

Chemical and Biological Aspects of Secondary Metabolites from Tongan Marine Sponges

by

Jacqueline Mary Elizabeth Kane Barber

Victoria

UNIVERSITY OF WELLINGTON

*Te Whare Wānanga
o te Ūpoko o te Ika a Māui*



A thesis
submitted to Victoria University of Wellington
in fulfilment of the
requirements for the degree of
Doctor of Philosophy
in Chemistry.

Victoria University of Wellington
2012

Abstract

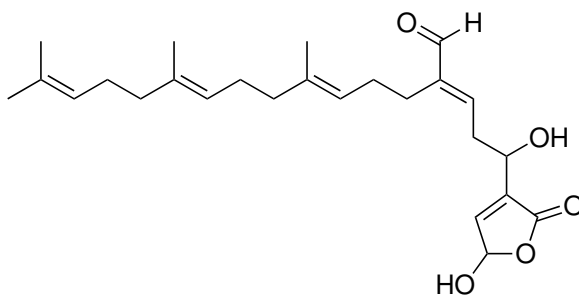
This thesis describes the isolation and structural elucidation of 17 new secondary metabolites from Tongan marine sponges including examples of alkaloids, polyketides and terpenoids. In the process of this work, 19 sponge specimens were subjected to preliminary NMR-guided investigation. Nine organisms were selected for further analysis on the basis of the structural novelty perceived within the HMBC spectrum of crude fractions generated by the first chromatographic purification of their crude extracts, and the apparent rarity of the specimen.

Investigation of two different demosponge specimens afforded the γ -hydroxybutenolide sesterterpenes (**23** and **24**), and small quantities of the potentially cytotoxic alkaloid 14-bromohomofascaplysin (**29**).

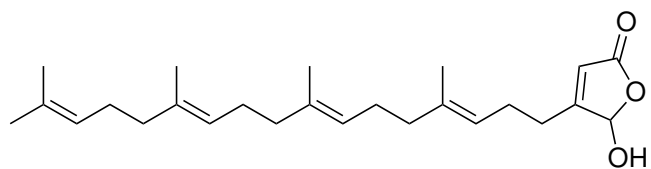
The analysis of two samples of a dictyoceratid sponge yielded the new labdane diterpenes luakuliides A–C (**33–36**), characterised by a bridging hemi-acetal function on the B-ring of the labdane bicycle. Luakuliide A (**33**) and its methyl acetal derivative **34** were found to display interesting immunomodulatory activity.

Seven new α -pyrone polyketides, lehualides E–K (**69–75**), were isolated from a *Plakortis* sp. Lehualides H–K (**72–75**) display a range of sulfur functionalities, the natures of which were determined by spectroscopic comparison with synthesised model compounds.

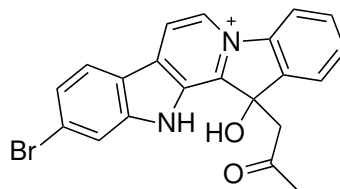
Another plakinid sponge specimen contained four new polyketides (**95–98**), all of which possess different cyclic peroxide moieties. Cyclic peroxides **95**, **97** and **98** displayed potent cytotoxicity against human promyelocytic leukemia cells (HL-60). Chemical genetic and phenotypic profiling studies of **95** were undertaken in *Saccharomyces cerevisiae* yeast using the homozygous diploid and heterozygous diploid deletion libraries. These studies indicate that **95** acts to disrupt Ca^{2+} homeostasis, leading to elevation of intracellular Ca^{2+} levels.



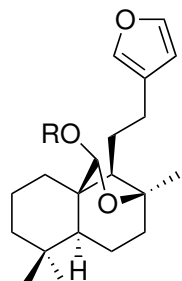
23



24

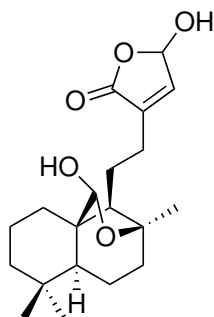


29

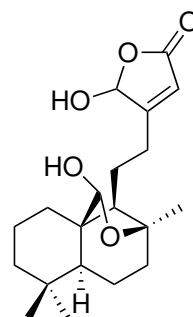


R = H 33

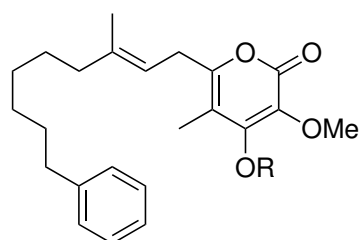
R = Me 34



35

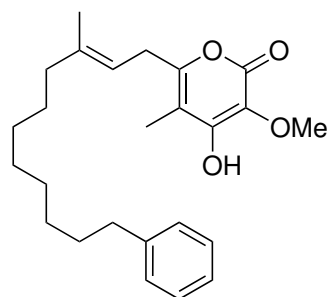


36

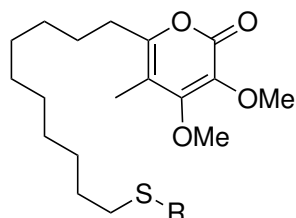


69 R = Me

70 R = H

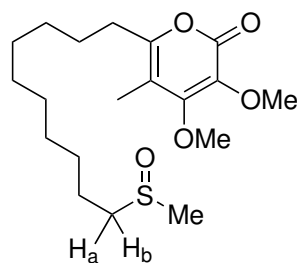


71

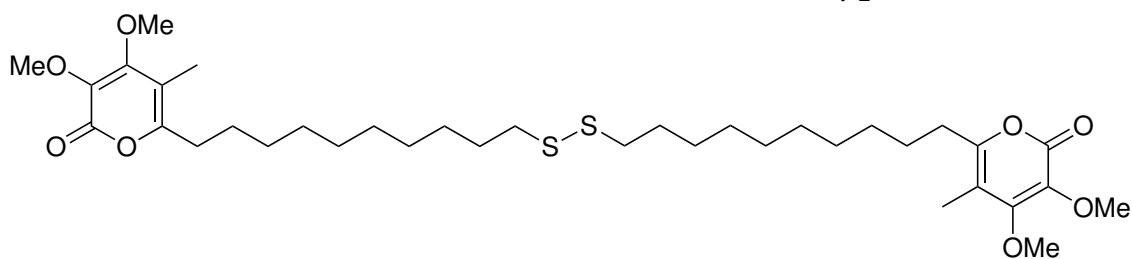


72 R = Ac

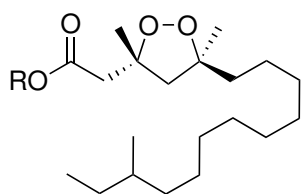
73 R = Me



74

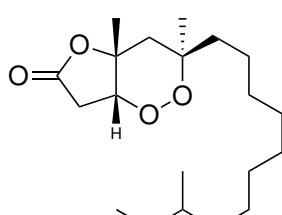


75

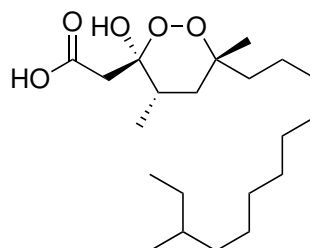


95 R = H

96 R = Me



97



98

Acknowledgments

Over the last three years I've been lucky enough to have tremendous support from family, friends and work-mates. Without your friendship and help I would not have been able to achieve this. Thank you very much.

My supervisor Peter, thank you for being such a fountain of knowledge and for your guidance throughout my studies. Your uncanny ability to solve the snarliest of problems and inspire me when even I was lacking in enthusiasm has more than made up for the difficulties I've encountered when trying to pin you down. To the Natural Products Groups and the occupants of LB212 and LB211 over the years; the Peter's Moore and Clark, Russel Hewitt and Nathaniel Dasyam. Particular thanks to Jono Singh, Helen Woolner, Rob Keyzers, Emma Aitken, and Taitusi Taufua for all the help and support you offered, and to John Ryan for all your help with NMR.

Everyone in the Chemical Genetics lab, thank you for all your help with my assays. I'm particularly grateful to David Bellows and Paul Atkinson for allowing me to work in your lab for so long, and to James Matthews for helping me with everything from assay design to proof-reading. Thank you also to Dora Leahy and Rosemary Heathcott for your technical guidance, and to Heather Best and Christina Roberts for help with writing and therapeutic hot chocolates in recent months. Ploi Yibmantasiri, I've loved finding someone who shares my enthusiasm for mid-afternoon cocktails.

Alec La Grow, Bryan O'Leary, Nick Monahan and Ash Dangerfield - we've had some good times over the years. Thank you for always believing in me and my abilities.

Ed Willis, Anne O'Driscoll, Graham Fairweather and Livvy Eaton - you all kept me sane at various points during my PhD, and were always there for a cup of tea (or coffee) and to go for a run. Patricia Stein and Shona de Sain, you helped me cope at the very end and for that I will be eternally grateful.

Mum, dad, James and Felix, thank you for always having been there to help me through whatever life has thrown at me over the years.

Paul, you helped me through everything in the last couple of months, thanks for cooking me dinner, drying my tears and making me laugh when I needed to. I will always cherish the time we've spent together.

For Florence,

*I know you would have been proud
and I miss you everyday.*

Contents

Abstract	iii
Acknowledgments	v
Dedication	vii
Table of Contents	ix
List of Figures	xv
List of Schemes	xxi
List of Tables	xxiii
Glossary	xxvii
1 Introduction	1
1.1 Natural products as therapeutic agents	1
1.2 Marine natural products	3
1.3 Sponges	5
1.3.1 Microbial symbiosis in marine sponges	7
1.4 The Tongan marine ecoregion	8
1.5 Organism selection and screening	10
1.5.1 Bioassay-guided isolation	10
1.5.2 Spectroscopy-guided isolation	11
1.5.3 Advances in NMR screening	12
1.6 Assigning biological applications	14
1.6.1 Chemical genetic profiling	15
1.6.2 Gene expression profiling	15

1.7	Research objectives	16
1.8	Summary	16
2	Organism Screening and Selection	19
2.1	Collection areas	19
2.2	Organism selection	19
2.3	The Vava'u group	20
2.3.1	PTN3_37F and PTN3_45E	22
2.3.2	PTN4_10B	24
2.4	'Eua Island	26
2.4.1	PTN3_19D	27
2.4.2	PTN3_20A	29
2.4.3	PTN3_20B	31
2.4.4	PTN3_21D	33
2.4.5	PTN3_21E and PTN3_50B	35
2.5	Concluding remarks	36
3	Luakuliides A–C	37
3.1	The order Dictyoceratida	37
3.2	Labdane diterpenoids from the dictyoceratid sponge “luakuli”	38
3.2.1	Isolation and identification of luakuliides A–C	38
3.2.2	Biological activity of the luakuliides	57
3.2.3	Labdane diterpenes	57
3.2.4	Biogenesis of luakuliides A–C	58
3.2.5	Concluding remarks	62
4	Chemical Analyses of Plakinid Sponges	63
4.1	The family Plakinidae	63

4.1.1	The <i>Plakortis</i> and <i>Plakinastrella</i> genera	64
4.2	α -Pyrone metabolites from <i>Plakortis</i> sp.	68
4.2.1	Isolation and identification of lehualides E–K	69
4.2.2	Bioactivity of the lehualides	92
4.2.3	Determination of sulfur functionalities	94
4.2.4	α - and γ -Pyrone metabolites from marine invertebrates	98
4.2.5	Biogenesis of the lehualides	101
4.2.6	Concluding remarks	104
4.3	Cyclic peroxides from a plakinid sponge	105
4.3.1	Isolation and identification of cyclic peroxides	105
4.3.2	Growth inhibition of eukaryotes	125
4.3.3	Organism classification	126
4.3.4	Cyclic peroxide natural products	126
4.3.5	Biogenesis of cyclic peroxides from plakinid sponges	130
4.3.6	Concluding remarks	136
5	Chemical Genetic Profiling of Marine Cyclic Peroxides	137
5.1	The biological effects of marine cyclic peroxides	137
5.2	Biological assessment in <i>S. cerevisiae</i>	138
5.3	Chemical genetic profiling in <i>S. cerevisiae</i>	139
5.3.1	Homozygous profiling	143
5.3.2	Haploinsufficiency profiling	143
5.4	Preliminary studies in <i>S. cerevisiae</i>	144
5.4.1	Phenotypic profiling of epiplakinic acid I and plakortolide X	146
5.5	Chemical genetic profile of epiplakinic acid I	149
5.5.1	Homozygous profiling of epiplakinic acid I	149
5.5.2	Haploinsufficiency profiling of epiplakinic acid I	151

5.5.3	Plakortide F acid	153
5.5.4	The Ca ²⁺ second messenger system	156
5.5.5	Epiplakinic acid I induces a Ca ²⁺ -related stress response . . .	156
5.5.6	Calcineurin signaling	158
5.5.7	Interactions between calcineurin signaling and TOR	160
5.6	Mechanistic insights from phenotypic and chemical genetic profiling .	162
5.6.1	Future directions	162
5.6.2	Concluding remarks	164
6	Concluding Remarks	165
7	General Experimental Procedures	167
7.1	Isolation of new diterpenes from PTN3_45E	168
7.1.1	Animal material	168
7.1.2	Extraction of PTN3_45E	168
7.2	Isolation of known terpenes from PTN4_10B	169
7.2.1	Animal material	169
7.2.2	Initial extraction of PTN4_10B	169
7.3	Isolation of 14-bromohomofascaplysin	170
7.3.1	Animal material	170
7.3.2	Extraction of PTN3_20B	170
7.3.3	Me ₂ CO-free extraction of PTN3_20B	170
7.4	Isolation of halenaquinone	171
7.4.1	Animal material	171
7.4.2	Extraction of PTN3_21D	171
7.5	Isolation of luakuliides A–C	171
7.5.1	Animal material	171
7.5.2	Screening extraction of PTN3_21E	172

7.5.3	Extraction of PTN3_50B	172
7.6	Isolation of lehuaalides E–K	174
7.6.1	Animal material	174
7.6.2	Initial extraction of <i>Plakortis</i> sp. PTN3_20A	174
7.6.3	Second extraction of <i>Plakortis</i> sp. PTN3_20A	175
7.6.4	Preparation of spectroscopic model compounds	176
7.7	Isolation of new cyclic peroxides	179
7.7.1	Animal material	179
7.7.2	Initial extraction of PTN3_19D	179
7.7.3	Second extraction of PTN3_19D	180
7.8	Biological evaluation of cyclic peroxides	182
7.8.1	Yeast strains	182
7.8.2	Preliminary assay protocols	182
7.8.3	Chemical genetic profiling of epiplakinic acid I	186
7.8.4	Imaging studies	191
7.8.5	Transformation of 8025- α strain	192
7.8.6	Attempted transformation of <i>zrt1</i> Δ / <i>zrt1</i> Δ and <i>cch1</i> Δ / <i>cch1</i> Δ strains	193
A	Sponge Screening and Cyclic Loading Protocol	195
A.1	Cyclic loading and backloading	195
A.2	Screening protocol	196
A.3	Cyclic loading	197
A.4	Processing and NMR analysis	198
A.5	Spicule analysis	200
B	Yeast Growth Media	201
C	NMR Data for Known Compounds	202

D ^1H NMR Spectra of Known Compounds	208
E NMR Spectra of Luakuliides A–C	217
F NMR Spectra of Lehualides E–K	248
G NMR Spectra of New Cyclic Peroxides	284
H Phenotypic Profile of Epiplakinic Acid I	305
I Chemical Genetic Profile of Epiplakinic Acid I	311
Bibliography	317

List of Figures

1.1	Taxonomic classification within the phylum Porifera.	6
1.2	The Kingdom of Tonga	9
1.3	A generic ^1H NMR spectrum.	12
1.4	A generic HMBC spectrum.	13
2.1	The Vava'u island group.	20
2.2	Surface photo of the sponge PTN3_45E	22
2.3	^1H NMR screen spectrum (CD_3OD) of PTN3_45E	23
2.4	HMBC screen spectrum (CD_3OD) of PTN3_45E	23
2.5	Surface photo of the sponge PTN4_10B	24
2.6	^1H NMR screen spectrum (CD_3OD) of PTN4_10B	25
2.7	HMBC screen spectrum (CD_3OD) of PTN4_10B	25
2.8	The Tongatapu island group.	26
2.9	Surface photo of the plakinid specimen PTN3_19D	27
2.10	^1H NMR screen spectrum (CD_3OD) of PTN3_19D	27
2.11	HMBC screen spectrum (CD_3OD) of PTN3_19D	28
2.12	Surface photo of the <i>Plakortis</i> specimen PTN3_20A	29
2.13	^1H NMR screen spectrum (CD_3OD) of PTN3_20A	30
2.14	HMBC screen spectrum (CD_3OD) of PTN3_20A	30
2.15	Surface photo of the sponge PTN3_20B	31
2.16	^1H NMR spectrum (CD_3OD) of PTN3_20B	32
2.17	HMBC experiment (CD_3OD) of PTN3_20B	32
2.18	Surface photo of the sponge PTN3_21D	33
2.19	^1H NMR spectrum (CD_3OD) of PTN3_21D	34
2.20	HMBC experiment (CD_3OD) of PTN3_21D	34

2.21	Vava'u collection of the dictyoceratid sponge "luakuli"	35
2.22	¹ H spectrum (CD ₃ OD) of PTN3_21E	35
2.23	HMBC experiment (CD ₃ OD) of PTN3_50B	36
3.1	Taxonomic classification of the order Dictyoceratida.	37
3.2	Correlations evidencing substructures in the screen HMBC spectrum of PTN3_21E	39
3.3	Purification strategy employed in the isolation of luakuliides A–C . . .	40
3.4	The furan system of luakuliide A	42
3.5	NMR correlations establishing the C-9 to C-12, C-5 to C-7 and C- 1 to C-3 alkyl segments in luakuliide A	42
3.6	The <i>gem</i> -dimethyl substructure of luakuliide A	43
3.7	COSY and HMBC correlations establishing the C-7 to C-9 connec- tions in luakuliide A	43
3.8	Establishment of the cyclodecane system of luakuliide A	44
3.9	COSY and HMBC correlations establishing the CH-20 hemi-acetal bridge in luakuliide A	45
3.10	The <i>trans</i> -fused [4.4.0]-bicyclodecane system of luakuliide A	45
3.11	Determination of relative stereochemistry in luakuliide A	46
3.12	NMR correlations establishing the C-9 to C-12, C-5 to C-7 and C- 1 to C-3 alkyl segments in luakuliide B	49
3.13	HMBC correlations establishing the connections from C-1 to C-5 in luakuliide B	50
3.14	COSY and HMBC correlations completing the cyclodecane system of luakuliide B	50
3.15	The [4.4.0]-bicyclodecane system and bridging hemi-acetal moiety of luakuliide B	51
3.16	The α -substituted α,β -unsaturated ester and γ - hemi-acetal methine in luakuliide B	52
3.17	The α -substituted γ -hydroxybutenolide moiety of luakuliide B	52
3.18	The β -substituted- γ -hydroxybutenolide moiety of luakuliide C	54

4.1	Taxonomic classification of the order Homoscleophorida.	63
4.2	Depiction of the PKS1 propagation units used in the biosynthesis of plakortether B	65
4.3	Diod spicules recovered from the <i>Plakortis</i> sponge PTN3_20A	69
4.4	Correlations evidencing substructures in the screen HMBC spectrum of PTN3_20A	70
4.5	Purification strategy employed in the isolation of lehualides E–K.	71
4.6	The mono alkyl-substituted benzene ring of lehualide E	72
4.7	COSY, HMBC and 1D NOE correlations confirming the C-7 to C-11 segment in lehualide E	73
4.8	COSY and HMBC correlations establishing the C-5 to C-8 connections in lehualide E	73
4.9	HMBC and 1D NOE correlations establishing the C-3 to C-6 tetra-substituted diene in lehualide E	74
4.10	1D TOCSY correlations confirming the linear connectivity in lehualide E	75
4.11	¹ H NMR spectral comparison between of lehualides E and F	77
4.12	COSY and selected HMBC correlations establishing the C-17 to C-23 segment of lehualide F	78
4.13	COSY and HMBC correlations confirming the C-5 to C-6 and C-8 to C-9 alkenes in lehualide F	78
4.14	HMBC and 1D NOE correlations establishing the C-4–C-5 bond and methoxy substitution of C-3 in lehualide F	79
4.15	The α -pyrone system present in lehualide F	79
4.16	¹ H NMR spectral comparison of lehualides F and G	81
4.17	1D TOCSY and bsHSQC-TOCSY correlations used to elucidate the aliphatic chain of lehualide G	82
4.18	The dimethoxy-substituted α -pyrone segment of lehualide H	84
4.19	The thioacetate moiety of lehualide H	85
4.20	Positive-ion mode HRESIMS spectra of lehualides I and J	87
4.21	The methyl sulfide function of lehualide I	88

4.22	¹ H NMR spectral study of lehualide I	89
4.23	The sulfoxide centre of lehualide J.	89
4.24	¹ H NMR spectral comparison of lehualide H and octanethioacetate.	95
4.25	¹ H NMR spectral comparison of lehualide I and methyloctylsulfide.	95
4.26	¹ H NMR spectral comparison of lehualide J and methyloctylsulfoxide.	95
4.27	A diod spicule recovered from the plakinid sponge PTN3_19D	105
4.28	Correlations evidencing substructures in the screen HMBC spectrum of PTN3_19D	106
4.29	Overall purification strategy employed during isolation of the cyclic peroxide metabolites	108
4.30	COSY and HMBC correlations establishing the C-1 to C-4 linkages of epiplakinic acid I	109
4.31	HMBC correlations establishing the C-3 to C-6, and C-19 linkages epiplakinic acid I	110
4.32	COSY and HMBC correlations establishing the C-14 to C-17 segment of epiplakinic acid I	110
4.33	1D TOCSY correlations establishing the C ₉ methylene chain of epiplakinic acid I	111
4.34	1D NOE correlations proving relative stereochemistry of the 1,2-dioxolane nucleus of epiplakinic acid I	111
4.35	The C-21 methyl ester moiety of epiplakinic acid I methyl ester.	113
4.36	COSY and HMBC correlations establishing the C-1 to C-5 connections within plakortolide X	115
4.37	COSY and HMBC correlations confirming the C-3 to C-5 connections in plakortolide X	116
4.38	HMBC correlations establishing the C-5 to C-7 linkages in plakortolide X	116
4.39	1D TOCSY correlations confirming linear connectivity in plakortolide X	117
4.40	Stereochemistry about the bicyclic nucleus of plakortolide X	117
4.41	COSY and selected HMBC correlations evidencing the C-3 to C-5 connections in the 1-hydroxy-1,2-dioxane metabolite	120

4.42	The C-1 to C-4 and C-5 to C-7 connections in the 1-hydroxy-1,2-dioxane metabolite	121
4.43	The completed linear structure of the 1-hydroxy-1,2-dioxane metabolite	121
4.44	1D NOE correlations evidencing relative configuration in the 1-hydroxy-1,2-dioxane metabolite	122
4.45	MTT-assays for cyclic peroxides against the HL-60 cell line	125
5.1	Open reading frame deletion within the <i>S. cerevisiae</i> YKO strains . .	140
5.2	Chemical genetic profiling revealing the importance of a deleted gene to strain fitness under assay conditions	142
5.3	Synthetic genetic interactions uncovered by the homozygous profiling assay	143
5.4	Depiction of drug-induced haploinsufficiency	144
5.5	The kinetics of epiplakinic acid I inhibiting growth of <i>S. cerevisiae</i> cells	145
5.6	Epiplakinic acid I, plakortolide X and CaCl ₂ cause a similar decrease in cell size in <i>S. cerevisiae</i> strains	146
5.7	Cell cycle of <i>S. cerevisiae</i>	148
5.8	Bud index of <i>S. cerevisiae</i> cells when treated with epiplakinic acid I and plakortolide X.	148
5.9	Depiction of the ion-channel and ATP-pump system for Ca ²⁺ homeostasis in <i>S. cerevisiae</i>	154
5.10	Translocation studies in the Crz1p-GFP strain	157
5.11	Qualitative staining of WT cells with Calcium Orange dye	158
5.12	Flow cytometry imaging ROS formation with DCF-DA and PI	159
5.13	Calcineurin signaling pathway in <i>S. cerevisiae</i>	160
5.14	Antagonistic interactions between the calcineurin and TORC2 signaling pathways	161
A.1	A depiction of the cyclic loading process.	196
H.1	Dose-response curves for epiplakinic acid I and plakortolide X against WT and Δpdr yeast strains	305
H.2	Activity of epiplakinic acid I and plakortolide X is enhanced in the presence of high Ca ²⁺	306

H.3	Dose-response curves for epiplakinic acid I and plakortolide X in the presence of EGTA	307
H.4	Epiplakinic acid I causes an increase in S-phase population in <i>S. cerevisiae</i> cells.	307
H.5	Epiplakinic acid I affects a decrease in cell size in <i>S. cerevisiae</i>	308
H.6	Hypersensitivity of cytoskeletal mutants to epiplakinic acid I	308
H.7	Dose-response curves for epiplakinic acid I against Ca ²⁺ -responsive deletions strains	309
H.8	Translocation studies in the Zrt1p-GFP strain	310

List of Schemes

3.1	Formation of the labdane, halimane and clerodane skeletons	60
3.2	Proposed generation of the hemi-acetal functions, furan and γ -hydroxybutenolide moieties of luakuliides A–C	61
4.1	Conversion of plakortolides to plakortones via <i>seco</i> -plakortolides.	66
4.2	Synthesis of the spectroscopic model compounds of lehualides H–J.	94
4.3	Mechanism for α -pyrone degradation as proposed by Kong <i>et al.</i>	101
4.4	Formation of coenzyme M from L-cysteine and sulfoactaldehyde.	102
4.5	Proposed biogenesis for lehualides H–K	103
4.6	Biosynthesis of cyclic peroxides via Diels-Alder cycloaddition of molecular oxygen	130
4.7	Proposed biosynthesis of 1,2-dioxolane cyclic peroxides	132
4.8	Proposed biosynthesis of 1,2-dioxane cyclic peroxides	133
4.9	Proposed biosynthesis of the plakortolide bicycle by intramolecular cyclisation	134
4.10	Proposed biosynthesis of the 1-hydroxy-1,2-dioxane metabolite	135

List of Tables

2.1	Sponge Specimens Analysed During This Study.	21
3.1	NMR Spectroscopic Data for the Acetal Moieties of Luakuliide A and Luakuliide A Methyl Acetal	46
3.2	NMR Spectroscopic Data of Luakuliide A	47
3.3	NMR Spectroscopic Data of Luakuliide A Methyl Acetal	48
3.4	NMR Spectroscopic Data of Luakuliide B	53
3.5	NMR Spectroscopic Data of γ -Hydroxybutenolide Moieties	55
3.6	NMR Spectroscopic Data of Luakuliide C	56
4.1	NMR Spectroscopic Data of Lehualide E	76
4.2	NMR Spectroscopic Data of Lehualide F	80
4.3	NMR Spectroscopic Data of Lehualide G	83
4.4	NMR Spectroscopic Data of Lehualide H	86
4.5	NMR Spectroscopic Data of Lehualide I	90
4.6	NMR Spectroscopic Data of Lehualide J	91
4.7	Inhibition of HL-60 Cells by Lehualides F–I	92
4.8	NMR Spectroscopic Data of Lehualide K	93
4.9	Chemical Shift Analysis of the Sulfur Moieties in Lehualides H–J	97
4.10	NMR Spectroscopic Data of Epiplakinic Acid I	112
4.11	NMR Spectroscopic Data of Epiplakinic Acid I Methyl Ester	114
4.12	Comparison of Salient NMR Chemical Shifts in Plakortolides T and X	118
4.13	NMR Spectroscopic Data of Plakortolide X	119
4.14	Comparison of Salient NMR Chemical Shifts of 1-hydroxy-1,2-dioxane Metabolites	123
4.15	NMR Spectroscopic Data of the 1-Hydroxy-1,2-Dioxane Metabolite	124
5.1	Synergistic Inhibitory Effects of Cyclic Peroxides and CaCl_2	146

5.2	Decrease in Cell Size Caused by Cyclic Peroxides and CaCl ₂	147
5.3	Effects of Epiplakinic Acid I on the <i>S. cerevisiae</i> Cell Cycle	148
5.4	Functional Categories of Deletion Strains Sensitive to Epiplakinic Acid I	150
5.5	Growth Inhibitory Effects of Epiplakinic Acid I on Cytoskeletal Deletion Mutant Strains	151
5.6	Functional Categories of Deletion Strains Haploinsufficient to Epiplakinic Acid I	152
5.7	Functional Categories of Genes Differentially Regulated in the Presence of Plakortide F Acid	153
5.8	Growth Inhibitory Effects of Epiplakinic Acid I on Ca ²⁺ -Responsive Deletion Strains	155
5.9	Growth Inhibitory Effects of Epiplakinic Acid I on Ca ²⁺ -Pump and Channel Deletion Strains	155
5.10	Proposed Ion Pump Deletion-GFP Strains	163
7.1	Yeast Strains Used During this Study	183
7.2	PCR Master Mix	188
C.1	NMR Spectroscopic Data of <i>iso</i> -Secothorectolide	202
C.2	NMR Spectroscopic Data of 1-Hydroxyluffarin Q	203
C.3	NMR Spectroscopic Data of Ambliol B	203
C.4	NMR Spectroscopic Data of Luffariellolide	204
C.5	NMR Spectroscopic Data of 5 α ,8 α -Epidioxysterol 27	205
C.6	NMR Spectroscopic Data of 5 α ,8 α -Epidioxysterol 28	206
C.7	NMR Spectroscopic Data of 14-Bromohomofascaplysin	207
C.8	NMR Spectroscopic Data of Halenaquinone	207
I.1	Homozygous Profile of Epiplakinic Acid I	311
I.2	Haploinsufficiency Profile of Epiplakinic Acid I	312
I.3	Haploinsufficiency Profile of Epiplakinic Acid I Continued	313

I.4	Functional Categories of Deletion Strains Resistant to Epiplakinic Acid I	314
I.5	Functional Categories of Heterozygous Deletion Strains Resistant to Epiplakinic Acid I	315

Glossary

Ac	Acetyl
br	Broad
C₁₈	Octadecyl derivatised silica gel
COSY	Correlation spectroscopy (¹ H to ¹ H correlations depicted by \rightarrow and \leftarrow)
d	Doublet
Δ	Indicates deletion of the preceding gene
Δ<i>pdr</i>	Drug-sensitised yeast strain
δ	Chemical shift (ppm)
DAD	Diode array detector
DCF-DA	Dichlorofluorescein diacetate
<i>d</i>₆-DMSO	Deuterated DMSO
DIOL	2,3-Dihydroxy-1-propoxypropyl-derivatized silica gel
DMSO	Dimethyl sulfoxide
EGTA	Ethylene glycol tetraacetic acid
Et	Ethyl
EU	European Union
FACS	Fluorescence-activated cell sorting
FDA	United States Food and Drug Administration
GC	Gas chromatography
GFP	Green fluorescent protein
HIP	Haploinsufficiency profiling
HL-60	Human promyelocytic leukemia cell line
HMBC	Heteronuclear multiple-bond correlation (¹ H to ¹³ C correlations depicted by \rightarrow)
HOP	Homozygous profiling
HPLC	High pressure (performance) liquid chromatography
HP20/HP20SS	PSDVB stationary support
HRESIMS	High resolution electrospray ionization mass spectrometry
HSQC	Heteronuclear single-quantum correlation
HTS	High-throughput screening
IC₅₀	Dose that is inhibitory to 50% of test subjects
ICP-MS	Inductively coupled plasma mass spectrometry
IPA	Isopropyl alcohol (2-propanol)
<i>J</i>	Scalar coupling constant
LB	Lysogeny broth, bacterial growth media
LH-20	Crosslinked dextran-based size exclusion resin
m	Multiplet (NMR coupling pattern)
<i>m/z</i>	Mass to charge ratio

MALDI-TOF	Matrix-assisted laser desorption/ionisation time of flight
MDR	Multiple drug resistance
Me	Methyl
MIC	Minimum inhibitory concentration
mult.	Multiplicity
MS	Mass spectrometry
MTT assay	Colorimetric cytotoxicity assay using 3-(4,5-dimethyl-thiazol-2-yl)-2,5-diphenyltetrazolium bromide
NMR	Nuclear magnetic resonance
NOE	Nuclear Overhauser effect (^1H to ^1H enhancements depicted by $\xrightarrow{\hspace{1cm}}$)
NOESY	Nuclear Overhauser enhancement spectroscopy
PCR	Polymerase chain reaction
PDR	Pleiotropic drug resistance
Pet. ether	Petroleum ether (hexanes)
PI	Propidium iodide
pos.	Position
ppm	Parts per million
PSDVB	Poly(styrene-divinylbenzene)
q	Quartet
quin	Quintet
RFP	Red fluorescent protein
s	Singlet (NMR coupling pattern)
SAM	<i>S</i> -adenosylmethionine
SC	Synthetic complete yeast growth media
SD	Synthetic deficient yeast growth media
SEM	Scanning electron microscope
sept	Septet
SCUBA	Self contained underwater breathing apparatus
t	Triplet
TLC	Thin layer chromatography
TOCSY	Total correlation spectroscopy (^1H to ^1H correlations depicted by $\xrightarrow{\hspace{1cm}}$ and $\xleftarrow{\hspace{1cm}}$)
VUW	Victoria University of Wellington
WT	Wild type yeast
YPD	Yeast extract peptone dextrose, complete medium for yeast growth

Chapter 1

Introduction

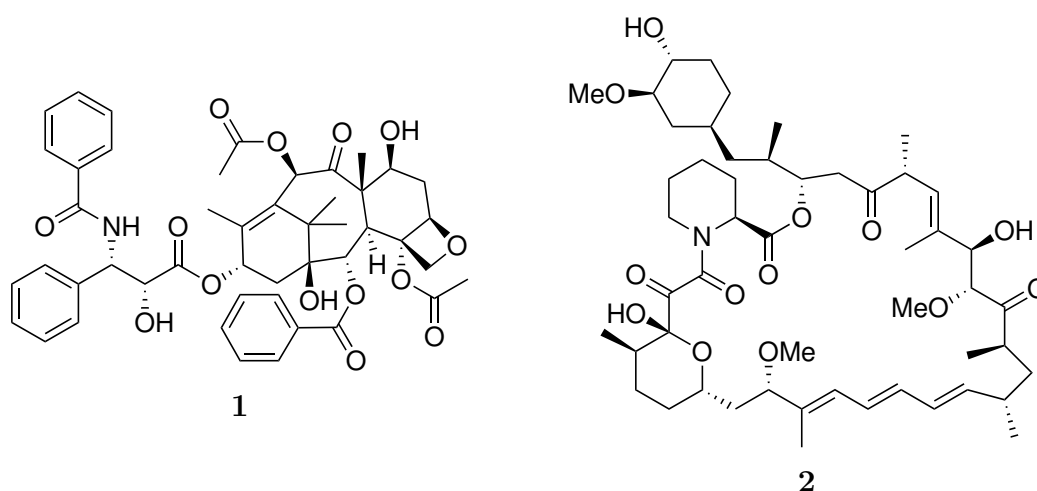
1.1 Natural products as therapeutic agents

For millennia human societies have relied upon nature for their fundamental needs, and for medicines in particular.¹ Egyptian documentation of this relationship dates back to 4000 BC,¹ however, the treatment of human disease is still a pressing and costly concern. Care and support of cancer patients alone in the US totaled more than 124 billion USD in 2010.² As the leading cause of death in New Zealand, cancers account for 29.4% of all deaths at an estimated cost of 511 million NZD per year.³ As such, the development of new therapeutic agents is beneficial to society, if only to lessen these financial burdens.

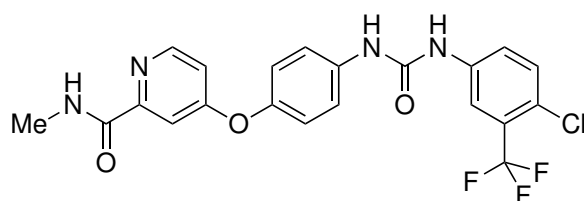
Naturally-derived compounds continue to play an integral role in the treatment of human disease, and the pharmaceutical landscape is heavily populated by non-synthetic compounds.⁴ Over the past 30 years roughly 60% of the introduced small molecule pharmaceutical leads have been natural products, derivatives thereof, or synthetic mimics of natural product pharmacophores.⁴⁻⁷ One such entity is the microtubule stabiliser paclitaxel (**1**, TAXOL[®], Bristol-Myers Squibb). Isolated from the Pacific yew tree, *Taxus brevifolia* in 1967, paclitaxel has been marketed from the early 1990s and is estimated to have extended the lives of several hundred thousands of lung, ovarian and breast cancer patients.⁸ Annual sales of TAXOL[®] peaked at 1.6 billion USD in 2000.⁹ Another significant example is the immunosuppressive macrolide rapamycin (**2**, Rapamune[®], Wyeth). First developed as an antifungal agent, rapamycin has been used widely since 1999 for the prevention of organ transplant rejection.⁴ In 2011 a total of 94,493 life-saving organ transplants were carried out in the US alone, with each patient then requiring immunosuppressive treatment for an average cost of more than 24,000 USD per annum.¹⁰

These two structurally different and important therapeutic agents are both products of a living organism's secondary metabolism. Secondary metabolites are non-essential to the immediate survival of an organism as they are not involved in

normal growth, development or reproduction.¹¹ Significant biochemical input is required during their synthesis, justified by the physiological advantages they confer upon the producing organism.¹² Organisms devoid of formal cellular immune systems and/or adequate forms of physical protection are thought to rely upon secondary metabolites to deliver an alternative chemical defence system against assault.¹³ Consequentially, a chemical arsenal of metabolites have been isolated from such organisms and display activities including antifungal, antimicrobial, and cytotoxicity.¹⁴ While these metabolites may not have co-evolved with human receptors they have been evolved to interact with biomolecules in general.⁶ It is this innate and varied biological activity that has made secondary metabolites and their derivatives integral to the development of medicinal chemistry to the point where they are estimated to have more than doubled the average life-span of human beings in the 20th century alone.¹⁵



In response to growing demand for new therapeutic agents, the 1990s saw the advent of high-throughput screening (HTS) methods and combinatorial chemistry techniques. These new HTS techniques made screening entire compound libraries faster than it was to isolate and characterise a single natural product. However, the use of molecular scaffolds and combinatorial techniques has resulted in libraries of topographically similar molecules,¹⁶ many of which have not demonstrated biological characteristics appropriate for clinical trials. Sorafenib (**3**, Nexavar, Bayer) is the only compound developed by these methods to have gained FDA approval,^{4,17} marketed since 2005 for the treatment of renal carcinomas.



3

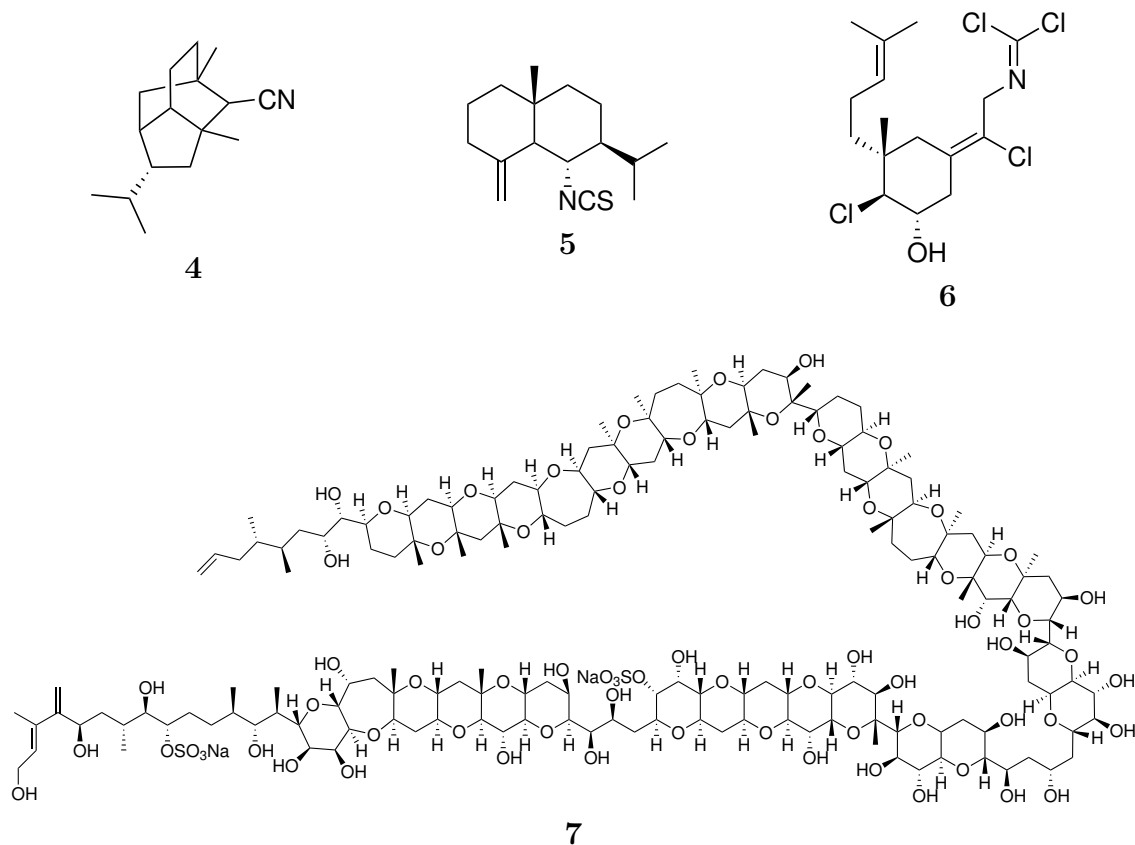
2

Structural trends have been observed between artificially designed and naturally occurring molecules, and although subtle, these differences between the compound classes appear to induce drastic differences in target specificity and biological potency.^{5,18,19} Compounds of natural derivation generally exhibit a greater number of chiral centres, and corresponding steric complexity. Oxygen-based functions predominate those of nitrogen, sulfur and the halogens, providing a high number of hydrogen-bond donors. There is also a trend towards greater aromaticity within the structures.²⁰⁻²³ As many of these aspects are readily incorporated into synthetic strategies, synthetic chemistry will maintain an integral role in pharmaceutical development. Although, our improving understanding of the genetic basis to the production of some natural products may offer new possibilities for large-scale production of such compounds in the future. It is clear, however, that the unmatched structural diversity and complexity evident within natural products will continue to inspire synthetic chemists in years to come. Natural products chemistry will remain essential to drug discovery,^{18,24} in the continued search for new and unexplored areas of chemical space.^{25,26}

1.2 Marine natural products

Oceans encompass 70% of the Earth's surface,²⁷ forming a myriad of ecosystems that are home to an estimated 90% of all species.²⁷ Of the 38 identified animal phyla, 26 are exclusively aquatic and 19 of these are exclusively marine. In comparison, Onchyophoria (the velvet worms) is the only living, solely terrestrial phylum. It is therefore unsurprising that environments such as coral reefs and the deep sea floor are estimated to house a greater diversity of flora and fauna than tropical rainforests,¹⁴ and are believed to contain a similar degree of chemical diversity.

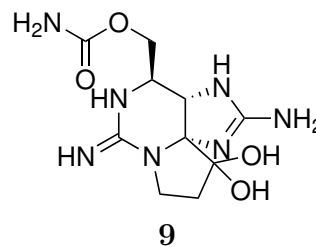
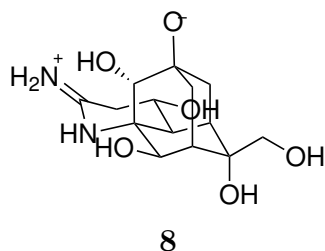
As of 2011 more than 24,000 novel marine natural products have been reported,²⁸ displaying a diverse array of structures and chemical functionality.²⁴ Owing to the availability of chlorine and bromine in seawater, halogen atoms are frequently observed in marine metabolites, in comparison to their terrestrial counterparts.²⁴ Cyanate (**4**), isothiocyanate (**5**) functions have appeared primarily in the marine environment, while the dichloro-imine function of compound **6** has only been observed in sponge metabolites.²⁴ Structural singularity in marine natural products also extends to carbon skeletons. The ladder-like cyclic polyether structure is characteristic of the marine toxins, exemplified by maitotoxin (**7**), the largest non-proteinaceous toxin known.²⁹



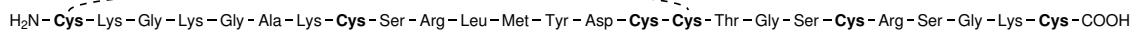
Many of the organisms investigated from the marine environment are sessile invertebrates, most of which lack both physical defences and formal cellular immune systems and require potent and diverse chemical defences.¹³ Owing to the intrinsic dilution factor of the marine environment, compounds for chemical defence must be highly potent to elicit an effect upon release into the surroundings.⁴

The isolation of potent toxins, particularly those known to humans, initially dominated the natural products field. Tetrodotoxin (**8**) was widely utilised in Voodoo practices in the creation of the 'living-dead'.³⁰ The neurotoxin acts by binding to site 1 of the fast voltage-gated Na⁺ channels found in most forms of muscle tissue detrimentally affecting muscle contraction and silencing neural activity.³¹ Tetrodotoxin (**8**) is produced by the bacteria *Vibrio alginolyticus*, which is harboured by *Taricha* sp. newts, *Atelopus* sp. toads, and the blue-ringed octopus *Hapalochlaena* sp.³² Occurrence of the bacteria within species of puffer fish led to the infamy of **8** as a source of lethal food poisoning.^{31,32}

The release of toxic chemical entities by sponges and other marine organisms is not solely restricted to defence. Pheromones are released for communication between organisms of many species, for instance quorum sensing by dinoflagellates preceding algal blooms.³³ Another dinoflagellate isolate, saxitoxin (**9**), has gained notoriety as the source of human paralytic shellfish poisoning (PSP) in tainted shellfish. The molecule shares the tetrodotoxin binding site, and has also been isolated from some species of puffer fish.³⁴



Investigation of marine cone snails of the genus *Conus* from the west and south-western Pacific eventually led to development of ziconotide (**10**, Prialt[®], Neurex/Elan), the first true marine natural product to gain FDA approval.³⁵ The fish-hunting cone snails spear their prey with harpoon-like hollow teeth filled with incapacitating venom. The peptidic toxins are highly potent and selective, acting as both agonists and antagonists of the ligand- and voltage-gated ion channels, and G-protein-coupled-receptors.³⁶ Intrathecal delivery of the synthetic ω -conotoxin **10** was approved by the FDA and EU in 2004 and 2005 respectively.³⁵ As the most potent non-opioid analgesic, the development of ziconotide has been a particularly important success in the marine natural products field.



10

1.3 Sponges

Sponges (phylum Porifera), are the oldest metazoans (multicellular organisms)³⁷ and have been in wide-spread existence since the pre-Cambrian era, ca. 560 million years ago.³⁸ Taxonomy within the Porifera phylum is uncertain, with reclassifications frequently taking place even at class level. Environmental factors exert a dramatic influence over physical characteristics of sponges such as size, colour and shape, preventing the use of macro-morphological and -physical characteristics as tools in sponge description.³⁸ Instead, skeletal networks form the basis of classification, dividing phylum Porifera into three classes. The class Demospongiae encompasses 80–90% of all sponge species, and the organisms contain siliceous and/or spongian fibres. Calcarea sponges exhibit calcite CaCO₃ spicules, while Hexactinellida sponges have a siliceous spicule network that comprises most of the mass of the organism (see Figure 1.1).

Sponges are devoid of features commonly found in other animals including developed circulatory, digestive, nervous and muscular systems.³⁸ In combination with a low level of cellular organisation and vegetative appearance, these absences prevented the classification of the phylum into Animalia until the 18th century.³⁸ These

sessile filter feeders are also devoid of a formal cellular immune system, and rely upon their secretion of toxic secondary metabolites to ward off unwanted bacterial, fungal, and parasitic infections.^{13,37} These metabolites also offer protection against encroachment,¹³ and surface encrustation resulting in the disruption of their water-pumping systems.³⁸ Perhaps unsurprisingly, sponges are the source of over 30% of the marine natural products isolated over the last few decades.^{28,39,40}

Kingdom Animalia

Phylum Porifera

Class Calcarea (calcareous sponges)

Order Clathrinida

Order Murrayonida

Order Leucosolenida

Order Lithonida

Order Baerida

Class Hexactinellida (glass sponges)

Order Amphodiscosida

Order Hexactinosida

Order Aulocalycoida

Order Lychnicosida

Order Lyssacinosida

Class Demospongiae (spongin fibres)

Order Homosclerophida

Order Spirophorida

Order Astrophorida

Order Hadromerida

Order Chondrosida

Order Poecilosclerida

Order Halichondrida

Order Agelasida

Order Haplosclerida

Order Dictyoceratida

Order Dendroceratida

Order Halisarcida

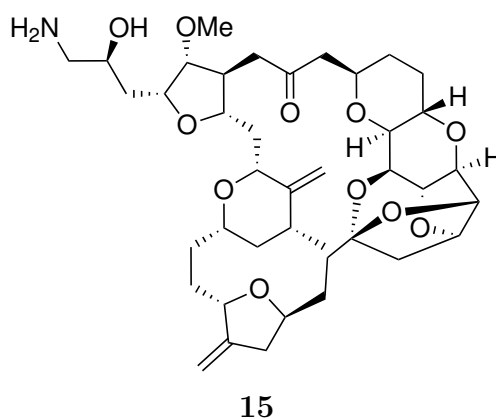
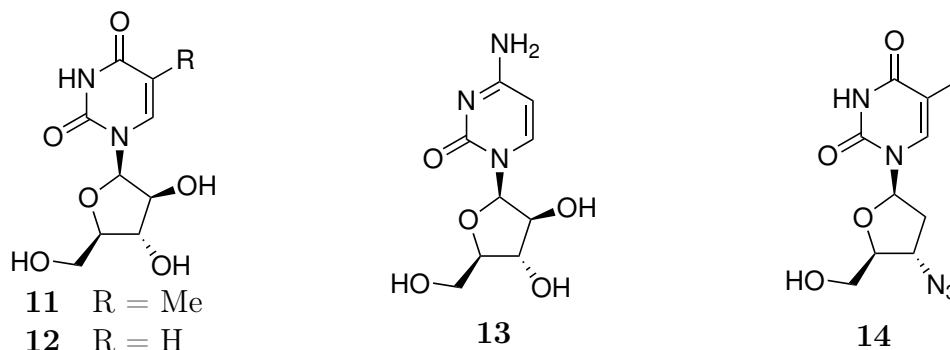
Order Verongida

Order Verticillitida

Figure 1.1 Taxonomic classification within the phylum Porifera to order level, after Hooper and van Soest.³⁸

An early foray into the metabolite profile of the sponge *Cryptotethia crypta* by Bergmann, Feeney and Burke yielded the unusual arabinosyl nucleosides spongothymidine (**11**) and spongouridine (**12**).^{41–43} Subsequent development of synthetic analogues generated the anticancer agent Ara-C (**13**) and the antiviral agent azidothymidine or AZT (**14**, Retrovir[®], Glaxo-SmithKline).^{44,45} AZT provided a major break-through in the AIDS therapy in 1990s, helping to dispel the notion that HIV/AIDS was a death sentence,⁴⁵ and is still in use today. Recent efforts have seen a synthetic reproduction of the pharmacophore of the macrocyclic-

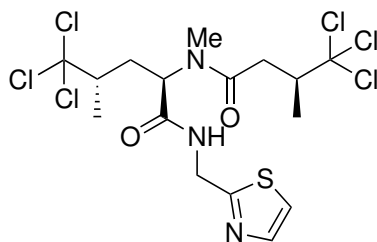
polyether halichondrin B, isolated from *Halichondria okadai*, gained FDA approval in November 2010. The microtubule-targeting qualities of halichondrin B were recognised shortly after its reported isolation in 1986, and administration of the derivative Halaven (**15**, Eisai Co.) for the treatment of non-small cell lung cancers, prostate cancer, sarcoma and breast cancers was approved 24 years later.^{46,47}



1.3.1 Microbial symbiosis in marine sponges

Many sponges are known to host an array of microbial symbionts, which can account for up to 60% of the living tissue in some sponges.^{48,49} The true extent of microbial contribution to the secondary metabolite profile of sponges is not known, primarily due the difficulties associated with ex-host culturing of many of these microbial symbionts.^{24,49} Microbial origins are often inferred when isolates from a single organism display unusual structural diversity, or conversely, metabolites classes are isolated from several unrelated sponges. Structural motifs typical of bacterial metabolism are also indicative of microbial origin, such as the polyketide cyclic peroxides frequently encountered in Indo-Pacific *Plakortis* and *Plakinastrella* sponges. Cellular localisation of many typical *Plakortis simplex* metabolites in cells of the *Sphingomonas* strain PS193 has been demonstrated, although polyketide cyclic peroxides were not among these.⁵⁰ Physical separation of sponge cells from their associated symbiotic cyanobacteria has also been successful. Such work has indicated cyanobacterial origins (*Oscillatoria spongelia*) for 13-dimethylisodysodenin

(**16**), which was previously classified as a metabolite of the sponge *Dysidea herbacea*.⁵¹



16

Investigations of *Svenzea*,⁵² *Mycale*,⁵³ *Myxilla* and *Haliclona* sponges⁵⁴ by Lee *et al.* have shown that up to 75% of sponge-associated bacteria are vertically transferred during embryogenesis, as opposed to horizontal transfer from the environment.⁵² This demonstrates a species-specific relationships between sponges and their bacterial communities.⁵⁴

1.4 The Tongan marine ecoregion

While the VUW marine natural products program has traditionally investigated organisms from New Zealand, the past few years have seen frequent recollection of the same organisms and the isolation of similar metabolites. Therefore in this study new collection areas were selected to provide new organisms for investigation. The Kingdom of Tonga was chosen as such a site (Figure 1.2).

The Tongan archipelago is located in the south-west Pacific Ocean, bordered to the west by the Fijian islands, and to the north by the Samoan territories. The Territorial Sea with and Exclusive Economic Zone of the kingdom comprises of 660,000 km² encompassing 171 islands, 52 of them inhabited,⁵⁶ which are divided into three main groups – Vava’u, Ha’apai and Tongatapu. The subtropical Tongan marine environment offers a range of habitats, which coupled with geographical isolation intrinsic to the island nation and a number of major ocean currents in the region create diverse marine communities.

Although Tonga is home to an abundance of marine life, there have been very few reports of secondary metabolites isolated from Tongan marine organisms. The last compound reported from Tongan waters was in 2001, although a number of polyketide and terpenoid structures were reported during the 1980s.^{57,58} However, environmental similarity across the Indo-Pacific region should allow parallels to be drawn with metabolites isolated from organisms collected in the neighbouring Fijian islands, while the change in geographical location may induce subtle chemical

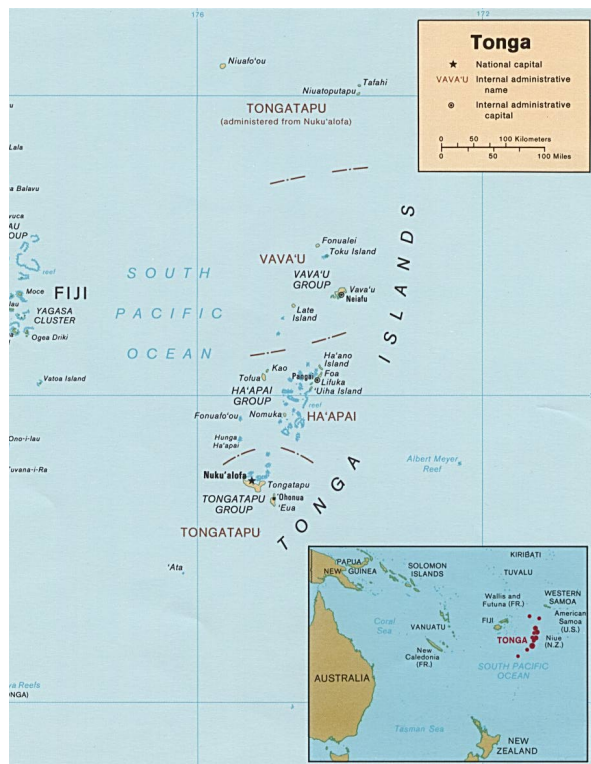
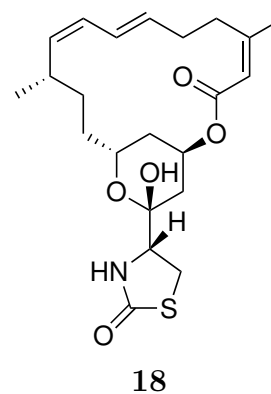
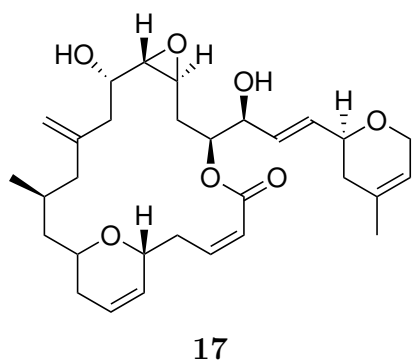
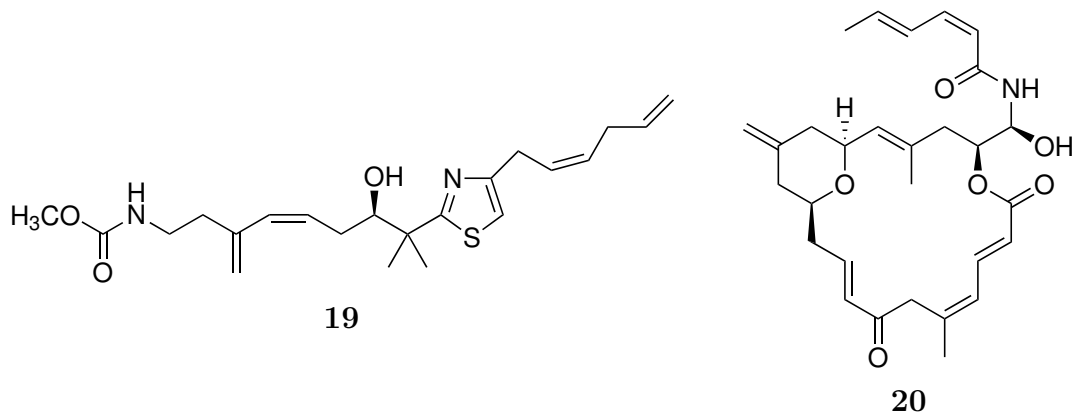


Figure 1.2 The Kingdom of Tonga.⁵⁵

differences. Chemical analysis of a Fijian *Cacospongia mycofijiensis* specimen during the 1980s yielded the macrolides laulimalide (**17**), latrunculin A (**18**) and mycothiazole (**19**).^{57–59} The hypothesis of chemical similarity across the Indo-Pacific region was proven by analysis of an ‘Euan *C. mycofijiensis* specimen within this laboratory, which afforded both **19**, **18**, and isomers of **17**. However, the ‘Euan specimen was also found to contain small quantities of zampanolide (**20**),⁶⁰ which had not been reported since its initial isolation in 1996.⁶¹ The potent microtubule stabilising activity of **20** was subsequently uncovered by Field *et al.*⁶²





1.5 Organism selection and screening

There are several approaches to the selection of organisms to screen. Organisms with ethnopharmacological* history are frequently investigated as probable sources of potentially bioactive compounds, albeit without structural novelty. Taxonomy is also considered; organisms closely related to species proven to produce unique and bioactive molecules are frequently collected.⁶³ Random sampling of organisms from several locations is a fruitful approach in discovering new metabolites, although laborious and expensive.⁶³ As the microbial populations within sponge specimens and their metabolites profiles vary in response to changes in environment stresses,^{39,60} the investigation of well-known species from different environments should culminate in isolation of new compounds.

The Indo-Pacific in general has been well examined by natural product research programs,^{57-59,61} and similar species diversity is observed across the region. Hence, this study will focus on the investigation of encrusting organisms that are difficult to collect, and those with cryptic colouration and sparse distribution. Such organisms are less likely to have been subject to prior investigation in Tonga and more likely to yield structural novelty. Analysis of organisms from unexplored or geographically isolated areas will also be undertaken, although logistical difficulties may hinder the recollection of organisms collected from remote areas.

1.5.1 Bioassay-guided isolation

Bioassay-guided isolation has been the governing paradigm in natural products research since the early 1980s. Used successfully for decades, the approach involves screening crude biological extracts from target organisms against assays for specific modes of activity. Although the method guarantees a biologically useful end-product, it is not without flaws. Such studies culminate in structural elucidation only

*Ethnopharmacology entails the study of plants used in traditional medications and their active constituents.

after iterative cycles of chromatography and bioassay assessment, hence frequently result in isolation of known compounds.²⁴ The monetary value of a bioactive compound is significantly lessened without structural novelty: one can claim rights to a specific use, but not governing ‘ownership’ rights to the structure. Assessing crude extracts also precludes the use of more sophisticated biological assays. Assay bias may also disregard a wide range of metabolites present in an organic extract, and risk an incomplete understanding of a given compound’s full biological potential. Pharmaceuticals such as rapamycin (**2**) are currently marketed for a use unrelated to the application for which they were initially intended. Furthermore, *in vitro* testing cannot adequately assess a compound’s *in vivo* activity.

From a practical perspective, the wide range of polarities present in a crude extract can render a compound insoluble in the assay media, further excluding potentially bioactive compounds. Potent activity of a low-level compound can also be masked by the mild activities of compounds present at high-levels, while synergistic interactions between compounds within an active fraction can smear a positive biological activity across many fractions during purification.⁶⁴

1.5.2 Spectroscopy-guided isolation

Spectroscopy-guided isolation uses chemistry to narrow the isolation focus. As opposed to a positive bioactivity, interesting and uncommon structural motifs are tracked throughout chromatographic cycles. Such focus on unusual structural motifs facilitates structural dereplication at an early stage, increasing the chances of discovering a novel structure free from prior patent claim.

Nuclear magnetic resonance (NMR) spectroscopy is an ideal tool for organism screening and monitoring expedient isolation procedures. Sample preparation and spectral acquisition is quick to perform, and the non-destructive technique allows sample recovery. The ability to discern chemical functionality from ¹H NMR spectra is useful in optimisation of chromatographic conditions; from the selection of an appropriate stationary-phase through to the use of ion-exchange media and pH buffers for acidic and basic chemical moieties. Comparative insensitivity of the technique relative to other forms of spectroscopic analysis is a significant disadvantage. However, new powerful instruments fitted with cryogenic electronics and micro-probes can accommodate small sample sizes (<1 mg) and have dramatically improved the detection of minor compounds. The use of such technologies in 2D correlation experiments allows facile observation of comparatively insensitive nuclei such as ¹³C and ¹⁵N.^{5,65}

In comparison to NMR, greater sensitivity is offered by mass spectrometry (MS), and

by MS-coupled liquid chromatography and gas chromatography systems (LC-MS and GC-MS). However, ionisation susceptibility can differ widely between molecular classes, hence assessment by NMR can prove more all-encompassing. Additionally, sub-structure identification offered by 2D NMR spectra can be more informative than that obtained from MS fragmentation patterns.

1.5.3 Advances in NMR screening

The use of NMR screening within the VUW marine natural products program has been well developed over the past decade. Expansion from analysis of ^1H NMR spectra (Figure 1.3) to digital compilation of 2D heteronuclear single quantum coherence (HSQC) spectra has led to the isolation of many structurally unique biologically active secondary metabolites from New Zealand sponges and red algae.^{48,60,66} The spectral ‘masks’ of compiled HSQC spectra proved highly useful in organism selection.^{48,60,66} By masking out the common correlations it is relatively simple to determine the degree of structural novelty present within a given spectrum. However, the HSQC spectrum is fundamentally limited to the observation of protonated centres and the application of New Zealand spectral masks to Tongan organisms is questionable. Drastic changes in the metabolite composition of crude extracts may circumvent the ‘masking’ function of the HSQC screen technologies.⁶⁰

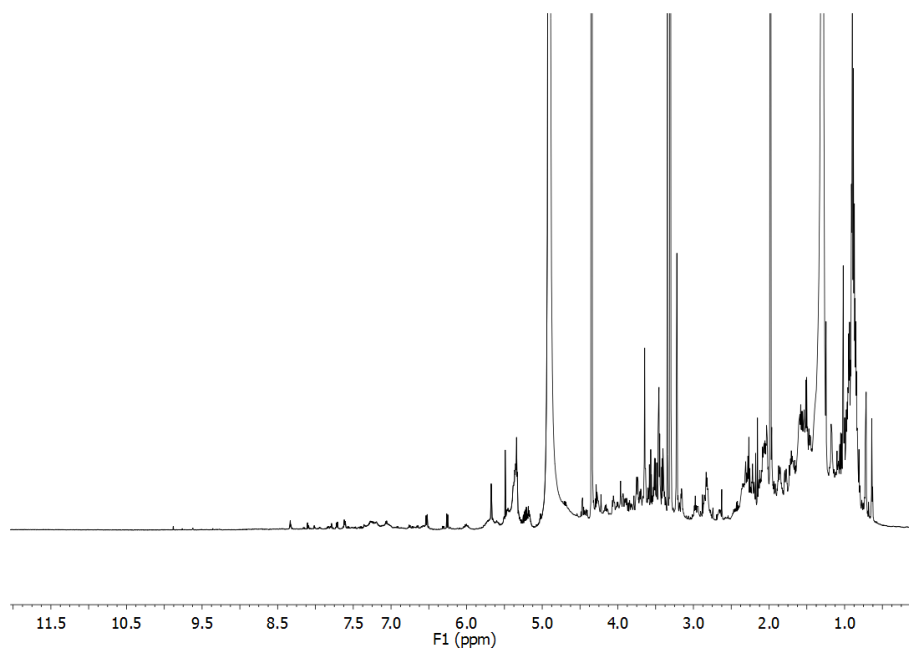


Figure 1.3 A generic ^1H NMR spectrum.

HMBC screening

Analysis by an heteronuclear multiple bond correlation (HMBC) experiment at the first stage of purification is the natural progression in NMR screening. The HMBC spectrum (Figure 1.4) provides multiple-bond correlations from ^1H nuclei to both protonated and non-protonated ^{13}C centres. As such, the experiment should prove a powerful tool allowing the identification of entire families of compounds at an early stage of isolation.⁶⁰ In combination with an HSQC screen, an interesting one-bond correlation can be extended upon by multiple-bond correlations in the HMBC spectrum. Although sub-structure screening can also be performed using the shorter COSY experiment (20 min vs $8\frac{1}{4}$ h), only protonated linkages are shown in the COSY spectrum and the experiment delivers less spectral dispersion as the ^1H spectrum forms both the real (F1) and synthetic (F2) dimensions.

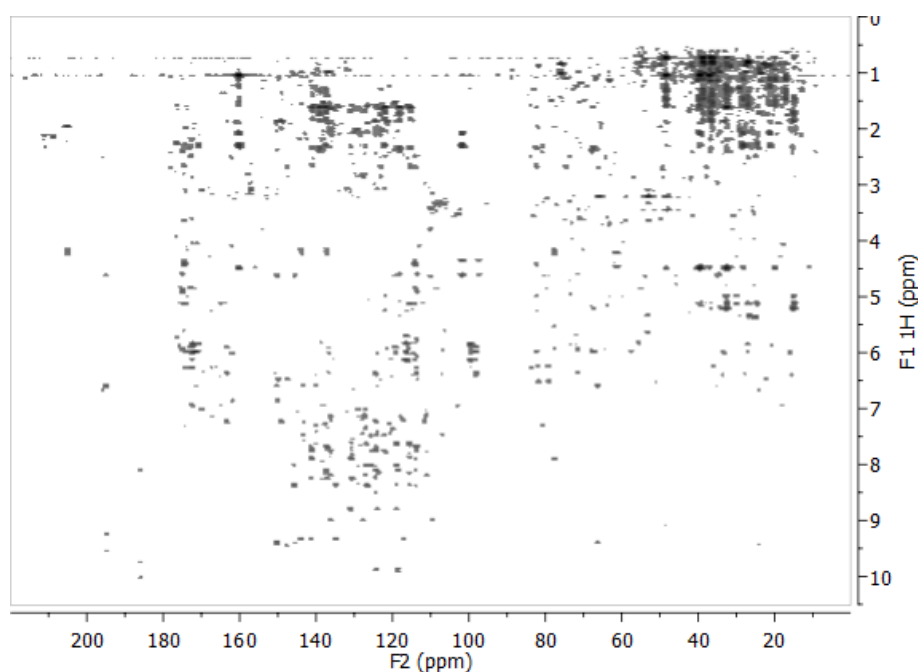


Figure 1.4 A generic HMBC spectrum.

Sub-structure analysis via the HMBC experiment was recently demonstrated by Bertelli *et al.* in the identification of sugar syrup contamination in various types of honey.⁶⁷ The experiment allowed discrimination between spectroscopic signals of very similar chemical moieties in very similar molecules, namely the anomeric hydroxyls of sugars. Spectral correlations were statistically grouped according to their relative integrations across several fractions, allowing the identification of adulterated honey samples, and for the degree of adulteration to be quantified.⁶⁷ The same approach has been used to determine the geographical origin of foodstuffs⁶⁸ and to assess age-related tainting.⁶⁹ Natural product studies have employed the techniques for chemotaxonomy, identifying the general classes of metabolites present within organism extracts. One such study allowed distinctions to be made between

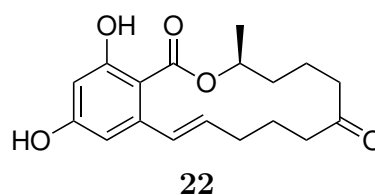
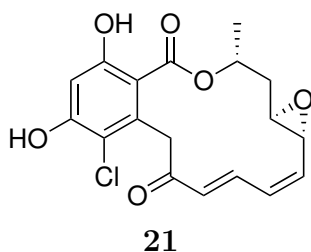
the extrudes from the conifer families Araucariaceae, Cupressaceae, and Pinaceae and the resins produced by the angiosperm family Fabaceae.⁷⁰

The premise behind NMR-based screening methodology is that a novel structure often corresponds to a novel biological activity, however, a novel structure still requires a biological application and as such, bioassay methods cannot be ignored. As the antithesis of bioassay-guided isolation, ignorance of potential biological application is the primary disadvantage of this structure-guided isolation method. For this reason, spectroscopy-guided isolation will in all likelihood remain subordinate to bioassay-guided studies, although the approach is a viable alternative for research groups without access to a wide variety of sophisticated biological assays.

1.6 Assigning biological applications

Assigning biological application to small molecules isolated in the absence of biological assessment requires a broad-spectrum assay approach. A viable option is to test pure compounds individually, or as part of a compound library against a series of selected cell lines or protein-based assays. Although library generation via either synthesis or isolation requires significant time and labour, the approach delivers highly specific and wide-ranging bioactivity information. Accurate determination of biological activities is invaluable to progression of drug leads through pre-clinical and clinical testing phases.

It is often assumed that structurally similar molecules will display similar modes of activity. This is not always the case, however. Despite structural similarities between members of the resorcylic acid lactone family, the compounds display a wide variety of biological activities.⁷¹ Radicol (**21**) potently and selectively competes for ATP-binding pocket of HSP90, a molecular chaperone responsible for the maturation and stability of several oncogenic genes.⁷² Conversely, zearalone (**22**) interacts with the estrogen pathway, and has been shown to adopt a conformation mimicing that of 17-estradiol,⁷³ and interact with the estrogen receptor in direct competition with the sterol.⁷⁴



In light of these findings assay selection requires great consideration. The most

logical approach would be to test a pure compound or library against common screening assays, followed by more specific and sophisticated assays. This is, however, strictly limited by the type of assays available, and by the quantities of purified material. Ideally, one could assess multiple activities with a single assay, making judicious use of the compound. This can be delivered by microarray profiling assays, such as those carried out in the eukaryote model *Saccharomyces cerevisiae* (baking yeast). Although the assays may not identify the exact mechanism of a compound, the profiles will hint towards a given biological function indicating which protein-based assays would be most informative to deciphering a compound's biological function.

1.6.1 Chemical genetic profiling

Chemical genetic profiling via microarray analysis delivers broad-ranging information about biological interactions. During chemical genetic profiling assays, a pooled population of mutant yeast strains is assessed for growth under a certain growing condition, such as the presence of a xenobiotic. Each of the mutant strains carries the deletion for a single non-essential gene, which is replaced by a unique molecular barcode. These barcodes allow the growth characteristics of each strain to be quantified relative to a control population.

A fundamental assumption in chemical genetic screening is that small molecules bind specifically to a cellular component and alter its activity, functionally mimicking a mutation at the corresponding gene locus.^{75,76} Increased sensitivity of a specific deletion mutant strain to a small molecule indicates that the deleted gene is related to the molecule's cellular target in either function or pathway. These "guilt by association" interactions show that the deleted gene is required to buffer the effects of the small molecule, and can be used to elucidate its cellular target.

1.6.2 Gene expression profiling

Orthogonal to chemical genetic profiling, gene expression profiling analysis quantifies the up- and down-regulation of messenger RNA (mRNA) expression of genes in response to an exogenous substance. Fluctuations in levels of specific mRNA sequences suggest a changed requirement for the protein coded by the sequence; for example, cells or tissues will increase levels of mRNA encoding alcohol dehydrogenase in response to increased levels of ethanol in their environment.⁷⁷

Both chemical genetic profiling and gene expression profiling techniques assess both the non-essential and essential gene cassettes simultaneously. However, under stress conditions, multiple gene products may be expressed but not be required for

expedient adaptation to environmental changes,⁷⁶ while genes essential for growth in particular environments may have an unchanged expression profile as their response is post-transcriptional.⁷⁶ Chemical genetic profiling therefore has the power to identify the specific target of a small molecule inhibitor in the absence of any change in mRNA-expression.⁷⁶

Chemical genetic profiling is an ideal form of biological assessment for small molecules isolated without knowledge of their biological activity. The profiles obtained from the assays will indicate which cellular functions are affected by a small molecule, aiding the identification of its precise cellular target and elucidation of its mechanism of action.

1.7 Research objectives

This thesis will encompass the isolation and structural elucidation of new secondary metabolites from Tongan marine sponges. To maximise the discovery of novel metabolites, the study of specimens with cyptic colouration and sparse distribution in geographically remote areas will be undertaken. This approach will hopefully uncover structural novelty from a well-examined region.

The principles of NMR-guided isolation will be applied throughout the chromatographic process, and the value of the HMBC experiment as a screening tool will be assessed through the identification of molecular substructures from within semi-purified fractions.

Following isolation, all metabolites will be assessed for activity against the human promyelocytic leukemia cell line HL-60. Inhibition of *Saccharomyces cerevisiae* yeast will also be assessed with the aim of identifying compounds with antifungal activity that is sufficient to allow characterisation of their biological mechanisms with chemical genetic techniques.

1.8 Summary

With its multiple island groups spanning many latitudes, the Kingdom of Tonga offers a host of different marine environments, providing an ideal location to study marine natural products. In comparison to New Zealand, Tonga should offer a multitude of organisms whose investigation will hopefully culminate in the characterisation of new and interesting secondary metabolites.

Bioassay-guided isolation has been used in the successful isolation of biologically-active secondary metabolites for decades. However, the partnership of spectroscopy-guided isolation practices and chemical genetic screening offers an alternative. Chemical genetic screening techniques have the potential to identify the specific mode of activity of such biologically active metabolites. The approach is unbiased towards any particular mode of biological activity, and complements a structure-based isolation approach. Used in tandem, the two have the potential to uncover new metabolites and fully characterise their biological activities.

Chapter 2

Organism Screening and Selection

Over the course of this study, 19 Tongan sponges were subjected to an NMR-based screening and selection process. 1D and 2D NMR spectra were acquired from the semi-purified screening fractions from each sponge, and the HMBC experiments in particular were assessed for apparent structural novelty. Nine specimens were selected for more thorough investigation on this basis. The metabolite profiles of each of these organisms is briefly detailed, and more comprehensive accounts of the structural classes from three organisms can be found in Chapters 3, 4 and 5.

2.1 Collection areas

Two excursions were made to the Kingdom of Tonga for sample collection yielding 260 sponge samples. In some cases multiple collections of the same organism were made, allowing study of changes in low-level metabolite profiles of specimens collected from geographically distinct locations. Collection sites visited during the first expedition in November 2008 included areas about the capital Nuku'alofa on the main island Tongatapu, the Houma blow-holes on the south side of the island, and the island of 'Eua to the east of Tongatapu. Several locations in the northern Vava'u island group were explored in November 2009.

2.2 Organism selection

Nineteen sponges that had been collected in small quantities from the Tongan islands were screened according to laboratory protocol (Appendix A). The crude methanol extracts of each sponge were individually partitioned over a column of HP20 resin beads, generating three Me₂CO in H₂O fractions of differing polarities, 30%, 75% and 100% Me₂CO in H₂O. Full NMR data sets of the 100% and 75% Me₂CO in H₂O fractions, including HMBC experiments, were acquired. Organism selection was

largely based upon the structural motifs evident within the crude HMBC spectra, with an emphasis placed on sub-structures including non-protonated carbon centres. Using these guidelines, nine specimens were chosen for further investigation. The remaining ten samples were discontinued when the spectral interest offered within was superseded by others, and when insufficient quantities of the organism had been collected (<10 g). A compilation of the masses of screened sponge fractions extracted is presented in Table 2.1.

2.3 The Vava'u group

The northern island group of Tonga, Vava'u, was visited in November 2009, and over 100 sponge samples were collected from eight dive sites within the island group. Comparison with sponge specimens also collected from 'Eua Island revealed subtle changes in metabolite profile between the two locations. In the case of the dictyoceratid sponge "luakuli" (PTN3_21E), new metabolites were isolated (see Chapter 3). Conversely, Vava'u collections of *Cacospongia mycofijiensis* investigated by Singh were deficient in the sought-after microtubule stabiliser zampanolide (20).^{60,62}



Figure 2.1 The Vava'u island group.

Table 2.1 Sponge Specimens Analysed During This Study

Specimen ID#	Collection location	Specimen masses (g)		Me ₂ CO in H ₂ O fraction (mg)	
		Total	Screening	100%	75%
PTN3_14C	Oho'una Harbour, Tongatapu	45.0	21.0	336.8	867.2
PTN3_17B	Houma, Tongatapu	7.0	7.0	48.1	45.6
PTN3_18E†	Houma, Tongatapu	3.0	3.0	15.2	12.7
PTN3_19D*	'Eua cave (SW), 'Eua	50.0	26.0	155.3	88.4
PTN3_20A*	'Eua cave (SW), 'Eua	37.0	21.0	588.2	460.8
PTN3_20B*	'Eua cave (SW), 'Eua	40.0	20.5	90.0	98.6
PTN3_20E	'Eua cave (SW), 'Eua	8.0	8.0	54.2	49.0
PTN3_21D*	'Eua cave (SW), 'Eua	50.0	22.0	53.5	95.4
PTN3_21E*	'Eua cave (SW), 'Eua	90.0	23.0	105.2	120.8
PTN3_23C	'Eua cave (SW), 'Eua	60.0	20.0	59.4	132.7
PTN3_25D	Fafa Island (SW), Tongatapu	80.0	22.0	56.6	35.6
PTN3_37F ^Ω *	Split Rock, Vava'u	115.0	17.0	90.2	17.4
PTN3_45B†	Tu'ungasika Island, Vava'u	344.0	19.0	69.1	14.3
PTN3_45E ^Ω *	Tu'ungasika Island, Vava'u	96.0	24.0	121.5	70.7
PTN3_49A	Shark's Tooth, Kitu's, Vava'u	875.0	17.0	72.1	80.6
PTN3_50B [§] *	Shark's Tooth, Kitu's, Vava'u	42.0	12.0	62.6	40.9
PTN4_08C†	Split Rock, Vava'u	44.0	17.0	19.3	14.2
PTN4_10B*	Fakalotul, Vava'u	125.0	16.0	96.2	65.8
PTN4_16C†	Sea fans, Vava'u	148.0	17.0	39.3	82.1

Arbitrarily assigned laboratory ID.

* Specimen was further investigated.

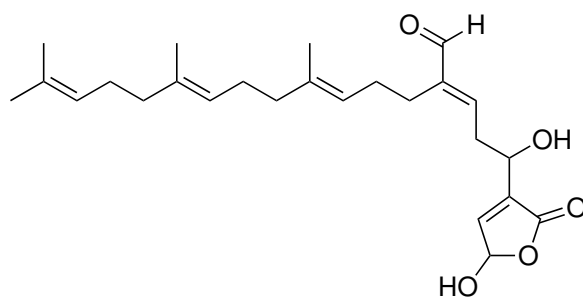
† ‡ ^Ω § Collections of the same organism from different locations.

2.3.1 PTN3_37F and PTN3_45E

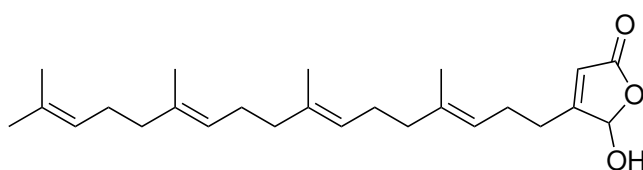


Figure 2.2 Surface photo of the sponge PTN3_45E.

Extraction of the demosponges PTN3_37F and PTN3_45E yielded two new diterpenes, *iso*-secothorectolide (**23**) and 1-hydroxyluffarin Q (**24**). The metabolites dominated the 1D and 2D NMR spectra of the 100% and 75% Me₂CO in H₂O HP20 fractions (Figures 2.3 and 2.4). Concurrent isolation of the two unreported metabolites within this laboratory from a bright orange 'Euan sample of *Fascaplysinopsis* sp. (order Dictyoceratida, family Thorectidae) by Taufa⁷⁸ aided structural elucidation of the compounds.



23



24

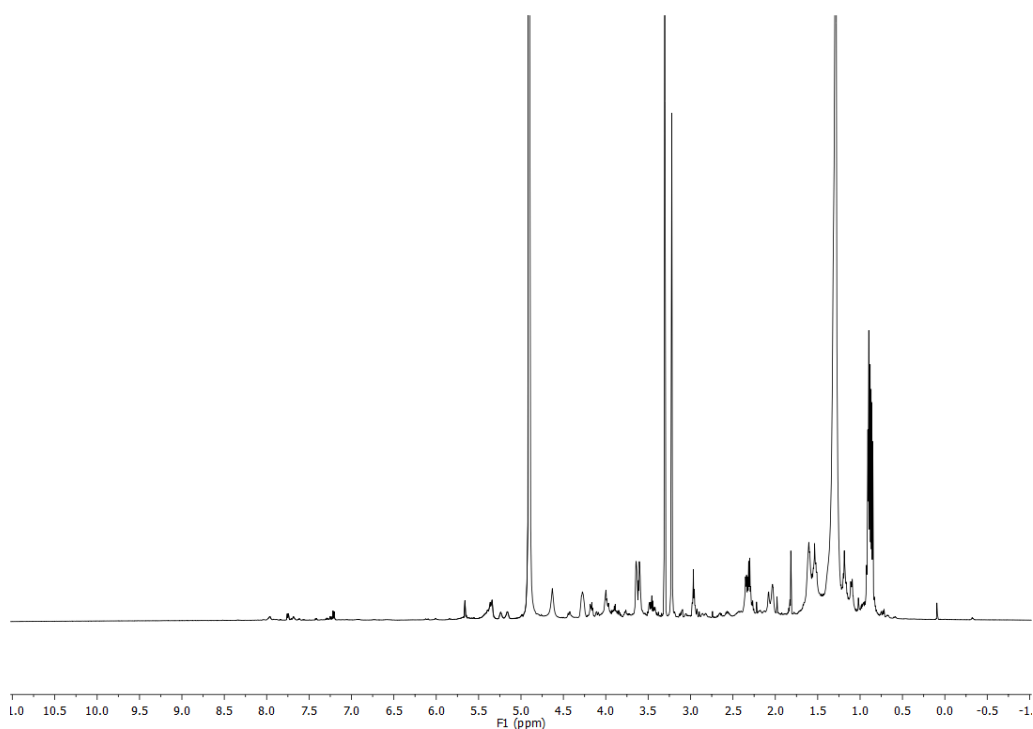


Figure 2.3 ^1H NMR spectrum (CD_3OD) of the 75% Me_2CO in H_2O HP20 fraction of PTN3_45E.

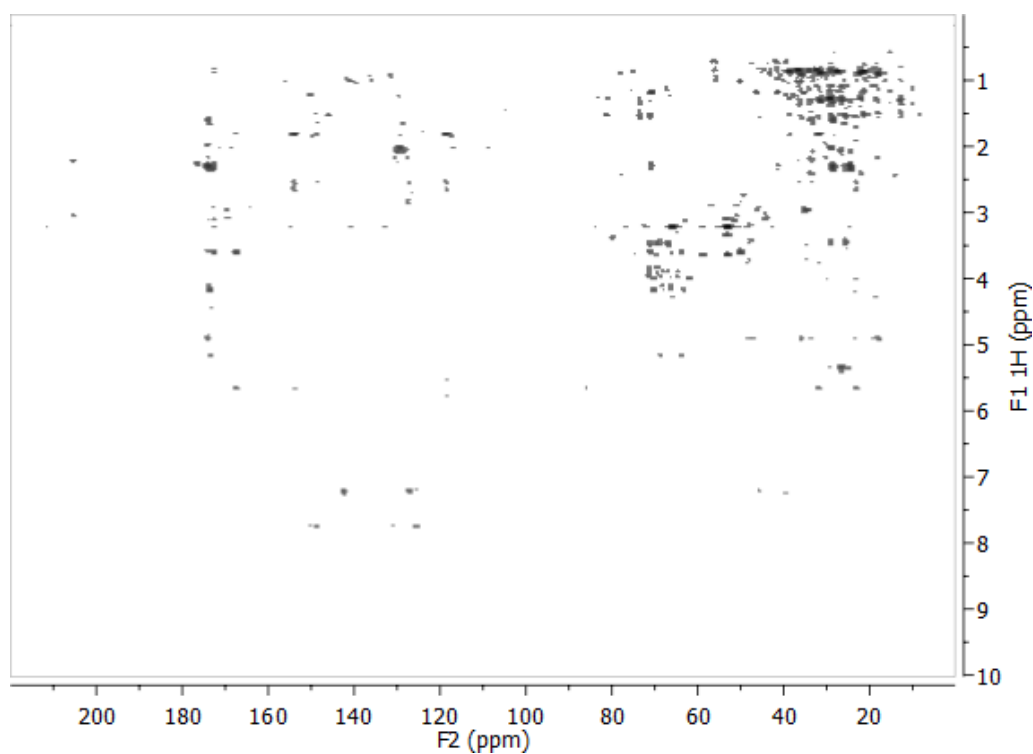


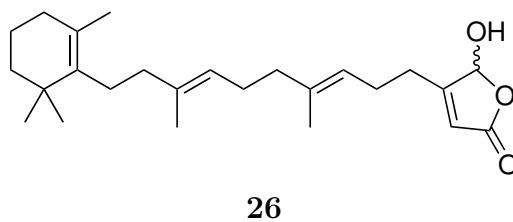
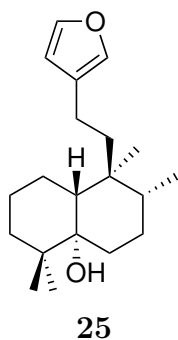
Figure 2.4 HMBC experiment (CD_3OD) of the 75% Me_2CO in H_2O HP20 fraction of PTN3_45E.

2.3.2 PTN4_10B



Figure 2.5 Surface photo of the sponge PTN4_10B

Several collections were made within the Vava'u island group of an unidentified demosponge, PTN4_10B. The lipophilic HP20 screening fraction (100% Me₂CO) of PTN4_10B was dominated by two compounds: ambliol B (**25**) and luffarielolide (**26**), while the ¹H and HMBC NMR spectra of the 75% Me₂CO in H₂O fraction indicated the presence of other metabolites (Figures 2.6 and 2.7). Further analysis of this specimen was not undertaken in this study, although subsequent investigations by Woolner⁷⁹ yielded several new members of the fascaplysin and homofascaplysin classes.



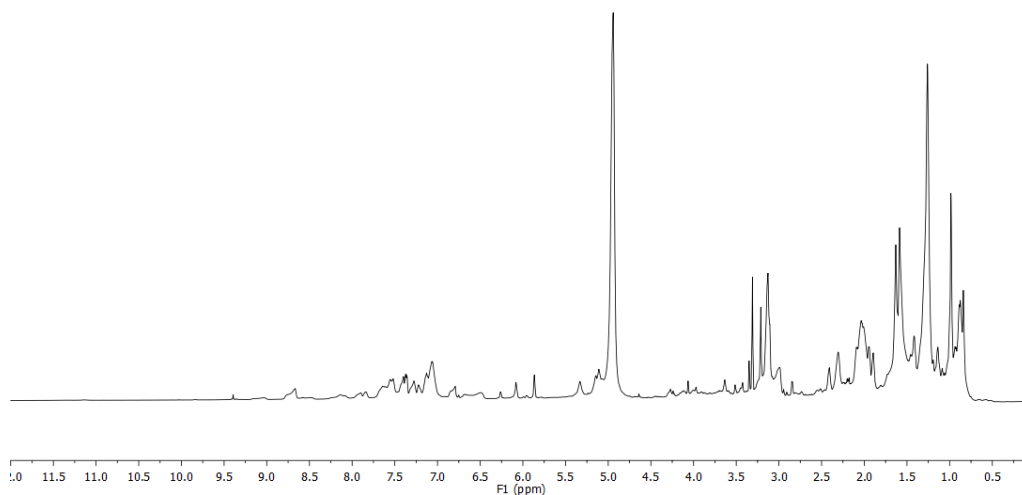


Figure 2.6 ^1H NMR spectrum (CD_3OD) of the 75% Me_2CO in H_2O HP20 fraction of PTN4_10B.

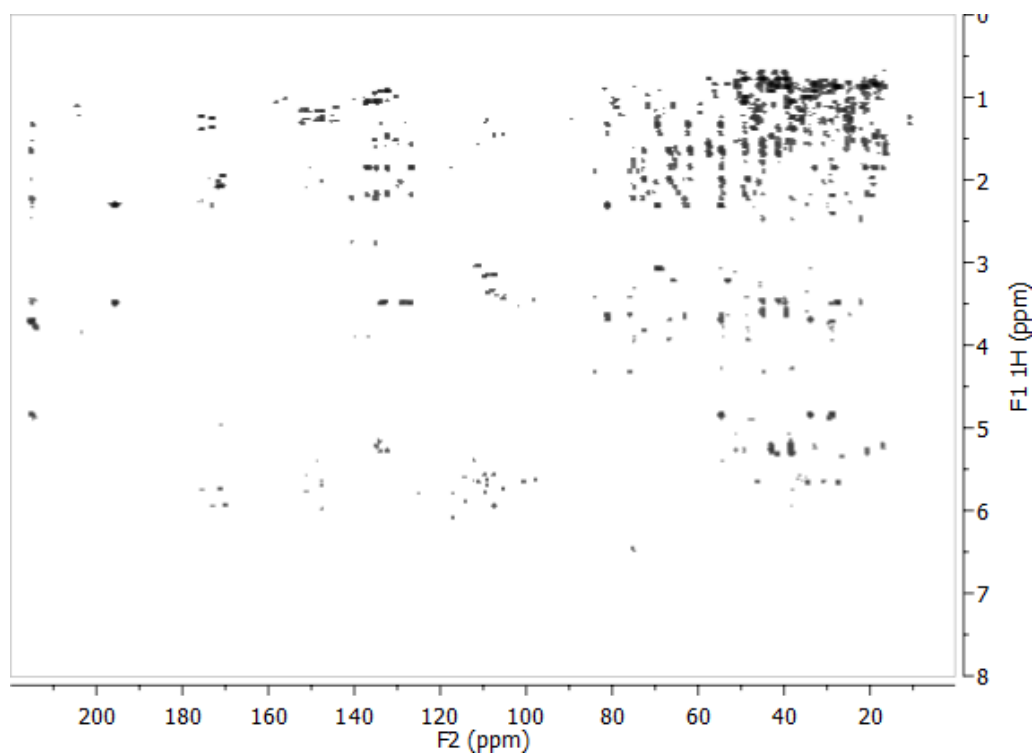


Figure 2.7 HMBC experiment (CD_3OD) of the 75% Me_2CO in H_2O HP20 fraction of PTN4_10B.

2.4 ‘Eua Island

‘Eua is the most ancient of Tongan islands, geologically distinct and geographically isolated from the other island groups.³⁹ No report has been made of natural product investigations in the area, and it was hoped that the unique marine environment about ‘Eua would produce novel chemistry.

A number of the specimens to receive further investigative attention during this work were collected at a depth of ca. 15 m in November 2008 from a marine cave on ‘Eua island. A second collection venture to the area was intended, but had to be abandoned due to safety concerns. Recollection of particularly rich sponges, such as the *Plakortis* specimen PTN3_20A was attempted in the Vava’u group, although such attempts were for the most part unsuccessful, owing to organism rarity or difficulties in sample recognition.

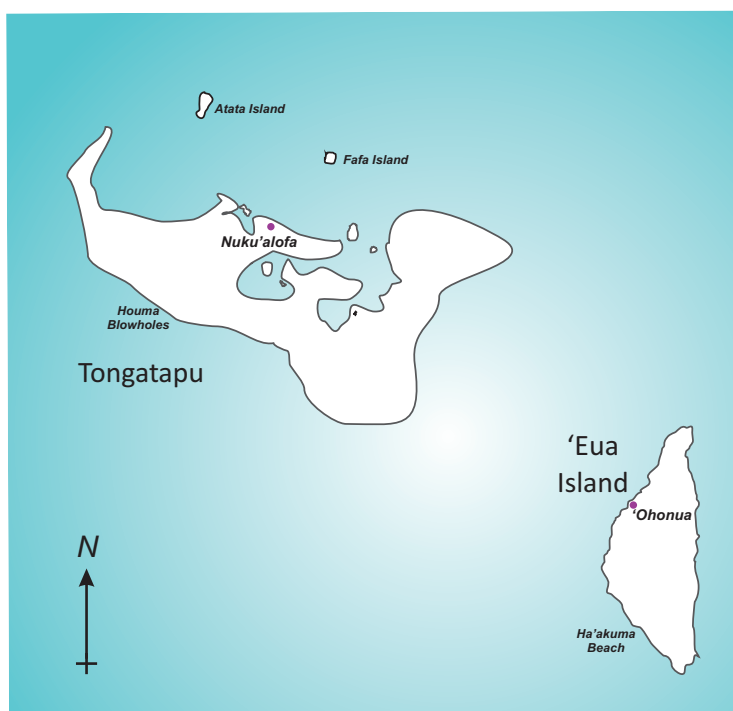


Figure 2.8 The Tongatapu island group.

2.4.1 PTN3_19D



Figure 2.9 Surface photo of the plakinid specimen PTN3_19D.

Investigation of the thinly-encrusting black plakinid sponge PTN3_19D (50 g) yielded four new polyketide metabolites and two $5\alpha,8\alpha$ -epidioxysterols. Evident within the HMBC experiment of the 75% Me₂CO in H₂O fraction were correlations from the protons of deshielded diastereotopic methylenes to oxycarbonyls and oxyquarternary centres (Figures 2.10 and 2.11). These interesting oxygenated structural fragments encouraged investigation of the specimen.

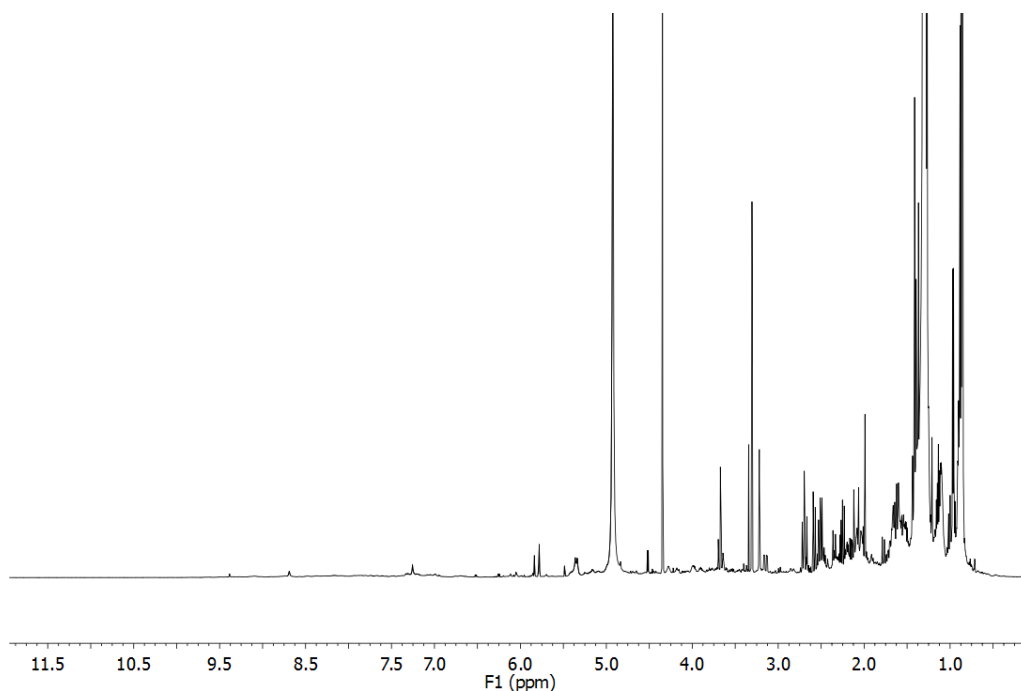


Figure 2.10 ¹H NMR spectrum (CD₃OD) of the 75% Me₂CO in H₂O HP20 fraction of PTN3_19D.

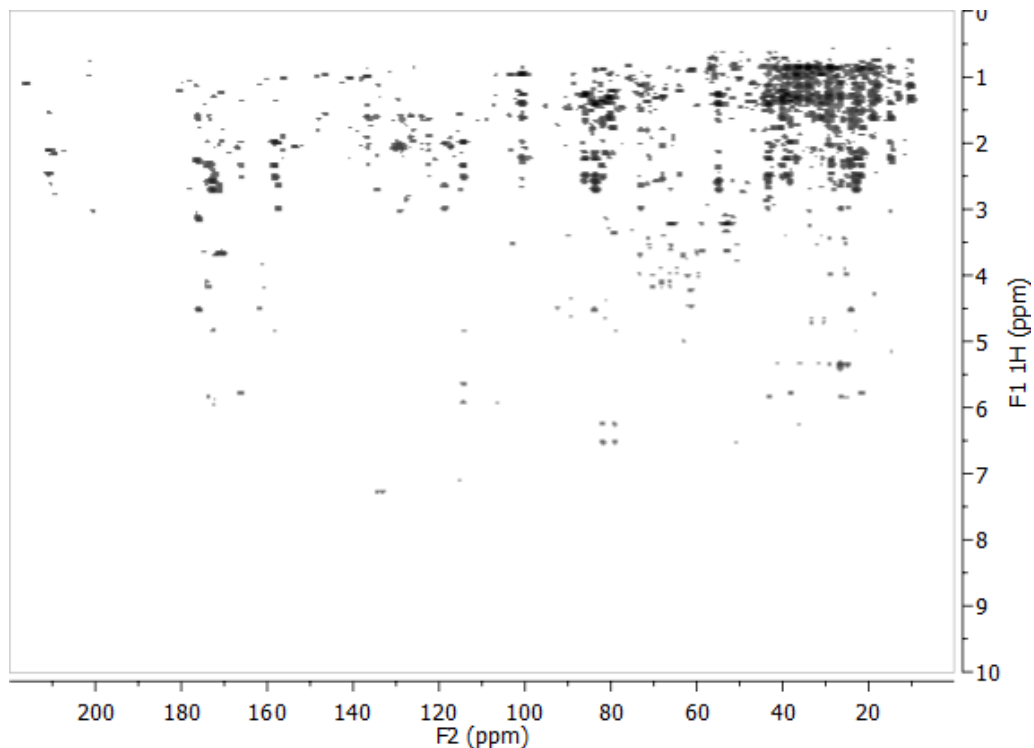
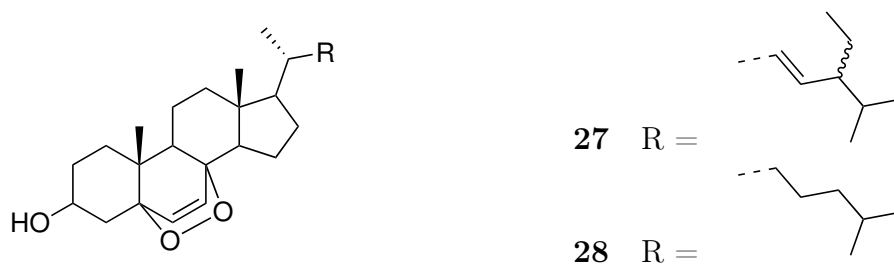


Figure 2.11 HMBC experiment (CD_3OD) of the 75% Me_2CO in H_2O HP20 fraction of PTN3_19D.

Two members of the $5\alpha, 8\alpha$ -epidioxysterol class **27** and **28** were isolated from PTN3_19D. The metabolites were first reported in 1978 by Gunatilaka *et al.* and have subsequently been encountered in a number of different sponge species,⁸⁰⁻⁸² the gorgonian *Eunicell cavolini* and the ascidian *Trididemnum inarmatum*.⁸³ Stereochemical analysis of the sterols was not undertaken during this study.



Investigation of PTN3_19D also afforded four new polyketide cyclic peroxides, the isolation and structural elucidation of which is detailed in Chapter 4. Biological assessment of the metabolites in *Saccharomyces cerevisiae* yeast follows in Chapter 5.

2.4.2 PTN3_20A



Figure 2.12 Surface photo of the *Plakortis* specimen PTN3_20A.

One of the first specimens to be analysed with our NMR-based screening protocol during this study was a dark purplish-brown *Plakortis* sponge, PTN3_20A. As detailed in Table 2.1, the 20 g screen sample yielded unusually high masses for the three Me₂CO in H₂O fractions. This was fortuitous as recollection of the sponge was never achieved.

Analysis of the ¹H NMR spectra of the 75% and 100% Me₂CO in H₂O fractions drew attention to unusual combination of signals, including shielded methyl protons, oxymethyl protons, aromatic protons, and evidence of a long alkyl chain (Figure 2.13). However, the HMBC spectra indicated the most interesting structural relationships: correlations between deshielded, methyl groups, methylene centres and two isolated, highly polarised and substituted carbon double bonds (Figure 2.14). The seven new isolates from this organism are discussed in Chapter 4.

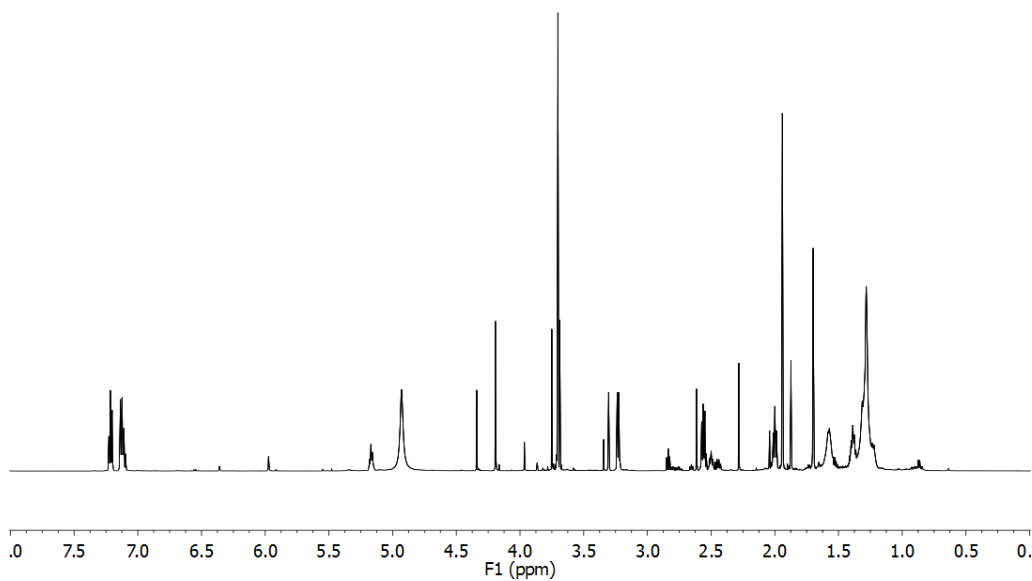


Figure 2.13 ^1H NMR spectrum (CD_3OD) of the 75% Me_2CO in H_2O HP20 fraction of PTN3_20A.

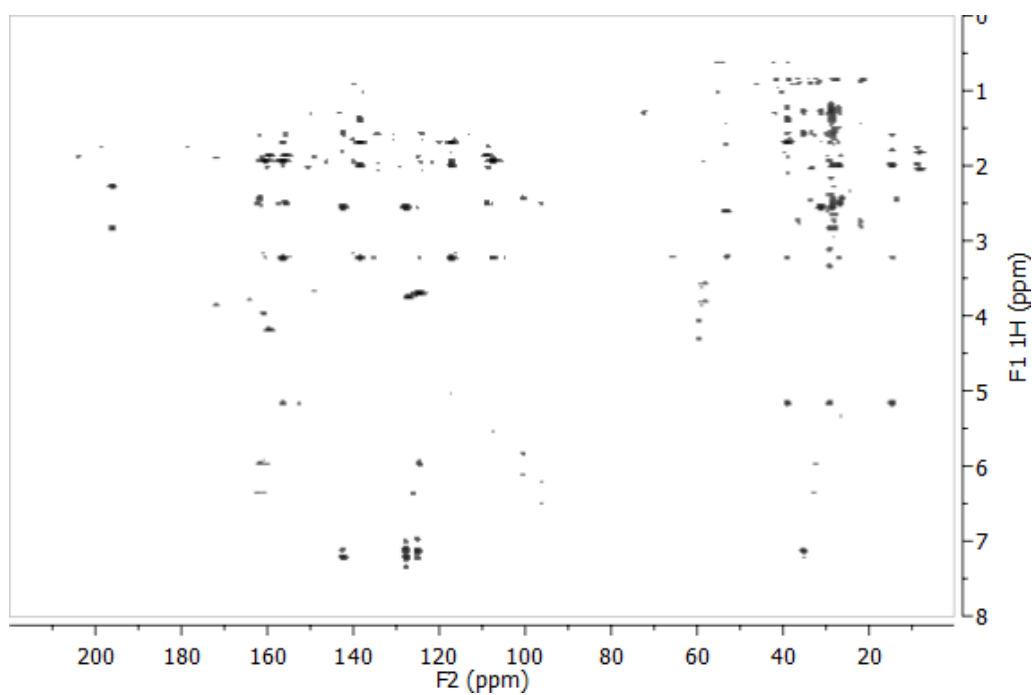


Figure 2.14 HMBC experiment (CD_3OD) of the 75% Me_2CO in H_2O HP20 fraction of PTN3_20A.

2.4.3 PTN3_20B

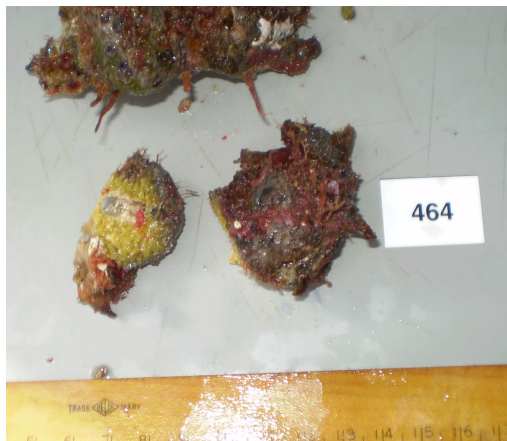
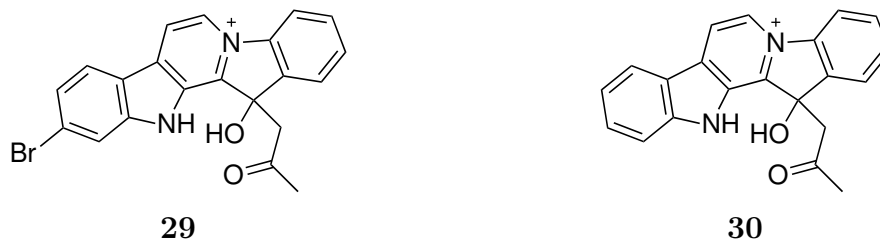


Figure 2.15 Surface photo of the slimy, mottled-green sponge PTN3_20B.

Analysis of the slimy, mottled-green demosponge PTN3_20B yielded the cytotoxic metabolite 14-bromohomofascaplysin (**29**). The alkaloid was present at low levels in the ^1H and HMBC NMR spectra of the 75% Me_2CO in H_2O HP20 fraction (Figures 2.16 and 2.17). A new addition to the homofascaplysin class, **29** was later isolated in greater quantities from PTN4_10B by Woolner.⁷⁹ The metabolite is a potent inhibitor of the HL-60 cell line, IC_{50} 33.8 nmol L^{-1} , and cell cycle analysis indicated that **29** induces S-phase delay.⁸⁴ 14-bromohomofascaplysin (**29**) was cytotoxic to wild type yeast with an IC_{50} value of 4.58 $\mu\text{mol L}^{-1}$.



The *des*-bromo analogue **30** was isolated by Taufa from the orange 'Euan specimen PTN3_13A,⁷⁸ allowing direct spectral and biological comparison between the compounds. Consistent with the trend observed by Crews *et al*,⁸⁵ HL-60 cells exhibited increased sensitivity to the brominated form. The presence of this class of compounds in three apparently unrelated organisms (PTN3_13A, PTN3_20B and PTN4_10B), may indicate spongal origin of the compounds, or that the producing bacterial symbiont is not specific to sponges of a particular class.

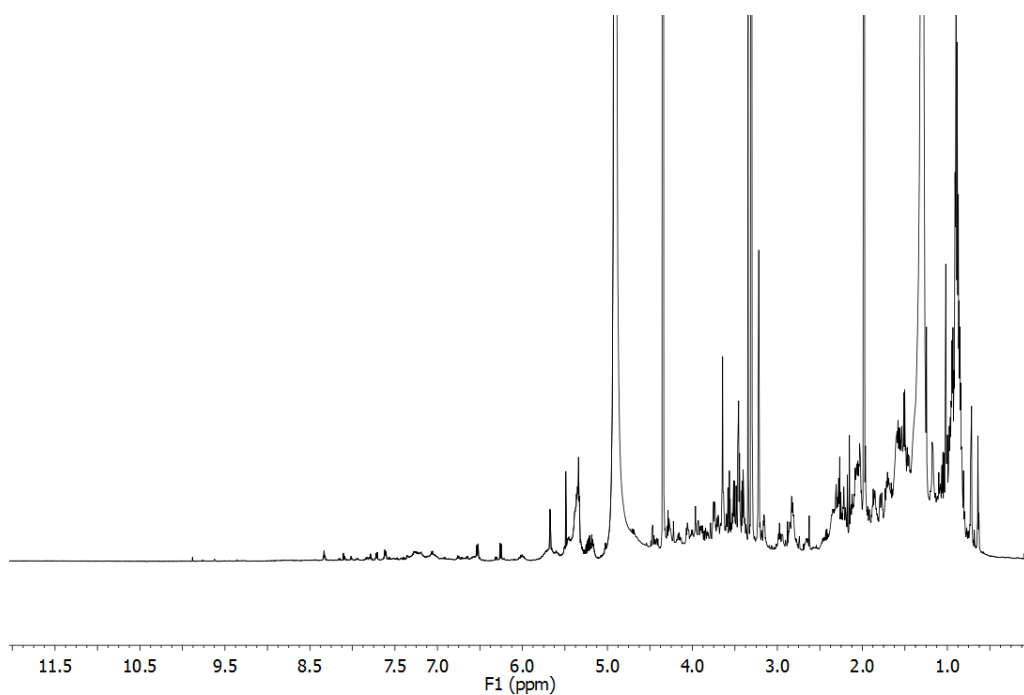


Figure 2.16 ^1H NMR spectrum (CD_3OD) of the 75% Me_2CO in H_2O HP20 fraction of PTN3_20B.

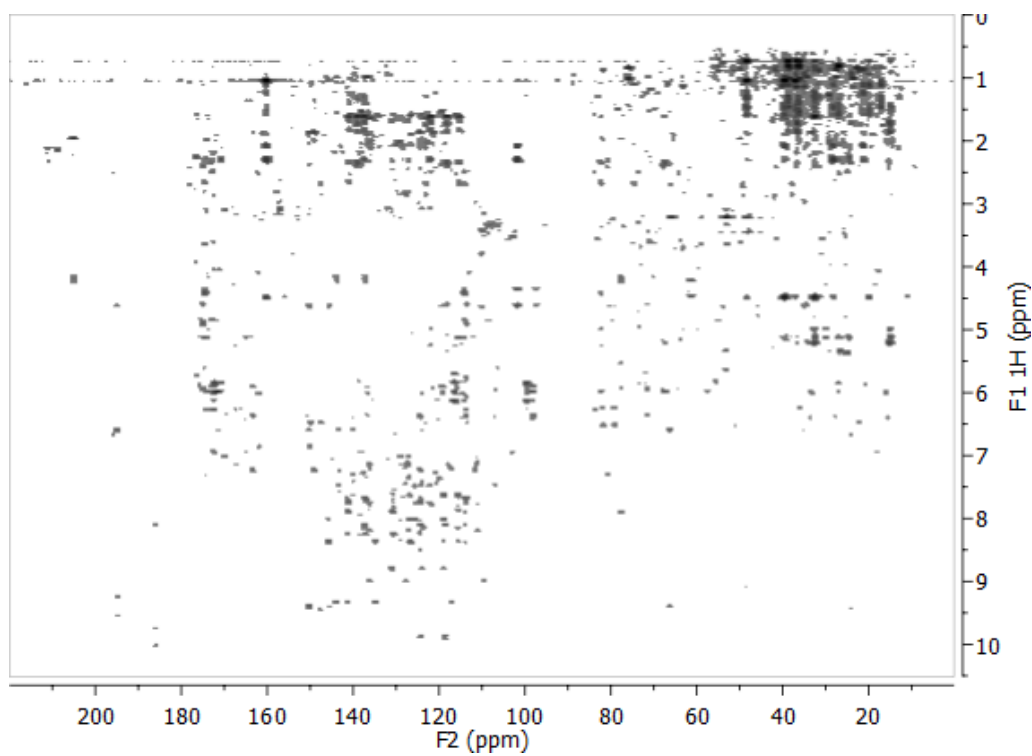


Figure 2.17 HMBC experiment (CD_3OD) of the 75% Me_2CO in H_2O HP20 fraction of PTN3_20B.

2.4.4 PTN3_21D

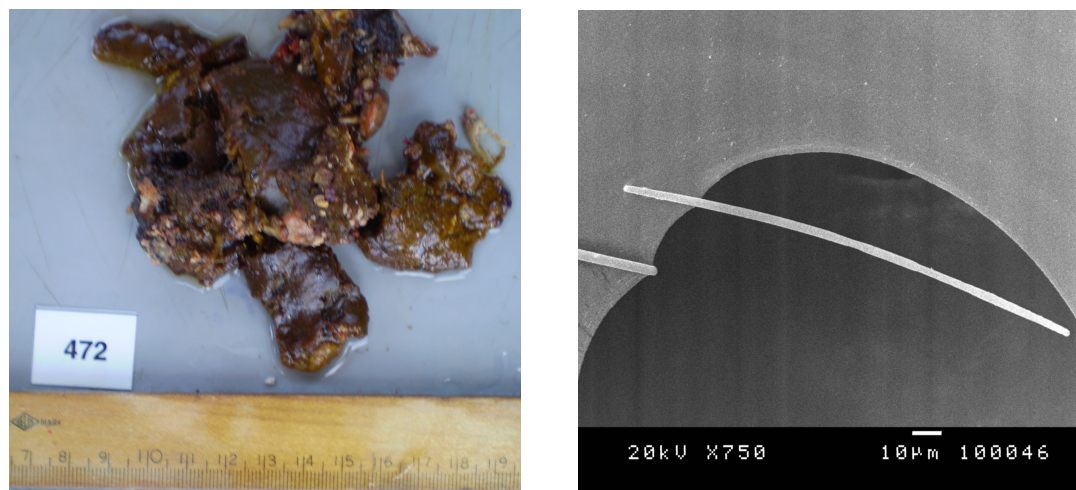
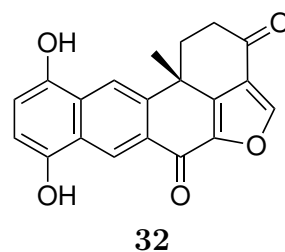
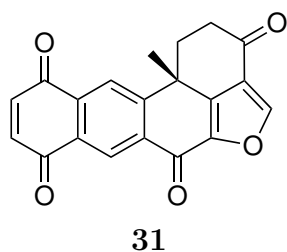


Figure 2.18 Surface photo of the sponge PTN3_21D and diod spicules recovered from the the organism.

Extraction of the blood red sponge specimen PTN3_21D (ca. 50 g) led to the isolation of the polyketide halenaquinone (**31**).⁸⁶ The compound dominated the ¹H and HMBC NMR spectra of the 100% and 75% Me₂CO in H₂O fractions from the initial HP20 screening column (Figures 2.19 and 2.20).

Identification of **31** was difficult; low level protonation about the fused penta cycle hindered structural elucidation. Connections between the tri-substituted furan and the adjoining α,β -unsaturated ketone were particularly difficult to establish. Further inspection of the 1D and 2D NMR spectra indicated the presence of the known dihydroxy reduction derivative **32**,⁸⁷ and other related compounds. Analysis of the sponge was problematic however; only MeCN appeared to dissolve the metabolites adequately, but also caused degradation of the metabolites. In light of solubility and stability issues and the presence of known metabolites within the organism, investigation of this specimen was discontinued. Diod spicules were recovered from the organism following HNO₃ tissue digest (Figure 2.18).



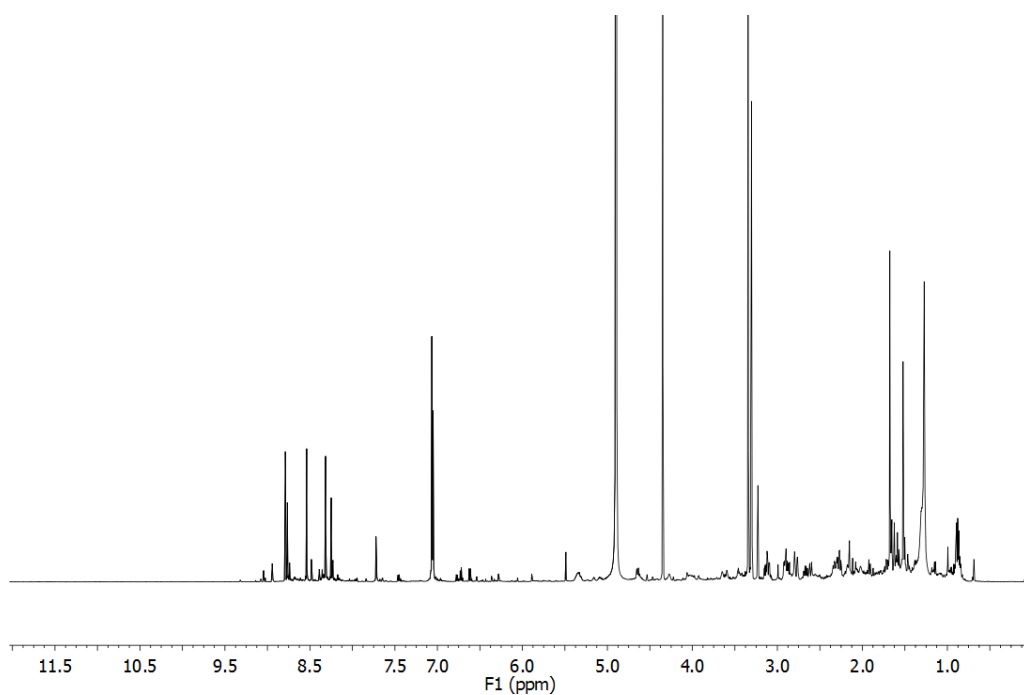


Figure 2.19 ^1H NMR spectrum (CD_3OD) of the 75% Me_2CO in H_2O HP20 fraction of PTN3_21D.

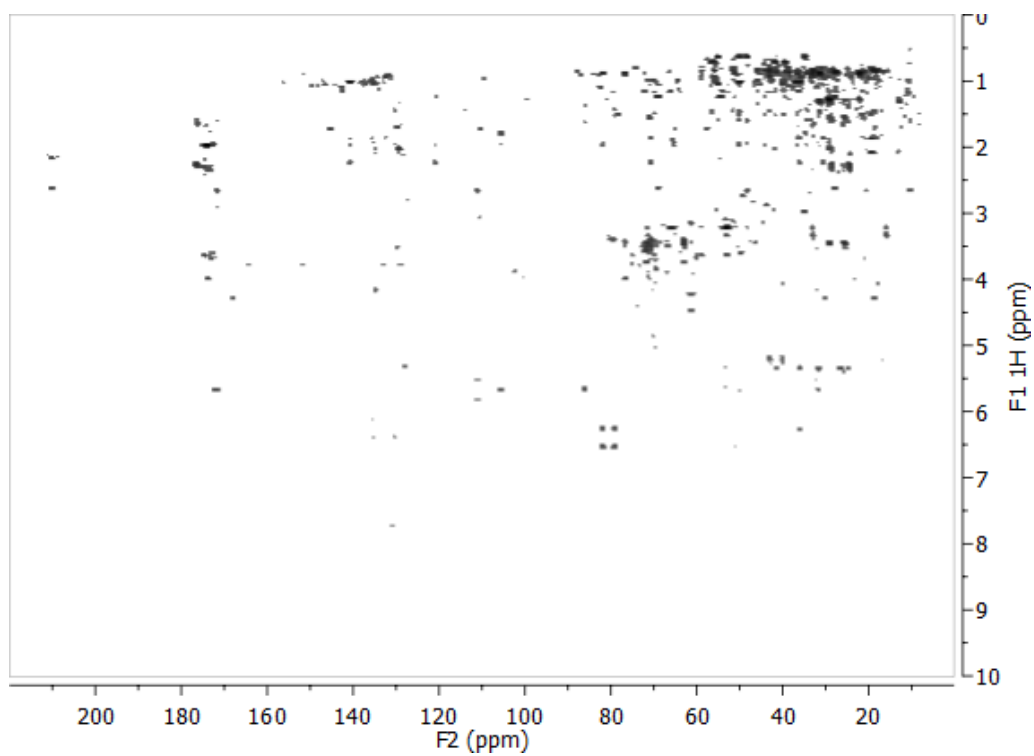


Figure 2.20 HMBC experiment (CD_3OD) of the 75% Me_2CO in H_2O HP20 fraction of PTN3_21D.

2.4.5 PTN3_21E and PTN3_50B



Figure 2.21 Surface photo of the Vava'u collection of the dictyoceratid sponge PTN3_50B.

A small quantity of an unidentified dictyoceratid sponge (see Figure 2.21) was collected from 'Eua island (PTN3_21E; 90 g, November 2008), and dubbed "luakuli"* owing to its unappetising appearance. Two closely related metabolites dominated the 75% and 100% Me₂CO in H₂O fractions; correlations characteristic of a *gem*-dimethyl pair were immediately apparent in the HMBC spectrum, while a 3-substituted furan ring was evident in the ¹H and HMBC spectra (Figures 2.22 and 2.23).

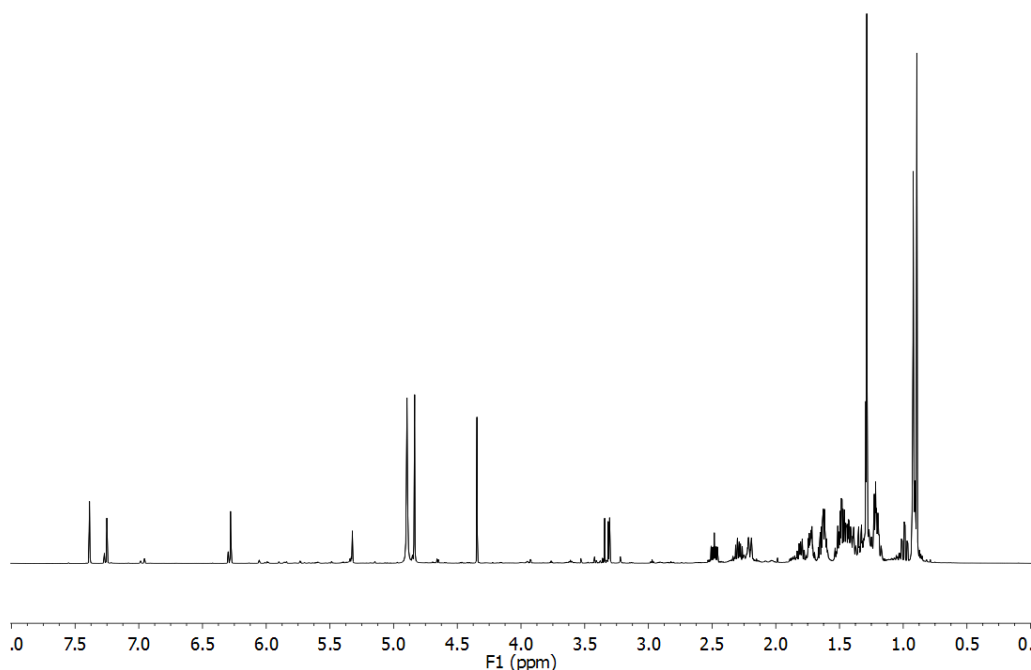


Figure 2.22 ¹H NMR spectrum (CD₃OD) of the 75% Me₂CO in H₂O HP20 fraction of PTN3_21E.

*Luakuli, Tongan term for the product(s) of canine stomach upheaval.

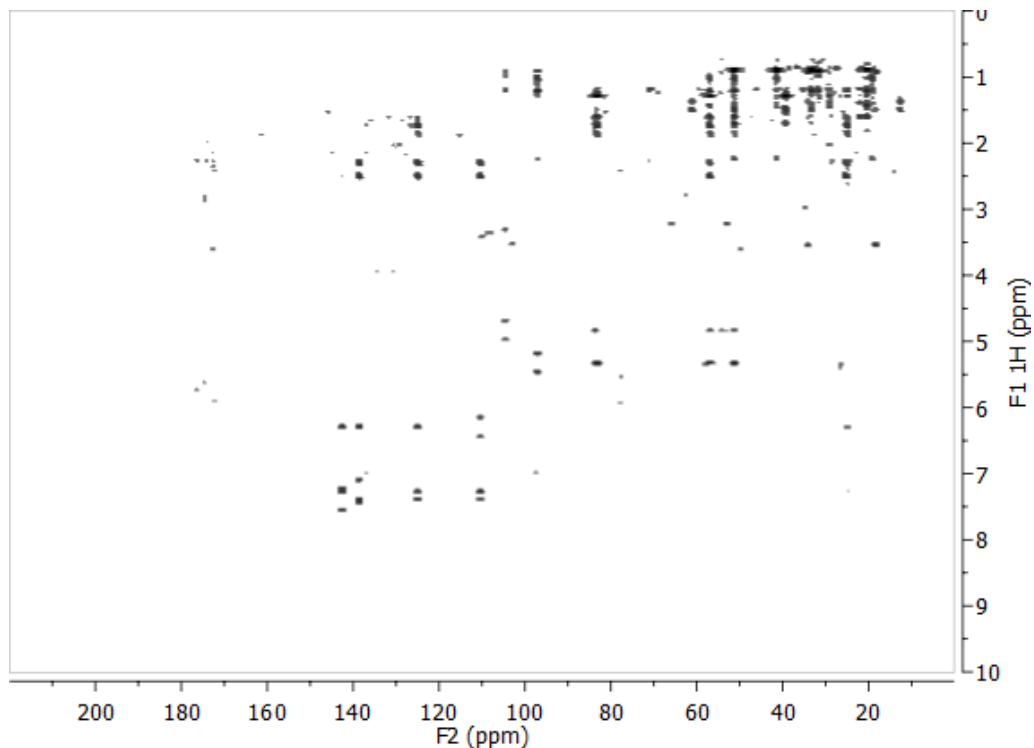


Figure 2.23 HMBC experiment (CD_3OD) of the 75% Me_2CO in H_2O HP20 fraction of PTN3_21E.

Subsequent study generated large quantities of a new labdane diterpene and its methyl acetal derivative. Targeted recollection of the “luakuli” sponge was achieved in the Vava’u group, and two minor metabolites were identified. An account of their isolation can be found in Chapter 3.

2.5 Concluding remarks

Investigation of nine Tongan sponges culminated in the isolation of a variety of terpene, alkaloid and polyketide metabolites. As postulated, the metabolite profiles of sponges, such as the dictyoceratid specimens PTN3_21E and PTN3_50B, were seen to vary subtly depending on the geographical origin of the specimen.

Organisms collected from the most ancient of the Tongan islands,⁸⁸ ‘Eua, appear to be chemically distinct from those collected in the Tongatapu and Vava’u island groups, yielding a greater proportion of new structures. Although the Vava’u island group boasts a wealth of marine life, organisms collected within the Vava’u group have displayed chemistry more similar to that observed in organisms from the neighbouring Fijian islands. This indicates that further investigation of organisms from ‘Eua island in particular should be undertaken.

Chapter 3

Luakuliides A–C

Analysis of an unidentified dictyoceratid sponge yielded three new labdane diterpenes; luakuliides A–C, which exhibit interesting immunomodulatory activity. Investigation of the specimen was undertaken following identification of the gem-dimethyl motif, characteristic of the cyclised labdane skeleton, in the HMBC screening spectrum.

3.1 The order Dictyoceratida

Dictyoceratida is an order in the class Demospongiae (sub-class Ceractinomorpha), and further divided into four families: Dysideidae, Irciniidae, Spongiidae and Thorectidae (Figure 3.1). Dictyoceratid sponges are characteristically devoid of an easily classified skeletal component, such as spicules, making their taxonomic identification particularly difficult. In place of spicules, they possess complex and ordered network of spongin fibres. This produces a tough, flexible tissue with a soft texture, while the textured surface is typically reticulated or conulose (marked with cone-shaped elevations). Modulation of surface pigmentation is frequently observed in demosponges – changes in light exposure can affect differences within the same organism. Hence, organisms growing in light exhibit a dark exterior with interiors ranging from white through to yellow and pale brown.³⁸

Order Dictyoceratida
Family Dysideidae
Family Irciniidae
Family Spongiidae
Family Thorectidae
Subfamily Phyllospongiinae
Subfamily Thorectinae

Figure 3.1 Taxonomic classification of Dictyoceratida, after Hooper and van Soest.³⁸

Owing to frequent phylogenetic restructuring and the ensuing taxonomic inconsistencies within the literature, a detailed account of dictyoceratid sponge metabolites is

difficult to present and would be outside of the scope of this study.

3.2 Labdane diterpenoids from the dictyoceratid sponge “luakuli”

The sponge PTN3_21E was initially collected from a dimly illuminated marine cave on the island of 'Eua, at a depth of ca. 15 m in November 2008. Tentatively assigned as belonging to the order Dictyoceratida, the sponge is porous and firm, with a reticulated surface and oscules of two size classes (see Figure 2.21). The organism contains no siliceous spicules and there is little difference in the pigmentation of its pinky-beige exterior and interior. Its nondescript appearance and sparse distribution made recollection in the Vava'u group difficult (November 2009), and only one small specimen (PTN3_50B) was recovered from the vertical interior of a cave.

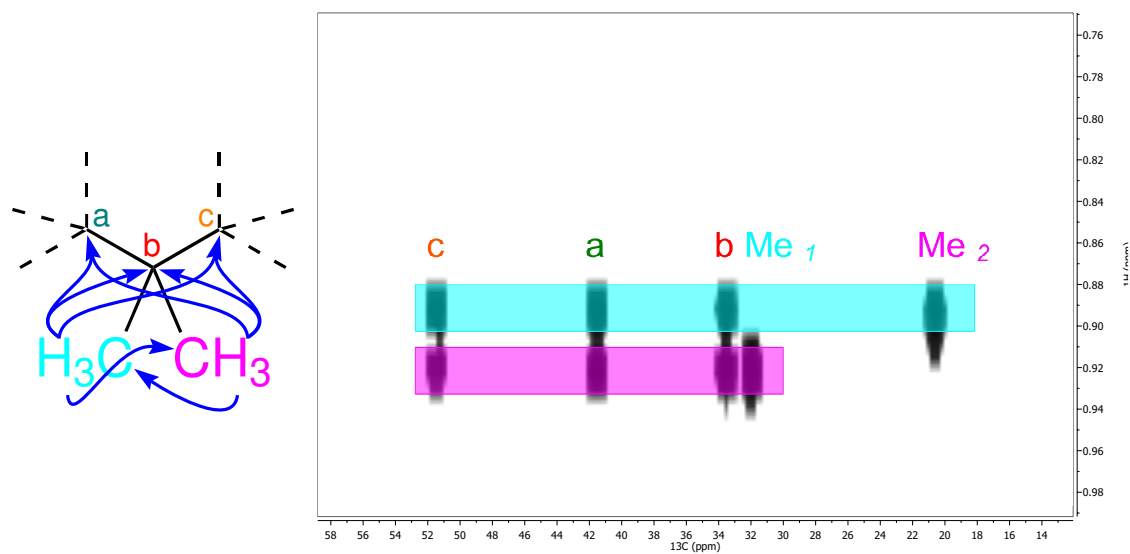
3.2.1 Isolation and identification of luakuliides A–C

The methanol extracts of a ca. 20 g screening sub-sample were chromatographically separated over HP20 resin (see Appendix A). Both the 100% and 75% and Me₂CO fractions displayed interesting NMR spectral signals, which appeared to belong to two closely related metabolites. The ¹H NMR spectrum contained the broad, deshielded signals of three heterocyclic olefinic methines, a hemi-acetal methine, deshielded diastereotopic methylene protons and shielded methyl singlets. Similarly, the ¹H and HMBC spectra of these fractions contained patterns characteristic of a *gem*-dimethyl pair and a 3-substituted furan system (Figure 3.2).

Portions of both HP20 fractions were partitioned further over HP20SS. The labdane diterpene luakuliide A (**33**) eluted in 60% and 70% Me₂CO in H₂O fractions, while further normal-phase purification of the 90% and 100% Me₂CO in H₂O fractions over DIOL yielded the presumed methanol artifact **34**, in the 100% CH₂Cl₂ fraction. Flash chromatography on DIOL of the 80% Me₂CO in H₂O HP20SS fraction generated further quantities of **33**, while the methoxy congener **34** eluted in the 10% CH₂Cl₂ in hexanes fraction.

The Vava'u specimen was extracted and partitioned over HP20 and HP20SS in a similar manner to the 'Eua specimen. Quantities of **33** and **34** were isolated following DIOL flash chromatography of the 100% Me₂CO in H₂O HP20SS fraction, and further purification of the 33% EtOAc in CH₂Cl₂ DIOL fraction by reversed-phase HPLC (C₁₈, 70% MeCN in H₂O) yielded luakuliides B and C (**35** and **36**). An overview of the isolation of the individual luakuliides is depicted in Figure 3.3.

A



B

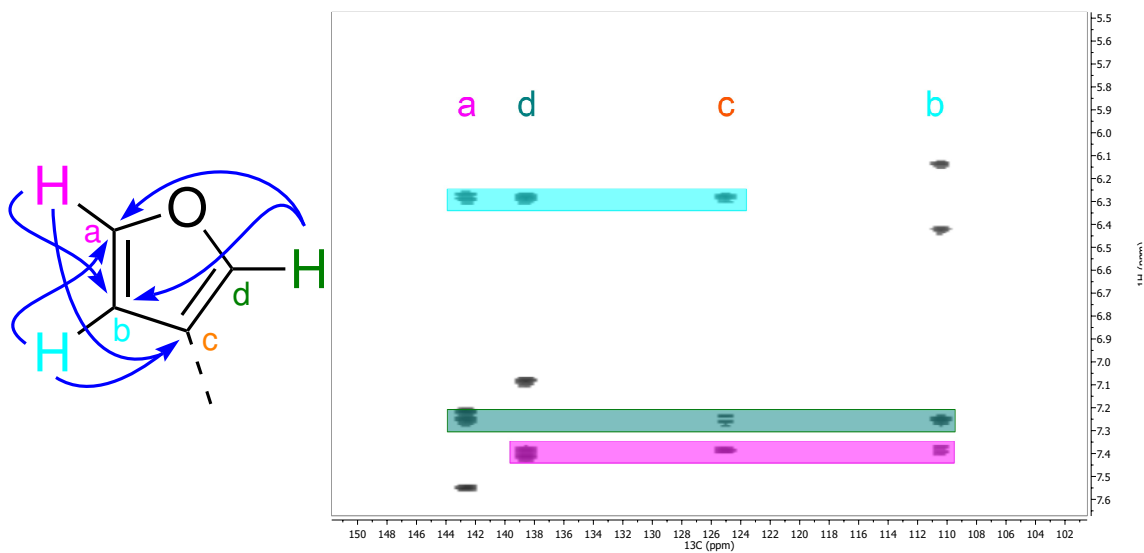


Figure 3.2 Proton to carbon correlations evidencing substructures in the HMBC spectrum of the 75% Me₂CO in H₂O HP20 screen fraction of PTN3_21E. A: the *gem*-dimethyl pair and B: the 3-substituted furan ring.

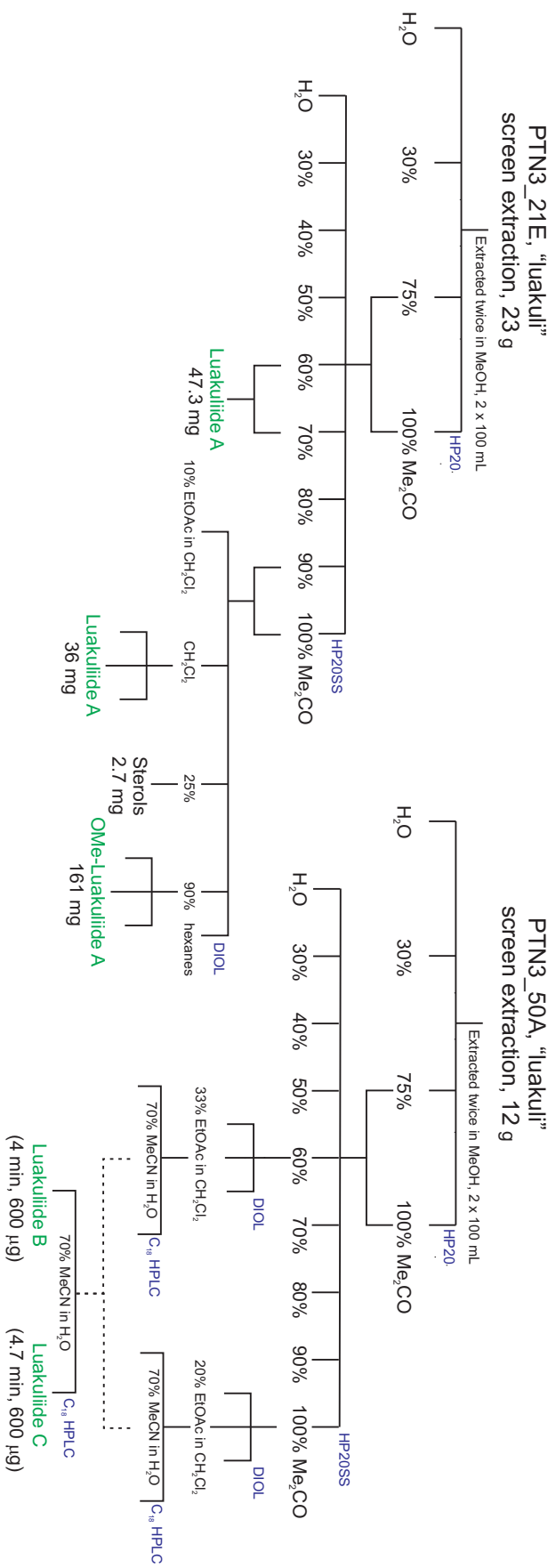


Figure 3.3 Purification strategy employed in the isolation of luakuliides A–C

Luakuliide A (**33**)

Luakuliide A (**33**), $[\alpha]_D^{25.4} -10.8^\circ$ (c 18.5, CHCl_3) was isolated as a colourless oil (92.7 mg in total). Positive-mode HRESIMS analysis of **33** revealed a $[\text{M} + \text{Na}]^+$ pseudo-molecular ion peak at m/z 341.2093, indicative of the molecular formula $\text{C}_{20}\text{H}_{30}\text{O}_3$, requiring six degrees of unsaturation. The ^{13}C NMR spectrum contained 20 distinct resonances, including four sp^2 centres, while the fully-coupled HSQC spectrum accounted for 29 of the 30 protons, indicating the presence of an exchangeable proton.

Analysis of the ^1H and HSQC NMR spectra (CDCl_3) suggested the presence of a 3-substituted furan system $[(\delta_{\text{C}} 111.0, \delta_{\text{H}} 6.26), (\delta_{\text{C}} 138.9, \delta_{\text{H}} 7.21)$ and $(\delta_{\text{C}} 142.9, \delta_{\text{H}} 7.34)]$, a hemi-acetal methine $(\delta_{\text{C}} 98.0, \delta_{\text{H}} 5.33)$, two deshielded diastereotopic methylene pairs $[(\delta_{\text{C}} 25.8, \delta_{\text{H}} \text{a } 2.52, \text{b } 2.29)$ and $(\delta_{\text{C}} 26.0, \delta_{\text{H}} \text{a } 1.88, \text{b } 1.72)]$, a deshielded methyl singlet $(\delta_{\text{C}} 23.0, \delta_{\text{H}} 1.31)$, two methines $[(\delta_{\text{C}} 51.7, \delta_{\text{H}} 1.18)$ and $(\delta_{\text{C}} 57.4, \delta_{\text{H}} 1.15)]$, a *gem*-dimethyl pair $[(\delta_{\text{C}} 21.7, \delta_{\text{H}} 0.89)$ and $(\delta_{\text{C}} 33.0, \delta_{\text{H}} 0.88)]$ and a region of diastereotopic methylene protons integrating for 10 resonances. Four spin systems were identified in the COSY spectrum: the sp^2 hybridised furan system, two isolated segments of contiguous deshielded diastereotopic methylenes and a methine, and a further isolated segment of three contiguous diastereotopic methylenes. Immediately apparent from the HMBC were the characteristic patterns of a *gem*-dimethyl pair and the 3-substituted furan system.

Olefinic methines CH-16 $(\delta_{\text{C}} 138.9, \delta_{\text{H}} 7.21)$ and CH-14 $(\delta_{\text{C}} 111.0, \delta_{\text{H}} 6.26)$ share reciprocal allylic COSY couplings and strong three-bond HMBC correlations. Vicinal COSY and HMBC correlations were observed between CH-14 and CH-15 $(\delta_{\text{C}} 142.9, \delta_{\text{H}} 7.34)$ and further HMBC correlations were observed from the three methines to the non-protonated olefinic carbon centre C-13 $(\delta_{\text{C}} 125.1)$, as depicted in Figure 3.4. Methines CH-16 and CH-15 both display large $^1J_{\text{CH}}$ couplings of 203 Hz and 201 Hz respectively, consistent with oxygen-substituted sp^2 centres, whereas CH-14 displays a smaller coupling consistent with carbon substitution. The ^{13}C chemical shifts of the four centres were consistent with oxygen substitution of CH-15 and CH-16. Placement of the oxygen between CH-15 and CH-16 completed the 3-substituted furan system, accounting for three degrees of molecular unsaturation.

As depicted in Figure 3.5, connection between CH_2 -12 $(\delta_{\text{C}} 25.8, \delta_{\text{H}} \text{a } 2.52, \text{b } 2.29)$ and CH_2 -11 $(\delta_{\text{C}} 26.0, \delta_{\text{H}} \text{a } 1.88, \text{b } 1.72)$ was evidenced by strong correlations in the COSY spectrum, corroborated by reciprocal HMBC correlations. Protons of CH_2 -11 shared further COSY correlations with methine CH-9 $(\delta_{\text{C}} 57.4, \delta_{\text{H}} 1.15)$, and reciprocal HMBC correlations were observed between the centres.

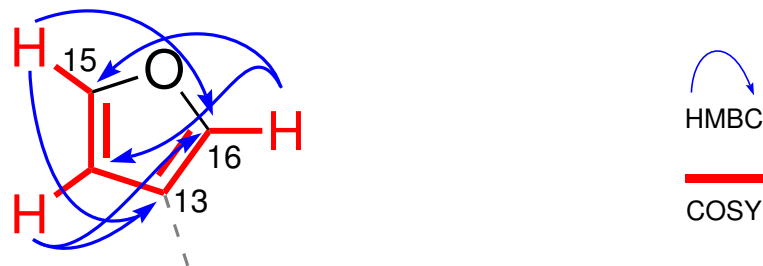


Figure 3.4 COSY and selected HMBC (H \rightarrow C) correlations observed within the furan system of **33**.

The third COSY spin system extends from methine CH-5 (δ_C 51.7, δ_H 1.18) to CH₂-7 (δ_C 39.8, δ_H a 1.62, b 1.42). Strong COSY coupling was observed between CH-5 and methylene CH₂-6 (δ_C 21.0, δ_H a 1.69, b 1.48), with the large coupling (17.4 Hz) between H-5 and H₂-6a indicating an anti-periplanar relationship. Protons of CH₂-6 further correlated with those of CH₂-7, with the connectivities corroborated by HMBC correlations as shown in Figure 3.5.

Identification of the final spin system by the COSY experiment began with the diastereotopic methylene CH₂-1 (δ_C 29.6, δ_H a 2.21, b 1.03), the protons of which shared reciprocal COSY correlations with CH₂-2 (δ_C 19.9, δ_H a 1.47, b 1.38). CH₂-2 displayed further COSY correlations to a third methylene CH₂-3 (δ_C 41.9, δ_H a 1.39, b 1.16). Selective irradiation of the H-1a methylene proton with a 1D-TOCSY experiment provided further evidence of the C-1 to C-3 segment. Over spin-lock mixing times of 20–60 ms, geminal partner H-1b, both H₂-2 protons and the resonances of H₂-3 were sequentially revealed, proving connection of CH₂-1 to CH₂-3 in this order (Figure 3.5).

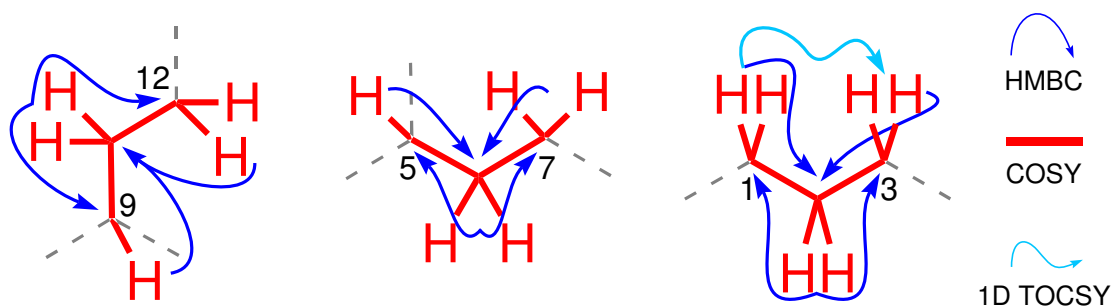


Figure 3.5 COSY, selected HMBC and 1D TOCSY correlations establishing the connectivities C-9 to C-12, C-5 to C-7 and C-1 to C-3 in **33**.

A *gem*-dimethyl pair, CH₃-18 (δ_C 21.7, δ_H 0.89) and CH₃-19 (δ_C 33.0, δ_H 0.88) was evidenced by reciprocal HMBC correlations between the methyls, and shared correlations to a quaternary centre C-4 (δ_C 34.1), methine CH-5, and methylene CH₂-3. Further HMBC correlations from the protons of CH₂-3 to C-4 and CH-5, and from CH-5 to C-4, established the connection between the C-1 to C-3 methylene series and the *gem*-dimethyl pair (Figure 3.6).

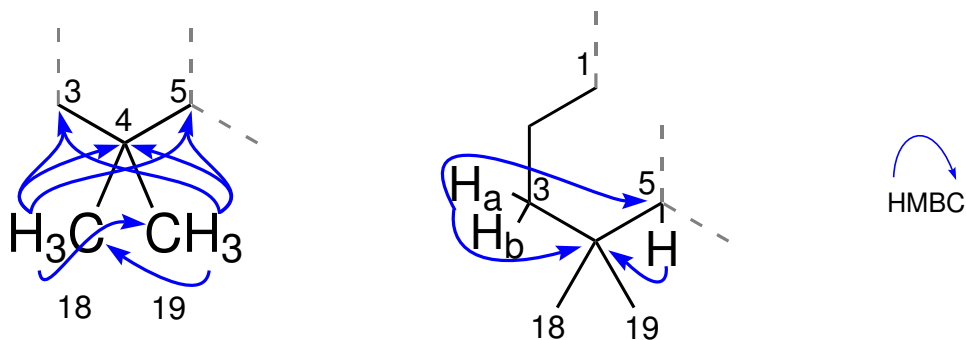


Figure 3.6 HMBC correlations establishing the *gem*-dimethyl substructure in **33**, and its connection to the C-1 to C-3 methylene segment.

The protons of methyl singlet CH₃-17 (δ_C 23.0, δ_H 1.31) shared weak COSY correlations with H-9 and H₂-7, and correlated strongly in the HMBC experiment with the two protonated centres and C-8. These correlations completed the linear sequence extending from CH₂-1 to CH-9 as shown in Figure 3.7.

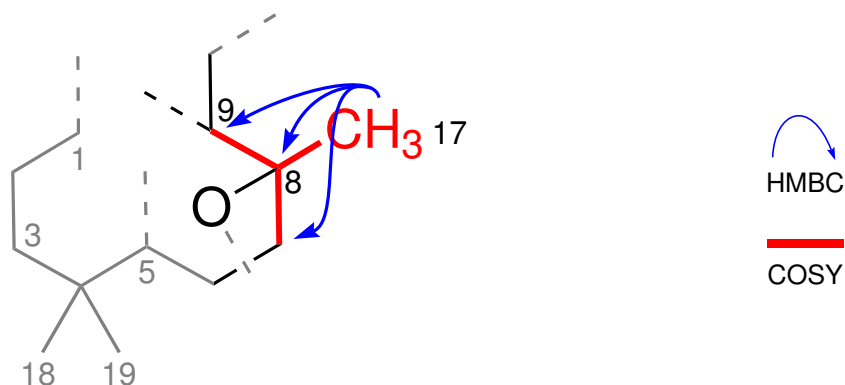


Figure 3.7 COSY and selected HMBC correlations establishing the linear connections from C-7 to C-9 and methyl substitution of C-8 in **33**.

Observation of HMBC correlations from the protons of CH₂-2 to the quaternary centre C-10 established the bond between C-1 and C-10, extending the linear sequence by one carbon atom. Similarly, an HMBC correlation from H-1b to C-9 established the C-10–CH-9 bond. Corroborating correlations were observed from H-9 to the oxygen-substituted C-8 (δ_C 84.0) and fully carbon-substituted C-10 (δ_C 51.9) quaternary centres. These correlations completed the cyclodecane system C-1 to C-10, accounting for a further degree of molecular unsaturation. Connection between the furan system (C-13 to C-16) and the substituted cyclodecane segment C-1 to C-12 was established by HMBC correlations from the protons of the diastereotopic methylene CH₂-12 to the *sp*² centres C-13, CH-14 and CH-16. This completed the carbon skeleton from C-1 to C-16 as shown in Figure 3.8.

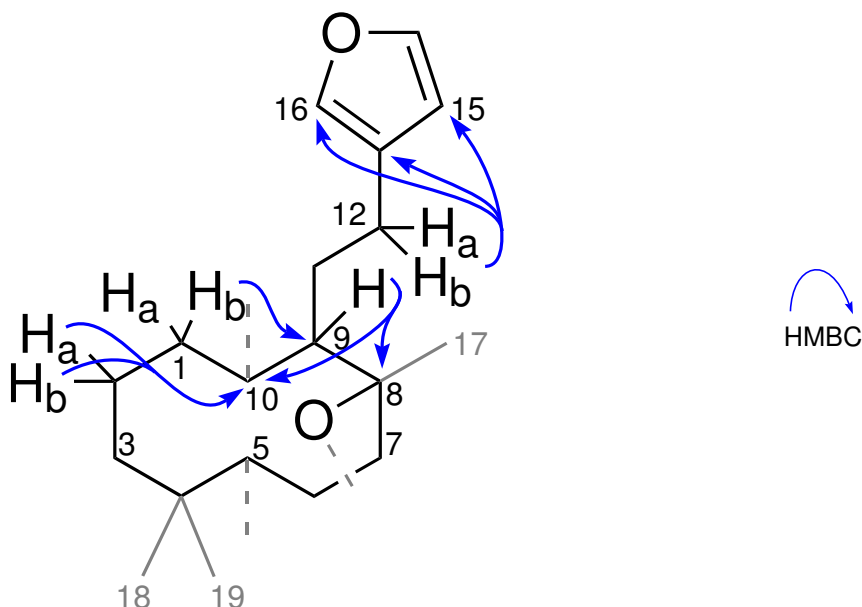


Figure 3.8 Selected HMBC correlations establishing the cyclodecane system of **33**, and attachment of the furan moiety.

All but the carbon resonance, CH-20 (δ_C 98.0, δ_H 5.33, $^1J_{CH}$ 170 Hz), was accounted for the by furan-substituted cyclodecane system, C-1 to C-19. The deshielded chemical shift and large $^1J_{CH}$ value of CH-20 are consistent with a hemi-acetal functionality. The exchangeable hydroxyl was evidenced by the IR and 1H NMR spectra (ν_{max} 3394 cm^{-1} , δ_H 4.08), and a COSY correlation observed with H-20. The hemi-acetal methine H-20 displayed HMBC correlations to C-10, and the methines CH-5 and CH-9, and a further HMBC correlation was observed from H-5 to C-10. These correlations established the bond between CH-5 and C-10, forming the two fused six-membered rings of the [4.4.0]-bicyclodecane system in luakuliide A (**33**), accounting for another double-bond equivalent in the fused bicyclic system. A weak HMBC correlation was observed from H-20 to the oxygen substituted C-8 (δ_C 84.0) establishing a hemi-acetal bridge. Somewhat surprisingly, reciprocal five-bond correlations were observed in the COSY experiment between H-20 and H₃-17, providing further evidence of their connection. The hemi-acetal bridge between C-10 and the oxygen-substituted C-8 completed the structure of **33** and accounted for the final degree of unsaturation in the tricyclic diterpene (Figure 3.9).

Requisite of the fused tricyclic system is the 1,3-diaxial positioning of the hemi-acetal, CH-20, and oxygen substituent of C-8, placing CH₃-17 in an equatorial position on ring B. A weak COSY coupling between H-5 and CH₃-19 established their 1,2-diaxial relationship on ring A, and the large coupling (12.8 Hz) between H-5 and H-6a indicated their 1,2-diaxial relationship on ring B (Figure 3.10).

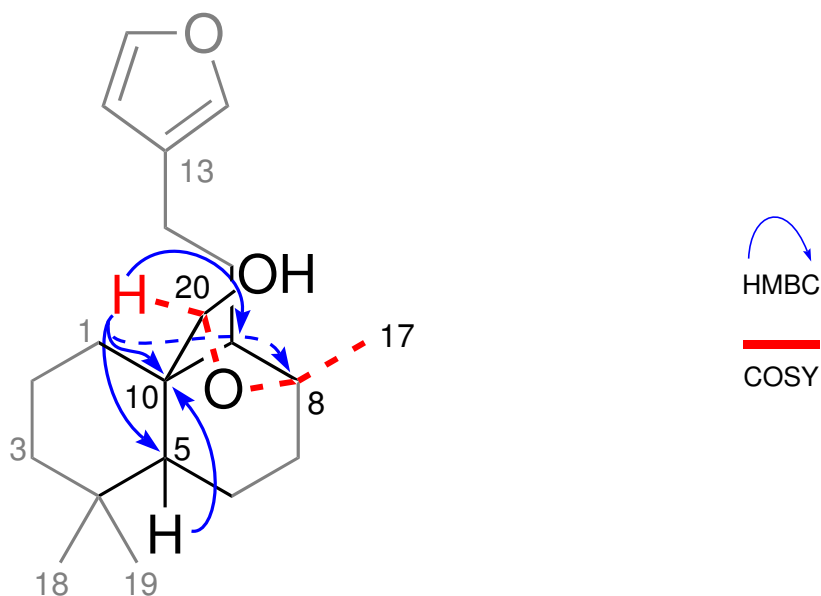


Figure 3.9 COSY and HMBC correlations establishing the hemi-acetal bridge between C-10 and C-8 in **33**. Dashed lines and arrows indicate a weak correlations.

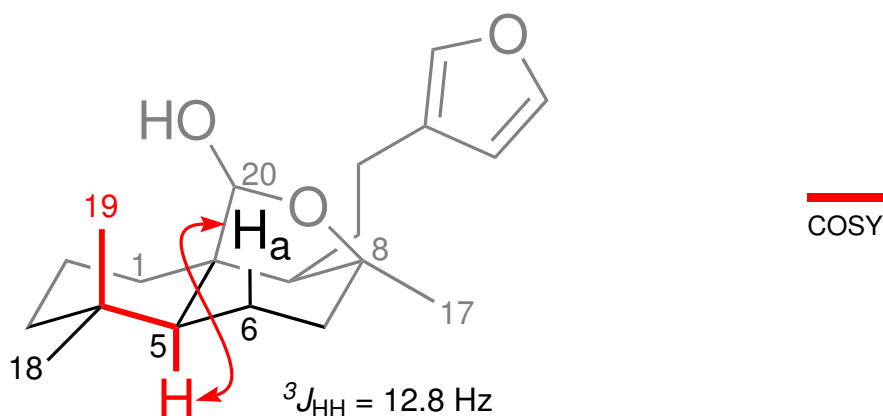


Figure 3.10 The *trans*-fused [4.4.0]-bicyclodecane system of **33** as evidenced by ${}^1\text{H}$ - ${}^1\text{H}$ coupling between H-5 and H-6a (${}^3J_{\text{HH}} = 12.8 \text{ Hz}$) and COSY correlations between H-5 and H₃-19.

Following selective irradiation of the hemi-acetal methine H-20 in a 1D NOE experiment, positive enhancements of H₃-19 and axial H-6a were observed, placing these protons on the same face of the [4.4.0]-bicyclodecane system. Irradiation of H-11a with a 1D TOCSY experiment revealed H-9 ($\delta_{\text{H}} 1.15$) after a 20 ms mixing time. The excited H-9 resonance provided a resolved target for a selective 1D NOE experiment. The experiment produced positive enhancement of the equatorial methyl H₃-17, and the protons H-5 ($\delta_{\text{H}} 1.18$), H-1b ($\delta_{\text{H}} 1.03$) and H-7b ($\delta_{\text{H}} 1.42$), placing them on the same face of the bicycle (Figure 3.11). These correlations firmly established the *trans*-fusion of the [4.4.0]-bicyclodecane system, and equatorial attachment of the furan-bearing segment to ring B.

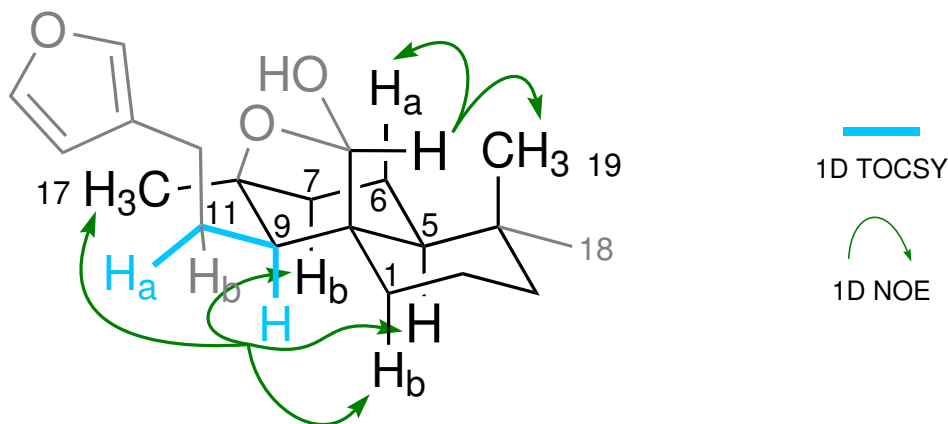
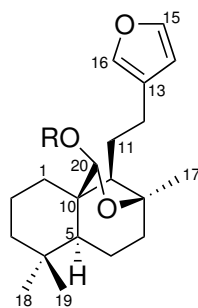


Figure 3.11 1D TOCSY-NOESY and 1D NOE correlations used to determination the relative stereochemistry about the *trans*-[4.4.0]-bicyclodecane system in **33**.

Isolation of the methyl-acetal analogue **34** and facile conversion of **33** into **34** confirmed the hemi-acetal functionality of luakuliide A (**33**). Positive ion-mode HRESIMS of the derivative **34** generated a pseudo-molecular ion corresponding to the molecular formula $C_{21}H_{32}O_3$ (m/z 355.2249 $[M+Na]^+$, Δ 2.3 ppm), and the two displayed similar optical rotations; **33**, $[\alpha]_D^{25.4} -10.8^\circ$ (c 18.5, $CHCl_3$) and **34**, $[\alpha]_D^{25.4} -75.0^\circ$ (c 0.14, $CHCl_3$). With the exception of the strong methoxy singlet signal (δ_C 55.4, δ_H 3.34) and the up-field shift of the acetal position (from δ_C 98.0, δ_H 5.33 to δ_C 104.9, δ_H 4.83), the two compounds proved to be very spectroscopically similar as shown in Table 3.1.

Table 3.1 NMR Spectral Data for the Acetal Moieties of **33** and **34**, (600 MHz, $CDCl_3$)



33 R = H
34 R = Me

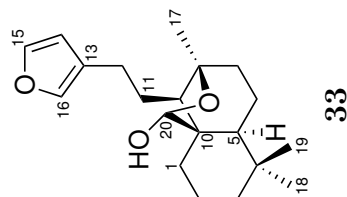
Position	mult	33		34		Difference*	
		δ_C (ppm)	δ_H (ppm)	δ_C (ppm)	δ_H (ppm)	$\Delta\delta_C$ (ppm)	$\Delta\delta_H$ (ppm)
8	C	84.0		83.7		-0.3	
9	CH	57.4	1.15	57.5	1.15	0.1	0.0
10	C	51.9		52.0		0.1	
20	CH	98.0	5.44	104.9	4.83	5.9	-0.50
OCH ₃	CH ₃			55.4	3.34		

* $\Delta\delta = \delta_{34} - \delta_{33}$

Absolute configuration is arbitrary.

Table 3.2 NMR Spectroscopic Data of Luakuliide A (**33**), (600 MHz, CDCl₃)

Position	¹³ C		¹ H		COSY	HMBC (¹ H → ¹³ C)	NOE [†]
	δ (ppm)	¹ J _{CH} (Hz)	δ (ppm)	mult			
1	a	29.6	131	d	13.2	1b, 2a, 2b, 3a, 3b	2, 3, 10
	b		122	td	13.4, 5.4	1a, 2a, 2b	2, 3, 9, 10
2	a	19.9	124	dd	12.7, 5.7	1a, 1b, 2b, 3a, 3b	1, 3, 4, 10
	b		128	d	13.8	1a, 1b, 2a, 3a, 3b	1, 3, 4, 10
3	a	41.9	126	td	13.2, 3.3	2a, 2b, 3b	1, 2, 4, 18, 19
	b		123	brd	14.4	1a, 1b, 2a, 2b, 3a	1, 2, 4, 5
4		34.1	C				
5		51.7	CH	dd	12.8, 4.6	6a, 7b w, 19*	4, 6, 7, 10, 18, 19
6	a	21.0	CH ₂	dq	12.8, 5.8	5, 6b, 7a, 7b, 17*	5, 7
	b		118	dd	13.5, 5.9	6a, 7a, 7b	5
7	a	39.8	CH ₂	d	8.7	6b, 7b, 17	5, 6, 8, 9, 17
	b		126	dd	12.4, 5.4	5, 6a, 7a, 9, 17	6, 8*, 9, 17
8		84.0	C				
9		57.4	CH	d	8.3	11a, 11b	8, 10, 11, 12, 20
10		51.9	C				
11	a	26.0	CH ₂	dtd	12.1, 7.3, 1.9	9, 11b, 12a, 12b	8, 9, 12, 13
	b		131	ddd	18.7, 9.2, 4.9	9, 11a, 12a, 12b	8, 9, 12, 13
12	a	25.8	CH ₂	ddd	14.8, 10.0, 4.9	11a, 11b, 12b	9, 12, 13, 14, 15
	b		126	dtd	16.6, 7.9, 7.9	11a, 11b, 12a	9*, 12, 13, 14, 15
13		126	C				
14		111.0	CH	brs	6.26	15, 16*	13, 15, 16
15		142.9	CH	brs	7.34	14*	13*, 14, 16
16		138.9	CH	brs	7.21	14	12*, 13, 15
17		23.0	CH ₃	s	1.31	7a, 7b, 9a, 20	6*, 7, 8, 9, 11*
18		21.7	CH ₃	s	0.89	3a, 3b, 19	2, 3, 4, 19
19		33.0	CH ₃	s	0.88	5*, 18	2, 3, 4, 18
20		98.0	CH	s	5.33	17*	5, 8, 9, 10
OH				brs	2.95		6a, 19



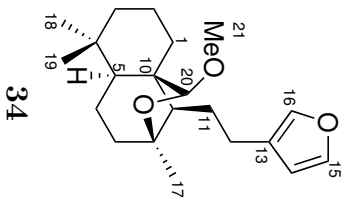
[†]Selected correlations.

*Weak correlations.

Absolute configuration is arbitrary.

Table 3.3 NMR Spectroscopic Data of Luakuliide A Methyl Acetal (**34**), (600 MHz, CDCl₃).

Position	¹³ C		¹ H		COSY	HMBC (¹ H → ¹³ C)	NOE†
	δ (ppm)	mult	δ (ppm)	mult			
1	29.5	CH ₂	2.20	d	1b, 2a, 2b, 3a	2, 3, 10	
2	20.0	CH ₂	0.97	td	1a, 2a, 2b	2, 3, 9, 10	
3	41.9	CH ₂	1.35	tt	1a, 1b, 2b, 3a, 3b	1, 3, 4, 10	
a			1.47	dt	1a, 1b, 2a, 3a, 3b	1, 3, 4, 10	
b			1.40	dd	1a, 1b, 2a, 2b, 3b	1, 2, 4, 5	
4	34.2	C	1.16	td	2a, 2b, 3a	1, 2, 4, 18, 19	
5	51.8	CH	1.18	dd	6a, 7b, 19*	4, 6, 7, 10, 18, 19	
6	21.2	CH ₂	1.51	dd	5, 7a, 7b, 17*	5, 7	19
a			1.72	dd		5, 7	
b			1.67	d			
7	40.0	CH ₂	1.42	dd	6a, 6b, 7b 17	5, 6, 8, 9, 17	
a					5, 6a, 7a, 9, 17	6, 8, 9, 17	
b							
8	83.7	C	1.15	d	11a, 11b	8, 10, 11, 12, 20	1b, 5, 7b
9	57.5	CH	1.82	ddd	11b, 12a, 12b	8, 9, 12, 13	
10	52.0	C	1.65	ddd	11a, 12a, 12b	8, 9, 12, 13	
11	26.0	CH ₂	2.50	ddd	11a, 11b, 12b;	9, 12, 13, 14, 15	
a					11a, 11b, 12a;	9, 12, 13, 14, 15	
b							
12	25.6	CH ₂	2.30	ddd	11a, 11b, 12a	9, 12, 13, 14, 15	
a							
b							
13	125.4	C					
14	111.2	CH	6.27	brs	15, 16*	13, 15, 16	
15	142.8	CH	7.35	brs	14*	13, 14, 16	
16	138.9	CH	7.21	brs	14	12, 13, 15	
17	23.4	CH ₃	1.30	s	7a, 7b, 9, 20	6, 7, 8, 9, 11*	
18	21.8	CH ₃	0.89	s	3a, 3b, 19	2, 3, 4, 19	
19	33.0	CH ₃	0.88	s	5, 18	2, 3, 4, 18	6a
20	104.9	CH	4.83	s	17*	5, 8, 9, 10	6a, 19
21	55.4	OMe	3.34	s		20	



†Selected correlations.

*Weak correlations.

Absolute configuration is arbitrary.

Luakuliide B (**35**)

Analysis of luakuliide B (**35**) by positive ion-mode HRESIMS revealed a $[M + Na]^+$ pseudo-molecular ion peak at m/z 373.1996, corresponding to the molecular formula $C_{20}H_{30}O_5$. The ^{13}C NMR spectrum displayed all 20 expected resonances, and analysis of the fully-coupled HSQC spectrum in conjunction with the 1H NMR spectrum accounted for all but two hydrogens, indicating the presence of an additional exchangeable proton relative to compound **33**.

Inspection of the 1H , ^{13}C NMR spectra and HSQC experiment of luakuliide B (**35**) revealed much structural similarity with that of **33**, particularly in the aliphatic region. As such, the structure was elucidated in the same fashion as luakuliide A (**33**). The characteristic furan signals were, however, replaced by an ester carbonyl (C-16: δ_C 171.5), an olefinic methine (δ_C 143.0, δ_H 6.87), a non-protonated olefinic centre (δ_C 131.0) and a hemi-acetal methine (δ_C 96.7, δ_H 6.10, $^1J_{CH}$ 176 Hz).

As illustrated in Figure 3.12, the methylene centres CH_2 -11 and CH_2 -12 appear at a slightly higher chemical shift, relative to those in **33** [$(CH_2$ -11: δ_C 23.6, δ_H a 1.91, b 1.73) and $(CH_2$ -12: δ_C 26.0, δ_H a 2.41, b 2.21)], and share reciprocal COSY and HMBC correlations with each other and the methine CH-9 (δ_C 58.0, δ_H 1.22). Connection from CH-5 to CH_2 -7 [$(CH$ -5: δ_C 51.8, δ_H 1.22), $(CH_2$ -6 δ_C 21.0, δ_H a 1.50, b 1.72) and $(CH_2$ -7 δ_C 41.9, δ_H a 1.68, b 1.42)] was evidenced by COSY correlations between the centres, and corroborating HMBC correlations. Further COSY and HMBC correlations established the C-1 to C-3 spin system [$(CH_2$ -1: δ_C 29.6, δ_H a 2.21, b 1.08), $(CH_2$ -2: δ_C 19.9, δ_H a 1.51, b 1.39) and $(CH_2$ -3: δ_C 39.8, δ_H a 1.43, b 1.19)], which was confirmed by a 1D TOCSY experiment as seen in **33**.

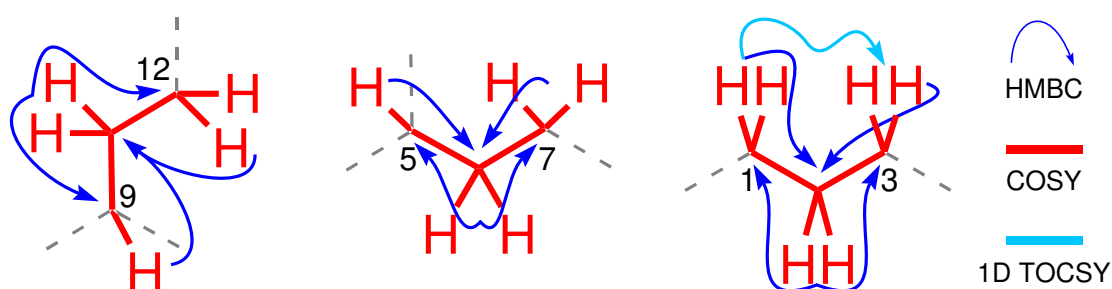


Figure 3.12 COSY, HMBC and 1D TOCSY correlations establishing the connections from C-9 to C-12, C-5 to C-7 and from C-1 to C-3 in **35**.

The *gem*-dimethyl pair [$(CH_3$ -18: δ_C 21.8, δ_H 0.90) and $(CH_3$ -19: δ_C 33.0, δ_H 0.90)] was again evidenced by the display of reciprocal HMBC correlations between the methyls and shared correlations to CH-5 (δ_C 51.8, δ_H 1.22), C-4 (δ_C 34.2) and CH_2 -3. As with **33**, HMBC correlations were observed from H_2 -3 and H-5 to the quaternary carbon C-4, and from H_2 -3 to CH-5, establishing the linear connections from C-1 to C-5 (Figure 3.13).

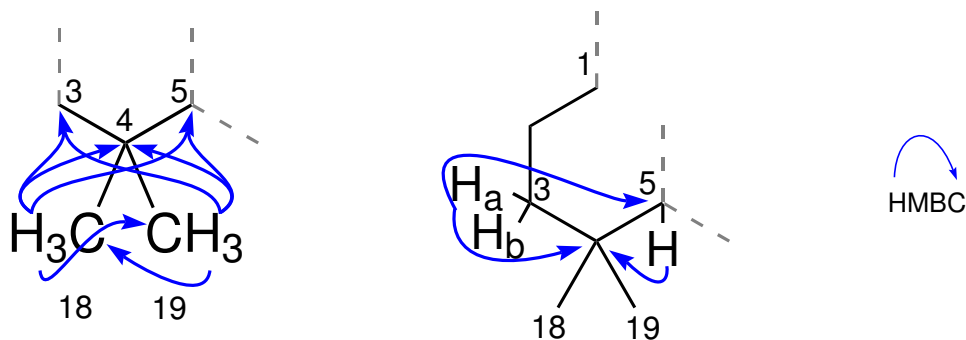


Figure 3.13 HMBC correlations establishing the *gem*-dimethyl substructure in **35** and the connections from C-1 to C-5.

As observed in compound **33**, the methyl singlet of **35**, CH₃-17 (δ_C 23.3, δ_H 1.31) shared weak COSY correlations with H-9 and CH₂-7 (δ_C 41.9, δ_H a 1.68, b 1.42), and displayed HMBC correlations to the oxygen-substituted C-8 (δ_C 84.0), CH-9 and CH₂-7. Protons of the methylenes CH₂-2 and CH₂-1 correlated to C-10 and C-9, respectively, completing the linear connectivity from C-1 to C-10, corroborated by HMBC correlations from H-9 to quaternary centres C-8 and C-10 (Figure 3.14).

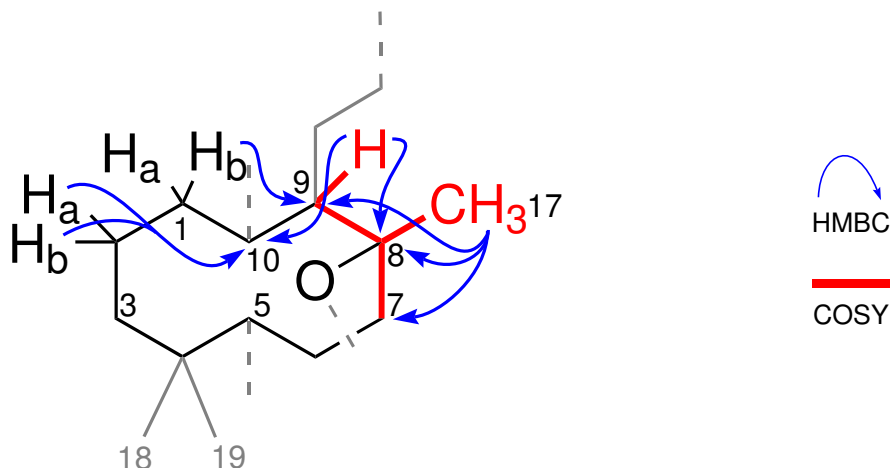


Figure 3.14 COSY and selected HMBC correlations completing the cyclodecane system of **35**.

The hemi-acetal methine CH-20 (δ_C 98.0, δ_H 5.35), displayed strong HMBC correlations to C-10 and weaker correlations to C-5 and C-9. These correlations reestablished the [4.4.0]-bicyclodecane system. Again, a weak HMBC correlation was observed from H-20 to C-8, establishing the hemi-acetal link in **35**, as shown in Figure 3.15.

As required by constraints of the fused tricyclic system, CH-20 and the oxygen-substituent of C-8 occupy 1,3-diaxial positions on ring A, with CH₃-17 equatorial at C-8. As in **33**, the large $^3J_{HH}$ coupling between H-5 and H-6a (13.6 Hz) was indicative of their 1,2-diaxial relationship on ring B. Similarly, the observation of

a weak COSY correlation between H-5 and H₃-19 placed these resonances as 1,2-diaxial with respect to ring A, confirming *trans*-fusion of the [4.4.0]-bicyclodecane system. The 1D TOCSY-NOESY experiment utilised in **33** to establishing configuration at CH-9 could not be employed here owing to small sample size. However, similarities in chemical shift and $^3J_{\text{HH}}$ couplings of CH-9 between **35** and **33** suggests retention of relative stereochemistry about C-9, placing the CH₂-11 to C-16 substructure in an equatorial position.

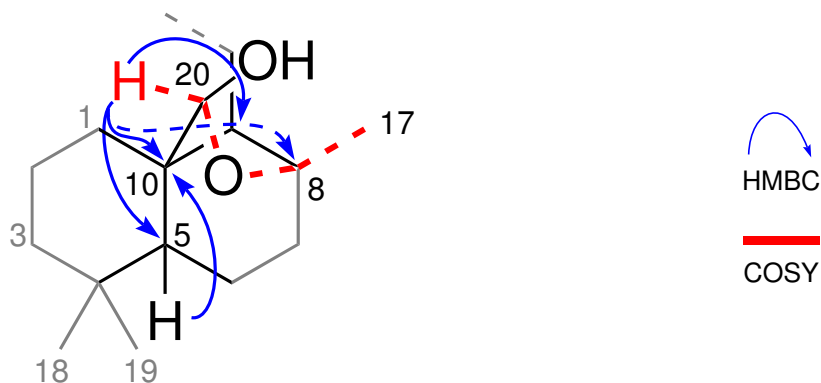


Figure 3.15 COSY and selected HMBC correlations used in completion of the [4.4.0]-bicyclodecane system and assignment of the bridging hemi-acetal moiety in **35**. Dashed lines and arrows indicate weak correlations.

Remaining unaccounted for by the tricyclic system were three sp^2 carbon resonances [(C-13: δ_{C} 131.0), (CH-14: δ_{C} 143.0, δ_{H} 6.87 $^1J_{\text{CH}}$ 177 Hz) and (C-16: δ_{C} 171.5)], and an oxygen-substituted methine (CH-15: δ_{C} 96.7, δ_{H} 6.10, $^1J_{\text{CH}}$ 176 Hz). On the basis of chemical shift and $^1J_{\text{CH}}$ couplings the resonances were assigned as a tri-substituted alkene, an ester carbonyl and a second hemi-acetal methine. The vicinal positioning of CH-14 and CH-15 was evidenced by reciprocal COSY and HMBC correlations. The C-12 to C-13 bond was established by HMBC correlations H-14 to quaternary C-13 and CH₂-12. Further HMBC correlations were observed from the CH₂-12 methylene protons to quaternary C-13, CH-14 and carbonyl C-16 confirming bonds from C-13 to C-14 and C-16. This established the α, β -unsaturated ester function, C-16–C-13–CH-14 (Figure 3.16).

The substituted [4.4.0]-bicyclodecane tricyclic system (C-1 to C-20) and the C-14 to C-16 enoate accounted for all but one degree of unsaturation associated with the molecular formula. The combination of chemical shift and high $^1J_{\text{CH}}$ for CH-15 (δ_{C} 96.7, δ_{H} 6.10, $^1J_{\text{CH}}$ 176 Hz) is consistent with dioxy-substitution of the centre. As such, an α -substituted γ -hydroxybutenolide moiety linking the hemi-acetal CH-15 and carbonyl C-16 is proposed (Figure 3.17). This final substructure satisfies the oxygen count and unsaturation requirements of the molecular formula.

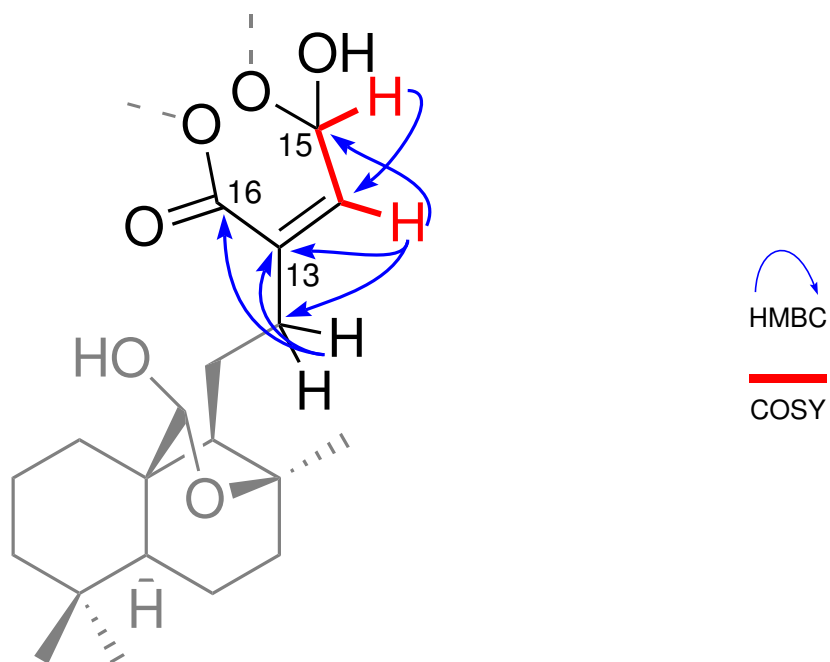


Figure 3.16 COSY and HMBC correlations evidencing the substituted α,β -unsaturated ester (C16–C13–C14) and γ -hemi-acetal methine (C-15) in **35**.

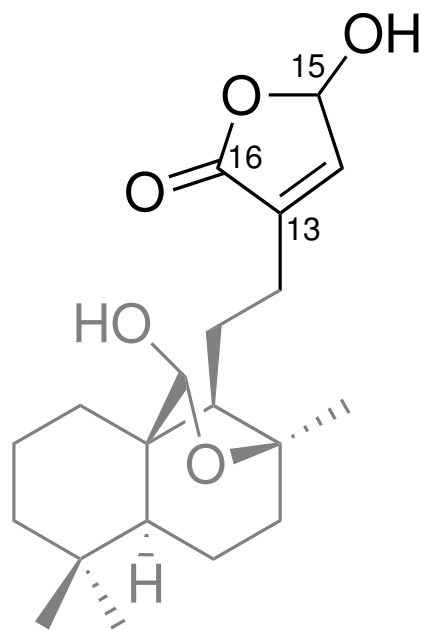
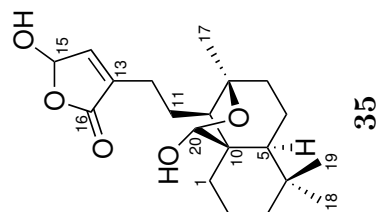


Figure 3.17 The α -substituted γ -hydroxybutenolide moiety of **35**.

Table 3.4 NMR Spectroscopic Data of Luakuliide B (**35**), (600 MHz, CDCl₃).

Position	¹³ C		¹ H		J (Hz)	COSY	HMBC (¹ H → ¹³ C)
	δ (ppm)	mult	¹ J _{CH} (Hz)	δ (ppm)			
1	a	29.6	mult	130	12.8	1b, 2a, 2b, 3a	2, 3, 10
	b		CH ₂	122	13.3, 3.8	1a, 2a, 2b	2, 3, 9, 10
2	a	19.9	CH ₂	128	14.2	1a, 1b, 2b, 3a, 3b	1, 3, 4, 10
	b			123	13.8, 3.0	1a, 1b, 2a, 3a, 3b	1, 3, 4, 10
3	a	39.8	CH ₂	128	12.5, 5.3	1a, 1b, 2a, 2b, 3b	1, 2, 4, 5
	b			122	13.9, 4.2	2a, 2b, 3a	1, 2, 18, 19
4		34.2	C				
5		51.8	CH	123	13.6, 4.8	6a, 7b, 19*	4, 6, 7, 10, 18, 19
6	a	21.0	CH ₂	126	1.50	5, 7a, 7b, 17*	5, 7
	b			126	1.72		5, 7
7	a	41.9	CH ₂	121	1.68	6b, 7b, 17	5, 6, 8, 9, 17
	b			127	1.42	5*, 6a, 7a, 9*, 17	6, 8*, 9, 17
8		84.0	C				
9		58.0	CH	129	1.20	11a, 11b	5*, 8, 10, 11, 12, 20
10		52.1	C				
11	a	23.6	CH ₂	124	7.2		
	b			126	1.91	9, 11b, 12a, 12b	8, 9, 12, 13
12	a	26.0	CH ₂	123	1.73	9, 11a, 12a, 12b	8, 9, 12, 13
	b			128	2.41	11a, 11b, 12a, 12b	9, 12, 13, 14, 15
13		131.0	C		2.21	11a, 11b, 12a	9*, 12, 13, 14, 15
14		143.0	CH	177	6.87	12a, 12b, 15	12*, 13, 15, 16
15		96.7	CH	176	6.10	14*	13*, 14, 16
16		171.5	C				
17		23.3	CH ₃	126	1.31	7a, 7b, 9, 20*	6*, 7, 8, 9, 11*
18		21.8	CH ₃	123	0.90	3a, 3b, 19	2, 3, 4, 19
19		33.0	CH ₃	124	0.90	5*, 18	2, 3, 4, 18
20		98.0	CH	171	5.35	17*	5, 8, 9, 10

*Weak correlations.
Absolute configuration is arbitrary.



Luakuliide C (**36**)

The observation of a $[M + Na]^+$ pseudomolecular ion peak (m/z 373.1990) by positive ion-mode HRESIMS analysis of luakuliide C (**36**), indicated that **36** has a molecular formula of $C_{20}H_{30}O_5$, like that of **35**. The differences in HPLC retention times between **35** and **36** implied an isomeric relationship between the metabolites. Inspection of the 1D and 2D NMR spectra of **36** indicated that the [4.4.0]-bicyclodecane system (C-1 to C-12) observed in **33–35** is conserved. However, subtle changes in chemical shift of the 1H and ^{13}C resonances associated with the γ -hydroxybutenolide moiety suggested some change in functionality.

Consistent with the isomeric relationship between **35** and **36**, the resonances C-13 to C-16 were assigned once more as an ester carbonyl (δ_C 171.0), a tri-substituted alkene (δ_C 168.9; δ_C 117.9, δ_H 5.90, $^1J_{CH}$ 181 Hz), and a hemi-acetal methine (δ_C 98.6, δ_H 5.99, $^1J_{CH}$ 177 Hz). Interpretation of COSY and HMBC correlations between the resonances, centres were assigned as a β -substituted- γ -hydroxybutenolide (Figure 3.18). The change in polarisation of the C-13 to CH-14 double bond in **36**, δ_C 168.9 and 117.9, compared to that of **35**, δ_C 131.0 and 143.0, is consistent with the change in alkyl substitution relative to the carbonyl centre.

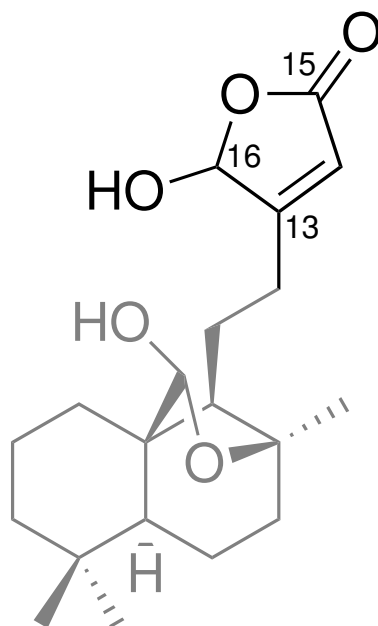


Figure 3.18 The β -substituted- γ -hydroxybutenolide moiety of **36**.

The same trends in chemical shift are also observed in the γ -hydroxybutenolide moieties of *iso*-secothorectolide (**23**), luffarin Q (**24**) and luffarielolide (**26**) isolated during this study (Tables C.1, C.2 and C.4). Similar trends in bond polarisation are also observed in the γ -hydroxybutenolides teuponin (**37**)⁸⁹ and acuminolide (**38**)⁹⁰, which were isolated from the terrestrial organisms *Teucrium japonicum* and *Neouvaria acuminatissima*, respectively.^{89,90} Single crystal X-ray analysis of

teuponin (**37**) and acuminolide (**38**) confirmed the substitution patterns of the two γ -hydroxybutenolide groups. Differences in hybridisation of the carbonyl and hemiacetal centres, and lengths of the C-O and C=O bonds are clearly illustrated in the crystal structures. Comparisons of the ^1H and ^{13}C NMR spectra of **35** and **37**, and **36** and **38**, are shown below in Table 3.5, providing support for the structural assignment of **35** and **36**.

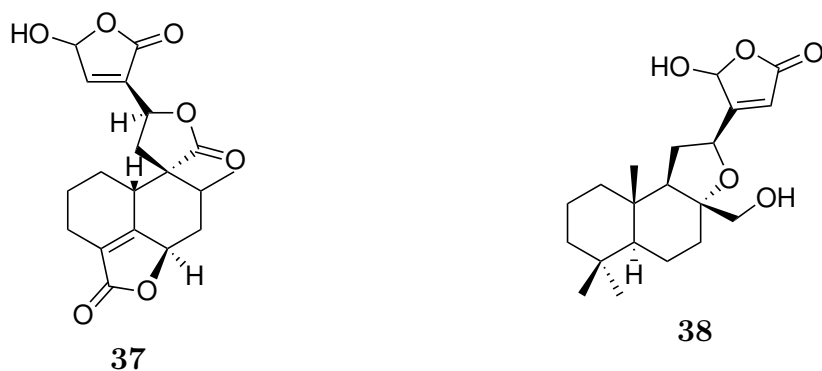
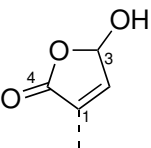
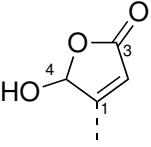


Table 3.5 NMR Spectral Data for the γ -Hydroxybutenolide Moieties in **35–38**.

Position	mult	35 * and 36 *		37 † and 38 ‡		Difference§	
		δ_{C}	δ_{H}	δ_{C}	δ_{H}	$\Delta\delta_{\text{C}}$	$\Delta\delta_{\text{H}}$
							
1	C	138.7		135.8		-2.9	
2	CH	142.8	6.87, brs	147.7	7.67, brs	5.1	0.8
3	CH	96.6	6.10, brs	100.5	6.61, brs	3.9	0.51
4	C	171.3		169.4		-1.9	
							
1	C	168.9		169.0		0.1	
2	CH	117.9	5.90	117.2	6.02	-0.7	0.12
3	CH	171.0		170.9		-0.1	
4	C	98.6	5.99	98.4	6.26	-0.2	0.27

* CDCl_3 , 600 MHz

† d_5 -pyridine, 400 MHz

‡ CDCl_3 , 300 MHz

§ $\Delta\delta = \delta_{\mathbf{37-38}} - \delta_{\mathbf{35-36}}$

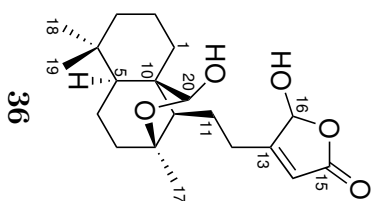
The high $^1J_{\text{CH}}$ values of the methines CH-15 and CH-16 in the γ -hydroxybutenolide moieties of **35** and **36** are noteworthy at 177 Hz and 181 Hz, respectively. An equivalent carbon-substituted sp^2 -hybridised centre could be expected to have a $^1J_{\text{CH}}$ value of ca. 160 Hz, and the coupling constants appear to have increased in magnitude due to the inductive electron-withdrawing qualities of the nearby oxygen atoms and strain imposed by the five-membered ring. Easily extracted from ^{13}C -coupled HSQC spectra, $^1J_{\text{CH}}$ values are frequently invoked in functional group determination, there is value in comprehensively compiling J -coupling values associated with these commonly isolated heterocycles, in addition to those found in more unusual synthetic substrates. Such a resource would be invaluable to spectroscopic structural elucidation.

Table 3.6 NMR Spectroscopic Data of Luakuliide C (**36**), (600 MHz, CDCl₃).

Position	¹³ C		¹ H		COSY	HMBC (¹ H → ¹³ C)		
	δ (ppm)	mult	¹ J _{CH} (Hz)	δ (ppm)			mult	J (Hz)
1	29.5	CH ₂	131	2.23	brd	16.6	1b, 2a, 2b, 3a	2, 3, 10
			122	1.08	td	13.4, 3.9	1a, 2a, 2b	2, 3, 9, 10
2	20.0	CH ₂	126	1.39	qd	13.7, 2.6	1a, 1b, 2b, 3a, 3b	1, 3, 4, 10
			122	1.52	dt	16.4, 2.4	1a, 1b, 2a, 3a, 3b	1, 3, 4, 10
3	41.9	CH ₂	125	1.44	d	13.4	1a, 1b, 2a, 2b, 3b	1, 2, 4, 5
			122	1.19	t	12.7	2a, 2b, 3a	1, 2, 18, 19
4	34.2	C						
5	51.8	CH	123	1.22	dd	10.1, 5.3	6a, 7b, 19*	4, 6, 7, 10, 18, 19
6	21.2	CH ₂	128	1.52	d	8.5	5, 7a, 7b, 17*	5, 7
			121	1.72	dt	13.3, 5.4		5, 7
7	40.0	CH ₂	122	1.68	dd	13.5, 5.5	6b, 7b, 17	5, 6, 8, 9, 17
			126	1.42	m		5*, 6a, 7a, 9, 17	6, 8, 9, 17
8	83.8	C						
9	57.8	CH	129	1.20	dd	8.4, 2.2	11a, 11b	5, 8, 10, 11, 12, 20
10	52.2	C						
11	23.0	CH ₂	128	1.92	brm		9, 11b, 12a, 12b	8, 9, 12, 13
			121	1.82	ddd	14.9, 8.8, 5.0	9, 11a, 12a, 12b	8, 9, 12, 13
12	28.6	CH ₂	127	2.48	ddd	16.4, 10.8, 4.7	11a, 11b, 12a, 12b	9, 12, 13, 14, 15
			128	2.38	dt	9.9, 5.4	11a, 11b, 12a	9, 12, 13, 14, 15
13	168.9	C						
14	117.9	CH	181	5.90	brs		12a, 12b, 15, 16*	13, 15, 16
15	171.0	C						
16	98.6	CH	177	5.99	brs		12a*, 12b, 14	12*, 13, 15
17	23.3	CH ₃	126	1.30	s		7a, 7b, 9, 20*	6*, 7, 8, 9, 11*
18	21.8	CH ₃	124	0.90	s		3a, 3b, 19	2, 3, 4, 19
19	33.0	CH ₃	124	0.90	s		5*, 18	2, 3, 4, 18
20	97.8	CH	170	5.36	s		17*	5, 8, 9, 10

*Weak correlations.

Absolute configuration is arbitrary.



3.2.2 Biological activity of the luakuliides

Labdane diterpenes have been associated with antimicrobial, antiinflammatory, immuno- and enzyme-modulatory biological activities.⁹¹ As such, **33** and **34** were assessed for cytotoxicity, antifungal and immunomodulatory activity.⁹² In a standard 48 h proliferation MTT assay **33** and **34** displayed weak inhibition HL-60 cell line with IC₅₀ values of 21.7 and 43.5 $\mu\text{mol L}^{-1}$, respectively, and negligible inhibition of a drug-sensitive *S. cerevisiae* strain.⁹³ Their immunomodulatory activities were far more significant. Luakuliide A (**33**) and the methyl acetal **34** inhibited production of nitric oxide (NO) in stimulated splenocytes, while **34** also affected an increase in interferon- γ (INF- γ).⁹⁴ Increased production of the proinflammatory cytokine, tumor necrosis factor- α (TNF- α) in stimulated macrophages was also observed and lesser response was affected in non-stimulated cells.⁹²

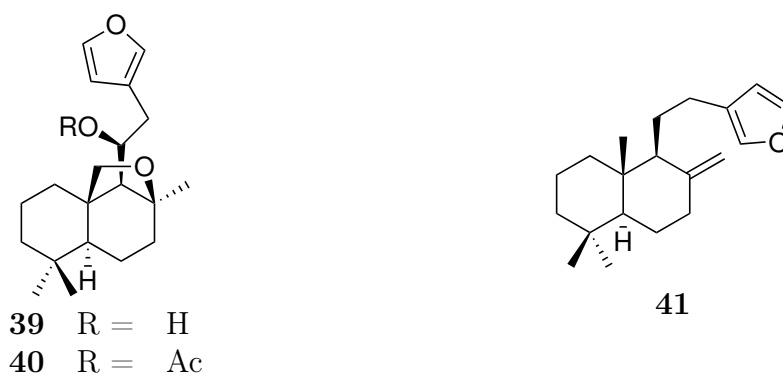
Inflammation is fundamental to many pathological conditions, from triggering and perpetuating autoimmune diseases through to immune responses to foreign bodies.⁹⁵ The macrophage white blood cells line are key to both the initiation and direction of inflammatory processes via TNF- α and NO.⁹⁶ TNF- α acts in transduction of signals pertaining to cell activation, proliferation and apoptosis, enhancing the overall inflammatory response.⁹⁷ Nitrous oxide has roles in the innate and adaptive immune systems including macrophage phagocytosis, neutrophil migration, and natural killer T-cell activity.⁹⁸ Hence, small molecules which affect the regulation of T-cell activation and influence NO and TNF- α are of interest with respect to the treatment of autoimmune and inflammatory disorders.^{92,99}

3.2.3 Labdane diterpenes

As products of the ubiquitous isoprenoid pathway, cyclised diterpene metabolites have been extensively isolated from terrestrial sources, especially the Angiosperm families Asteraceae and Labiatae.¹⁰⁰ The skeleton name is derived from “labdanum”, a resin extracted from the rockroses *Cistus* (family Cistaceae), from which the first members of the class were initially obtained.¹⁰¹

The labdane skeleton is infrequently encountered within the marine environment, examples including cacofurans A (**39**) and B (**40**), isolated from an Okinawan sponge specimen of *Cacospongia* sp. (order Dictyoceratida, family Thorectidae).¹⁰² As seen in the luakuliide skeleton, oxidation of C-8 and subsequent nucleophilic attack on the CH₃-20 methyl (aldehyde) generates the C-8 to C-20 ether or hemi-acetal bridge. The source of differentiation between the luakuliides and cacofurans is oxidation at C-11 compared to further oxidation at C-20.¹⁰² Investigation of another *Cacospongia* specimen from the Philippines yielded several furano and meroquinone diterpenes

metabolites, including **41**, where the C-8 methyl substituent is replaced by an exocyclic methyldiene. Sesterterpene luffariellolide (**26**, isolated from PTN4_10B) was encountered during the same investigation, illustrating the promiscuity of the compound.¹⁰³



Furan moieties, such as that of luakuliide A (**33**), frequently undergo further oxidation forming the entities such as butenolide or 2-furanone functions, and the γ -hydroxybutenolide moieties featured in **35** and **36**. Many metabolites featuring both these functions have been reported, although this oxidation could conceivably occur naturally within the organism or during isolation.¹⁰⁴

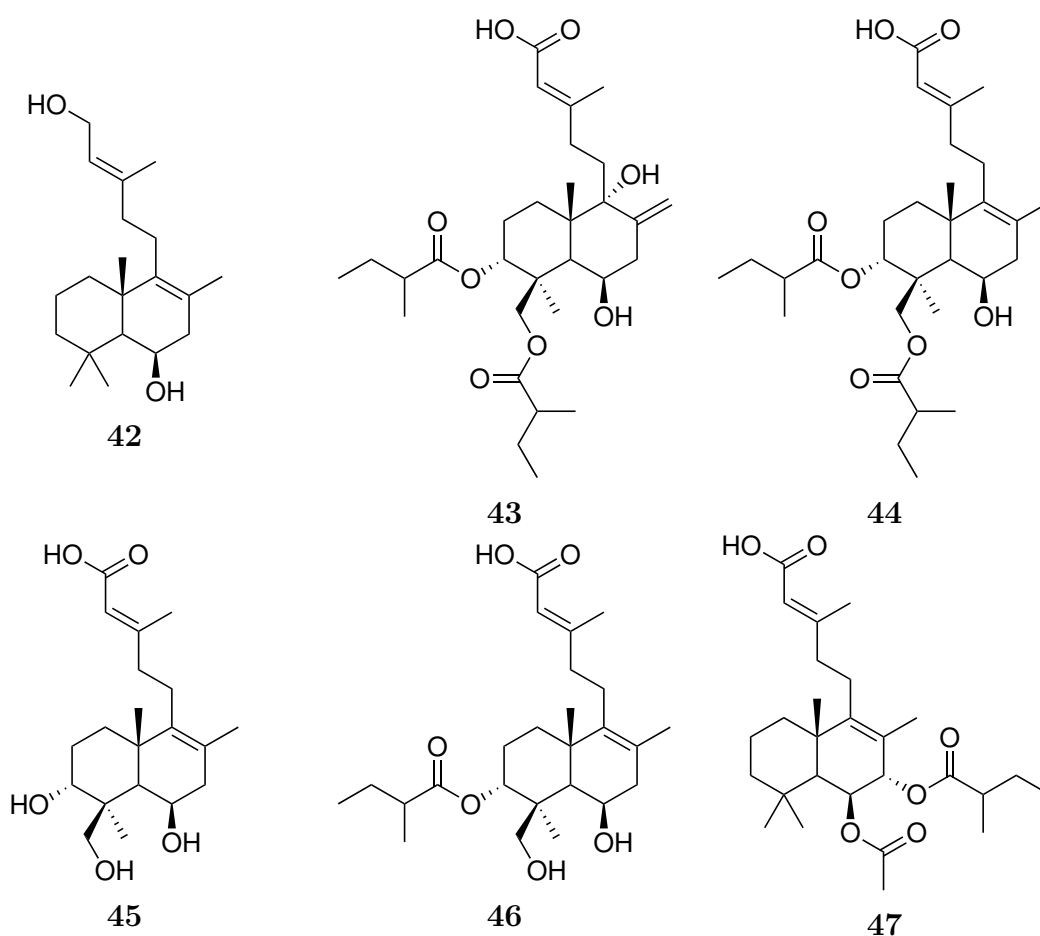
Intertidal limpets of the *Trimusculus* genus, are also rich sources of such cyclic diterpenes. Collections from central Chile of *T. peruvianus* yielded four new diterpenes metabolites with the characteristic labdane bicycle and an acyclic terminal isoprene unit.¹⁰⁵ Further investigation of the same species led to the isolation of several new additions to this class including **42–47**, which differ in oxidative substitution of the labdane bicycle.^{106,107} South African collections of *T. costatus* yielded similar labdanes,¹⁰⁸ in addition to $5\alpha,8\alpha$ -epidioxy sterols similar to **27** and **28** isolated from the plakinid sponge PTN3_19D.¹⁰⁹

3.2.4 Biogenesis of luakuliides A–C

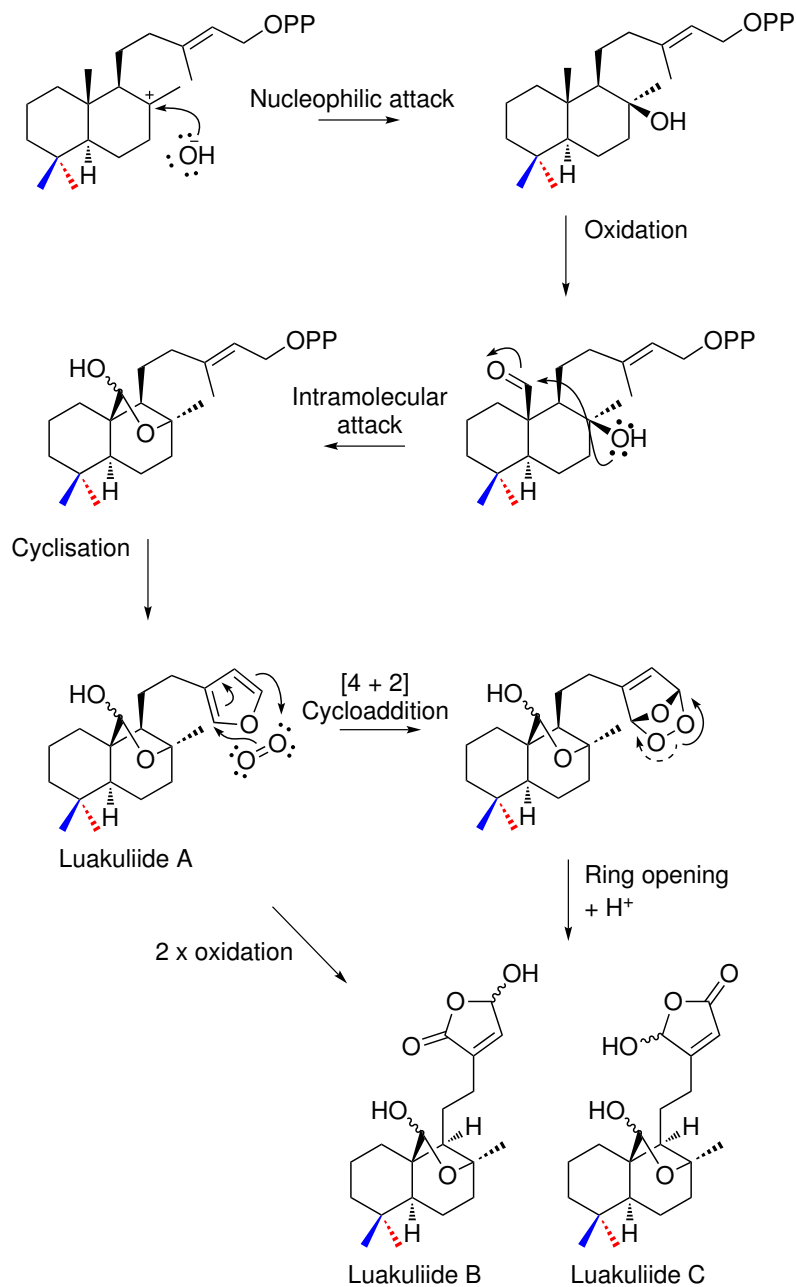
Isoprene biosynthesis and formation of the different terpene classes is well documented. Formation of many carbon skeletons, including that of the labdanes, has also been well explored and confirmed via both the mevalonate and non-mevalonate pathways.¹¹⁰

Cyclisation of geranylgeranyl pyrophosphate (GGPP) by either of two ways forms the four diastereomers of the labdane skeleton, differing in configuration at C-5 and C-9.¹⁰⁴ The labdane skeleton is a precursor to many other diterpenes skeletons; diastereomers of the labdadienyl cation can undergo a series of 1,2-hydride and methyl shifts. Concerted migrations generate a *trans*-decalin product, and

cis- relationship between C-8 and C-10 methyls. However, the series of stepwise migrations pauses at the C-5 cation intermediate, giving rise to either *cis*- or *trans*-fused clerodane products depending on which of the two C-4 methyl substituents migrates. This process is depicted in Scheme 3.1 for one labdadienyl diastereomer. Alternatively, capture of the C-5 cation of the halimane skeleton by an exogenous nucleophile generates species including ambliol B (**25**),¹¹¹ isolated in this study from PTN4_10B. This theory of dual mechanisms is supported by the high proportion of *trans*- over *cis*-decalin products, and the isolation of partially rearranged labdanes such as the halimane **25**.



Historical confusion within the literature has arisen over the absolute stereochemistry of the labdane, halimane and clerodane skeletons and the governing nomenclature. Stereochemical classification is now made in reference to the original isolate clerodin (**48**); those with the same absolute configuration are *neo*- while the enantiomeric forms are *ent-neo*-labdanes and -clerodanes. As indicated in Scheme 3.1, further division is made in reference to the *cis*- or *trans*-decalin ring junction. Relative orientation of C-8 and C-9 methyls is the final source of differentiation within the skeletons.



Scheme 3.2 Proposed pathway for generation of the hemi-acetal functions, furan and γ -hydroxybutenolide moieties of luakuliides A–C (**33–36**).

3.2.5 Concluding remarks

Labdane metabolites are infrequently encountered in marine organisms. In this case their characteristic *gem*-dimethyl feature was identified early during analysis of the HMBC spectra from crude fractions, prompting further purification and eventual isolation of the luakuliides. Differentiating these structures from other labdanes is the hemi-acetal bridge from C-20 to C-8, which also provides evidence for capture of the C-8 labdadienyl cation. The 1D TOCSY-NOESY NMR experiment was integral to assigning the *trans*-fusion of the [4.4.0]-bicyclodecane system and relative stereochemistry of the luakuliides.

Luakuliide A (**33**) and its methyl acetal derivative (**34**) display interesting biological activity. The metabolites have significant macrophage stimulatory activity, promoting a proinflammatory response, which is complemented by increased activity in T-cells. Although in contrast to antiinflammatory properties frequently demonstrated by labdane diterpenes, these findings illustrate the potential of the luakuliides as new immunomodulatory agents.

Chapter 4

Chemical Analyses of Plakinid Sponges

Investigation of two plakinid sponge specimens yielded several new polyketide metabolites: the α -pyrones lehualides E–K and four cyclic peroxides. Analysis of the HMBC experiments of semi-purified fractions from each of the organisms was integral to their selection for further study. During the selection process the α -pyrone of the lehualides, and the oxygenated backbones of the cyclic peroxides were partially elucidated, prompting further investigation of the organisms.

4.1 The family Plakinidae

Plakinidae, the sole family of the order Homosclerophorida¹¹³ encompasses several valid genera: *Plakina*, *Plakortis*, *Plakinastrella*, *Placinolopha*, *Corticium*, *Pseudocorticium*, and *Oscarella* (Figure 4.1). Except for *Oscarella*, these genera possess a siliceous skeleton, formed by either a uniform arrangement of calthrops, diod and triod spicules, or a combination of the two. Found mainly in warm waters, the encrusting sponges are generally dark purple and grey in appearance, with a lighter tan and beige interior. With cork-like, dense and rubbery textures, their velveteen surfaces are frequently covered with wide, shallow nodules.^{38,113}

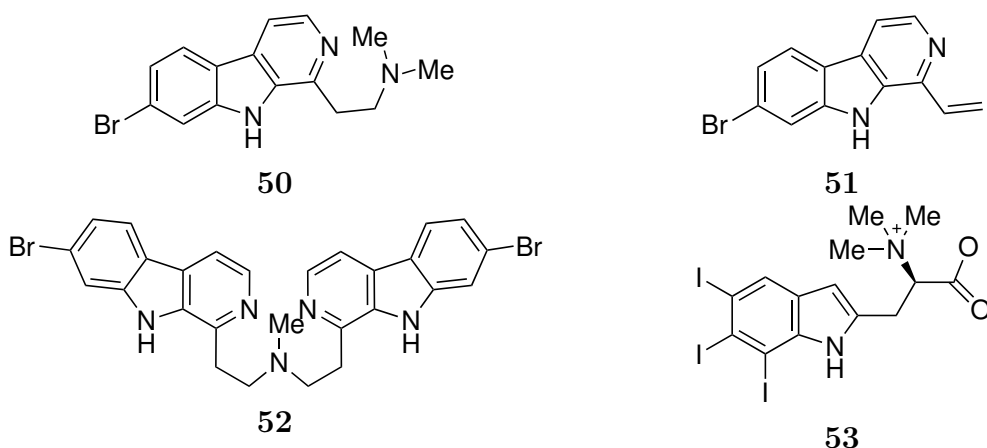
Order Homosclerophorida
Family Plakinidae
Genus *Plakina*
Genus *Plakortis*
Genus *Plakinastrella*
Genus *Placinolopha*
Genus *Corticium*
Genus *Pseudocorticium*
Genus *Oscarella*

Figure 4.1 Taxonomic classification of the order Homosclerophorida, after Hooper and van Soest.³⁸ Genera encountered during this study are shown in blue.

4.1.1 The *Plakortis* and *Plakinastrella* genera

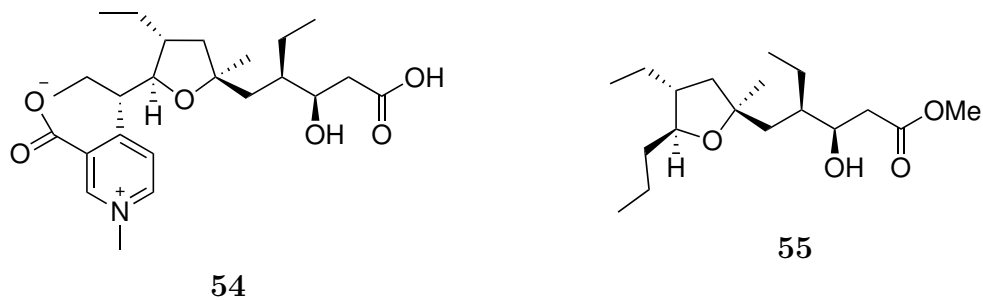
The phylum Porifera is notorious for its taxonomic uncertainty. In the case of the closely related genera *Plakortis* and *Plakinastrella*, their simple spiculation makes generic distinction and further speciation particularly difficult to establish. The spicule profile of *Plakortis* specimens is mainly composed of irregular diods in a single size-class and the occasional triod, while *Plakinastrella* sponges are thought to exhibit up to three size-classes of diods, triod spicules and calthropes.

A range of biologically active compounds have been reported from species within these two genera. A series of β -carboline, the plakortamines (**50–52**), were isolated in conjunction with epiplakinic acids.¹¹⁴ These simple brominated alkaloids are often associated with ascidians (phylum Chordata), such as the antiviral eudistomins from the Caribbean ascidian *Eudistoma olivaceum*.¹¹⁵ Although uncommon, this class of metabolites is preceded within sponges, sharing structural features with the polycyclic fascaplysin alkaloids, such as 14-bromohomofascaplysin (**29**).



Chemical investigations by Costantino and co-workers of Caribbean collections of *Plakortis simplex* have also yielded a series of iodoindole metabolites.^{116,117} Plakohypaphorine E (**53**) and others of the class represent the first naturally occurring iodoindole metabolites. Subsequently, the same research group reported the pyridinium derivatives simplakidine (**54**)¹¹⁸ and simplexidine¹¹⁹ from the same organism. Simplakidine combines the pyridinium nucleus shared by simplexidine with the polyketide framework observed in plakortether B (**55**), an archetypal isolate of sponges from this family.

A rich complement of type I polyketide metabolites have been isolated from *Plakortis* sponges. The type I polyketide synthesis pathway (PKS1) is also active in macrolactone biosynthesis, although the *Plakortis* metabolites generally feature an acid-substituted five- or six-membered heterocycle within a long, largely saturated carbon skeleton. Such carbon backbones, in combination with a terminal carboxylic



acid, contributed to their assumed origins in fatty acid synthesis.¹²⁰ The mechanisms of PKS1 and fatty acid synthesis both involve chain growth by C₂, however, PKS1 utilises a great variety of starter units, and the different propagation units specify acetate, propionate, butyrate and methyl-propionate groups.¹²¹ These generate a carbon skeleton featuring methyl, ethyl, propyl and *gem*-dimethyl side-branches, as observed in plakortether B (**55**, Figure 4.2). Products of PKS1 frequently exhibit great variation in oxidation, and the various reduction units used in PKS1 are also enantiospecific.

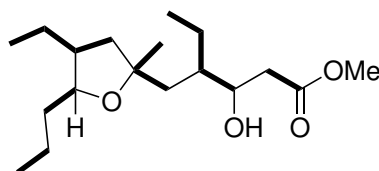
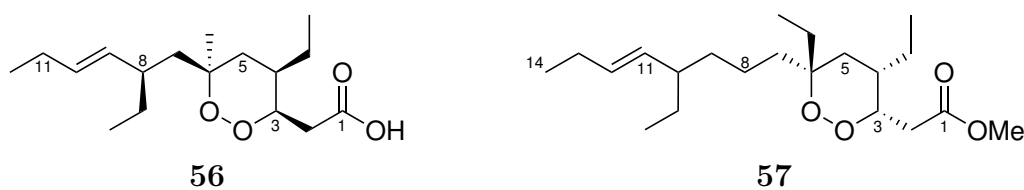


Figure 4.2 Depiction of the PKS1 propagation units used in the biosynthesis of plakortether B (**55**). The metabolite comprises three acetate, one propionate and two butyrate units.

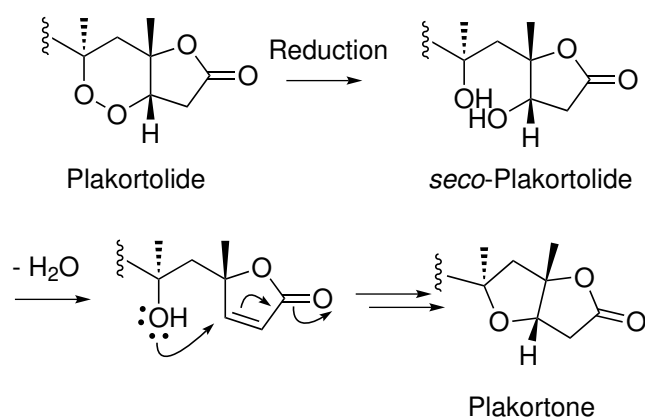
Cyclic peroxides are a distinctive class of polyketide metabolite frequently isolated from both the *Plakortis* and *Plakinastrella* genera. The first example, plakortin (**56**), a potent antibiotic, was isolated from a *Plakortis halichondrioides* specimen in 1978.¹²² Rich augmentation of both the acid-substituted 1,2-dioxolane nucleus and substituents of **56** has given rise to a contingent of structurally related compounds categorised into several arbitrary classes. Plakortide F (**57**), retains the acid-substituted peroxide nucleus of **56** although the compounds differ in absolute configuration. Variation in substitution about the cyclic peroxide core at C-4 and C-6 reflects a change in propagation units during biosynthesis, while the inclusion of an additional acetate monomer during formation of **57** (C-7–C-8) accounts for the difference in chain length.



Cyclisation of the acid forms the peroxy-lactone bicyclic system, characteristic of

the plakortolide class. The first example was described in 1980, although not fully characterised until 1991 by Davidson *et al.*¹²³ The absence of the free acid in the plakortolide skeleton frequently corresponds to decreased biological activity compared to the carboxylic acid analogue. Although the ring fusion is exclusively *cis*, varied configuration at C-6 forms two diastereomeric carbon skeletons. The two are easily distinguishable by NOE correlations between the C-4 and C-6 methyl substituents and changes in the ¹H chemical shift of H-5a, ca. 0.1 ppm.

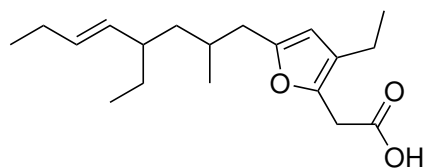
Ring-opening of the plakortolide cyclic peroxide generates the *seco*-plakortolide diols. Loss of ring-strain lessens diastereotopic differentiation of the CH₂-5 methylene protons allowing spectroscopic distinction between the two forms. Upon isolation, *seco*-plakortolides are known to undergo facile intramolecular condensation and Michael-type addition of the C-6 hydroxyl to C-3 of a butenolide intermediate forming hydrofuran derivatives, plakortones (Scheme 4.1).¹²⁴ Co-isolation of all three forms of the same carbon skeleton could cast doubt over the natural origins of *seco*-plakortolide and plakortone structures.¹²⁵ However, plakortone skeletons bearing ethyl substituents at C-4 and C-6 have been isolated in the absence of plakortolide analogues from Caribbean *Plakortis halicondrioides* and *P. simplex* specimens.^{126,127}



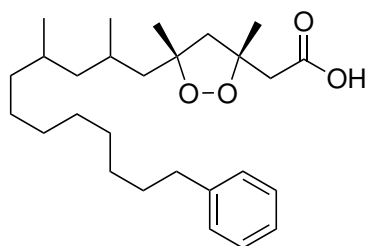
Scheme 4.1 Conversion of plakortolides to plakortones via *seco*-plakortolides by reduction, intramolecular condensation and Michael-type addition, after Yong *et al.*¹²⁴

This parade of polyketide metabolites displays further structural variation. Isolated from a Dominican *Plakortis halichondrioides* specimen, glánvillic acids A and B (A, **58**),¹²⁸ for which stereochemistry has not been defined, bear an aromatic furan ring (C-3–C-6). A host of other *Plakortis* metabolites bear an alkyl group varying in saturation, branching and chain length. Further additions to the contingent of cyclic peroxides are the plakinic and epiplakinic acids, which were first encountered from Palauan specimens of *P. nigra*. As demonstrated by **59** and **60**, the two classes possess lengthy methyl-branched alkyl backbones terminating in a phenyl ring, derived from a benzoate starting unit.¹¹⁴ These structural characteristics are shared with members of the plakortolide class.¹²⁴ The two acid classes are differentiated by

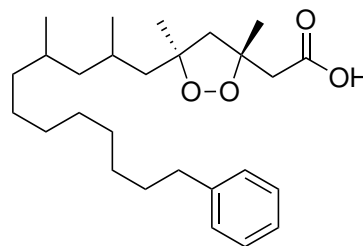
the orientation of the C-3 and C-5 methyl substituents about the 1,2-dioxane ring, *cis*- in the plakinic acids (**59**), and *trans*- in the epiplakinic acids (**60**). One example of epiplakinic acid decarboxylation has been reported.¹²⁹



58

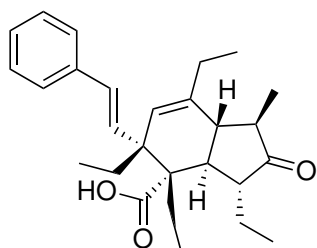


59

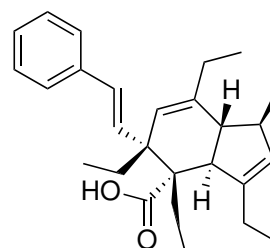


60

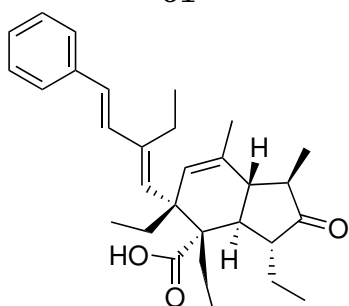
Spiculoic acids A and B (**61** and **62**) were isolated from a *P. angulospiculatus* specimen,¹³⁰ and possess an unprecedented carbon skeleton. The biosynthetic origins of the polyketide-derived structures are not clear, but the skeleton is thought to incorporate a phenyl acetate starter unit and four butyrate units. A post-assembly enzyme-catalysed intramolecular [4+2] cycloaddition is proposed for formation of the fused bicycle, which contains the expected cyclohexene ring.¹³⁰ Recent investigation of a *P. zygompha* specimen by Berrue *et al.* uncovered three further spiculoic acids, and two zygomphic acids (**63** and **64**).¹³¹ Common to both classes is the fused bicyclic nucleus, with structural variation arising from the inclusion of different PKS1 monomers.



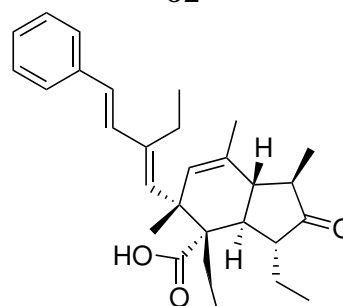
61



62

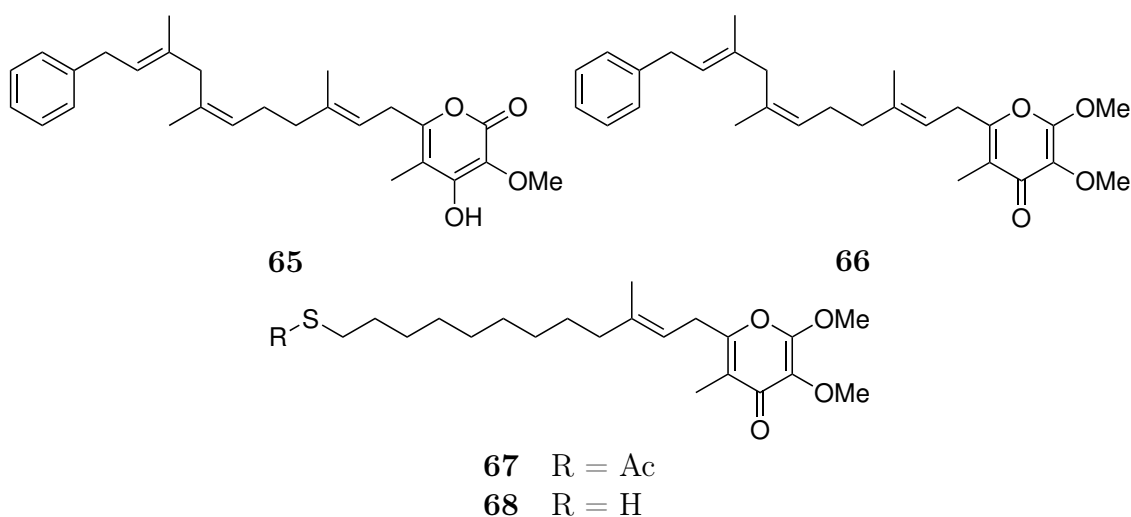


63



64

While this series of polyketide metabolites are most probably of bacterial origin, they appear to be exclusive to sponges of the *Plakortis* and *Plakinastrella* genera, indicating a taxonomically-specific symbiosis. Another class of polyketide metabolites unique to plakinid sponges is the lehualides. The class differs from more common plakinid isolates, bearing α - or γ -pyrone moieties in place of the cyclic peroxides. The first members of the class have a pseudo-terpenoid appearance owing to the number of methyl-substituted alkene functions present in the extended alkyl chain. Terminal substituents encountered in the lehualides include phenyl rings, and a variety of sulfur functionalities of which the biosynthetic origins are unclear. The first members of this series, lehualides A–D (**65**–**68**), were reported in 2005 from a Hawai’ian *Plakortis* specimen,¹³² and the succinct synthesis of lehualide B (**66**) was reported in 2010 by Jeso *et al.*¹³³ Seven additions to this class, lehualides E–K (**69**–**75**), were isolated during this study from a Tongan *Plakortis* sp. and are detailed in the following sections.¹³⁴



4.2 α -Pyrone metabolites from *Plakortis* sp.

The sponge specimen PTN3_20A (Figure 2.12) was collected at a depth of 12–15 m from the ceiling of a large cave on ‘Eua Island in November 2008. Identified as a species of *Plakortis*, similar to *P. ceylonica* (Dendy, 1905), the sponge morphologically formed small oval pendant encrustations about 3 cm thick, with a cork-like, rubbery and dense texture. Smooth to the touch, the surface was dark chocolate-purplish brown in colour and covered in wide shallow nodules ca. 3 mm high. Diod spicules (180–250 μm long, Figure 4.3) were isolated via centrifuge following HNO_3 treatment of the tissue, aiding classification of the organism as a *Plakortis* species. Attempts were made to recollect the organism in the Vava‘u group but were unsuccessful. The nondescript appearance and growth of the sponge

in dimly-lit caves may have both been contributing factors leading to specimens going unnoticed.

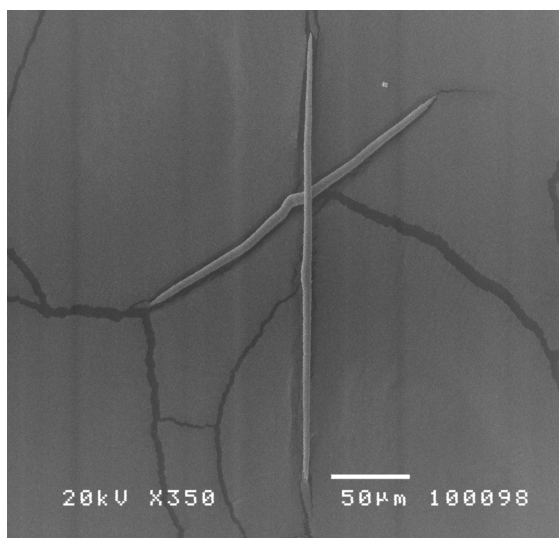


Figure 4.3 Diod spicules recovered from the *Plakortis* sponge PTN3_20A.

4.2.1 Isolation and identification of lehualides E–K

Methanolic extracts of the *Plakortis* specimen PTN3_20A were partitioned over reversed-phase HP20 resin, generating three fractions with differing polarity; 30%, 75% and 100% Me₂CO in H₂O. NMR analysis of the less polar 75% and 100% Me₂CO in H₂O fractions showed the presence of one major component and several closely related compounds. Immediately apparent in the ¹H NMR spectra of the two fractions were the resonances of an aromatic system, olefinic methines (δ_{H} 5.20 ppm), methoxy groups (δ_{H} 3.80–4.20 ppm), deshielded methylenes and methyls (δ_{H} 2.60–3.20 and 1.60–1.90 ppm), and a large aliphatic methylene envelope (δ_{H} 1.15–1.30 ppm).

Analysis of correlations within the HMBC spectra of the 75% and 100% Me₂CO in H₂O fractions confirmed the value of investigating the organism further. Protons of deshielded methylene doublets displayed correlations to two separate methyl-substituted carbon double bonds (Figure 4.4). One of the double bonds appeared to be oxy-substituted, and another deshielded methylene correlated to a mono-substituted phenyl ring. Interpretation of these structural fragments indicated that the structure in question could be closely related to the *Plakortis* isolates lehualides A–D (**65–68**). The lehualides were originally isolated from a *Plakortis* sponge collected from the vertical interior of large caves on Niihwa Island, Hawai'i, which appeared morphologically similar to the specimen from 'Eua.¹³² The moderate toxicity associated with lehualides A–D, coupled with subtle variations in the NMR

spectra of the 'Eua sample pointed towards a targeted and spectroscopically guided chemical evaluation of the *Plakortis* sp.

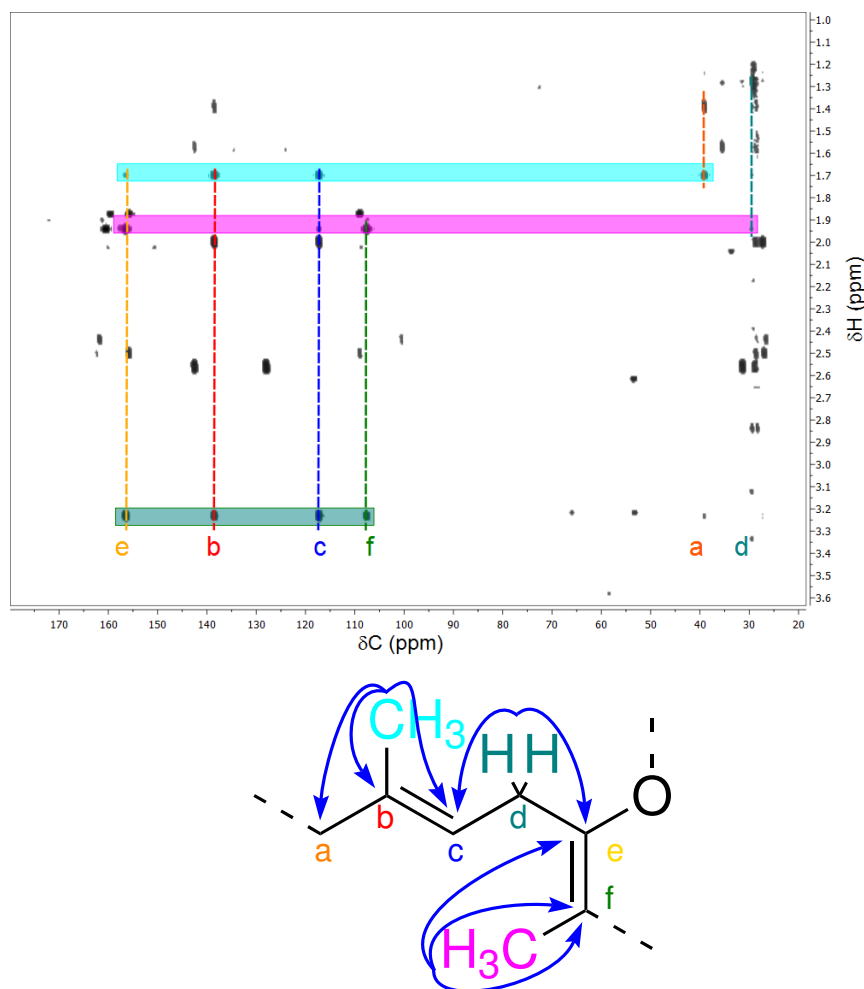


Figure 4.4 Proton to carbon correlations evidencing the methyl-substituted carbon double bonds present in the HMBC spectrum of the 75% Me₂CO in H₂O screen fraction of PTN3_20A.

Following the initial partitioning over HP20, the non-polar fractions derived from PTN3_20A were subjected to further reversed-phase chromatography (HP20SS, Me₂CO in H₂O). All fractions retained signals associated with the oxy-substituted double bond and tri-substituted double bond, indicating the separation was dependent upon a secondary structural feature. Relatively good separation was apparent on silica gel thin layer chromatography (TLC) plates, however, the α - and γ -pyrone groups present in **65–68** were suspected to be acid-sensitive. In light of this, and given the small quantities of the specimen available for analysis, DIOL was chosen as a normal-phase material for isolation. The closely related compounds were found to elute from DIOL in CH₂Cl₂, and final purification of the DIOL fractions was completed by C₁₈ HPLC. The overall isolation strategy of lehualides E–K (**69–75**) is summarised in Figure 4.5.

Lehualide E (69)

The positive-ion mode HRESIMS data of **69** showed a $[M+Na]^+$ pseudo-molecular ion peak at m/z 385.2399, consistent with the molecular formula of $C_{24}H_{32}O_4$, requiring nine degrees of unsaturation. The ^{13}C NMR spectrum contained 22 distinct resonances, including 11 sp^2 centres, indicating some form of molecular symmetry, while interpretation of the 1H and the fully-coupled HSQC NMR spectra accounted for all of the 32 protons.

Immediately apparent in the $CDCl_3$ 1H NMR spectrum were the resonances of a mono alkyl-substituted benzene ring (δ_H 7.27–7.16) an olefinic methine (δ_H 5.18), two methoxy singlets (δ_H 4.19, 3.81), a deshielded methylene doublet and triplet each integrating for two protons (δ_H 3.17, 2.57), two olefinic methyl singlets (δ_H 1.85, 1.66) and an aliphatic methylene envelope integrating for 12 protons.

Three spin systems were identified from the COSY spectrum: a mono alkyl-substituted phenyl ring, an isolated methyl-substituted alkene and an extended aliphatic chain. As illustrated in Figure 4.6, COSY and HMBC correlations allowed the facile assembly of the mono alkyl-substituted benzene ring C-16 to C-21 [(C-16: δ_C 143.1), (CH-17 and CH-21: δ_C 128.3, δ_H 7.27, 2H), (CH-18 and CH-20: δ_C 128.5, δ_C 7.17, 2H) and (CH-19: δ_C 125.7, δ_H 7.16, 1H)]. The ring accounted for four of the 11 observed sp^2 resonances, four of the degrees of unsaturation required by the molecular formula and the element of molecular symmetry indicated by the ^{13}C spectrum. HMBC correlations were observed between the protons of a methylene triplet CH_2 -15 (δ_C 36.1, δ_H 2.57) and C-16, while reciprocal correlations between the methines CH-17/-21 and CH_2 -15 established the attachment point of the aromatic ring.

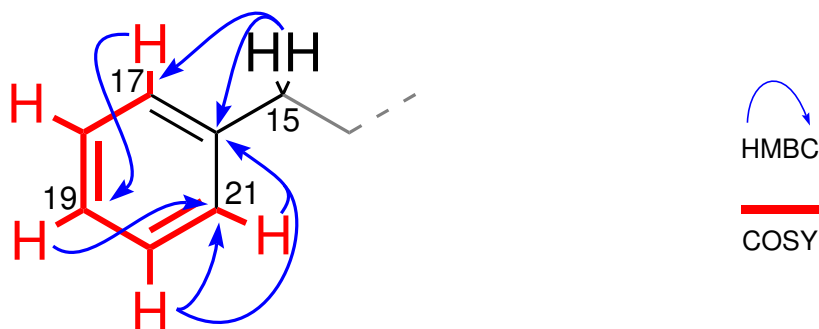


Figure 4.6 The mono alkyl-substituted benzene ring (C-16 to C-21) of **69** as evidenced by COSY and HMBC correlations.

The protons of the upfield olefinic methyl singlet CH_3 -23 (δ_C 16.4, δ_H 1.66) showed HMBC correlations to two sp^2 carbons CH-8 (δ_C 118.2, δ_H 5.18), and C-9 (δ_C 138.7), and shared an allylic COSY correlation with H-8. A further HMBC

correlation from H₃-23 to a methylene carbon CH₂-10 (δ_C 39.7, δ_H 1.96), and a COSY correlation from H-8 to the protons of another methylene CH₂-7 (δ_C 30.2, δ_H 3.17) established an isolated, tri-substituted double bond. The *E* geometry of the alkene was established from selective irradiation of H₃-23 in a 1D NOE experiment and subsequent enhancement of H₂-7 and H-11. Methylenes H₂-7 and H₂-10 were similarly enhanced after irradiation of H-8, confirming the *E* geometry of the tri-substituted double bond (Figure 4.7).

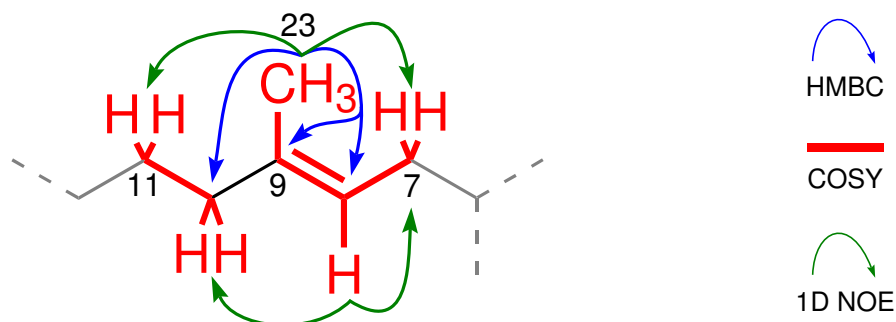


Figure 4.7 COSY, HMBC and 1D NOE correlations confirming the geometry and connectivity of the C-7 to C-11 segment in **69**.

The remaining five non-protonated *sp*² carbons C-2 (δ_C 162.7), C-3 (δ_C 128.3), C-4 (δ_C 159.0), C-5 (δ_C 108.3) and C-6 (δ_C 154.8) could only be accounted for by two fully substituted carbon-carbon double bonds and a carbonyl. HMBC correlations were observed from H₂-7 to C-5 and C-6, indicating the double-allylic character of H₂-7, consistent with its chemical shift (δ_C 30.2, δ_H 3.17). An HMBC correlation from H-8 to C-6, established the C-6–C-7 bond. Further HMBC correlations were observed from the protons of the final olefinic methyl CH₃-22 (δ_C 10.1, δ_H 1.85) to C-4, C-5 and C-6, which combined with a homoallylic COSY correlation between H₂-7 and H₃-22 established attachment of the methyl at C-5 and the connections from C-4 to C-5 and from C-5 to C-6 (Figure 4.8).

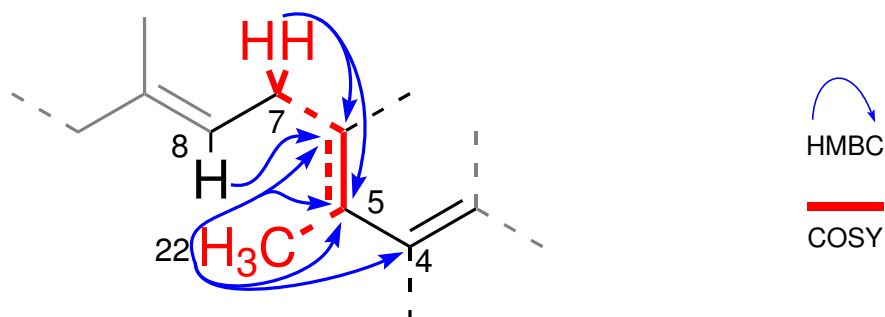


Figure 4.8 COSY and HMBC correlations firmly establishing the C-5 to C-8 connections in **69**. Dashed lines indicate weak correlations.

The substructure was extended by an HMBC correlation from the protons of a methoxy OCH₃-4 (δ_C 60.5, δ_H 4.19) to C-4, while a second methoxy OCH₃-3

(δ_C 60.4, δ_H 3.81) correlated with C-3, revealing the final carbon-carbon double bond. Reciprocal NOE correlations between OCH_3 -3 and OCH_3 -4 established the C-3 to C-4 connectivity and the *cis* relationship of the methoxy substituents. NOE correlations between OCH_3 -4 and H_3 -22, and H_2 -7 to H_3 -22 confirmed the tetra-substituted diene C-3 to C-6, with CH_2 -7 and CH_3 -22 on the same side of the C-5 to C-6 double bond. With one carbon and two oxygen atoms remaining from the molecular formula and two double-bond equivalents, the remaining sp^2 centre C-2 (δ_C 162.7), which must be a carbonyl was therefore assigned as an α, β -unsaturated ester on the basis of its shielded chemical shift (Figure 4.9). The shielded chemical shift of the oxygenated C-3 (δ_C 126.2) is also consistent with the attachment of the carbonyl.^{132,135}

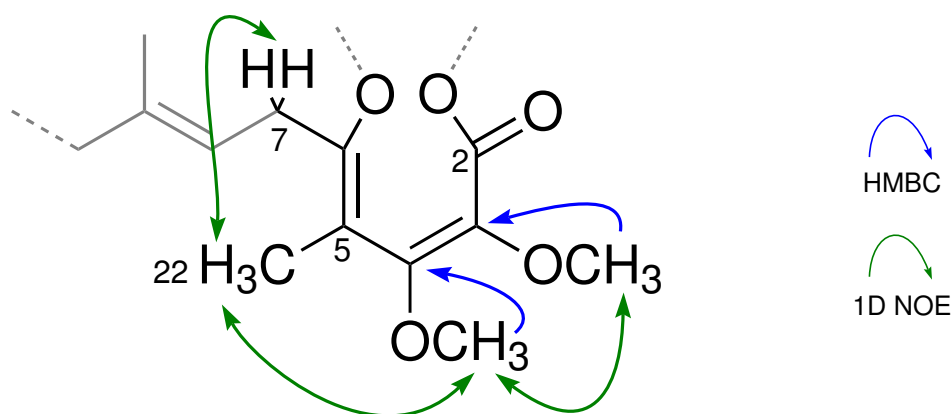


Figure 4.9 HMBC and 1D NOE correlations used to establish the C-3 to C-6 tetra-substituted diene in **69**, and the geometry of the substituents. Double headed arrows indicate reciprocal correlations.

All but one degree of unsaturation associated with the molecular formula were accounted for by the phenyl ring, the isolated double bond C-8–C-9, and the C-2 to C-6 dienolate. Furthermore, the four oxygen atoms required by the molecular formula are accounted for by the two oxymethyls and the ester functionality. The deshielded chemical shift of C-6 (δ_C 154.8) is consistent with oxygen substitution, and therefore an α -pyrone moiety, C-2 to C-6, similar to that of lehualide A (**65**), is established (Figure 4.10). UV absorption maxima (λ_{max} 291 nm), and IR stretching frequencies (ν_{max} 1686, 1649 cm^{-1}) support this assignment,¹³⁶ while the chemical shifts of the sp^2 carbon resonances are consistent with those reported for similar systems.¹³²

A series of sequential COSY and HMBC correlations, beginning at the H_2 -15 methylene triplet, and terminating with H_2 -10 established a C_6 methylene chain linking the mono alkyl-substituted benzene ring and the C-2 to CH_2 -10 segment. Selective excitation of the methylenes CH_2 -10 (δ_C 39.7 δ_H 1.96) and CH_2 -15 (δ_C 36.1 δ_H 2.57) with mixing times of 20–120 ms revealed the resonances within the methylene envelope (CH_2 -12 – CH_2 -14: δ_C 27.8, 29.9, 29.3, 31.6 δ_H 1.24–1.38) and

gave reciprocal revelation of CH₂-10 and CH₂-15 (Figure 4.10). This completed the structure of lehualide E (**69**). NMR data for **69** is presented in Table 4.1.

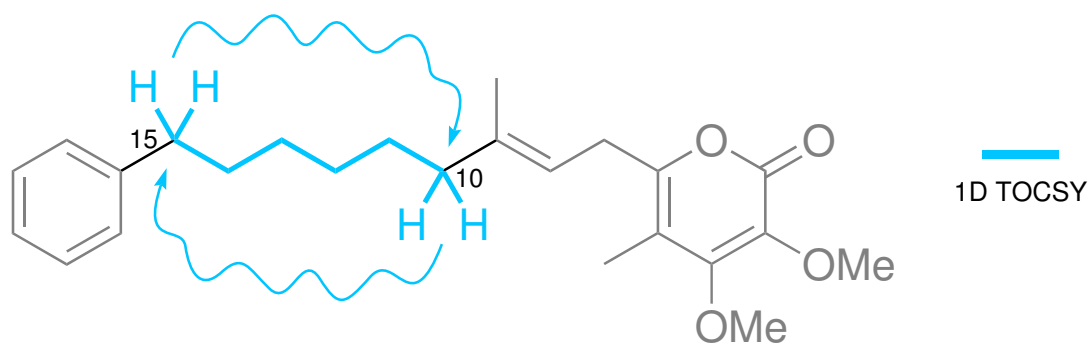
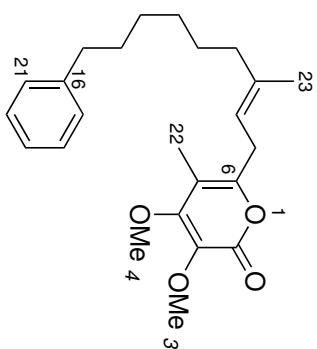


Figure 4.10 1D TOCSY correlations confirming connection between the extended α -pyrone segment (C-2 to C-11) and the mono alkyl-substituted benzene ring (C-15 to C-21) in **69**.

Table 4.1 NMR Spectroscopic Data of Lehnalide E (**69**), (600 MHz, CDCl₃).

Position	¹³ C		¹ H		COSY	HMBC (¹ H → ¹³ C)	NOE†
	δ (ppm)	¹ J _{CH} (Hz)	δ (ppm)	J (Hz)			
2	162.7	mult					
3	128.3	C					
OCH ₃	60.5	CH ₃	3.81	s		3	OCH ₃ -4
4	159.0	C					
OCH ₃	60.6	CH ₃	4.19	s		4	OCH ₃ -3, 22
5	108.3	C					
6	154.8	C					
7	30.3	CH ₂	3.17	d	7, 22*	5*, 6, 8, 23,	23
8	117.5	CH	5.17	t	6, 23	6*, 7, 23	10
9	138.7	C					
10	39.7	CH ₂	1.96	t	11	8, 9, 11, 23	8
11	27.8	CH ₂	1.38	quin	10, 12	8, 9, 11, 23	23
12	29.9	CH ₂	1.32	quin	11, 13	10, 11, 13	
13	29.3	CH ₂	1.24-1.29	m	12, 14	12, 14	
14	31.6	CH ₂	1.59	quin	12, 14	13, 15, 16	
15	36.1	CH ₂	2.57	t	13	14, 16, 17, 21	
16	143.0	C					
17	128.5	CH	7.19	d	18	19, 21	
18	128.4	CH	7.29	t	17, 19	16, 20	
19	125.7	CH	7.19	t	18, 20	17, 21	
20	128.4	CH	7.29	t	19, 21	16, 18	
21	128.5	CH	7.19	d	20	17, 19	
22	10.3	CH ₃	1.85	s	7*	4, 5, 6, 7	OCH ₃ -3, 7
23	16.4	CH ₃	1.66	s	8	8, 9, 10	7, 11



69

†Selected correlations.

*Weak correlations.

Lehualide F (70)

Lehualide F (**70**) was isolated as a white solid. Positive-ion mode HRESIMS analysis of **70** revealed a $[M + Na]^+$ pseudo-molecular ion peak at m/z 393.2042. This indicated the molecular formula $C_{23}H_{30}O_4$, differing from that of **69** by an additional CH_2 equivalent. The multiplicity-edited HSQC spectrum accounted for 32 of the 33 protons, indicating the presence of one exchangeable proton, while the 1H spectrum of **70** displayed resonances for a mono alkyl-substituted benzene ring (δ_H 7.22–7.16) an olefinic methine (δ_H 5.17), a deshielded methylene doublet and triplet (δ_H 3.20, 2.57), two olefinic methyl singlets (δ_H 1.85, 1.66) and an aliphatic methylene envelope integrating for 12 protons. As demonstrated in Figure 4.11, the 1H NMR spectrum of **70** appeared very similar to that of lehualide E (**69**), except for the broad resonance of an exchangeable proton (δ_H 6.50), the presence of only one methoxy (δ_H 3.90) and slight downfield change in the chemical shift of the CH_3 -22 methyl signal (δ_H 1.96).

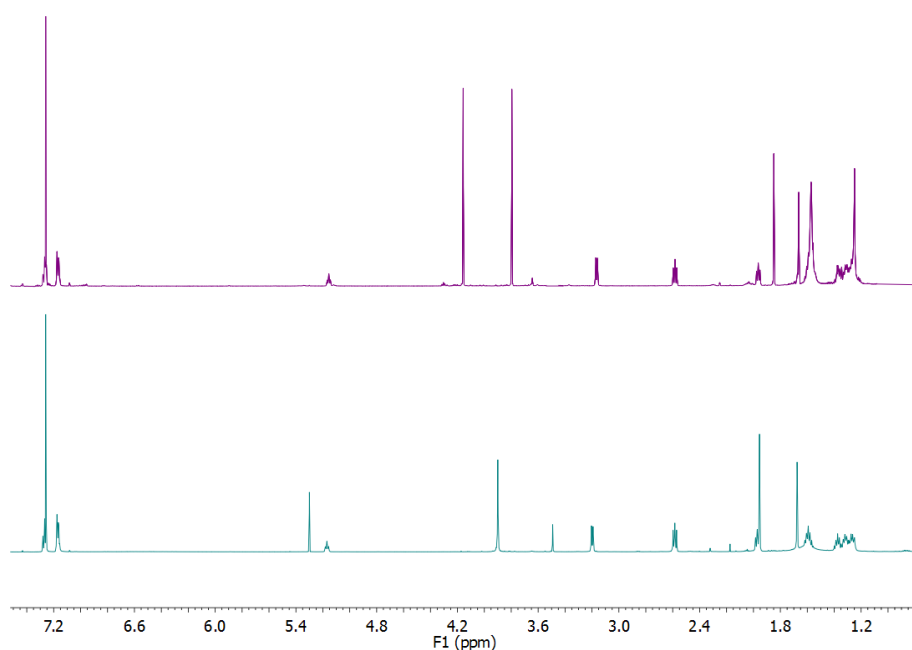


Figure 4.11 1H NMR spectra of lehualides **E** (**69**) and **F** (**70**); differing in the number of methoxy signals and chemical shift of CH_3 -22 (**69** δ_H 1.85; **70** δ_H 1.96).

As with **69**, COSY and HMBC correlations allowed the facile assembly of the mono alkyl-substituted benzene ring C-16 to C-21 [(C-16: δ_C 143.0), (CH-17 and CH-21: δ_C 128.5, δ_H 7.17, 2H), (CH-18 and CH-20: δ_C 128.4, δ_H 7.22, 2H) and (CH-19: δ_C 125.6, δ_H 7.16, 1H)]. Substitution of the aromatic ring was established via HMBC correlation from protons of a methylene triplet CH_2 -15 (δ_C 36.1, δ_H 2.57) to C-16, and reciprocal correlations between the methines CH-17/-21 and CH_2 -15 (Figure 4.12).

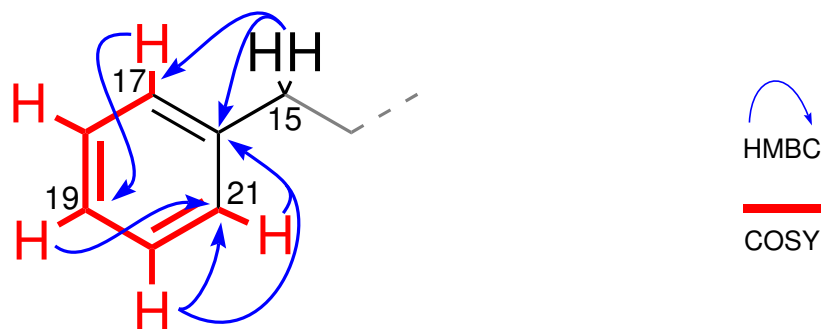


Figure 4.12 COSY and selected HMBC correlations establishing the C-17 to C-23 segment of **70**.

The isolated double bond C-8–C-9 was again assembled on the basis of HMBC correlations from protons of the olefinic methyl singlet CH₃-23 (δ_C 16.3, δ_H 1.68) to the *sp*² carbons CH-8 (δ_C 117.2, δ_H 5.17), and C-9 (δ_C 139.0). A further HMBC correlation from H₃-23 to a methylene carbon CH₂-10 (δ_C 39.7, δ_H 1.96), and a COSY correlation from H-8 to the protons of another methylene CH₂-7 (δ_C 30.2, δ_H 3.17) extended the *sp*² substructure. Selective irradiation of H₃-23 in a 1D NOE experiment induced enhancement of H₂-7 and H₂-11, while H₂-7 and H₂-10 were similarly enhanced after irradiation of H-8. This established the *E* geometry of the C-8 to C-9 alkene.

An α -pyrone (λ_{max} 298 nm) similar to that of **69** was quickly identified. The oxy-substituted double bond between C-5 and C-6 was established on the basis of the strong HMBC correlations from the protons of the *sp*² methyl H₃-21 and methylene H₂-7 to both C-5 and C-6. Evidence of weak homoallylic COSY coupling between H₃-21 and H₂-7 confirmed the CH₂-7–C-6–C-5–CH₃-21 bonds (Figure 4.13).

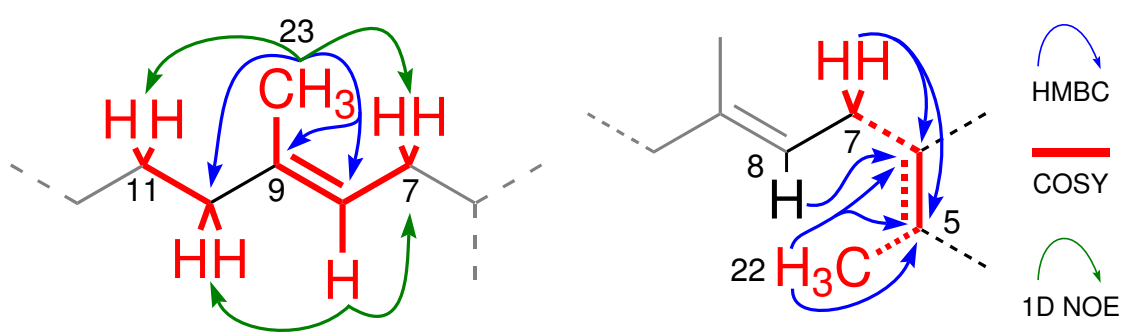


Figure 4.13 COSY, HMBC and 1D NOE correlations confirming the tri-substitution of the *E* alkene C-8–C-9, and the tetra-substituted alkene C-5–C-6 in **70**. Dashed lines indicate weak correlations.

A further HMBC correlation from H₃-22 to C-4 (δ_C 162.1) was observed, the deshielded chemical shift again indicating oxygen-substitution of C-4. However, the methoxy observed in **69** was absent suggesting a hydroxyl functionality. This accounted for the exchangeable proton (IR: ν_{max} 3250 cm⁻¹, δ_H 6.50 ppm). HMBC

correlations from protons of the lone methoxy OCH_3 -3 (δ_C 60.0, δ_H 3.86) to C-3 (δ_C 125.0) were observed as in **69**, as was an NOE correlation between the protons of CH_2 -7 and CH_3 -21 (Figure 4.14).

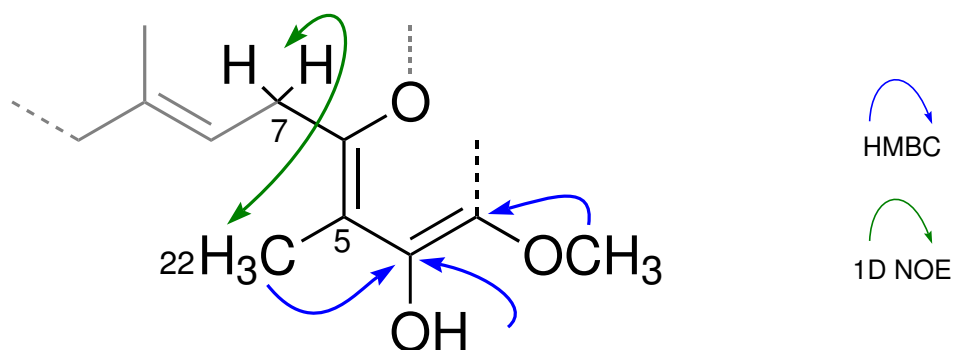


Figure 4.14 HMBC and 1D NOE correlations establishing the C-4–C-5 bond and methoxy substitution of C-3 in **70**. Double headed arrows indicate reciprocal correlations.

The α -pyrone system was completed by the α,β -unsaturated ester carbonyl C-2 (δ_C 160.4), Figure 4.15. All other chemical shifts and correlations observed in the NMR spectra were essentially identical to that of **69**, thereby establishing **70** as the C-4 *des*-methoxy congener of **69**. NMR data for **70** is presented in Table 4.2.

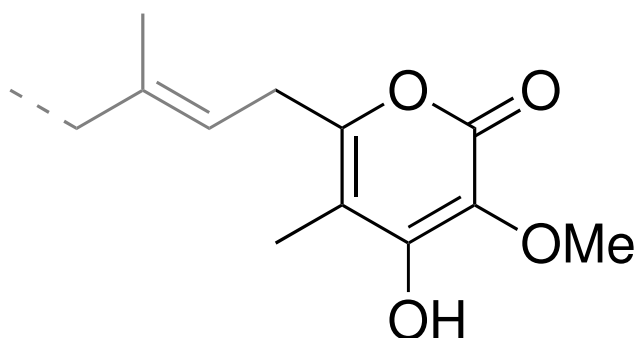


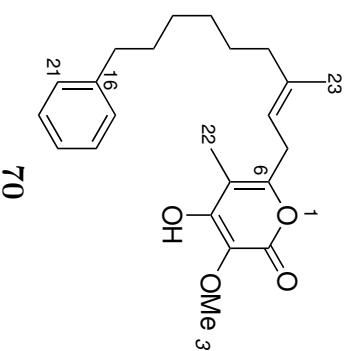
Figure 4.15 The α -pyrone system present in **70**, the *des*-methoxy congener of **69**.

Table 4.2 NMR Spectroscopic Data of Lehnalide F (**70**), (600 MHz, CDCl₃).

Position	¹³ C			¹ H			COSY	HMBC (¹ H → ¹³ C)	NOE†
	δ (ppm)	mult	¹ J _{CH} (Hz)	δ (ppm)	mult	J (Hz)			
2	160.3	C							
3	125.0	C							
OCH ₃	59.8	CH ₃	146	3.90	s			3	
4	157.9	C							
5	105.6	C							
6	157.3	C							
7	30.2	CH ₂	128	3.20	d	7.2	8, 22*	5*, 6, 8	22, 23
8	117.2	CH	158	5.17	t	7.0	7, 23*	7, 9, 23	10
9	139.0	C							
10	39.7	CH ₂	125	1.97	t	8.4	11	9, 11	8
11	27.8	CH ₂	125	1.38	quin	7.6	10, 12	8, 9, 11, 23	23
12	29.29	CH ₂	126	1.32	quin	8.0	11, 13	10, 11, 13	
13	29.26	CH ₂	126	1.24–1.29	m		12, 14	12, 14	
14	31.5	CH ₂	125	1.59	quin	8.0	13, 15	13, 15	
15	36.1	CH ₂	125	2.57	t	7.2	13, 14	14, 15, 16	
16	143.0	C							
17	128.5	CH	157	7.16	d	6.0	18	19, 21	
18	128.4	CH	160	7.22	t	7.7	17, 19	16, 20	
19	125.6	CH	161	7.17	t	8.2	18, 20	17, 21	
20	128.4	CH	160	7.22	t	7.7	19, 21	16, 18	
21	128.5	CH	157	7.16	d	6.0	20	17, 19	
22	9.4	CH ₃	130	1.96	s		7*	4, 5, 6	7
23	16.3	CH ₃	125	1.68	s		8*	8, 9, 10	7, 11
OH				6.51	brs				

†Selected correlations.

*Weak correlations.



Lehualide G (71)

A $[M+Na]^+$ pseudo-molecular ion peak observed in the positive-ion mode HRESIMS spectrum for lehualide G (**71**) at m/z 421.2355, indicated a molecular formula of $C_{25}H_{34}O_4$, differing from **70** by an additional C_2H_2 equivalent. Detailed analysis of the 1D and 2D NMR spectra of **70** and **71** determined that the two were chain-length congeners. The only perceivable differences between the spectra of the two compounds were the methylene regions of the 1H and ^{13}C spectra (Figure 4.16).

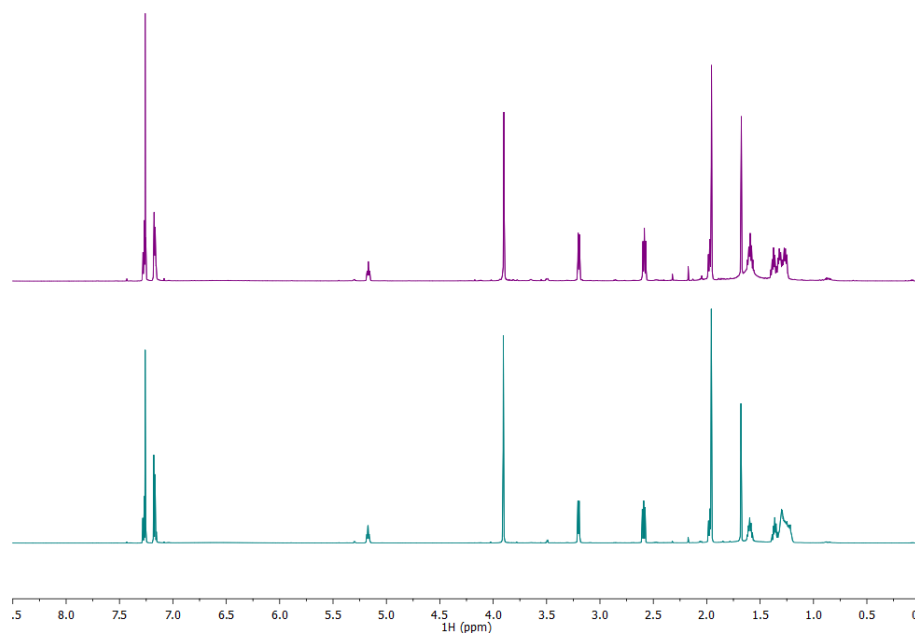


Figure 4.16 1H NMR spectra of lehualides **F** (**70**) and **G** (**71**). The compounds differ only integration of the methylene region (δ_H 1.28–1.45 ppm, **69** 6H, **70** 8H).

Much of the 1D and 2D NMR data of **71** were consistent with the α -pyrone moiety present in **70**, and UV and IR spectroscopic data (λ_{max} 235 and 291 nm, ν_{max} 3250 cm^{-1}) supported this assignment. The extended methylene chain of **71**, C-10 to C-17, was established by selective 1D TOCSY irradiation of CH_2 -17 (δ_C 36.1, δ_H 2.61). As the mixing time was increased from 0 to 120 ms, the methylene resonances H_2 -16 to H_2 -10 (C-10: δ_C 40.5, δ_H 2.01) were sequentially revealed. Analogous 1D TOCSY irradiation of H_2 -10 coupled with COSY and HMBC correlations within the chain provided confirmation of this assignment and the connection between the methylenes (Figure 4.17).

HSQC-TOCSY analysis of **71** in CD_3OD over a selected band-width, δ_C 10–50 ppm, allowed elucidation of the aliphatic chain: [(C-12 to C-15: δ_C 32.8, 30.6, 30.5, 30.3, δ_H 1.25–1.29) and (C-16: δ_C 30.1, δ_C 1.22)]. Using this method the overlapping methylene resonances from C-12 to C-16 were clearly resolved, while the TOCSY correlations aided concise ordering of the resonances. NMR data for **71** is presented in Table 4.3.

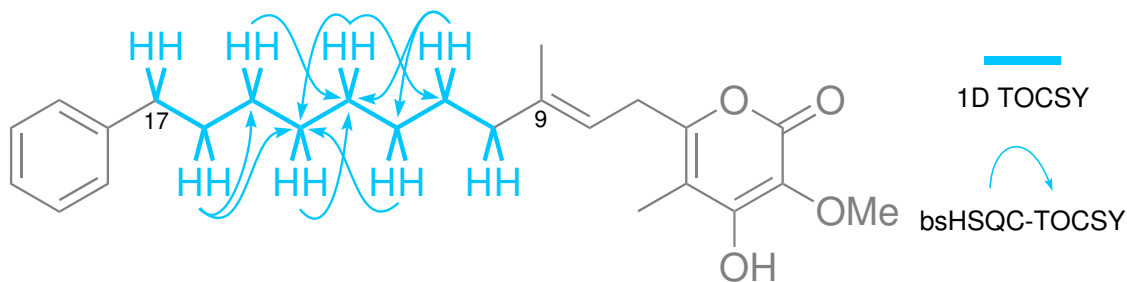
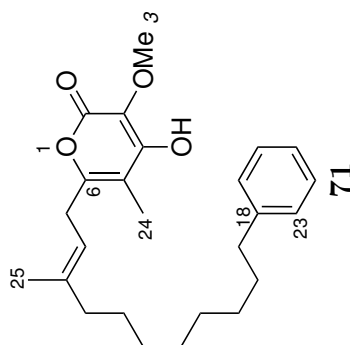


Figure 4.17 1D TOCSY and bsHSQC-TOCSY correlations established the connection between methylenes CH₂-10 and CH₂-17 in the extended aliphatic chain of **71**.

The structural similarities between lehualides F and G made resolution of the chain-length congeners impossible under normal-phase chromatographic conditions. With no discernable difference in polarity, the two compounds would co-elute in an approximate 1:20 ratio. Exploitation of the differences in lipophilicity granted separation of the two congeners under reversed-phase conditions (C₁₈ HPLC, 85% MeCN in H₂O). Conversely, resolution of mixed fractions of lehualides E and F could be nearly achieved under normal-phased conditions. Although the lipophilic chains induced streaking across the stationary phase, polarity differences between the methoxy and hydroxyl forms were sufficient to afford some separation.

Table 4.3 NMR Spectroscopic Data of Lehualide G (**71**), (600 MHz, CDCl₃).

Position	¹³ C		¹ H		COSY	HMBC (¹ H → ¹³ C)	NOE [†]
	δ (ppm)	mult	¹ J _{CH} (Hz)	δ (ppm)			
2	160.4	C					
3	125.0	C					
OCH ₃							
4	158.0	CH ₃	147	3.86		3	
5	105.7	C					
6	157.3	C					
7	30.3	CH ₂	128	3.21	24*	6, 8	24, 25
8	117.1	CH	157	5.16	7, 25*	6*, 7, 25	10
9	139.1	C					
10	39.7	CH ₂	125	1.97		8, 11, 25	8
11	27.8	CH ₂	124	1.36		9, 10, 12	25
12	29.4	CH ₂		1.20-1.33			
13	29.55	CH ₂		1.20-1.33			
14	29.58	CH ₂		1.20-1.33			
15	29.45	CH ₂		1.20-1.33			
16	31.7	CH ₂	126	1.59	15, 17	15, 17	
17	36.1	CH ₂	126	2.61	16	16, 18, 19, 23	
18	143.1	C					
19	128.5	CH	157	7.17	20	21, 23	
20	128.3	CH	160	7.27	19, 21	18, 22	
21	125.7	CH	162	7.16	20, 22	19, 23	
22	128.3	CH	160	7.27	21, 23	18, 20	
23	128.5	CH	157	7.17	22	19, 21	
24	9.5	CH ₃	129	1.96	7*	4, 5, 6	7
25	16.5	CH ₃	126	1.68	8*	8, 9, 10	7, 11
OH				6.50	brs		



[†]Selected correlations.
*Weak correlations.

Lehualide H (72)

Positive-ion mode HRESIMS analysis of lehualide H (**72**) generated a $[M + Na]^+$ pseudo-molecular ion peak at m/z 407.1864, suitable for the formula $C_{20}H_{32}O_5S$, requiring five degrees of unsaturation, and incorporation of a sulfur atom. Analysis of the 1H NMR spectrum of **72** revealed, in contrast with the lehualides E–G, the absence of the phenyl moiety, olefinic proton, and doubly allylic methylene signals.

Similar 2D NMR, IR and UV spectroscopic data to that of **69**, and the presence of two methoxy signals indicated retention of the dimethoxy α -pyrone. This accounted for four of the five oxygen atoms, and four degrees of molecular unsaturation. As with **69**, the non-protonated α -pyrone ring was assigned on the basis of HMBC and NOE correlations between H₂-7, H₃-21 and the methoxy groups OCH₃-4 and OCH₃-3. The doubly allylic methylene doublet of **69**, CH₂-7 (δ_C 30.2, δ_H 3.17), is replaced in **72** by a singly allylic methylene triplet, CH₂-7 (δ_C 30.9, δ_H 2.44), as evidenced by homoallylic COSY correlation between CH₂-7 and H₃-21, and HMBC correlations to C-5 and C-6 (Figure 4.18). These data confirmed the absence of the isolated double bond and associated olefinic methyl of the previously described structures.

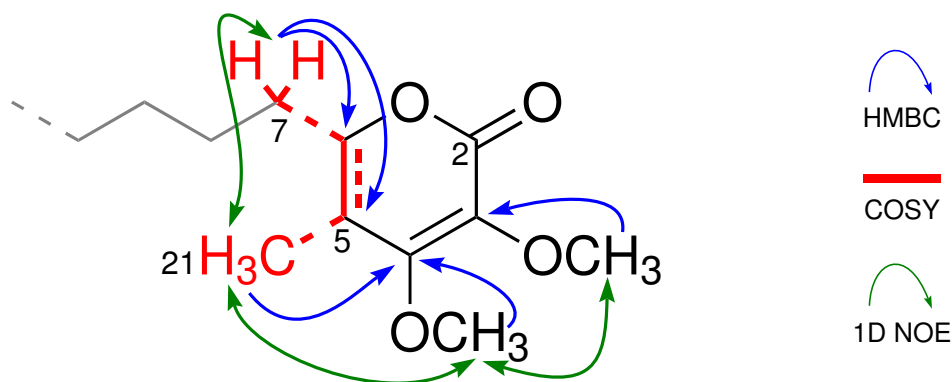


Figure 4.18 The dimethoxy-substituted α -pyrone and singly-allylic methylene substituent of **72** as evidenced by COSY, HMBC and 1D NOE correlations. Double headed arrows indicate reciprocal correlations, and dashed lines indicate weak correlations.

The long alkyl chain characteristic of the lehualides extended between CH₂-7 and CH₂-16 (δ_C 29.2, δ_H 2.86), selective 1D TOCSY irradiations of methylenes H₂-7 and H₂-16, with increasing mixing times (0–200 ms) established the connection between the two centres.

The final substructure began at the deshielded methyl singlet terminus (δ_C 30.8, δ_H 2.35). Strong HMBC correlations from the protons of both the methyl and H₂-16 to an ester carbonyl (δ_C 196.3) were observed. The large $^1J_{CH}$ coupling constant and low 1H and ^{13}C chemical shifts of the C-16 methylene (δ_C 29.2, δ_H 2.86, $^1J_{CH}$ 141 Hz) indicated sulfur attachment.^{137,138} The chemical shift of the acetate carbonyl (δ_C 196.3) is consistent with the thioacetate moiety previously observed in lehualide

C (**67**). As illustrated in Figure 4.19, reciprocal weak HMBC correlations observed from the protons of methylene H₂-16 and methyl terminus to the respective carbons confirmed the thioacetate linkage. Elucidation of this substructure accounted for the sulfur atom, the fifth oxygen atom, and the final degree of unsaturation required by the molecular formula. This completed the structure of lehualide H (**72**), the NMR data of which is presented in Table 4.4.

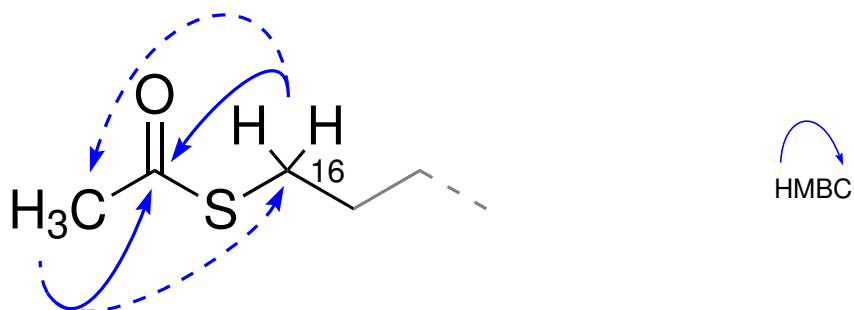


Figure 4.19 The thioacetate moiety of **72** as evidenced by HMBC correlations. Dashed arrows indicate weak correlations.

Lehualides I and J (73 and 74)

The sulfur functionalities in lehualides I and J presented challenges during structural elucidation of the compounds, beginning with establishing their respective molecular formulae. Interpretation of the positive-ion mode HRESIMS spectrum of lehualide I (**73**) led to a proposed molecular formula of $C_{19}H_{32}O_5S$ (m/z 395.1867 $[M + Na]^+$, m/z 379.1920 $[M - 16 + Na]^+$). A pseudo-molecular ion peak correlating to the same formula was also observed in the HRESIMS spectrum of **74**: $C_{19}H_{32}O_5S$ (m/z 395.1868 $[M + Na]^+$) (Figure 4.20). Relative peak heights of the $[M + Na]^+$ and $[M - 16 + Na]^+$ signals in the spectrum of **73** varied slightly between injections, suggesting they may not be products of fragmentation. Following further interpretation of the HRESIMS and NMR spectra of both compounds, the formula of **73** was revised to $C_{19}H_{32}O_4S$ (m/z 379.1920 $[M + Na]^+$, 395.1867 $[M + 16 + Na]^+$). This new formula contains one less oxygen atom than that of **74**, and the strong $[M + 16 + Na]^+$ peak was thought to represent an oxygen adduct formed in the positive-ion mode conditions.

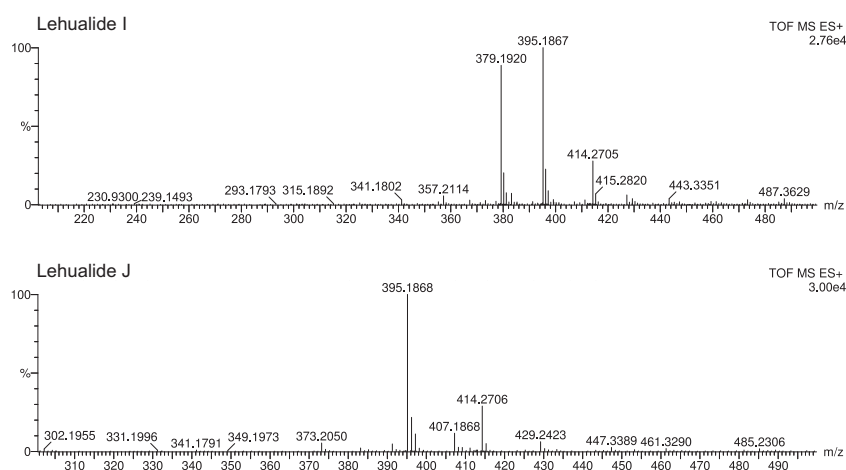


Figure 4.20 Positive-ion mode HRESIMS spectra of lehualides I and J. Both compounds appear to have the same molecular weight and corresponding chemical formula.

Analysis of the 1D and 2D NMR spectroscopic data of lehualide I (**73**), in conjunction with IR and UV spectra, confirmed the same C-6 alkyl-substituted α -pyrone system present in **72**. This accounted for the four degrees of unsaturation, and the four oxygen atoms required by the molecular formula. The alkyl chain was again elucidated by irradiation of methylenes H₂-16 and H₂-7 using a 1D TOCSY pulse with sequentially increasing mixing times. When acquired in CDCl₃, the ¹³C NMR spectrum was devoid of one methylene resonance, although no discernable differences in peak height or line width were observed between resonances in the region. Analysis of **73** in both C₆D₆ and CD₃OD allowed resolution and observation of the missing methylene centre.

Similar to lehualide H (**72**), a methyl singlet (CH₃-17: δ_C 15.6, δ_H 2.09) was observed

in the ^1H spectrum of lehualide I (**73**). Inspection of 2D NMR spectroscopic data revealed weak HMBC and COSY correlations between CH_3 -17 and the CH_2 -16 methylene (δ_{C} 34.3, δ_{H} 2.49), indicating the presence of a heteroatom between them (Figure 4.21). The high $^1J_{\text{CH}}$ values and shielded chemical shifts of the aliphatic centres CH_2 -16 ($^1J_{\text{CH}}$ 137 Hz) and CH_3 -17 ($^1J_{\text{CH}}$ 137 Hz) indicated the linkage was a sulfur atom.¹³⁷ This was corroborated by a weak C-S stretch present in the IR spectrum at 698 cm^{-1} indicative of a sulfide function.

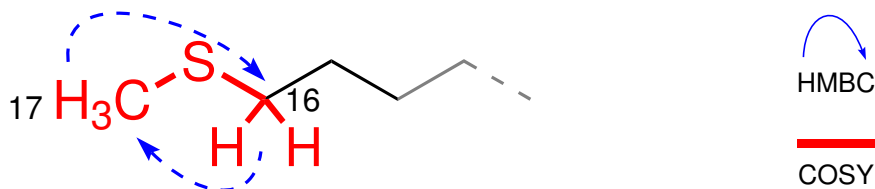


Figure 4.21 The methyl sulfide function of **73** as evidenced by COSY and HMBC correlations. Dashed arrows indicate weak correlations.

As shown in Figure 4.22, acquisition of the ^1H NMR spectrum of lehualide I (**73**) in CDCl_3 resulted in broadening of the signals for the centres adjacent to the sulfur (CH_3 -17 and CH_2 -16) after an hour in solution. The effect was initially attributed to acid-catalysed H-D exchange. Acidic α -protons of dicarbonyl sulfone centres have been observed to undergo H-D exchange,¹³⁹ although presence of the function was negated by the HRESIMS evidence. Dissolution of the compound in a polar solvents such as CD_3OD alleviated the broadness, presumably due to hydrogen-bonding between the solvent and the sulfur centre. The broadness observed in CDCl_3 is therefore attributed to fluctuating intramolecular interactions between the sulfur and the pyrone core in the absence of intermolecular hydrogen-bonding.

The ^1H NMR spectrum of lehualide J (**74**) was very similar to that of lehualides H and I (**72** and **73**), the primary difference being the presence of a deshielded diastereotopic methylene (δ_{C} 54.9, δ_{H} a 2.73, b 2.66), observed in the HSQC experiment. As with compounds **72** and **73**, the C-6 alkyl-substituted α -pyrone system was identified through detailed analysis of both 1D and 2D NMR data, corroborated by UV and IR spectroscopic data. In this case, the aliphatic chain extending from the pyrone terminates in the methylene centre CH_2 -16 (δ_{C} 54.9, δ_{H} a 2.73, b 2.66), the diastereotopic nature of which indicated close proximity to a chiral centre. A deshielded methyl singlet CH_3 -17 (δ_{C} 38.7, δ_{H} 2.56) was also observed at significantly higher chemical shift to that of **73**. As depicted in Figure 4.23, the centres displayed weak reciprocal COSY and HMBC correlations, indicating the presence of a heteroatom between them, while the large $^1J_{\text{CH}}$ couplings associated with the centres (CH_2 -16: $^1J_{\text{CH}}$ Ha 137 Hz, Hb 135 Hz; CH_3 -17: $^1J_{\text{CH}}$ 137 Hz) in conjunction with their chemical shifts was again indicative of a bridging sulfur functionality.¹³⁷ Incorporation of an oxygen-bearing stereogenic sulfoxide centre

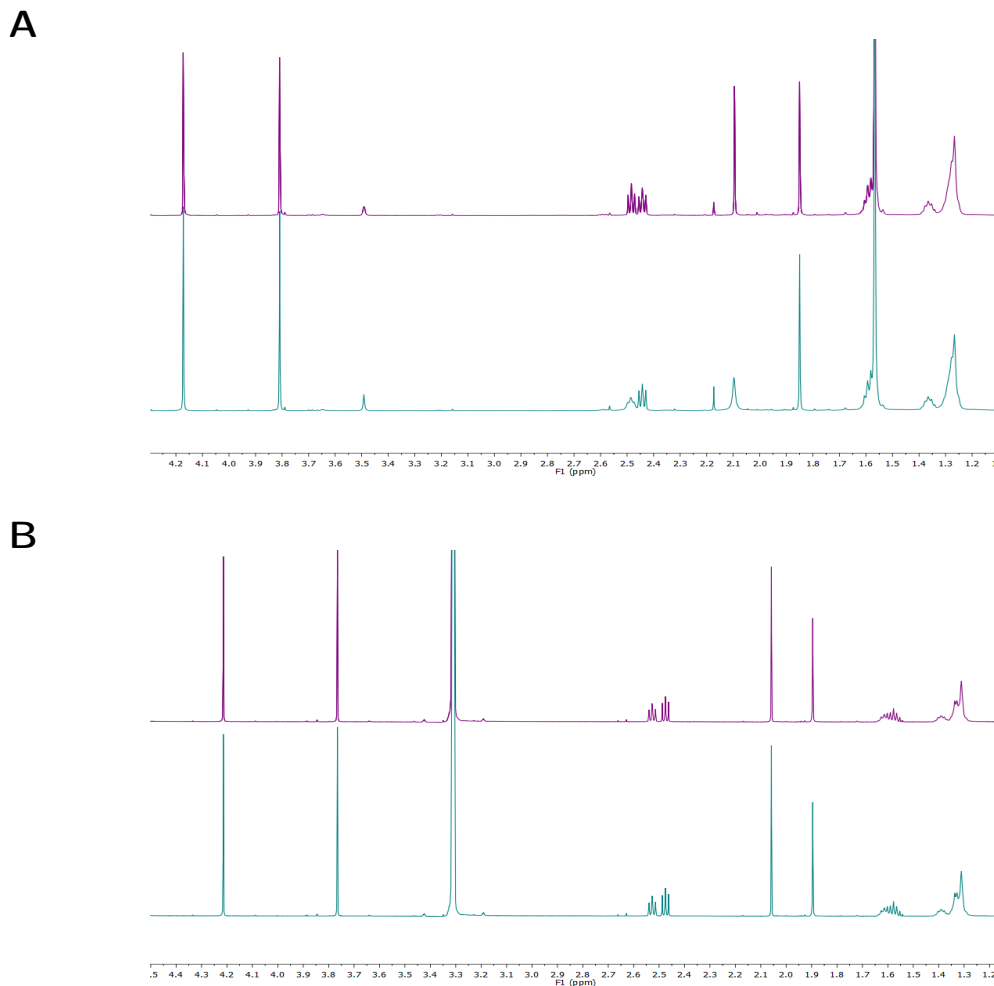


Figure 4.22 ¹H NMR spectrum of lehualide I (**73**) acquired in A: CDCl₃ and B: CD₃OD. Broadening of the methylene and methyl signals (δ_{H} 2.48, 2.08 ppm) adjacent to the sulfur centre is apparent after 60 min in CDCl₃, but not observed in CD₃OD.

accounted for both the diastereotopic nature of CH₂-16 and deshielded chemical shifts of the methylene and CH₃-17, while incorporating the remaining oxygen indicated by the molecular formula. The IR stretch of the functionality was observed at 1027 cm⁻¹.¹⁴⁰ It is unclear, however, whether the apparent lack of optical activity ($[\alpha]_{\text{D}}^{19.1}$ 0.0° (*c* 3.69 × 10⁻³, CHCl₃)) is due to natural occurrence of lehualide J (**74**) as a racemic mixture or small sample size. NMR data for the structures of lehualides I and lehualide J (**73** and **74**) is presented in Tables 4.5 and 4.6.

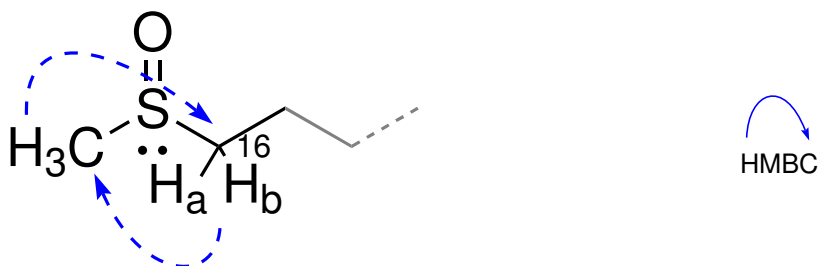


Figure 4.23 The stereogenic sulfoxide centre of **74** as evidenced by HMBC correlations. Dashed arrows indicate weak correlations.

Table 4.5 NMR Spectroscopic Data of Lehuamide I (**73**), (600 MHz, CDCl₃).

Position	¹³ C		¹ H		COSY	HMBC (¹ H → ¹³ C)	NOE†
	δ (ppm)	¹ J _{CH} (Hz)	δ (ppm)	<i>J</i> (Hz)			
2	162.6	mult					
3	127.7	C					
OCH ₃ -3	60.4	CH ₃	3.85	s		3	OCH ₃ -4
4	158.9	C					
OCH ₃ -4	60.5	CH ₃	4.21	s		4	OCH ₃ -3, 17
5	108.3	C					
6	155.8	C					
7	30.8	CH ₂	2.45	t		8, 17*	
8	27.4	CH ₂	1.59	quin		5*, 6, 8	
9	29.5	CH ₂	1.23-128	m		7, 9	6*, 7, 9
10	29.5	CH ₂	1.23-128	m			
11	29.5	CH ₂	1.23-128	m			
12	29.5	CH ₂	1.23-128	m			
13	29.5	CH ₂	1.23-128	m			
14	28.8	CH ₂	1.37	quin		13, 15	13, 15, 16
15	27.4	CH ₂	1.59	quin		7, 9	6*, 7, 9
16	34.3	CH ₂	2.49	brt		15, SMe*	15, SMe*
SMe	15.6	CH ₃	2.09	brs		16*	16*
17	10.3	CH ₃	1.85	s		7*	4, 5, 6

†Selected correlations.
*Weak correlations.

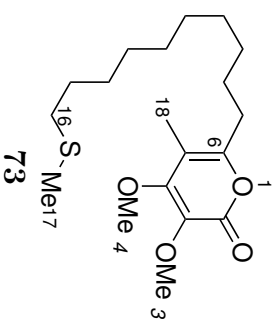
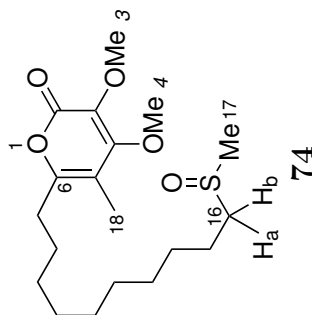


Table 4.6 NMR Spectroscopic Data of Lehuaide J (**74**), (600 MHz, CDCl₃).

Position	¹³ C		¹ H		COSY	HMBC (¹ H → ¹³ C)	NOE†
	δ (ppm)	mult	¹ J _{CH} (Hz)	J (Hz)			
2	162.7	C					
3	127.8	C					
OCH ₃ -3	60.5	CH ₃	146			3	OCH ₃ -4
4	158.9	C					
OCH ₃ -4	60.6	CH ₃	149			4	OCH ₃ -3, 17
5	108.5	C					
6	155.9	C					
7	30.9	CH ₂	128	7.7	8, 17*	5*, 6, 8	17
8	27.5	CH ₂	127	7.7	7, 9	6*, 7, 9	
9	29.36	CH ₂					
10	29.28	CH ₂					
11	28.9	CH ₂	119				
12	29.44	CH ₂					
13	29.39	CH ₂					
14	29.24	CH ₂					
15	22.7	CH ₂	128	7.0	14, 16a, 16b	14, 16	
16	54.9	CH ₂	137	13.0, 9.0, 6.1	15, 16*	14, 15, S(O)Me*	
a			135	12.7, 9.2, 6.6	15, 16a	14*, 15, S(O)Me*	
b			137		16a, 16b	16*	
S(O)Me	38.7	CH ₃	130		7*	4, 5, 6	OCH ₃ -4, 7
17	10.4	CH ₃					



†Selected correlations.

*Weak correlations.

Lehualide K (75)

The final addition to the lehualide suite, K (**75**) was not isolated in any purity exceeding approximately 85%. Persistent impurities of **70** and **72** remained within the sample despite multiple normal phase column chromatographic purifications, and attempted isolation by C₁₈ and DIOL HPLC under various solvent conditions. The ¹H and ¹³C NMR spectra of **75** are remarkably similar to those of **72**, except the absence of the acetyl group. As is typical of the latter lehualides, compounds **72–74**, the terminating methylene of the extended aliphatic chain, CH₂-16 has a large ¹J_{CH} value (δ_C 39.3, δ_H 2.67, ¹J_{CH} 139 Hz) and shielded chemical shift, consistent with a terminal sulfur-containing functional group. Further analysis of both the 1D and 2D NMR spectra suggested **75** to be the thiol analogue of **72**. The signal attributed to the S-H proton diminished during the purification process, however, while the positive-ion mode HRESIMS spectrum showed a [M + Na]⁺ pseudo-molecular ion peak at *m/z* 705.3477. This mass was consistent with the molecular formula C₃₆H₅₈O₈S₂, indicating formation of a disulfide dimer. In light of the isolation of the thiol lehualide D (**68**), dimerisation of **75** during the isolation process is suspected. NMR data for the disulfide **75** is presented in Table 4.8.

4.2.2 Bioactivity of the lehualides

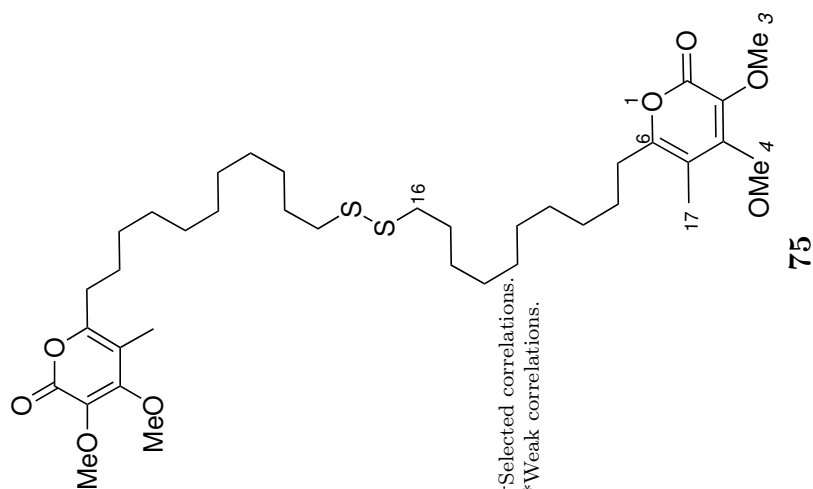
Lehualides F–I (**70–73**) displayed mild growth inhibition (60–70%) of a drug-sensitive *Saccharomyces cerevisiae* strain at 100 $\mu\text{mol L}^{-1}$, and mild cytotoxicity against the human promyelocytic leukemia (HL-60) cell line (Table 4.7). Unfortunately, the limited quantities of material available for assessment combined with compound instability prevented further biological investigation of the lehualides.

Table 4.7 Inhibition of HL-60 Cells by Lehualides F–I (**70–73**).

Compound	IC ₅₀ ($\mu\text{mol L}^{-1}$)
70	6.2
71	5.4
72	14.6
73	10.8

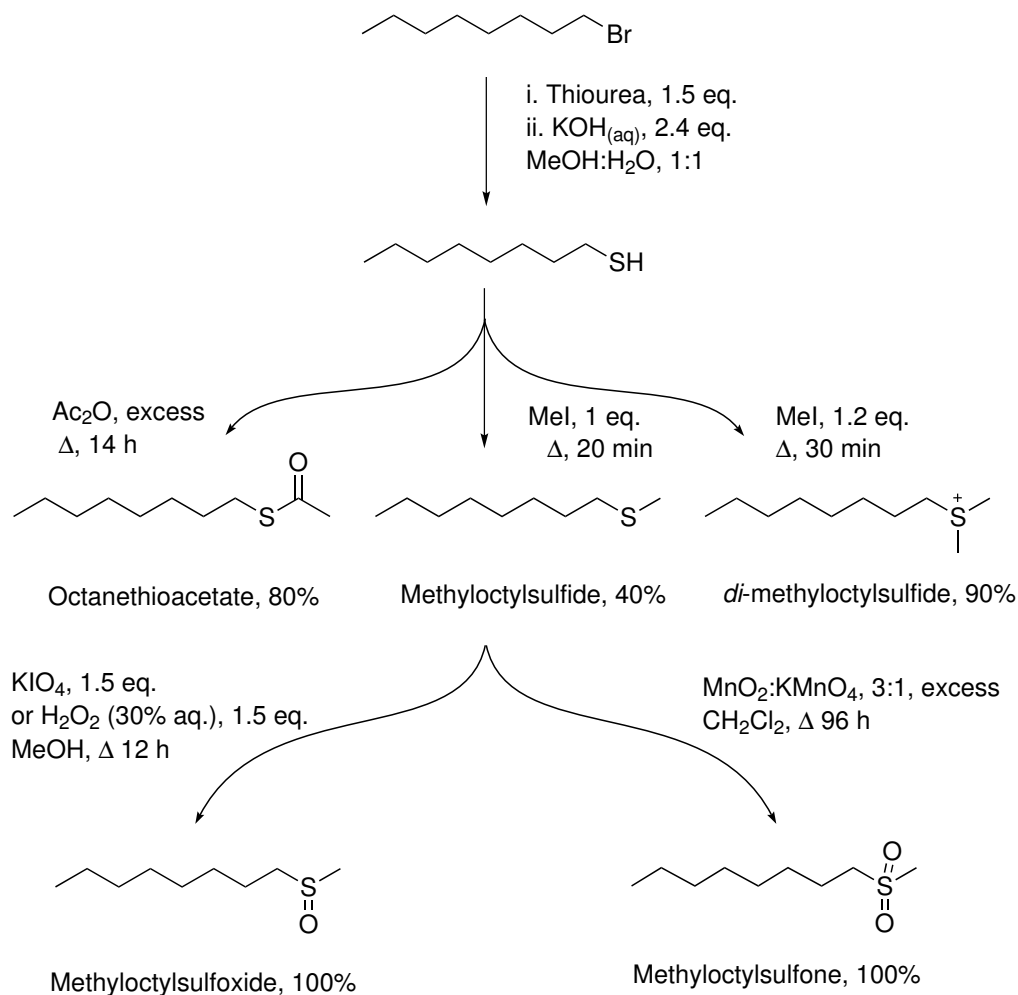
Table 4.8 NMR Spectroscopic Data of Leuhualide K (**75**), (600 MHz, CDCl₃).

Position	¹³ C		¹ J _{CH} (Hz)		¹ H		J (Hz)	COSY	HMBC (¹ H → ¹³ C)	NOE†
	δ (ppm)	mult	δ (ppm)	mult	δ (ppm)	mult				
2	162.7	C								
3	128.4	C								
OCH ₃ -3	60.5	CH ₃	146		3.81	s			3	OCH ₃ -4
4	158.9	C								
OCH ₃ -4	60.6	CH ₃	148		4.17	s			4	OCH ₃ -3, 17
5	108.5	C								
6	155.9	C								
7	30.9	CH ₂	128		2.44	t	7.7	8, 17*	5*, 6, 8, 9	17
8	27.5	CH ₂	128		1.59	quin	7.5	7, 9	6*, 7, 9	
9	29.33	CH ₂			1.24-1.28	m				
10	29.62	CH ₂			1.24-1.28	m				
11	29.59	CH ₂			1.24-1.28	m				
12	29.55	CH ₂			1.24-1.28	m				
13	29.44	CH ₂			1.24-1.28	m				
14	28.6	CH ₂	118		1.37	quin	7.6	13, 15	13, 15, 16	
15	29.3	CH ₂	127		1.66	quin	7.4	14, 16	14, 15, 16	
16	39.2	CH ₂	139		2.67	t	7.4			
17	10.4	CH ₂	129		1.84	s		7*	4, 5, 6	OCH ₃ -4, 7



4.2.3 Determination of sulfur functionalities

The NMR-silent nature of the ^{32}S nuclei present in lehualides H–K (**72–75**) presented particular difficulties during characterisation of the compounds via NMR. A suite of sulfur functional groups were prepared in order to confirm the structures of **72–74** through comparison of spectroscopic data (Scheme 4.2).



Scheme 4.2 Synthesis of the spectroscopic model compounds of lehualides H–J: octanethioacetate, methyloctylsulfide and methyloctylsulfoxide.

Octanethiol was prepared and derivatised to yield octanethioacetate,¹⁴¹ the mono- and di-methylsulfide products and the corresponding sulfoxide and sulfone species. The thioacetate proved a spectroscopic match for the aliphatic portion of lehualide H (**72**), supporting the proposal of **72** as its final structure. Methyloctylsulfide was found to have identical spectroscopic characteristics to the aliphatic portion of the natural product **73**, confirming the methylsulfide substructure of lehualide I and its final structure as **73**. Stoichiometric oxidation of methyloctyl sulfide with both H₂O₂ and KIO₄ provided the sulfoxide product,^{142,143} a spectroscopic match for the aliphatic portion of the metabolite **74** in chemical shift and $^1J_{\text{CH}}$ coupling constants, confirming the structure of lehualide J as **74** (Figures 4.24–4.26).

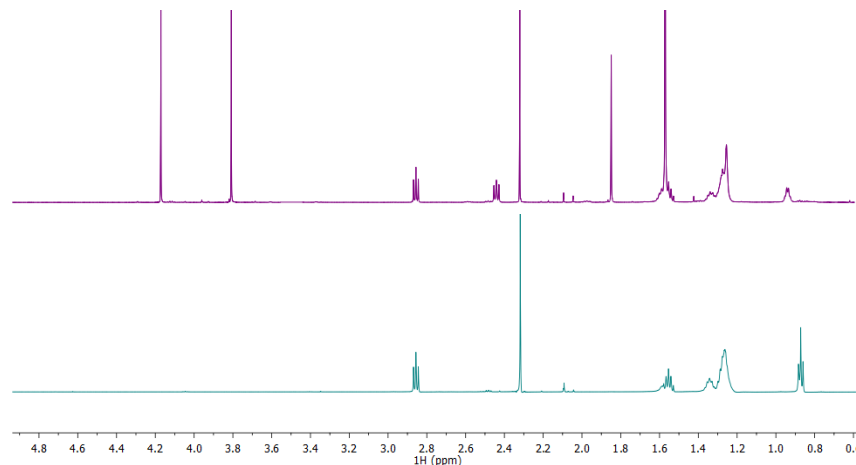


Figure 4.24 ^1H NMR spectral comparison of **lehuamide H (72)** and **octanethioacetate**. The methylene (δ_{H} 2.86 ppm) and methyl (δ_{H} 1.84 ppm) centres adjacent to the sulfur moiety share chemical shifts.

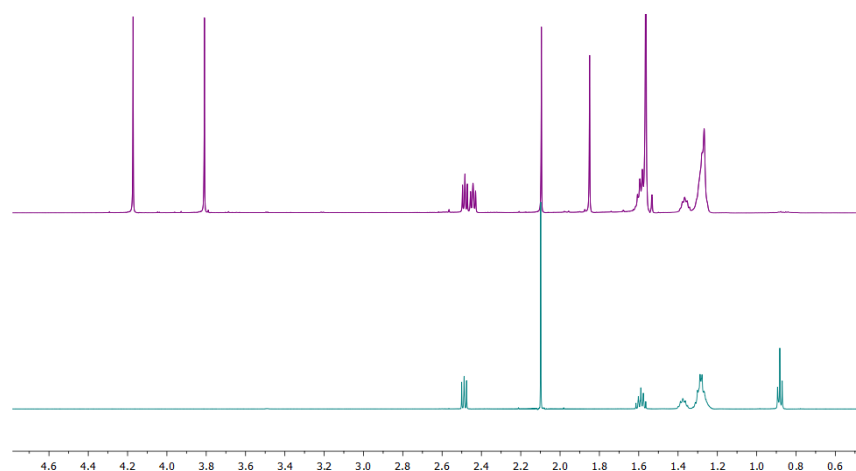


Figure 4.25 ^1H NMR spectral comparison of **lehuamide I (73)** and **methyloctylsulfide**. The methylene (δ_{H} 2.49 ppm) and methyl (δ_{H} 2.09 ppm) centres adjacent to the sulfur nucleus share chemical shifts.

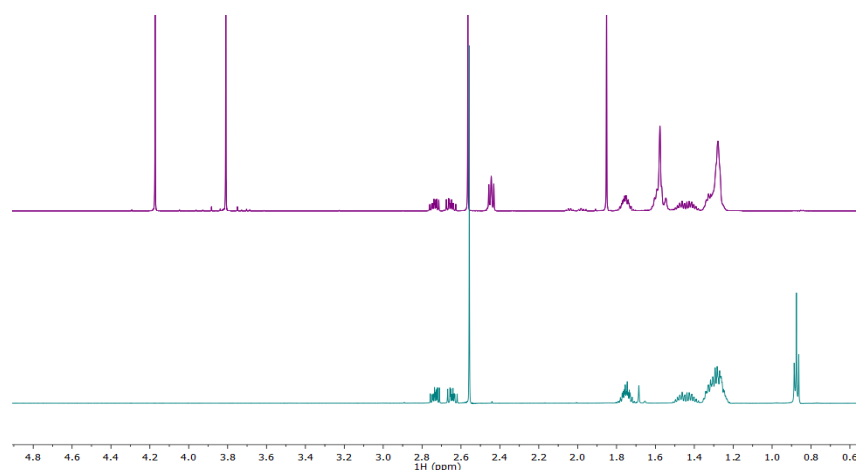


Figure 4.26 ^1H NMR spectral comparison of **lehuamide J (74)** and **methyloctylsulfoxide**. The methylene (δ_{H} 2.73, 2.66 ppm) and methyl (δ_{H} 2.56 ppm) centres adjacent to the sulfoxide centre share chemical shifts.

For further spectroscopic comparison with the natural products dimethyloctylsulfide and methyloctylsulfone were prepared via established methods,¹⁴⁴ and were found

to display significant spectroscopic differences (see Table 4.9). Analysis by TLC of the three model compounds and the natural products gave corroborating evidence for the nature of the sulfur moieties.

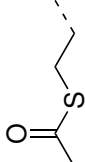
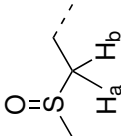
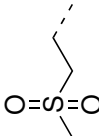
NMR detection of sulfur functionalities

Direct bonding to sulfur has little effect on the chemical shifts of spin-active carbon and hydrogen nuclei, as the three elements have similar relative electronegativities.¹⁴⁵ In the absence of a deshielding effect upon chemical shifts, analysis of the $^1J_{\text{CH}}$ coupling of adjacent C-H bonds is the best way to analyse sulfur in an NMR spectrum. Orientation of the sulfur lone pairs increases the $^1J_{\text{CH}}$ values of adjacent C-H bonds, as interaction with the filled *p*-orbitals decreases the *s*-character of the C-H bonds. Interaction with π -systems has a similar effect.^{137,145} $^1J_{\text{CH}}$ values can be obtained from fully-coupled HSQC spectra (and strong HMBC data), but as it is common practice to conduct decoupled HSQC experiments, there are few literature references. Bonding to oxygen similarly affects $^1J_{\text{CH}}$ values, but the electronegativity of the nucleus also significantly deshields adjacent nuclei, facilitating indirect observation of the nucleus through the changes in chemical shift. Only when the sulfur itself is bonded to a more electronegative element are chemical shifts significantly affected. As observed in **73** and its spectroscopic model, the sulfur lone-pair can act as a fourth substituent, thereby forming a chiral centre and inducing diastereotopic splitting of adjacent methylenes. The deshielding oxygen substituent induces downfield shifts of ca. 0.5 ppm in the ^1H spectrum, while dioxy-substituted sulfones can deshield chemical shifts by ca. 1 ppm, relative to aliphatic chemical shifts.¹⁴⁶ Formation of the oxygen-adduct of **73** during HRESIMS analysis illustrates the potential danger of relying solely upon MS data for confirmation of molecular formula(e). In the absence of isolation of **74**, the sulfide analogue **73** may have been mischaracterised and falsely reported.

Sulfur functionalities in the marine environment

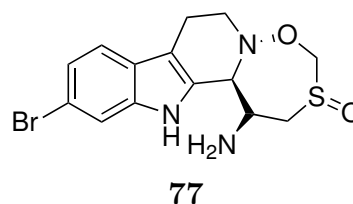
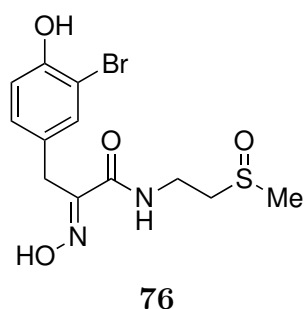
While the sulfur functionalities of lehualides H and K (**72** and **75**) have been previously encountered in lehualides C and D (**67** and **68**), the methyl sulfide and sulfoxide functionalities present in lehualides I and J (**73** and **74**) appear to be unprecedented in metabolites from sponges of this genus. Sulfoxides and sulfides are reported rarely from marine organisms, although there have been numerous examples reported from terrestrial plants including methionine and cysteine sulfoxides from brassicaceous and alliaceous vegetables,^{140,147} and trisulfides from the roots of some angiosperms.¹⁴⁸ Examples from sponge literature include

Table 4.9 Chemical Shift Comparisons of the Sulfur Moieties in Lethualides H–J (**72–74**) and their Spectroscopic Models, (600 MHz, CDCl₃).

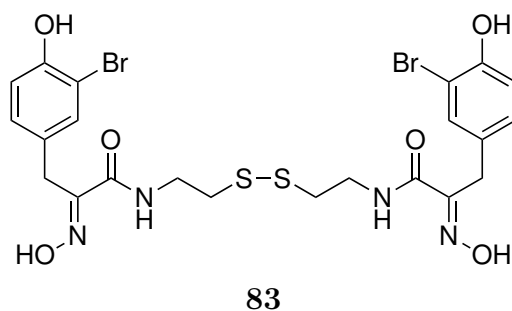
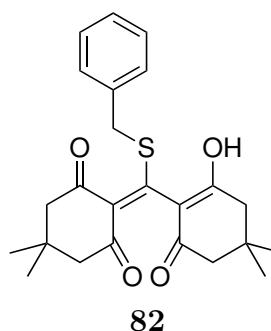
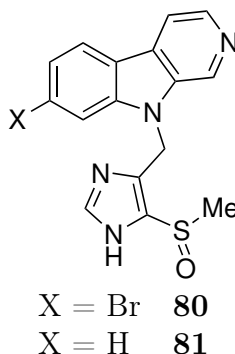
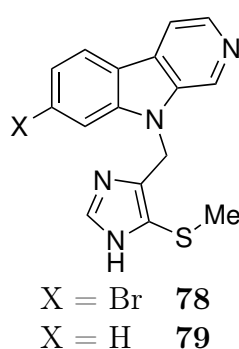
Position	72–74				Spectroscopic Model				Difference*	
	δ_C (ppm)	δ_H (ppm)	$^1J_{CH}$ (Hz)	δ_C (ppm)	δ_H (ppm)	$^1J_{CH}$ (Hz)	$\Delta\delta_C$ (ppm)	$\Delta\delta_H$ (ppm)	Δ^1J_{CH} (Hz)	Δ^1J_{CH} (Hz)
	CH ₂ SC(O)CH ₃	29.2	2.86	141	31.9	2.86	139	-2.7	0.0	2
	CH ₂ SC(O)CH ₃	196.3			196.3			0.0		
	CH ₂ SC(O)CH ₃	30.8	2.29	129	30.9	2.32	127	-0.1	0.03	2
	CH ₂ SCH ₃	34.3	2.49	137	34.2	2.48	137	0.1	0.01	0
	CH ₂ SCH ₃	15.4	2.08	137	15.5	2.08	137	0.1	0.00	0
	CH ₂ S(O)CH ₃	54.9	a 2.73 b 2.68	137	54.9	a 2.73 b 2.66	137	0.0	0.00	0
	CH ₂ S(O)CH ₃	38.7	2.56	137	38.7	2.56	138	0.0	0.02 0.00	1 -1
	CH ₂ S ⁺ (CH ₃) ₂				25.7	3.75	145			
	CH ₂ S ⁺ (CH ₃) ₂				42.7	3.34	146			
	CH ₂ S(O) ₂ CH ₃	55.0			55.0	3.00	136			
	CH ₂ S(O) ₂ CH ₃				40.5	2.89	139			

* $\Delta\delta = \delta_{\text{Spectroscopic Model}} - \delta_{\text{72-74}}$

psammaplin N (**76**),¹⁴⁹ eudistomin K (**77**),¹⁵⁰ didemnolines A–D (**78–81**),¹³⁸ and the sulfide benzylthiocrellidone (**82**) from *Crella spinulata*.¹⁵¹



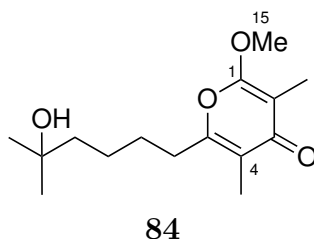
Formation of disulfide species, as is suspected in the case of **75**, has also been encountered in the marine environment. Psammaplin A (**83**), isolated from a Tongan specimen of *Psammaphysilla* sp.,¹⁵² was the first example of a disulfide species originating from a marine sponge. The isolation of lehualides E–K (**69–75**), particularly in light of the sulfur functionalities present in the latter members of the class, adds to the diversity of chemical functionality obtained from *Plakortis* sponges.



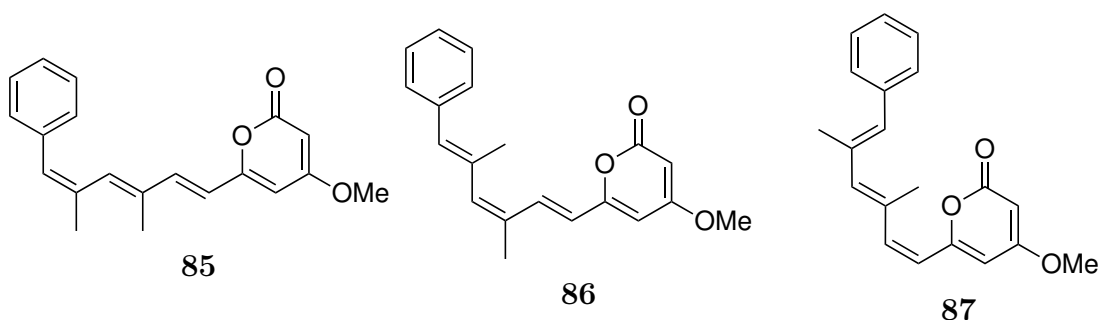
4.2.4 α - and γ -Pyrone metabolites from marine invertebrates

Lehualides A–K are the stand-alone pyrone metabolites from Plakinidae sponges, although the heterocycle function has been encountered within a variety of sponge metabolites and cultures of microbial sponge symbiotes. Examples include nocapyrone A (**84**), discovered within cultures of the *Nocardiopsis* strain HB383,

isolated from a *Halichondria panacea* specimen. Successful ex-host culturing also allowed biosynthetic characterisation of the γ -pyrones via feeding experiments with ^{13}C -labeled acetate, propionate, and methionine. Feeding of 1- ^{13}C -propionate led to an enhancement of the ^{13}C NMR signals of C-1 and C-3, while 1- ^{13}C -acetate enhanced the carbon resonances of C-5 and C-7. The signal of C-15 was enhanced after feeding with *S*Me- ^{13}C -methionine, indicating that the C-1 methoxy substituent is derived from *S*-adenosylmethionine (SAM).¹⁵³ These observations led Schneeman and co-workers to propose the initial formation of an α -pyrone, which tautomerises into the γ -pyrone in the course of methylation by an *O*-methyltransferase.¹⁵³



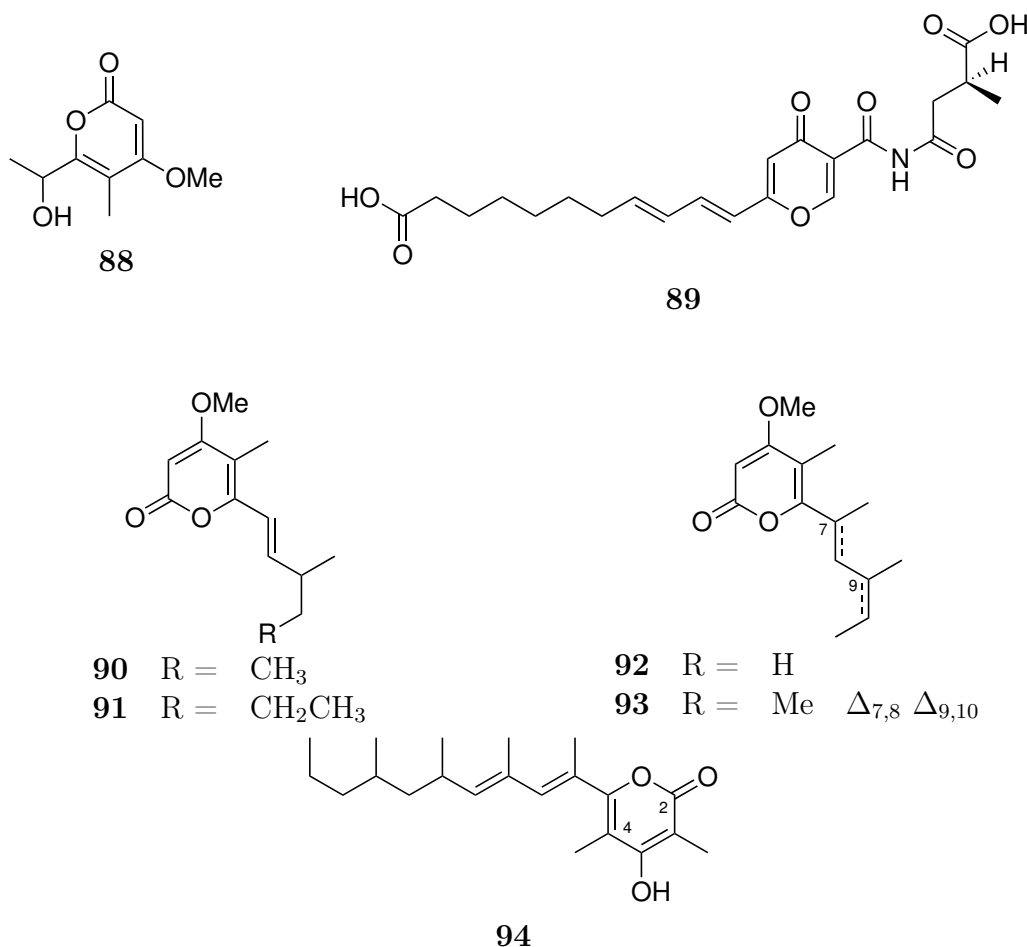
Marine fungi have produced many pyrone metabolites, such as the phenethyl- α -pyrone derivatives from a marine *Aspergillus niger* strain (EN-13).¹⁵⁴ The endophytic fungus was isolated from the inner tissue of the brown algae *Colpomenia sinuosa*, cultured *ex vivo* to yield four pyrone metabolites, and three cyclo-dipeptides.¹⁵⁴ Similar *ex vivo* culturing of another endophytic *A. niger* strain (MA-132), isolated from the marine mangrove plant *Avicennia marina*, afforded the α -pyrone metabolites nigerapyrones A–H.¹⁵⁵ Similar to lehualides A and B, the nigerapyrones have tails with varied regiochemistry about the methyl-substituted double bonds. The structures of nigerapyrones F–H (**85–87**) terminate with a phenyl function.¹⁵⁵



The new α -pyrone nigrosporapyrone (**88**) was isolated from cultured *Nigrospora* sp. fungus (PSU-F5) harvested from an *Annella* sp. sea fan.¹⁵⁶ The fungus *Microsphaeropsis* sp. was isolated from the Mediterranean sponge *Aplysina aerophoba* and subsequent investigation yielded the γ -pyrones microsphaerones A (**89**) and B.¹⁵⁷ Investigation of other marine invertebrates has also yielded examples of this heterocycle. Isolated from the Mediterranean mollusc *Placida dendritica*

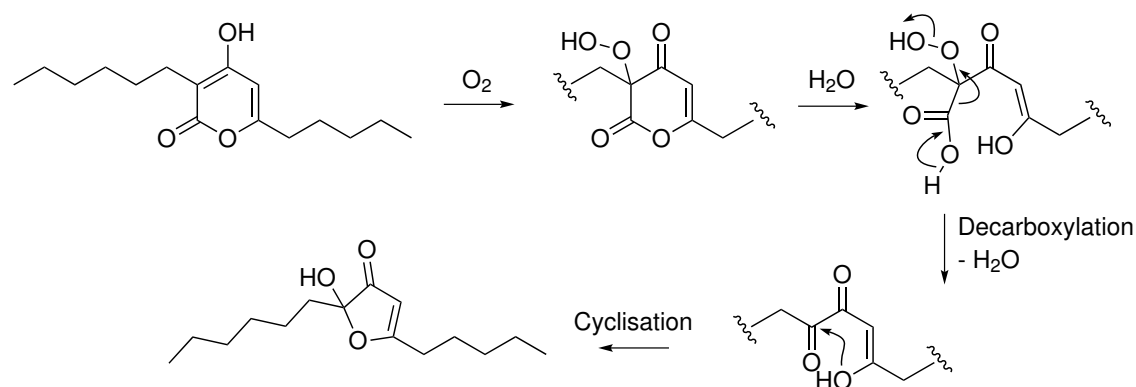
(order Sacoglossa), placidenes C–F (**90–93**) exhibit α -pyrone groups, differing from plakinid polyketides in that they comprise entirely of propionate groups.¹⁵⁸

More akin to the lehualides, recent isolates from another mollusc, *Aplysiopsis formosa*, the aplysiopsenes have a mixed acetate/propionate pathway.¹⁵⁹ Polypropionate skeletons are frequently uncovered within marine gastropods: Chilean specimens of *Siphonaria lessoni* yielded the α -pyrone norpectinatone in addition to acyclic congeners,¹⁶⁰ while collections of *Siphonaria diemenensis* from Sydney Harbour, Australia yielded the α -pyrone diemenensin A (**94**).¹⁶¹ Like lehualides A and E–K, **94** bears a C-4 hydroxyl and an olefinic methyl at C-5, yet differs in methylation in place of oxygen substitution at C-3.



Oxidative degradation of α -pyrone tautomers is frequently encountered, particularly in C-3 carbon-substituted systems. Kong *et al.* observed transformation of 3,6-alkyl-substituted 4-hydroxy- α -pyrones into 3-furanone substrates following storage of the metabolites in CDCl_3 at ambient temperatures for 11 days.^{162,163} Scheme 4.3 depicts their proposed mechanism, which entails C-3 oxidation by O_2 , followed by hydrolysis of the lactone, decarboxylation of the C-2 carboxylate and intramolecular cyclisation. Popplewell *et al.* proposed a similar degradation pathway for similarly substituted oxylipin pyrone substrates from a New Zealand red macroalgae *Phacelocarpus labillardieri*.⁶⁶ To circumvent such degradation lehualides E–K were

stored frozen in benzene/ethanol solutions, a more practical storage method than some methods previously employed.⁶⁶



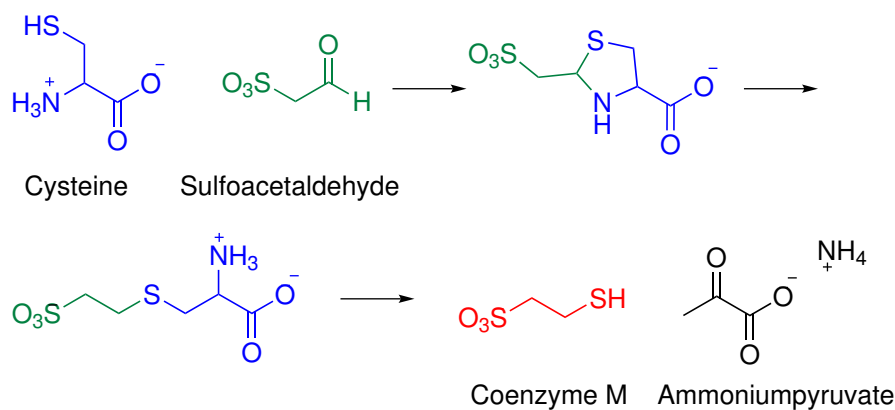
Scheme 4.3 Mechanism for degradation of pseudopyrone B into furanone 3 as proposed by Kong *et al.*¹⁶²

4.2.5 Biogenesis of the lehualides

The polyketide derivation of the lehualides is apparent; the skeletons primarily comprise fully reduced acetate monomers, with little post-translational modification required to introduce chemical functionalities such as the C-2 methoxy groups. The terminal phenyl group of **65**, **66** and **69–71** involves a phenylacetate chain starter unit. Incorporation of propionate monomers into the predominantly acetate-based chain introduces the C-5 methyl substituent of the α -pyrone ring, and the tri-substituted $\Delta_{8,9}$ alkene of lehualides E–G (**69–71**). Installation of the α -pyrone occurs during cleavage of the final module from the ACP domain.

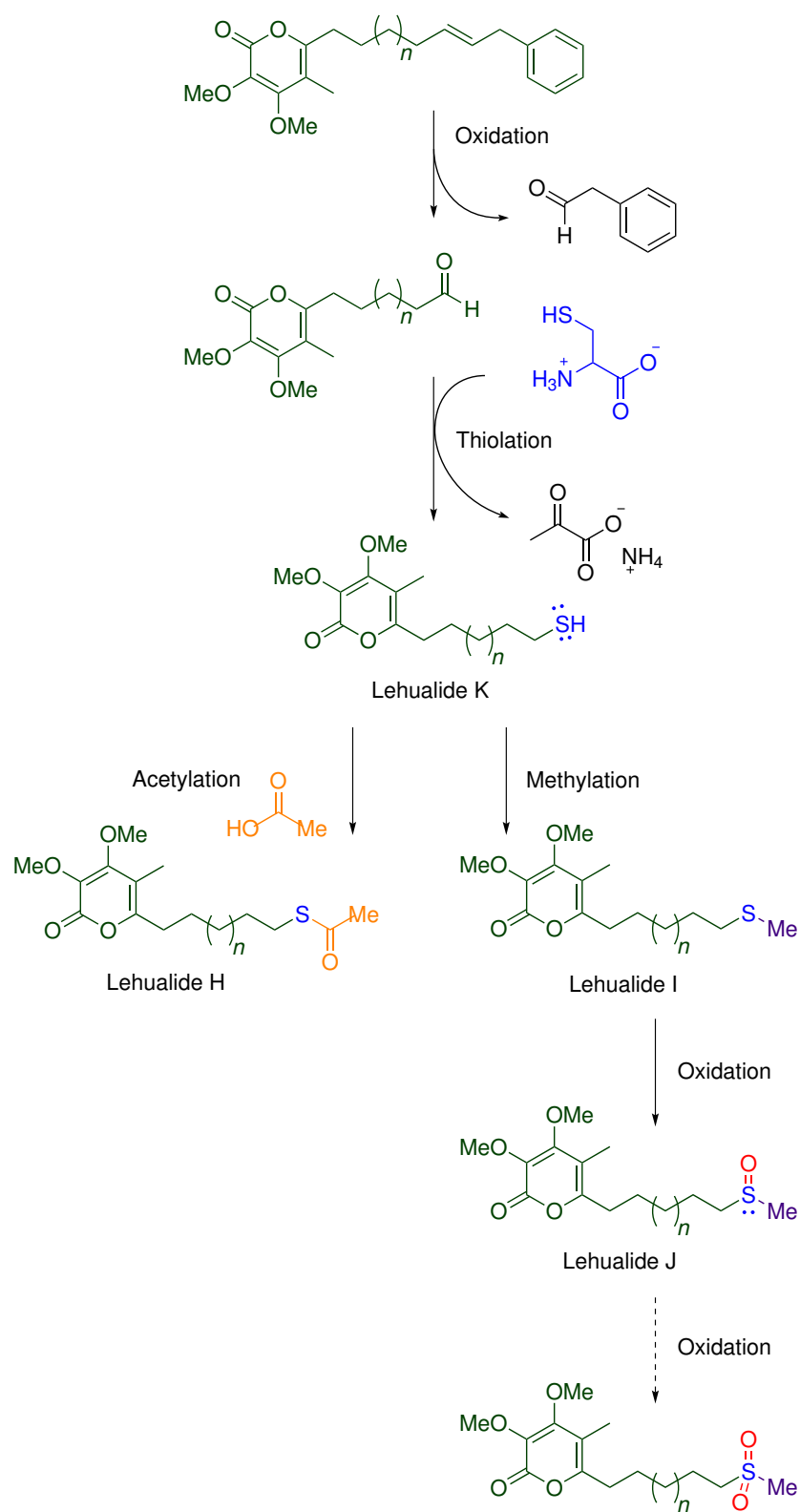
Occurrence of the four different sulfur functionalities in lehualides H–J pose interesting biosynthetic questions. While synthetic introduction of C-S bonds often involves (facile) attack of an electrophilic carbon by a sulfur nucleophile, biological formation of C-S bonds is more complex. Multiple sulfur cofactors have been identified in biological systems, these include coenzymes A and M, SAM, thiamine pyrophosphate, biotin, molybdopterin, lipoic acid and N-(7-mercaptoheptanoyl)threonine phosphate.¹⁶⁴ Introduction of thiol functionalities to the lehualide polyketide skeleton is most probably analogous to the conversion of L-cysteine and sulfoactaldehyde into coenzyme M. As depicted in Scheme 4.4, sulfoactaldehyde is attacked by the cysteine SH nucleophile forming a thiazolidine adduct. The new C-N bond undergoes reductive ring-opening generating S-(sulfoethyl)-L-cysteine. Pyridoxyl-P assists β -elimination in the 2-aminoacrylic acid portion generating coenzyme M and ammoniumpyruvate.¹⁶⁵

The uneven number of carbons in the backbones of lehualides H–J indicates chain-truncation within the structures, similar to that observed by Yong *et al.*¹⁶⁶



Scheme 4.4 Thiolation of sulfoacetaldehyde by L-cysteine to form coenzyme M.

The lehualides may share a common phenylacetate starter unit, with incomplete reduction of an adjacent acetate group allowing for oxidative cleavage of the alkene producing an aldehyde function. A similar reaction to that above between L-cysteine and the new aldehyde functionality in the polyketide can be envisaged generating a monomeric form of lehualide K (**75**). As would be the case in organic synthesis, the thioacetate of lehualide H (**72**) could easily form via nucleophilic attack of an electrophilic centre such as ethanoic acid by the thiol function of the polyketide product. Similarly, enzyme-mediated methyl transfer to the thiol group would give rise to the sulfide lehualide I (**73**). Oxidation of the methylsulfide group forming the sulfoxide functionality present in lehualide J (**74**), and hypothetically a sulfone moiety, could proceed by a host of enzymatic processes. Synthetic experimentation with the heme enzyme chloroperoxidase of *Caldariomyces fumago* and the vanadium-dependant bromoperoxidase of *Ascophyllum nodosum* has proven the applicability of the enzymes to a range of synthetic substrates and such enzymes could play a role in this biosynthesis.¹⁶⁷



Scheme 4.5 Proposed biogenesis for lehualides H–K (**72–75**), $n = 6$.

4.2.6 Concluding remarks

Analysis of the HMBC spectra of screening fractions from the *Plakortis* specimen PTN3_20A was of great import identifying the potential for structural novelty within the extracts and selection of this sponge for further evaluation. Further use of the HMBC NMR spectrum in the early stages of purification led to determination of the non-protonated α -pyrone substructure, further demonstration of the value in analysing HMBC spectra early on in the isolation process.

The isolation of lehualides E–K has added to chemical knowledge pertaining to spectral characteristics of substituted pyrone systems. Structural elucidation of the fully-substituted α -pyrone system of lehualides E–K (**69–75**) presented a challenge. Similarly unprotonated systems have previously been proposed on the basis of chemical shifts alone, however, the substitution pattern here allowed for the indisputable establishment of the α -pyrone substructure.

The suite of sulfur functional groups isolated during this study are of interest biosynthetically and from a characterisation perspective. Unequivocal identification of the moieties containing the NMR-silent ^{32}S nucleus was provided by generating model compounds for comparison of their ^1H and ^{13}C NMR spectra. Although in agreement with the proposed structures, this experience highlights the necessity of structural determination via some means other than NMR spectroscopic analysis.

Finally, as encountered throughout this work, investigation of metabolites from infrequently identified organisms is double-edged. The benefits of expedient isolation of new metabolites are countered by the realities of isolation, especially when the metabolites in question are potentially structurally unstable. This also impacted on the quantities of isolated material available for biological assessment.

4.3 Cyclic peroxides from a plakinid sponge

Identified as a species of *Plakinastrella* or *Plakortis*, the sponge specimen PTN3_19D (Figure 2.9), was collected at a depth of 12–15 m from the horizontal ceiling of a large cave on ‘Eua Island in November 2008. The specimen formed thick, dense encrustations 0.5–1.5 cm thick, appearing smooth but with a rough reticulated surface covered in wide shallow nodules ca. 3 mm high. The black-grey exterior contrasted against the tan-pink interior, which turned grey during methanol extraction, and the texture was dense and cork-like. The abundant diod spicules (40–60 $\mu\text{m} \times 1\text{--}1.5 \mu\text{m}$, Figure 4.27) were isolated via centrifuge following HNO_3 treatment of the tissue, aiding classification of the specimen as a plakinid sponge. As with the *Plakortis* specimen which yielded the lehualides, unsuccessful recollection attempts were made in the Vava’u group. The nondescript appearance and growth of the specimen in dimly-lit caves may have again been contributing factors leading to specimens going unnoticed.

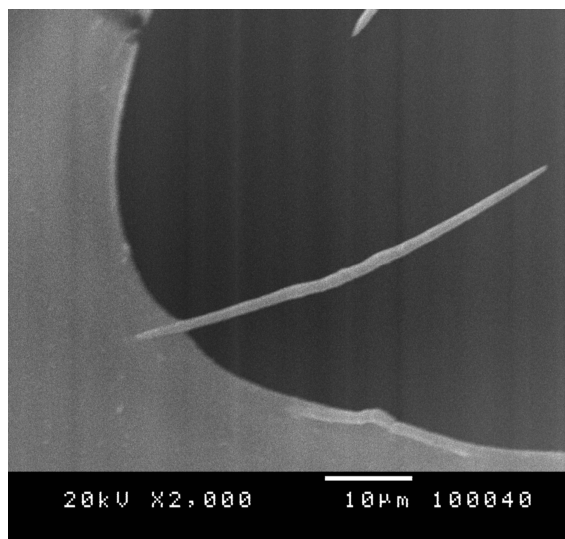


Figure 4.27 A diod spicule recovered from the plakinid sponge PTN3_19D.

4.3.1 Isolation and identification of cyclic peroxides

The MeOH extracts of the frozen screen sample of PTN3_19D were partitioned over HP20 resin beads, generating fractions of 30%, 75% and 100% Me_2CO in H_2O . HMBC NMR analysis of the less polar 75% and 100% Me_2CO in H_2O fractions showed the presence of several closely related compounds containing multiple deshielded diastereotopic methylenes correlating to oxycarbonyls (δ_{C} 170–174 ppm) and oxyquaternary centres (δ_{C} 80–84 ppm). Similarly deshielded methyl doublet and singlet signals shared HMBC correlations with the same oxyquaternaries (Figure 4.28). The ^1H and ^{13}C NMR spectra also showed the presence of saturated alkyl

systems, evidenced by COSY and HMBC correlations. This interesting combination of NMR correlations suggested that this plakinid specimen would be ideal for an NMR-guided isolation. Furthermore, reports of plakinid isolates displaying antifungal activity^{168–171} indicated that any isolates could be suitable for analysis by chemical genetic methods in *Saccharomyces cerevisiae* yeast.

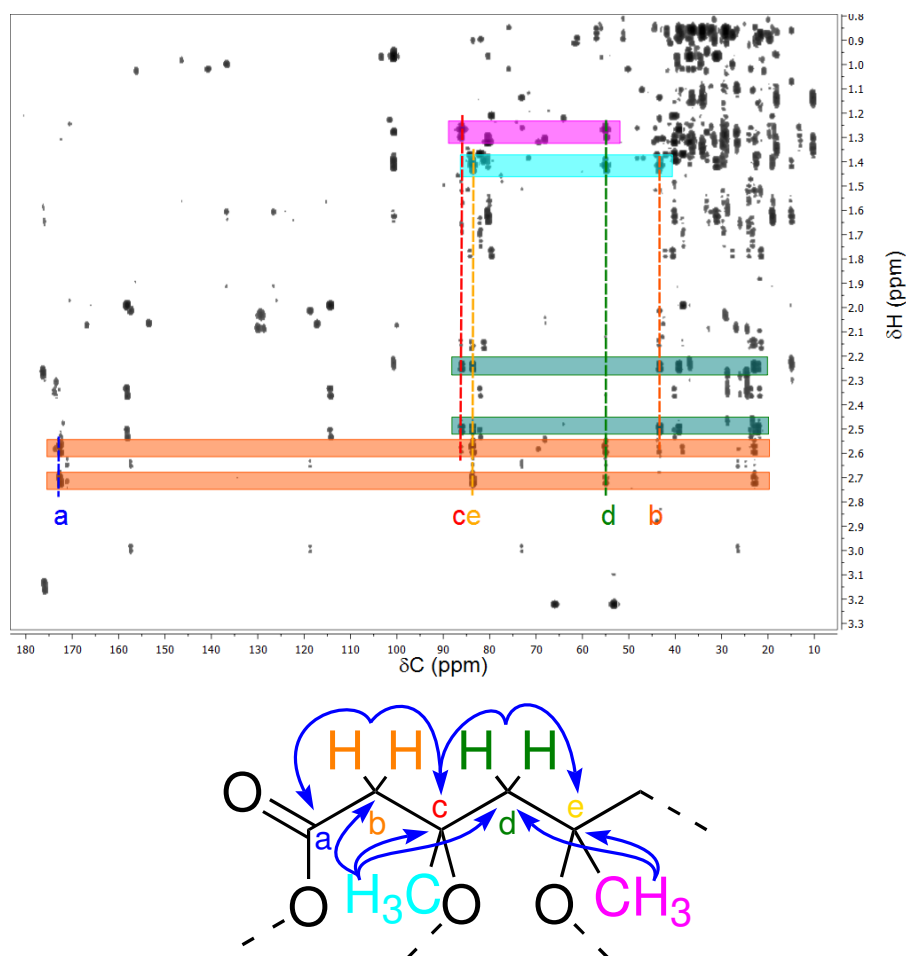


Figure 4.28 Correlations evidencing the methyl-substituted oxyquaternary centres and nearby diastereotopic methylenes and oxycarbonyls present in the HMBC spectrum of the Me₂CO in H₂O screen fraction of PTN3_19D.

Following initial partitioning of the crude methanol extracts over HP20, the non-polar fractions were subjected to further reversed-phase chromatography (HP20SS, Me₂O in H₂O). Analysis by ¹H NMR of the non-polar 80–100% Me₂CO in H₂O fractions showed retention of the diastereotopic methylene signals associated with the oxygenated quaternary centres, indicating relatively non-polar compounds despite the oxygenation.

Relatively good separation was apparent on silica gel TLC plates, however the oxygenated functionalities were anticipated to be acid-sensitive, as such DIOL was chosen as a normal-phase material for further purification. Batch elution on DIOL resulted in elution of the closely related compounds in the CH₂Cl₂ fraction, indicative of significant lipophilicity within the structures. As the structures were deficient in a chromophore, the choice of chromatographic methods for the isolation of the

metabolites was limited. Cyclic peroxides epiplakinic acid I (**95**), its methyl ester derivative (**96**), plakortolide X (**97**) and an unusual 1-hydroxy-1,2-dioxane (**98**) were all isolated via LH20 size-exclusion chromatography followed by cycles of bench-top DIOL chromatography with mixtures of hexanes, CH₂Cl₂ and MeOH. Although DAD-HPLC was used successfully in the isolation of the lehualides, the technique could not be applied here, excepting final purification of the 5 α ,8 α -epidioxysterols (**27**) and (**28**) (C₁₈ HPLC, MeCN in H₂O). A summary of the overall isolation strategy for the cyclic peroxides is depicted in Figure 4.29.

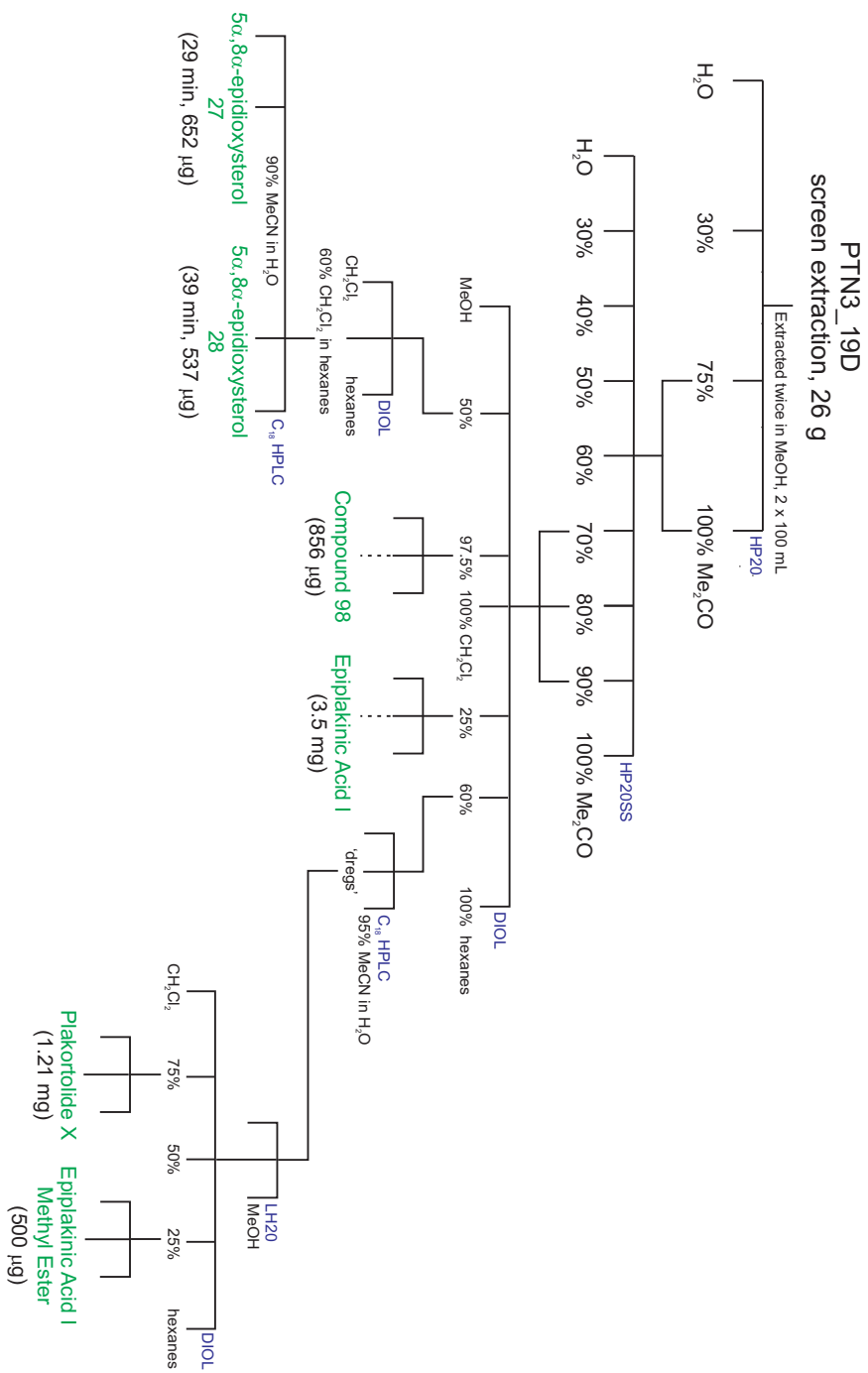


Figure 4.29 Overall purification strategy employed during isolation of cyclic peroxides **27**, **28** and **95–98**.

Epiplakinic acid I (95)

Epiplakinic acid I (**95**), $[\alpha]_D^{25.2} +1.9^\circ$ (c 0.068, CHCl_3), was isolated as a colourless oil. Positive-ion mode HRESIMS analysis of **95** generated a $[\text{M} + \text{Na}]^+$ pseudo-molecular ion peak at m/z 365.2668, suitable for the formula $\text{C}_{20}\text{H}_{38}\text{O}_4$, which required two degrees of unsaturation. This was supported by negative-ion mode HRESIMS analysis of the compound. Analysis of the ^1H and ^{13}C data showed a carboxylic acid carbonyl (δ_{C} 174.3), two oxyquaternary centres (δ_{C} 86.8, 84.0), two isolated deshielded diastereotopic methylenes [$(\delta_{\text{C}}$ 55.7, δ_{H} a 2.45, b 2.25) and $(\delta_{\text{C}}$ 39.9, δ_{H} a 1.70, b 1.53)], a third diastereotopic aliphatic methylene (δ_{C} 36.8, δ_{H} a 1.26, b 1.06), resonances corresponding to an extended aliphatic chain, two methyl singlets [$(\delta_{\text{C}}$ 23.9, δ_{H} 1.45) and $(\delta_{\text{C}}$ 23.3, δ_{H} 1.29)], an aliphatic methine (δ_{C} 34.5, δ_{H} 1.28), an aliphatic methyl doublet (δ_{C} 19.7, δ_{H} 0.83) and a terminal aliphatic methyl triplet (δ_{C} 11.6, δ_{H} 0.84). All but one hydrogen atom was accounted for by the fully-coupled HSQC spectrum; with corroborating evidence for an acid functionality indicated by ^{13}C NMR and IR spectra (ν_{max} 3428 (OH), 1717 (C=O) cm^{-1}).

As illustrated by Figure 4.30, HMBC NMR correlations were observed from the protons of a methyl singlet CH_3 -18 (δ_{C} 23.9, δ_{H} 1.45) to methylenes CH_2 -2 and CH_2 -4 [$(\text{CH}_2$ -2: δ_{C} 44.1, δ_{H} a 2.80, b 2.72) and $(\text{CH}_2$ -4: δ_{C} 55.7, δ_{H} 2.45, 2.25)] and oxyquaternary C-3 (δ_{C} 84.0). This established connection between the methyl singlet CH_3 -18 and the non-protonated oxyquaternary centre, and the adjacent positioning of methylenes CH_2 -2 and CH_2 -4. A weak COSY correlation between H_3 -18 and H_2 -2 confirmed the CH_2 -2-C-3 bond, corroborated by an HMBC correlation from H_2 -2 to C-3. Further HMBC correlations from the protons of H_2 -2 to a carbonyl C-1 (δ_{C} 174.3) extended the linear segment C-1 to C-4. The absence of further spectral correlations to the carbonyl C-1 indicated an acid function.

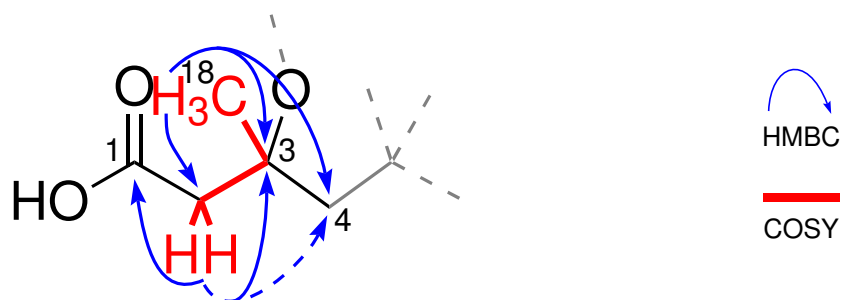


Figure 4.30 Salient COSY and HMBC NMR correlations establishing the C-1 to C-4 linkages in **95**, and methyl substitution of C-4. Dashed arrows indicate weak correlations.

The second methyl singlet CH_3 -19 (δ_{C} 23.3, δ_{H} 1.29) displayed HMBC correlations to a second oxyquaternary C-5 (δ_{C} 86.8), and methylenes CH_2 -4 and CH_2 -6 (δ_{C} 39.9, δ_{H} a 1.70, b 1.53). This established substitution of the non-protonated C-5 with the

methyl singlet CH₃-19, and adjacent positioning of the methylenes CH₂-4 and CH₂-6 (Figure 4.31). Corroborating HMBC correlations were observed from H₂-4 to both quaternary centres, C-3 and C-5, confirming the linear sequence from C-1 to CH₂-6.

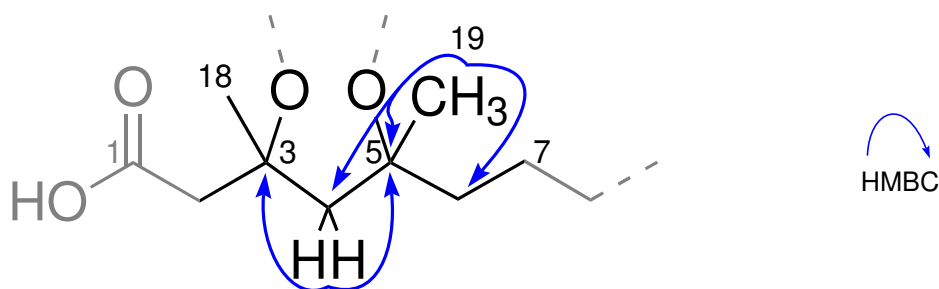


Figure 4.31 Salient HMBC NMR correlations establishing the C-3 to C-6 linkages of **95**, and methyl substitution of C-5.

COSY correlations clearly established the connectivity between the terminal methyl triplet CH₃-17 (δ_C 11.6, δ_H 0.84), aliphatic methylene CH₂-16 (δ_C 29.73, δ_H 1.11), methine CH-15 (δ_C 34.5, δ_H 1.28), its methyl doublet substituent CH₃-20 (δ_C 19.7, δ_H 0.83) and a second aliphatic methylene CH₂-14 (δ_C 36.8, δ_H a 1.26, b 1.06). This series was corroborated by HMBC correlations from methyl doublet CH₃-20 to the methine CH-15 and the adjacent methylenes CH₂-14 and CH₂-16. Selective excitation of CH₃-17 with a 1D TOCSY experiment over mixing times of 20–80 ms, confirmed connection between the protonated centres (Figure 4.32).

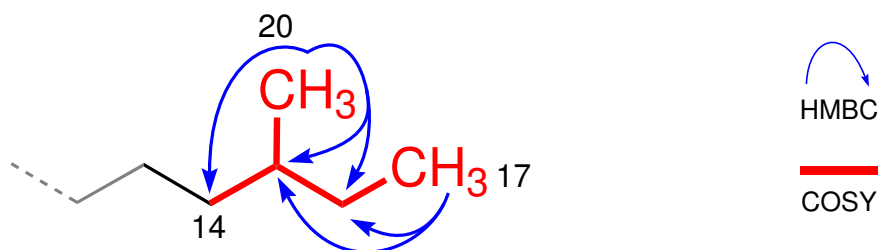


Figure 4.32 COSY and HMBC NMR correlations establishing γ -methyl-substituted motif C-14 to C-17 of **95**.

A C₉ methylene chain beginning with CH₂-6, terminating at CH₂-14, was established by a series of sequential COSY and HMBC correlations. Selective irradiation of both methylene centres (CH₂-6 and CH₂-14) and subsequent revelation of the other in a series of 1D TOCSY experiments with mixing times of 20–120 ms confirmed the connection (Figure 4.33).

As all of the protons of the molecular formula were accounted for, a cyclic structure is required to account for the final degree of unsaturation associated with the molecular formula. Two of the oxygen atoms were incorporated into the acid functionality,



Figure 4.33 1D TOCSY correlations establishing the C₉ methylene chain of **95**.

implying substitution of the oxyquaternaries C-3 and C-5 with different oxygen atoms. A peroxide linkage between the oxyquaternary centres is therefore proposed, completing the structure of **95**.

The 1,2-dioxolane core of **95** is consistent with common *Plakortis* and *Plakinastrella* metabolites, the plakinic and epiplakinic acids. The classes are diastereomeric in their orientation of alkyl substituents about the 1,2-dioxolane nucleus, *cis* in plakinic acids, and *trans* in the epiplakinic acids. Comparison of the ¹H and ¹³C NMR chemical shifts of the methyl groups in known plakinic and epiplakinic acids was consistent with *trans* configuration of the methyl groups in **95**.¹⁷¹ The *cis* orientation of methyls within plakinic acids increases diastereotopic differentiation of the CH₂-4 protons in the ¹H NMR spectra, and the C-5 methyl substituent has a higher chemical shift relative to the analogous positions in epiplakinic acids.^{114,123}

Trans orientation of CH₃-18 and CH₃-19 about the 1,2-dioxolane nucleus of **95** was confirmed by a series of 1D NOE experiments. Selective irradiation of H-4a and H-4b gave exclusive enhancement of H₃-19 and H₃-18 respectively, while irradiation of the H₃-18 and H₃-19 methyls resulted in reciprocal enhancements of the methylene protons, and only weak enhancement of the other methyl (Figure 4.34).

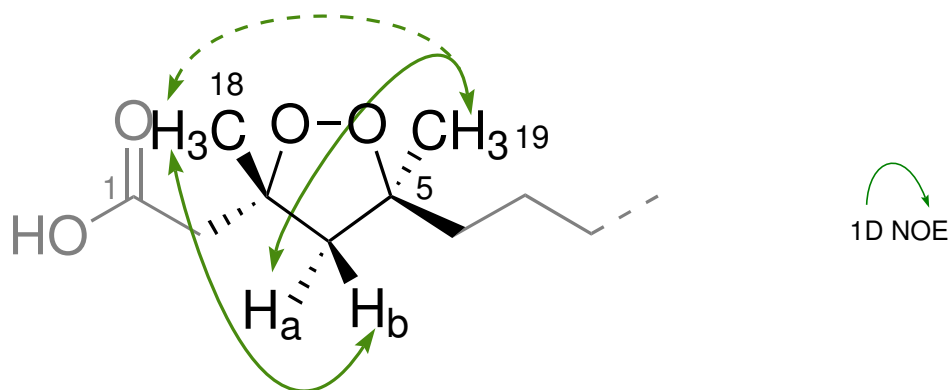


Figure 4.34 1D NOE correlations used to establish relative stereochemistry in the 1,2-dioxolane nucleus of **95**. Double headed arrows indicate reciprocal correlations, and dashed arrows indicate weak correlations.

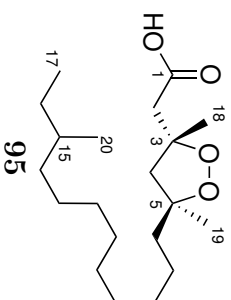
Table 4.10 NMR Spectroscopic Data of Epiplakinic Acid I (**95**), (600 MHz, CDCl₃).

Position	¹³ C			¹ H			COSY	HMBC (¹ H → ¹³ C)	NOE [†]
	δ (ppm)	mult	¹ J _{CH} (Hz)	δ (ppm)	mult	J (Hz)			
1	174.3	C							
2	44.1	CH ₂	129	2.80	d	14.9	2b	1, 3, 4, 18	4a, 4b*, 18
a									
b									
3	84.0	C	129	2.72	d	14.8	2a	1, 3, 4, 18	4a, 4b*, 18
4	55.7	CH ₂	131	2.45	d	12.5	4b	2, 3, 5, 6, 19	2a, 2b*, 19
5	86.8	C	131	2.25	d	12.4	4a	2, 3, 5, 6, 18	18
6	39.9	CH ₂	126	1.70	td	12.9, 4.5	6b, 7, 19	5, 7	4b, 18, 19
a									
b									
7	24.7	CH ₂	125	1.53	td	13.6, 3.9	6a, 7, 19	5, 7	4b, 18, 19
a									
b									
8	29.6	CH ₂	125	1.37	m		6b	8	
9	29.74	CH ₂	127	1.34	m				
10	29.8	CH ₂	123	1.22–1.30	m				
11	30.17	CH ₂	125	1.22–1.30	m				
12	30.16	CH ₂	127	1.22–1.30	m				
13	27.2	CH ₂	127	1.28	m		13b	14	
a									
b									
14	36.8	CH ₂	123	1.18	m		13a	14	
a									
b									
15	34.5	CH	122	1.26	m		13, 14b, 15	13, 15	
16	29.73	CH ₂	124	1.06	m		14a, 13, 15	13, 15	
17	11.6	CH ₃	124	1.11	sept	6.9	14, 16, 20	14, 16, 20	
18	23.9	CH ₃	125	0.84	t	6.4	15, 17	15, 17	
19	23.3	CH ₃	127	1.45	s		15, 16	15, 16	4b
20	19.7	CH ₃	126	1.29	s			2, 3, 4	4a
			123	0.83	d	8.6	15	5, 4, 6	

[†]Selected correlations.

*Weak correlations.

Absolute configuration is arbitrary.



Epiplakinic acid I methyl ester (**96**)

The methyl ester **96** eluted earlier from DIOL than its acid analogue **95**. Analysis by positive-ion mode HRESIMS revealed a $[M + Na]^+$ pseudo-molecular ion peak at m/z 371.2790, which correlated to the formula $C_{21}H_{39}O_5$. This established the presence of an additional CH_2 equivalent in the structure, relative to **95**. Comparison of 1D and 2D NMR data showed compounds **95** and **96** to be identical in structure and relative stereochemistry, except for the presence of a methoxy singlet (CH_3 -21: δ_C 52.0, δ_H 3.69) in **96**. The observation of an HMBC correlation from it (CH_3 -21) to an ester carbonyl (C-1: δ_C 171.4) confirmed the methyl ester function (Figure 4.35).

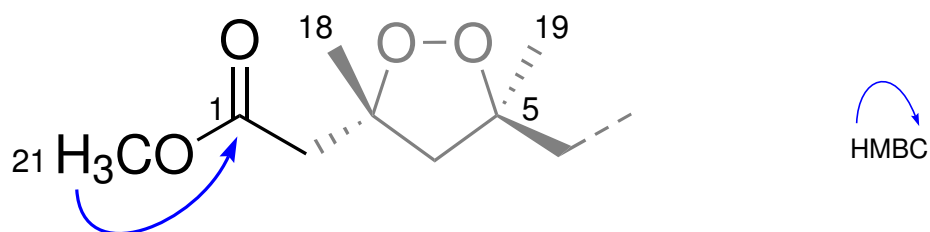


Figure 4.35 HMBC NMR correlation establishing the C-21 methyl ester moiety of **96**.

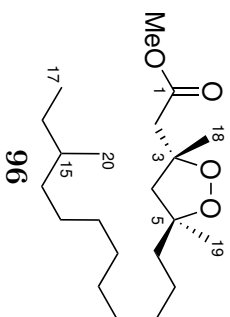
Table 4.11 NMR Spectroscopic Data of Epiplakinic Acid I Methyl Ester (**96**), (600 MHz, CDCl₃).

Position	¹³ C		¹ H		COSY	HMBC		NOE [†]
	δ (ppm)	¹ J _{CH} (Hz)	δ (ppm)	J (Hz)		(¹ H → ¹³ C)		
1	171.3	C						
2	44.1	CH ₂	129	2.80	d	14.9	2b	1, 3, 4, 18
			129	2.72	d	14.8	2a	1, 3, 4, 18
3	84.1	C						4a, 4b*, 18
4	55.5	CH ₂	131	2.45	d	12.5	4b	2, 3, 5, 6, 19
			131	2.25	d	12.4	4a	2, 3, 5, 6, 18
5	86.7	C						18
6	39.8	CH ₂	126	1.70	td	12.9, 4.5	6b, 7, 19	4b, 18, 19
			126	1.53	td	13.6, 3.9	6a, 7, 19	4b, 18, 19
7	24.7	CH ₂	125	1.37	m		6b	8
			126	1.28	m			
8	29.6	CH ₂	125	1.34	m			
9	29.74	CH ₂		1.22-1.30	m			
10	29.8	CH ₂		1.22-1.30	m			
11	30.17	CH ₂		1.22-1.30	m			
12	30.16	CH ₂		1.22-1.30	m			
13	27.2	CH ₂	127	1.28	m		13b	14
			124	1.18	m		13a	14
14	36.8	CH ₂	124	1.26	m		13, 14b, 15	13, 15
			123	1.06	m		13, 14a, 15	13, 15
15	34.5	CH	125	1.28	m		14, 16, 20	14, 16, 20
16	29.73	CH ₂	124	1.11	sep	6.9	15, 17	15, 17
17	11.6	CH ₃	125	0.84	t	6.4	15, 16	15, 16
18	24.3	CH ₃	127	1.45	s			2, 3, 4
19	23.4	CH ₃	126	1.29	s			4, 5, 6
20	19.4	CH ₃	124	0.83	d	8.6	15	15, 16
OCH ₃ -1	51.9	CH ₃	144	3.69	s		1	

[†]Selected correlations.

*Weak correlations.

Absolute configuration is arbitrary.



Plakortolide X (97)

Plakortolide X (**97**), $[\alpha]_D^{24.6} +0.0^\circ$ (c 0.08, CHCl_3), was isolated as a colourless oil. The apparent lack of rotation may indicate the isolation of a racemic mixture. Positive-ion mode HRESIMS analysis of **97** revealed a $[\text{M} + \text{H}]^+$ pseudo-molecular ion peak (m/z 349.2355) correlating to the molecular formula $\text{C}_{20}\text{H}_{38}\text{O}_4$, which required three degrees of unsaturation. A $[\text{M} - \text{H}]^-$ ion peak was observed at m/z 325.2379 by negative-ion mode analysis, confirming this formula. Evident in the 1D and 2D NMR data was conservation of the γ -methyl branched alkyl chain seen in **95** and **96**. The oxygenated end of the molecule displayed NMR resonances significantly different from those of **95** and **96**, indicating a different arrangement of functionality. The absence of an OH stretch in the IR spectrum and the continued presence of an oxy-substituted carbonyl (δ_{C} 174.3) and an additional oxy-substituted methine (δ_{C} 81.3, δ_{H} 4.46) suggested the presence of a lactone.

Strong HMBC correlations were observed from the protons of a methyl singlet, CH_3 -18 (δ_{C} 25.9, δ_{H} 1.39) to three carbon centres; oxymethine CH-3 (δ_{C} 81.3, δ_{H} 4.46), oxyquaternary C-4 (δ_{C} 83.0) and an isolated methylene CH_2 -5 (δ_{C} 40.5, δ_{H} a 2.17, b 1.71). These correlations established attachment of the methyl singlet to the non-protonated C-4, and the bonds from CH-3 to C-4 and between C-4 and CH_2 -5. COSY correlations between the methine CH-3 and a second diastereotopic methylene CH_2 -2 (δ_{C} 34.3, δ_{H} a 2.92, b 2.62) extended the substructure. HMBC correlations from the protons of CH_2 -2 to the oxycarbonyl C-1 (δ_{C} 174.3) indicated linkage from C-1 to C-2, firmly establishing the C-1 to C-5 terminus of the molecule (Figure 4.36).

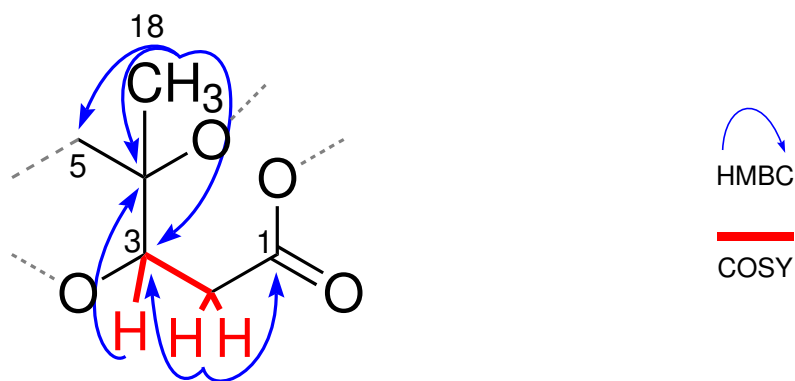


Figure 4.36 COSY and HMBC correlations establishing the C-1 to C-5 linkages in **97**.

Further evidence of the bond between C-4 and the isolated methylene CH_2 -5 was given by HMBC correlations from the protons of CH_2 -5 to the oxyquaternary C-4 and oxymethine CH-3, further extending the δ -methyl branched carbon chain (Figure 4.37). The remaining methyl singlet CH_3 -19 (δ_{C} 22.4, δ_{H} 1.29), also showed strong HMBC correlations to CH_2 -5, its non-protonated attachment point

C-6 (δ_C 80.3) and a further methylene CH₂-7 (δ_C 41.0, δ_H 1.48). Corroborating HMBC correlations were observed from H₂-5 to C-6 and CH₂-7. These correlations fully established the 4,6-dimethyl-substituted carbon chain with oxy-substitution at carbonyl C-1 and at CH-3, C-4 and C-6 (Figure 4.38).

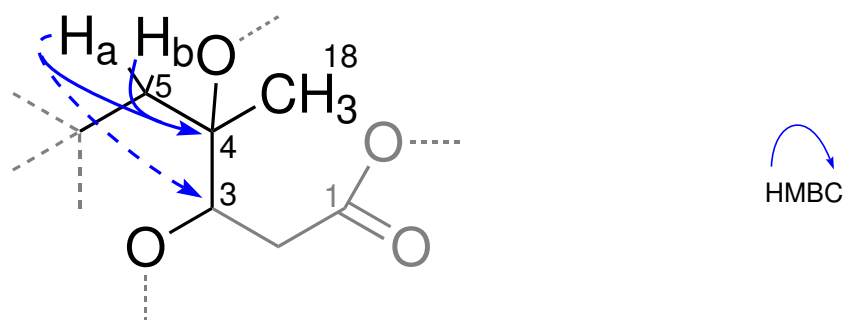


Figure 4.37 COSY and selected HMBC correlations confirming the C-3 to C-5 connections in **97**. Dashed arrows indicate weak correlations.

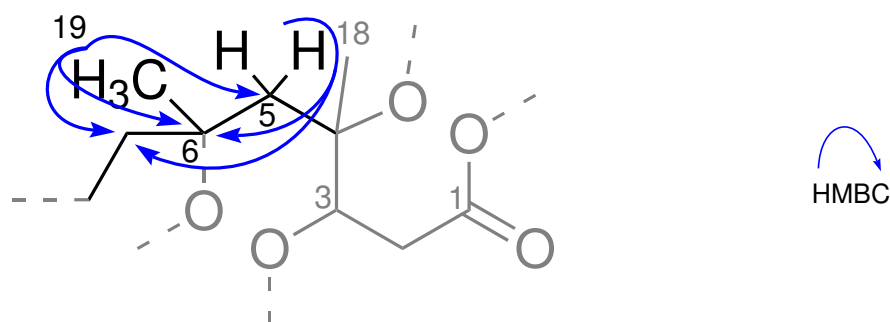


Figure 4.38 HMBC correlations establishing the linkages from C-5 to C-7 in **97**.

The remaining carbon resonances of the molecule included one methine, eight methylenes and two methyl groups. These centres were readily assembled into the γ -methyl substituted alkyl chain observed in **95** and **96** through interpretation of COSY and HMBC correlations. The attachment of this chain to CH₂-7 was confirmed by selective irradiation of the methylenes H₂-7 and H₂-14 with a 1D TOCSY experiment. Over mixing times of 20–120 ms the other resonance was revealed, confirming the connection between the C-1 to C-7 and C-14 to C-17 segments.

The γ -methyl substituted alkyl chain, C-8 to C-20, accounted for all other protons associated with the molecular formula, however, two degrees of unsaturation remained and four oxygenated linkages required incorporation via three oxygen atoms. These criteria are satisfied by formation of a bicyclic structure, with a lactone linkage between C-1 and C-4, and a peroxy bridge between C-3 and C-6 as seen in the plakortolide skeleton (Figure 4.39).

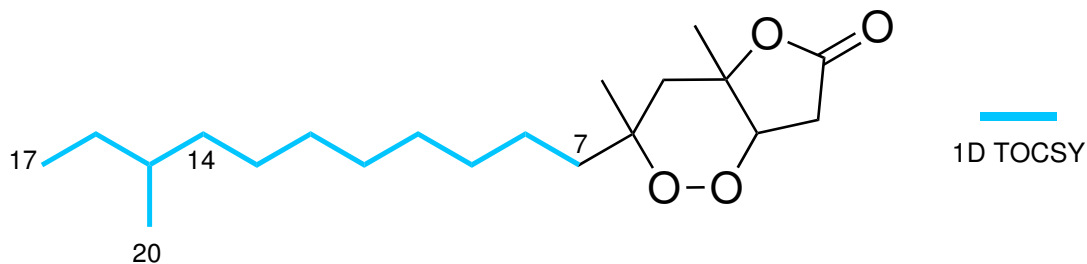


Figure 4.39 1D TOCSY correlations in **97**, confirming connection between the segments C-1 to C-7 and C-14 to C-17. Incorporation of the two final degrees of molecular unsaturation completes the structure of **97**.

Selective irradiation of H₃-18 and H-3 during 1D NOE experiments gave reciprocal enhancement of these resonances, confirming the configurations at C-3 and C-4, and the *cis* fusion of peroxy lactone bicycle. Reciprocal 1,3-diaxial correlations observed between H-3 and H-5a, and weaker correlations between H₃-18 and H-5a, placed the resonances on the same side of the six-membered 1,2-dioxane ring, while H₃-19 shared a strong NOE correlation with H-5b and a weaker correlation with H-5a. Following 1D NOE irradiation of H₃-19 and H₃-18, enhancement of neither methyl singlet was observed, indicating that the two methyls occupy opposing faces of the 1,2-dioxane ring (Figure 4.40).

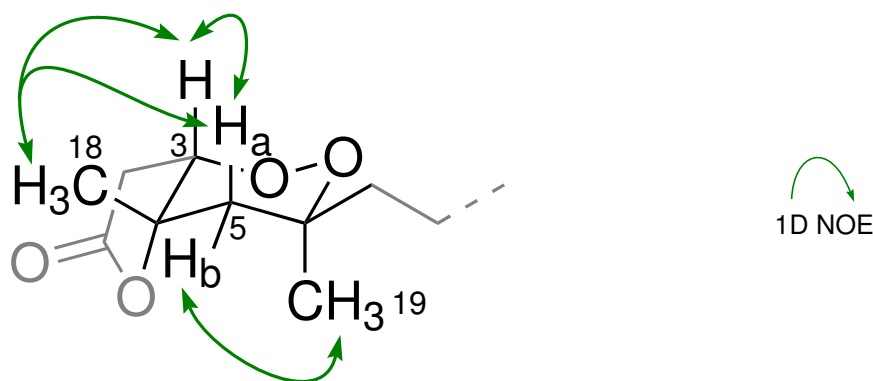


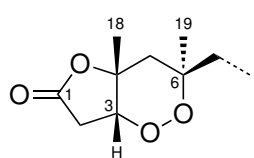
Figure 4.40 Stereochemistry about the bicyclic nucleus of **97** as evidenced by selected 1D NOE correlations. Double headed arrows indicate reciprocal correlations.

The plakortolide class has primarily been isolated from sponges identified as *Plakinastrella* sp. although some examples have been reported from specimens identified as *Plakortis* sponges. Comparison of the NMR spectral data of **97** with that of plakortolide T,¹⁶⁶ as shown in Table 4.12, supported the structural assignment of **97**. A complete tabulation of the NMR spectroscopic data for **97** can be found in Table 4.13.

Fusion of the plakortolide bicycle at C-3 and C-4 is exclusively *cis*, although varied configuration at C-6 forms two diastereomeric carbon skeletons, which display significant differences in ¹H chemical shift of CH₂-5 and the C-4 methyl

substituent.¹⁷² Orientation of the C-4 and C-6 methyls on opposing faces decreases diastereotopic differentiation of the H₂-5 protons, and ¹H NMR chemical shift of the C-4 methyl increases ca. 0.1 ppm.¹²⁴ Hydrolysis of the peroxide bridge produces another structural variant, the *seco*-plakortolide diols, which have been reported as both true isolates and as synthetic degradation products of plakortolides.¹²⁴ One can easily distinguish the peroxide and diol forms through analysis of the H₂-5 ¹H NMR shifts. Ring strain in the peroxide form increases the diastereotopic differentiation of H-5a and H-5b relative to the diol form. Furthermore, the ¹H NMR shifts of the C-4 and C-6 methyl groups are deshielded by ca. 0.1 ppm in plakortolides, relative to *seco*-plakortolides.¹²⁴

Table 4.12 Comparison of Salient NMR Chemical Shifts in Plakortolide T¹⁶⁶ relative to those of Plakortolide X (**97**).



Pos	mult	97 *		Plakortolide T [†]		Difference [‡]	
		¹³ C δ (ppm)	¹ H δ (ppm)	¹³ C δ (ppm)	¹ H δ (ppm)	¹³ C Δδ (ppm)	¹ H Δδ (ppm)
1	C	174.3		174.9		0.6	0.00
2 a	CH ₂	34.5	2.92	34.5	2.91	0.0	-0.01
b			2.62		2.62		0.0
3	CH	81.2	4.46	81.3	4.45	0.1	-0.01
4	C	83.0		83.3			
5 a	CH ₂	40.7	2.17	40.8	2.17	0.1	0.00
5 b			1.71		1.71		0.00
6	C	80.2		80.5		0.3	
18	CH ₃	26.0	1.39	26.4	1.39	0.4	0.00
19	CH ₃	22.5	1.29	22.6	1.29	0.1	0.00

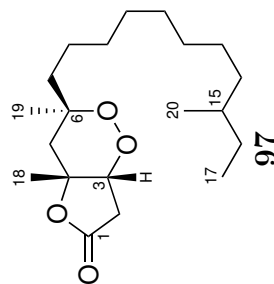
*CDCl₃, ¹H 600 MHz; ¹³C 150 MHz.

†CDCl₃, ¹H 500 MHz; ¹³C 125 MHz.

‡Δδ = δ_{Plakortolide T} - δ₉₇

Table 4.13 NMR Spectroscopic Data of Plakortolide X (**97**), (600 MHz, CDCl₃).

Position	¹³ C		¹ H		J (Hz)	COSY	HMBC (¹ H → ¹³ C)	NOE†
	δ (ppm)	mult	¹ J _{CH} (Hz)	δ (ppm)				
1	174.3	C						
2 a	34.46	CH ₂	130	2.92	dd	2b, 3	1, 3, 4	3
b			141	2.62	d	2a, 3	1, 3, 4	4a, 4b
3	81.2	CH	158	4.46	d	2a, 5a	4	5a, 18
4	83.0	C						
5 a	40.7	CH ₂	129	2.17	d	3, 5b	4, 6, 19	18, 19
b			126	1.71	d	5a	1*, 4, 6, 19	4, 5a, 7, 18
6	80.2	C						
7	41.2	CH ₂	123	1.48	m	8	6, 8, 19	
8	30.0	CH ₂	127	1.27	m	7, 9	7, 9, 10*	
9	23.2	CH ₂	127	1.28	m	8, 10	10	
10	30.2	CH ₂	124	1.26	quin	9, 11	9, 11	
11‡	29.7	CH ₂	124	1.26	m	10, 12	10, 12	
12‡	29.7	CH ₂	124	1.26	m	11, 13	11, 13	
13 a	27.2	CH ₂	127	1.28	m	14	6, 8, 19	
b			124	1.21	m	14	6, 8, 19	
14 a	36.7	CH ₂	119	1.27	m	13, 14b, 15	13, 15, 16	
b			122	1.05	m	13, 14a, 15	13, 15, 16	
15	34.51	CH ₂	125	1.28	quin	5.7	14a, 14b, 16a, 16b	14, 16, 17
16 a	29.6	CH ₂	124	1.32	quin	5.5	15a, 16b, 17	15, 17, 19
b			122	1.11	sep	6.7	15, 17, 19	15, 17, 19
17	11.6	CH ₃	125	0.85	t	7.1	16	15, 16
18	26.0	CH ₃	128	1.39	s		3, 4, 5	3, 5a, 5b*
19	22.5	CH ₃	127	1.29	s		5, 6, 7	5b
20	19.4	CH ₃	124	0.83	d	5.9	15	14, 15, 16



†Selected correlations.

*Weak correlations.

‡Indistinguishable

Absolute configuration is arbitrary.

Cyclic peroxide **98**

Isolated as colourless oil, positive- and negative-ion mode HRESIMS analysis of **98**, $[\alpha]_D^{24.6} +4.1^\circ$ (c 0.03, CHCl_3), indicated a molecular formula of $\text{C}_{21}\text{H}_{40}\text{O}_5$; $[(m/z$ 395.2771 $[\text{M} + \text{Na}]^+$, Δ -0.8 ppm) and $(m/z$ 371.2790 $[\text{M} - \text{H}]^-$, Δ -1.9 ppm)]. This formula required the incorporation of an additional oxygen atom, relative to compounds **95–97**. Evident in the 1D and 2D NMR data was conservation of the γ -methyl branched alkyl chain. However, the oxygenated terminus of the molecule displayed NMR resonances differing again from those observed in the spectra of compounds **95–97**, indicating a further variation in functional arrangement. In particular, the chemical shift of one of the oxyquaternary centres had increased significantly to δ_{C} 100.9 ppm, from the δ_{C} 80–84 ppm observed in the previous three compounds. An OH stretch was observed in the IR spectrum (ν_{max} 3374 cm^{-1}), which in combination with an oxy-substituted carbonyl (δ_{C} 174.7; ν_{max} 1717 cm^{-1}) was again suggestive of a carboxylic acid functionality.

As illustrated in Figure 4.41, correlations were observed in the COSY experiment between the aliphatic methyl doublet CH_3 -19 (δ_{C} 16.2, δ_{H} 0.99), methine CH -4 (δ_{C} 32.7, δ_{H} 1.99) and the diastereotopic methylene CH_2 -5 (δ_{C} 37.3, δ_{H} a 1.66, b 1.41). The C-19–C-4–C-5 bonds were confirmed by HMBC correlations from the methyl doublet CH_3 -19 to the methine CH -4 and the adjacent methylene CH_2 -5. A third HMBC correlation was observed from CH_3 -19 to the highly deshielded oxyquaternary C-3 (δ_{C} 100.9), whose chemical shift is consistent with dioxy-substitution. These correlations established the connections from C-3 to C-5.

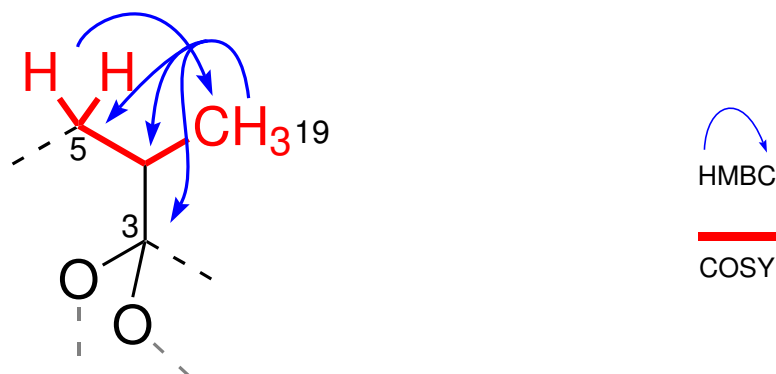


Figure 4.41 COSY and selected HMBC correlations evidencing the C-3 to C-5 connections and methyl substitution of C-4 in **98**.

An isolated diastereotopic methylene CH_2 -2 (δ_{C} 39.4, δ_{H} a 2.89, b 2.55) displayed HMBC correlations to C-4 and C-3, confirming the C-3–C-4 bond and connection between CH_2 -2 and C-3. HMBC correlations from both protons of the methylene CH_2 -2 were observed to the oxy-substituted carbonyl C-1 completing the γ -methyl

substituted carbon chain C-1 to C-5. Strong HMBC correlations were observed from the methyl singlet CH₃-20 (δ_C 20.1, δ_H 1.34) to the methylene CH₂-5, its attachment point the oxyquaternary centre C-6 (δ_C 81.1) and another methylene CH₂-7 (δ_C 40.6, δ_H 1.42). These were corroborated by HMBC correlations observed from H₂-5 to both C-4 and C-6. As shown in Figure 4.42, these correlations established the linear connectivity from C-1 to C-7 with oxycarbonyl substitution at C-1, dioxy-substitution at C-3 and monooxygenation at C-6.

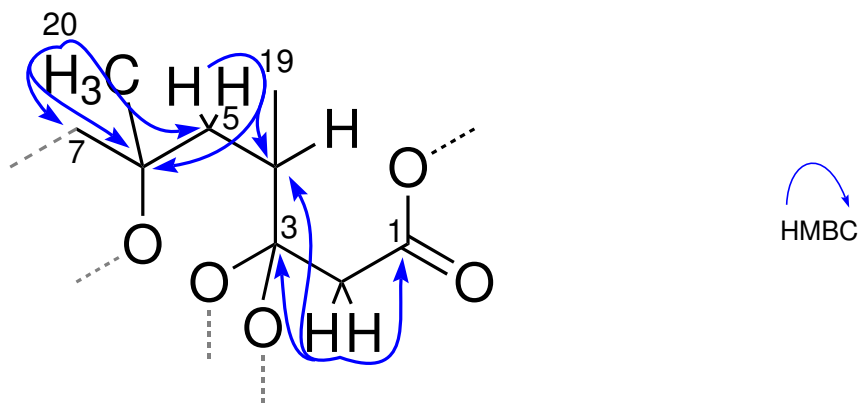


Figure 4.42 HMBC correlations proving the connections C-1 to C-4 and C-5 to C-7 and methyl substitution of C-6 in **98**.

A series of sequential COSY and HMBC correlations established the aliphatic chain extending from CH₂-7 to CH₃-18, with methyl substitution at CH-16. Connection between the protonated centres H₂-7 to H₃-18 was proven via irradiation of H₂-7, H₂-14 and H₃-18 with 1D TOCSY experiments over mixing times of 20–200 ms, as shown in Figure 4.43.

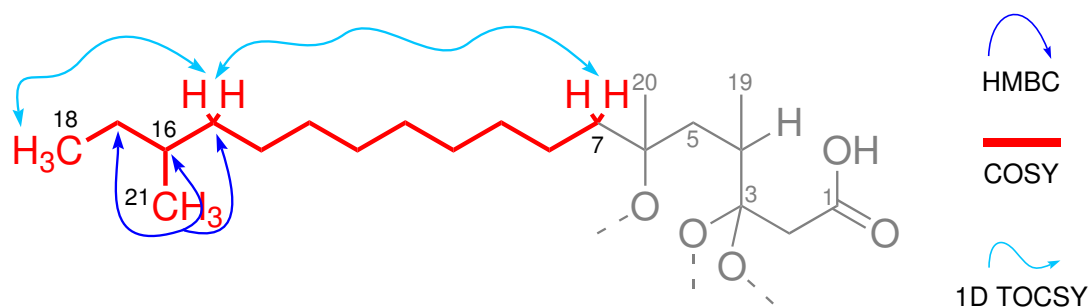


Figure 4.43 The completed linear structure of **98** as evidenced by COSY, 1D TOCSY and selected HMBC correlations. Double headed arrows indicate reciprocal correlations.

The presence of five oxygen atoms in the molecular formula, implied that C-1, C-3 and C-6 are substituted by different oxygens. As only two hydrogen atoms remained from the molecular formula, another degree of unsaturation required incorporation. Formation of a six-membered cyclic peroxide function bridging from the hemiacetal centre C-3 to C-6, and an acid function at C-1 satisfied these requirements. The strong, reciprocal NOE correlations observed between methine CH-4 and the C-6

substituent, CH₃-20, are consistent with their 1,3-diaxial positioning on the six-membered peroxide ring. The methyl H₃-20 and CH-4 shared further strong NOE correlations with H-5b, while the C-4 substituent H₃-19 correlated strongly with H-5a and weakly with H-5b. NOE enhancement was not observed between H₃-19 and H₃-20, indicating that they occupied opposing faces on the 1,2-dioxane ring (Figure 4.44).

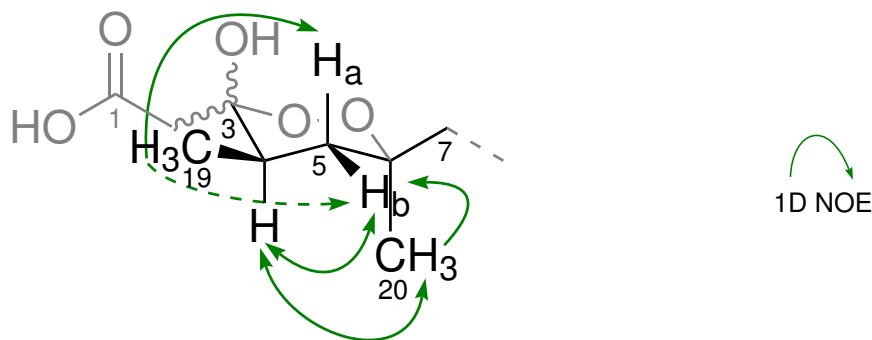
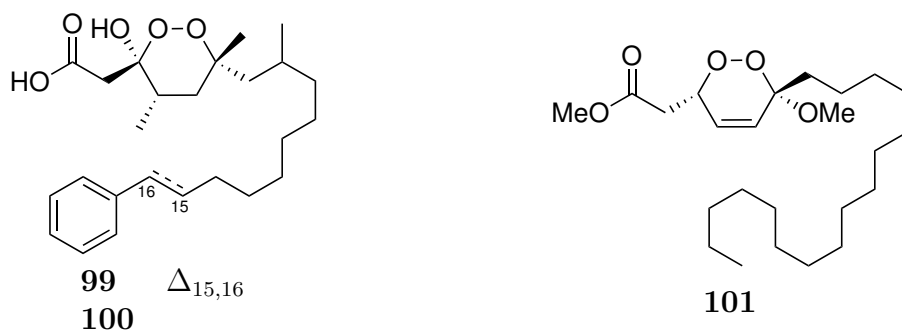
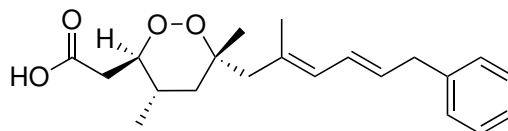


Figure 4.44 1D NOE correlations evidencing the 1,3-diaxial positioning of CH-4 and CH₃-20 and relative configuration at C-4 and C-6 in **98**. Double headed arrows indicate reciprocal correlations.

The only other report of the 1-hydroxy-1,2-dioxane moiety of **98** is in compounds **99** and **100**, metabolites isolated from a *Plakortis* (or *Plakinastrella*) specimen collected in Guam.¹⁷³ Manzo *et al.* reported that **99** and **100** underwent degradative decarboxylation during the isolation process (reversed-phase HPLC in MeOH).¹⁷³ Such degradation was not encountered during this study. Compound **98** also bears structural similarity to plakorin (**101**),¹²⁰ although differing in the position of the hemi-acetal oxygen.



While the configuration at C-4 and C-6 in **98** was readily assigned by NOE correlations, configuration of C-3 was more difficult to determine, and was assigned through spectroscopic comparison with methyl capucinoate (**102**). Isolated from a Caribbean *Plakinastrella onkodes* specimen,¹²⁸ **102** shares the methylation pattern of **98**, **99** and **100** but bears an axial hydrogen at C-3 in place of the hydroxyl group.



102

As with **98**, the 1,3-diaxial orientation of H-4 and the C-6 methyl in compounds **99** and **100** was assigned on the basis of 1D NOE experiments.¹⁷³ Chemical shift comparison of **99** and **100** with **102** led Manzo *et al.* to position the C-3 hydroxyl in **99** and **100** axially. The configuration at C-3 in **99** and **100** was inferred from the downfield chemical shift of the H-5_{ax} proton in **99** relative to **102**.¹⁷³ The same argument can be applied to **98**. Consistent with 1,3-diaxial interactions with a hydroxyl function, the H-5_{ax} proton resonance appears 0.31 ppm further downfield in **98** and **99** compared with the corresponding proton in **102** [(**98**: δ_{H} 1.66, t, $J = 12.8$ Hz), (**99**: δ_{H} 1.70, dd, $J = 13.1, 13.1$ Hz) and (**102**: δ_{H} 1.39, t, $J = 12.8$)].¹⁷³ Other spectral data about the peroxide cores of compounds **98–100** are virtually identical, implying conservation of relative configuration between the three compounds. Comparison of the chemical shift differences about the cyclic peroxide nuclei of **98** and **99** can be found in Table 4.14. NMR spectroscopic data for **98** is detailed in Table 4.15.

Table 4.14 Comparison of Salient NMR Chemical Shifts in **98** and **99**.

Pos	mult	98 *		99 †		Difference‡	
		¹³ C δ (ppm)	¹ H δ (ppm)	¹³ C δ (ppm)	¹ H δ (ppm)	¹³ C $\Delta\delta$ (ppm)	¹ H $\Delta\delta$ (ppm)
4	CH	32.9	1.99	32.7	1.99	-0.2	0.00
5 a	CH ₂	37.4	1.66	36.6	1.67	0.8	0.01
b			1.41		1.36		-0.05
19	CH ₃	16.2	0.99	16.1	0.98	-0.1	-0.01
20	CH ₃	20.3	1.34	20.3	1.31	0.0	0.03

*CDCl₃, ¹H 600 MHz; ¹³C 150 MHz.

†CDCl₃, ¹H 400 MHz; ¹³C 75 MHz.

‡ $\Delta\delta = \delta_{99} - \delta_{98}$

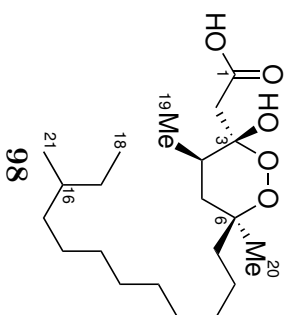
Table 4.15 NMR Spectroscopic Data of Compound **98**, (600 MHz, CDCl₃).

Position	¹³ C			¹ H			COSY	HMBC (¹ H → ¹³ C)	NOE†
	δ (ppm)	mult	¹ J _{CH} (Hz)	δ (ppm)	mult	J (Hz)			
1	174.7	C							
2	39.4	CH ₂	128	2.89	d	15.9	2b	1, 3, 4	
a									
b			132	2.55	d	15.9	2a	1, 3, 4, 18	4, 20
3	100.9	C							
4	32.9	CH	127	1.99	sep	6.2	5a, 5b, 19	2b, 3, 5, 19	2b, 5a*, 5b, 20
5	37.4	CH ₂	128	1.66	t	12.8	4, 5b	3, 6, 7, 19, 20	
a									
b			128	1.41	dd	13.5, 4.7	4, 5a	3, 6, 7, 19, 20	
6	81.1	C							
7	40.7	CH ₂	122	1.53	td	13.6, 3.9	6a, 7, 19	5, 7	5b, 18, 19
a									
b			122	1.42	m		8	5b, 8, 9	
8	23.0	CH ₂							
9	30.1	CH ₂	122	1.31	m		7, 9	7, 9	
10	30.2	CH ₂	120	1.24	m		8		
11	29.8	CH ₂	121	1.23	m		8		
12	29.7	CH ₂	121	1.25	m		8		
13	29.65	CH ₂	123	1.11	quin	6.9		12, 14	
14	27.2	CH ₂	122	1.20	m			13, 15	
15	36.8	CH ₂	123	1.26	m			14, 16	
a								15a, 16	
b								15, 17, 19	
16	34.5	CH	124	1.28	m	7.4	15, 16, 21	15, 17, 19	
17	29.64	CH ₂	121	1.28	m		16, 18	16, 18	
18	11.6	CH ₃	120	0.85	t	7.5	16*, 17	16, 17	
19	16.2	CH ₃	126	0.99	d	7.0	4	2, 4, 5	5a, 5b*
20	20.3	CH ₃	125	1.34	s			5, 6, 7	
21	19.4	CH ₃	123	0.88	d	7.1	16	15, 16, 17	4, 5b

†Selected correlations.

*Weak correlations.

Absolute configuration is arbitrary.



4.3.2 Growth inhibition of eukaryotes

Cyclic peroxides **95**, **97** and **98** displayed cytotoxicity against the HL-60 cell line (Figure 4.45).⁹³ Using a standard 48 h cell proliferation MTT assay, **95**, **97** and **98** exhibited IC₅₀ values for growth inhibition of 13.43, 285.09 and 3.59 nmol L⁻¹ respectively, while 5 α ,8 α -epidioxysterols **27** and **28** showed far weaker inhibition of the same cell line with respective IC₅₀ values of 6.48 and 7.90 μ mol L⁻¹ (not shown).⁹³

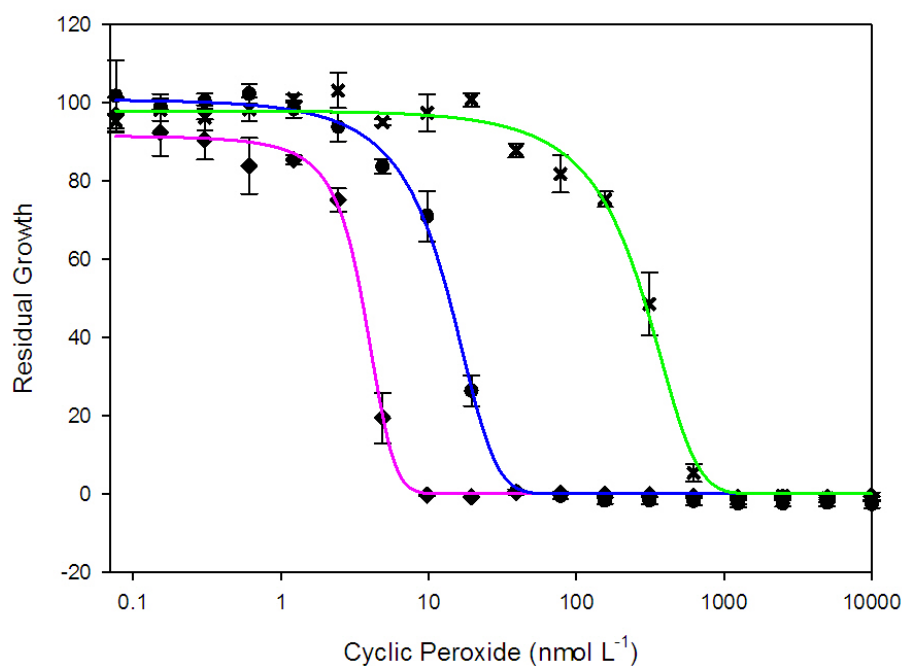


Figure 4.45 MTT-assay showing inhibition of the HL-60 cell line by **95** (●), IC₅₀ 13.43 nmol L⁻¹; **97** (×), IC₅₀ 285.09 nmol L⁻¹; and **98** (◇), IC₅₀ 3.59 nmol L⁻¹.

The biological activities of epiplakinic acid I (**95**) and plakortolide X (**97**) were further investigated using two strains of *Saccharomyces cerevisiae* yeast, a wild-type (WT) and a drug-sensitive mutant strain (Δpdr). The Δpdr strain carries deletions for the transcription factor genes, *PDR3* and *PDR3*, which regulate expression of the pleiotropic drug resistance pump network.¹⁷⁴ Unable to upregulate the PDR response, the Δpdr strain is up to 3–100-fold more sensitive to some xenobiotics than WT yeast.¹⁷⁵ Interestingly, **95** displayed similar inhibition of WT and the Δpdr mutant strain, IC₅₀ 3.36 and 3.50 μ mol L⁻¹ respectively, indicating **95** is not a substrate for the PDR pump network. Conversely, **97** was ineffective against WT, and inhibited the Δpdr strain (IC₅₀ 4.45 μ mol L⁻¹). This suggests that **97** is a substrate for one of the PDR pumps; a change in biological activity that may be due to the change in carbonyl functionality. Chemical genetic screening of **95** and **97** is discussed in Chapter 5.

4.3.3 Organism classification

Chemotaxonomic analysis of the sponge PTN3_19D, in combination with physical examination, points irrevocably to the plakinid genera *Plakinastrella* and *Plakortis*, although further distinction is difficult. A larger proportion of cyclic peroxides have been isolated from the *Plakinastrella* genus in comparison to *Plakortis*. Epiplakinic acids and plakortolide compounds have been found almost exclusively in *Plakinastrella* specimens, although the single report of the 1-hydroxy-1,2-dioxane nucleus of compound **98** is from a specimen of *Plakortis* sp.¹⁷³ In all these cases the initial organism identification can be debated given the close relationship between the genera. In the case of **99** and **100**, the specimen was originally identified as *Plakinastrella clathrata* (Kilpatrick, 1911), but only one size-class of diod spicules and few irregularly-shaped triods were observed and the organisms was eventually reclassified as *Plakortis*.¹⁷³

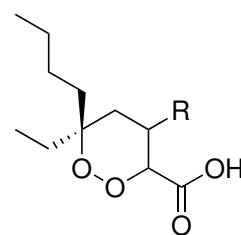
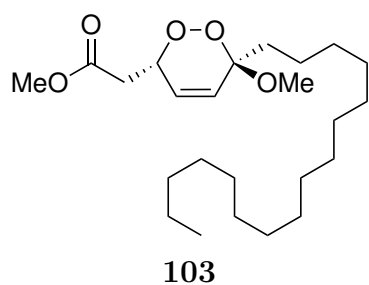
The exclusive occurrence of cyclic peroxides such as **95–98** in sponges of the *Plakortis* and *Plakinastrella* genera may indicate singular symbiosis of specific bacteria with sponges from the Plakinidae family, similar to that observed in *Myxilla* and *Haliclona* sponges.⁵² Microbial origins for the plakinid polyketides further explains subtle changes in metabolite profiles between specimens collected from different environments and locations.⁵³ In stark contrast, the 5 α ,8 α -epidioxysterols **27** and **28** have been isolated from sponges of many orders from different locations. This may indicate that **27** and **28** are products of sponge metabolism, which is less affected by subtle environmental variation, or simply products of bacteria common to both locations and sponge orders.

4.3.4 Cyclic peroxide natural products

A great number of cyclic peroxide sponge metabolites of both polyketide and terpenoid derivation have been isolated in addition to those from plakinidae sponges, a selection of which are detailed below.

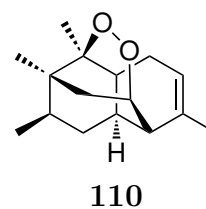
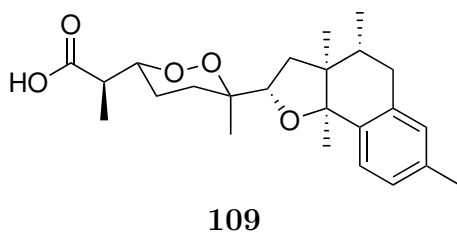
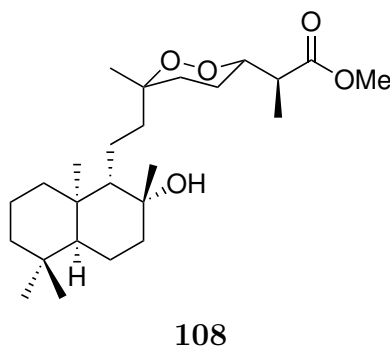
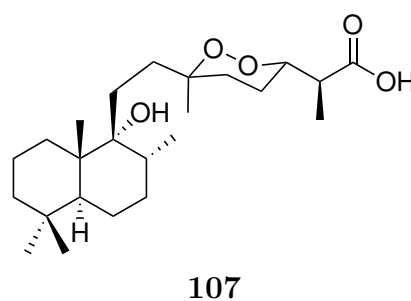
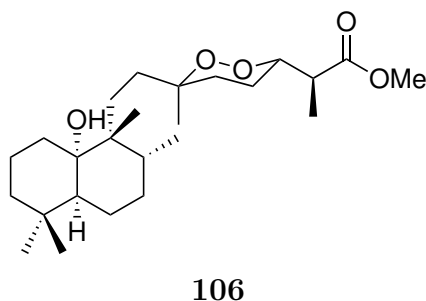
Plakorin (**101**) was first isolated from an Okinawan *Plakortis* specimen,¹²⁰ while its C-3 epimer chondrillin (**103**) has been encountered in *Plakortis*^{176,177} and *Chondrilla* sponges.¹⁷⁸ Six plakorin-like metabolites were reported in 1993 from another collection of Okinawan *Plakortis* sponge, the crude extracts of which displayed potent antifungal activity.¹⁶⁸ However, the metabolites were found to be too reactive to allow isolation by either (preparative) TLC or HPLC (the stationary phase was not specified), and their structures were elucidated from a semi-pure mixture.¹⁶⁸ A specimen of *Callyspongia* sp. collected in New Guinea was found to contain two

modestly cytotoxic alkyl-branched 1,2-dioxane carboxylates **104** and **105**,¹⁷⁹ sharing great structural similarity with *Plakortis* isolates the plakortides.^{127,180}

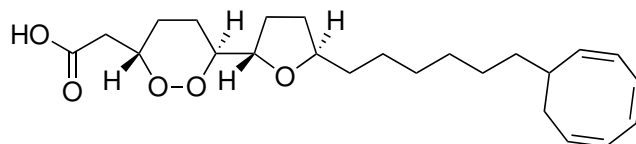


104 R = CH(CH₃)₂
105 R = CH₂CH₃

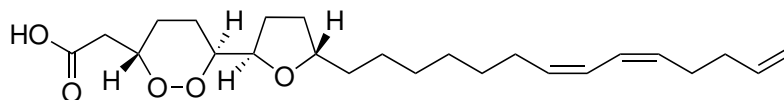
A Thai collection of *Mycale* sp. yielded two norsesterterpene 1,2-dioxanes **106** and **107**.¹⁸¹ differing by the hydroxyl and methyl substitution of C-9 and C-10. The two compounds show diverse biological activity: inhibition of several tumor cell lines, antiviral activity against the vesicular stomatitis virus and HSV-1, and growth inhibition of some gram positive bacteria. An Australian collection of the same genus afforded several similar norsesterterpene 1,2-dioxanes including **108**, while an Australian *Latrunculia conulosa* specimen yielded several rearranged norsesterterpenes including **109**, and the aptly named pentacycle contrunculin B (**110**).¹⁸²



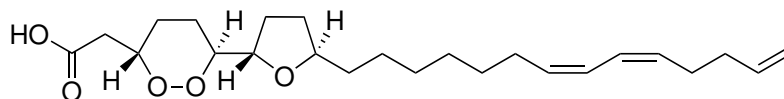
Cyclic peroxides have widely been encountered in sponges, other marine invertebrates and their predators. The ascidian *Stolonica socialis* has produced metabolites most similar to those of plakinid origins.¹⁸³ The stolonoxides feature a 2,5-*trans*-substituted tetrahydrofuran ring adjoined by a 1,2-dioxolane carboxylate, and a partially unsaturated long alkyl chain extending from the 5-position of the tetrahydrofuran ring. Recent additions to the class, stolonoxide E (**111**) and its diastereomer stolonoxide F, were isolated from a Spanish specimen of the ascidian. Both terminate in an unusual cyclooctatriene function, thought to form from an unstable terminal tetraene function. As stolonoxides A and C (**112** and **113**) both possess a terminal alkene separated from an internal diene by two methylene groups, the formation of a tetraene is not implausible. Whether formation of the 2,4,6-cyclooctatriene moiety occurs *in vivo* or during isolation is uncertain, however.¹⁸⁴ The stolonoxides all display low micromolar cytotoxicity across several mammalian cancer cell lines including the breast cancer (MDA-MB-231), colon adenocarcinoma (HT-29) and lung epithelial cell adenocarcinoma (A549).¹⁸³



111

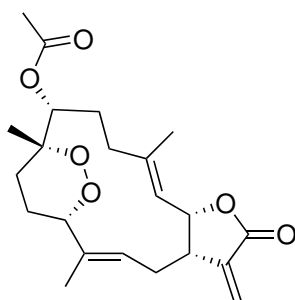


112

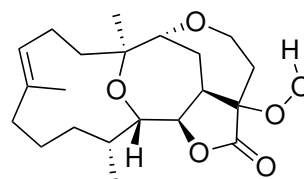


113

Soft corals, such as *Labophytum denticulatum* and other species within the genus have also been observed to incorporate peroxide linkages within their characteristic cembranolide diterpene carbon skeletons giving rise to structures such as 7-epidenticulatolide (**114**).¹⁸⁵ Hydroperoxides are also encountered within the marine environment, such as cembranoid **115** from the mollusc *Planaxis sulcatus*.¹⁸⁶



114

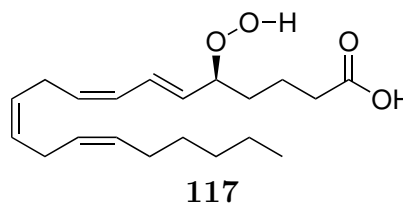
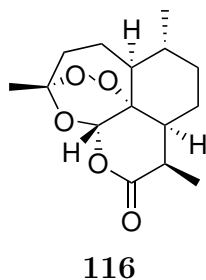


115

Derived from the sweet wormwood *Artemisia annua*, the sesquiterpene artemisininins are the most noted terrestrial cyclic peroxide metabolites.¹⁸⁷ Derivatives of the parent artemisinin skeleton (**116**), first reported in 1971, are now the standard treatment worldwide for *Plasmodium falciparum* malaria, delivering the most rapid action of all pharmaceuticals currently available to combat the disease.¹⁸⁸

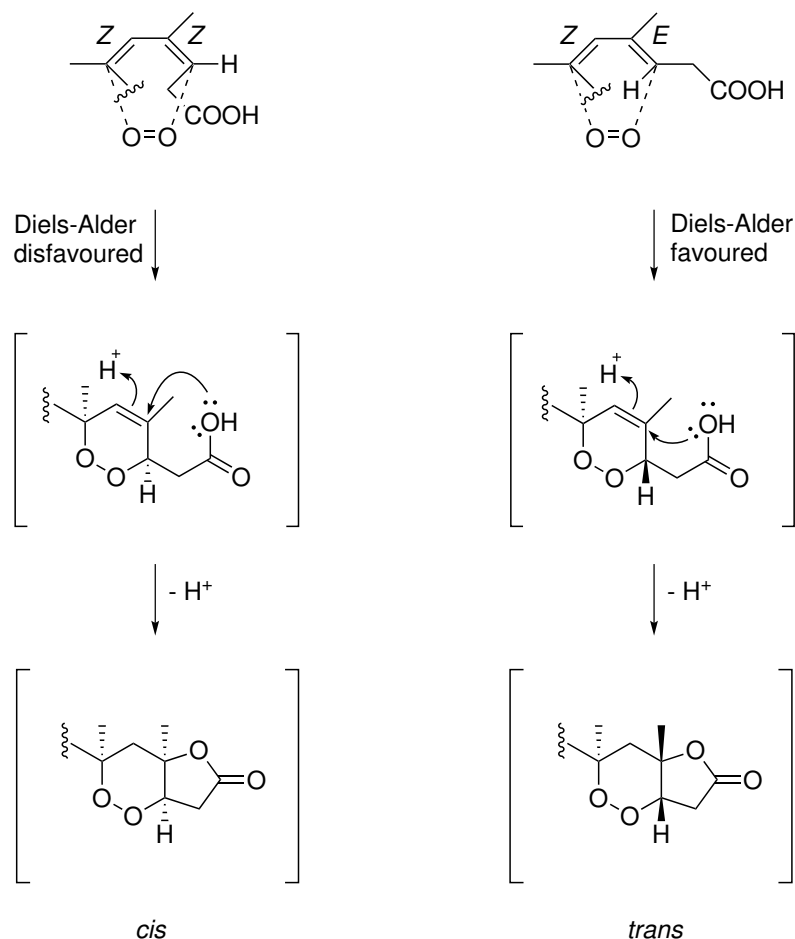
A wide-range of monoterpene and diterpene cyclic peroxide metabolites have also been reported from terrestrial sources, as have steroidal peroxides such as the ubiquitous 5 α ,8 α -epidioxysterols. These classes are encountered widely in sponges,⁸⁰ gorgonians and ascidians,⁸³ with the peroxide function thought to form by addition of molecular oxygen across the $\Delta_{5,7}$ diene. Both the 5 α ,8 α - and 5 β ,8 β -epidioxysterols have been the focus of many biological studies attributing antiviral,⁸⁰ cytotoxic,^{80,83} immunosuppressive,¹⁸⁹ and modest antibacterial¹⁹⁰ activities to the carbon skeletons.

Fatty acid metabolites of both marine and terrestrial origins are final additions to this complement of cyclic peroxides. Lipoxygenase enzymes, present within a variety of organisms, act upon arachidonic acid and derivatives of linoleic acid producing a number of hydroperoxy-eicosatetraenoic acids such as **117**, which affect a wide range of biological functions.¹⁹¹



4.3.5 Biogenesis of cyclic peroxides from plakinid sponges

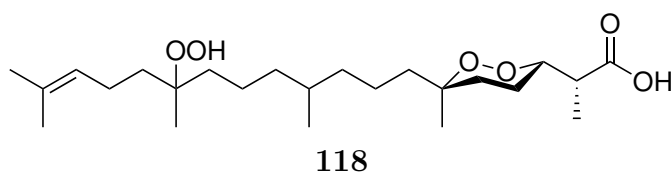
Cyclic peroxides **95–98** are of polyketide derivation, comprised predominantly of acetate monomers with three propionate units forming the methyl side-branches. There are two primary mechanisms proposed for formation of the cyclic peroxide moiety. The first involves Diels-Alder cycloaddition of singlet oxygen across a diene.^{192,193} Such an approach was employed in the synthesis of 6-*epi*-plakortolide E,¹⁹⁴ however, as shown in Scheme 4.6, the regiospecific mechanism cannot account for the stereochemistry evident within some natural product classes.¹²⁴ Attack of molecular oxygen at C-6 from the bottom face installs an arbitrary 6*S* configuration, and a (3*E*,5*Z*)-diene acid provides *trans* configuration of methyl groups as seen in **97**. Yong *et al.*¹²⁴ have noted that generation of *cis* plakortolides is unlikely by this mechanism, requiring either a change in diene configuration to 3*Z*,5*Z* introducing unfavourable steric congestion, or attack of oxygen from the top face of a 3*E*,5*Z* precursor disallowing 6*S* configuration.



Scheme 4.6 Biosynthesis of cyclic peroxides via Diels-Alder cycloaddition of molecular oxygen as proposed by Yong *et al.*¹²⁴

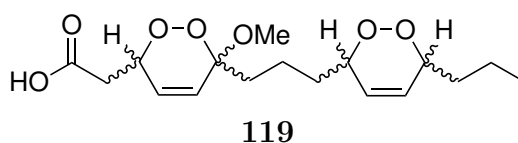
An alternate model from Ovenden and Capon rationalises biosynthesis of the norterpene sigmosceptrrellins, such as **118**, in a manner comparable to oxylipin

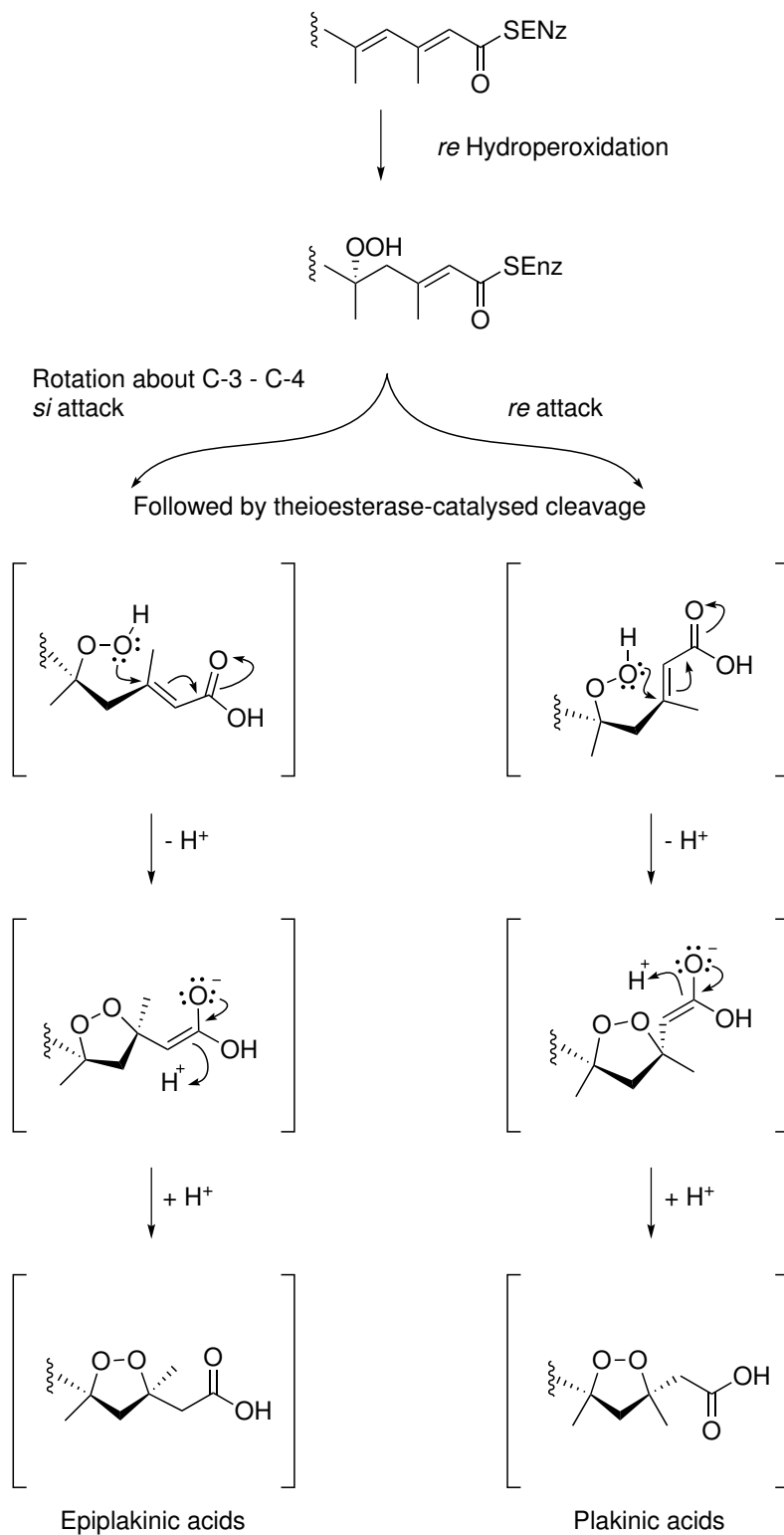
biosynthesis,¹⁹¹ and can be applied to plakinid polyketide metabolites.¹⁹⁵ As shown in Scheme 4.7, stereochemistry is defined in the first step where hydroperoxidation occurs on the *re* or *si* face of a skipped diene. The adjacent carbonyl activates the alkene to oxa-Michael addition by the hydroperoxide nucleophile, defining stereochemistry about the C-3 position. Conceivably, the overall mechanism could occur pre- or post-cleavage from the polyketide ACP domain. Support for the theory of carbonyl activation can be found in the structure of **118**, which bears a γ -alkene and hydroperoxide in addition to an acid-substituted cyclic peroxide moiety. The absence of an activating carbonyl group appears to have impeded cyclisation of the hydroperoxide and γ -alkene functions.¹⁹⁶



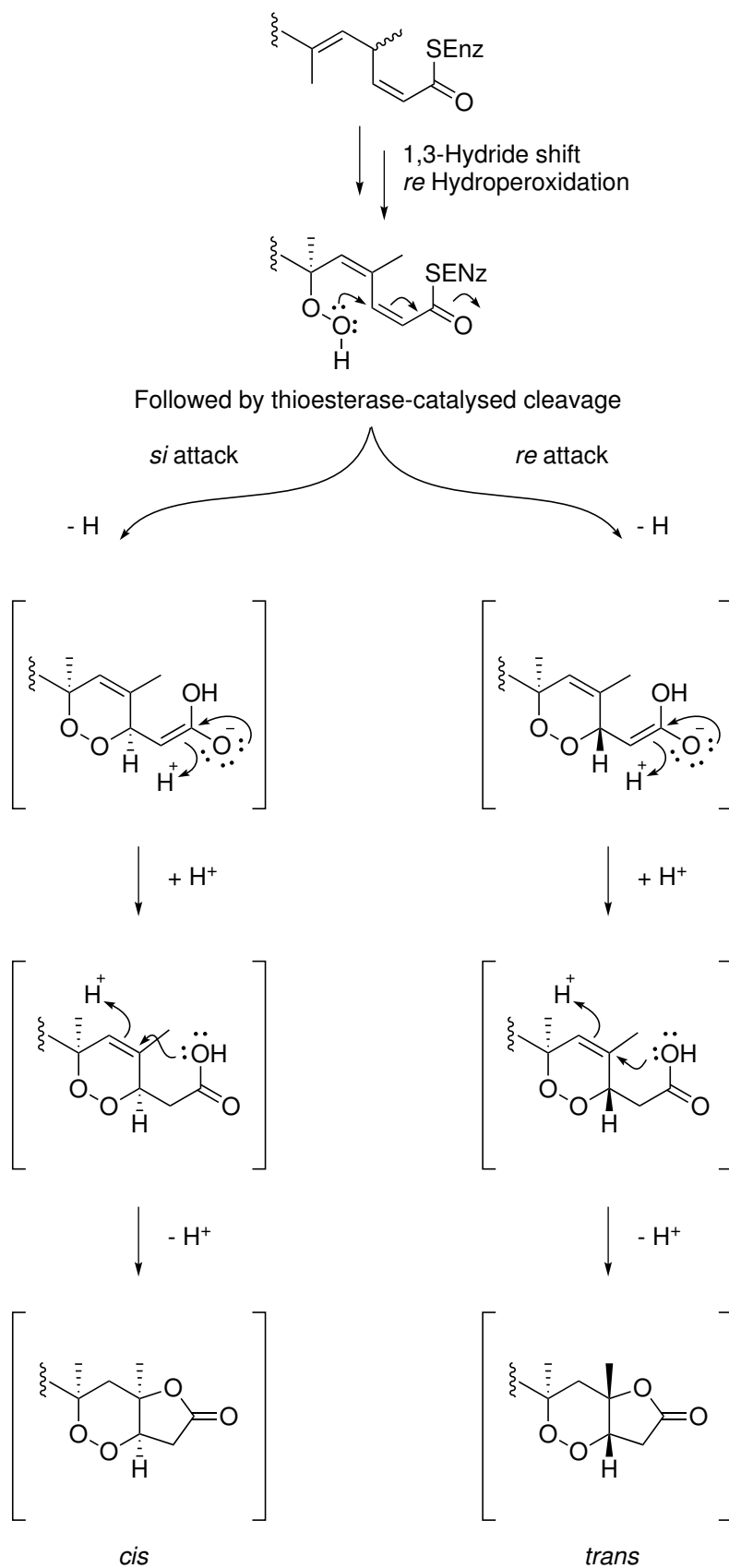
Application of the Oviden-Capon mechanism to conjugated diene substrates generates diastereomeric plakinic and epiplakinic acids (see Scheme 4.8). As noted by Yong *et al.*, migration of the Δ_5 alkene to Δ_4 via a 1,3-hydride shift prior to the initial hydroperoxidation introduces unsaturation observed in the plakortide skeleton (see Scheme 4.9). This provides a suitable electrophile for *re* or *si* attack by the terminal carboxylic acid generating both diastereomers of the plakortide bicycle.¹²⁴ Finally, as depicted in Scheme 4.10, the same mechanism can be invoked in the proposed biosynthesis of the 1-hydroxy-1,2-dioxane core of **98**. The presence of a ketone at C-3 allows formation of both epimers of the hemi-acetal function.

However, the *bis*-1,2-dioxene polyketides, represented by **119**, isolated from South African *Plakortis aff. simplex* specimens question the theory of carbonyl-activated cyclisation, or raises the possibility of cyclisation occurring by more than one mechanism within the same substrate. The second cyclic peroxide group could be a product of a [4+2] cycloaddition of singlet oxygen across a diene; the stereochemical constraints discrediting this mechanism in some substrates are not present here.¹²⁹

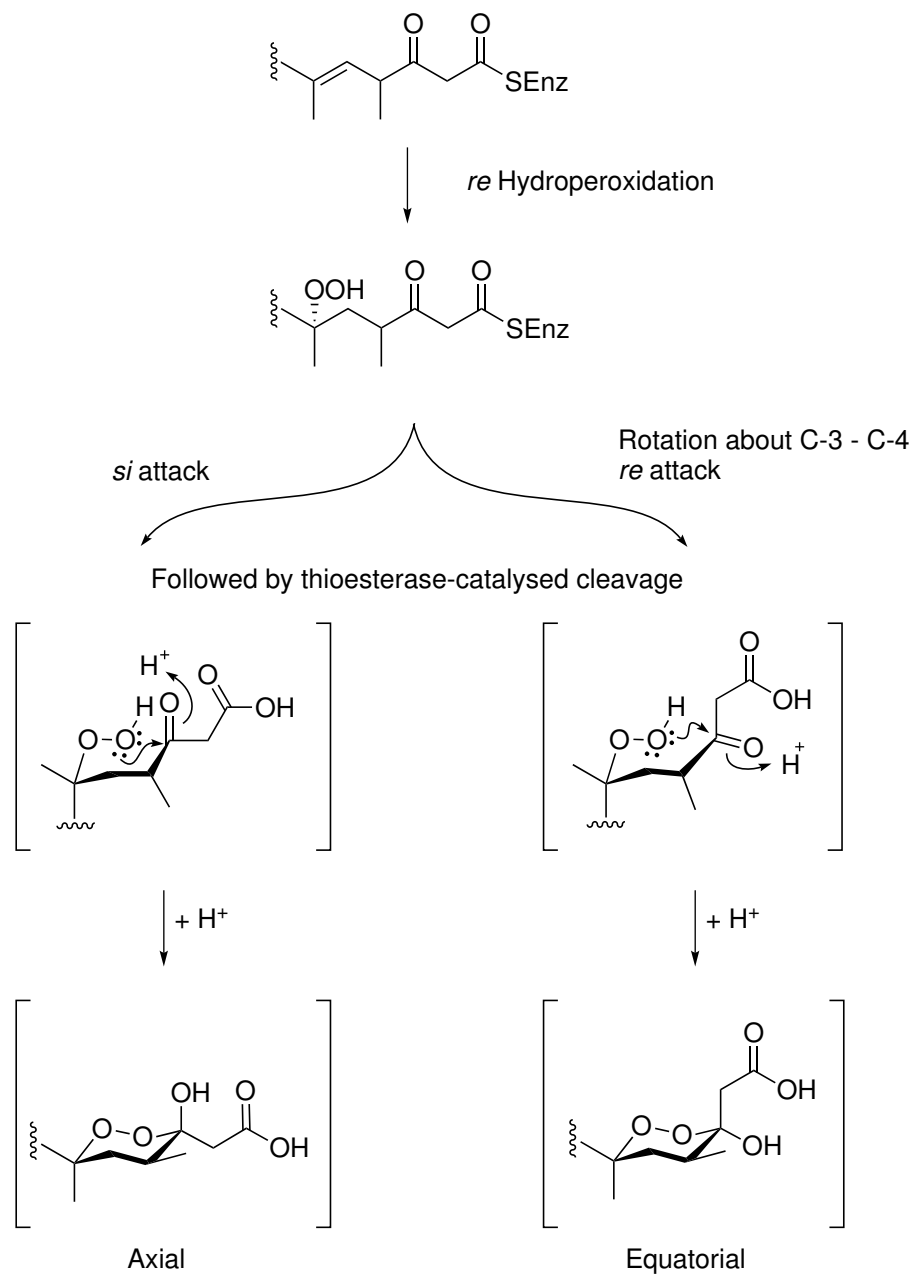




Scheme 4.8 Proposed biosynthesis of the 1,2-dioxane nuclei of plakinic and epiplakinic acids via hydroperoxidation and oxa-Michael addition.



Scheme 4.9 Proposed biosynthesis of the plakortolide bicycle by intramolecular cyclisation, after Yong *et al.*¹²⁴



Scheme 4.10 Proposed biosynthesis of both epimeric forms of the 1-hydroxy-1,2-dioxane nucleus of **98**.

4.3.6 Concluding remarks

Overall, this study has furthered the chemical knowledge pertaining to the cyclic peroxide complement of plakinid sponges. Identification of the substituted peroxide functions was facilitated greatly by analysis of HMBC spectra during organism screening and selection. Correlations were observed from diastereotopic methylenes to the oxyquaternary centres within the cyclic peroxide moieties and to the adjacent oxycarbonyl centres. Identification of these oxygenated structural fragments at the screening stage was integral to the selection of this organism for further analysis.

Examples from three different cyclic peroxide classes were encountered: compounds **95** and **96** display the 1,2-dioxane moiety of the epiplakinic acids, the peroxide lactone bicycle of the plakortolide class is demonstrated by **97**, while an uncommon 1-hydroxy-1,2-dioxane moiety was encountered in **98**. These cyclic peroxides all exhibited surprising stability to oxidative degradation, despite precedence for degradation among similar compounds.

Metabolites **95**, **97** and **98** were potently active against the HL-60 cell line, and their assessment against other cell lines will be undertaken in the future. The decreased sensitivity of HL-60 cells to **97** compared with **95** and **98** may reflect the absence of the free carboxylic acid moiety, an observation that may be useful to future development of the structures as structural leads.

Chapter 5

Chemical Genetic Profiling of Marine Cyclic Peroxides

*The spectroscopy-guided isolation approach applied during this study requires an unbiased assay technique for the biological characterisation of small molecules following their isolation. The suitability of genome-wide screening techniques as such an approach was explored. Chemical genetic profiling assays were carried out in *Saccharomyces cerevisiae* yeast in an effort to elucidate the precise biological mechanism of the cyclic peroxides presented in Chapter 4.*

5.1 The biological effects of marine cyclic peroxides

Since the late 1980s, cyclic peroxide polyketides have been implicated in Ca^{2+} modulation.^{120,169,173,180} Plakorin (**101**) was shown to increase Ca^{2+} uptake by the cardiac sarcoplasmic reticulum ATPase in rabbit white skeletal muscle in 1989,¹²⁰ and the same activity was assigned to the plakortone class in 1996.¹⁹⁷ Excessive release of Ca^{2+} inside cardiac muscle can cause sudden cardiac death in heart failure patients.¹⁹⁸ As such, the therapeutic potential of the plakortones in treating some forms of heart failure prompted efforts towards the synthesis of the 2,6-dioxabicyclo[3.3.0]octane-3-one core of the class.¹⁹⁹ Molluscan isolates, stolonoxides A and C (**112** and **113**), have been identified as inhibitors of the mitochondrial respiratory chain,¹⁸⁴ specifically affecting the function of two protein complexes that are reliant upon Ca^{2+} -signaling: complex II (succinate: ubiquinone oxioeductase) and complex III (ubiquinol: cytochrome C oxioeductase).²⁰⁰ Similarly, the plakortides have also been found to promote activation of the ATP-dependent sarcoplasmic reticulum (SR) Ca^{2+} pump.¹⁸⁰ The antimalarial drug artemisinin (**116**) has also been shown to inhibit the SERCA-type Ca^{2+} transporter of the malaria parasite *Plasmodium falciparum*.²⁰¹ Although structurally distinct from plakinid isolates, the Ca^{2+} -modulatory activity of **116** is attributed to the peroxide moiety, and is

easily cultured in defined media, and exhibits obvious phenotypes such as growth inhibition and morphological changes. Furthermore, approximately 31% of the human genes implicated in disease have an orthologue in *S. cerevisiae*.²⁰³ The cell cycle of *S. cerevisiae* has been well studied and its extremely short replication time (ca. 90 min) aids culturing in a laboratory environment, significantly decreasing growth-based assay times. The robust organism can be stably maintained in both haploid and diploid states, facilitating the generation of deletion strain libraries.

Yeast cells of all species are remarkably robust and resistant to many xenobiotics. Much of this innate resistance is due to their extensive network of membrane-bound pumps, termed the pleiotropic drug resistance (PDR) network. The PDR pumps presumably defend the cell, acting to eject xenobiotics within the cell before they can reach levels that affect growth.²⁰⁴ The transcription factor genes *PDR1* and *PDR3* encode the master regulators of the PDR pump network, and their simultaneous deletion in a haploid strain (Δpdr) confers 3–100-fold greater sensitivity to inhibitory compounds compared to a wild type (WT) strain.¹⁷⁵ Hence, molecules which display little or no activity in the WT can often be assessed in the drug-sensitive Δpdr background, when the lack of activity is due to drug efflux.

5.3 Chemical genetic profiling in *S. cerevisiae*

The complete deletion of anyone of around 80% of *S. cerevisiae* genes has no obvious effect on cell viability,²⁰⁵ a phenomenon attributed to the functional overlap exhibited by many genes, termed genetic buffering. This buffering mechanism means the deletion of a single gene can be compensated for by other genes that can functionally assume its role. Chemical genetic interactions are observed when a deletion strain is exposed to a small molecule whose cellular target is encoded by another gene that is genetically buffering the initial deletion. These interactions are manifested as inhibition or death of the deletion strain, termed synthetic sickness or synthetic lethality, indicating processes or pathways that are affected by the small molecule and require compensation in its presence. In this way chemical genetic interactions identify genetic networks that buffer the phenotype induced by the small molecule.

Since completion of the *S. cerevisiae* genome sequence and functional annotation of much of the genome,^{206,207} a comprehensive and ordered array of haploid and diploid Yeast Knock-Out (YKO) strains covering the entire yeast genome have been described.⁷⁵ Each carrying deletions for a single gene, the YKO strains have been utilised in the study of biologically active small molecules, aiding elucidation of biological mechanisms and identification of cellular targets.²⁰⁸

The presence of a unique molecular barcode within each deletion strain is integral to chemical genetic assays used in this study. In each strain the open reading frame is replaced by a growth-selection marker for resistance to the antifungal agent kanamycin. The marker is flanked by two 20-nucleotide barcodes (Up and Dn tags) unique to each yeast strain, which are adjoined on either side by a universal primer sequence common to the strains (Figure 5.1). These features allow identification of all deletion strains, and quantification of their relative representation from within a mixed population by PCR amplification. Incorporation of the universal primer sites allows tandem amplification of all barcodes, while the use of two tags makes for more robust data.⁷⁵

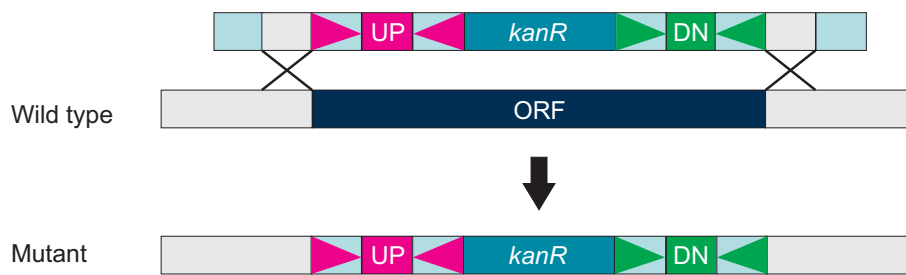


Figure 5.1 Deletion of the open reading frame deletion within the *S. cerevisiae* genome and insertion of the kanamycin resistance marker, after Boone *et al.*⁷⁵ In each YKO strain, the kanamycin resistance marker is flanked by two unique molecular barcode tags, each adjoined by universal primers.⁷⁵

As depicted in Figure 5.2, under assay conditions a mixed culture containing every deletion mutant is grown in the presence of a potential drug at a concentration that inhibits 30% of the population - IC₃₀. The genomic DNA is then extracted and the tags of each strain amplified in two tandem PCR reactions for the Up and Dn tags. The barcode amplicons of each YKO are hybridised to an oligonucleotide microarray, which carries the the complementary barcode sequences for the tags of each YKO. From the array, the relative abundance of each deletion strain can be quantified via the fluorescence signal intensity of their respective barcodes. High or low intensity of a barcode signal corresponds to high or low growth of that particular deletion strain within the population pool.^{75,203,209}

Mutants carrying deletions for genes that are important for growth under a specific condition compete less effectively within the assay pool and diminish in population size decreasing the signal intensity of their molecular barcode. Hence, one experiment can identify the genes required for growth under a given condition, and rank them in order of their importance to fitness, i.e. their sensitivity to the experimental conditions. Homozygous profiling (HOP) analyses ca. 4,000 non-essential gene deletions using the homozygous diploid deletion set in which each strain is deleted for both alleles of a single non-essential gene.²¹⁰ Interactions with essential genes are probed via haploinsufficiency profiling (HIP), which is conducted

using the genome-wide heterozygous diploid deletion set in which only one allele of a given gene (essential and non-essential) is removed from a strain.^{76,209,211}

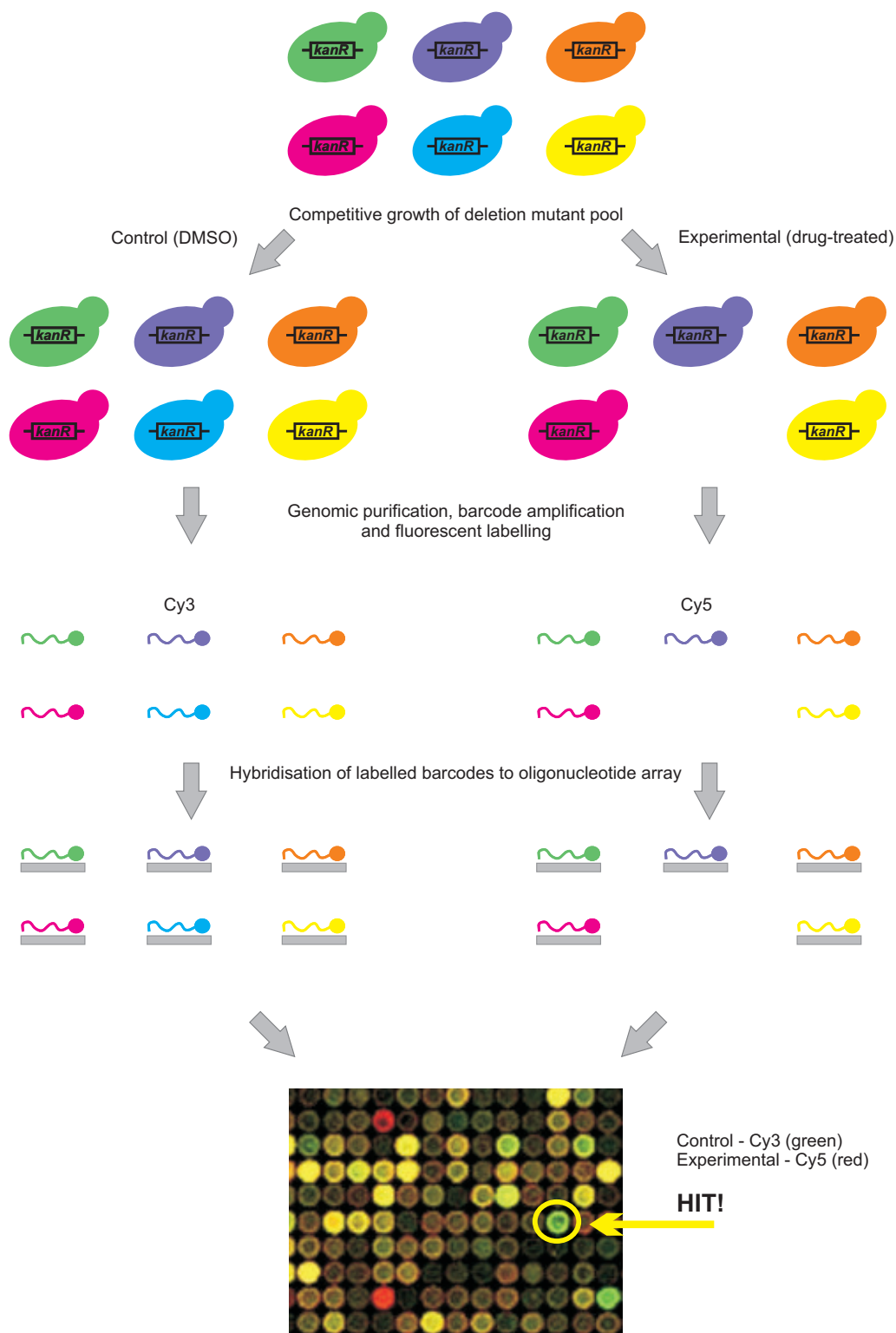


Figure 5.2 Chemical genetic profiling revealing the importance of a deleted gene to strain fitness under assay conditions, adapted from Boone *et al.*⁷⁵ The deletion strains compete for growth in the assay pool, and those lacking genes important for growth under experimental conditions are out-competed and removed from the assay pool, as shown by the blue strain. This diminishes barcode intensity of the experimental population (Cy5) relative to the control population (Cy3) on the microarray slide. Strains unaffected by either condition appear yellow, while those detrimentally affected appear green.

5.3.1 Homozygous profiling

Interactions uncovered by homozygous profiling (HOP) assays cannot reveal the primary cellular target of a bioactive molecule. Instead, synthetically sick or lethal interactions identify “friends of the target”, genes which are related to the target of a small molecule in either cellular function or pathway and genetically buffer its absence. These genetic interactions point back to the unknown target in a “guilt by association” manner.

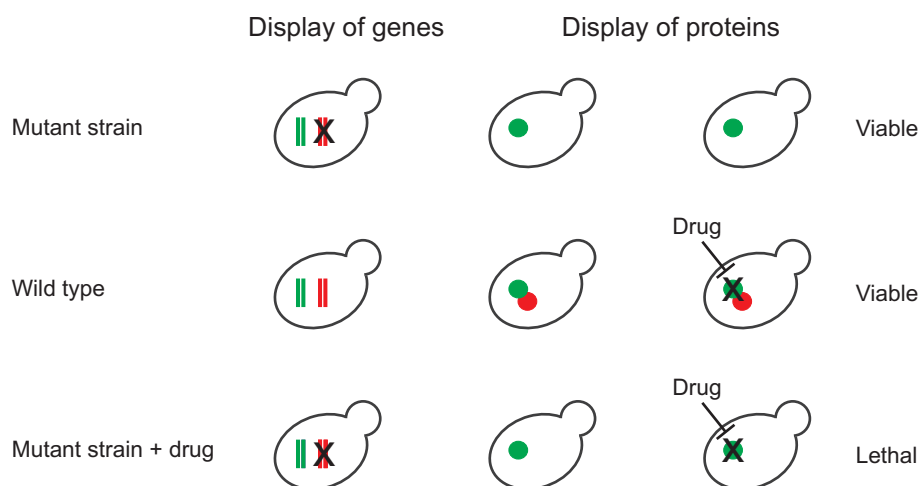


Figure 5.3 Synthetic genetic interactions uncovered by the homozygous profiling assay. A deletion mutant strain is viable except in the presence of a xenobiotic whose primary target is encoded by a gene buffering the initial deletion. These interactions identify genes related to the target of a small molecule in either cellular function or pathway.

5.3.2 Haploinsufficiency profiling

Concurrent assessment of both essential and nonessential gene interactions has the potential to identify a cellular target directly by the mechanism of drug-induced haploinsufficiency.^{212,213} This is achieved by screening the heterozygous diploid deletion mutant library, a near complete collection that omits only a few hundred (ca. 3%) haploinsufficient genes.²¹³

Haploinsufficiency profiling is based on gene dosage dependence. A heterozygous diploid mutant is deleted for one of two gene copies, halving the quantity of a given protein that can be produced by the cell. Under normal growth conditions, this reduced quantity of protein is sufficient to maintain proper function of the mutant strain.^{212,213} However, in the presence of a small molecule which targets the protein encoded by the heterozygous deletion, the mutant strain will be sensitised in comparison to strains with a full complement of the protein.^{212,213} This phenomenon is known as drug-induced haploinsufficiency. Synthetically lethal interactions are

also revealed by HIP, therefore using both homozygous and heterozygous mutant screens is a complementary approach for identifying a cellular target.²¹⁴

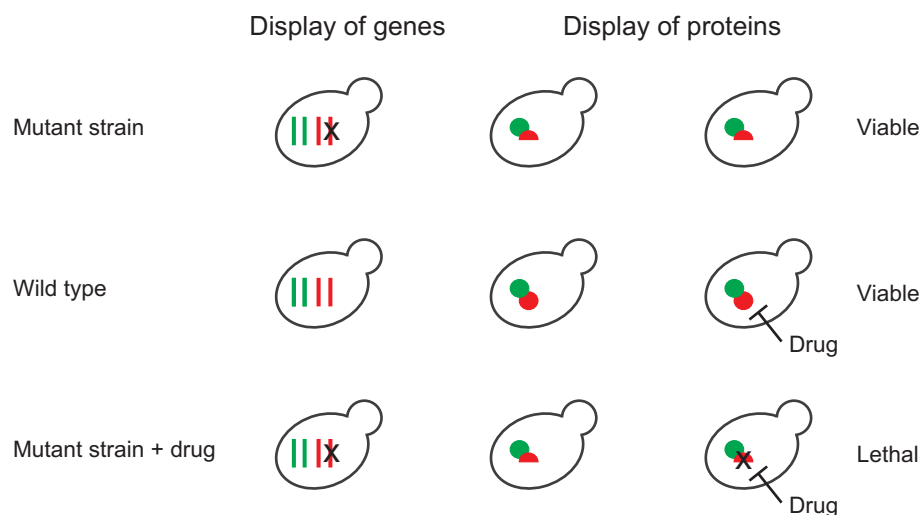


Figure 5.4 Depiction of drug-induced haploinsufficiency. A heterozygous deletion mutant can only produce half the quantity of a given protein in comparison to wild type yeast. However, the mutant remains viable except in the presence of a small molecule that targets the protein encoded by the heterozygous deletion. This sensitises the deletion strain relative to the wild type.

It is thought that the HIP assay is not applicable to compounds whose primary cellular target is encoded by an essential gene that is under dosage control.^{212,213} Upregulation of single gene copies is thought to circumvent the haploinsufficiency mechanism,²¹³ potentially rendering important drug – gene-product interactions insignificant. It now appears however, that in general, protein levels in *S. cerevisiae* are not directly monitored and adjusted to a desired level.²¹⁵

5.4 Preliminary studies in *S. cerevisiae*

As stated in Chapter 4, epiplakinic acid I (**95**) inhibited both haploid WT and Δpdr strains, with IC_{50} values of 3.36 and 3.50 $\mu\text{mol L}^{-1}$ respectively and a minimum inhibitory concentration (MIC) of 10 $\mu\text{mol L}^{-1}$ (Figure H.1 A*). Plakortolide X (**97**) was found to have no effect on the haploid WT strain but inhibited the haploid Δpdr strain with an IC_{50} value of 4.45 $\mu\text{mol L}^{-1}$, and a MIC of 10 $\mu\text{mol L}^{-1}$ (Figure H.1 B). These results indicate that **95** is not subject to PDR efflux, whereas **97** may be a substrate for one of the PDR pumps. The primary structural difference between **95** and **97** is the absence of the free acid in **97**, and it is fascinating that this results in such a difference in biological activity in yeast.

Owing to the robust nature of yeast cells, compounds that affect the growth of yeast are frequently cytostatic and inhibit their growth rather than killing

*Growth curves for all dose response assays can be found in Appendix H

them (cytotoxic).²¹⁶ Some are truly cytotoxic, however, and induce a cell death process analogous to mammalian apoptosis.^{216,217} Colony-forming assays showed that following exposure to **95** for 17 h at its MIC, the drug-treated cells were unable to repropagate on solid growth medium on the absence of **95**. This is consistent with **95** causing irreversible cytostatic inhibition of yeast cells or being cytotoxic. Time-course assessment of the growth effects of **95** in WT yeast, indicated that **95** caused its effects within two hours of treatment at the MIC (Figure 5.5 A).

As cyclic peroxides are thought to affect Ca^{2+} modulation, inhibition assays were conducted in high and low Ca^{2+} environments. Consistent with **95** and **97** influencing intracellular Ca^{2+} levels, phenotypic enhancement was observed following co-treatment of WT and Δpdr cells with a non-inhibitory concentration of CaCl_2 and **95** or **97** (Table 5.1 and Figure H.2). Ethyleneglycol tetraacetic acid (EGTA) is a chelating ligand with a much higher affinity for Ca^{2+} over Mg^{2+} ions, and the ligand was used to produce a low Ca^{2+} environment.²¹⁸ No recovery was observed upon co-treatment of WT cultures with **95** and EGTA (Figures 5.5 B and H.3).

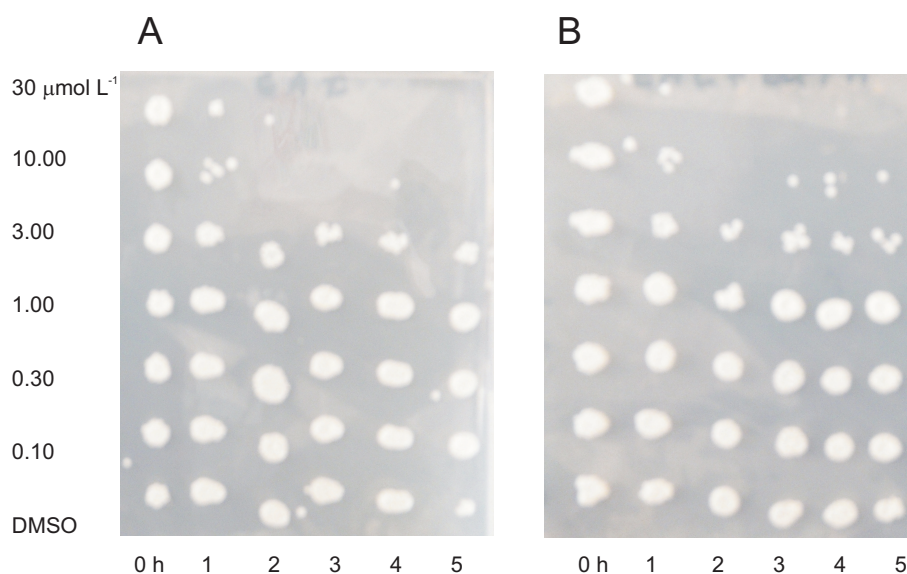


Figure 5.5 The kinetics of epiplakinic acid I (**95**) inhibiting *S. cerevisiae* cells are unchanged by the presence of EGTA. Plates were incubated for 72 h following inoculation.

A: **95** (10 $\mu\text{mol L}^{-1}$) for 1 h B: EGTA (50 mmol L^{-1}) and **95** (10 $\mu\text{mol L}^{-1}$)

The observation of a significant increase in growth inhibition during co-treatment of cells with **95** and **97** and non-inhibitory concentration of Ca^{2+} is consistent with **95** and **97** affecting intracellular Ca^{2+} levels. However, the absence of phenotype recovery during co-treatment with EGTA is unexpected if the cyclic peroxides do affect their toxicity by modulating levels of the Ca^{2+} ion. However, the activities of **95** and **97** may also arise from release of Ca^{2+} from intracellular stores, in addition to influx of the ion from external sources. As such, an apparent lack of phenotype recovery may reflect an inability for the ligand to traverse the cell membrane and internally chelate cytosolic calcium.

Table 5.1 Synergistic Inhibitory Effects of Cyclic Peroxides **95** and **97** and CaCl₂.

Agent	Strain	Concentration		Residual Growth (%)	Error (\pm %)
		95 and 97 (μmolL^{-1})	CaCl ₂ (mmolL^{-1})		
95	WT	3.33		90.4	0.5
95	WT	3.33	50	13.8	0.5
97	Δpdr	6.35		104.3	2.5
97	Δpdr	6.35	50	4.6	9.0

5.4.1 Phenotypic profiling of the cyclic peroxides

Cellular Morphology

Changes in cellular morphology were also analysed during assessment of epiplakinic acid I (**95**) and plakortolide X (**97**). Both compounds were found to decrease cell size and bud formation, with a similar decrease in cell size observed in response to CaCl₂. Analysis by light microscopy showed a ca. 25% decrease in cell size in drug-treated populations (Table 5.2 and Figure 5.6).^{219,220} This may be symptomatic of cellular starvation. This was also observed using a GFP-tagged plasma membrane reporter strain (Figure H.5).

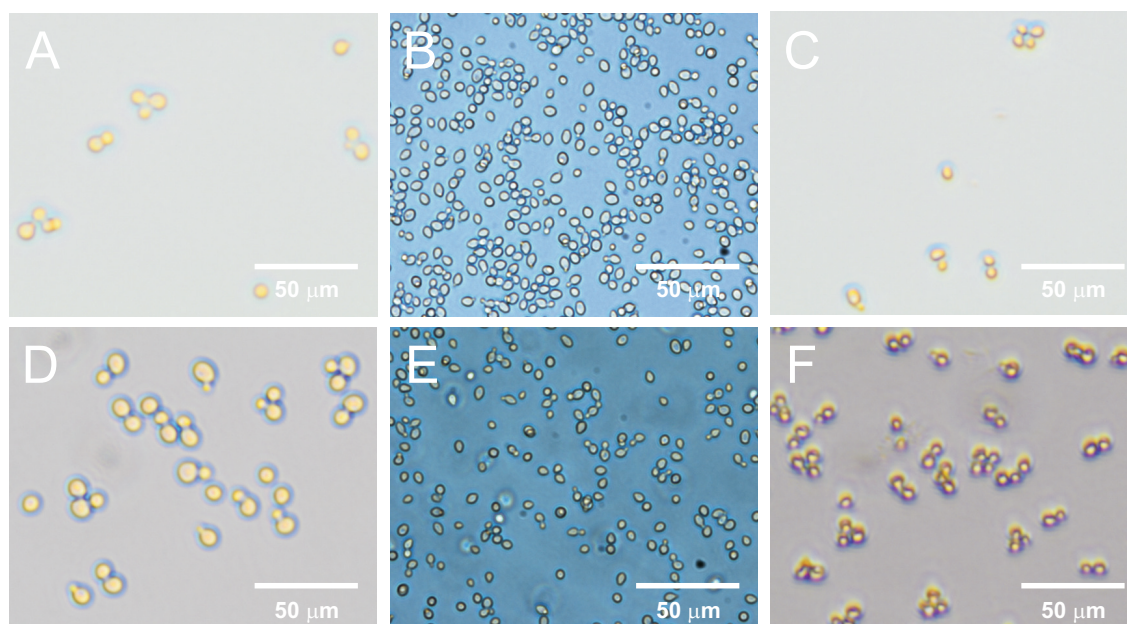


Figure 5.6 Epiplakinic acid I (**95**), plakortolide X (**97**) and CaCl₂ cause a similar decrease in cell size in WT and Δpdr *S. cerevisiae* strains, respectively.

WT A: DMSO, 1%, 2 h B: CaCl₂, 50 mmol L^{-1} , 2 h C: **95**, 10 $\mu\text{mol L}^{-1}$, 2 h
 Δpdr D: DMSO, 1%, 2 h E: CaCl₂, 50 mmol L^{-1} , 2 h F: **97**, 10 $\mu\text{mol L}^{-1}$, 2 h

Table 5.2 Decrease in Cell Size Caused by **95**, **97** and CaCl₂ after 2 h.

Agent	Strain	Concentration	Cell Size (μm)	Error ($\pm\mu\text{m}$)
95	WT	10 $\mu\text{mol L}^{-1}$	5.6	1.1
DMSO	WT	1%	7.2	0.6
CaCl ₂	WT	50 mmol L^{-1}	4.9	0.6
97	Δpdr	10 $\mu\text{mol L}^{-1}$	3.9	1.6
DMSO	Δpdr	1%	8.6	1.1
CaCl ₂	Δpdr	50 mmol L^{-1}	4.9	0.6

Cell cycle analyses

The eukaryotic cell cycle consists of four distinct phases: G₁-phase, S-phase, G₂-phase (collectively known as interphase), and M-phase (comprising mitosis, in which the cell's duplicated chromosomes are divided between the two daughter cells, and cytokinesis, when the cytoplasm is divided in half, forming distinct cells). Initiation of each phase relies upon proper progression and completion of the previous phase, which is ensured by the phase-boundary checkpoints. A fifth phase, G₀ or stationary phase, is entered when cells have temporarily stopped dividing. In yeast, this phase is entered in response to periods of environmental hardship or cellular starvation.²²¹

As depicted in Figure 5.7, progression through the mitotic cell cycle of *S. cerevisiae* can be observed through bud analysis. The G₁-S-phase transition is characterised by the formation of the bud site.²²² The bud develops throughout S-phase, concurrent with DNA replication, as polarised actin migrates within the cell to the bud site, outwardly distorting the cell membrane and directing growth of the bud in the direction of polarisation. This continues into G₂-phase. Budding yeast differ from mammalian cells systems in that the replicated genetic material only migrates into the bud/daughter cell during the G₂-M transition. At this point the bud/daughter cell is fully formed, and nearly the same size as the mother cell, mitosis occurs followed by cytokinesis and the daughter cells are released.

An increase in small budded cells was observed in WT and Δpdr cells in response to **95** and **97**, confirmed by bud index (Figure 5.8). This indicated cell cycle delay during either the G₁-S transition, or early S-phase, leading to a decrease of the G₂ population. Flow cytometry analysis of WT populations treated with **95** supported this hypothesis, revealing a 50% increase S-phase populations in cells treated with **95** at the IC₅₀, while treatment at the MIC appeared to inhibit during G₂ (Table 5.3 and Figure H.4). These different results may be due to difficulties in distinguishing between the two phases in yeast via flow cytometry.²¹⁶

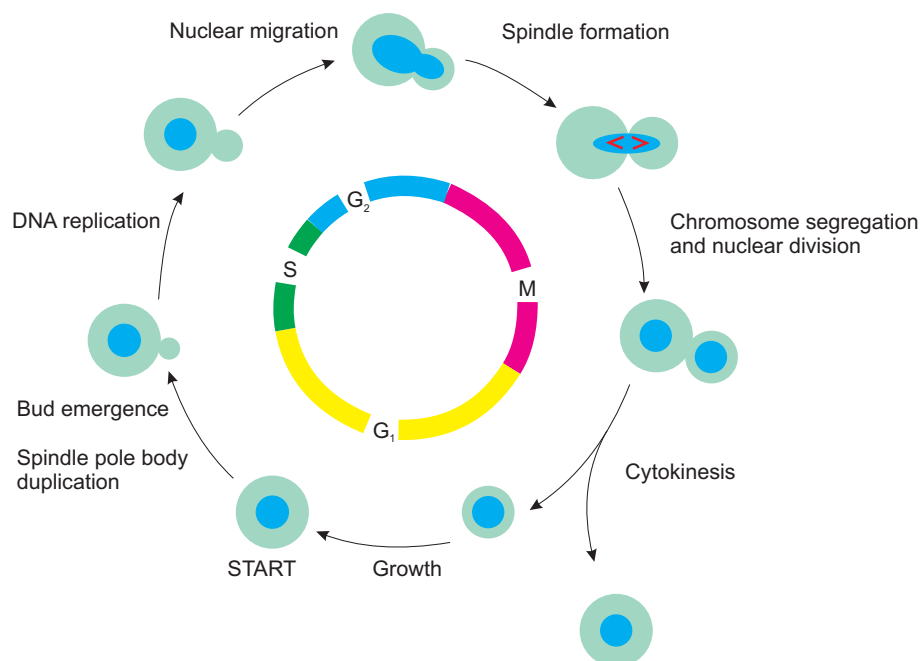


Figure 5.7 Cell cycle of *S. cerevisiae* after Calzone *et al.*²²³

Table 5.3 Effects of **95** on the *S. cerevisiae* Cell Cycle.

Agent	Concentration	Phase population (%)		
		G ₁	S	G ₂
95	3.4 $\mu\text{mol L}^{-1}$ (IC ₅₀)	30.5	40.9	58.9
95	7.0 $\mu\text{mol L}^{-1}$	31.0	18.8	67.1
95	10 $\mu\text{mol L}^{-1}$ (MIC)	26.9	29.9	52.3
DMSO	1%	40.4	18.4	55.6

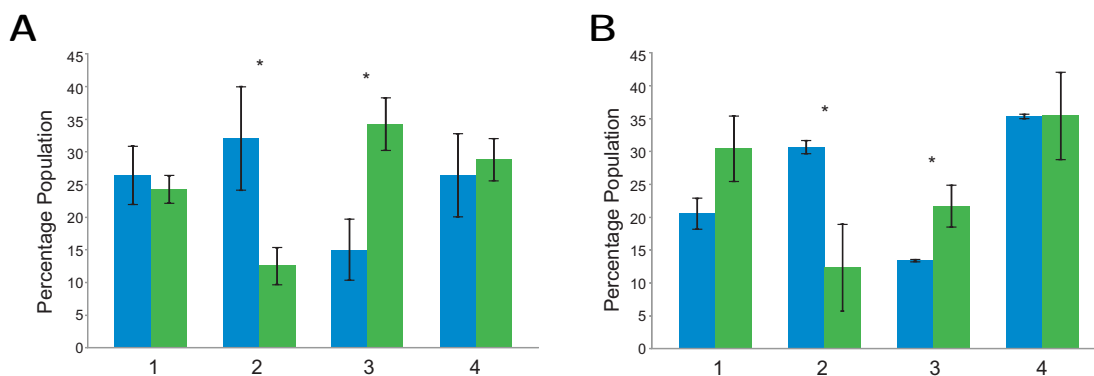


Figure 5.8 *S. cerevisiae* WT and Δpdr cell populations displayed a small bud phenotype when treated with **95** and **97**, correlating to an increase in S-phase populations at the expense of the G₂ populations. 1 = no bud, 2 = small bud, 3 = medium, 4 = equal size.

* Indicates statistical significance as determined by T-test.

A: WT cells treated with **95**, 10 $\mu\text{mol L}^{-1}$ and DMSO, 1%

B: Δpdr cells treated with **97**, 10 $\mu\text{mol L}^{-1}$ and DMSO, 1%

5.5 Chemical genetic profile of epiplakinic acid I

Cyclic peroxides epiplakinic acid I (**95**) and plakortolide X (**97**) were both subjected to genome-wide homozygous profiling. The homozygous diploid deletion set was used to assess for chemical genetic interactions with **95**, while Coorey assessed **97** in a hemizygous screen using the haploid deletion set (Δpdr background).²²⁴ Subsequent analysis for haploinsufficiency in the presence of **95** was undertaken with the heterozygous diploid deletion set. A full tabulation of the HOP and HIP profiles of **95** can be found in Appendix I.

5.5.1 Homozygous profiling of epiplakinic acid I

Functional annotation of the *S. cerevisiae* genome can be used to establish functional and physical relationships between the hits found in a chemogenomic screen.²¹⁶ Grouping hits according to their gene ontology term annotation with on-line data analysis software such as FunSpec²²⁵ or YeastMine²²⁶ has significant advantages as all of the data used has been experimentally defined.

The removal of strains implicated in multi-drug resistance (MDR) has become common-place prior to gene ontology-based cluster analysis, owing to the observation that the inclusion of such genes places a bias on clusters formed within the dataset.²¹⁰ Conversely, exclusion of MDR hits may lose information salient to the action of a specific compound. For example genes involved in vesicular mediated transport are frequently removed as their role in drug efflux recycling is thought to be compound-non-specific. However, exclusion of these genes from the profile of a compound which directly affected these processes would severely devalue the chemical genetic screen. Hence, removal of MDR genes should be done with caution.²¹⁶

The HOP profile of **95** identified 48 genes whose deletion caused increased sensitivity to **95**. The removal of 19 genes which frequently occur in chemical genetic screens and five genes encoding dubious open reading frames left 21 genes displaying chemical genetic interactions in the presence of **95**.²²⁷ After removal of MDR genes, the profile of **95** showed functional clustering in the areas of cytoskeleton binding, vacuolar protein sorting, ribosome biogenesis, metabolism under stress conditions, response to stress, membrane organisation, Golgi sorting and mitochondrial function and repair, as classified by FunSpec²²⁵ and YeastMine.²²⁶ The unfiltered profile included a number of genes involved in vacuolar protein sorting (Table 5.4). The HOP profile of **95** did not identify any genes involved in upholding the PDR response, consistent with **95** not being subject to PDR efflux, as indicated by its similar activity in both the WT and Δpdr strains.

Table 5.4 Functional Categories of Deletion Strains Sensitive to Epiplakinic Acid I (**95**, 3 $\mu\text{mol L}^{-1}$).

GO Molecular Functions	p-value	Gene deletion strain
Cytoskeletal actin polarisation and cytoskeleton binding	8.844 E-06	<i>end3Δ/end3Δ</i> , <i>hcm1Δ/hcm1Δ</i> , <i>rcy1Δ/rcy1Δ</i> , <i>rvs161Δ/rvs161Δ</i> , <i>rvs167Δ/rvs167Δ</i> , <i>sla1Δ/sla1Δ</i> , <i>sli15Δ/sli15Δ</i> , <i>spo74Δ/spo74Δ</i>
Golgi sorting	0.002195	<i>apl2Δ/apl2Δ</i> , <i>chs5Δ/chs5Δ</i> , <i>gos1Δ/gos1Δ</i> , <i>och1Δ/och1Δ</i> , <i>rgp1Δ/rgp1Δ</i>
Membrane organisation	0.004122	<i>hcm1Δ/hcm1Δ</i> , <i>spo74Δ/spo74Δ</i> and <i>vac7Δ/vac7Δ</i>
Metabolism under stress	0.001258	<i>aro7Δ/aro7Δ</i> , <i>crz1Δ/crz1Δ</i> , <i>csg2Δ/csg2Δ</i> , <i>hog2Δ/hog2Δ</i> , <i>grr1Δ/grr1Δ</i> , <i>pfk2Δ/pfk2Δ</i> , <i>vac7Δ/vac7Δ</i>
Ribosome biogenesis	0.00048	<i>dbp7Δ/dbp7Δ</i> , <i>rsa1Δ/rsa1Δ</i> , <i>rps9bΔ/rps9Δ</i> , <i>sfp1Δ/sfp1Δ</i> , <i>tod6Δ/tod6Δ</i> , <i>yor019wΔ/yor019wΔ</i>
Divalent cation and heavy metals sensitivity	0.0009385	<i>csg2Δ/csg2Δ</i> , <i>vps4Δ/vps4Δ</i> , <i>crz1Δ/crz1Δ</i> and <i>sod1Δ/sod1Δ</i>
Vacuolar protein sorting and transport	3.25 E-06	<i>bro1Δ/bro1Δ</i> , <i>did2Δ/did2Δ</i> , <i>snf7Δ/snf7</i> , <i>stp22Δ/stp22Δ</i> , <i>vps4Δ/vps4Δ</i> , <i>vps24Δ/vps24Δ</i> , <i>vps28Δ/vps28Δ</i> , <i>vps36Δ/vps36Δ</i>

* Genes implicated in MDR appear in blue.

Consistent with the small-cell and small-bud phenotype, the HOP profile included the mutant strains of cytoskeletal genes involved in bud formation and endocytosis; *SLA1*, *RSA1*, *RVS161* and *RVS167*. Sla1p is a cytoskeletal binding protein, required for assembly of the cortical actin cytoskeleton. Sla1p plays an integral role in both bud formation and endocytosis through its interactions with proteins regulating actin dynamics. End3p forms a complex with Sla1p and Pan1p, which is involved in endocytosis, actin cytoskeletal organisation and cell wall morphogenesis.²²⁸ Rvs161p and Rvs167p interact to regulate polarisation of the actin cytoskeleton and are directly involved in endocytosis and exocytosis. They also play a role in maintaining cell polarity and viability in the event of osmotic stress or starvation. Hence, disruption or impairment of these genes and their functions can be detrimental to bud formation and endocytosis, consistent with the observed phenotype of **95**. Furthermore, as **95** appears to affect cell size and budding, the deletion of actin-related genes may result in a synergistic increase in sensitivity to the compound, down-stream of an initial chemical genetic interaction with **95**. Hypersensitivity of the deletion strains of *SLA1*, *RSA1*, *RVS161* and *RVS167* to **95** was validated by a dose-response assay (Table 5.5 and Figure H.6), indicating that **95** may affect related cellular processes, such as actin coordination and endocytosis.

Although implicated in multi-drug resistance, *SFP1* is integral to ribosome biogenesis in yeast, and genetic deficiency of *SFP1* imparts translation-specific defects, significantly reducing the cell's ability to synthesise ribosomes, contributing to the

observed starvation response.²²⁹ Hypersensitivity of the deletion strain to **95** may imply interaction of **95** with the target of rapamycin (TOR) pathway, Section 5.5.7.

Analysis was also undertaken on genes, the deletion of which appeared to confer resistance to **95** (z-score > 2). The 44 resistant strains were submitted for gene ontology analysis (FunSpec²²⁵), however, time constraints prevented more in depth analysis of trends within the data. Full tabulation of the analysis can be found in Table I.4.

Table 5.5 Growth Inhibitory Effects of **95** on Cytoskeletal Deletion Mutant Strains.

Strain	Concentration ($\mu\text{mol L}^{-1}$)	Residual Growth (%)	Error (\pm %)
BY4743 WT	3.3 (IC_{50})	100.3	2.0
<i>sla1</i> Δ / <i>sla1</i> Δ	3.3	15.1	3.0
<i>sfp1</i> Δ / <i>sfp1</i> Δ	3.3	4.8	0.5
<i>rsa1</i> Δ / <i>rsa1</i> Δ	3.3	46.3	3.0
<i>rvs167</i> Δ / <i>rvs167</i> Δ	3.3	46.3	5.5

5.5.2 Haploinsufficiency profiling of epiplakinic acid I

The HIP assay identified 124 genes which displayed haploinsufficiency in the presence of **95**, eight of which are classified as essential according to the *Saccharomyces* Genome Database,²²⁶ (Table 5.6). Eleven genes implicated in multi-drug resistance,²²⁷ and 21 genes encoding genes with an unknown function were excluded from the profile. FunSpec²²⁵ cluster analysis of the homozygous gene profile, and the essential genes indicated by the heterozygous array displayed functional overlap in ribosome biogenesis (p-value = 0.00048). This may further indicate interaction of **95** with the TOR starvation response pathway. The HIP profile also contained many genes functioning to mitochondrial repair, cytoskeletal polarisation and binding, ribosome generation, and plasma membrane organisation.²²⁶ The combined HOP and HIP profiles displayed functional clustering in response to Zn^{2+} ions (p-value = 0.000192), and Zn^{2+} homeostasis (p-value = 0.009733) as determined by FunSpec.²²⁵ The 99 strains deemed to display resistance to **95** (z-score > 2) were similarly assessed by FunSpec cluster analysis, a full tabulation of which can be found in Table I.5. Significant insight into the biological mechanisms of small molecules can be gained through analysis of resistant deletion strains, and is worth undertaking. However, complete analysis and investigation of the resistant deletion strains was prevented by the time constraints on this project.

Table 5.6 Functional Categories of Deletion Strains Haploinsufficient to Epiplakinic Acid I (**95**, 2 $\mu\text{mol L}^{-1}$).

GO Molecular Functions	Gene deletion strain*
Metal ion homeostasis	<i>ddp1Δ/ddp1Δ</i> , <i>inp52Δ/inp52Δ</i> , <i>irc7Δ/irc7Δ</i> , <i>izh1Δ/izh1Δ</i> , <i>izh2Δ/izh2Δ</i> , <i>ybr016wΔ/ybr016wΔ</i>
Cytoskeletal polarisation and binding	<i>abp140Δ/abp140Δ</i> , <i>cik1Δ/cik1Δ</i> , <i>ede1Δ/ede1Δ</i> , <i>kin4Δ/kin4Δ</i> , <i>mad3Δ/mad3Δ</i> , <i>nap1Δ/nap1Δ</i> , <i>pcl1Δ/pcl1Δ</i> , <i>rax1Δ/rax1Δ</i>
Ribosomal subunit proteins	<i>asc1Δ/asc1Δ</i> , <i>crf1Δ/crf1Δ</i> , <i>rcl1Δ/rcl1Δ</i> , <i>rpl27AΔ/rpl27AΔ</i> , <i>rpl33AΔ/rpl33AΔ</i> , <i>rpl39Δ/rpl39Δ</i> , <i>rps14BΔ/rps14BΔ</i> , <i>rps15Δ/rps15Δ</i> , <i>sip1Δ/sip1Δ</i> , <i>ydr223wΔ/ydr223wΔ</i> , <i>yor019wΔ/yor019wΔ</i>
RNA binding proteins	<i>prp43Δ/prp43Δ</i> , <i>rpc1Δ/rpc10Δ</i> , <i>tan1Δ/tan1Δ</i> , <i>ygl232wΔ/ygl232wΔ</i> , <i>yra2Δ/yra2Δ</i>
Mitochondrial and oxidative stress conditions	<i>aim2Δ/aim2Δ</i> , <i>aim14Δ/aim14Δ</i> , <i>crc1Δ/crc1Δ</i> , <i>cox17Δ/cox17Δ</i> , <i>maf1Δ/maf1Δ</i> , <i>mne1Δ/mne1Δ</i> , <i>mrm2Δ/mrm2Δ</i> , <i>mrpl11Δ/mrpl11Δ</i> , <i>mrpl16Δ/mrpl16Δ</i> , <i>mrs1Δ/mrs1Δ</i> , <i>pxr1Δ/pxr1Δ</i> , <i>rps7AΔ/rps7AΔ</i> , <i>yir003wΔ/yir003wΔ</i>
Golgi sorting	<i>gga1Δ/gga1Δ</i> , <i>gmh1Δ/gmh1Δ</i> , <i>ste13Δ/ste13Δ</i> , <i>top23Δ/top23Δ</i>
Utilisation of alternative carbon sources	<i>ath1Δ/ath1Δ</i> , <i>dal7Δ/dal7Δ</i> , <i>gac1Δ/gac1Δ</i> , <i>gal3Δ/gal3Δ</i> , <i>pyk2Δ/pyk2Δ</i> , <i>tps1Δ/tps1Δ</i> , <i>ysa1Δ/ysa1Δ</i>
Amino acid biosynthesis	<i>ado1Δ/ado1Δ</i> , <i>asi1Δ/asi1Δ</i> , <i>car2Δ/car2Δ</i> , <i>fsh3Δ/fsh3Δ</i> , <i>gnp1Δ/gnp1Δ</i> , <i>imd3Δ/imd3Δ</i> , <i>map2Δ/map2Δ</i> , <i>pho81Δ/pho81Δ</i> , <i>stp2Δ/stp2Δ</i> , <i>thi12Δ/thi12Δ</i> , <i>yfr055wΔ/yfr055wΔ</i>
Fatty acid biosynthesis	<i>fox2Δ/fox2Δ</i> , <i>frm2Δ/frm2Δ</i> , <i>ylr400wΔ/ylr400wΔ</i>
Plasma membrane organisation	<i>ast1Δ/ast1Δ</i> , <i>azr1Δ/azr1Δ</i> , <i>erv46Δ/erv46Δ</i> , <i>rrt8Δ/rrt8Δ</i> , <i>sur2Δ/sur2Δ</i> , <i>pmt6Δ/pmt6Δ</i> , <i>pst1Δ/pst1Δ</i> , <i>yeh1Δ/yeh1Δ</i>
Meiosis	<i>mum3Δ/mum3Δ</i> , <i>ndt80Δ/ndt80Δ</i> , <i>osw1Δ/osw1Δ</i> , <i>slz1Δ/siz1Δ</i> , <i>ssp2Δ/ssp2Δ</i> , <i>vhs1Δ/vhs1Δ</i>
DNA assembly and repair	<i>hht1Δ/hht1Δ</i> , <i>rad4Δ/rad4Δ</i> , <i>rts2Δ/rts2Δ</i> , <i>shu1Δ/shu1Δ</i> , <i>ubr2Δ/ubr2Δ</i>
Transcription	<i>rtr1Δ/rtr1Δ</i> , <i>rtr2Δ/rtr2Δ</i> , <i>ynl187wΔ/ynl187wΔ</i>
Protein synthesis	<i>eug1Δ/eug1Δ</i> , <i>ost5Δ/ost5Δ</i> , <i>ptp1Δ/ptp1Δ</i> , <i>ssa3Δ/ssa3Δ</i>
Proteasome degradation	<i>pci1Δ/pci1Δ</i> , <i>yuh1Δ/yuh1Δ</i>

* Essential genes appear in blue.

5.5.3 Plakortide F acid

Comparison of the gene expression profile of plakortide F acid (**122**)¹⁶⁹ and the homozygous profile of **95** proved informative. Plakortide F acid (**122**) induces upregulation of genes associated with response to stress, protein transport and sorting, carbohydrate metabolism, organelle organisation, amino acid metabolism, membrane organisation, cell wall organisation and sporulation. Functions pertaining to the activity of **95**, namely cell cycle and ribosome biogenesis experienced downregulation in the presence of **122**. Their study also showed an overall increase in intracellular Ca²⁺ and Zn²⁺-levels by ICP-MS.¹⁶⁹

Only one direct overlap was observed between the RNA-expression profile of **122**¹⁶⁹ and the homozygous profile of **95** - the Ca²⁺-sensitive stress response transcription factor Crz1p,[†] which is activated in response to elevated Ca²⁺ levels (Sections 5.5.5 and 5.5.6). Other calcium-responsive genes to experience upregulation in the presence of **122** included those encoding membrane bound ion pumps and ion channels. Calcium influx through the plasma membrane is mediated by the Ca²⁺ channels Cch1p and Mid1p, as shown in Figure 5.9. Intracellular levels are modulated by the pumps Pmr1p and Pmc1p, with Pmr1p sequestering Ca²⁺ and Mg²⁺ within the Golgi bodies. Pmc1p and the H⁺/Ca²⁺ exchanger Vcx1p affect Ca²⁺ detoxification by increasing vacuolar storage, while Vcx1p will also release vacuolar Ca²⁺ stores into the cytoplasm in response to hyperosmotic stress.^{169,226,230}

Table 5.7 Functional Categories of Genes Differentially Regulated in the Presence of Plakortide F Acid (**122**).

Status	Functional category
Upregulated	Response to stress
	Transport
	Carbohydrate metabolism
	Transcription
	Protein modification
	Organelle organisation
	Amino acid metabolism
	Membrane organisation
	Cell wall organisation
	Sporulation
	Downregulated
Ribosome biogenesis	
Conjugation Translation	
Amino acid metabolism	
Signal transduction	
Meiosis	

Sensitivity of the ion channel and ATP-pump deletion strains to plakortide F acid

[†]This is not unexpected: 7% is the highest reported overlap between the two techniques, observed when galactose is provided as a carbon source as opposed to glucose.⁷⁶

(122) was established by Xu *et al.*¹⁶⁹ The ATP-pump mutants *pmr1Δ/pmr1Δ* and *pmc1Δ/pmc1Δ* and the ion channel mutants *cch1Δ/cch1Δ* and *mid1Δ/mid1Δ* displayed hypersensitivity to epiplakinic acid I (95) relative to the WT control. As Cch1p and Mid1p are required for passage of Ca²⁺ into the cells, deletion of the genes should confer resistance. Hence, sensitivity of the deletion mutants to the cyclic peroxides is counterintuitive. However, one can imagine that the channels also allow exit of ions from within the cell, mitigating intracellular toxicity. Xu *et al.* also postulate that “Ca²⁺ deprivation in these mutants might result in a compensatory induction in intracellular Ca²⁺ levels, causing 122 (and 95) to be more toxic under these conditions”.¹⁶⁹

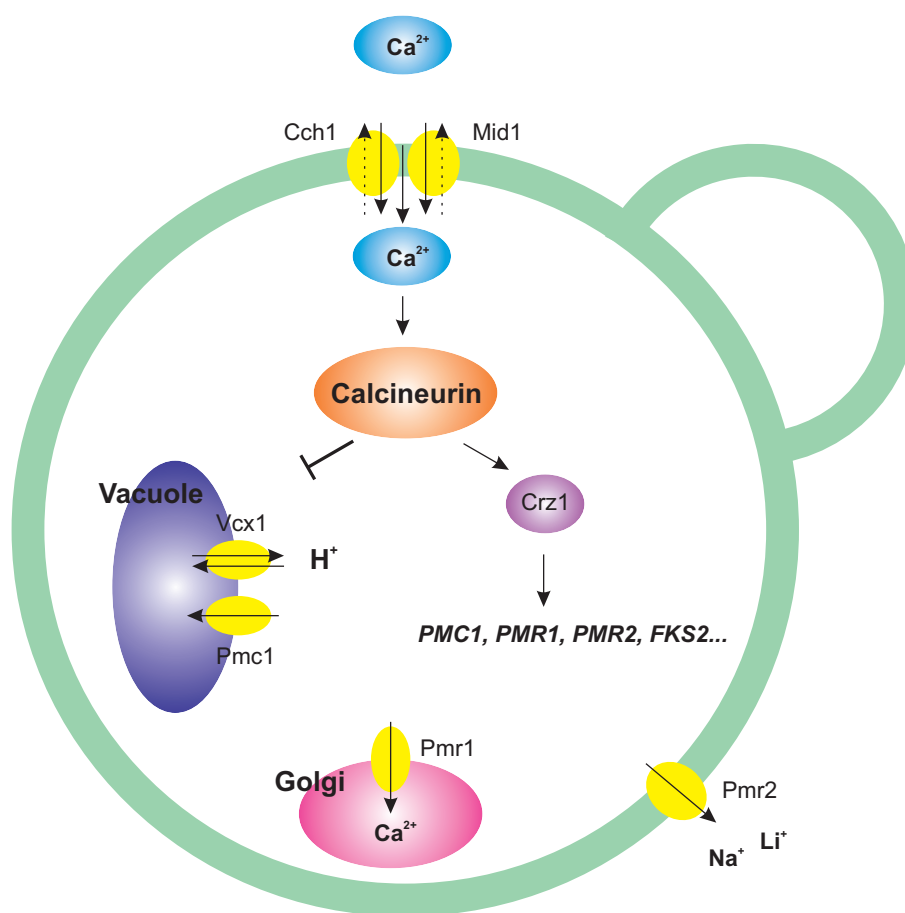


Figure 5.9 Depiction of the ion-channel and ATP-pump system for Ca²⁺ homeostasis in *S. cerevisiae*, adapted from Miyakawa *et al.*²³⁰

Another Ca²⁺-modulating agent, amiodarone,²³¹ is thought to interact with Mid1p.²³² Courchesne *et al.* observed some resistance of the *mid1Δ, cch1Δ* double deletion to amiodarone. Furthermore, the *mid1Δ/mid1Δ* strain did not show the same growth inhibition as the *cch1Δ/cch1Δ* strain in response to amiodarone. Sensitivity of the Mid1p and Cch1p deletion strains to 122 and 95 indicates that neither are the cellular target of the cyclic peroxides 122 and 95. However, the compounds could potentially interact with the membrane-bound ion channels of another divalent ion, such the Fe²⁺ transporter Fet3p. The Mid1p and Cch1p channels has been shown

to be essential to iron toxicity tolerance,²³³ as such it is not unreasonable that a reciprocal interaction may be occurring.

Consistent with plakortide F acid (**122**) increasing intracellular levels of Ca²⁺ and causing Ca²⁺ stress, Xu *et al.* also observed hypersensitivity in the deletion strain of genes essential to the function of calcineurin, a Ca²⁺/calmodulin-dependent protein phosphatase.[‡] *CNB1* encodes the regulatory subunit of the calcineurin heterodimer in yeast and the catalytic subunit of calcineurin is encoded by the functionally redundant genes *CNA1* and *CNA2*.²¹⁸ Mutation of both *CNA1* and *CNA2*, and the regulatory gene *CNB1*, or exposure to calcineurin inhibitors such as FK506 and cyclosporin A compromises activity of the calcineurin phosphatase. *CRZ1* encodes a Ca²⁺-responsive transcription factor that directs calcineurin-dependent transcription genes to mitigate Ca²⁺ toxicity. Hypersensitivity to **122** was displayed by the strains *crz1Δ/crz1Δ*, *cnb1Δ/cnb1Δ*, *cna1Δ/cna1Δ* and *cna2Δ/cna2Δ*.¹⁶⁹ The deletion strains *crz1Δ/crz1Δ*, and *cna2Δ/cna2Δ* displayed similar hypersensitivity to epiplakinic acid I (**95**). Slight sensitivity was observed in the *cnb1Δ/cnb1Δ* strain, although assessment over a more restricted concentration range is required for definitive conclusion. Unexpectedly, the *cna1Δ/cna1Δ* strain did not display sensitivity to **95** (Tables 5.8, 5.9 and Figure H.7).

Table 5.8 Growth Inhibitory Effects of **95** on Ca²⁺-Responsive Deletion Strains.

Strain	Concentration ($\mu\text{mol L}^{-1}$)	Residual Growth (%)	Error (\pm %)
BY4743 WT	7.6	99.0	5.0
<i>cna1Δ/cna1Δ</i>	7.6	70.5	3.0
<i>cna2Δ/cna2Δ</i>	7.6	7.1	2.5
<i>cnb1Δ/cnb1Δ</i>	7.6	11.5	4.5
<i>crz1Δ/crz1Δ</i>	7.6	4.7	3.5
<i>hcm1Δ/hcm1Δ</i>	7.6	42.3	0.5

Table 5.9 Growth Inhibitory Effects of **95** on Ca²⁺-Pump/Channel Deletion Strains.

Strain	Concentration ($\mu\text{mol L}^{-1}$)	Residual Growth (%)	Error (\pm %)
BY4743 WT	3.3	113.3	2.0
<i>cch1Δ/cch1Δ</i>	3.3	56.9	1.2
<i>mid1Δ/mid1Δ</i>	3.3	4.5	0.5
<i>pmc1Δ/pmc1Δ</i>	3.3	69.3	5.2
<i>pmr1Δ/pmr1Δ</i>	3.3	56.2	1.1
<i>ygl167wΔ/ygl167wΔ</i>	3.3	3.5	0.5

[‡]The calcium-modulated protein, calmodulin is a calcium-binding protein conserved in all eukaryotic systems. It can bind up to four calcium ions, and once activated it binds to and regulates many different protein targets affecting a myriad of cellular responses.

5.5.4 The Ca^{2+} second messenger system

Calcium ions are integral to many physiologically important functions, including cytoskeletal dynamics, and as key regulators of the protein calmodulin, the ions play a pivotal role in muscle contraction in higher eukaryotes. The ion is an important second messenger, relaying signals from cell surface receptors to target molecules within the cell (in the cytoplasm or nucleus), inducing changes in cellular activity, and amplifying the strength of the initial signal through signal transduction cascades.[§] The Ca^{2+} second messenger system acts through cellular traffic of the metal ions via membrane ion channels and membrane-bound ion pumps, carefully monitoring cytoplasmic and organelle-located stores of the ion. The second messenger must be tightly controlled as disruption to the system has far-reaching effects, and as such, foreign molecules which in any way influence this system can be extensively detrimental to cellular function. While Ca^{2+} -overload can trigger apoptosis in mammalian cells,²³⁴ decreased viability of WT *S. cerevisiae* has not been reported in response to disruption of Ca^{2+} levels alone.²³⁵ As such, a rise in intracellular Zn^{2+} levels could also contribute to the cellular starvation phenotype induced by **95** and **97**. Translocation studies in the Zrt1p-GFP strain do not necessarily support this, however. In response to increased intracellular Zn^{2+} , the Zn^{2+} -specific membrane pump, Zrt1p, is rapidly endocytosed then degraded in the vacuole.²³⁶ This response was not apparent upon exposure of the Zrt1p-GFP strain to **95** for 40 min (Figure H.8). This may indicate that **95** does not increase intracellular levels of Zn^{2+} . However, if **95** does inhibit actin coordination, the lack of Zrt1p endocytosis may be accounted for.

5.5.5 Epiplakinic acid I induces a Ca^{2+} -related response

Translocation studies were conducted in the Crz1p-GFP strain showing nuclear relocalisation of the GFP signal upon exposure to CaCl_2 or epiplakinic acid I (**95**). This indicates that **95** induces the same cellular response as a spike in intracellular Ca^{2+} . Coorey observed similar relocation in the Crz1p-GFP- Δpdr strain in response to plakortolide X (**97**),²²⁴ consistent with **95** and **97** inducing a spike in intracellular Ca^{2+} . Illustrating the Ca^{2+} -specificity of the Crz1p response, the Crz1p-GFP displayed weak and transient nuclear relocalisation upon exposure to Mg^{2+} , Zn^{2+} and Fe^{2+} (data not shown). The calcium-modulator amiodarone also induces translocation in the Crz1p-GFP strain,²³⁷ indicating the two compounds

[§]There are three main classes: hydrophilic molecules such as cAMP, cGMP, IP3, and Ca^{2+} located in the cytosol; hydrophobic molecules, including diacylglycerol, and phosphatidylinositols are associated with cellular membranes and diffuse from the plasma membrane into the intermembrane space where they can affect membrane-associated effector proteins; gases, such as NO, CO and H_2S form the third division, and are capable of diffusing both through the cytosol and across cellular membranes.

may have similar cellular effects. Amiodarone also induces a starvation response and decreases cell size, while flow cytometry studies with amiodarone have indicated cell cycle delays at both S-phase and the G₂-M transition as seen with **95**.²³⁷

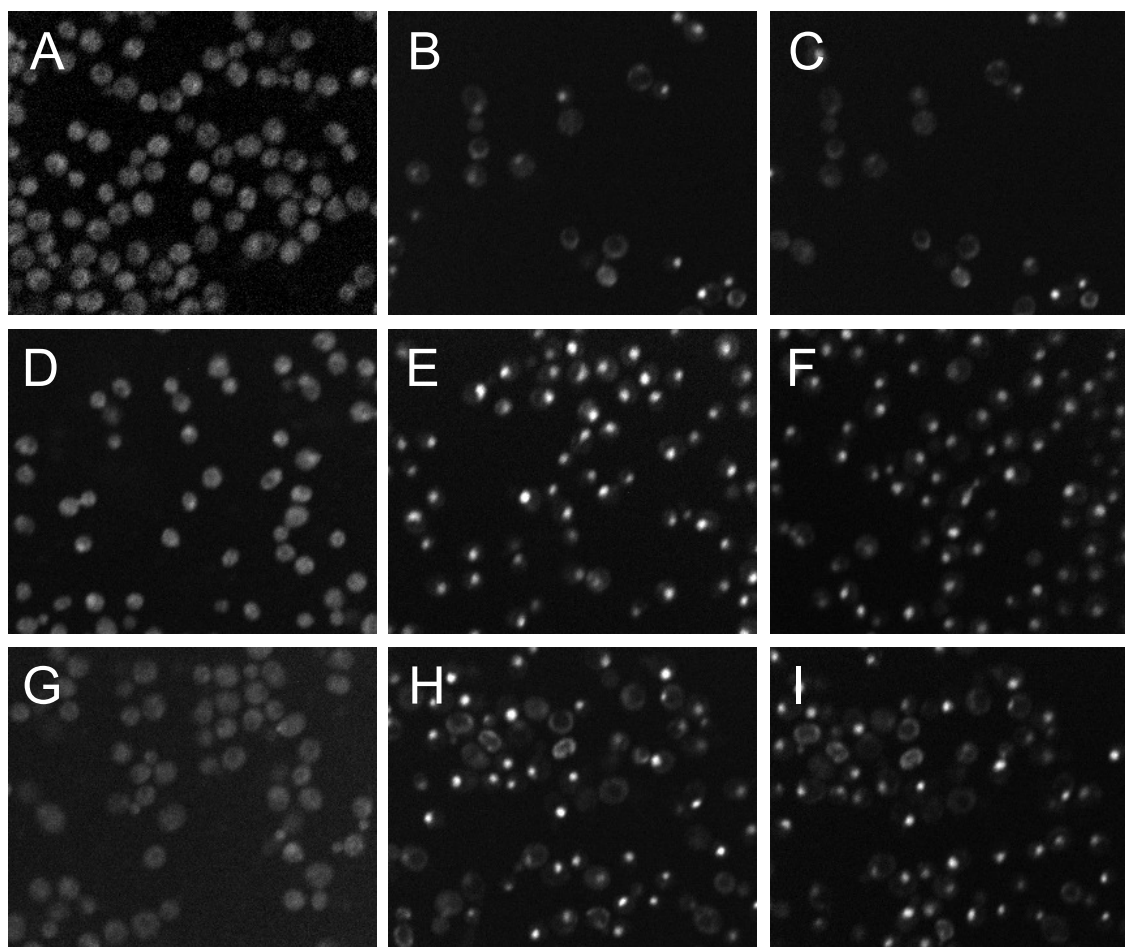


Figure 5.10 Translocation studies in the Crz1p-GFP strain indicating a similar response to a rise in intracellular Ca²⁺ and exposure to epiplakinic acid I (**95**).

A: DMSO (1%), 0 min	B: 95 (10 $\mu\text{mol L}^{-1}$), 0 min	C: CaCl ₂ (50 mmol L ⁻¹), 0 min
D: DMSO, t = 5 min	E: 95 , t = 5 min	F: CaCl ₂ , t = 5 min
G: DMSO, t = 40 min	H: 95 , t = 40 min	I: CaCl ₂ , t = 40 min

Qualitative staining of WT cells with Calcium Orange fluorescent dye also indicated an increase in cellular Ca²⁺ levels in response to epiplakinic acid I (**95**). Consistent with **95** causing an increase in intracellular Ca²⁺ levels, the fluorescence intensity of the Calcium Orange probe was increased in WT cells treated separately with **95** and CaCl₂, relative to the DMSO control (Figure 5.11). This is in agreement with Xu *et al.* who observed an increase in the intracellular levels of Ca²⁺ and Zn²⁺ in WT cells exposed to plakortide F (**122**) by ICP-MS analysis.¹⁶⁹

Increased Ca²⁺ signaling is known to contribute to formation of reactive oxygen species (ROS), and associated cellular toxicity.²³⁸ Although a significant number of genes implicated in mitochondrial damage and response to oxidative stress displayed sensitivity to **95** in the HOP and HIP assays, no evidence for formation of ROS was found. To test for the formation of ROS in the presence on **95**, translocation studies

were conducted in a GFP-tagged reported strain with a red fluorescent protein (RFP) nuclear membrane localisation marker, Yap1p-GFP-NLS-mCherry. Yap1p is a stress response transcription factor, which normally resides in the cytoplasm and translocates to the nucleus in response to oxidative stress. Co-localisation of the GFP and RFP signals was not observed in response to **95**, indicating that Yap1p did not undergo nuclear relocalisation (data not shown). This suggests that **95** does not cause the formation of ROS.

Flow cytometry analysis was also carried out in haploid WT cells using with dichlorofluorescein diacetate (DCF-DA) and propidium iodide (PI) to study the formation of ROS and cell death (Figure 5.12). Although PI staining in the upper left quadrant indicated increased cell death in presence of **95**, the assay did not indicate that formation of ROS was responsible for the increase. However, PI staining is indicative of increased cell wall permeabilisation as a consequence of cell death, and as such this may indicate that **95** (and presumably **97**) is truly cytotoxic to yeast.

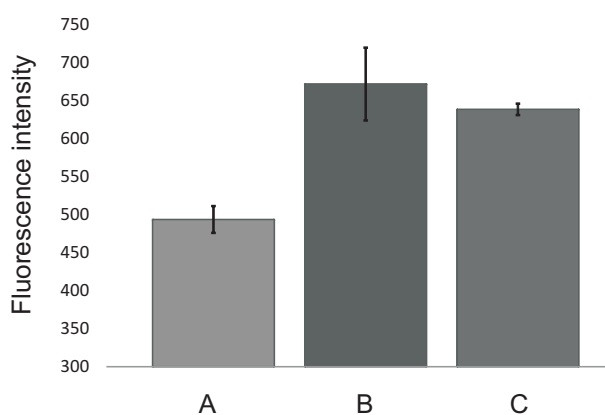


Figure 5.11 Qualitative staining of WT cells with Calcium Orange dye. A: DMSO, 1% B: CaCl₂, 50 mmol L⁻¹ C: Epiplakinic acid I, 10 μmol L⁻¹ Increased fluorescence intensity is indicative of Ca²⁺-coordination by the fluorophore, as observed in the presence of CaCl₂ (B) and **95** (C), relative to the DMSO control (A).

5.5.6 Calcineurin signaling

In *S. cerevisiae* calcineurin is required to maintain cell viability, becoming activated in response to environmental conditions, including exposure to high intracellular levels of Ca²⁺ and Na⁺, and to elevated temperature. In yeast (and mammals), Crz1p is the best-characterised substrate for activated calcineurin.^{239,240} The transcription factor Crz1p resides in the cytoplasm when calcineurin signaling is low, and is dephosphorylated upon activation of calcineurin, rapidly translocating to the nucleus where it affects cellular responses to mitigate Ca²⁺ toxicity. In addition to its role in yeast ion homeostasis, calcineurin is involved in recovery from G₁ arrest

caused by mating pheromones, such as α -factor,²⁴⁰ and is essential to the function of deletion strains with defective cell walls.^{239,241}

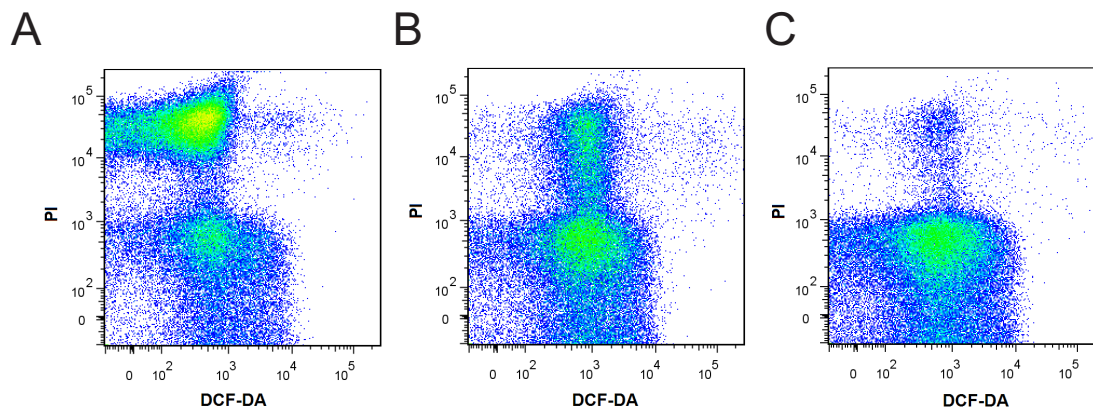


Figure 5.12 Flow cytometry imaging ROS formation with DCF-DA and PI in haploid WT cells.

A: Epiplakinic acid I, $10 \mu\text{mol L}^{-1}$ B: H_2O_2 , $10 \mu\text{mol L}^{-1}$ C: DMSO, 1%
 The lower quadrants represent live cells stained with DCF-DA and cell death is indicated by PI staining of the populations in the top left quadrant. As indicated by the controls, the majority of the live cell population predominantly occupies the left quadrant, while a shift to the right indicates the presence of ROS. The increased cell death observed in the presence of **95** does not appear to be caused by the generation of ROS.

Upon activation of calcineurin, a suite of genes required for ion homeostasis is upregulated in a calcineurin/Crz1p-dependent manner. Following nuclear relocalisation, Crz1p binds specifically to a region of 24 base pairs within the promoter regions of the upregulated genes, termed the calcineurin dependent response element (CDRE). In this way, Crz1p functions downstream of calcineurin to affect calcineurin-dependent responses that mitigate Ca^{2+} -related toxicity. Overproduction of Crz1p in WT cells also increases tolerance to Mn^{2+} and Li^+ , and is known to suppress the phenotypes of calcineurin mutants.²⁴²

The ion homeostasis genes which experience calcineurin/Crz1p-dependent regulation include the vacuolar and Golgi-bound Ca^{2+} and $\text{Ca}^{2+}/\text{Mn}^{2+}$ -ATPases encoded by *PMC1* and *PMR1* (Figure 5.9).^{218,242} The ion-pumps are integral to intracellular ion homeostasis, and their Crz1p-mediated transcription is required for growth under high Ca^{2+} conditions. *PMR2* encodes a plasma membrane Na^+/Li^+ -ATPase required for growth in the presence of high concentration of the two ions. Expression of the pumps is induced by (high) Ca^{2+} and Na^+ in a calcineurin/Crz1p-dependent manner, and in response to high osmotic stress by the high osmolarity glycerol (HOG1) pathway. Deletion of these genes confers sensitivity to **95** (Figure H.7) and **122**.

Independent of Crz1p, increased calcineurin signaling also causes depolarisation of the actin cytoskeleton (Section 5.5.7). Mulet *et al.* observed formation of small actin balls about the cellular peripheries upon brief exposure to 0.2 mol L^{-1}

CaCl₂,²⁴¹ although the effect was observed simultaneously in wt, *cnb1Δ/cnb1Δ* and *crz1Δ/crz1Δ* mutants, indicating actin depolarisation is independent of Crz1p.[¶]

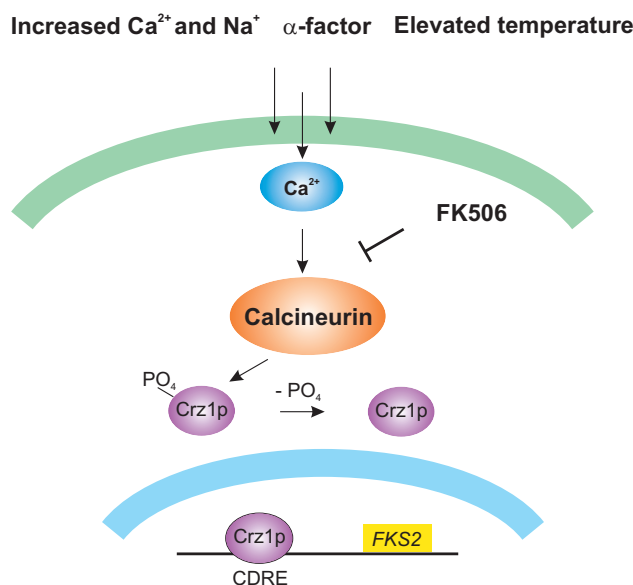


Figure 5.13 Calcineurin signaling pathway in *S. cerevisiae* and activation of Crz1, adapted from Yoshimoto *et al.*²⁴³ Calcineurin is activated by external stimuli, including elevated temperature and levels of Na⁺ and Ca²⁺, and presence of the mating pheromone α-factor. Calcineurin dephosphorylates Crz1, which undergoes nuclear translocation and initiates Ca²⁺-dependent transcription of genes, such as *FKS2*, containing the CDRE in their promoter regions. The calcineurin signaling cascade is rapidly and specifically inhibited by the presence of immunosuppressive drug FK506.

5.5.7 Interactions between calcineurin signaling and TOR

The TOR pathway is conserved among eukaryotes, controlling cell growth in response to nutrient availability and environmental stress. The TOR protein kinase comprises two functionally and structurally distinct protein complexes, TORC1 (TOR complex 1) and TORC2. In yeast, TORC1 contains either *TOR1* or *TOR2*, whereas TORC2 contains exclusively *TOR2*. TORC1 is rapamycin-sensitive and controls growth-related processes such as transcription, translation, ribosome biogenesis, nutrient transport and autophagy in response to nutrient levels.²²⁰ Inactivation of TORC1 leads to a rapid downregulation of genes involved in ribosome biogenesis, with the carryon effect of decreased protein synthesis and cell growth.²⁴⁵ TORC2 is rapamycin-insensitive and controls polarisation of the actin cytoskeleton, acting to inhibit calcineurin-mediated depolarisation of the actin cytoskeleton. In this way, TORC2 allows a cell to resume growth after a stress has been overcome.²⁴¹

The TORC2-calcineurin relationship is mutually antagonistic, and a downstream effect of increased Ca²⁺ levels and calcineurin signaling is inhibition of the TOR

[¶]A similar phenotype is seen upon exposure to latrunculin A, known to stabilise monomeric actin by coordinating to thymosinβ.²⁴⁴

pathway (Figure 5.14).²⁴⁶ Calcineurin prevents TOR-mediated growth under stress conditions in one way by inhibiting signaling between TORC2 and the proteins Slm1p and Slm2p, which act to regulate the actin cytoskeleton organisation in response to stress.²⁴⁷ Increased Ca^{2+} levels and calcineurin signaling promote dephosphorylation of the SLM proteins disrupting their function in actin regulation.²⁴¹ Hence, calcineurin-activating agents, such as **122** and potentially **95** can initiate depolarisation of the actin cytoskeleton leading to the phenotype observed in this study. Similarly, TORC2 phosphorylation of Slm1p and Slm2p inhibits calcineurin-mediated depolarisation of the actin cytoskeleton and Crz1p-dependent gene transcription.

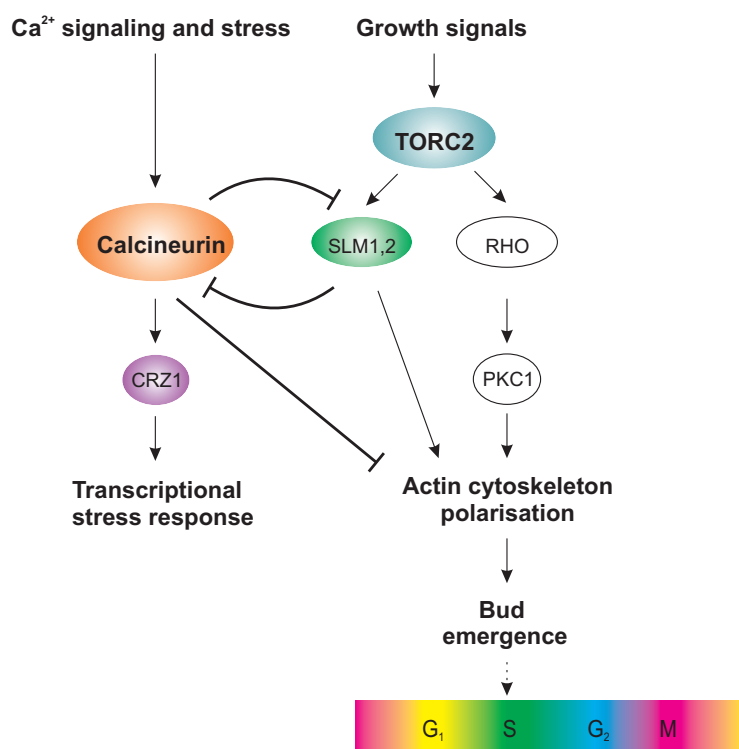


Figure 5.14 Antagonistic interactions between the calcineurin and TORC2 signaling pathways after Mulet *et al.*²⁴¹

Inactivation of the TOR pathway, or treatment with rapamycin, produces a phenotype similar to that of epiplakinic acid I (**95**) and plakortolide X (**97**). Rapamycin inhibits cell cycle progression, initiating arrest at the G₁-S phase boundary, and induces physiological changes consistent with cellular starvation, including reduced cell size.²¹⁹ Xu *et al.* observed that co-treatment of cells with plakortide F acid (**122**) and non-inhibitory concentrations of calcineurin-specific inhibitors FK506 and cyclosporin A greatly enhanced the potency of **122**.¹⁶⁹ From this one can infer that **122**, and presumably compounds **95** and **97**, influence a cellular process closely related to that of FK506 and cyclosporin A, i.e. calcineurin signaling. Additionally, cyclosporin A has a similar effect as plakinid cyclic peroxides on Ca^{2+} -pumping in the mammalian cardiac sarcoplasmic reticulum.^{120,197,248}

5.6 Mechanistic insights from phenotypic and chemical genetic profiling

The phenotypic profiling assays carried out during this study, in combination with the expression profile of **122**, suggests that **95** disrupts intracellular Ca^{2+} homeostasis. Translocation of the Ca^{2+} -responsive transcription factor Crz1p was observed in the GFP strain following exposure to **95** and the same response was observed following addition of exogenous Ca^{2+} to growth media (Figure 5.10). This alone indicates that **95** causes increases in intracellular Ca^{2+} . An overall increase in cellular Ca^{2+} following exposure to **95** was also shown by Calcium Orange staining (Figure 5.11). Furthermore, the deletion strains of *CCH1*, *CNA2*, *CNB1*, *CRZ1*, *MID1*, *PMC1* and *PMR1*, which are required to mitigate Ca^{2+} toxicity, displayed hypersensitivity to **95** (Tables 5.8 and 5.9). Disruption of Ca^{2+} homeostasis could account for the phenotype caused by **95**; reduced cell size and an increase in cells with small buds. The same decrease in cell size was observed following the addition of exogenous CaCl_2 to yeast growth media (Table 5.2 and Figure 5.6).

Although the deletion strains of several genes integral to cell viability in environments of high Ca^{2+} were revealed in the HOP and HIP profiles of **95**, significant enrichment of these functions was not indicated via FunSpec cluster analysis. It may be that when a small molecule inhibits a process so fundamental to cellular function, such as Ca^{2+} signaling, that too many pathways are affected to allow statistically significant enrichment of any one particular process. Such a phenomenon has also been hypothesised in the case of protein synthesis inhibitors, such as pateamine A.²¹⁶ The combined HOP and HIP profiles of **95** did display enrichment in Zn^{2+} homeostasis (p-value = 0.009733) and response to Zn^{2+} ions (p-value = 0.000192), although the p-values associated with the enrichment does not appear particularly significant if disruption of ion homeostasis is the primary mechanism of the compound. Enrichment in Zn^{2+} regulation is, however, consistent with Xu *et al.* who observed increases in intracellular Zn^{2+} and Ca^{2+} in response to **122**. In light of this dual increase in levels of the ions, it may be that the cyclic peroxides are causing an increase in intracellular levels of either Zn^{2+} or Ca^{2+} , with a downstream effect of interfering with homeostasis of the other. Hence, both Zn^{2+} and Ca^{2+} may be responsible for inhibition of yeast cells by **95** and **97**.

5.6.1 Future directions

The mechanism by which the cyclic peroxides **95**, **97** and **122** raise intracellular ion levels requires addressing. Membrane hyperpolarisation has been hypothesised in the case of amiodarone; the amphiphilic molecule and has been shown to associate with

the plasma membrane of yeast cells, hyperpolarising the membrane, which may allow influx of the ion.²³⁷ Epiplakinic acid I (**95**), plakortolide X (**97**) and plakortide F acid (**122**) could also behave in this manner given their polar cyclic peroxide moieties and aliphatic backbones. The aliphatic portions of the three compounds, particularly the C₁₂ and C₁₀ carbon chains of **95** and **97**, could potentially incorporate into the plasma membrane. This could induce membrane curvature allowing both the passage of the compounds into the cell, and influx of Ca²⁺ and/or Zn²⁺ into the cytoplasm.

Interaction of **95** and **97** with membrane-bound ion pumps and channels is a likely mechanism by which cytosolic ion levels could rise. Efforts were made during this study towards the construction of a suite of strains carrying ion pump deletions and a corresponding GFP reporter (Table 5.10). Once compiled, the suite of GFP/deletion strains will be assessed for response to Ca²⁺ and Zn²⁺-induced stress. *ZAP1* encodes a Zn²⁺-responsive transcription factor, which resides in both the nucleus and cytoplasm. Unlike Crz1p, Zap1p does not undergo nuclear translocation, however, application of FRET dyes to Zap1p can allow *in vivo* observation of Zn²⁺ traffic.²⁴⁹ Analysis of both transcription factors in the absence of membrane-pumps should provide insight into the mechanism of these cyclic peroxides.

Table 5.10 Proposed Ion Pump Deletion-GFP Strains

Target metal ion	Target genes	
	Deletion	GFP-reporter
Ca ²⁺	<i>mid1Δ</i>	Crz1p-GFP
Ca ²⁺	<i>cch1Δ</i>	Crz1p-GFP
Ca ²⁺	<i>pmc1Δ</i>	Crz1p-GFP
Ca ²⁺	<i>pmr1Δ</i>	Crz1p-GFP
Ca ²⁺	<i>cch1Δ, mid1Δ</i>	Crz1p-GFP
Ca ²⁺ and Zn ²⁺	<i>zrt1Δ, zrt2Δ</i>	Crz1p-GFP
Ca ²⁺ and Zn ²⁺	<i>cch1Δ, mid1Δ</i>	Zap1p-GFP
Zn ²⁺	<i>zrt1Δ, zrt2Δ</i>	Zap1p-GFP

Imaging studies will also be undertaken to further characterise the cellular effects of **95**, including actin labeling with a fluorescent phalloidin conjugate, and visualisation of the endocytotic pathway with the fluorescent dye FM4-64FX. The effects of increased Zn²⁺ on cell size and the impact of exogenous Ca²⁺ and Zn²⁺ on bud formation will also be assessed.

5.6.2 Concluding remarks

In summary, phenotypic and chemical genetic assessment of epiplakinic acid I (**95**) suggests that the growth inhibitory effects of **95** are caused by increased intracellular Ca^{2+} levels, leading to an increase in small budded cells and reduced cell size. This verifies the work of Xu *et al.*¹⁶⁹ which attributes Ca^{2+} -modulatory behaviour to the structurally related plakortide F acid (**122**). It may also be that increased levels of intracellular Zn^{2+} contribute to the activity of **95** and **122** in yeast.

Increases in cytosolic levels of Ca^{2+} and potentially Zn^{2+} may occur through interaction with the cyclic peroxide and either a membrane-bound ion pump or channel, or with the membrane itself. As such, generation of the ion pump deletion-GFP strains is integral to elucidation of this mechanism, and future research will focus on the generation of these strains. Analysis of the double deletion mutants in particular should grant insight into the mechanism behind the activity of this class of compounds.

Unfortunately, further characterisation may be prevented owing to insufficient quantities of the cyclic peroxides available for analysis. This thesis has benefited from the assessment of specimens with a small sample size, however, this is a limiting factor for this particular arm of research. Complete characterisation of these compounds may be postponed until recollection of the same organism, or one containing similar metabolites.

Chapter 6

Concluding Remarks

Natural products chemistry continues to play an important role in the identification of new pharmaceutical leads for the development of new therapeutic agents. Using a spectroscopy-guided isolation approach, the metabolite profiles of nine Tongan sponge specimens were investigated during this research. Analysis of HMBC experiments acquired from semi-purified fractions from each organism was integral to their selection for study. In order to maximise the probability of uncovering structural novelty in a well-explored environment, only specimens collected in small quantities and those with sparse distribution were chosen for investigation. While this particular facet presented challenges and restricted creative freedom during chromatography, it was also rewarding with seventeen new metabolites expediently isolated from five different organisms over the course of this study. These include two hydroxybutenolide sesterterpenes **23** and **24**, and the alkaloid 14-bromohomofascaplysin (**29**). As five of the four sponges that afforded new metabolites were collected from ‘Eua island, further investigation of organisms from this location in particular may be worthwhile.

Three labdane diterpenes, luakuliides A–C (**33–36**) were isolated from an unidentified dictyoceratid sponge. The *gem*-dimethyl pair, characteristic of the labdane skeleton was evident in the HMBC experiment of the screening fraction, prompting further purification of the fractions. The luakuliide skeleton also features a hemiacetal moiety bridging the B-ring of the labdane bicycle. Luakuliide A (**33**) and its acetal derivative (**34**) were found to modulate NO and TNF- α levels in macrophages, demonstrating their immunomodulatory potential.

Investigation of two plakinid sponge specimens yielded the α -pyrones lehualides E–K (**69–75**), and a series of cyclic peroxides (**95–98**). In both cases the observation of heavily oxygenated sub-structures prompted further investigation of the organisms. The non-protonated nature of the major functional groups in both the lehualides and the cyclic peroxides makes it unlikely that either of these structural classes would have been revealed during spectroscopic organism screening without analysis of the HMBC experiment.

Structural elucidation of the fully-substituted α -pyrone system of lehualides E–K (**69–75**) presented a challenge. Similarly unprotonated systems have previously been proposed on the basis of chemical shift alone, however, the substitution pattern of the compounds found in this study allowed for the unequivocal establishment of the α -pyrone substructure. Lehualides H–K (**72–75**) also demonstrate several different sulfur-containing functional groups. The presence of the NMR-silent ^{32}S nuclei was determined by analysis of $^1J_{\text{CH}}$ couplings of adjacent methylene and methyl centres. However, unequivocal identification of the functional groups required synthetic modeling of the proposed structural fragments and analysis of their ^1H and ^{13}C NMR spectra.¹³⁴ Although NMR spectroscopy is an important tool to structural elucidation, the technique has its limits. As such it is important to provide further evidence of a structure wherever possible, be it through chemical derivatisation, X-ray analysis of an isolated compound, or synthesis.

A variety of cyclic peroxides have been uncovered from plakinid sponges, however, the isolation of multiple classes from one organism is less frequently observed. In this case, three different polyketide cyclic peroxide classes, including the rare 1-hydroxy-1,2-dioxolane metabolite **98**, were encountered alongside two $5\alpha,8\alpha$ -epidioxysterols. Cyclic peroxides **95–98** all displayed demonstrated potent inhibition of the HL-60 cell line, with the more heavily oxygenated compounds affecting greater inhibition. As such, the significantly decreased sensitivity of HL-60 cells to **97** compared with **95** and **98** may be due to the absence of the free carboxylic acid moiety.

Isolation of secondary metabolites without knowledge of their biological potential requires a technique capable of delivering an unbiased assessment of biological activity. Genome-wide profiling assays were conducted in an attempt to biologically characterise epiplakinic acid I (**95**), using the *Saccharomyces cerevisiae* homozygous and heterozygous diploid deletion sets. This study required the development of new laboratory techniques, and an understanding of foreign experimental concepts. Although no definitive cellular target was determined, this study verified the widely held opinion that plakinid cyclic peroxides disrupt cellular calcium homeostasis.

While in this instance chemical genetic screening was not successful in identifying the precise mechanism of action of a small molecule, it has indicated specific assays that could pinpoint the precise molecular target of the molecule. Future research into the elucidation of this mechanism is planned, although the realities of isolation from rare organisms may prevent these characterisation studies. While the investigation of uncommon organisms from geographically isolated locations may yield structural novelty, recollection difficulties can hinder the development of new bioactives.

Chapter 7

General Experimental Procedures

Optical rotations were performed on a Autopol II Automatic Polarimeter while UV spectra were acquired on an Agilent 8453 UV/Visible Spectrometer and IR spectra were recorded using a Perkin Elmer Spectrum One FT-IR spectrometer. NMR spectra were obtained using a 600 MHz Varian DirectDrive spectrometer equipped with a triple resonance HCN cryogenic probe, operating at 600, 150 and 60 MHz for ^1H , ^{13}C and ^{15}N nuclei, respectively. All HSQC spectra were acquired without carbon-decoupling. Spectra were recorded in CD_3OD (Cambridge Isotopes), CDCl_3 (Merck), $(\text{CD}_3)_2\text{SO}$ (Cambridge Isotopes) and C_6D_6 (Cambridge Isotopes), with chemical shifts δ (ppm) referenced to the residual solvent peak [(CD_3OD : δ_{C} 49.00, δ_{H} 3.31), (CDCl_3 : δ_{C} 77.16, δ_{H} 7.26), ($(\text{CD}_3)_2\text{SO}$: δ_{C} 39.52, δ_{H} 2.50) and (C_6D_6 : δ_{C} 128.06, δ_{H} 7.16)].²⁵⁰ HRESIMS measurements were obtained using a Waters Q-TOF PremierTM Tandem Mass Spectrometer.

GFP and RFP cell studies were performed on a Perkin Elmer EvoTec OPERA. GFP and RFP were excited using 488 nm and 561 nm with emission fluorescence collected through 520/35 and 600/40 bandpass filters respectively. Cells were imaged using an Olympus IXF1 optical microscope operating with a CC12 Soft Imaging System. Cell growth was quantified using a Wallac EnVision 2102 Multilabel Plate Reader (Perkin Elmer) while cell population studies were performed on a FACS CantoTM II Flow Cytometer (BD HTS) and manipulated on FlowJo version 7.6.1 flow cytometry analysis software (Tree Star Inc., Ashland, OR, USA). Cultures were concentrated using an Eppendorf 5810 Centrifuge and a 5415 R Microcentrifuge and suspended with a TallBoys Standard Vortex Mixer and an Eppendorf MixMate plate mixer.

2,3-Dihydroxypropoxypropyl-derivatised silica gel (DIOL) was used for all normal-phased column chromatography while Supelco dianion HP20 and HP20SS polystyrene (divinylbenzene) resins were used for reversed-phase column chromatography unless otherwise stated. Size exclusion chromatography was performed using Sephadex LH20. HPLC-grade CH_2Cl_2 (Merck) and MeCN (Fluka) were used for general purposes and for HPLC purification, all other solvents (including H_2O) were distilled from glass immediately prior to use. TLC analyses were performed using Machery-

Nagel Alugram Sil G/UV254 plates. The plates were analysed by fluorescence quenching under UV light ($\lambda = 254$ nm) followed by dipping in 5% H₂SO₄ in MeOH then dipping in 0.1% vanillin in EtOH and heating. Chemical reagents were purchased from Sigma-Aldrich and Penta International Corporation, unless otherwise specified, and used without further purification.

7.1 Isolation of new diterpenes from PTN3_45E

7.1.1 Animal material

A garlic-odoured specimen, PTN3_45E (96 g) was collected from the vertical rock sides of Tu'ungasika Island in the Vava'u group, at a depth of 12–15 m in November 2009. The specimen was frozen immediately and maintained at -18°C until extraction. A voucher specimen (PTN3_45E) has been deposited at the School of Chemical and Physical Sciences, VUW, Wellington.

7.1.2 Extraction of PTN3_45E

A frozen 24 g sample was extracted twice in 100 mL MeOH overnight. The filtered extracts were passed through a column of 40 mL HP20 resin in reverse order and the combined eluents were diluted 1:1 with 200 mL H₂O. The diluted eluent was passed through the column again, further diluted with 400 mL H₂O to 25% MeOH and passed through the column once more. The column was washed with H₂O then eluted generating three 100 mL fractions of 30%, 75% and 100% Me₂CO in H₂O of 10.5 mg, 70.7 mg and 121.5 mg respectively.

Further reversed-phase purification of the 75% Me₂CO in H₂O fraction was undertaken on HP20SS, generating Me₂CO in H₂O fractions of 30–100% Me₂CO. The 80% Me₂CO in H₂O HP20SS fraction was further partitioned over HP20SS resin with 70–80% Me₂CO in H₂O in 2% intervals. Analysis by TLC (5% MeOH in CH₂Cl₂) indicated two metabolites of similar polarity were present in the 70% and 72% Me₂CO in H₂O fractions (rf. 0.32 and 0.35). Resolution of the metabolites was achieved by reversed-phase HPLC (C₁₈, 85% MeCN in H₂O) with **23** (0.0007 g) and **24** (0.0015 g) eluting at 10 and 12 min respectively.

***iso*-Secothorectolide (23)**: Clear oil, 0.7 mg; ¹H and ¹³C NMR data, see Table C.1; HRESIMS m/z 439.2458 [M + Na]⁺ (calcd for C₂₅H₃₆O₅Na, 439.2460; Δ -0.5 ppm); m/z 415.2487 [M – H][–] (calcd for C₂₅H₃₅O₅, 415.2484; Δ 0.3 ppm).

1-Hydroxyluffarin Q (24): Clear oil, 1.5 mg; ^1H and ^{13}C NMR data, see Table C.2; HRESIMS m/z 439.2458 $[\text{M} + \text{Na}]^+$ (calcd for $\text{C}_{25}\text{H}_{36}\text{O}_5\text{Na}$, 439.2460; Δ -0.5 ppm); m/z 415.2476 $[\text{M} - \text{H}]^-$ (calcd for $\text{C}_{25}\text{H}_{35}\text{O}_5$, 415.2484; Δ -0.8 ppm).

7.2 Isolation of known terpenes from PTN4_10B

7.2.1 Animal material

The odorous sponge specimen PTN4_10B (125 g) was collected using SCUBA from a vertical rock face at a depth of ca. 15 m on Fakalotulā island in the Vava'u group in November 2009. The specimen was frozen immediately and maintained at -18°C until extraction. A voucher specimen is deposited at the School of Chemical and Physical Sciences, VUW, Wellington.

7.2.2 Initial extraction of PTN4_10B

A frozen 16.0 g sample was extracted twice for 20 h in 100 mL MeOH at room temperature. In reverse order the extracts were passed through a column of 40 mL HP20 resin, the combined eluents were diluted 1:1 with 200 mL H_2O , passed through the column again, further diluted with 400 mL H_2O to 25% MeOH and passed through the column once more. The column was washed with H_2O then eluted, generating three 100 mL fractions of 30%, 75% and 100% Me_2CO in H_2O . The Me_2CO in H_2O fractions (39.3 mg, 65.8 mg and 96.2 mg respectively) were evaporated to dryness under reduced pressure and subjected to 1D and 2D NMR analysis.

The crude NMR spectra of the 100% Me_2CO in H_2O fraction was dominated by two compounds identified as ambliol B (**25**) and luffariellolide (**26**). Bench-top column chromatography of the lipophilic fraction (DIOL, $\text{CH}_2\text{Cl}_2/20\%$ MeOH) yielded CH_2Cl_2 fractions rich in ambliol B (**25**) and spectroscopically pure luffariellolide (**26**, 11.3 mg). Further bench-top purification afforded ambliol B (7.3 mg, 75% hexane in CH_2Cl_2).

Ambliol B (25): Clear oil, 7.3 mg; $[\alpha]_D^{17.5} +67.6^\circ$ (c 0.06, CHCl_3); ^1H and ^{13}C NMR data, see Table C.3.

Luffariellolide (26): Clear oil, 11.3 mg; $[\alpha]_D^{17.5} +4.9^\circ$ (c 0.1, CHCl_3); ^1H and ^{13}C NMR data, see Table C.4.

7.3 Isolation of 14-bromohomofascaplysin

7.3.1 Animal material

The slimy green sponge, PTN3_20B (40 g) was collected from the interior of a large cave at a depth of 12–15 m on ‘Eua Island in November 2008. The specimen was frozen immediately then stored at -18°C until extraction. A voucher specimen is deposited at the School of Chemical and Physical Sciences, VUW, Wellington.

7.3.2 Extraction of PTN3_20B

A frozen 20.5 g screening sample of PTN3_20B was extracted twice overnight for 18 h with 100 mL MeOH at room temperature. The filtered extracts were passed through a column of 40 mL HP20 resin in reverse order and the combined eluents were diluted 1:1 with 200 mL H_2O . The diluted eluent was passed through the column again, further diluted with 400 mL H_2O to 25% MeOH and passed through the column once more. The column was washed with H_2O then eluted generating three 100 mL fractions of 30%, 75% and 100% Me_2CO in H_2O (13.0 mg, 98.6 mg and 90.0 mg respectively).

The 75% and 100% Me_2CO in H_2O fractions were further partitioned over HP20SS and the fractions (30%, 40%, 50%, 60%, 70% 80% and 100% Me_2CO in H_2O) analysed by ^1H NMR. The 50% and 60% Me_2CO in H_2O HP20SS fractions were further purified by bench-top chromatography (DIOL, hexane/ CH_2Cl_2 /EtOAc/MeOH/ H_2O) with small quantities of the charged 14-bromohomofascaplysin (**29**) eluting slowly from the column in the 10% MeOH in H_2O fraction.

14-bromohomofascaplysin (29): Clear oil, ca. 700 μg ; ^1H and ^{13}C NMR data, see Table C.7; HRESIMS m/z 407.0395 [$\text{M} + \text{H}$] $^+$ (calcd for $\text{C}_{21}\text{H}_{16}\text{N}_2\text{O}_2\text{Br}$, 407.0395; Δ 0.0 ppm).

7.3.3 Me_2CO -free extraction of PTN3_20B

The remaining 19.5 g of PTN3_20B was extracted twice overnight for 18 h in 100 mL MeOH, and the extracts were partitioned over HP20 resin. The column was eluted with eight fractions ranging from 30–100% MeOH in H_2O , which were analysed by ^1H NMR. Further 2D analysis was performed in an attempt to identify either 14-bromohomofascaplysin or 14-bromofascaplysin, although neither compound was identified by these methods.

7.4 Isolation of halenaquinone

7.4.1 Animal material

A red liver-coloured sponge specimen, PTN3_21D (50 g) was collected using SCUBA from the horizontal ceiling of a large cave at a depth of 12–15 m on ‘Eua Island in November 2008. The specimen was frozen immediately and maintained at -18°C until extraction. A voucher specimen is deposited at the School of Chemical and Physical Sciences, VUW, Wellington.

7.4.2 Extraction of PTN3_21D

The frozen sample (22.0 g) was extracted twice for 20 h in 100 mL MeOH at room temperature. In reverse order the filtered extracts were passed through a column of 40 mL HP20 resin, the combined eluents were diluted 1:1 with 200 mL H_2O , passed through the column again, further diluted with 400 mL H_2O to 25% MeOH and passed through the column once more. The column was washed with H_2O then eluted generating three 100 mL fractions of 30%, 75% and 100% Me_2CO in H_2O (41.5 mg, 95.4 mg and 53.5 mg respectively). The 75% and 100% Me_2CO in H_2O fractions were evaporated to dryness under reduced pressure and subjected to 1D and 2D NMR analysis. Normal-phase chromatography of the 75% Me_2CO in H_2O HP20 fraction (DIOL, hexane/ CH_2Cl_2 /EtOAc/MeOH) and subsequent NMR analysis showed concentration of the signals of interest in the 75% hexane in CH_2Cl_2 fraction. Subsequent reversed-phase HPLC (C_{18} , 90% MeCN in H_2O) yielded halenaquinone (**31**) (10.1 mg) as a red solid.

Halenaquinone (31): red solid, 10.1 mg; ^1H and ^{13}C NMR data, see Table C.8.

7.5 Isolation of luakuliides A–C

7.5.1 Animal material

The dictyoceratid sponge sample PTN3_21E (90 g) was collected at 12–15 m from an unlit cave on ‘Eua Island in November 2008. The specimen was frozen immediately and maintained at -18°C until extraction. A second collection PTN3_50B (42 g) was made from a similar cave location at Shark’s Tooth, Kitu’s in the Vava’u Island group in November 2009. A voucher specimen is deposited at the School of Chemical and Physical Sciences, VUW, Wellington.

7.5.2 Screening extraction of PTN3_21E

A 23 g sample was extracted while frozen in MeOH and partitioned over HP20 according to laboratory protocol (Appendix A). 1D and 2D NMR analysis of the 100% and 75% Me₂CO in H₂O fractions (105.2 mg, 120.8 mg respectively) revealed the presence of two closely related metabolites. Further reversed-phase fractionation of both fractions was undertaken over HP20SS resin producing fractions of Me₂CO in H₂O (30–100%, 10% intervals). ¹H NMR analysis of the 60% and 70% Me₂CO in H₂O HP20SS fractions revealed luakuliide A (**33**, 92.7 mg) in exceptionally high spectroscopic purity.

The 100% Me₂CO fraction was further partitioned (DIOL, hexane/CH₂Cl₂/EtOAc) generating a steroid rich fraction (4.7 mg, 50% hexane in CH₂Cl₂). Bench-top chromatography of the 90% Me₂CO in H₂O fraction (DIOL, CH₂Cl₂/EtOAc) yielded methyl-acetal analogue of luakuliide A, **34** (16.1 mg), while the 80% Me₂CO in H₂O HP20SS fraction contained a mixture of the two compounds.

Ethanol extraction of PTN3_21E

The remaining 67 g of PTN3_21E were extracted twice overnight in 200 mL EtOH and the extracts were partitioned over HP20 generating 30%, 75% and 100% Me₂CO in H₂O fractions. Compound **33** was clearly present within the extracts, however, the methyl-acetal analogue **34** was absent, indicating it was an artifact of MeOH extraction.

Derivatisation of luakuliide A (33): Luakuliide A (**33**, 5.0 mg) was dissolved in 5 mL 10% CDCl₃ in MeOH and maintained at 4 °C for 72 h. ¹H NMR analysis showed quantitative conversion to the methyl-acetal analogue **34**.

7.5.3 Extraction of PTN3_50B

The 42 g sample was extracted twice overnight in 200 mL MeOH and partitioned over 40 mL HP20 according as above. The 100% and 75% Me₂CO in H₂O fractions were partitioned over HP20SS with 30–100% Me₂CO in H₂O mixtures (10% intervals). As previously observed, the 80–100% Me₂CO in H₂O fractions contained compounds **33** and **34**, while the 70% and 60% Me₂CO in H₂O HP20SS fractions appeared to contain previously unencountered resonances, and was further partitioned over DIOL (hexane/CH₂Cl₂/EtOAc). The 33% EtOAc in CH₂Cl₂ fraction was then

partitioned by HPLC (C₁₈, 70% MeCN in H₂O) with the butenolide diterpenes **35** and **36** eluting between 4.0–4.7 min.

The 100% Me₂CO HP20SS fraction was devoid of both **33** and **34**, and subjected to further normal-phase chromatography (DIOL, hexane/CH₂Cl₂/EtOAc). The minor terpenoid metabolites eluted in the 20% EtOAc/CH₂Cl₂ fraction, HPLC purification of which (C₁₈, 70% MeCN in H₂O) yielded **35** and **36**, eluting closely at 4.2 and 4.5 min. Fractions from different collections of the two butenolide metabolites were combined and subjected to further chromatographic purification by HPLC (C₁₈, 70% MeCN in H₂O) generating ca. 600 μg of both **35** and **36**.

Normal-phase chromatography of the 70% Me₂CO in H₂O HP20SS fraction (DIOL, CH₂Cl₂/EtOAc) yielded an uncharacterised labdane diterpene in the 2.5% EtOAc in CH₂Cl₂ fraction, which was also identified within previously acquired spectra from the ‘Eua specimen.

Luakuliide A (33): Clear oil, 92.7 mg; $[\alpha]_D^{25.4} -10.8^\circ$ (*c* 18.5, CHCl₃), UV (MeOH) λ_{\max} (log ϵ), 213 (2.90); IR (film) ν_{\max} 3385, 2923, 2851, 1727, 1458, 1376, 1161, 1027 cm⁻¹; ¹H and ¹³C NMR data see Table 3.2; HRESIMS *m/z* 341.2097 [M + Na]⁺ (calcd for C₂₀H₃₀O₃Na, 341.2093; Δ 1.2 ppm).

Luakuliide A methyl-acetal (34): Clear oil, 16.1 mg; $[\alpha]_D^{25.4} -75.0^\circ$ (*c* 0.14, CHCl₃), UV (MeOH) λ_{\max} (log ϵ), 215 (3.89) nm; IR (film) ν_{\max} 2954, 2926, 2860, 1727, 1460, 1377, 1274, 1073, 999 cm⁻¹; ¹H and ¹³C NMR data see Table 3.3; HRESIMS *m/z* 355.2257 [M + Na]⁺ (calcd for C₂₁H₃₂O₃Na, 355.2249; Δ 2.3 ppm).

Luakuliide B (35): Clear oil, ca. 600 μg; UV (MeOH) λ_{\max} (log ϵ), 235 (3.80), 295 (3.73); IR (film) ν_{\max} 3250, 2928, 2853, 1687, 1647, 1561, 1440, 1221, 1094 cm⁻¹; ¹H and ¹³C NMR data see Table 3.4; HRESIMS *m/z* 373.1996 [M + Na]⁺ (calcd for C₂₀H₃₀O₅Na, 373.1991; Δ 1.3 ppm).

Luakuliide C (36): Clear oil, ca. 600 μg; UV (MeOH) λ_{\max} (log ϵ), 235 (3.80), 295 (3.73); IR (film) ν_{\max} 3250, 2928, 2853, 1687, 1647, 1561, 1440, 1221, 1094 cm⁻¹; ¹H and ¹³C NMR data see Table 3.2; HRESIMS *m/z* 373.1990 [M + Na]⁺ (calcd for C₂₀H₃₀O₅Na, 373.1991; Δ -0.3 ppm).

7.6 Isolation of lehualides E–K

7.6.1 Animal material

The *Plakortis* sponge PTN3_20A (36.0 g) collected was using SCUBA from the horizontal ceiling of a large cave at a depth of 12–15 m on ‘Eua Island in November 2008. The specimen was frozen immediately and kept at -18°C until extraction. The surface of the corky specimen is covered in wide shallow nodules ca. 3 mm high, and the organism forms small oval pendant encrustations. Diod spicules of 180–250 μm in length were recovered following HNO_3 digest of the organic material. A voucher specimen (PTN3_20A) has been deposited in the collection of Dr James Bell at the School of Biological Sciences, VUW, Wellington.

7.6.2 Initial extraction of *Plakortis* sp. PTN3_20A

The frozen sample (21.0 g) was extracted twice for 14 h in 100 mL MeOH at room temperature. The second extract, followed by the first, were passed through a column of 40 mL HP20 resin, the eluents combined and diluted with 200 mL H_2O . The diluted eluent was passed through the column again, further diluted to 25% MeOH and passed through the column once more. The column was washed with H_2O then eluted generating three 100 mL fractions of 30%, 75% and 100% Me_2CO in H_2O . The 75% and 100% Me_2CO in H_2O fractions were evaporated to dryness under reduced pressure then analysed by 1D and 2D NMR.

Sub-samples of the 75% Me_2CO in H_2O fraction (ca. 40 mg) were further partitioned over 3 mL reversed-phase resin (HP20SS) with MeOH and H_2O . The columns were washed with 20 mL H_2O then eluted generating 10 mL fractions of Me_2CO in H_2O (30–100%, 10% intervals). The 50–100% Me_2CO in H_2O fractions were assessed by ^1H NMR (CDCl_3). The 80% Me_2CO in H_2O HP20SS fractions were evaporated to dryness then further partitioned over DIOL ($\text{CH}_2\text{Cl}_2/\text{EtOAc}/\text{MeOH}$). The 100% CH_2Cl_2 fractions of the DIOL column was partitioned on reversed-phase HPLC (C_{18} , 85% MeCN in H_2O) with lehualides F and G (**70** and **71**) eluting at 6.5 and 10.5 min respectively (2.8 mg, and 14.5 mg total).

Sub-samples of the 100% Me_2CO fraction (ca. 40 mg) were partitioned over 3 mL HP20SS resin with MeOH and H_2O , the columns were washed with 20 mL H_2O then eluted generating 10 mL fractions of Me_2CO in H_2O (30–100%, 10% intervals). The 80% Me_2CO in H_2O fractions from the HP20SS columns were evaporated to dryness then further purified with bench-top DIOL chromatography (hexane/ $\text{CH}_2\text{Cl}_2/\text{EtOAc}$). Bench-top SiO_2 chromatography ($\text{CH}_2\text{Cl}_2/\text{EtOAc}$) of the

CH₂Cl₂ DIOL fraction, followed by normal-phase HPLC (DIOL, 4% IPA in hexane) of the 2.5% EtOAc in CH₂Cl₂ SiO₂ fraction yielded lehualide H (**72**, 700 μg) eluting at 16.1 min.

7.6.3 Second extraction of *Plakortis* sp. PTN3_20A

The remaining 15 g of *Plakortis* sp. was extracted from frozen with 100 mL MeOH for 14 h. The extract was filtered and the sponge tissue extracted for a further 14 h with 100 mL MeOH. The second extract was filtered and loaded onto 40 mL of equilibrated HP20 resin beads followed by the first extract. The combined eluents diluted 50% with H₂O and re-loaded onto the column, the eluent was further diluted 50% with H₂O and passed through the column once again. The column was washed with 100 mL H₂O, and eluted with 100 mL fractions of 30%, 75% and 100% Me₂CO in H₂O. Further reversed-phase partitioning of the 100% Me₂CO HP20 fraction over HP20SS generated eight Me₂CO in H₂O fractions, 30–100% in 10% Me₂CO increments.

Normal-phase bench-top chromatography (DIOL, CH₂Cl₂/EtOAc/MeOH) of the combined 80% Me₂CO in H₂O HP20SS fractions followed. The 100% CH₂Cl₂ fractions were evaporated to dryness and subsequent NMR analysis showed that the signals of interest were concentrated within the fractions. Subsequent reversed-phase HPLC (C₁₈, 85% MeCN in H₂O) of the 100% CH₂Cl₂ fraction yielded lehualides J (**74**, 500 μg), H (**72**, 800 μg), I (**73**, 646 μg) and E (**69**, 540 μg). Two related metabolites bearing terminal α-pyrone and thioacetate moieties were also recovered, although not fully characterised.

The 100% Me₂CO HP20SS fractions were further partitioned over DIOL (CH₂Cl₂/EtOAc/MeOH) with lehualide K (**75**) eluting late in the 100% CH₂Cl₂ fractions. Iterative cycles of bench-top chromatography (DIOL, hexane/CH₂Cl₂) yielded lehualide K in ca. 85% purity (2.12 mg). Partitioning of the 60% and 70% Me₂CO in H₂O HP20SS by reversed-phase HPLC (C₁₈, 75% MeCN in H₂O) afforded lehualide J (**74**, 1.95 mg total).

Lehualide E (69): Clear oil, 540 μg; UV (MeOH) λ_{max} (log ε), 235 (3.80), 295 (3.73); IR (film) ν_{max} 3250, 2928, 2853, 1687, 1647, 1561, 1440, 1221, 1094 cm⁻¹; ¹H and ¹³C NMR data, see Table 4.1; HRESIMS *m/z* 385.2399 [M + Na]⁺ (calcd for C₂₄H₃₂O₄Na, 385.2398; Δ 0.2 ppm).

Lehualide F (70): White solid, 2.8 mg; UV (MeOH) λ_{max} (log ε), 235 (3.81), 282 (3.70) nm; IR (film) ν_{max} 3250, 2929, 2854, 1686, 1648, 1560, 1439, 1220, 1094

cm⁻¹; ¹H and ¹³C NMR data, see Table 4.2; HRESIMS *m/z* 393.2042 [M + Na]⁺ (calcd for C₂₃H₃₀O₄Na, 393.2042; Δ 0.0 ppm).

Lehualide G (71): White solid, 18.3 mg; UV (MeOH) λ_{max} (log ε), 235 (3.44), 291 (3.55) nm; IR (film) ν_{max} 3250, 2926, 2854, 1686, 1649, 1563, 1439, 1276, 1094 cm⁻¹; ¹H and ¹³C NMR data, see Table 4.3; HRESIMS *m/z* 421.2355 [M + Na]⁺ (calcd for C₂₅H₃₄O₄Na, 421.2355; Δ 0.0 ppm).

Lehualide H (72): White solid, 1.5 mg; UV (MeOH) λ_{max} (log ε), 255 (3.68), 297 (4.29) nm; IR (film) ν_{max} 2925, 2853, 1709, 1690, 1651, 1569, 1458, 1227, 670 cm⁻¹; ¹H and ¹³C NMR data, see Table 4.4; HRESIMS *m/z* 407.1864 [M + Na]⁺ (calcd for C₂₀H₃₂O₅SNa, 407.1868; Δ -1.0 ppm).

Lehualide I (73): Clear oil, 646 μg; UV (MeOH) λ_{max} (log ε), 249 (3.12), 297 (3.96) nm; IR (film) ν_{max} 2926, 2854, 1712, 1652, 1570, 1460, 1370, 1229, 699 cm⁻¹; ¹H and ¹³C NMR data, see Table 4.5; HRESIMS *m/z* 379.1920 [M + Na]⁺ (calcd for C₁₉H₃₂O₄SNa, 379.1919; Δ 0.3 ppm).

Lehualide J (74): Clear oil, 2.0 mg; [α]_D^{19.1} 0.0° (*c* 3.69 × 10⁻³, CHCl₃), UV (MeOH) λ_{max} (log ε), 249 (2.88), 288 (3.52) nm; IR (film) ν_{max} 2925, 2855, 1713, 1652, 1569, 1458, 1371, 1228, 1098, 699 cm⁻¹; ¹H and ¹³C NMR data, see Table 4.6; HRESIMS *m/z* 395.1868 [M + Na]⁺ (calcd for C₁₉H₃₂O₅SNa, 395.1868; Δ 0.0 ppm).

Lehualide K (75): Clear oil, 2.1 mg (impure); UV (MeOH) λ_{max} (log ε), 240 (3.41), 296 (3.60) nm; IR (film) ν_{max} 2926, 2852, 1690, 1651, 1569, 1458, 1227, 672 cm⁻¹; ¹H and ¹³C NMR data, see Table 4.8; HRESIMS *m/z* 705.3477 [M + Na]⁺ (calcd for C₃₆H₅₈O₈S₂Na, 705.3471; Δ 0.9 ppm).

7.6.4 Preparation of spectroscopic model compounds

Preparation of octanethiol: 1-bromooctane (5.95 mL, 34.20 mmol) was stirred in 30 mL MeOH under ambient conditions. Thiourea (3.91 g, 0.05 mol) was dissolved in 30 mL H₂O then added to the 1-bromooctane solution. The reaction was heated to reflux for 3.5 h, then allowed to cool to room temperature. KOH (4.83 g, 0.09 mol) was added and the reaction heated at reflux for a further hour to hydrolyse the isothiuronium salt. The reaction was cooled to room temperature, extracted

twice with 30 mL CH₂Cl₂, the aqueous phase washed with 3 mL concentrated HCl and re-extracted with 30 mL CH₂Cl₂. The combined organic fractions were dried with MgSO₄, filtered and evaporated under reduced pressure. The crude product was distilled under reduced pressure affording octanethiol in high purity as judged by ¹H NMR.

Preparation of octylthioacetate: Octanethiol (0.89 g, 6.10 mmol) was stirred under ambient conditions, treated with a molar excess of acetic anhydride (15.00 mL, 159.00 mmol) then heated with stirring to 90 °C overnight. The reaction was cooled to room temperature, placed on ice and quenched with 20 mL H₂O. Addition of H₂O induced separation of the alkyl product and the aqueous phase was further extracted twice with 20 mL Et₂O. The organic phase was dried over MgSO₄, filtered and evaporated under reduced pressure. The crude product was then distilled under reduced pressure affording octylthioacetate in an 80% yield (0.92 g, 4.90 mmol).

Octylthioacetate: Colourless liquid, IR (film) ν_{\max} 698 cm⁻¹; ¹H NMR (CDCl₃, 600 MHz) δ 2.86 (2H, t, J = 7.5 Hz, H-1), 2.32 (3H, s, SC(O)CH₃), 1.55 (2H, quin, J = 7.6 Hz, H-2), 1.33 (2H, quin, J = 7.4 Hz, H-3), 1.23–1.30 (8H, m, H₂-4–H₂-7), 0.87 (3H, t, J = 6.5 Hz, H-8); ¹³C NMR (CDCl₃, 150 MHz) δ 196.3 (SC(O)CH₃), 30.9 (SC(O)CH₃), 31.9 (C-1), 30.8 (C-2), 29.6 (C-4–C-7), 29.30, 29.29, 29.22, 29.0 (C-3), 22.8 (C-5), 14.3 (C-8); HRESIMS [M + Na]⁺ m/z 199.1133 (calcd for C₉H₂₀OS, 199.1138; Δ -2.0 ppm).

Preparation of dimethyloctylsulfide: Octanethiol (0.42 g, 2.88 mmol) was stirred under ambient conditions in 20 mL MeOH. 1.2 equivalents of MeI were added and the reaction was heated at reflux for 30 min. The reaction was cooled to room temperature, quenched with 20 mL H₂O, and the reaction mixture was extracted twice with 20 mL Et₂O. The organic phase was dried over MgSO₄, filtered and evaporated under reduced pressure affording the dimethylation product in a 90% yield.

Dimethyloctylsulfide: Colourless liquid, ¹H NMR (CDCl₃, 600 MHz) δ 3.72 (2H, t, J = 7.8 Hz, H-1), 3.33 (6H, s, S(CH₃)₂), 1.78 (2H, quin, J = 6.6 Hz, H-2), 1.44 (2H, quin, J = 6.6 Hz, H-3), 1.30 (2H, quin, J = 6.6 Hz, H-4), 1.20–1.28 (6H, m, H-5–H-7), 0.81 (3H, s, H-8); ¹³C NMR (CDCl₃, 150 MHz) δ 43.6 (C-1), 31.7 (C-2), 29.0 (C-3), 28.9 (C-4), 28.3 (C-5), 25.6 (S(CH₃)₂), 24.3 (C-6), 22.7 (C-7), 14.2 (C-8); HRESIMS [M + H]⁺ m/z 175.1523 (calcd for C₁₀H₂₃S, 175.1520; Δ 1.7 ppm)

Preparation of methyloctylsulfide: Octanethiol (0.5 mL, mmol) was stirred under ambient conditions in 20 mL MeOH. One equivalent of MeI was added, and the reaction was heated at reflux for 20 min. The reaction was cooled to room temperature, quenched with 20 mL H₂O, and the reaction mixture was extracted twice with 20 mL Et₂O. The organic phase was dried over MgSO₄, filtered and evaporated under reduced pressure affording the mono-methylation product in a 40% yield.

Methyloctylsulfide: Colourless liquid, IR (film) ν_{\max} 698 cm⁻¹; ¹H NMR (CDCl₃, 600 MHz) δ 2.48 (2H, t, $J = 7.2$ Hz, H-2), 2.09 (3H, s, H-1), 1.58 (2H, quin, $J = 7.2$ Hz, H-3), 1.37 (2H, quin, $J = 7.2$ Hz, H-4), 1.23–1.30 (8H, m, H-5–H-8), 0.88 (3H, t, $J = 7.2$ Hz, H-9); ¹³C NMR (CDCl₃, 150 MHz) δ 34.2 (C-2), 31.8 (C-8), 29.15 (C-5), 29.13 (C-7), 29.1 (C-3), 28.8 (C-4), 22.6 (C-6), 15.5 (C-1), 14.0 (C-9).

Preparation of methyloctylsulfoxide A: Methyloctylsulfide (0.5 mL, 2.6 mmol) was stirred in 30 mL MeOH, after which 1.5 equivalents (4.0 mmol) KIO₄ in 3 mL H₂O were added and the cloudy solution stirred at room temperature for 12 h. Methyloctylsulfoxide was produced in 100% yield. No purification was performed.

Preparation of methyloctylsulfoxide B: Methyloctylsulfide (0.5 mL, 2.6 mmol) was stirred in 30 mL MeOH, and treated with 1.5 equivalents (4.0 mmol) 30% H₂O₂ aqueous solution. The reaction was stirred for 12 h under ambient conditions affording the sulfoxide product in 100% yield. No purification was performed.

Methyloctylsulfoxide: White crystalline solid; IR (film) ν_{\max} 1027, 748 cm⁻¹; ¹H NMR (CDCl₃, 600 MHz) δ 2.73 (1H, ddd, $J = 14.9, 9.8, 5.8$ Hz, H-2a), 2.64 (1H, ddd, $J = 16.2, 9.3, 5.8$ Hz, H-2b), 2.56 (3H, s, H-1), 1.75 (2H, quin, $J = 7.0$ Hz, H-3), 1.44 (2H, sept, $J = 8.4$ Hz, H-4), 1.22–1.34 (8H, m, H-5–H-8), 0.88 (3H, t, $J = 7.1$ Hz, H-9); ¹³C NMR (CDCl₃, 150 MHz) δ 54.9 (C-2), 38.7 (C-1), 31.9 (C-8), 29.3 (C-5), 29.2 (C-7), 28.9 (C-4), 22.8 (C-6), 22.7 (C-3), 14.2 (C-9); HRESIMS [M + Na]⁺ m/z 199.1129 (calcd for C₉H₂₀OS, 199.1133; Δ -2.0 ppm).

Preparation of methyloctylsulfone: Methyloctylsulfide (0.5 mL, 2.6 mmol) was stirred in 25 mL CH₂Cl₂ with excess of 3:1 activated MnO₂:KMnO₄. The suspension was stirred for 96 h, filtered, and the residue washed with a 1:1 mixture of MeOH and CH₂Cl₂. The filtrate was evaporated affording a white crystalline solid in 100% yield. No further purification was deemed necessary.

Methyloctylsulfone: White crystalline solid; IR (film) ν_{\max} 1273, 1141, 1128, 1117, 765, 749 cm^{-1} ; ^1H NMR (CDCl_3 , 600 MHz) δ 3.00 (2H, t, $J = 8.4$ Hz, H-2), 2.89 (3H, s, H-1), 1.85 (2H, quin, $J = 7.8$ Hz, H-3), 1.44 (2H, quin, $J = 7.2$ Hz, H-4), 1.24–1.34 (8H, m, H-5–H-8), 0.88 (3H, t, $J = 7.2$ Hz, H-9); ^{13}C NMR (CDCl_3 , 150 MHz) δ 55.0 (C-2), 40.5 (C-1), 31.8 (C-8), 29.14 (C-5), 29.05 (C-6), 28.5 (C-4), 22.7 (C-7), 22.6 (C-3), 14.2 (C-9).

7.7 Isolation of new cyclic peroxides

7.7.1 Animal material

The sponge PTN3_19D was collected from the horizontal ceiling of a large cave at a depth of 12–15 m on ‘Eua Island and frozen immediately. Identified as a plakinid sponge species (order Homosclerophorida), the specimen forms thick, dense lobule encrustations 0.5–1.5 cm thick, appearing smooth but with a rough reticulated surface covered in wide shallow nodules ca. 3 mm high in some places. The texture is dense and cork-like, and the black-grey exterior contrasts against a tan-pink interior, which turns grey in alcohol. The abundant diods are 40–60 $\mu\text{m} \times 1$ –1.5 μm , triods were not observed. A voucher specimen is deposited in the School of Chemical and Physical Sciences, VUW, Wellington.

7.7.2 Initial extraction of PTN3_19D

A 26 g sample of PTN3_19D was extracted twice for 14 h in 100 mL MeOH at room temperature then filtered. The second extract, followed by the first were passed through a column of 40 mL HP20 resin, the eluents combined and diluted with 200 mL H_2O . The eluent was passed through the column again, further diluted to 25% MeOH with 400 mL H_2O and passed through the column once more. The column was washed with H_2O then eluted, generating three 100 mL fractions of 30%, 75% and 100% Me_2CO in H_2O . The 75% and 100% Me_2CO in H_2O fractions (88.4 mg and 155.3 mg respectively) were evaporated under reduced pressure and analysed by 1D and 2D NMR. Sub-samples of the 75% and 100% Me_2CO in H_2O fractions (ca. 40 mg) were further partitioned over 3 mL reversed-phase resin (HP20SS) resin with MeOH/ H_2O . The columns were washed with 20 mL H_2O then eluted generating 10 mL fractions of Me_2CO in H_2O (30–100% Me_2CO , in 10% increments). Further purification of the 70–100% Me_2CO in H_2O fractions by DIOL oil chromatography (hexane/ CH_2Cl_2 /MeOH) gave a mixture of cyclic peroxides and long-chain fats within the different CH_2Cl_2 fractions.

NMR spectra of the 50% CH₂Cl₂ in MeOH DIOL fraction indicated steroidal content and the fraction was purified further on DIOL (hexane/CH₂Cl₂). The 40% hexane in CH₂Cl₂ fraction was again partitioned over DIOL and purification of the 20% hexane in CH₂Cl₂ fraction by reversed-phase HPLC (C₁₈, 90% MeCN in H₂O) yielded 5 α ,8 α -epidioxy sterols **27** (652 μ g) and **28** (537 μ g) with retention times of 29 min and 39 min respectively.

The 25% hexane in CH₂Cl₂ DIOL fraction was found to contain epiplakinic acid I (**95**) in high spectroscopic purity. Analysis of the 2.5% MeOH in CH₂Cl₂ fraction revealed compound **98** in reasonable purity. Attempts were made to further purify both compounds, however, the lipophilic nature of the long-chains induced co-elution on reversed phase. Further partitioning over DIOL (hexane/CH₂Cl₂) at 0.5 drop sec⁻¹ collecting 2 mL fractions was not observed to increase spectroscopic purity.

The non-polar 60% hexane in CH₂Cl₂ fractions generated by the initial DIOL column were partitioned by HPLC (C₁₈, 95% MeCN in H₂O). Fractions collected in between chromophore peaks were rich in the cyclic peroxide metabolites. Size-exclusion chromatography (LH20, 1.5 m, MeOH) was utilised to remove the residual long-chain fat contamination from the HPLC dregs, 170 fractions were collected with the material of interest eluting in fractions 37–41. The combined LH20 fractions were partitioned over DIOL (hexane/CH₂Cl₂) with epiplakinic acid I methyl ester (**96**) eluting early in CH₂Cl₂ and plakortolide X (**97**) eluting in the 75% hexane in CH₂Cl₂ fractions.

7.7.3 Second extraction of PTN3_19D

Following accidental defrost, the remaining 75 g of PTN3_19D was extracted twice in MeOH and partitioned over HP20 as above. Analysis of the 100% and 75% Me₂CO in H₂O fractions (69.3 mg and 252.4 mg) by ¹H and HMBC NMR confirmed the presence of the cyclic peroxides epiplakinic acid I (**95**) and plakortolide X (**97**) although in lower concentration than observed in the initial screening evaluation. One step of normal-phase purification was performed on the 100% Me₂CO fraction (DIOL, hexane/CH₂Cl₂/10% MeOH).

The 75% Me₂CO in H₂O HP20 fraction was partitioned over HP20SS generating ten fractions of 30–100% Me₂CO in H₂O. The 85% and 90% Me₂CO in H₂O fractions were combined and partitioned again on HP20SS over a smaller window generating fractions of 75%, 80%, 82%, 84%, 86%, 88% and 90% Me₂CO in H₂O. The metabolites were all found to co-elute within the 75% and 80% Me₂CO in H₂O fractions, which were subsequently partitioned on normal-phase. Epiplakinic acid I (**95**, ca. 2 mg) eluted in 100% CH₂Cl₂.

5 α 8 α -epidioxysterol 27: Clear oil, 652 μ g; $[\alpha]_D^{24.6}$ -0.1° (*c* 0.044, CHCl₃); UV (MeOH) λ_{\max} (log ϵ), 222 (3.73), 275 (2.94) nm; IR (film) ν_{\max} 3391, 2957, 2929, 2871, 1734, 1460, 1381, 1278, 1126, 969, 766 cm⁻¹; ¹H and ¹³C NMR data, see Table C.5; HRESIMS *m/z* 465.3345 [M + Na]⁺ (calcd for C₂₁H₄₀O₅Na, 465.3379; Δ 0.9 ppm), *m/z* 477.3135 [M + Cl]⁻ (calcd for C₂₉H₄₆O₃Cl, 477.3145; Δ 2.1 ppm).

5 α 8 α -epidioxysterol 28: Clear oil, 537 μ g; $[\alpha]_D^{24.6}$ -0.4° (*c* 0.036, CHCl₃); UV (MeOH) λ_{\max} (log ϵ), 228 (2.84) nm; IR (film) ν_{\max} 3366, 2929, 2870, 2362, 1717, 1629, 1467, 1381, 1270, 1047, 936, 748 cm⁻¹; ¹H and ¹³C NMR data, see Table C.6; HRESIMS *m/z* 439.3188 [M + Na]⁺ (calcd for C₂₁H₄₀O₅Na, 439.3192; Δ 0.9 ppm), *m/z* 451.2979 [M + Cl]⁻ (calcd for C₂₇H₄₄O₃Cl, 451.2976; Δ -0.7 ppm).

Epiplakinic acid I (95): Clear oil, ca. 3.5 mg; $[\alpha]_D^{25.2}$ $+1.9^\circ$ (*c* 0.068, CHCl₃); UV (MeOH) λ_{\max} (log ϵ), 273 (2.70) nm; IR (film) ν_{\max} 3388, 2928, 2920, 2854, 1717, 1464, 1374, 1220, 1024 cm⁻¹; ¹H and ¹³C NMR data, see Table 4.10; HRESIMS *m/z* 365.2668 [M + Na]⁺ (calcd for C₂₀H₃₈O₄Na, 365.2664; Δ -1.1 ppm), *m/z* 341.2692 [M - H]⁻ (calcd for C₂₀H₃₇O₄, 365.2692; Δ -2.3 ppm).

Epiplakinic acid I methyl ester (96): Clear oil, ca. 500 μ g; UV (MeOH) λ_{\max} (log ϵ), 273 (2.70) nm; IR (film) ν_{\max} 3388, 2928, 2920, 2854, 1717, 1464, 1374, 1220, 1024 cm⁻¹; ¹H and ¹³C NMR data, see Table 4.11; HRESIMS *m/z* 371.2790 [M + Na]⁺ (calcd for C₂₁H₃₉O₅Na, 371.2797; Δ -1.9 ppm).

Plakortolide X (97): Clear oil, 1.21 mg; $[\alpha]_D^{24.6}$ 0.0° (*c* 0.08, CHCl₃); UV (MeOH) λ_{\max} (log ϵ), 275 (2.80), 282 (2.57) nm; IR (film) ν_{\max} 2928, 2921, 2854, 1782, 1717, 1463, 1381, 1270, 1167, 1073 cm⁻¹; ¹H and ¹³C NMR data, see Table 4.13; HRESIMS *m/z* 349.2355 [M + H]⁺ (calcd for C₁₉H₃₄O₄Na, 349.2355; Δ -0.6 ppm), *m/z* 325.2379 [M - H]⁻ (calcd for C₂₀H₃₇O₄, 325.2374; Δ -1.5 ppm).

Compound 98: Clear oil, 856 μ g; $[\alpha]_D^{24.6}$ $+4.1^\circ$ (*c* 0.03, CHCl₃); UV (MeOH) λ_{\max} (log ϵ), 280 (3.05) nm; IR (film) ν_{\max} 3374, 2928, 2920, 2854, 1717, 1464, 1374, 1220, 1143 1024 cm⁻¹; ¹H and ¹³C NMR data, see Table 4.15; HRESIMS *m/z* 395.2771 [M + Na]⁺ (calcd for C₂₁H₄₀O₅Na, 395.2773; Δ -0.8 ppm), *m/z* 371.2790 [M - H]⁻ (calcd for C₂₁H₃₉O₅, 371.2797; Δ -1.9 ppm).

7.8 Biological evaluation of cyclic peroxides

7.8.1 Yeast strains

All strains were derived from a 15% glycerol stock stored at -80°C . The deletion strains (Table 7.1) were streaked out onto 10 cm diameter agar plates containing synthetic complete (SC) medium or synthetic deficient in uracil medium (SD-ura), supplemented with the appropriate antibiotics to ensure selective growth; $200\ \mu\text{g mL}^{-1}$ Geneticin antibiotic (G418, Gibco, Invitrogen) and/or $100\ \mu\text{g mL}^{-1}$ mourseothricin antibiotic (Nat, Werner BioAgents). The diploid BY4743 strain was streaked onto yeast extract peptone dextrose (YPD) agar and the diploid deletion strains were grown on YPD agar supplemented with G418 antibiotic ($200\ \mu\text{g mL}^{-1}$). The GFP-localised strains were streaked out onto 10 cm diameter agar plates containing SD-histidine medium. The freshly plated strains were incubated at 30°C for 48 h to allow the formation of single colonies then stored at 4°C .

Growth media

Y7092 (wt) was cultured in SC medium; homozygous deletion strains were cultured in 5 mL SC + with $200\ \mu\text{g mL}^{-1}$ G418 antibiotic; Δpdr was cultured in 5 mL SD-ura + Nat $100\ \mu\text{g mL}^{-1}$; haploid strains with GFP-localisation markers were cultured immediately prior to use by serial-dilution in SD-his; and BY4743 was cultured in 5 mL SC. YPD was used during assessment of **29** as a growth inhibitor and during transformation procedures (refer Appendix B for growth media recipes).

7.8.2 Preliminary assay protocols

Liquid-phase dose-reponse assays

Three 5 mL aliquots of SC, SD-ura or YPD growth media were inoculated with different single colonies of a given yeast strain and cultures were grown to saturation overnight in a rotating drum at 30°C .²⁵¹ The saturated cultures were diluted to 5×10^5 cells mL^{-1} in fresh media (SC, SD-ura or YPD), as determined by haemocytometer, and $99\ \mu\text{L}$ aliquots were added to 96-well tissue culture plates in a triplicate format. Seven point, half-log serial dilutions of compounds **29**, **95** and **97** (10.00 – $0.10\ \text{mmol L}^{-1}$) were prepared from $10.00\ \text{mmol L}^{-1}$ working stocks dissolved in DMSO. A $1\ \mu\text{L}$ volume of diluent was added per well, giving a final concentration range of 100.00 – $0.01\ \mu\text{mol L}^{-1}$. DMSO (1% final concentration) was added to one well as a control.

Table 7.1 Yeast Strains Used During this Study.

Strain	Ploidy	Genotype	Origin
yCG 117	haploid	<i>MATα can1Δ1::STE2pr-Sp_ Sp_ HIS5; lyp1Δ; ura3Δ0::NAT; leu2Δ0; his3Δ; met1Δ50; LYS2+</i>	Starting lab strain
8025- α	haploid	<i>MATα can1Δ::STE2pr-Sp_ his5 lyp1 Δ::STE3pr-LEU2 his3Δ1 leu2Δ0 ura3Δ0 LYS2+</i>	yCG 112
Δ <i>pdr</i>	haploid	<i>MATα pdr1Δ::NAT pdr3Δ::URA3 can1Δ::STE2pr-Sp_ HIS5; lyp1Δ::STE3pr- Sp-LEU2; his3Δ1 leu2Δ0 ura3Δ0</i>	yCG 198
BY4743 (wt)	diploid	<i>MATα/MATα his3Δ1/his3Δ leu2Δ0/leu2Δ0 lys2Δ0/+met15Δ0 /+ura3Δ0/ura3Δ0</i>	Starting lab strain
<i>sla1Δ/sla1Δ, rsa1Δ/rsa1Δ, crz1Δ/crz1Δ, hcm1Δ/hcm1Δ, sfp1Δ/sfp1Δ, pmc1Δ/pmc1Δ, ygk167wΔ/ygk167wΔ, rvs167Δ/rvs167Δ, pmr1Δ/pmr1Δ, cch1Δ/cch1Δ, mid1Δ/mid1Δ cna1Δ/cna1Δ, cna2Δ/cna2Δ, cnb1Δ/cnb1Δ</i>	diploid	Homozygous deletion strains with G418 resistance	Homozygous deletion set (Open Biosystems)
Crz1p-GFP	diploid	<i>MATα-Crz1p-GFP-HIS5 his3Δ1 leu2Δ0 met15Δ0 ura3Δ0</i>	MAT α -GFP Library (Invitrogen)
Zrt1p-GFP	diploid	<i>MATα-Zrt1p-GFP-HIS5 his3Δ1 leu2Δ0 met15Δ0 ura3Δ0</i>	MAT α -GFP Library (Invitrogen)
Zap1p-GFP	diploid	<i>MATα-Zap1p-GFP-HIS5 his3Δ1 leu2Δ0 met15Δ0 ura3Δ0</i>	MAT α -GFP Library (Invitrogen)
Yap1p-GFP mCherry	haploid	<i>MATα-Yap1p-GFP- HIS5 can1Δ::STE2pr- URA3 lyp1Δ::mCherry</i>	yCG 379
Mrh1p-GFP + mCherry/NLS-RS2	haploid	<i>MATα-Mrh1p-GFP- HIS5 can1Δ::STE2pr- URA3 lyp1Δ::mCherry/ NLS-RS2</i>	yCG 321

Plates were mixed by vortexing for 1 min at 950 rpm and incubated at 30 °C for a maximum of 18 h. After incubation, cells were resuspended by vortexing, and their growth was quantified by measuring optical density (OD) at 590 nm. Residual growth (%) was calculated for each concentration using the formula $((OD_{\text{exp}} - OD_{\text{blank}}) / (OD_{\text{DMSO}} - OD_{\text{blank}})) * 100$. Results are reported as the mean \pm standard error for two independent experiments performed in triplicate. The IC₅₀ values were determined using SigmaPlot and the MIC values were inferred from the plots.

Cytotoxicity assays

Colony forming assay: Stationary-phase cultures of WT cells and Δpdr were diluted to 5×10^5 cells mL^{-1} in fresh SC or SD–ura, then treated with either **95** (wt) or **97** (Δpdr) at final concentrations of 10 and 100 $\mu\text{mol L}^{-1}$. Rapamycin (2.00 nmol L^{-1}) and cycloheximide ($3.35 \mu\text{mol L}^{-1}$) served as positive controls for cytotoxic and cytostatic activity respectively, with DMSO acting as the negative control. The drug-treated cells were vortexed then incubated at 30 °C for 18 h. The cells were washed with fresh media and inoculated onto solid agar plates of SC or SD–ura medium then incubated for 48 h at 30 °C. The plates were inspected visually for colony growth and compared to the controls. Colony growth indicated cytostatic inhibition by the experimental compound and the absence of growth was indicative of cytotoxicity or irreversible inhibition.

Kill curve: The effective rate of cytotoxicity was measured by removing 1 μL aliquots from each dilution point within a dose-response assay and spotting them onto a 10×15 cm rectangular YPD plate hourly from 0 to 6 h and once more after 24 h. As there was a set volume rather than a set cell count spotted, the DMSO control is expected to show increased growth with time relative to the drug-treated cultures. The plate was incubated for 24 h and inspected visually for colony growth. The assay was performed for **95** and **97** with WT and Δpdr cultures respectively.

Inhibition in the presence and absence of Ca^{2+} : To determine the effect of Ca^{2+} concentration upon the cytotoxicity of **95** and **97**, inhibition assays in high and low environments of Ca^{2+} (50 mmol L^{-1} CaCl_2 and 100 mmol L^{-1} EGTA). Dose-response assays were performed in triplicate over a narrow concentration range ($30\text{--}1 \mu\text{mol L}^{-1}$ final concentration) against the WT and Δpdr strains in the presence of **95** and **97**. Three growth conditions were tested: inhibitory agent; agent + 50 mmol L^{-1} CaCl_2 ; and agent + 100 mmol L^{-1} EGTA. As with the kill curve assay, 1 μL aliquots from each dilution point within the assays were removed and spotted onto a 10×15 cm rectangular YPD plate hourly at $t = 0\text{--}6$ and 24 h. The plate was incubated for 24 h and inspected visually for colony growth. The assay was performed for **95** and **97** with WT and Δpdr cultures respectively. Residual growth of the dose-response assays was calculated after 17 h incubation and the IC_{50} values calculated for the different conditions (Figures H.2 and H.3). Dose-response assays were performed against the WT and Δpdr strains with **95** and **97** in high and low Ca^{2+} environments.

Cell cycle inhibition studies

Analysis by bud index: Fresh overnight cultures of haploid WT and Δpdr cells were diluted to 5×10^5 cells mL^{-1} in fresh SC or SD-ura, then treated with either **95** (wt) or **97** (Δpdr) at their MIC ($10 \mu\text{mol L}^{-1}$ final concentration). DMSO served as a negative control. At 2, 4 and 6 h time-points, $10 \mu\text{L}$ aliquots were removed, diluted 1:100 in H_2O and $10 \mu\text{L}$ samples of the populations were assessed by haemocytometer. Cell counts were made at each time-point, and the individual cells were scored according to bud size corresponding to their stage in the cell cycle. Cells were visually assessed and imaged at $t = 2$ and 4 h and the assays were repeated periodically to assess potential degradation of the inhibitory agents **95** and **97**.

Cell cycle analysis by flow cytometry: Three fresh overnight cultures of haploid WT cells were diluted to 5×10^6 cells mL^{-1} in fresh SC and cultured for a further 4 h to mid-log growth phase. Aliquots were taken and diluted to give 1 mL cultures 1×10^7 cells mL^{-1} . Cells were treated with DMSO and **95** at 10, 7 and $3.4 \mu\text{mol L}^{-1}$ and incubated at 30°C for 4 h. Cells were pelleted and washed with 5 mL Tris HCl buffer (50 mmol L^{-1}) and resuspended in 1.5 mL H_2O . To each 1.5 mL sample, 3.5 mL absolute EtOH was added as a fixative (70% EtOH final concentration) and the cells were incubated at 4°C overnight. Cells were pelleted, EtOH removed and the cells were washed twice with 2 mL Tris HCl buffer (50 mmol L^{-1}), resuspending each time by sonication. Cells were treated with 1.25 mL RNase solution (diluted 10-fold in 50 mmol L^{-1} Tris HCl buffer) and incubated for 2 h at 37°C with shaking. The cells were again pelleted, the RNase solution was removed, and then treated with 2 mL of fresh pepsin solution for 5 min at room temperature. $100 \mu\text{L}$ aliquots were then added to 2 mL solutions of SytoxGreen ($1 \mu\text{mol L}^{-1}$ in Tris HCl buffer), placed on ice and imaged immediately. A FACScan flow cytometer was used to visualise cells and CellQuest Pro software (BD Biosciences) was used to generate contour plots for each sample. Flow cytometry cell population data was manipulated with FlowJo version 7.6.1 flow cytometry analysis software. Populations were manually gated according to the untreated control and recorded as percentage of total population within the sample.²⁵²

RNase stock solution, 10x:

RNase	100 mg
NaOAc (3 mol L^{-1})	$333 \mu\text{L}$
H_2O	9.7 mL

Pepsin solution:

Pepsin	50 mg
HCl (1 mol L^{-1})	$550 \mu\text{L}$
H_2O	9.45 mL

Analysis of reactive oxygen species formation by flow cytometry Overnight liquid cultures of haploid WT and Δpdr cells were diluted to 1×10^7 cells mL^{-1} in fresh SC medium. In duplicate, 100 μL aliquots of WT and Δpdr culture were treated with experimental and control agents for 1 h in microcentrifuge tubes. Wild-type and Δpdr cells were treated by **95** and **97** respectively and positive controls of both strains were treated with 1 μL aliquots of 1 mmol L^{-1} H_2O_2 and DMSO then incubated for 30 min at 30°C . DCF-DA was added ($50 \mu\text{mol L}^{-1}$ final concentration) and the cells were incubated for a further 15 min. The cultures were placed on ice, diluted with 400 μL H_2O , and co-stained with 6 mg mL^{-1} propidium iodide prior to visualisation. Cells were visualised on the FACScan flow cytometer and CellQuest Pro software (BD Biosciences) was used to generate contour plots for each sample. Cell population data obtained from the flow cytometer was modelled on FlowJo version 7.6.1 flow cytometry analysis software. Populations were manually gated according to the untreated control and recorded as percentage of total population within the sample.

7.8.3 Chemical genetic profiling of epiplakinic acid I

Homozygous profiling by microarray

A 0.5 mL aliquot of the homozygous deletion set pool was inoculated into 10 mL SC and supplemented with 10 μL G418 (200 mg mL^{-1} in a 50 mL falcon tube). The culture was incubated overnight at 30°C in a rotating drum. Five parallel 10 mL cultures SC were seeded with 5×10^6 cells from the fresh culture of the YKO pool. Four of the cultures were treated with **95** to final concentrations of 4, 3, 2 and 1 $\mu\text{mol L}^{-1}$ and a 100 μL aliquot of DMSO served as control in the fifth culture. The cultures were incubated for 10 generations ca. 15 h at 30°C in a rotating drum. It was determined that 3 $\mu\text{mol L}^{-1}$ of **95** inhibited cellular growth by 30% (IC_{30}) relative to the DMSO control. The cultures treated with DMSO and 3 $\mu\text{mol L}^{-1}$ **95** were then diluted to 5×10^6 cells in 10 mL fresh SC, treated again DMSO or **95** and cultured for a further 10 generations.

Cell populations were determined by haemocytometer and duplicate 1.5 mL aliquots of both control and **95**-treated cultures were pelleted for 2 min at 10,000 rpm in microcentrifuge tubes and the supernatant discarded. Genomic DNA was then extracted from the cell pellets in accordance with the Master PureTM Yeast DNA Purification Kit. The cell pellets were resuspended in 300 μL of yeast cell lysis solution by vortexing then incubated at 65°C for 15 min then placed on ice for 5 min. A 150 μL aliquot of MPC protein precipitation reagent was added to each lysed sample, mixed by vortex for ca. 10 s and the cellular debris pelleted by centrifugation

at 10,000 rpm for 10 min.

The supernatant was transferred into a clean microcentrifuge tube and the genomic DNA was precipitated out by the addition of 500 μL IPA. This was mixed by inverting the tube and the DNA pelleted by centrifugation at 10,000 rpm for 10 min. The DNA was washed twice with 70% EtOH solution then dried briefly at room temperature. The DNA was dissolved in 35 μL Tris EDTA buffer and incubated at 65 °C for 10 min. A 1 μL aliquot of RNase ($5 \mu\text{g mL}^{-1}$) was added to each microcentrifuge tube and the samples were incubated at 37 °C with shaking for 30 min.

The duplicate samples were combined and H₂O was added to a final volume of 0.5 mL. The DNA was extracted with 500 μL of phenol/CHCl₃/isoamyl alcohol mix (25:24:1). The phases were emulsified by vortex and separated by centrifugation for 10 min at 16,000 rpm. The organic layer was removed and the aqueous phase washed with 500 μL of CHCl₃. 1 mL EtOH and 40 μL NaOAc were added to the aqueous layer and shaken gently. The DNA was precipitated during incubation for 25 min at 4 °C, and the pellets recovered following centrifugation (10 min, 13,000 rpm). The DNA pellets were washed twice with 70% EtOH then dissolved in 35 μL Tris EDTA (10 min, 60 °C) and maintained at 4 °C until further use.

The DNA was quantified using a Hoechst 33258 dye and calf thymus as the DNA standard. Four separate PCR reactions were conducted with 100 ng of starting DNA template. These consisted of the Up and Dn tags for both the control and experimental DNA samples. The Up tags were labeled with Cy3-dye markers and Dn tags with Cy5. The experimental conditions and primer sequences are shown below.

Primer sequences:

D1	5'-CGGTGTCGGTCTCGTAG-3'
U1	5'-GATGTCCACGAGGTCTCT-3'
D2comp-Cy3 or -Cy5	5'-Cy [3/5]-CGAGCTCGAATTCATCGAT-3'
U2comp-Cy3 or -Cy5	5'-Cy [3/5]-GTCGACCTGCAGCGTACG-3'

PCR primer combinations:

Control DNA (no compound)	Up tag PCR	Primers U1 and U2comp-Cy3
	Dn tag PCR	Primers D1 and D2comp-Cy3
Experimental (compound)	Up tag PCR	Primers U1 and U2comp-Cy5
	Dn tag PCR	Primers D1 and D2comp-Cy5

Each PCR reaction was performed in 60 μL final volume, containing 1.5 mmol L⁻¹ MgCl₂, 0.2 mmol L⁻¹ dNTPs, and 1 $\mu\text{mol L}^{-1}$ primers. PCR Master Mix was made up as follows. Four negative controls were also prepared with 4.0 μL H₂O in place

of DNA.

Table 7.2 PCR Master Mix

Component	Volume (μL)	
	1 \times	9 \times (1 array)
10 \times Platinum taq buffer	6.0	54.0
50 mmol L ⁻¹ MgCl ₂	1.8	6.2
5 mmol L ⁻¹ (each) dNTPs	2.4	21.6
Platinum taq (5 units μL^{-1})	0.2	1.8
H ₂ O	40.8	367.2
Total volume	51.2	460.8

PCR reaction components, 8 \times 0.2 mL tubes:

Labelled primer (25 $\mu\text{mol L}^{-1}$)	2.4 μL
Unlabelled primer (25 $\mu\text{mol L}^{-1}$)	2.4 μL
Master mix	51.2 μL
DNA (25 ng μL^{-1}) or H ₂ O	4.0 μL

PCR conditions:

94 $^{\circ}\text{C}$	3 m
94 $^{\circ}\text{C}$	30 s
50 $^{\circ}\text{C}$	30 s 38 cycles
72 $^{\circ}\text{C}$	30 s
72 $^{\circ}\text{C}$	5 m
10 $^{\circ}\text{C}$	hold

A 5 μL aliquot of each PCR condition was combined with 1 μL loading dye and run on a high resolution 4% MetaPhor Agarose gel with 1.5 μL 10-bp ladder (Invitrogen) checking for both contamination and amplification of the 56-bp Up and Dn tags.

A 20 μL aliquot of blocking primer mix (12.5 μL , 100 $\mu\text{mol L}^{-1}$ U1 primer; 12.5 μL , 100 $\mu\text{mol L}^{-1}$ D1 primer; 12.5 μL , 100 $\mu\text{mol L}^{-1}$ U2 block; 12.5 μL , 100 $\mu\text{mol L}^{-1}$ D2 block; 50 μL H₂O) was combined with 55 μL each PCR product. The complimentary oligonucleotide sequences bind with the priming regions of the PCR products preventing them from binding with each other and allowing them to hybridise to the microarray. The barcode tags were precipitated by adding 24 μL NaOAc (3 mol L⁻¹, pH 5.2), 600 μL EtOH and 1 μL 5 mg mL⁻¹ linear acrylamide to initiate precipitation. Solutions were mixed by vortex and the PCR products precipitated at -20 $^{\circ}\text{C}$ over 2 h.

Blocking primer sequences:

D2block	5'-ATCGATGAATTCGAGCTCG
U2block	5'-CGTACGCTGCAGGTCGAC

The PCR products were recovered by centrifugation at 13,000 rpm at 4 °C for 30 m and at washed at 4 °C with 70% EtOH. The EtOH was removed and the PCR products and washed were dried briefly in the dark, at room temperature, then redissolved 50 μL H_2O and maintained at $-20\text{ }^\circ\text{C}$ until hybridisation.

DNA hybridisation to microarray slide: The 50 μL PCR products were combined with 50 μL filter-sterilised 2x hybridisation buffer (2 mol L^{-1} NaCl, 20 mmol L^{-1} Tris HCl pH 7.5, 1% Triton X-100. DTT (1 mmol L^{-1} final concentration) was added to the hybridisation buffer immediately prior to use. The buffer and PCR products were pipetted gently to mix, avoiding bubbles, and the hybridisation mix was denatured at 95 °C for 2 min.

A 100 μL aliquot of hybridisation mix was applied to the gasket slide avoiding bubble formation. The microarray slide was placed active side down, on to gasket slide, the chamber was assembled and rotated gently to ensure wetting of the entire slide and continuous movement of the hybridisation mix. The slide was then rotated at a moderate speed for 4 h at 42 °C in a hybridisation oven. After baking, the gasket slide was removed, rinsed 5 times (210 mL H_2O , 90 mL SSPE and 0.15 mL Triton X), centrifuged to remove residual H_2O and dried in the dark with SiO_2 dessicant. The microarray slide was sent to Les McNoe at Otago Genomics Facility, Department of Biochemistry, University of Otago.

Microarray data analysis: GenePix 6.0 (Molecular Devices, Sunnyvale, CA, USA) was used to align the microarray image and extract data from the image file. The GenePix results file (.gpr file) was opened in a spreadsheet program and the control spots, spots flagged as poor quality, and those corresponding to essential gene deletions were removed. The Up and Dn tags were separated into separate worksheets and saved as .txt files. Each .txt file was uploaded into the web-based SNOMAD software (standardisation and normalisation of microarray data) and normalised according to the **median F635 (Cy5)** and **median F532 (Cy3)** data columns (as the data types “ONEintensities” and “TWOintensities”, respectively). Transformation parameters are as follows; **Perform** and **Graph** the transformation in **Steps 3**, Log transformation (Log base 2), **4**, calculation of mean log (intensities) and log (ratios), and **5**, local mean normalization across element signal intensity, (Span 0.3, Trim 0.1).²⁵³ The data was submitted for processing and the results were copied into a fresh worksheet. Data spots with low (<500) **median F532** scores were removed to reduce the level of noise in the data, and replicates were removed using a “replicate removal” script.²⁵⁴ The normalised log ratios for tag replicates were averaged, and z -scores (x -mean/standard deviation) were calculated. The data was sorted by z -scores, with z -scores < -3.0 denoted as a probable significant hit.

Database searches: Gene hits were categorised according to their molecular and biological functions and their cellular components using the web-based program FunSpec²²⁵. The *Saccharomyces* Genome Database²²⁶ was used to define the molecular and biological functions of gene hits and to analyse the synthetic lethal interactions of each genetic hit.

Haploinsufficiency profiling by microarray

The essential and nonessential gene cassettes of *S. cerevisiae* were assessed simultaneously for haploinsufficiency in the presence of **95**. All practical proceedings were the same as for the HOP, however 2 $\mu\text{mol L}^{-1}$ **95** was found to elicit a 30% growth reduction of the heterozygous deletion pool relative to the DMSO control. Data analysis differed in that values corresponding to essential genes were included during processing.

Microarray validation by dose-response: The sensitivity of homozygous deletion strains *sla1 Δ /sla1 Δ* , *rsa1 Δ /rsa1 Δ* , *crz1 Δ /crz1 Δ* , *hcm1 Δ /hcm1 Δ* , *sfp1 Δ /sfp1 Δ* , *rvs167 Δ /rvs167 Δ* , *mid1 Δ /mid1 Δ* , *cna1 Δ /cna1 Δ* , *cna2 Δ /cna2 Δ* and *cnb1 Δ /cnb1 Δ* to epiplakinic acid I (**95**) was assessed by dose-response relative to the diploid wild-type starting strain BY4743. The same general protocol as above was followed during these validation assays with half-log dilutions from 100–0.1 $\mu\text{mol L}^{-1}$ final concentration. The ion-pump deletion mutants *pmc1 Δ /pmc1 Δ* , *pmr1 Δ /pmr1 Δ* and *cch1 Δ /cch1 Δ* were also assessed relative to the diploid WT strain with an eight-point dilution across two orders of magnitude; 30, 20, 10, 3, 2, 1 and 0.03 $\mu\text{mol L}^{-1}$ final concentration.

Microarray validation by single-concentration growth inhibition: Slow growing strains (*sla1 Δ /sla1 Δ* , *rsa1 Δ /rsa1 Δ* , *sfp1 Δ /sfp1 Δ* and *rvs167 Δ /rvs167 Δ*) were assessed for inhibition relative to the WT at the IC₃₀ value used for the microarray experiment, and at the WT IC₅₀. Overnight cultures were prepared in triplicate from different single colonies and incubated for 18 h at 30 °C in a rotating drum. The strains were diluted to 5×10⁴ cells mL⁻¹ in 2 mL fresh SC supplemented with G418 antibiotic (200 $\mu\text{g mL}^{-1}$). Nine 99 μL aliquots of each culture were added to a 96-well tissue culture plate and treated in triplicate at 3.5 and 3.0 $\mu\text{mol L}^{-1}$. DMSO, 1 μL , served as control. Optical density measurements were taken hourly ($t = 0$ –8 h) and again at 20 h to quantify growth relative to the BY4743 WT strain.

7.8.4 Imaging studies

Prior to all imaging studies, GFP-labelled strains were cultured overnight on solid agar plates (SD-his). Cells were transferred into 384-well clear bottomed microtitre plates (Perkin Elmer Cell Carrier) by pipette and four 50 μL liquid cultures (SC) were made by serial dilution. Cultures were inoculated with control and experimental agents and incubated for a given period at 30 °C imaging with the OPERA microscope at specified time points.

Assessment of the nuclear-cytoplasmic ratio: The plasma-membrane protein GFP strain Mrh1p-GFP with nuclear membrane marker NLS-RS2/mCherry was cultured overnight on solid nutrient medium (SC-his). Cells of the GFP/mCherry strain were transferred into a 384-well clear bottomed microtitre plate (Perkin Elmer Cell Carrier) by pipette and a four-point serial dilution of 50 μL liquid cultures (SC) was made in duplicate. Cultures were inoculated with 1% DMSO control and **95** at the MIC concentration then incubated for 4 h, imaging at 2 and 4h.

Translocalisation of Crz1p-GFP in response to Ca^{2+} : Freshly cultured Crz1p-GFP cells were transferred from solid medium into a 384-well clear-bottomed microtitre plate as above. Parallel serial dilutions (50 μL liquid SC) were prepared over four points and cultured for 2 h prior to exposure to 1% DMSO, 50 mmol L^{-1} CaCl_2 and 10 $\mu\text{mol L}^{-1}$ **95**. Cells were imaged at 5 min intervals from $t = 0$ –40 min.

Specificity of Crz1p-GFP translocation to Ca^{2+} : Freshly cultured Crz1p-GFP cells were transferred from solid medium into a 384-well clear-bottomed microtitre plate as above. Parallel serial dilutions (50 μL liquid SC) were prepared over four points and cultured for 2 h prior to exposure to 1% DMSO, 50 mmol L^{-1} of the following metal salts: CaCl_2 , MgCl_2 , ZnSO_4 , CuSO_4 and KCl , and 10 $\mu\text{mol L}^{-1}$ **95**. Cells were imaged at 5 min intervals from $t = 0$ –40 min.

ROS induction with H_2O_2 in the Yap1p-GFP/mCherry strain: Freshly cultured Yap1p-GFP/mCherry cells were transferred into a 384-well clear-bottomed microtitre plate as above. Four, parallel serial dilutions (50 μL liquid SC) were prepared over four points and cultured for 2 h prior to exposure to 1% DMSO, 50 mmol L^{-1} CaCl_2 , 10 $\mu\text{mol L}^{-1}$ **95**, and 1 mmol L^{-1} H_2O_2 . Cells were imaged at 5 min intervals from $t = 0$ –40 min.

Effect of epiplakinic acid I upon membrane-bound ion pumps: Cultures of the Zrt1-GFP, Zap1-GFP and Crz1-GFP strains were prepared as stated above and transferred into 4-point serial dilutions of liquid SC in a clear-bottomed 384-well microtitre plate. The three GFP strains were simultaneously exposed to 1% DMSO control, 50 mmol L⁻¹ CaCl₂, MgCl₂ and ZnSO₄ and 10 μmol L⁻¹ **95**. Response to these species was assessed at 5 min intervals from t = 0–40 min.

Quantification of intracellular Ca²⁺ levels: Calcium Orange (Molecular Probes, Invitrogen) was used to quantify changes in the level of intra-cellular Ca²⁺ upon exposure to **95** relative to the DMSO control. Three 5 mL SC cultures of the diploid WT BY4743 strain were incubated at 30 °C in a rotating drum for 18 h then diluted to 5×10⁵ cells mL⁻¹ in fresh SC. Cultures were treated with **95** at the MIC (10 μmol L⁻¹), and DMSO served as positive control. As per the methods of use protocol, following 4 h exposure to **95** and DMSO control, cells were resuspended by vortexing and three 300 μL aliquots of each experimental condition were individually transferred into fresh microcentrifuge tubes, and incubated 30 min in the presence of Calcium Orange (5 μmol L⁻¹). Emission intensity was measured in two ways: Cells were washed twice with H₂O to remove free ligand and resuspended in 100 μL and the emission intensity of the probe measured (excitation 549 nm, emission 576 nm). Emission intensity of the cell/dye suspension was also measured to determine the effects of cell loss during the washing process.

7.8.5 Transformation of 8025-α strain

Plasmid purification: Cultures of bacteria expressing the pRS-316 plasmid were grown overnight in 2 mL LB supplemented with 2 μL ampicillin. The cells were harvested and subjected to RNA digest and the extracted plasmids were purified with the Invitrogen Plasmid Preparation kit. Purity of the extracted plasmid was determined by gel electrophoresis (1% agarose). The plasmid was stored at -20 °C prior to use in transformation.

Preparation of yeast cell cultures for transformation: Cells from a fresh overnight culture of the yeast strain 8025-α were diluted to 2.5×10⁸ in 150 mL pre-warmed YPD and incubated with shaking at 30 °C for 4 h in 250 mL conical flasks to achieve mid-log growth of the culture. After 4 h growth the OD₅₉₀ was measured and duplicate 25 mL aliquots of the culture (1.75×10⁸ cells) were washed twice with 25 mL H₂O. The cells were harvested by centrifuge and resuspended in 1 mL H₂O, transferred into microcentrifuge tubes, washed again with H₂O and 570 μL aliquots of cell concentrate (10⁸ cells) were further diluted in H₂O to a total volume of 1 mL

then harvested by centrifuge. To each microcentrifuge tube 360 μL transformation mix (including plasmid DNA) was added and the yeast cells resuspended by vortex.

Transformation mix:

PEG 3350	50% w/w	240 μL
LiOAc	1 mol L^{-1}	36 μL
single-stranded carrier DNA	2.0 mg mL^{-1}	50 μL
Plasmid DNA in H_2O		34 μL

Heat-shock was applied by placing the microcentrifuge tubes in a 42 °C water-bath for 40 min, after which the tubes were centrifuged at 10,000 rpm for 30 s and the supernatant was removed by pipette. The cell pellet was resuspended in 1 mL YPD and incubated for 3 h at 30 °C with shaking. A 150 μL aliquot of transformed cell culture were plated onto YPD agar, and the remainder harvested and resuspended in 150 μL YPD and plated similarly. Plates were incubated for 36 h at 30 °C and four transformants were randomly selected then streaked again on YPD then incubated for 24 h at 30 °C.

7.8.6 Attempted transformation of *zrt1* Δ /*zrt1* Δ and *cch1* Δ /*cch1* Δ strains

Plasmid purification: As above, bacteria expressing the pMT 2932 and 2916 plasmids encoding the URA3 MX cassette were cultured overnight in 2 mL LB supplemented with 2 μL ampicillin. The cells were harvested and the plasmids extracted and purified as per the Invitrogen Plasmid preparation kit. Restriction digests were performed on both plasmids.

Restriction digest as performed in microcentrifuge tubes:

Plasmid DNA in H_2O	50 μL
10x Buffer 2	5 μL
<i>Eco</i> R1 enzyme	1 μL
<i>Bam</i> H1 enzyme	1 μL
Bovine serum albumin	0.5 μL

Appendix A

Sponge Screening and Cyclic Loading Protocol

A.1 Cyclic loading and backloading

Cyclic loading is a technique developed by Northcote and West²⁵⁵ and was frequently employed during this research. The technique was used to fractionate crude extracts of organisms during the screening process, separating the undesirable non-polar fats and highly polar salts and carbohydrates from the intermediate polarity compounds of interest, i.e. secondary metabolites. This laboratory employs PSDVB (poly(styrene-divinylbenzene)) cross-linked polymeric resin beads as the stationary phase. PSDVB is a macro-porous, rigid resin which is chemically inert and stable across a large pH range, and can be reused a number of times without decreased performance. The beads are devoid of polar functional groups so irreversible binding or degradation of polar substrates has not been observed.

As depicted in Figure A.1 the crude (MeOH) extract is passed through a PSDVB column, allowing adhesion of non-polar metabolites within the extract to the column. The eluent is diluted 1:1 with H₂O and re-cycled through the column iteratively, diluted 1:1 with H₂O at each stage. Increased eluent polarity facilitates adsorption of increasing polar metabolites to the stationary phase, in effect the opposite of conventional chromatography. After adhesion of the desired material to the column, it is eluted with mixtures of H₂O and an organic modifier of decreasing polarity, commonly 30%, 75% and 100% Me₂CO in H₂O.

The 30% and 75% Me₂CO in H₂O fractions are then backloaded onto the screening column using the same cyclic technique, the column is air dried and then eluted with organic solvent. This generates fractions devoid of H₂O which can be easily evaporated under reduced pressure.

This laboratory uses water-miscible solvents such as MeOH and Me₂CO, which are

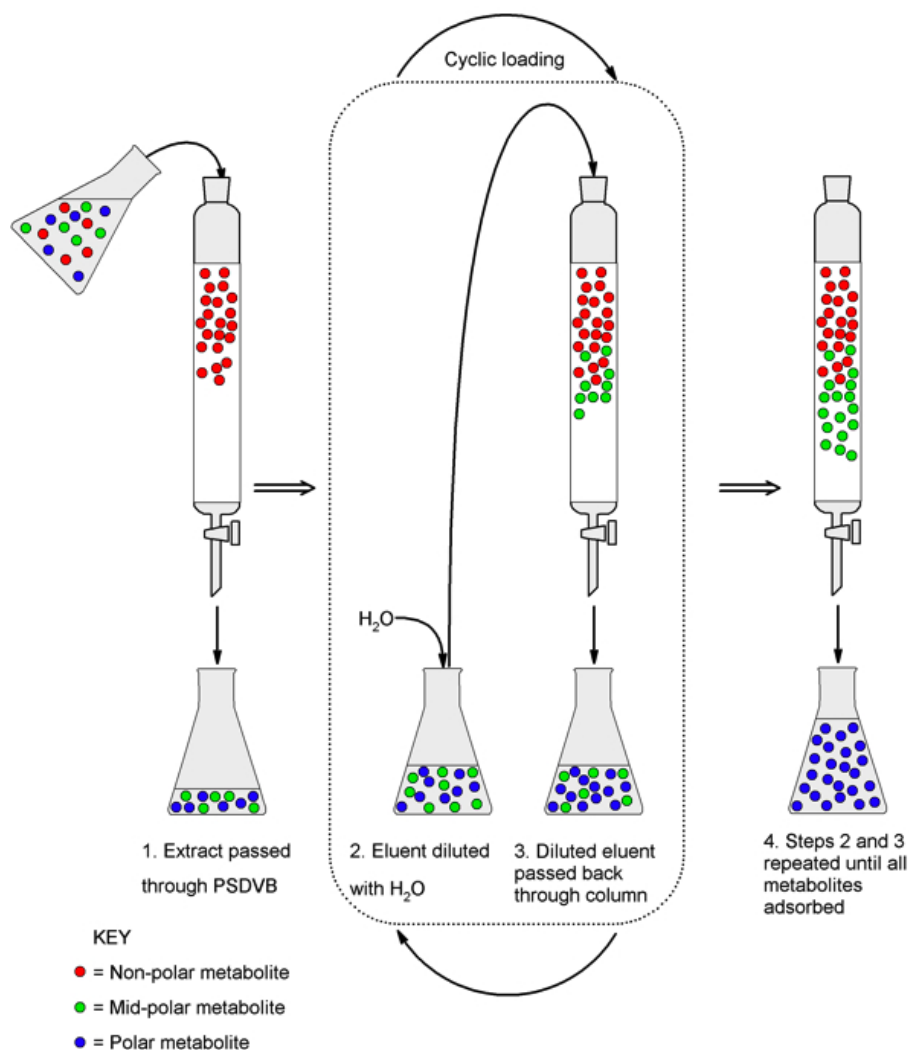


Figure A.1 A depiction of the cyclic loading process.

considerably more environmentally friendly than the halogenated solvents frequently used in other approaches such as liquid-liquid partitioning. Large quantities of eluent are generated during the procedure - the major draw-back of the technique. For a 20 g screening sample of sponge, 4.1 L of eluent is produced. However, an automated set-up is available for large-scale extractions using an HPLC pump system.

A.2 Screening protocol

Equipment required (per screen)

1× screening column loaded with 40 mL of HP20 resin beads equilibrated in MeOH.

Standard Preparation

Prepare an NMR quantification standard of 100 μL nitromethane in 5 mL CDCl_3 .

Voucher sample preparation

Take a voucher specimen of ca. 10 g of the crude sponge material ensuring that both the ectoderm and the endoderm are represented. Label and store the voucher sample in 75% IPA in H₂O.

Extraction

- Extract ~20 g of crude sponge material in 100 mL MeOH overnight.
- Filter the first extract and set aside.
- Re-extract the sponge material (and any filter paper/celite as necessary) in 100 mL MeOH overnight.
- Filter the second extract. Keep all sponge material (and any filter paper/celite as necessary) until the screen is complete at which time it may be discarded.

A.3 Cyclic loading

- Pass the second extract through the screen column with a flow rate of ca. 10 mL min⁻¹.
- Pass the first extract through the screen column with a flow rate of ca. 10 mL min⁻¹. Combine both eluents.
- Dilute the combined eluents with 200 mL H₂O. Pass the diluted eluents back through the screen column at a flow rate of ca. 10 mL min⁻¹.
- Dilute the eluent with 400 mL H₂O. Pass the diluted eluent back through the screen column at a flow rate of ca. 10 mL min⁻¹. The eluent should be kept until the screen is complete at which time it may be discarded.

Elution

- Elute the screen column with 100 mL of H₂O at a flow rate of ca. 10 mL min⁻¹. The H₂O eluent can be discarded immediately.
- Elute the screen column with 100 mL of 30% Me₂CO in H₂O at a flow rate of ca. 10 mL min⁻¹.
- Elute the screen column with 100 mL of 75% Me₂CO in H₂O at a flow rate of ca. 10 mL min⁻¹.

- Elute the screen column with 100 mL of Me₂CO at a flow rate of ca. 10 mL min⁻¹.

Backloading the 75% Me₂CO Fraction

- Dilute the 75% Me₂CO fraction with 100 mL H₂O. Pass the diluted eluent through the backloading column at a flow rate of ca. 8 mL min⁻¹.
- Dilute the eluent with 200 mL of H₂O. Pass the diluted eluent back through the backloading column at a flow rate of ca. 8 mL min⁻¹. The eluent should be kept until the screen is complete at which time it may be discarded.
- Elute the backloading column with 100 mL of Me₂CO.

Backloading the 30% Me₂CO Fraction

- Dilute the 30% Me₂CO fraction with 100 mL of H₂O. Pass the diluted eluent through the backloading column at a flow rate of ca. 8 mL min⁻¹.
- Dilute the eluent with 200 mL of H₂O. Pass the diluted eluent back through the backloading column at a flow rate of ca. 8 mL min⁻¹. The eluent should be kept until the screen is complete at which time it may be discarded.
- Elute the backloading column with 100 mL of Me₂CO.

A.4 Processing and NMR analysis

Processing the 75% Me₂CO Fraction

- Rotary-evaporate the Me₂CO eluent of the backloading column to dryness and transfer to a pre-weighed sample vial. Evaporate to dryness and record the mass.
- Prepare an NMR sample of the sample in 500 μL CD₃OD in a 5 mm NMR tube with 10 μL of the nitromethane standard.

NMR Analysis of the 75% Me₂CO Fraction

- Run a ¹H spectrum of the sample using the standard ¹H experiment with 64 transients (ca. 4 min)

- Run a COSY spectrum of the sample using the standard gCOSY parameter set. (ca. 20 min)
- Run a fully-coupled HSQC spectrum of the sample using the standard H-coupled HSQCad parameter set. (ca. 5 1/2 h)
- Run a fully-coupled HMBC spectrum of the sample using the standard H-coupled gHMBC parameter set. (ca. 8 1/4 h)

Processing the 30% Fraction

- Rotary-evaporate the Me₂CO eluent of the backloading column to dryness and transfer to a pre-weighed sample vial. Evaporate to dryness and record the mass.

Processing the 100% Fraction

- Rotary-evaporate the Me₂CO eluent of the screen column to dryness and transfer to a pre-weighed sample vial. Evaporate to dryness and record the mass.
- Prepare an NMR sample of the sample in 700 μ L of CDCl₃ in a 5 mm NMR tube with 10 μ L of the nitromethane standard.

NMR Analysis of the 100% Fraction

- Run a ¹H spectrum of the sample using the standard ¹H experiment with 64 transients (ca. 4 min).
- Run a COSY spectrum of the sample using the standard gCOSY parameter set. (ca. 20 min).
- Run a fully-coupled HSQC spectrum of the sample using the standard H-coupled HSQCad parameter set. (ca. 5 1/2 h).
- Run a fully-coupled HMBC spectrum of the sample using the standard H-coupled gHMBC parameter set. (ca. 8 1/4 h).

A.5 Spicule analysis

- Submerge a 1 cm³ piece of extracted sponge in 3 mL HNO₃ in a glass test tube. Ensure that both ecto- and endo-derms are represented in the tissue sample.
- Monitor decomposition of the organic tissue (ca. 24 h).
- When the organic matter is dissolved, dilute the acid with 5 mL H₂O.
- Centrifuge for 5 min to pellet the spicules.
- Remove the aqueous solution and wash the recovered spicules with 5 mL H₂O. Repeat the washing procedure twice more.
- Air dry the spicules for 24 h then analyse by SEM.

Appendix B

Yeast Growth Media

YPD liquid media

Liquid volume (total)	1000 mL	800 mL
Yeast extract	10 g	8 g
Peptone	20 g	16 g
Adenine	0.12 g	0.096 g
Agar	20 g	16 g

Autoclave and cool to 65 °C, add 40% glucose solution to a final concentration of 2% and antibiotics as required.

SD liquid media

Liquid volume (total)	1000 mL	800 mL
2x Agar solution		
Agar	20 g	16 g
H ₂ O	500 mL	400 mL

2x SD solution

H ₂ O	500 mL	400 mL
Yeast nitrogen base	1.7 g	1.36 g
Monosodium glutamate	1 g	0.8 g
Required amino acids	2 g	1.6 g

Autoclave and cool the 2x agar and 2x SD solutions to 65 °C, and combine the solutions while stirring, add 40% glucose solution (5% final concentration) and supplements as required.

Appendix C

NMR Data for Known Compounds

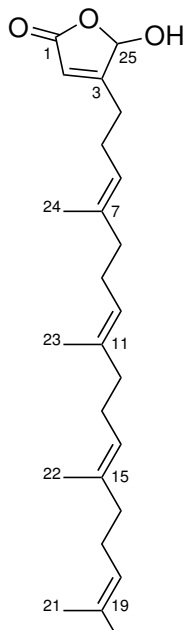
Table C.1 ^1H and ^{13}C NMR Data (600 MHz, CDCl_3) for *iso*-Secothorectolide (**23**).

Position	^{13}C		^1H			
	δ_{C}	mult	$^1J_{\text{CH}}$ (Hz)	δ_{H}	mult	J (Hz)
1	170.2	C				
2	146.1	C				
3	69.0	CH	146	4.80	brs	
4	34.8	CH ₂	128	2.85	brd	
5	147.5	CH	154	2.80		
6	124.3	C		6.54	t	6.6
7	24.7	CH ₂	128	2.29	t	7.0
8	26.7*	CH ₂	128	2.04–2.10	m	
9	123.0	CH	151	5.10	m	
10	136.7	C				
11	39.71**	CH ₂	120	1.95	brt	8.4
12	26.73*	CH ₂	128	2.04–2.10	m	
13	123.5	CH	151	5.09	m	
14	135.3	C				
15	39.68**	CH ₂	120	1.93	brt	8.4
16	26.54*	CH ₂	128	2.04–2.10	m	
17	124.1	CH	151	5.08	m	
18	131.5	C				
19	25.7	CH ₃	125	1.67	s	
20	17.9	CH ₃	125	1.60	s	
21	16.16	CH ₃	125	1.57	s	
22	16.2	CH ₃	125	1.59	s	
23	194.5	CHO	175	9.4	s	
24	147.51	CH	188	6.20	brs	
25	119.1	CH	§	6.12	brs	

* and **Assignment interchangeable

§Signal unresolved and immeasurable

Table C.2 ^1H and ^{13}C NMR Data (600 MHz, CDCl_3) for 1-Hydroxyluffarin Q (**24**).

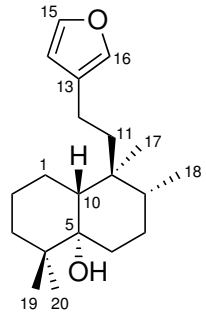


Position	^{13}C			^1H		
	δ_{C}	mult	$^1J_{\text{CH}}$ (Hz)	δ_{H}	mult	J (Hz)
1	171.5	C				
2	117.8	CH	184	6.09	s	
3	168.3	C				
4	26.1	CH_2	122	2.16	m	
5	26.8	CH_2	120	2.06	quin	7.5
6	120.9	CH	161	5.70	brd	5.1
7	135.21	C				
8	27.0**	CH_2		2.05–2.11	m	
9	32.7	CH_2	128	2.12	m	
10	124.2	CH	151	5.10	brt	7.6
11	137.5	C				
12	39.9	CH_2	123	1.97	m	
13	26.9**	CH_2		2.05–2.11	m	
14	123.5	CH	152	5.12	brt	6.8
15	136.1	C				
16	39.8	CH_2	123	1.97	m	
17	26.95**	CH_2		2.05–2.11	m	
18	124.5	CH	151	5.08	brt	7.6
19	131.5	C				
20	25.9	CH_3	124	1.67	s	
21	17.8	CH_3	124	1.59	s	
22	16.24*	CH_3	124	1.60	s	
23	16.21*	CH_3	124	1.60	s	
24	16.1	CH_3	125	1.59	s	
25	91.4	CH	168	5.31	s	

24

* and **Assignment interchangeable

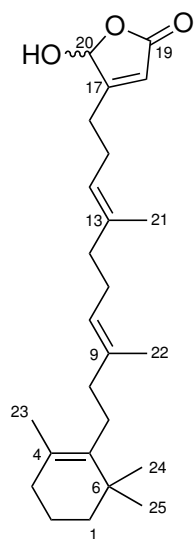
Table C.3 ^1H and ^{13}C NMR Data (600 MHz, CDCl_3) for ambliol B (**25**).



Position	^{13}C			^1H		
	δ_{C}	mult	$^1J_{\text{CH}}$ (Hz)	δ_{H}	mult	J (Hz)
1	21.4	CH_2	125	1.59	brd	
a				1.34	td	14.0, 4.4
2	22.4	CH_2	128	1.56		
b				1.46		
3	36.8	CH_2	124	1.64	td	
a				1.09	brd	13.4
4	39.1	C				
5	76.4	C				
6	25.5	CH_2	122	1.71	td	14.0, 4.2
a				1.41	dt	
7	24.6	CH_2	126	2.08	tt	17.8, 4.0
a				1.25	m	
8	40.5	CH	120	1.58	d	7.1
9	37.5	C				
10	35.1	CH	127	1.70	quin	4.5
11	40.2	CH_2	125	1.64	m	
a				1.29	m	
12	18.1	CH_2	125	2.36	dt	9.8, 8.0
13	126.2	C				
14	138.6	CH	202	7.2	s	
15	111.1	CH	174	6.25, s		
16	142.8	CH	202	7.35, s		
17	23.7	CH_3	123	1.01	s	
18	24.6	CH_3	124	0.86	s	
19	14.3	CH_3	123	0.95	d	
20	21.0	CH_3	124	1.13	s	

25

Table C.4 ^1H and ^{13}C NMR Data (600 MHz, CDCl_3) for Luffariellolide (**26**).



Position	^{13}C			^1H		
	δ_{C}	mult	$^1J_{\text{CH}}$ (Hz)	δ_{H}	mult	J (Hz)
1	19.7	CH_2	123	1.56	ddd	12.1, 6.2, 6.0
2	32.9	CH_2	124	1.90	t	6.1
3	39.9	CH_2	125	1.41	ddd	9.0, 6.1, 2.6
4	35.1	C				
5	137.2	C				
6	127.1	C				
7	28.1	CH_2	130	2.06	m	
8	40.4	CH_2	128	2.00	m	
9	136.5	C				
10	123.4	CH	150	5.10	t	7.0
11	26.6	CH_2	127	2.08	q	7.7
12	39.8	CH_2	128	2.02	m	
13	137.6	C				
14	122.1	CH	151	5.12	t	7.2
15	25.3	CH_2	125	2.31	q	6.9
16	27.9	CH_2	125	2.45	brs	
17	169.4	C				
18	117.8	CH	181	5.86	s	
19	171.5	C				
20	99.1	CH	173	5.99	s	
21	28.8*	CH_3	124	0.97	s	
22	28.8*	CH_3	124	0.97	s	
23	20.0	CH_3	125	1.59	s	
24	16.2	CH_3	124	1.63	s	
25	16.3	CH_3	124	1.62	s	

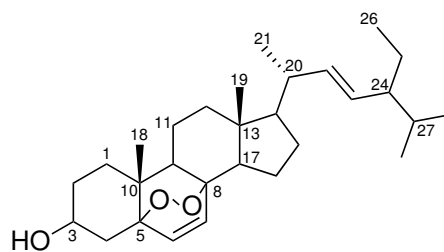
*Indistinguishable

Table C.5 ^1H and ^{13}C NMR Data (600 MHz, CDCl_3) for $5\alpha,8\alpha$ -Epidioxysterol (**27**).

Position	^{13}C			^1H			
	δ_{C}	mult	$^1J_{\text{CH}}$ (Hz)	δ_{H}	mult	J (Hz)	
1	a	34.8	CH_2	128	1.95	td	13.5, 3.4
	b			129	1.69	dtd	13.2, 3.4
2	a	30.2	CH_2	125	1.84	dd	12.9, 3.9
	b			125	1.53	q	14.0, 3.9
3		66.6	CH	144	3.81	s	
4	a	37.1	CH_2	141	2.11	ddd	13.9, 5.3, 1.9
	b			125	1.94	dd	13.1, 11.3
5		82.3	C				
6		135.5	CH	168	6.14	d	8.5
7		130.9	CH	170	6.51	d	8.7
8		79.6	C				
9		51.2	CH	130	1.49	t	5.1
10		37.0	C				
11	a	23.5	CH_2	127	1.50	dd	10.1, 7.0
	b			127	1.21	dd	18.6, 3.2
12	a	39.5	CH_2	127	1.96	d	14.4
	b			124	1.23	brd	5.8
13		44.7	C		1.23	brd	6.0
14		51.8	CH	123	1.56	m	
15	a	20.8	CH_2	125	1.77	dtd	7.4, 12.2, 3.2
	b			116	1.4	dd	11.9, 6.1
16	a	29.1	CH_2	126	1.69	dt	13.7, 3.5
	b			127	1.34	dd	22.4, 9.8
17		56.2	CH	123	1.23	m	
18		13.0	CH_3	125	0.82	s	
19		18.3	CH_3	125	0.88	s	
20		40.1	CH	126	2.03	dtd	23.6, 7.9, 2.7
21		21.3	CH_3	125	1.01	d	6.4
22		137.8	CH	148	5.14	dd	15.0, 8.3
23		130.0	CH	152	5.04	dd	15.3, 8.7
24 (1)	a	25.5	CH_2	124	1.41	m	
	b			124	1.17	d	10.1
24 (2)		12.6	CH_3	128	0.80	t	7.5
25		31.2	CH	127	1.52	m	
26		19.1	CH_3	122	0.79	d	6.7
27		21.1	CH_3	124	0.84	d	6.4

†Selected correlations.

*Weak correlations.



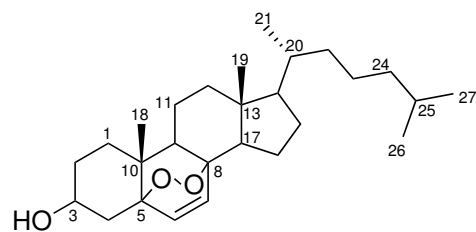
27

Table C.6 ^1H and ^{13}C NMR Data (600 MHz, CDCl_3) for $5\alpha,8\alpha$ -Epidioxysterol (**28**).

Position	^{13}C			^1H			
	δ_{C}	mult	$^1J_{\text{CH}}$ (Hz)	δ_{H}	mult	J (Hz)	
1	a	34.8	CH_2	127	1.95	td	13.3, 3.6
	b		CH_2	129	1.69	dt	13.7, 3.4
2	a	30.2	CH_2	133	1.83	brd	12.6
	b			125	1.54	m	
3		66.6	CH	144	3.97	m	
4	a	37.1	CH_2	126	2.11	ddd	13.8, 5.1, 2.0
	b		CH_2	127	1.91	dd	11.7, 13.6
5		82.3	C-O				
6		135.5	CH	166	6.24	d	9.1
7		130.9	CH	168	6.51	d	9.1
8		79.6	C-O				
9		51.2	CH	128	1.48	m	
10		37.0	C				
11	a	23.5	CH_2	127	1.50	m	
	b		CH_2	126	1.21	m	
12	a	39.5	CH_2	128	1.98	d	9.4
	b			126	1.22	m	
13		44.9					
14		51.7	CH	121	1.54	m	
16	a	28.4	CH_2	125	1.91	m	
	b			127	1.36	m	
17		56.5	CH	124	1.17	quin	8.0
18		12.8	CH_3	122	0.80	s	
19		18.3	CH_3	126	0.88	s	
20		35.4	CH	123	1.36	quin	2.7
21		18.7	CH_3	124	0.89	d	6.7
22	a	36.1	CH_2	124	1.34	t	12.7
	b		CH_2	124	1.00	d	6.9
23	a	23.9	CH_2		1.32	m	
	b				1.14	m	
24		39.6	CH_2		1.1		
25		28.1	CH_2	125	1.51	m	
26		22.7	CH_3	125	0.86	d	6.6
27		23.0	CH_3	124	0.87	d	6.6
28		33.2	CH	124	1.46	qd	11.7, 6.1

†Selected correlations.

*Weak correlations.



28

Table C.7 ^1H and ^{13}C NMR Data (600 MHz, CDCl_3) of 14-Bromohomofascaplysin (**29**).

Position	^{13}C			^1H		
	δ_{C}	mult	$^1J_{\text{CH}}$ (Hz)	δ_{H}	mult	J (Hz)
1	137.21	C				
2	124.4	CH	165	7.90	dd	7.7, 0.9
3	130.6	CH	164	7.70	td	7.4, 0.7
4	130.9	CH	165	7.8	d	7.9
5	113.8	CH	167	8.28	d	8.5
6	141.2	C				
N ⁺ -1						
7	124.0	CH	192	9.38	d	8.6
8	117.2	CH	175	8.83	d	8.6
9	135.0	C				
10	119.1	C				
11	124.5	CH	167	8.4	d	8.5
12	125.8	CH	171	7.66	dd	8.48, 1.66
13	126.7	C				
14	115.6	CH	172	8.02	d	1.37
15	146.0	C				
NH-2						
16	131.0	C				
17	143.95	C				
18	77.81	C				
19	50.1	CH ₂	130	4.20	dd	24.1, 18.6
20	205.1	C				
21	28.0	CH ₃	128	1.98	s	

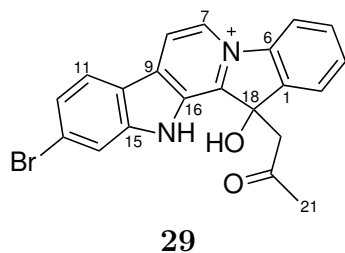
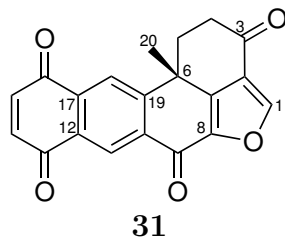


Table C.8 ^1H and ^{13}C NMR Data (600 MHz, d_3 -MeCN) of Halenaquinone (**31**).

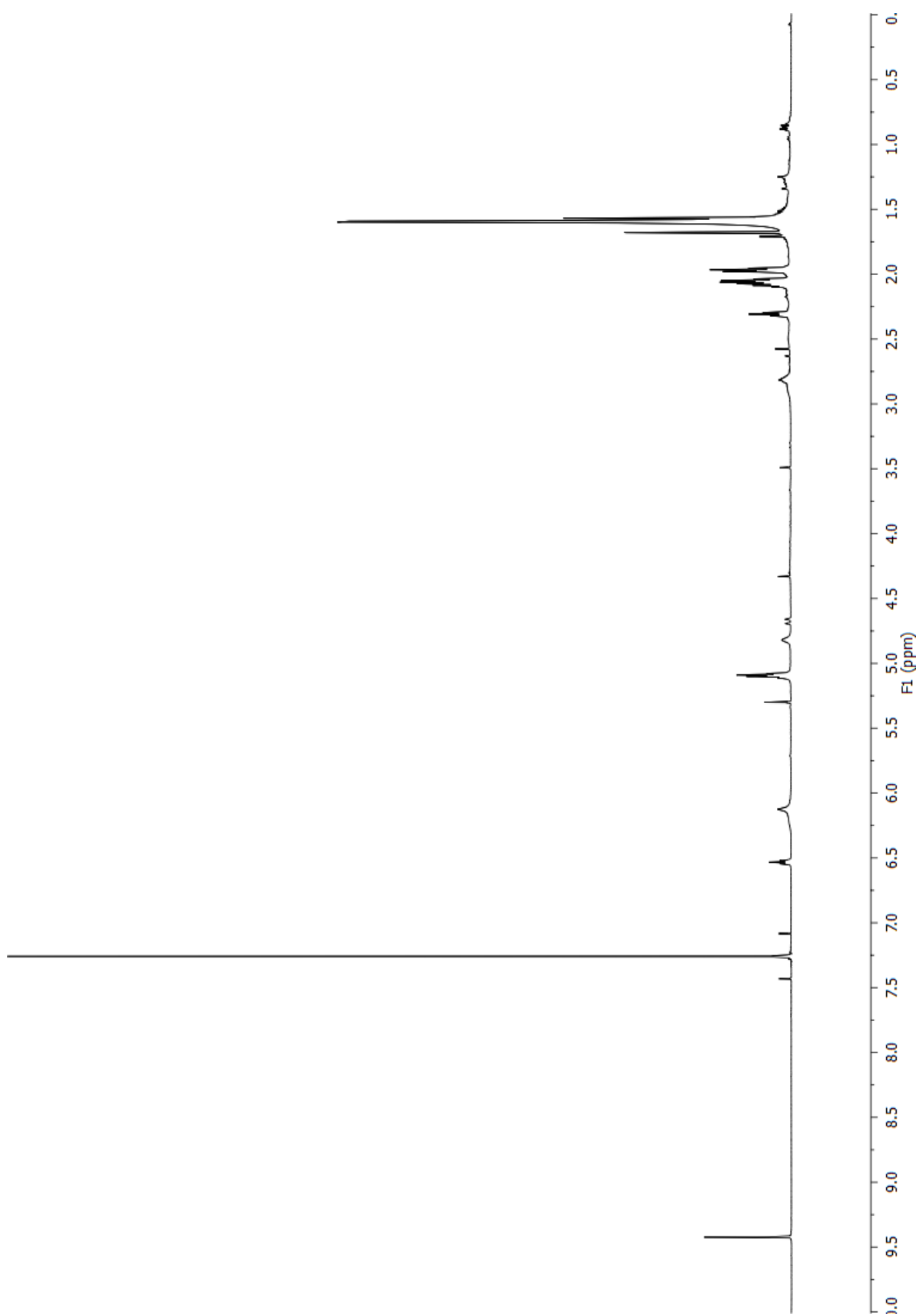
Position	^{13}C			^1H			
	δ_{C}	mult	$^1J_{\text{CH}}$ (Hz)	δ_{H}	mult	J (Hz)	
1	149.7	CH	211	8.37	s		
2	122.7	C					
3	191.5	C					
4	a	36.2	CH ₂	125	3.05	ddd	18.7, 13.3, 5.4
				132	2.72	ddd	18.6, 4.7, 1.9
5	b	32.7	CH ₂	134	2.89	ddd	13.1, 5.4, 1.9
				131	2.25	td	13.2, 4.8
6	36.9	C					
7	148.4	C					
8	144.7	C					
9	170.5	C					
10	137.0	C					
11	125.6	CH	167	9.08	s		
12	130.7	C					
13	184.1	C					
14	139.0	CH	170	7.06	d	11.4	
15	139.6	CH	170	7.08	d	11.1	
16	184.5	C					
17	134.0	C					
18	123.8	CH	163	8.30	s		
19	154.7	C					
20	29.4	CH ₃	130	1.66	s		



Appendix D

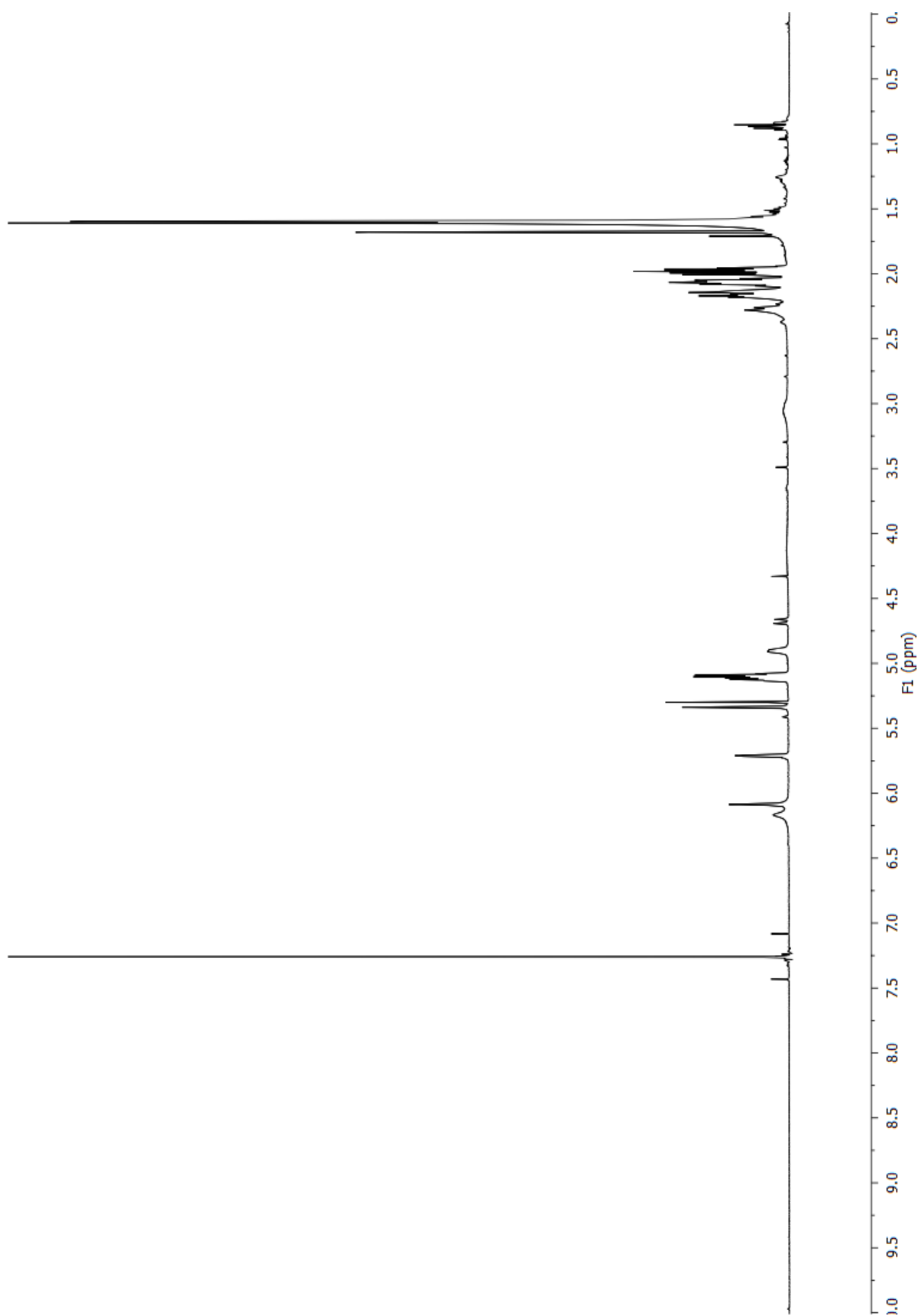
¹H NMR Spectra of Known Compounds

iso-Secothorectolide



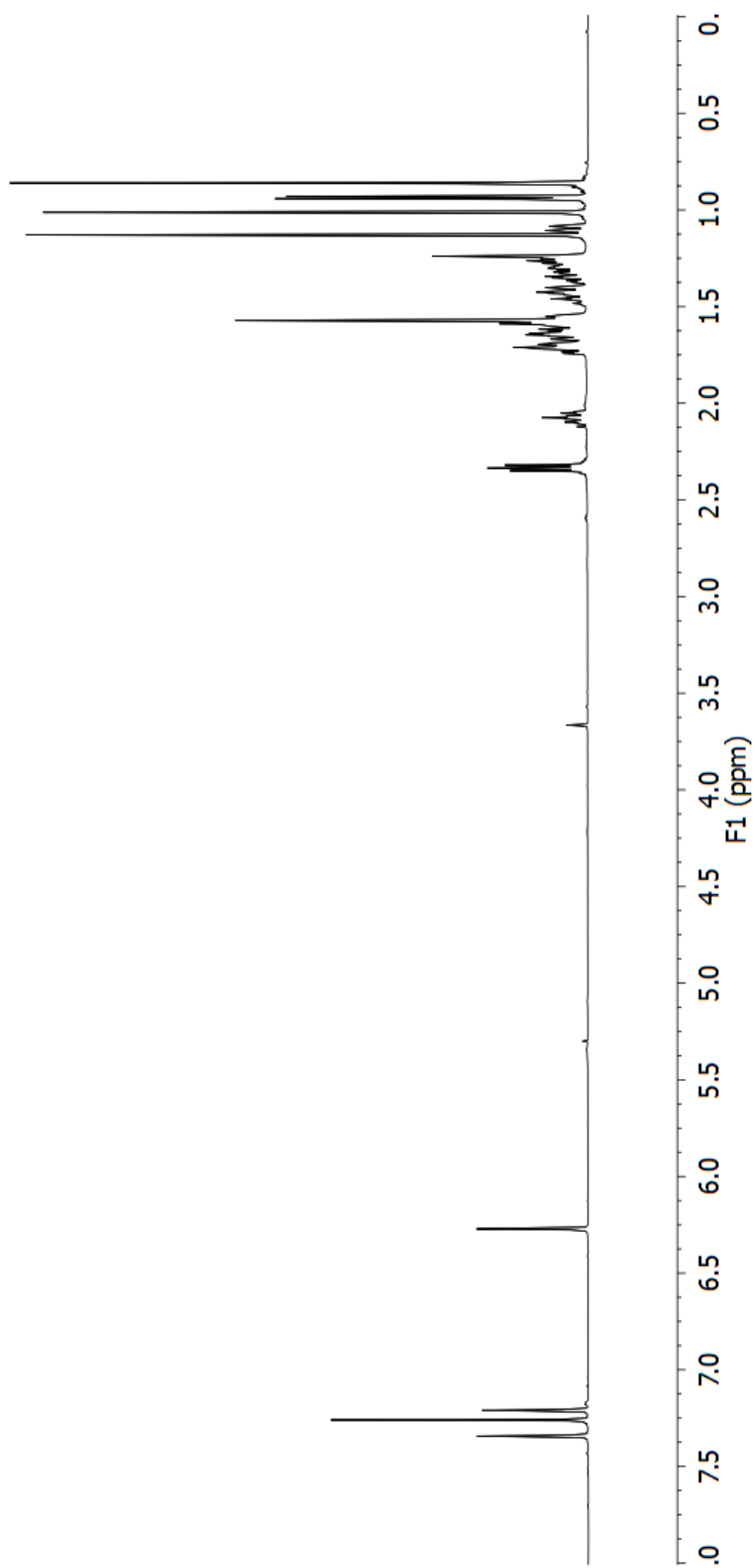
¹H NMR spectrum of *iso*-secothorectolide (**23**) (600 MHz, CDCl₃).

1-Hydroxyluffarin Q



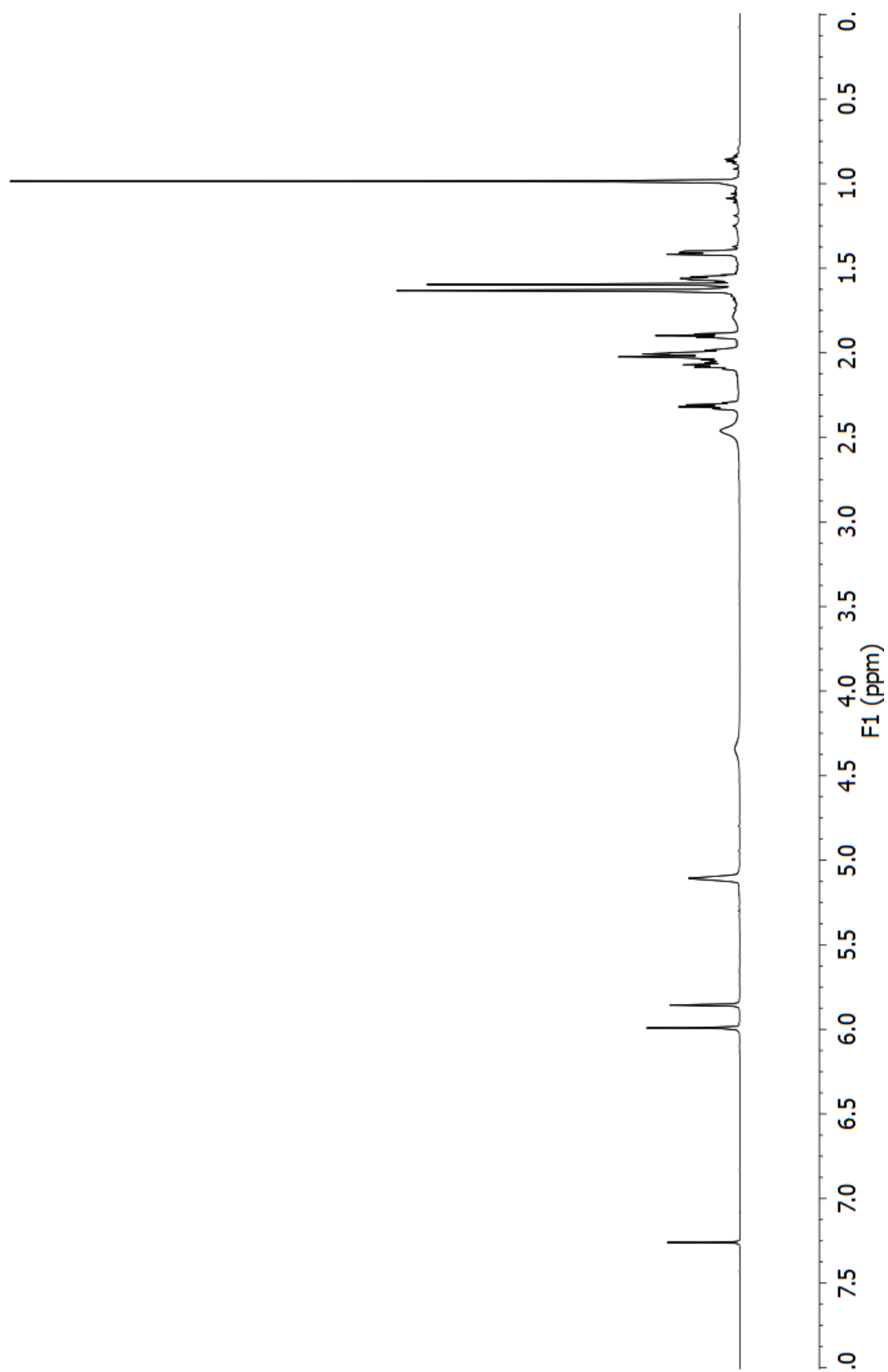
^1H NMR spectrum of 1-hydroxyluffarin Q (**24**) (600 MHz, CDCl_3).

Ambliol B



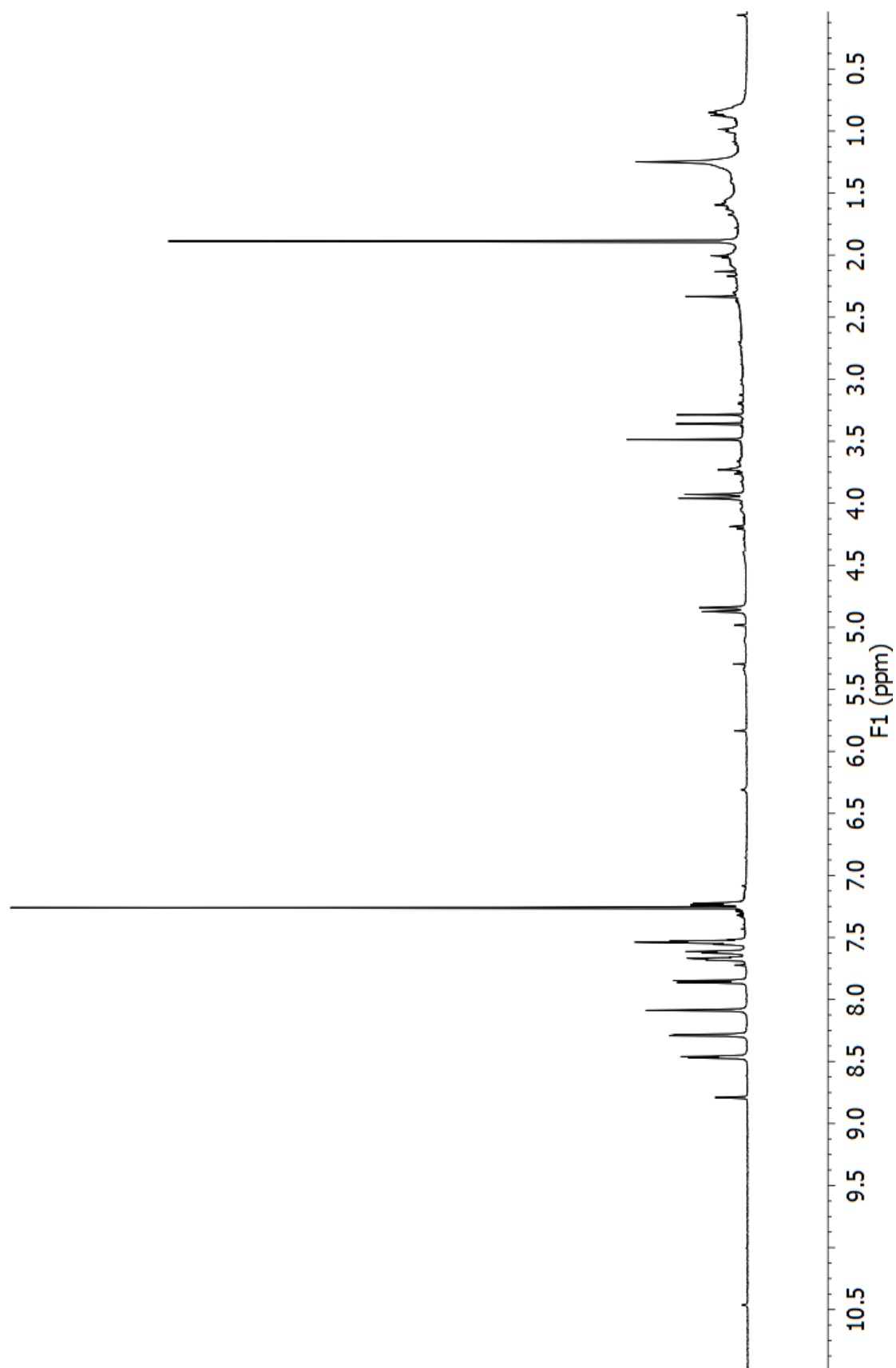
¹H NMR spectrum of ambliol B (**25**) (600 MHz, CDCl₃).

Luffarielolide



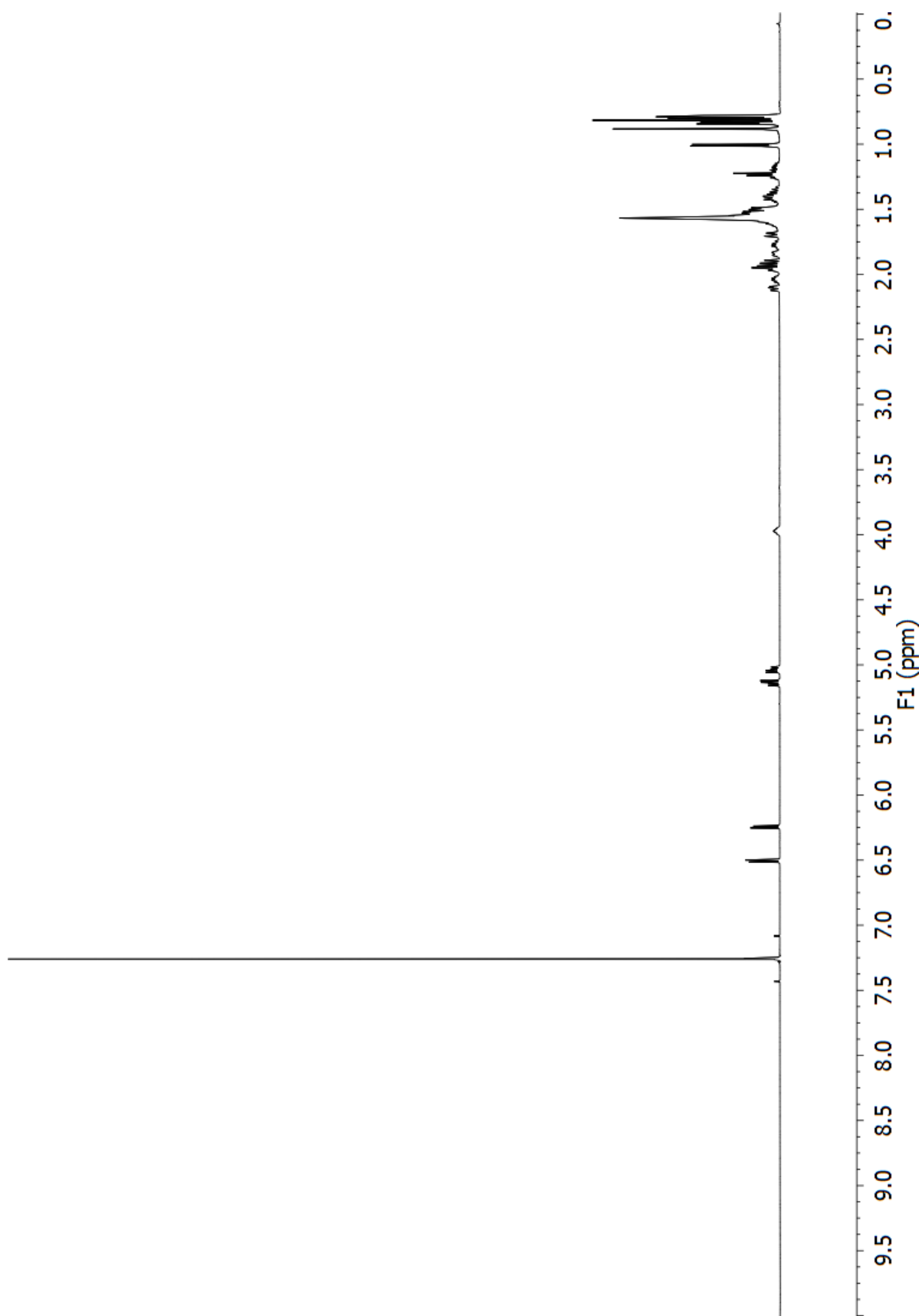
^1H NMR spectrum of luffarielolide (**26**) (600 MHz, CDCl_3).

14-Bromohomofascaplysin



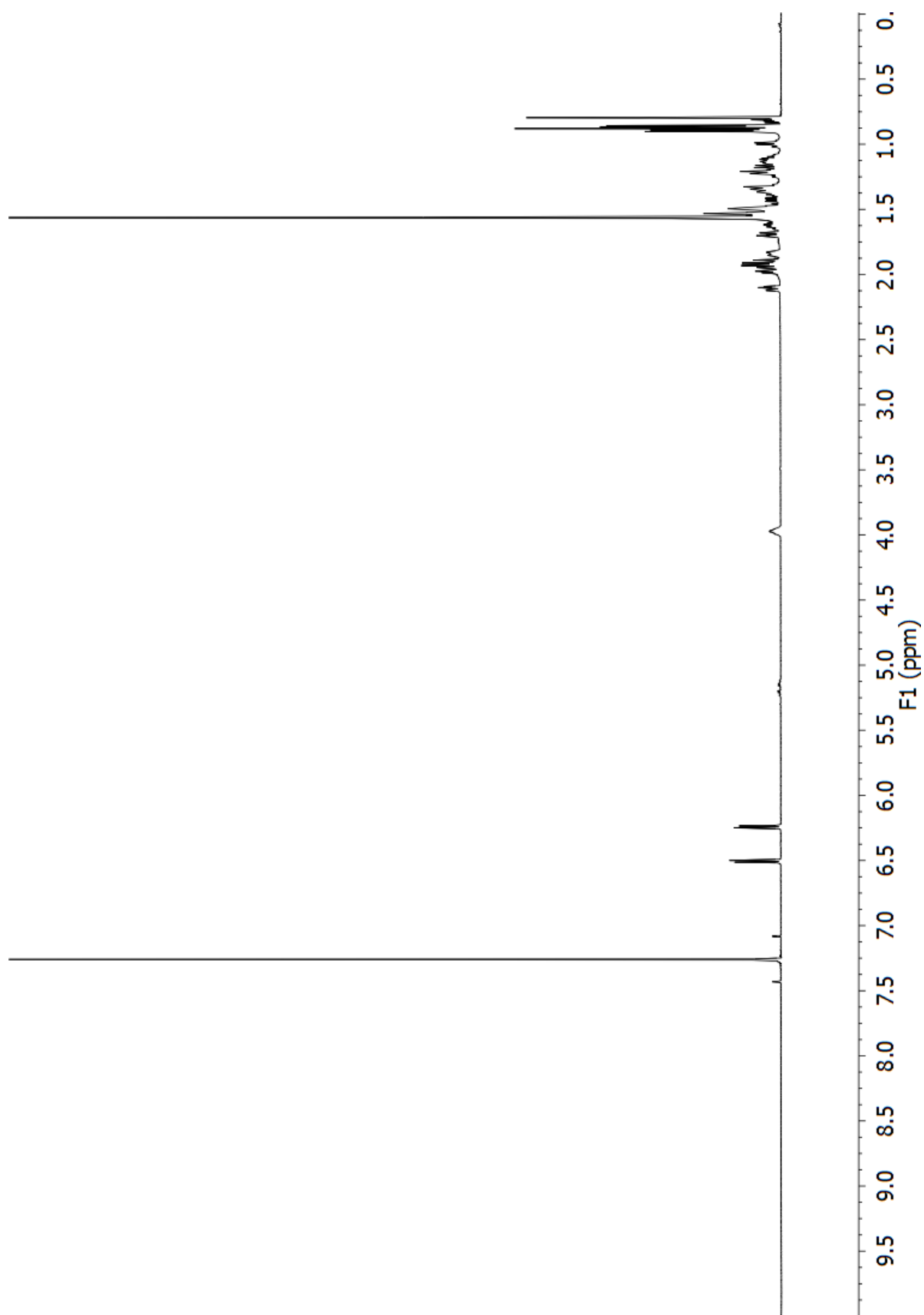
^1H NMR spectrum of 14-bromohomofascaplysin (**29**) (600 MHz, CDCl_3).

5 α ,8 α -Epidioxysterol **27**



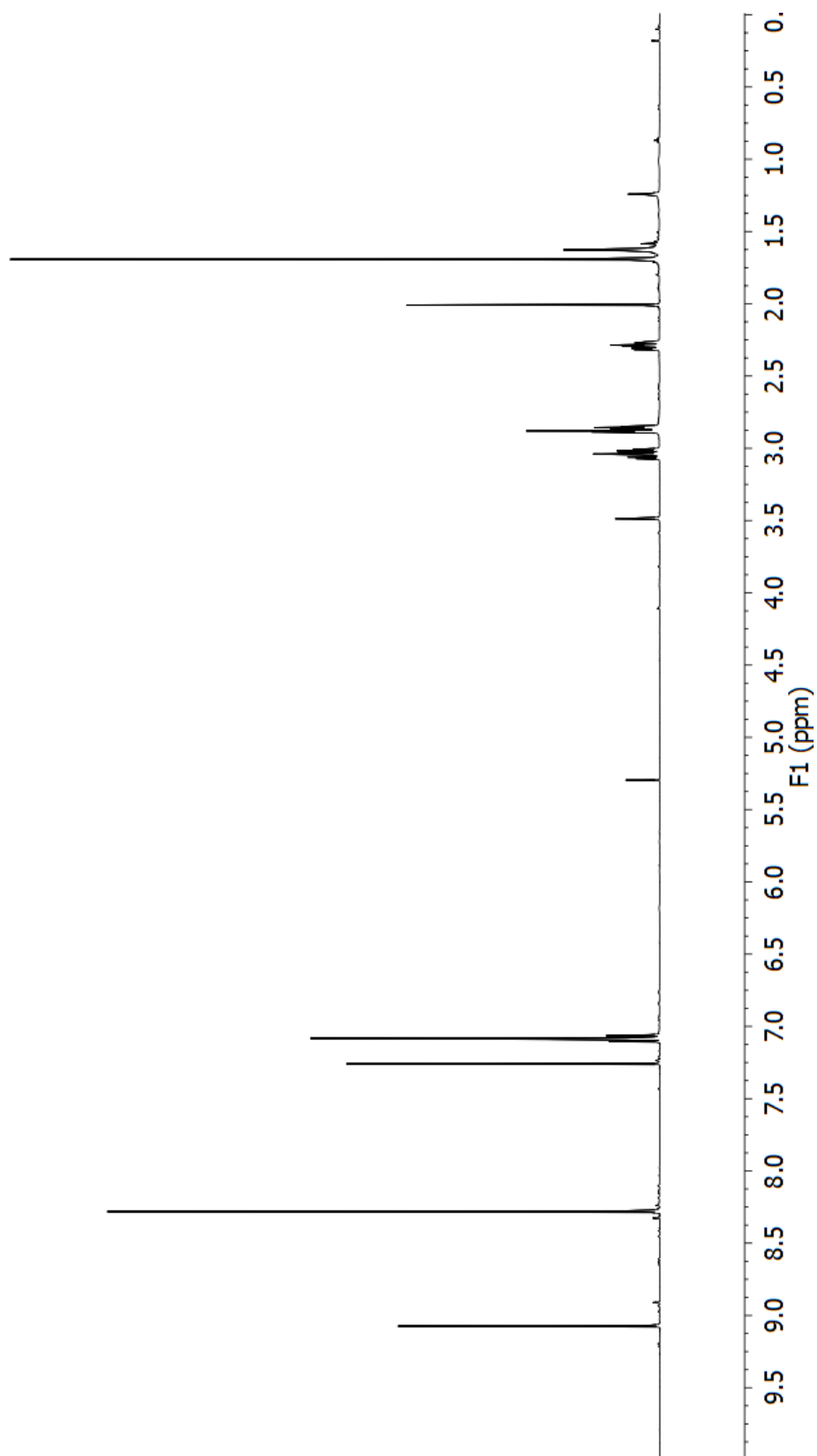
^1H NMR spectrum of 5 α ,8 α -epidioxysterol **27** (600 MHz, CDCl_3).

5 α ,8 α -Epidioxysterol 28



¹H NMR spectrum of 5 α ,8 α -epidioxysterol **28** (600 MHz, CDCl₃).

Halenaquinone

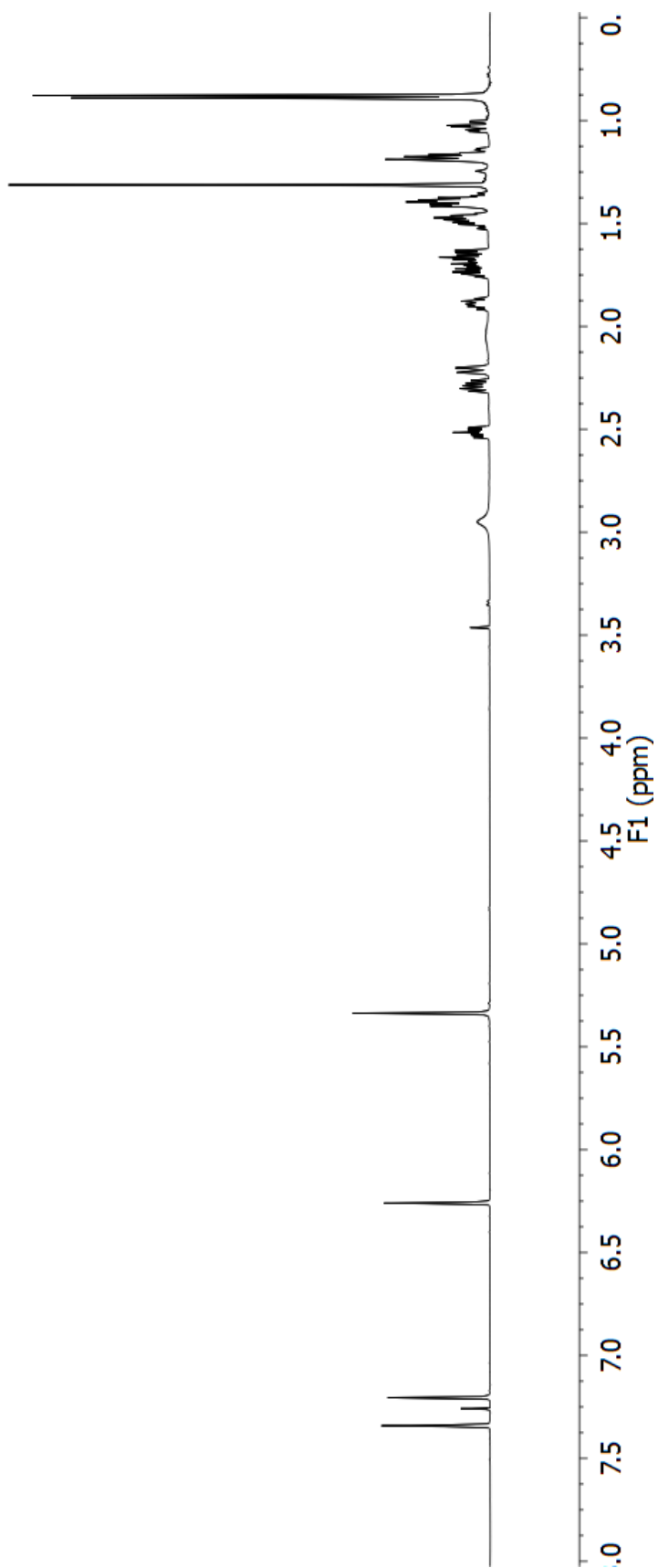


^1H NMR spectrum of halenaquinone (**31**) (600 MHz, CDCl_3).

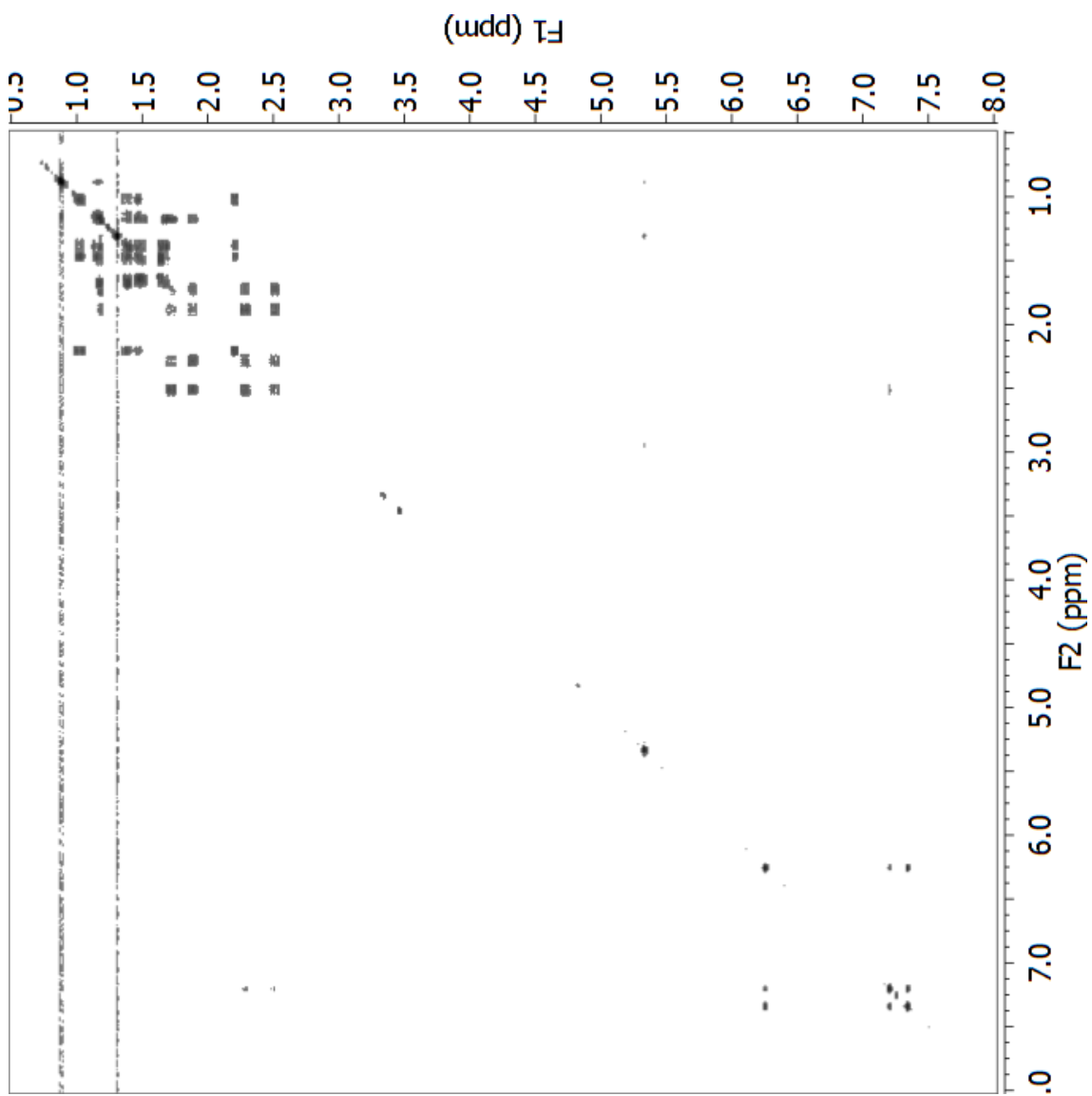
Appendix E

NMR Spectra of Luakuliides A–C

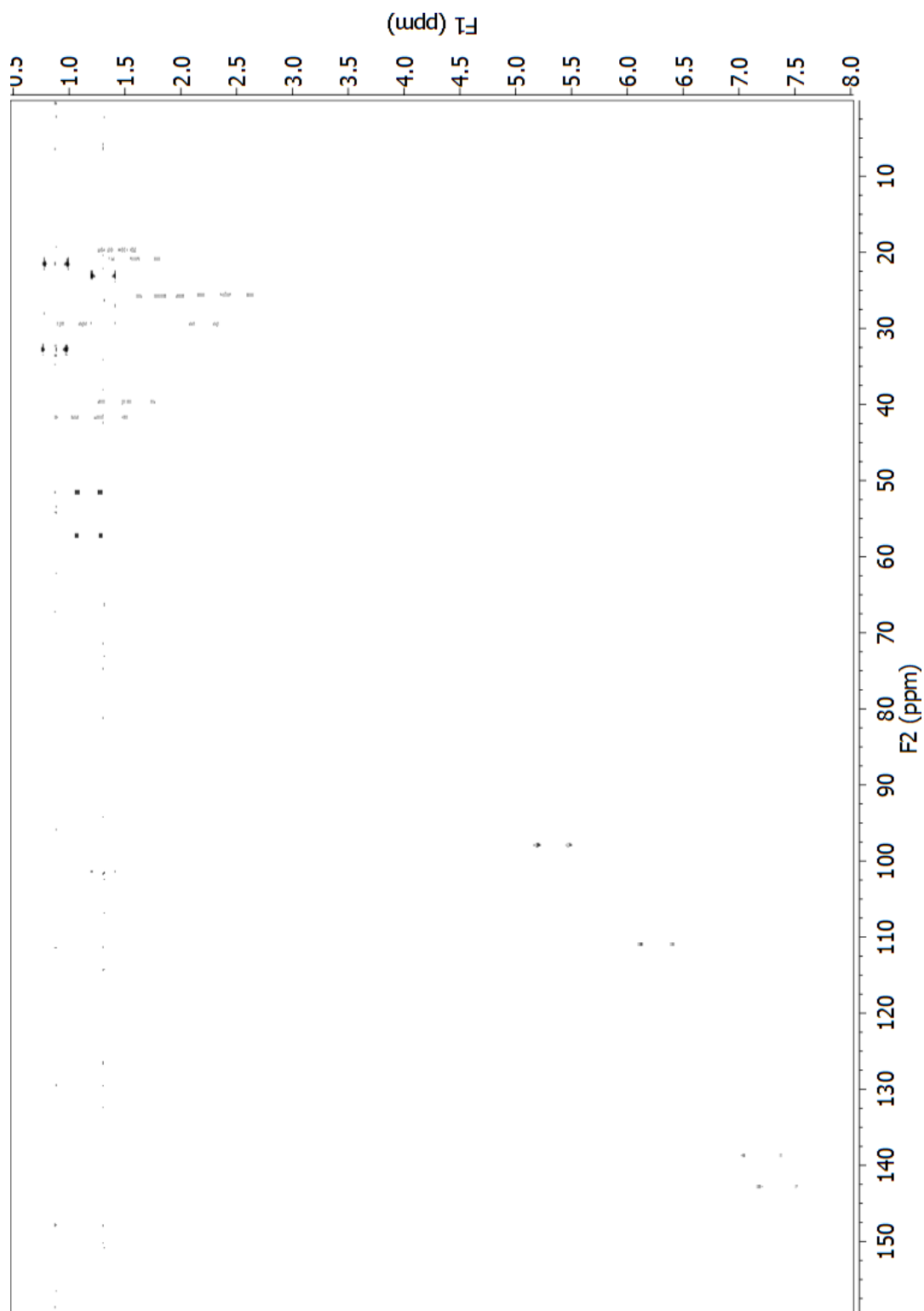
Luakuliide A



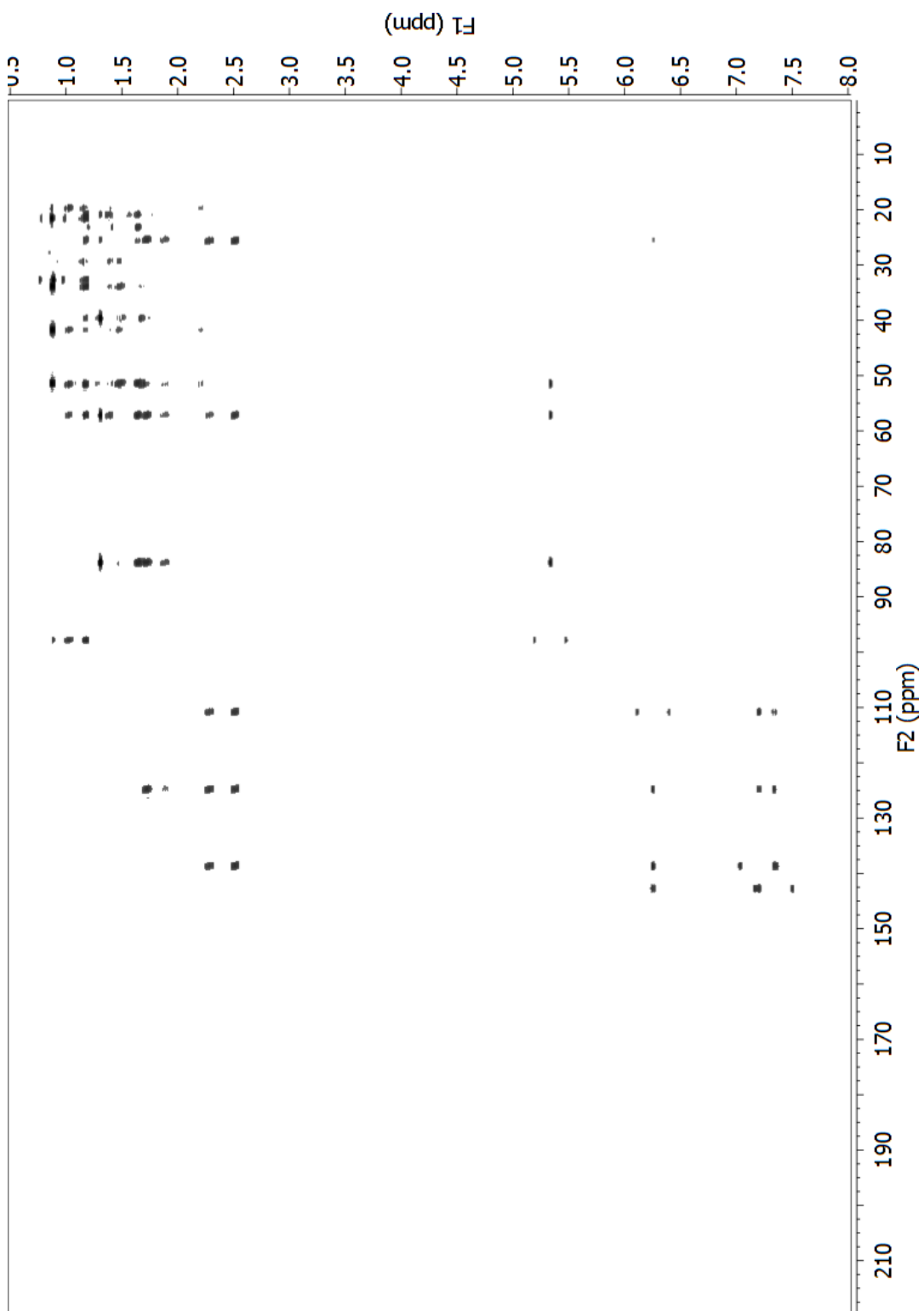
^1H NMR spectrum of Luakuliide A (**33**) (600 MHz, CDCl_3).



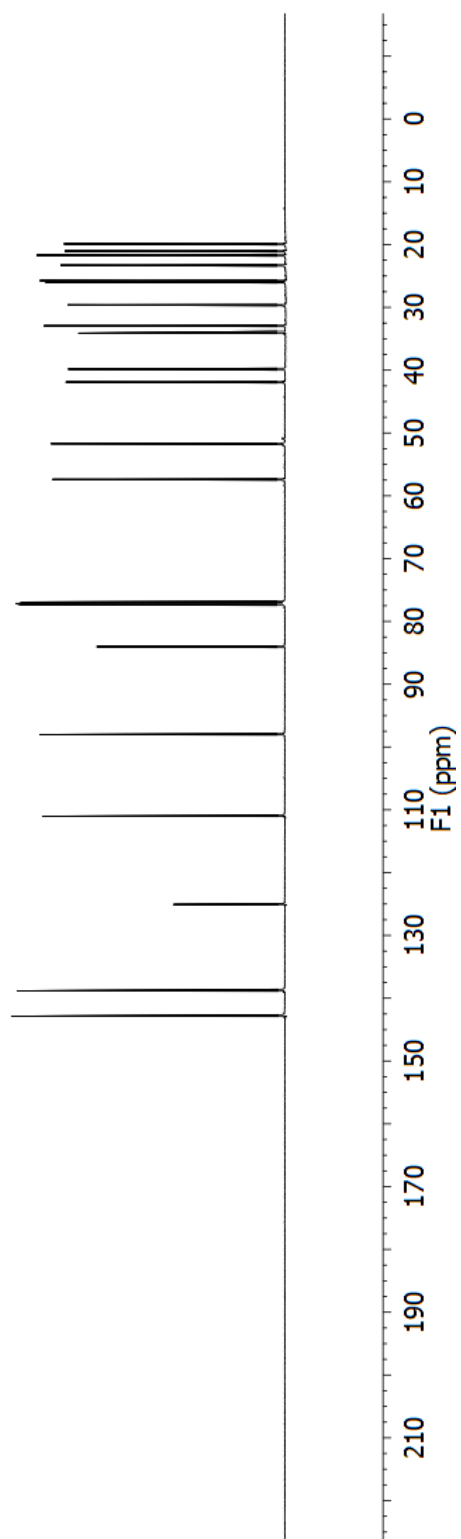
COSY spectrum of luakuliide A (**33**) (600 MHz, CDCl_3).



Fully-coupled HSQC spectrum of luakuliide A (**33**) (600 MHz, CDCl₃).

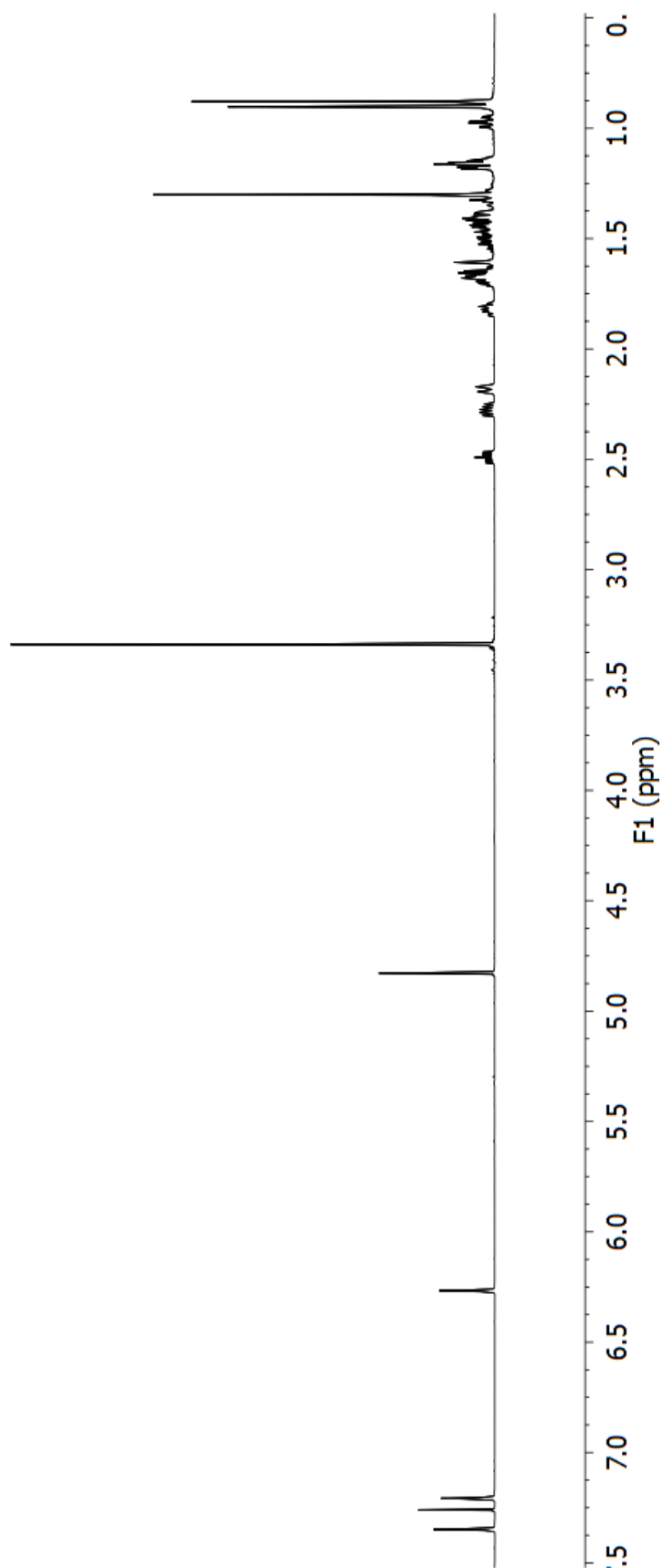


HMBC spectrum of luakuliide A (**33**) (600 MHz, CDCl₃).

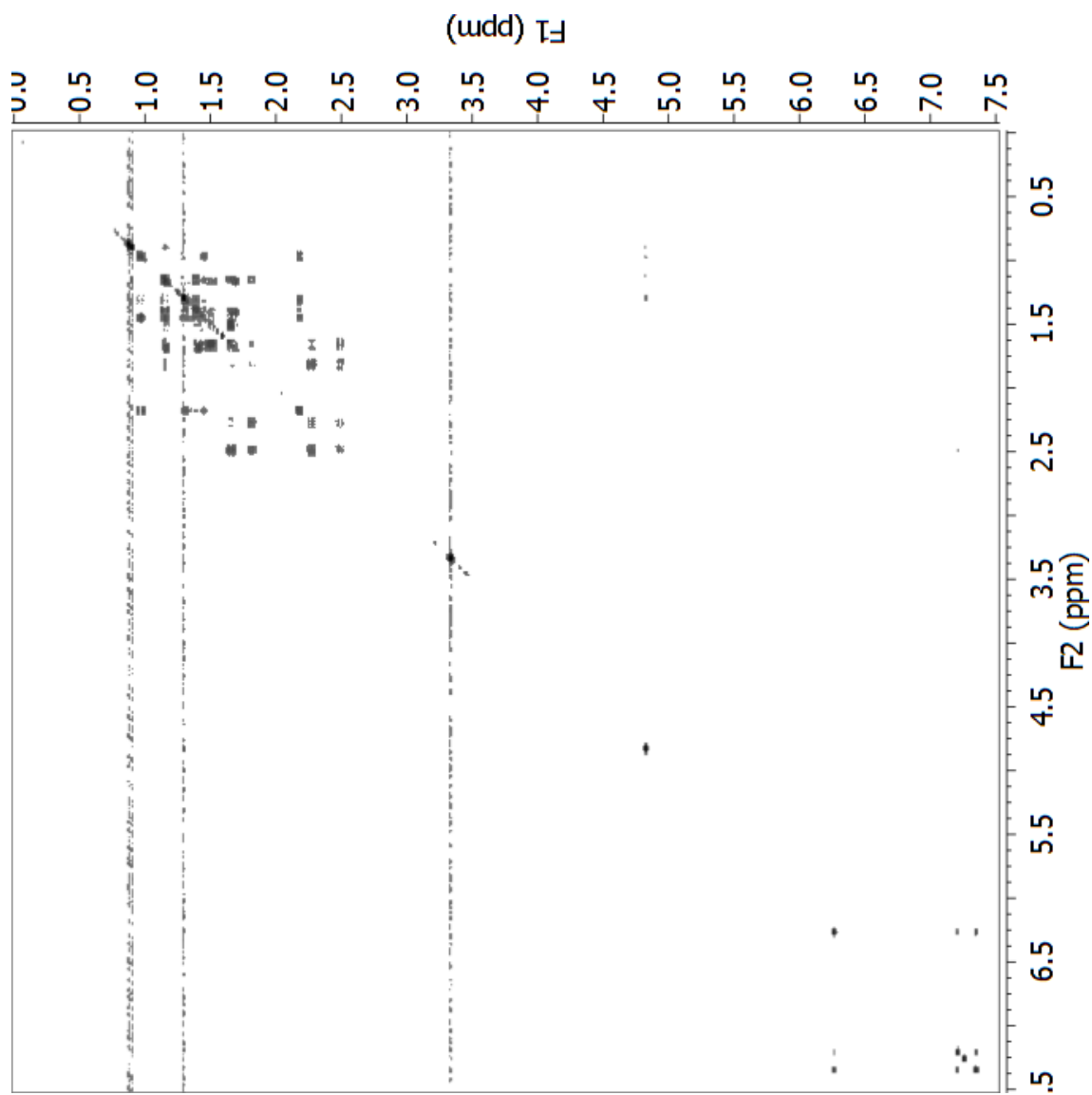


^{13}C NMR spectrum of luakuliide A (**33**) (150 MHz, CDCl₃).

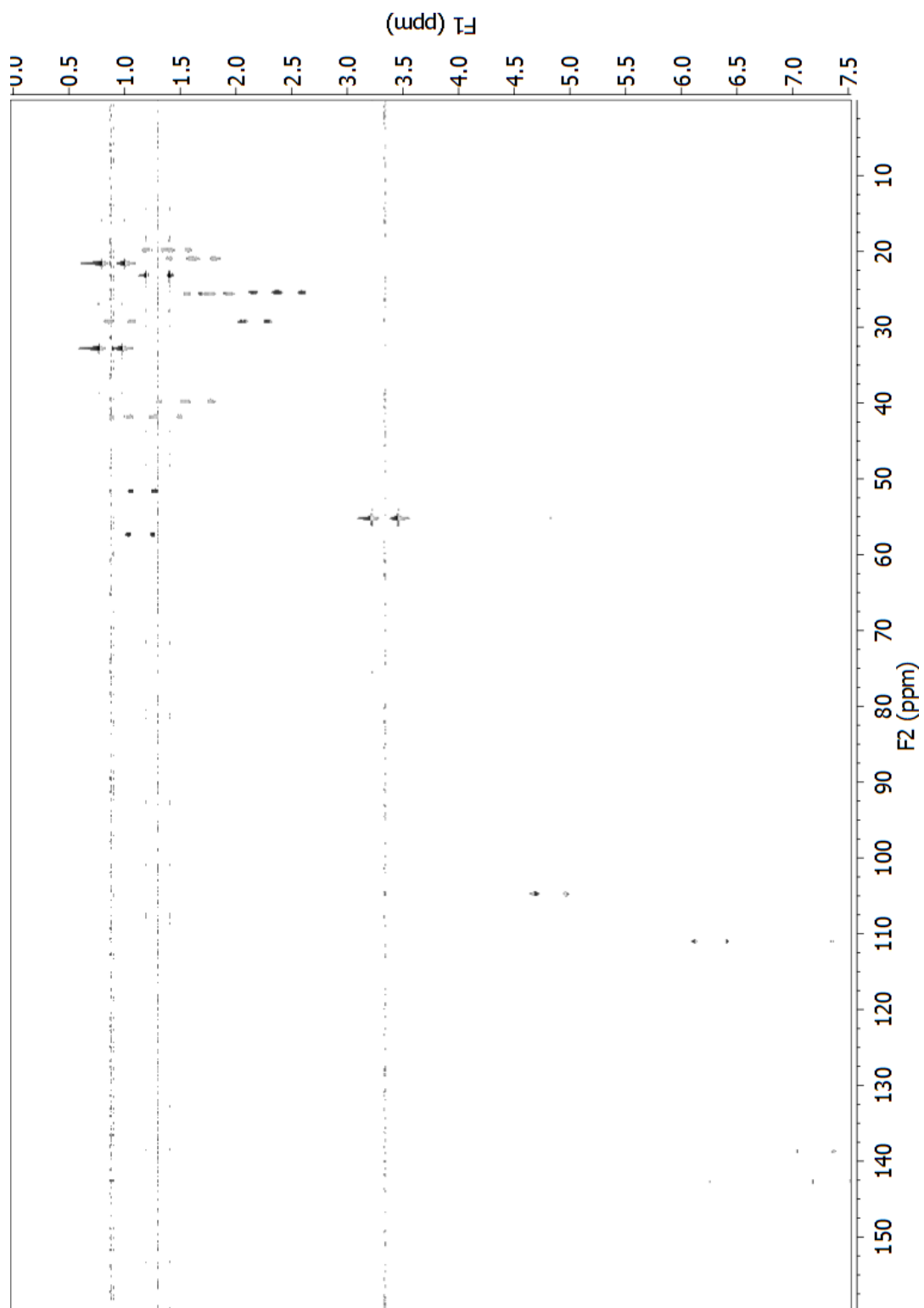
Luakuliide A Methyl Acetal



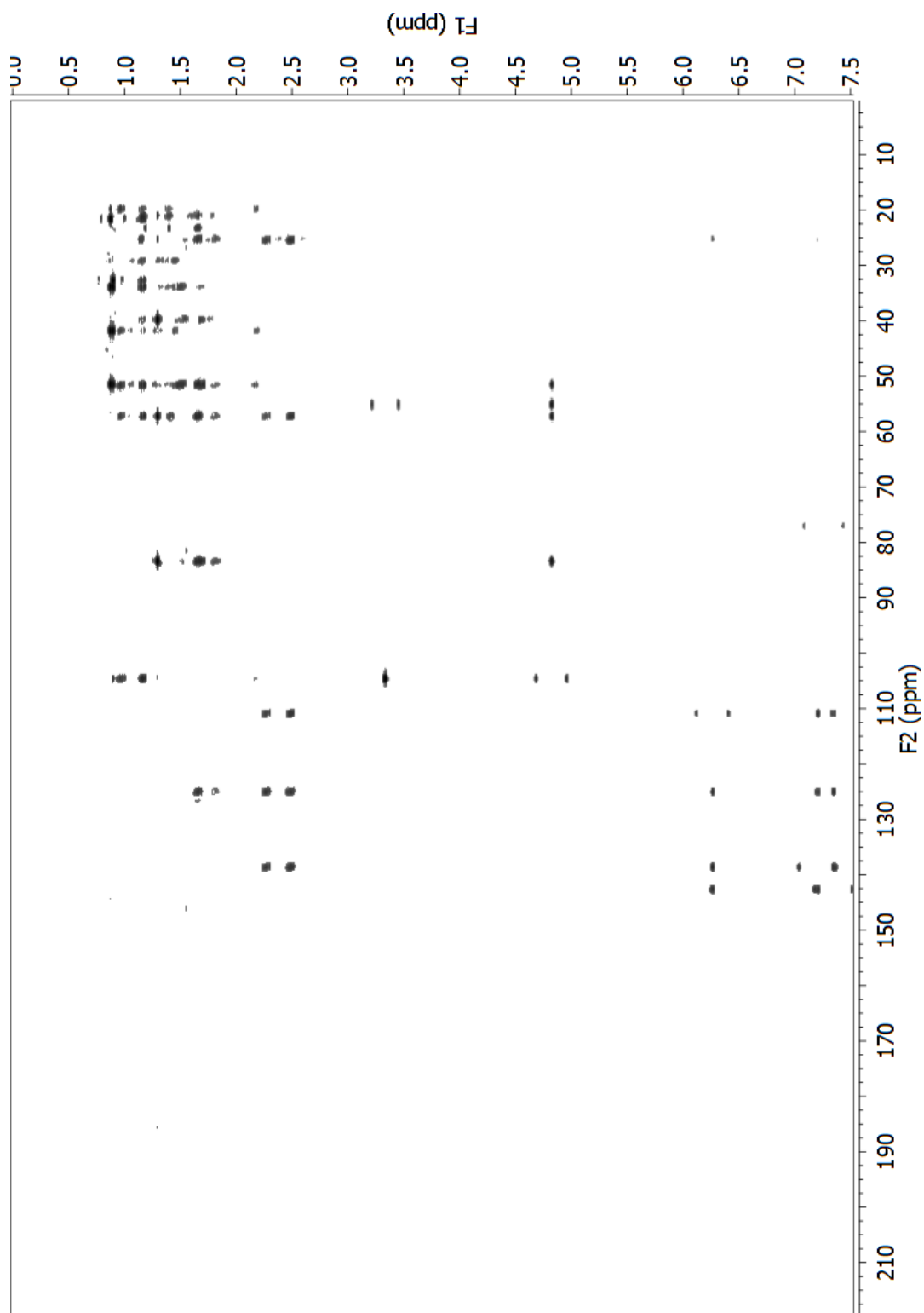
^1H NMR spectrum of luakuliide A methyl acetal (**34**) (600 MHz, CDCl_3).



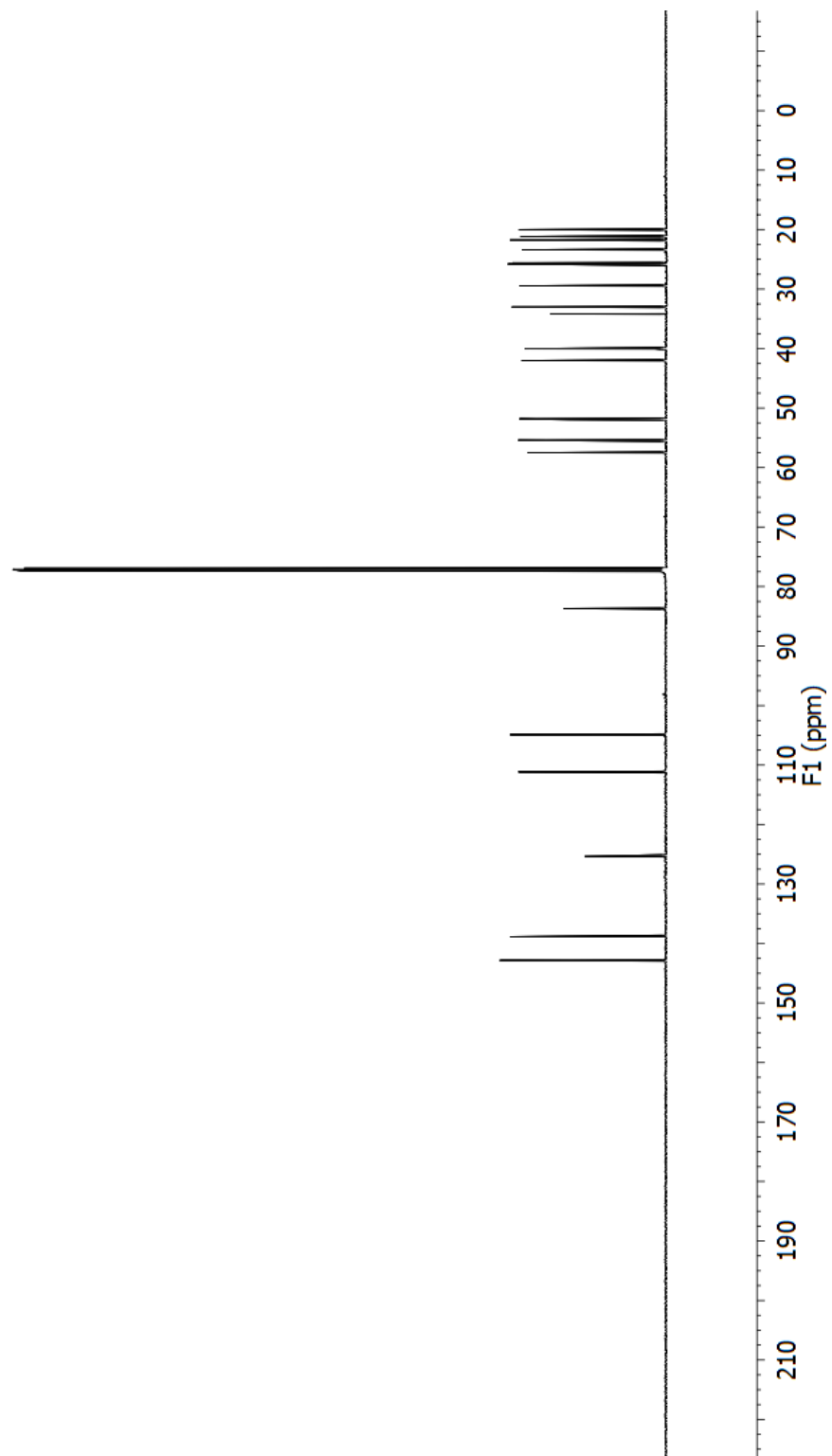
COSY spectrum of luakuliide A methyl acetal (**34**) (600 MHz, CDCl₃).



Fully-coupled HSQC spectrum of luakuliide A methyl acetal (**34**) (600 MHz, CDCl₃).

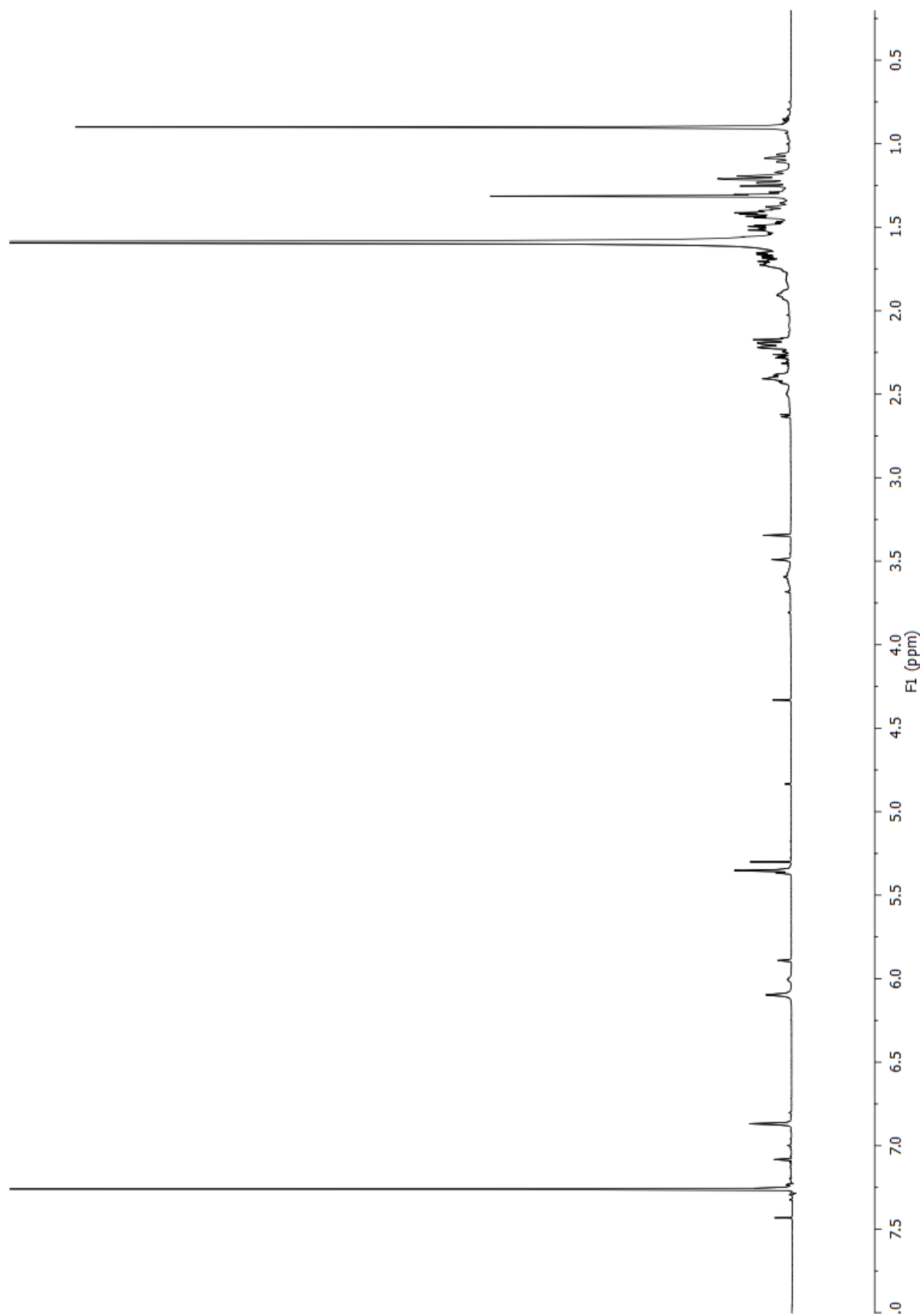


HMBC spectrum of luakuliide A methyl acetal (**34**) (600 MHz, CDCl₃).

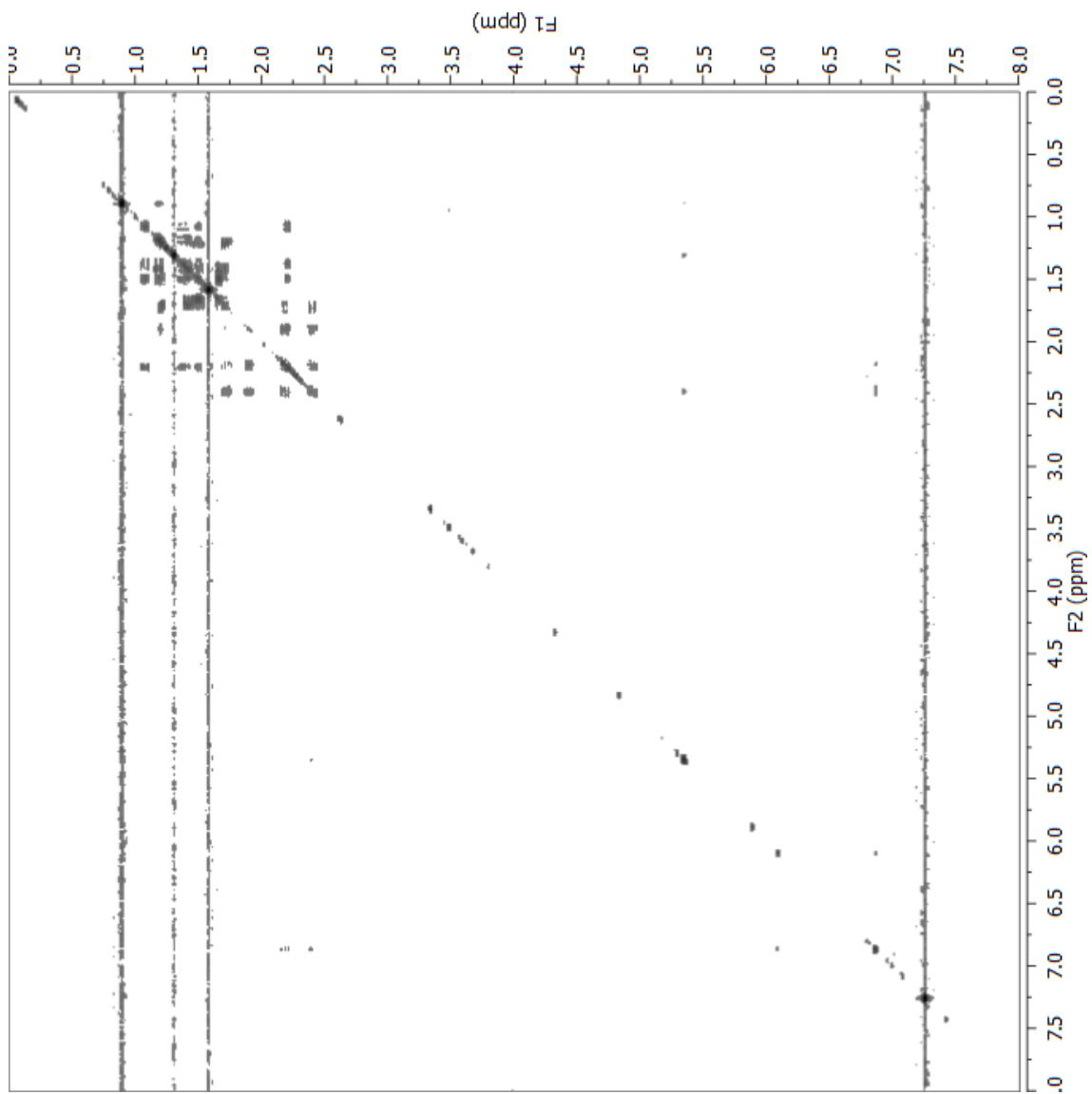


^{13}C NMR spectrum of luakuliide A methyl acetal (**34**) (150 MHz, CDCl_3).

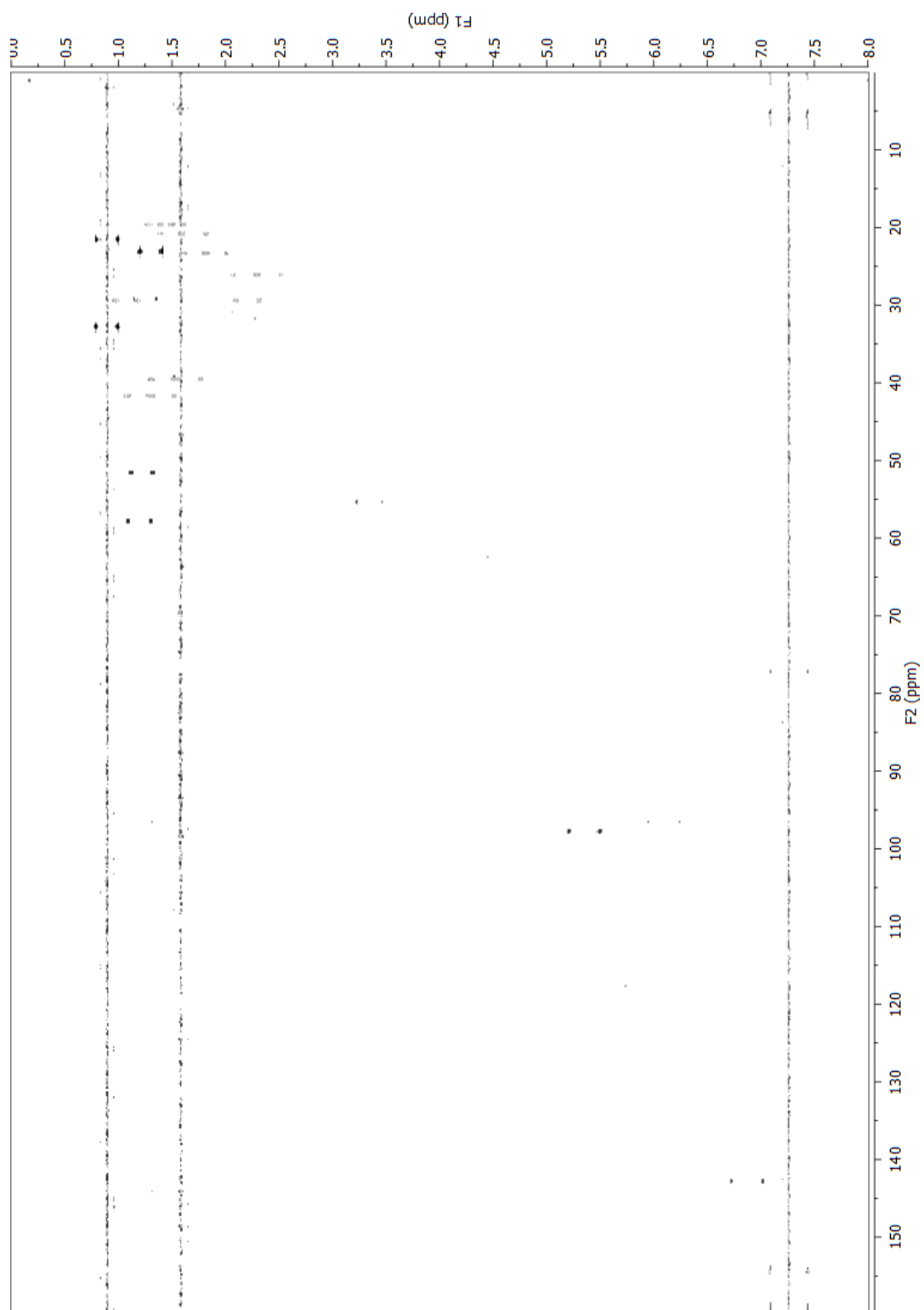
Luakuliide B



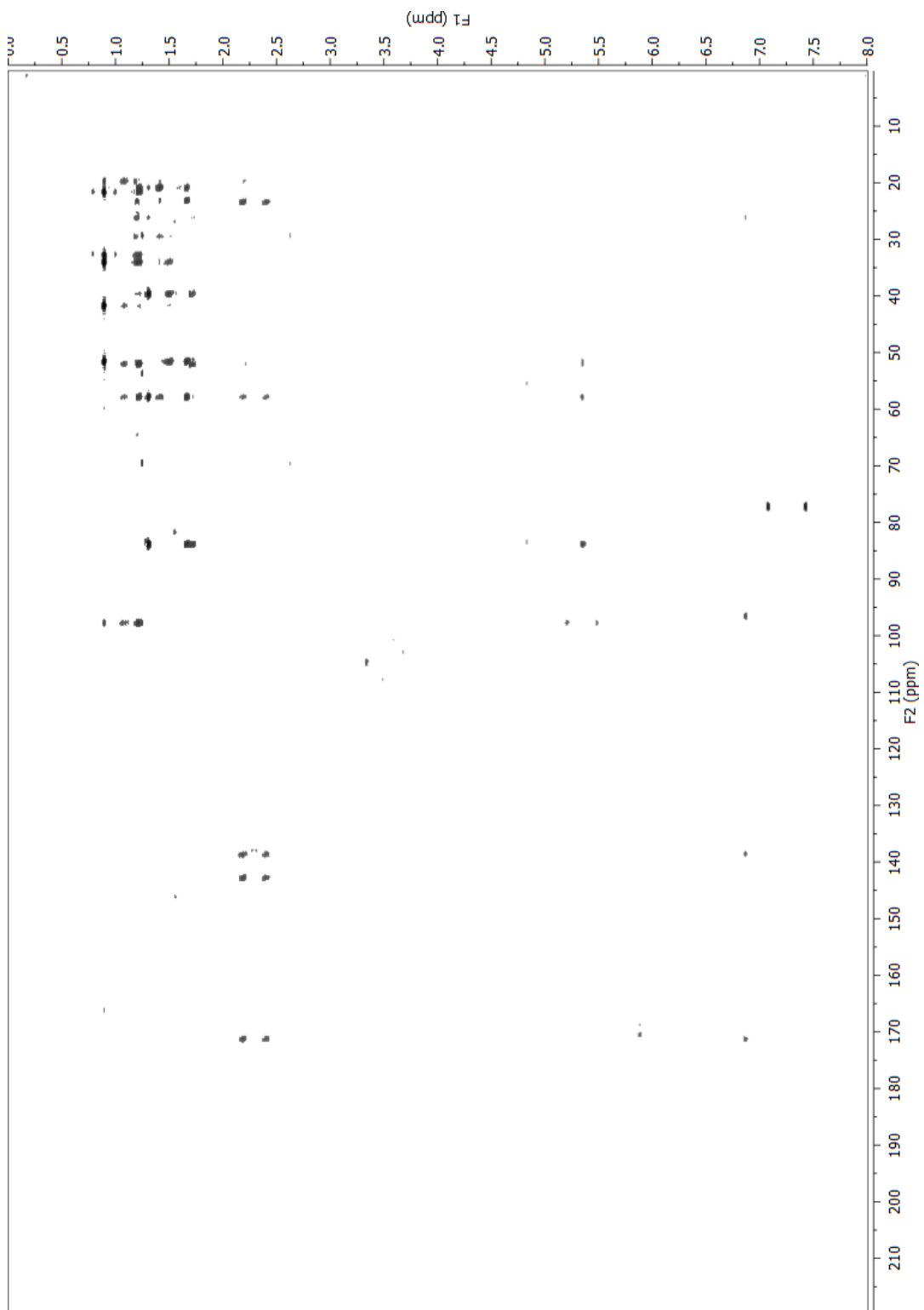
^1H NMR spectrum of Luakuliide B (**35**) (600 MHz, CDCl_3).



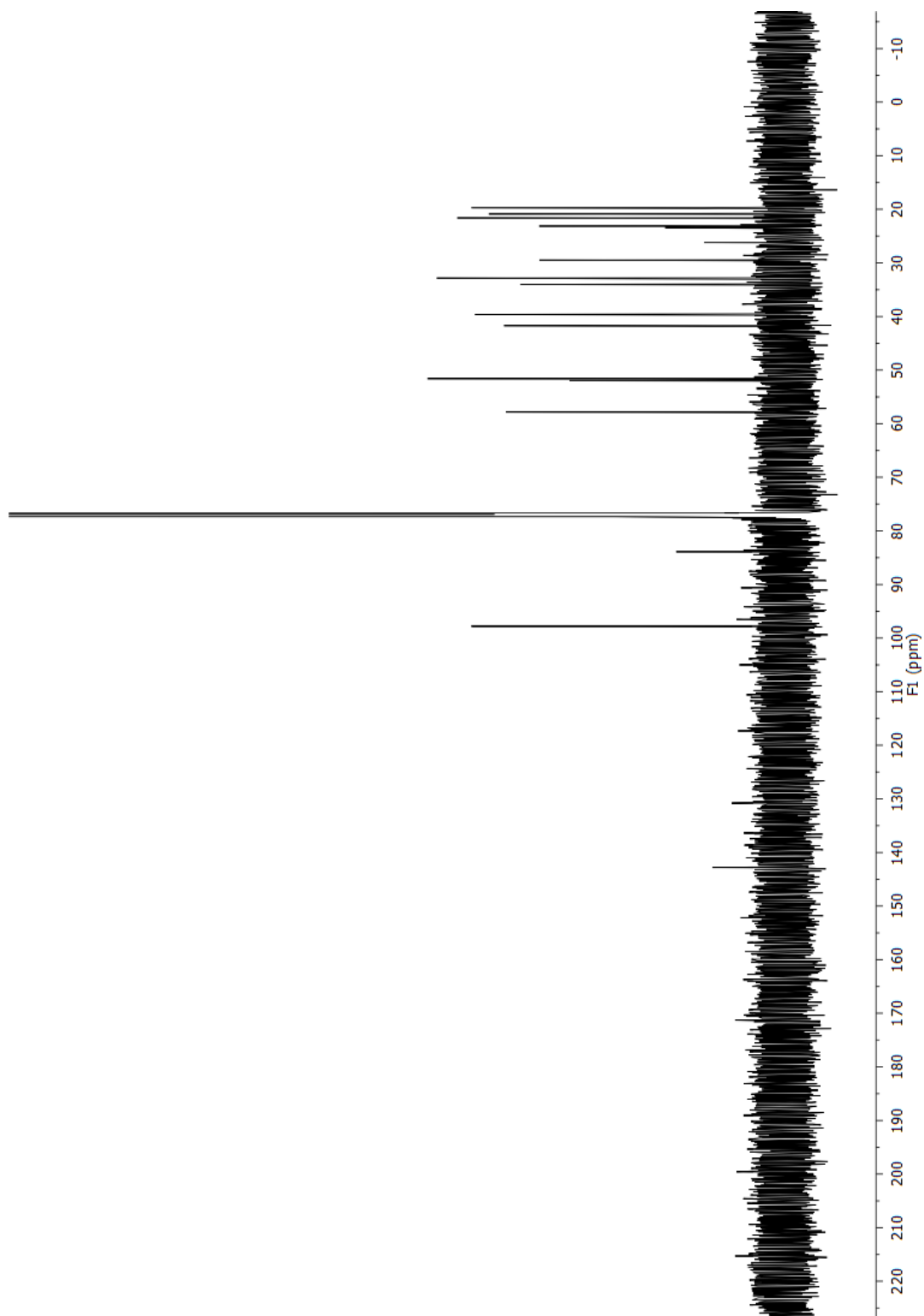
COSY spectrum of luakuliide B (**35**) (600 MHz, CDCl₃).



Fully-coupled HSQC spectrum of luakuliide B (**35**) (600 MHz, CDCl₃).

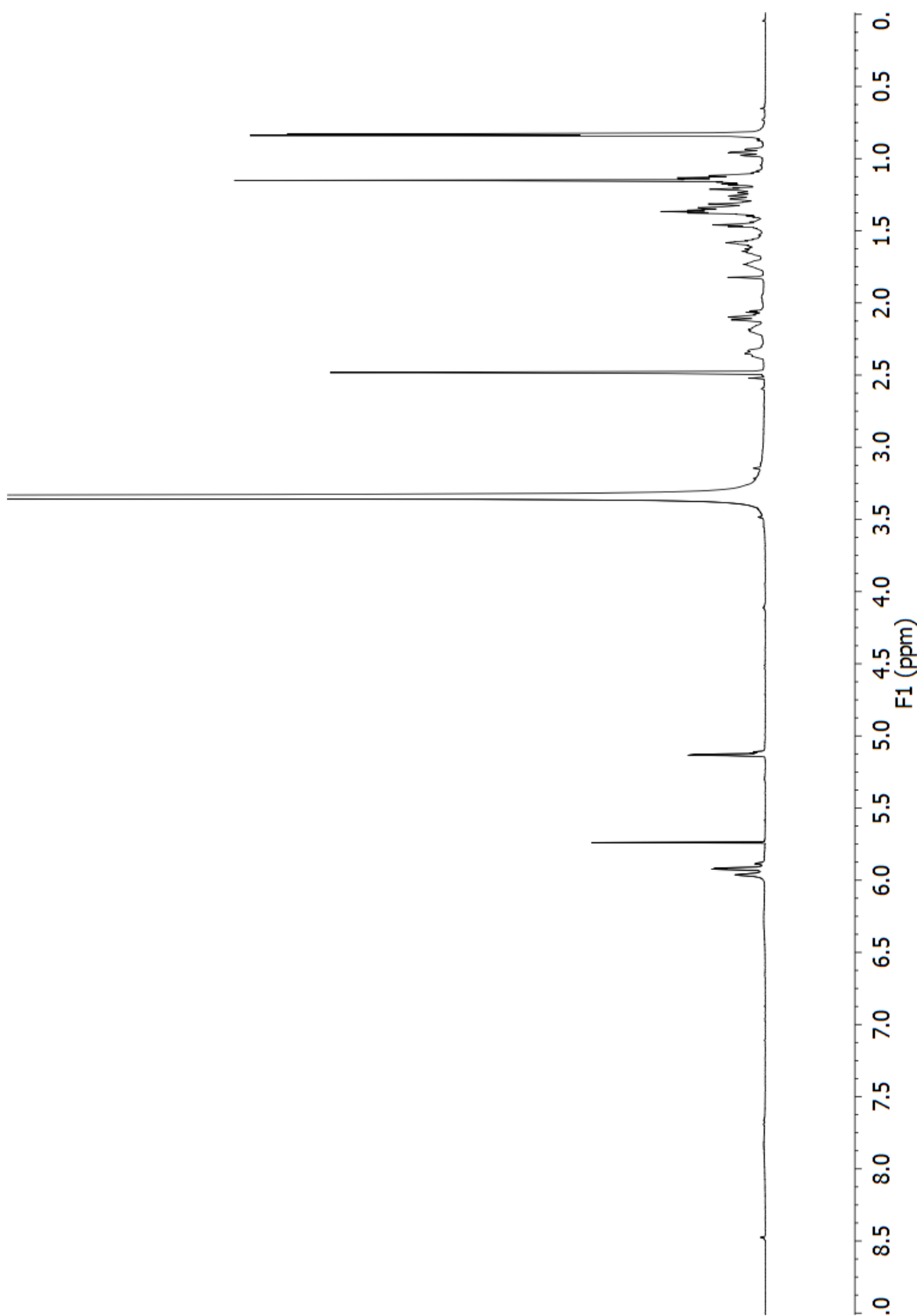


HMBC spectrum of luakuliide B (**35**) (600 MHz, CDCl₃).

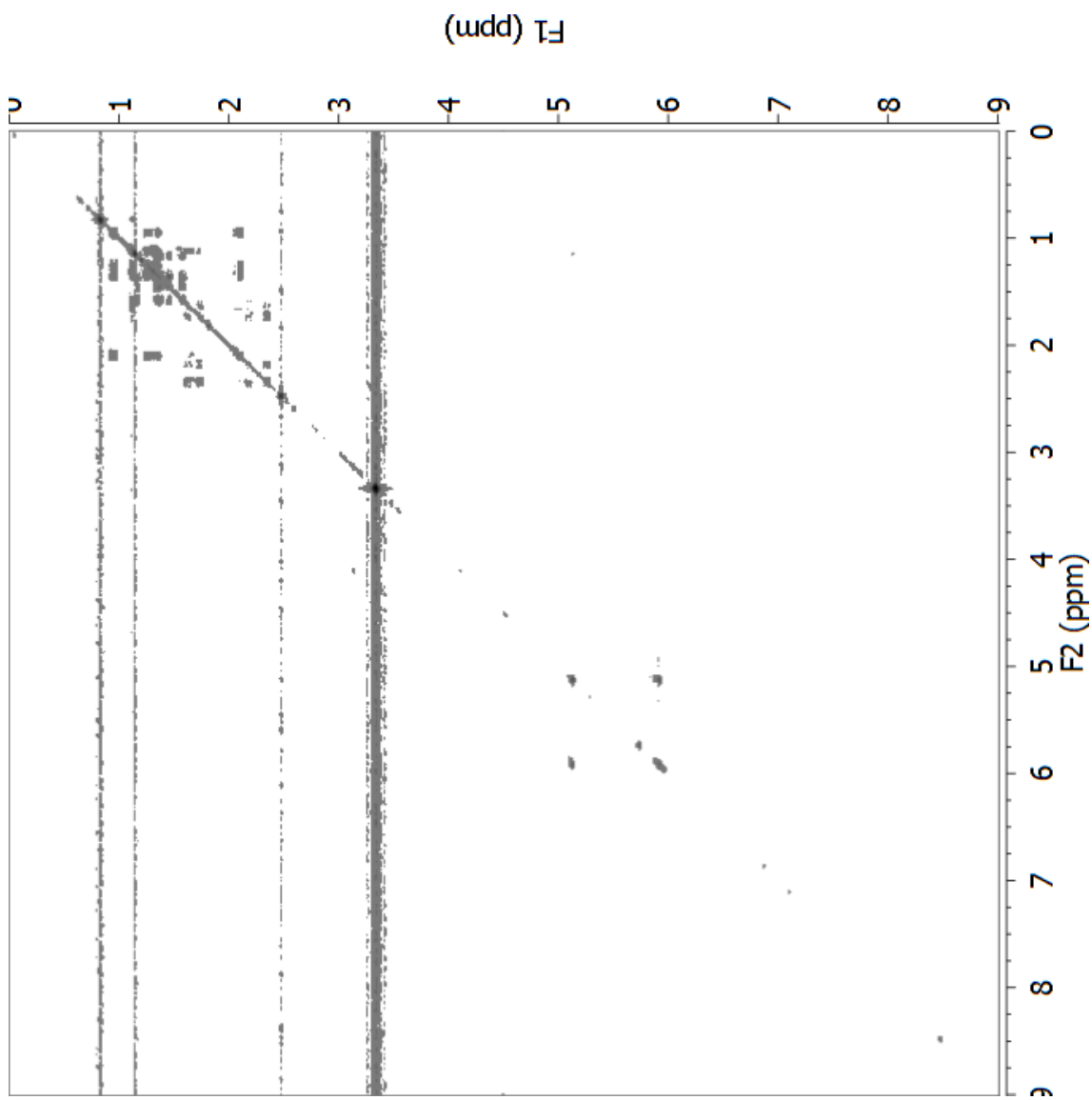


^{13}C NMR spectrum of luakuliide B (**35**) (150 MHz, CDCl_3).

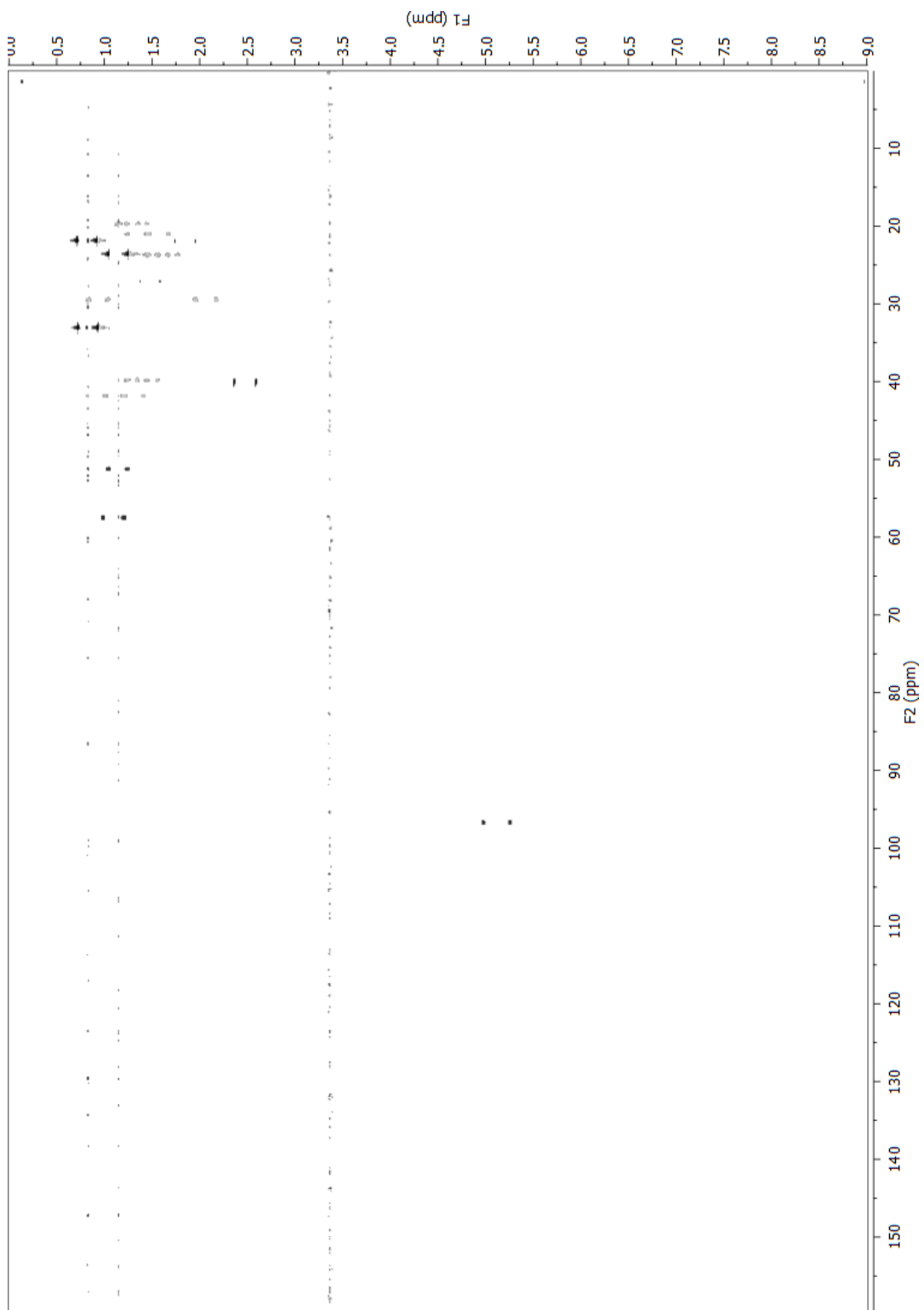
Luakuliide B



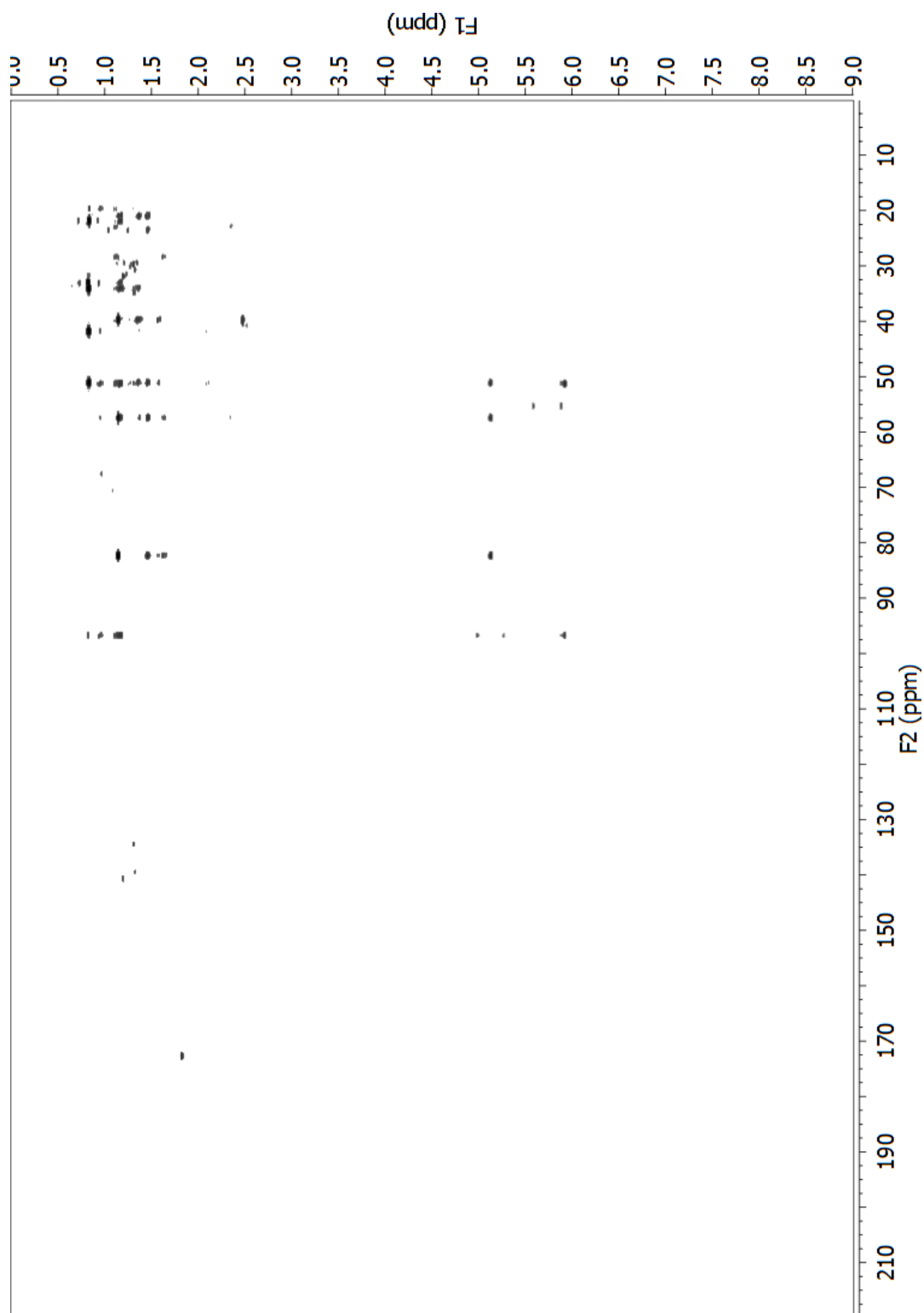
^1H NMR spectrum of Luakuliide B (**35**) (600 MHz, DMSO)



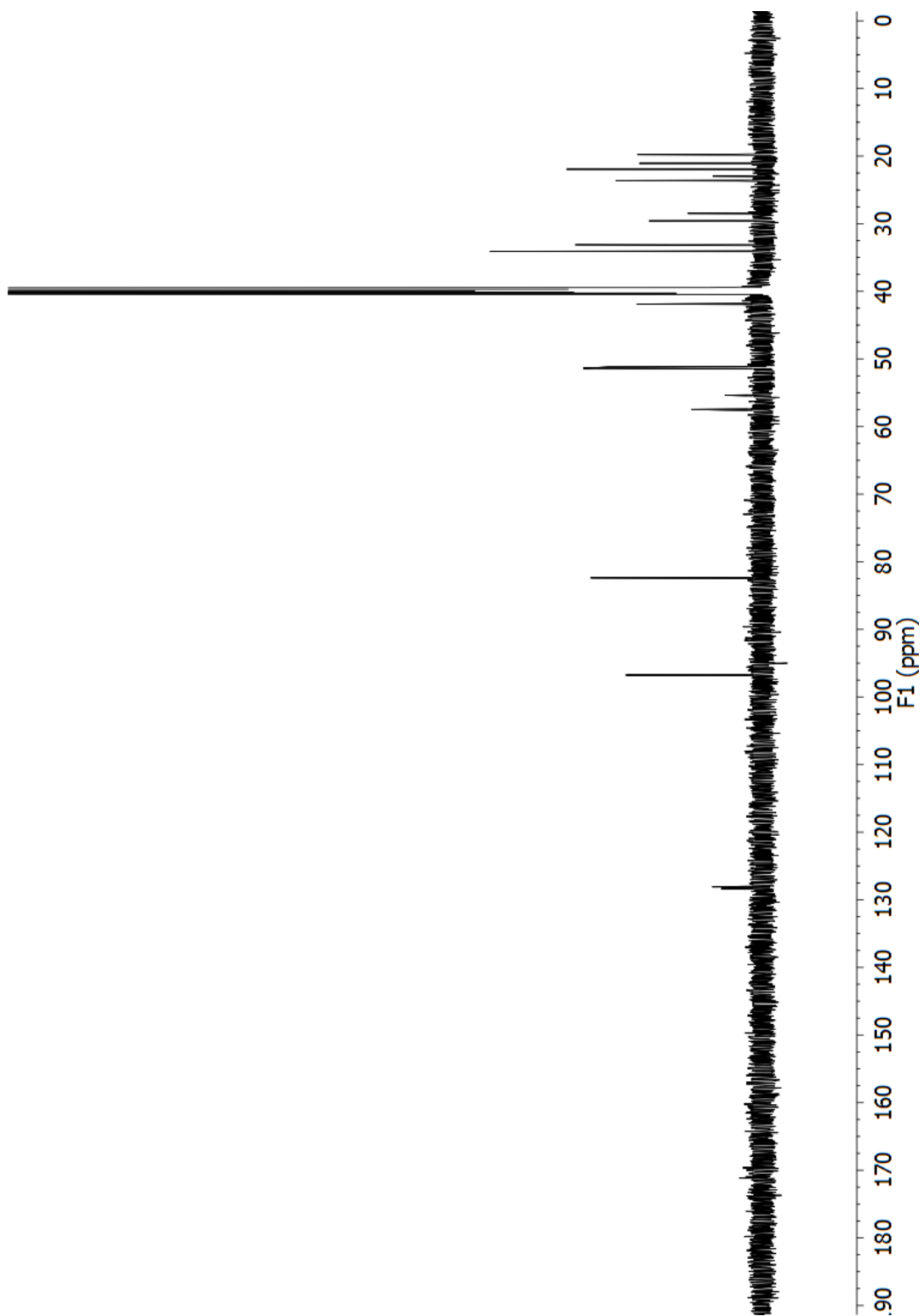
COSY spectrum of luakuliide B (**35**) (600 MHz, DMSO)



Fully-coupled HSQC spectrum of luakuliide B (**35**) (600 MHz, DMSO)

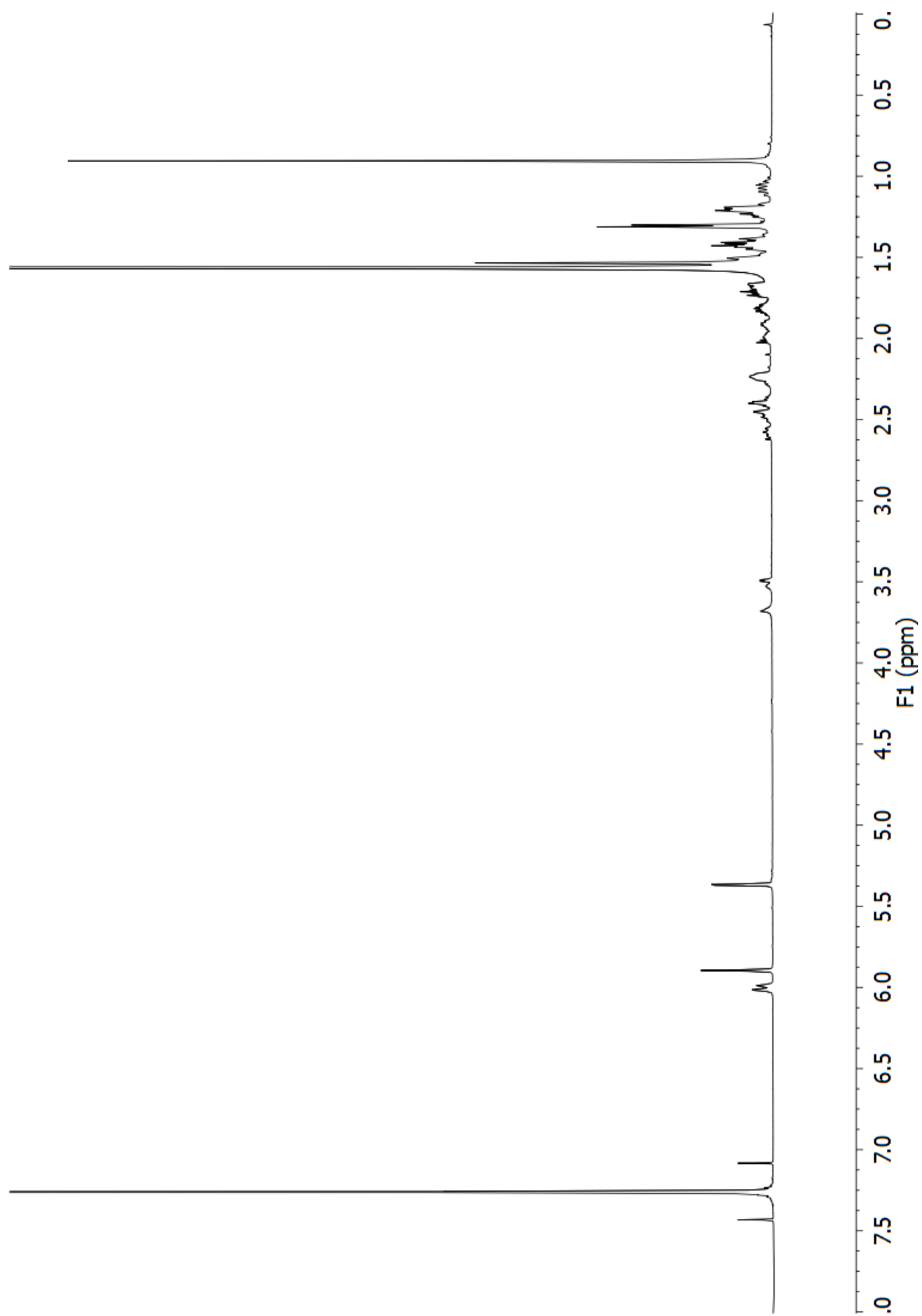


HMBC spectrum of luakuliide B (**35**) (600 MHz, DMSO)

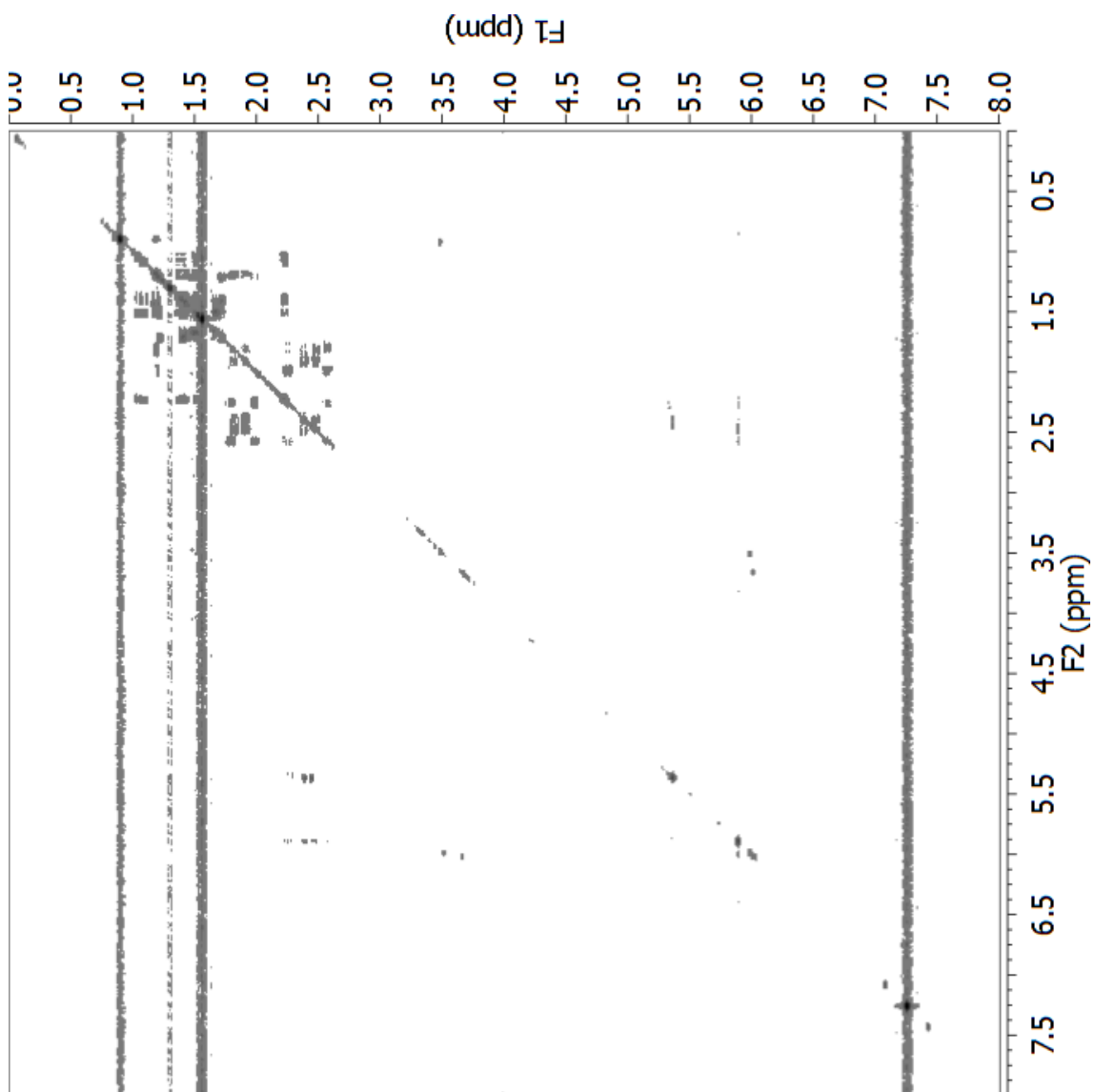


^{13}C NMR spectrum of luakuliide B (**35**) (150 MHz, DMSO)

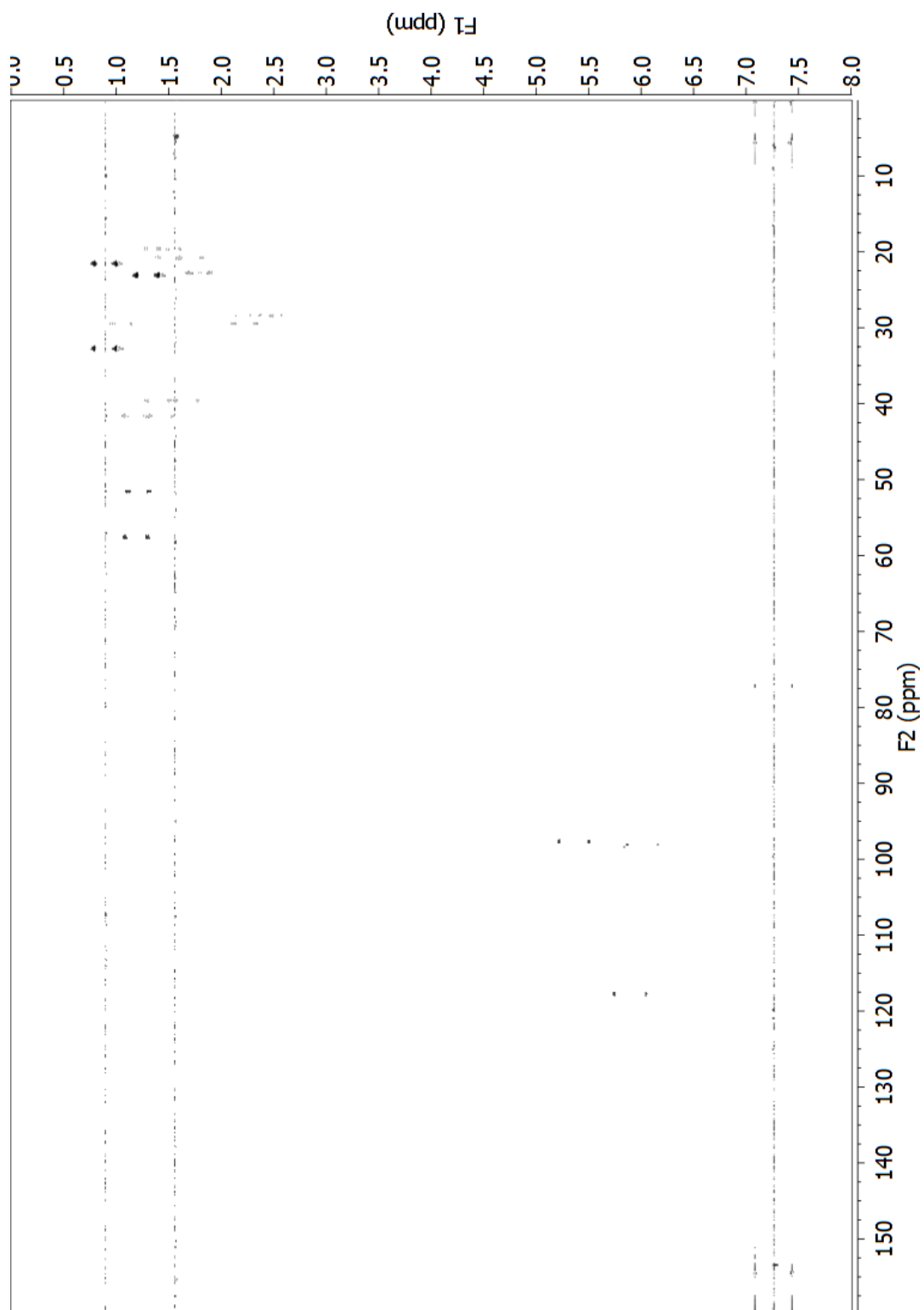
Luakuliide C



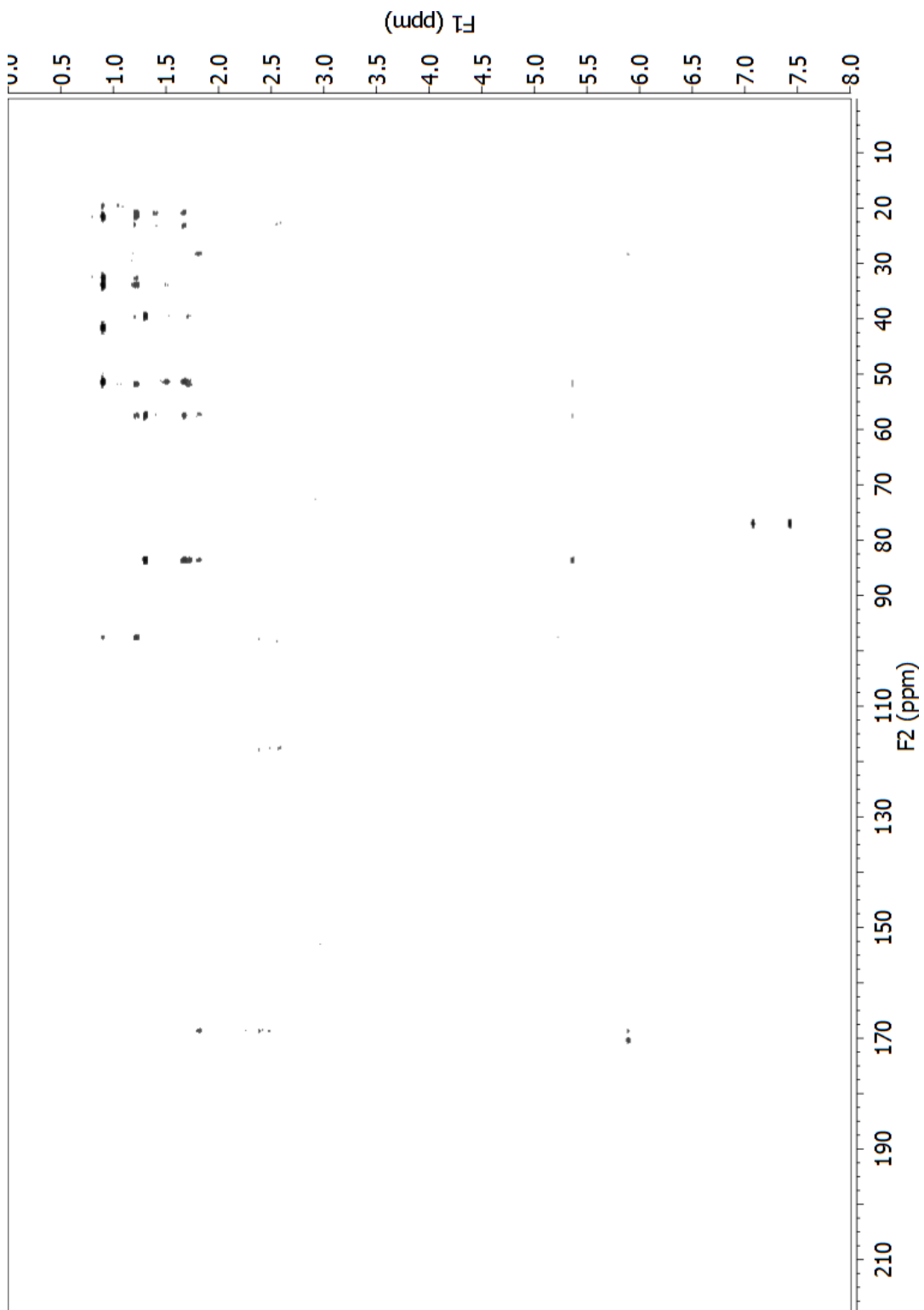
^1H NMR spectrum of Luakuliide C (**36**) (600 MHz, CDCl_3).



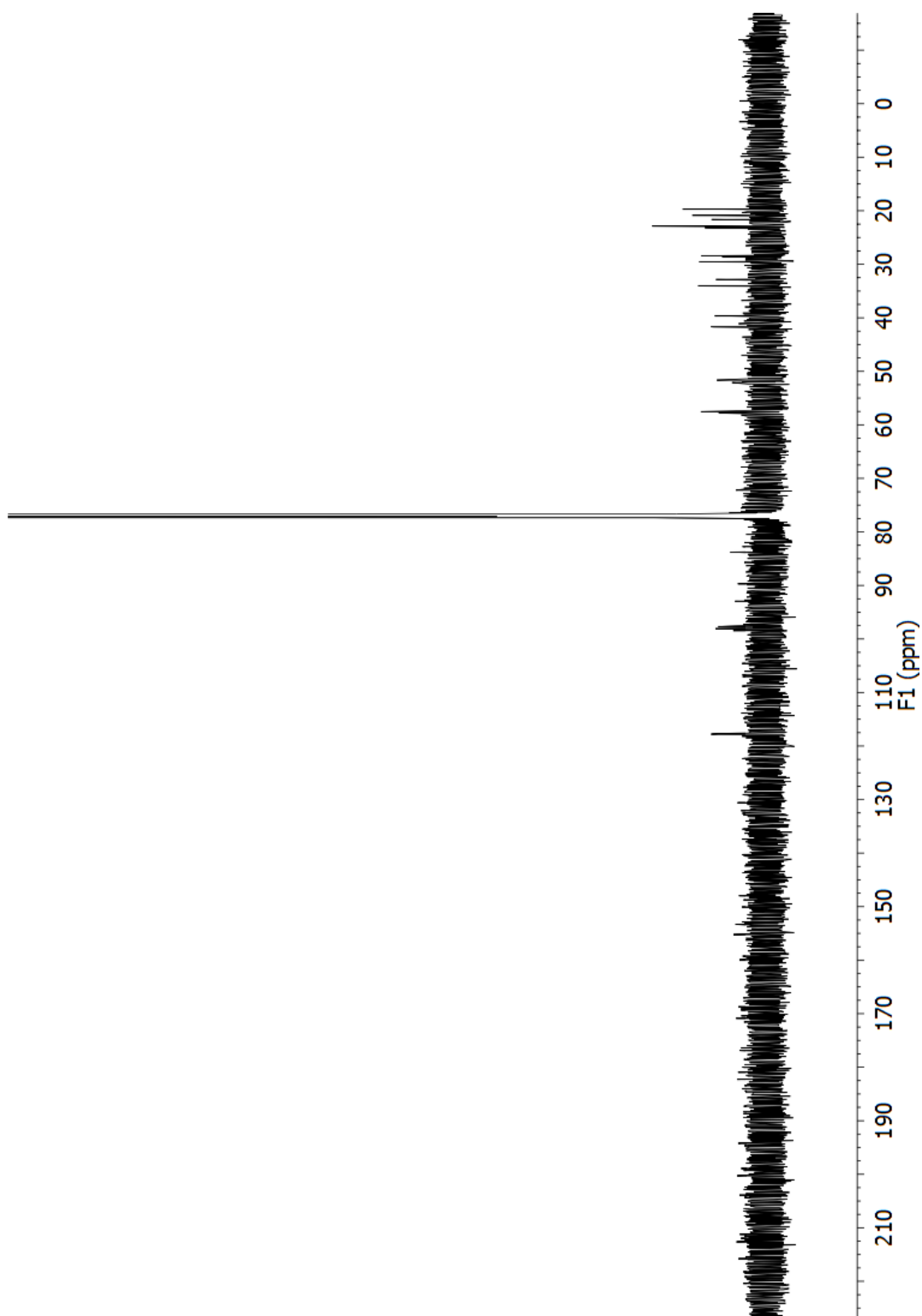
COSY spectrum of luakuliide C (**36**) (600 MHz, CDCl₃).



Fully-coupled HSQC spectrum of luakuliide C (**36**) (600 MHz, CDCl₃).

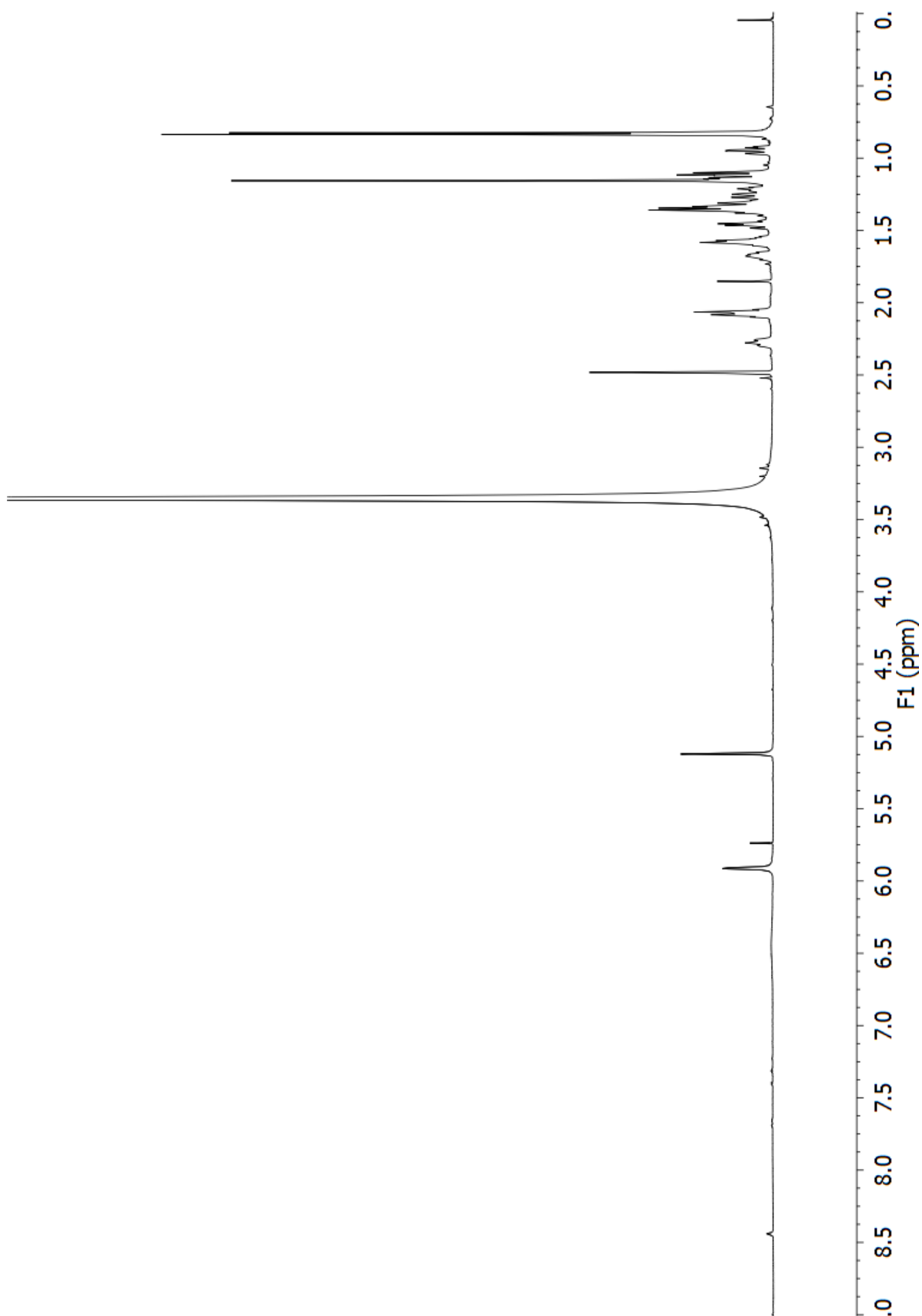


HMBC spectrum of luakuliide C (**36**) (600 MHz, CDCl₃).

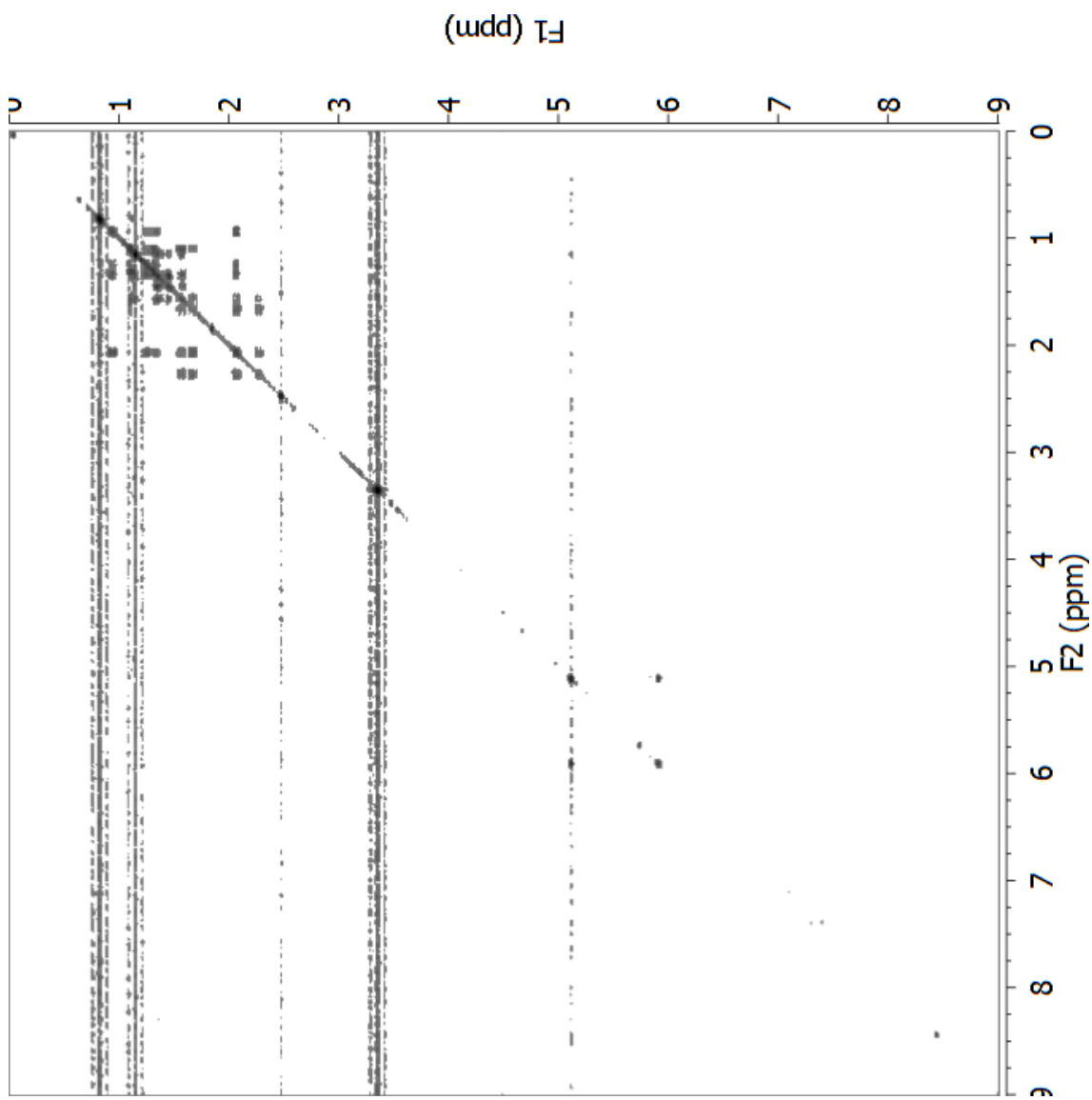


^{13}C NMR spectrum of luakuliide C (**36**) (150 MHz, CDCl_3).

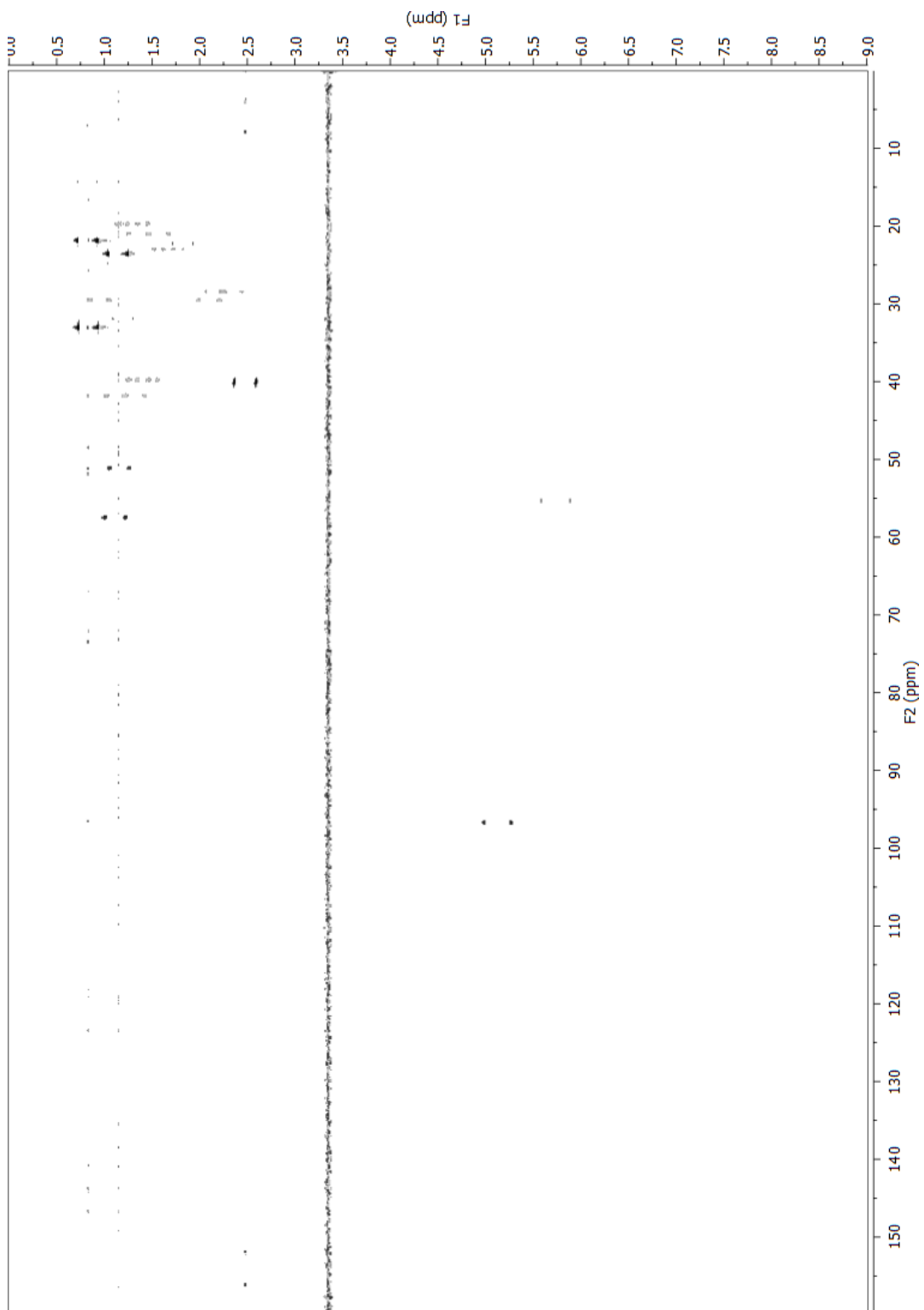
Luakuliide C



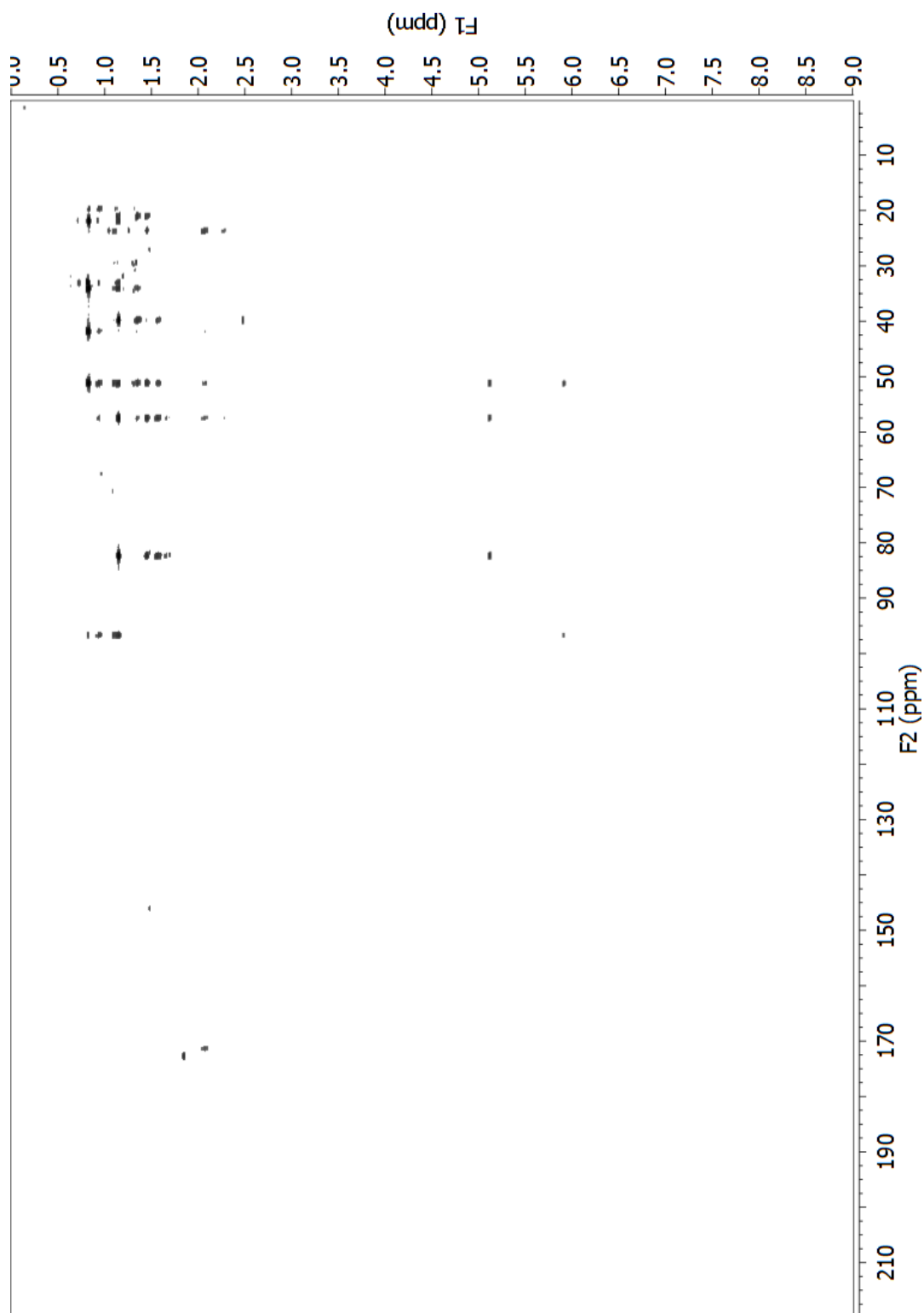
^1H NMR spectrum of Luakuliide C (**36**) (600 MHz, DMSO)



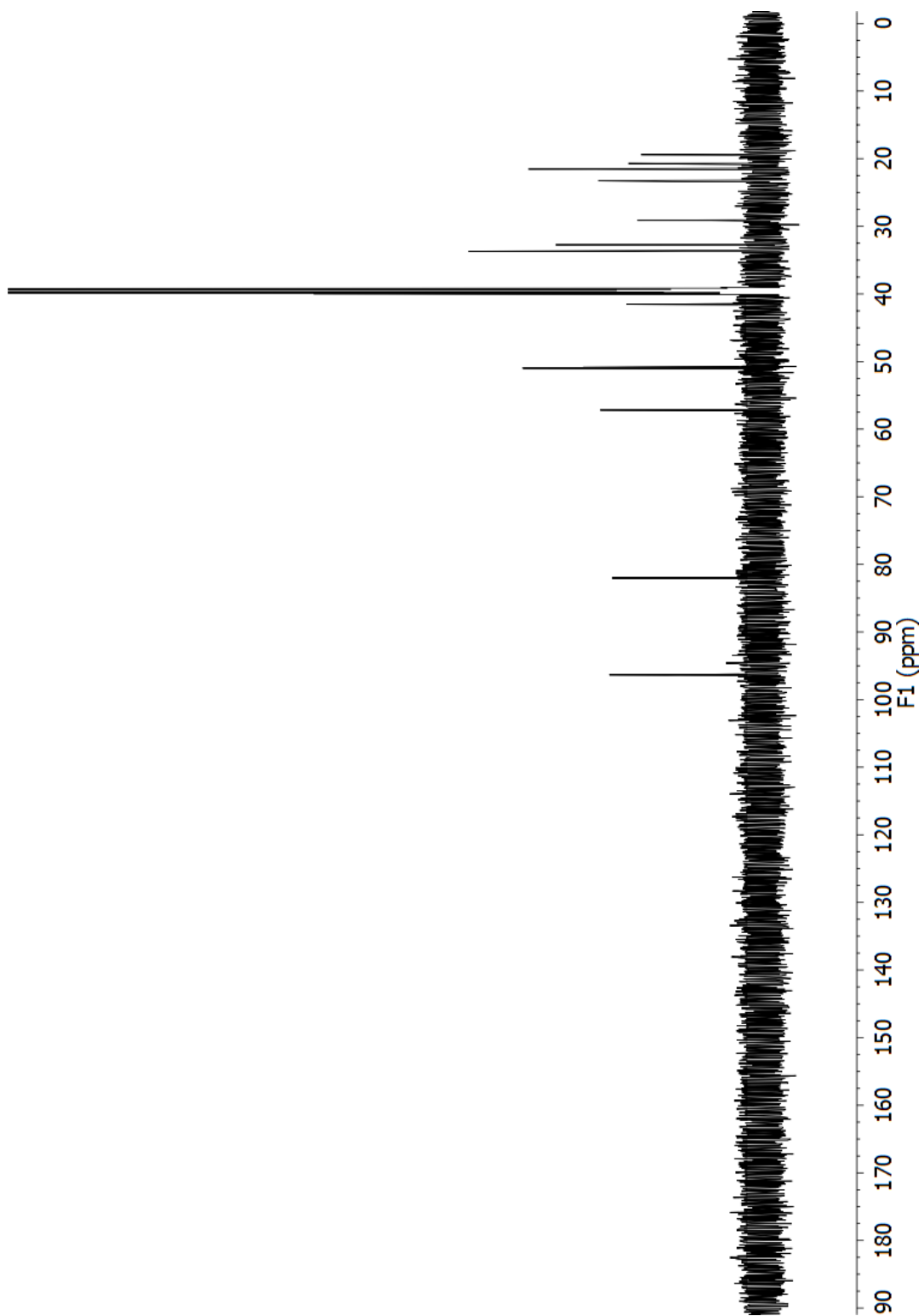
COSY spectrum of luakuliide C (**36**) (600 MHz, DMSO)



Fully-coupled HSQC spectrum of luakuliide C (**36**) (600 MHz, DMSO)



HMBC spectrum of luakuliide C (**36**) (600 MHz, DMSO)

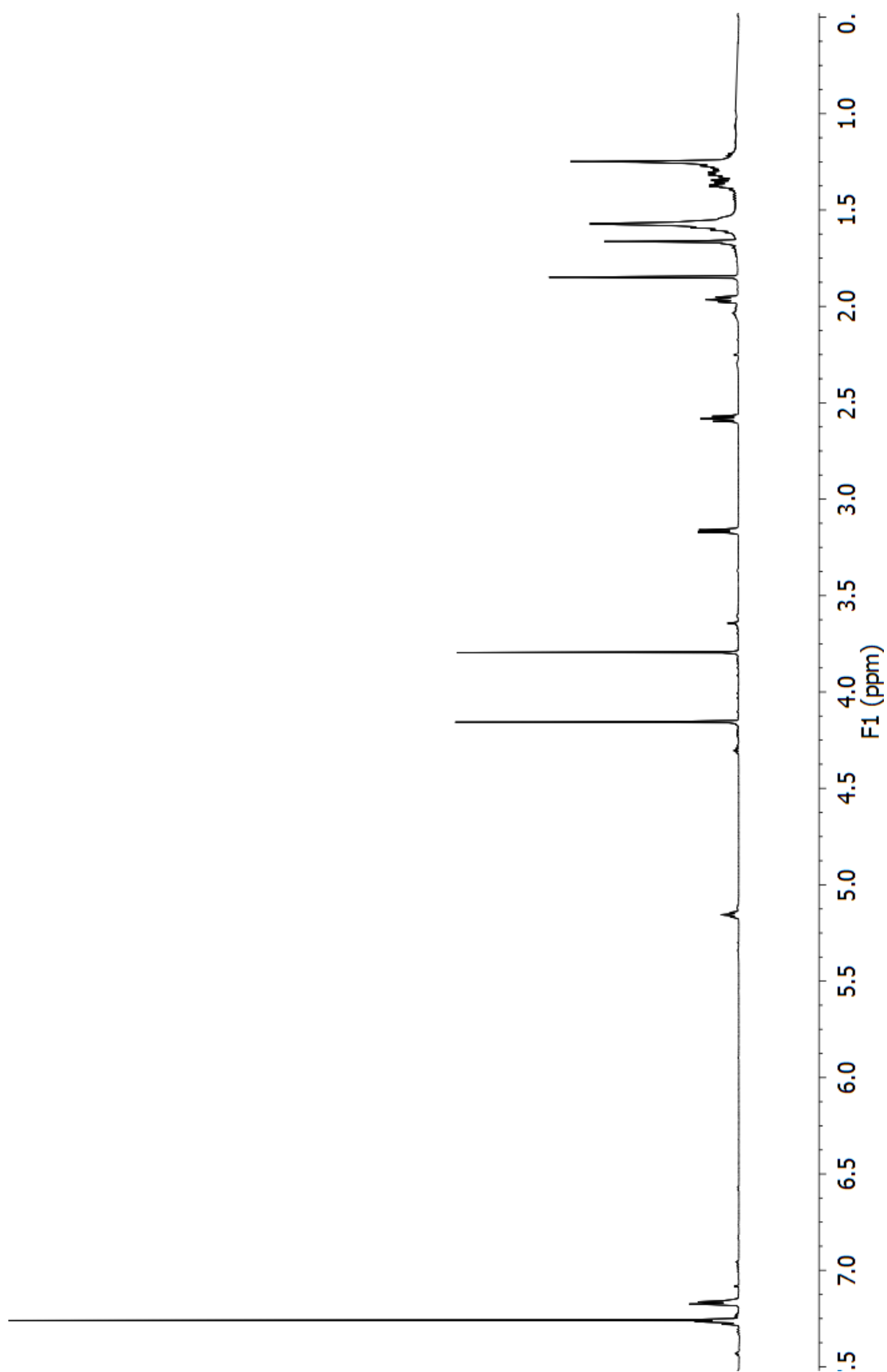


^{13}C NMR spectrum of luakuliide C (**36**) (150 MHz, DMSO)

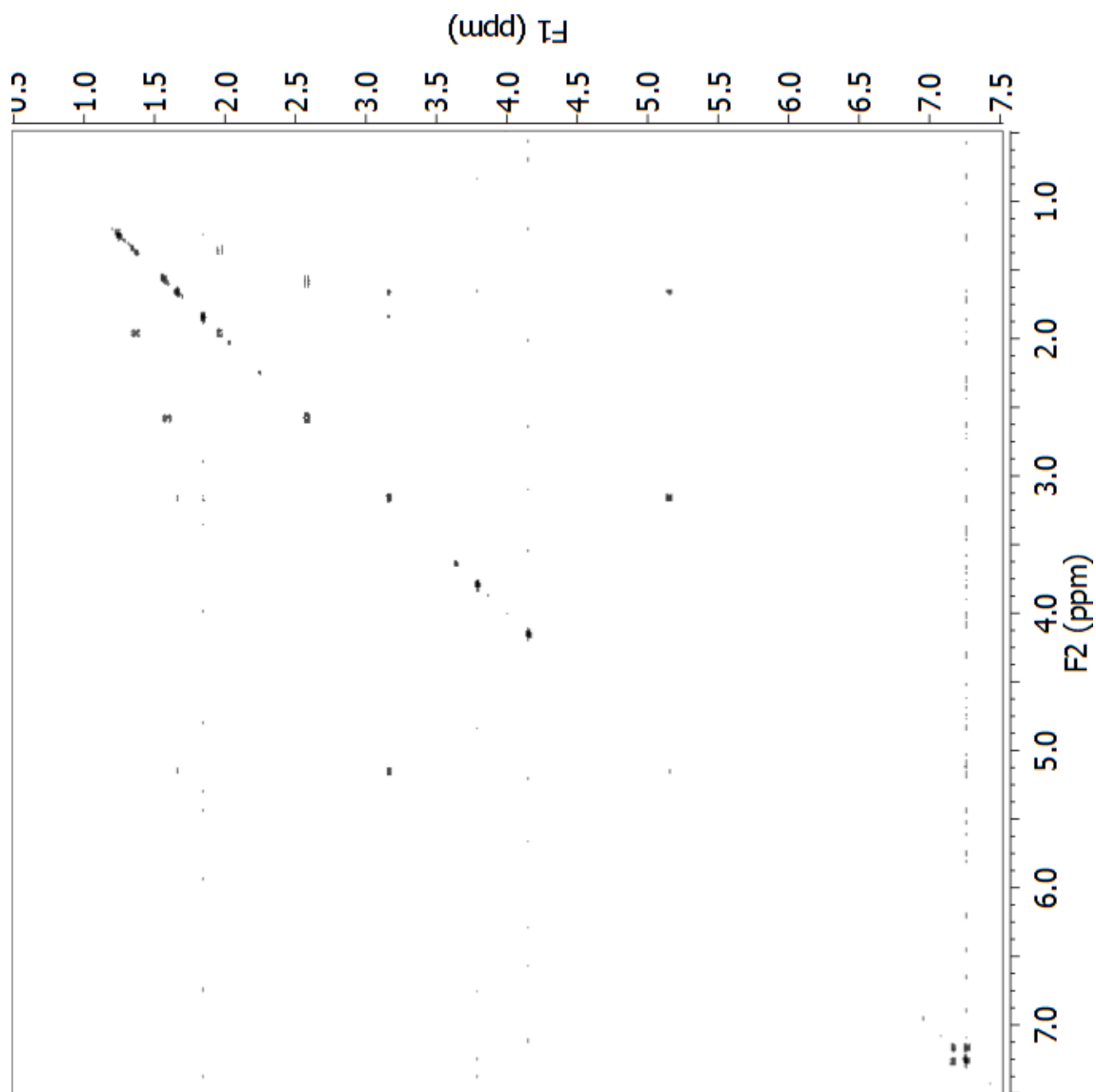
Appendix F

NMR Spectra of Lehualides E–K

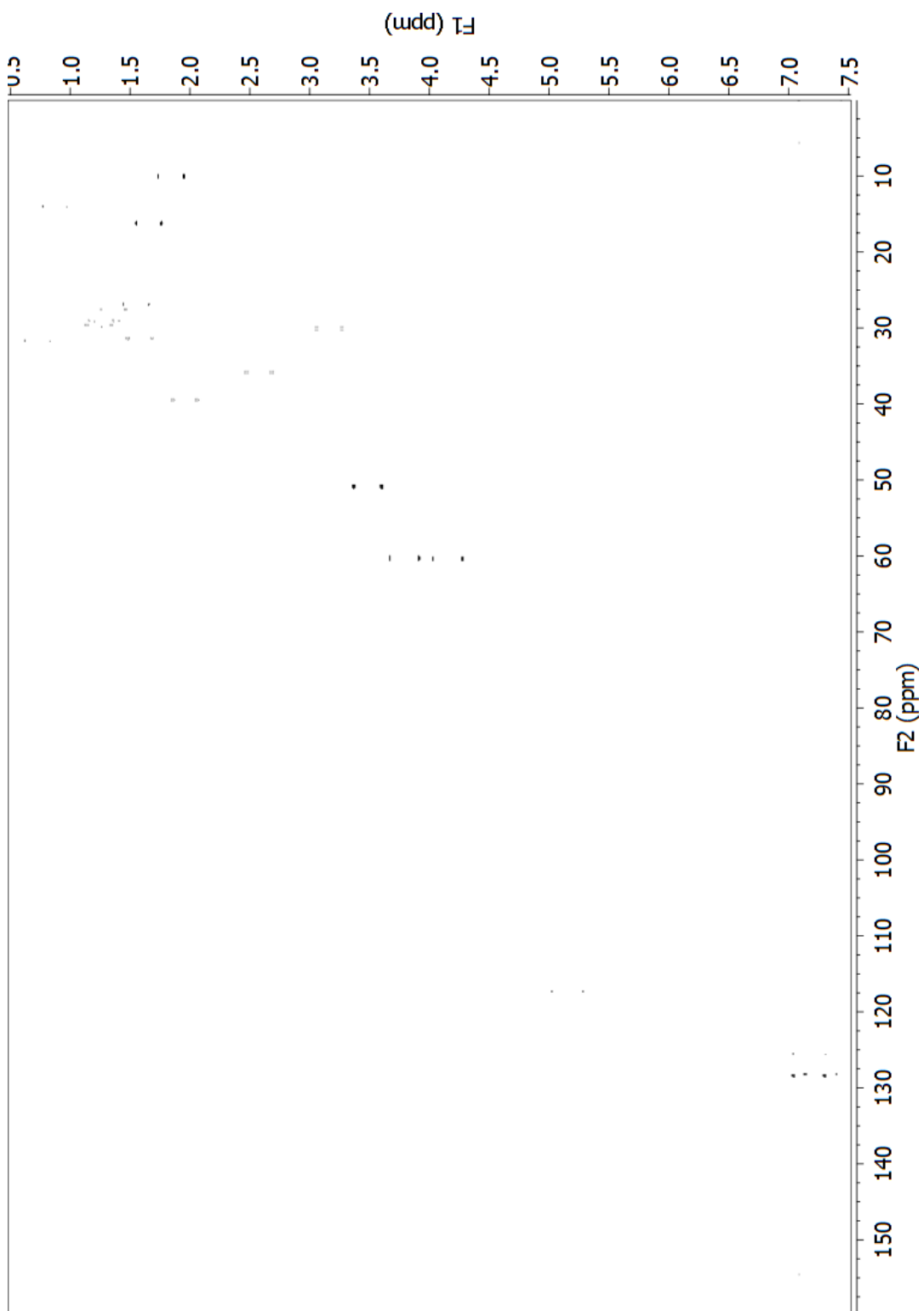
Lehualide E



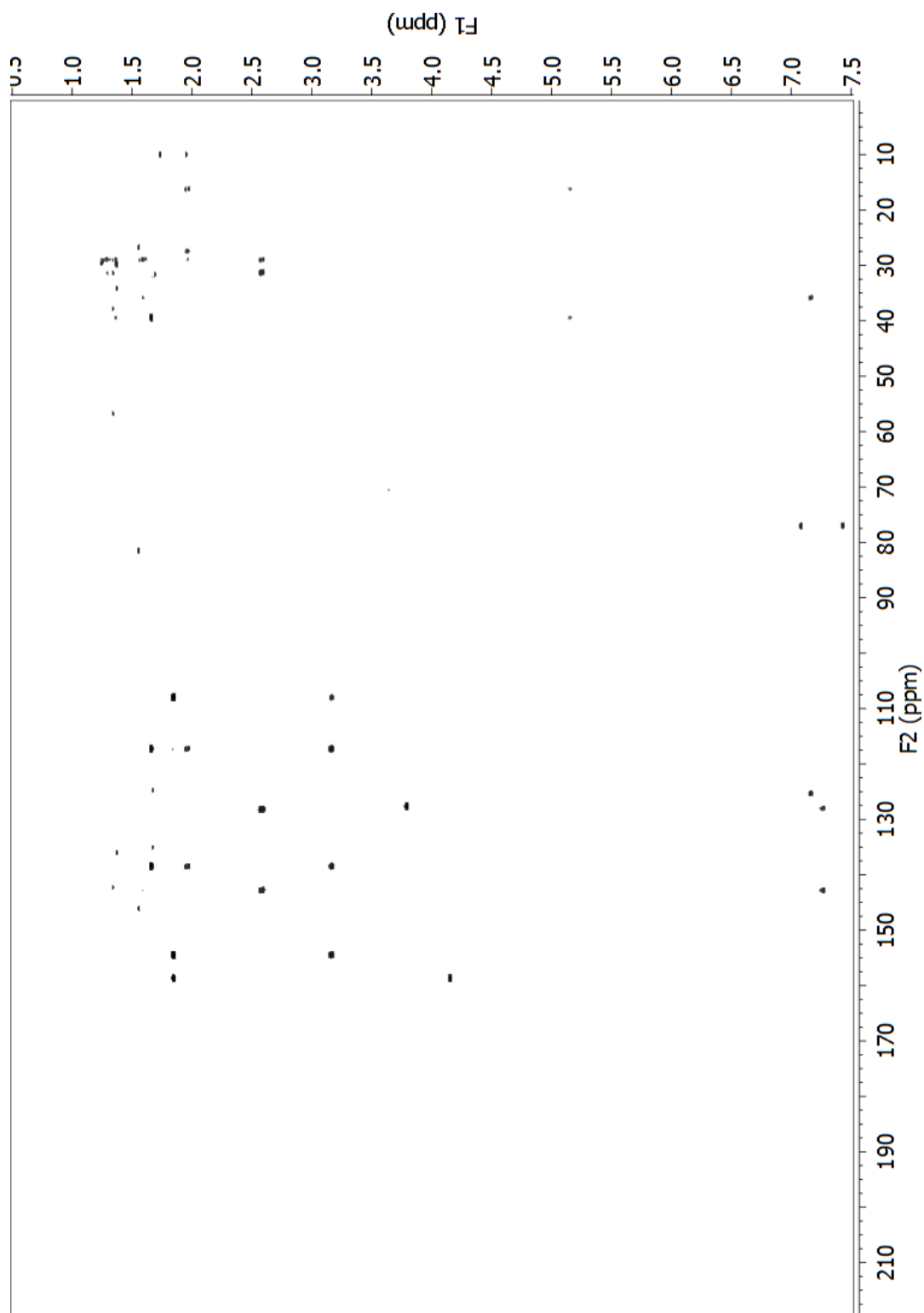
^1H NMR spectrum of lehualide E (**69**) (600 MHz, CDCl_3).



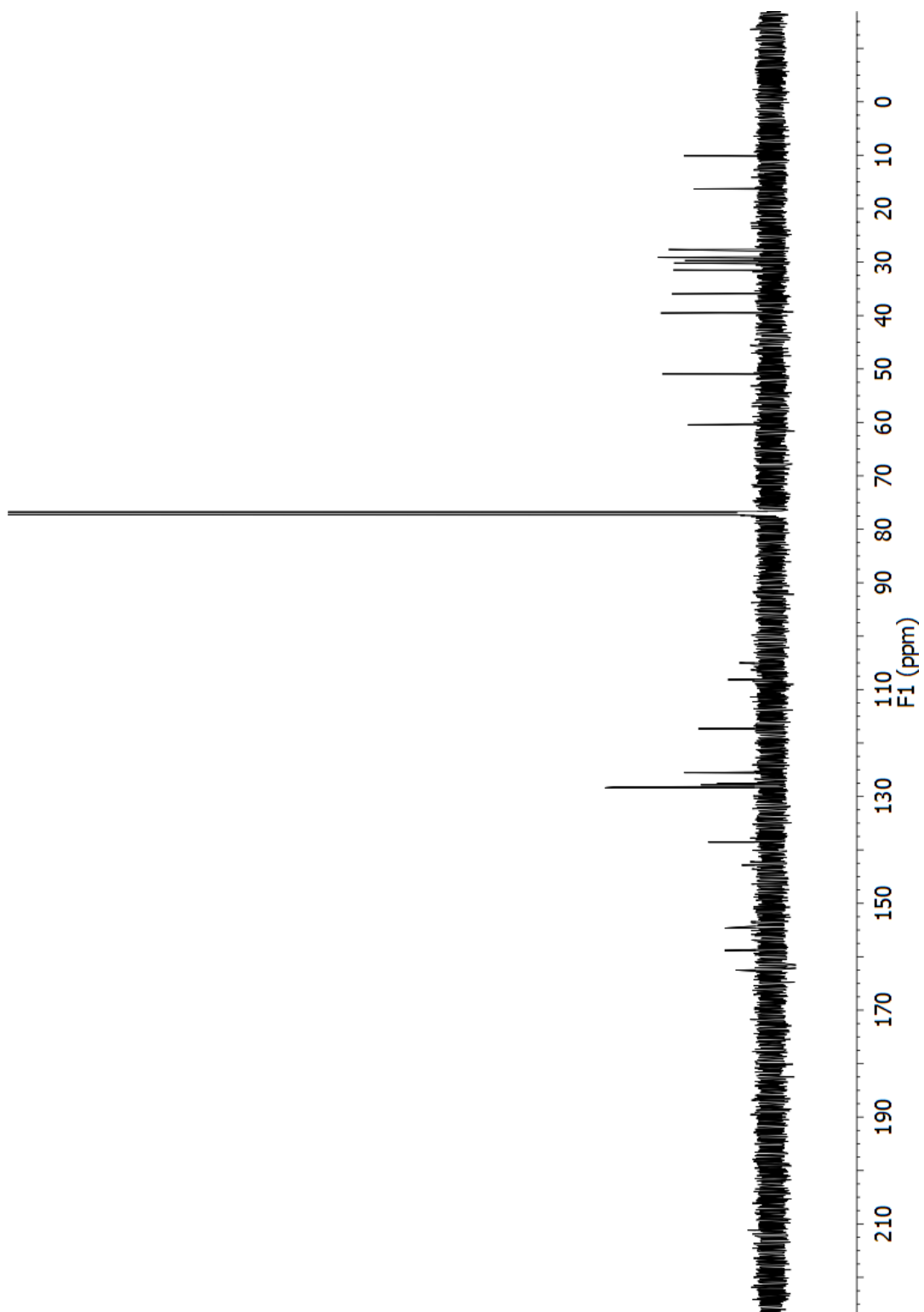
COSY spectrum of lehuaide E (**69**) (600 MHz, CDCl₃).



Fully-coupled HSQC spectrum of lehuaide E (**69**) (600 MHz, CDCl₃).

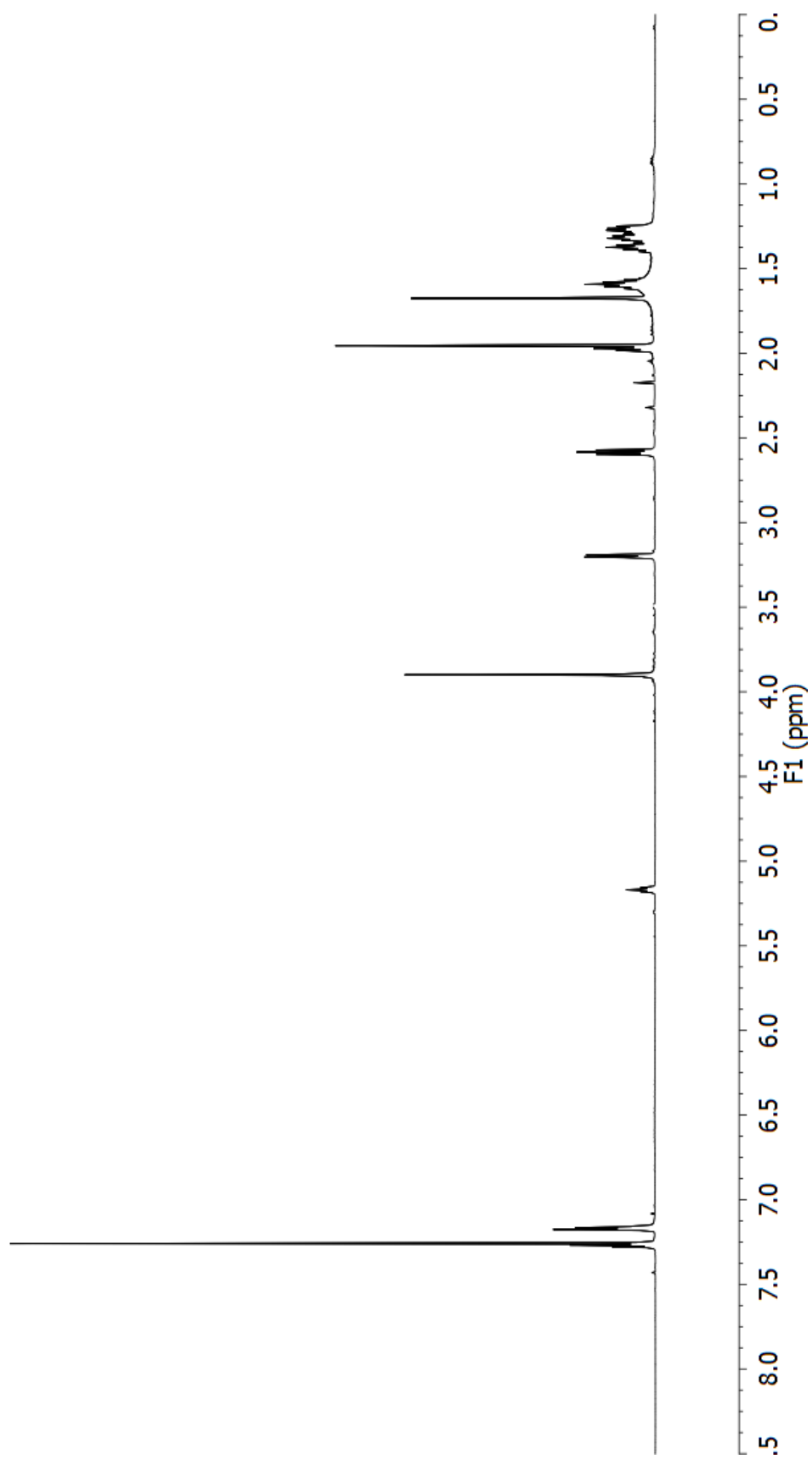


HMBC spectrum of lehuaide E (**69**) (600 MHz, CDCl₃).

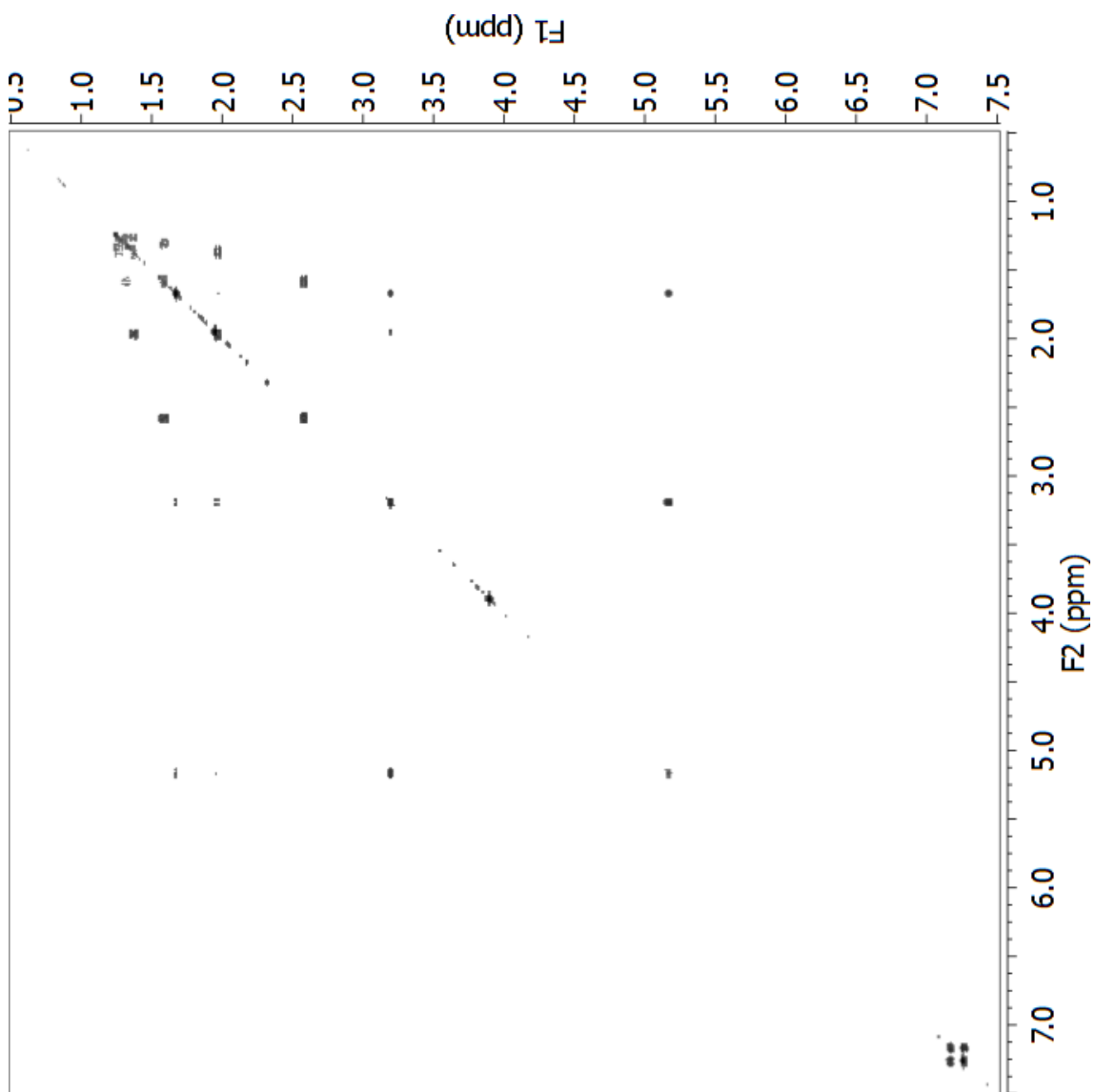


^{13}C NMR spectrum of lehuaide E (**69**) (150 MHz, CDCl_3).

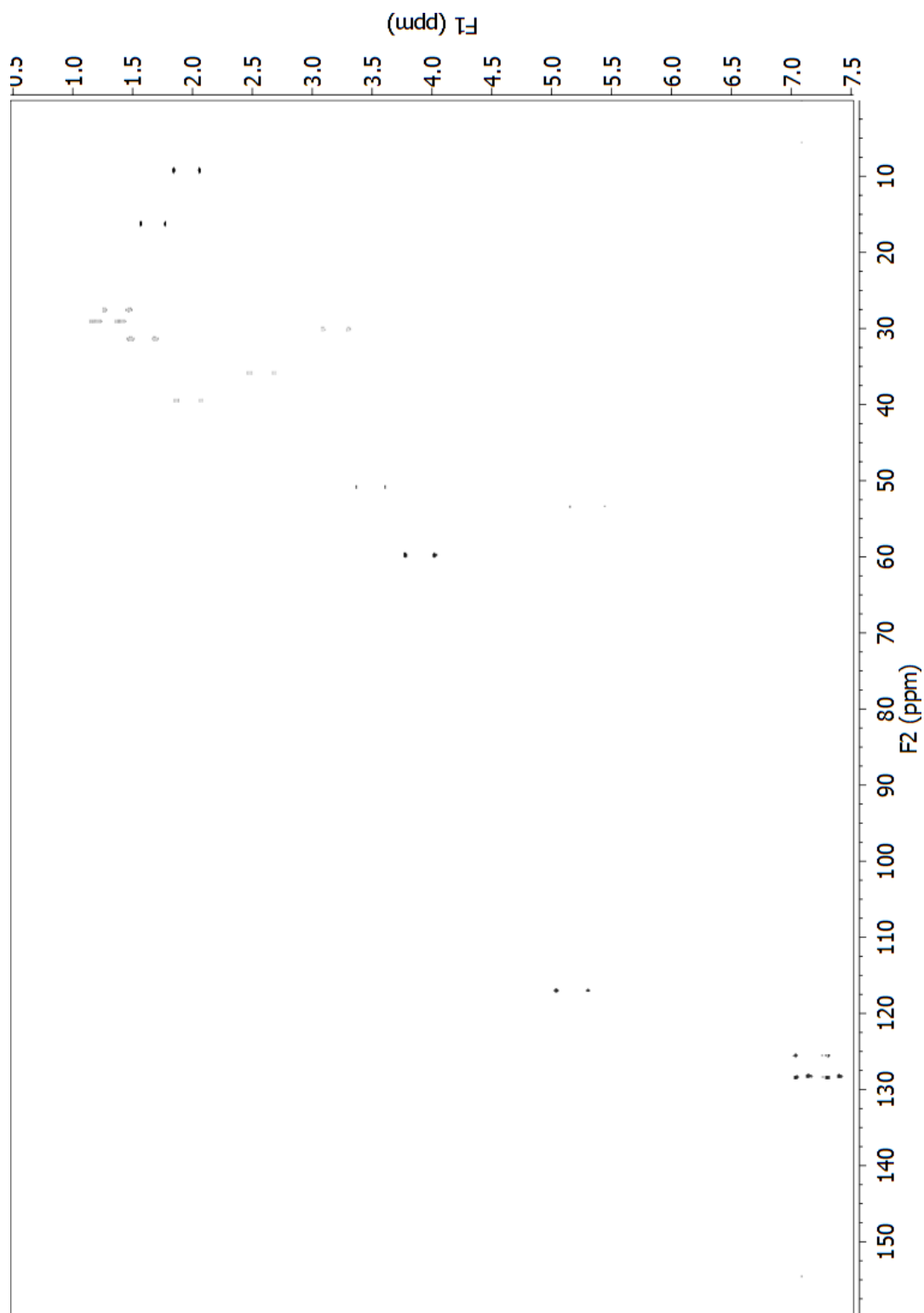
Lehualide F



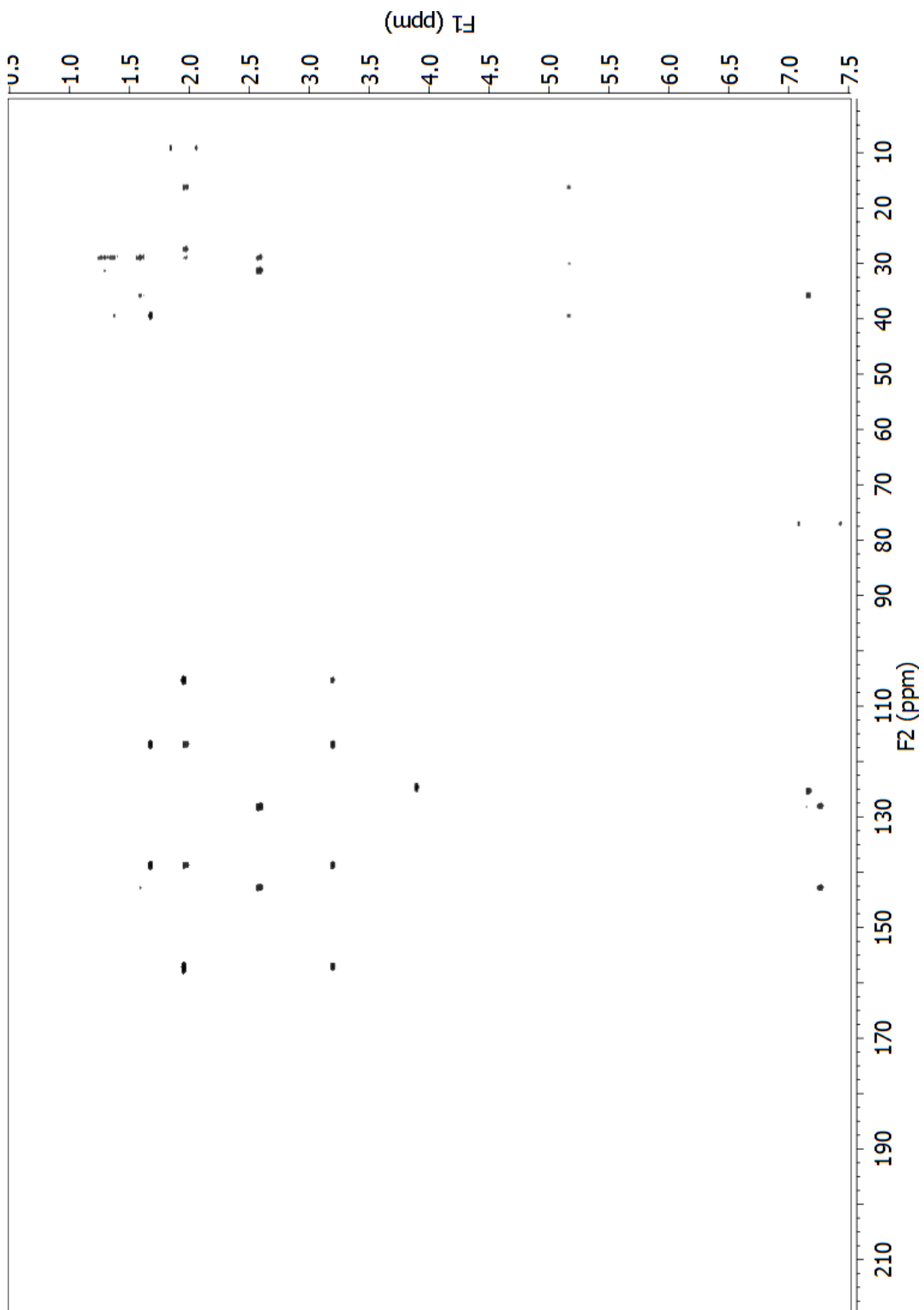
¹H NMR spectrum of lehualide F (**70**) (600 MHz, CDCl₃).



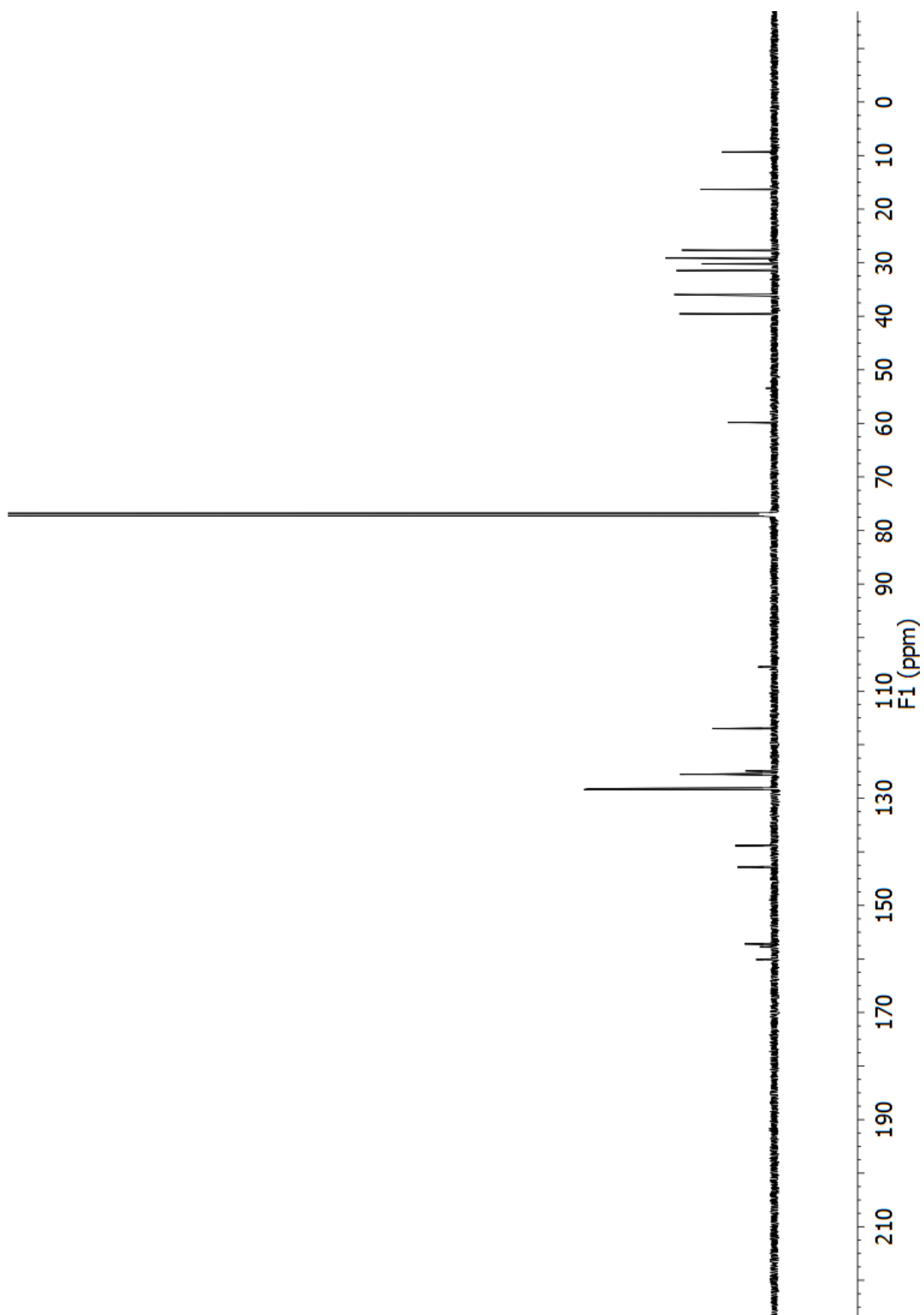
COSY spectrum of lehualide F (**70**) (600 MHz, CDCl₃).



Fully-coupled HSQC spectrum of lehuaide F (**70**) (600 MHz, CDCl₃).

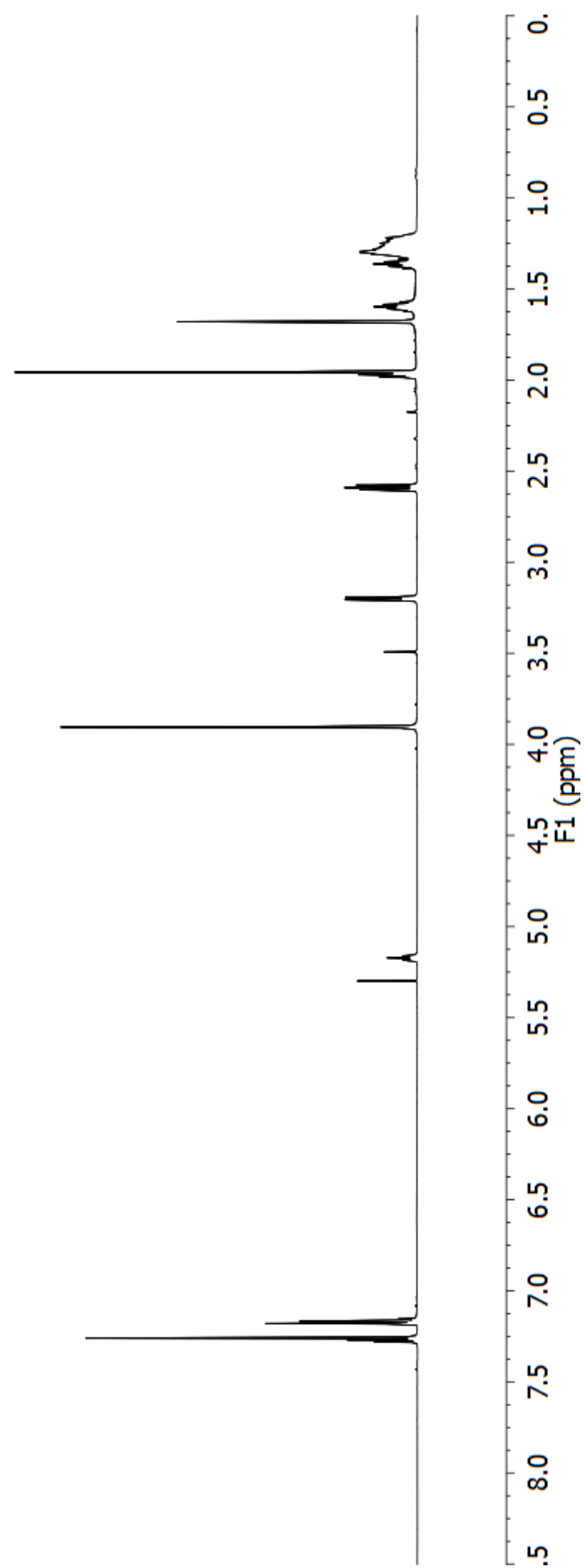


HMBC spectrum of lehuaide F (**70**) (600 MHz, CDCl₃).

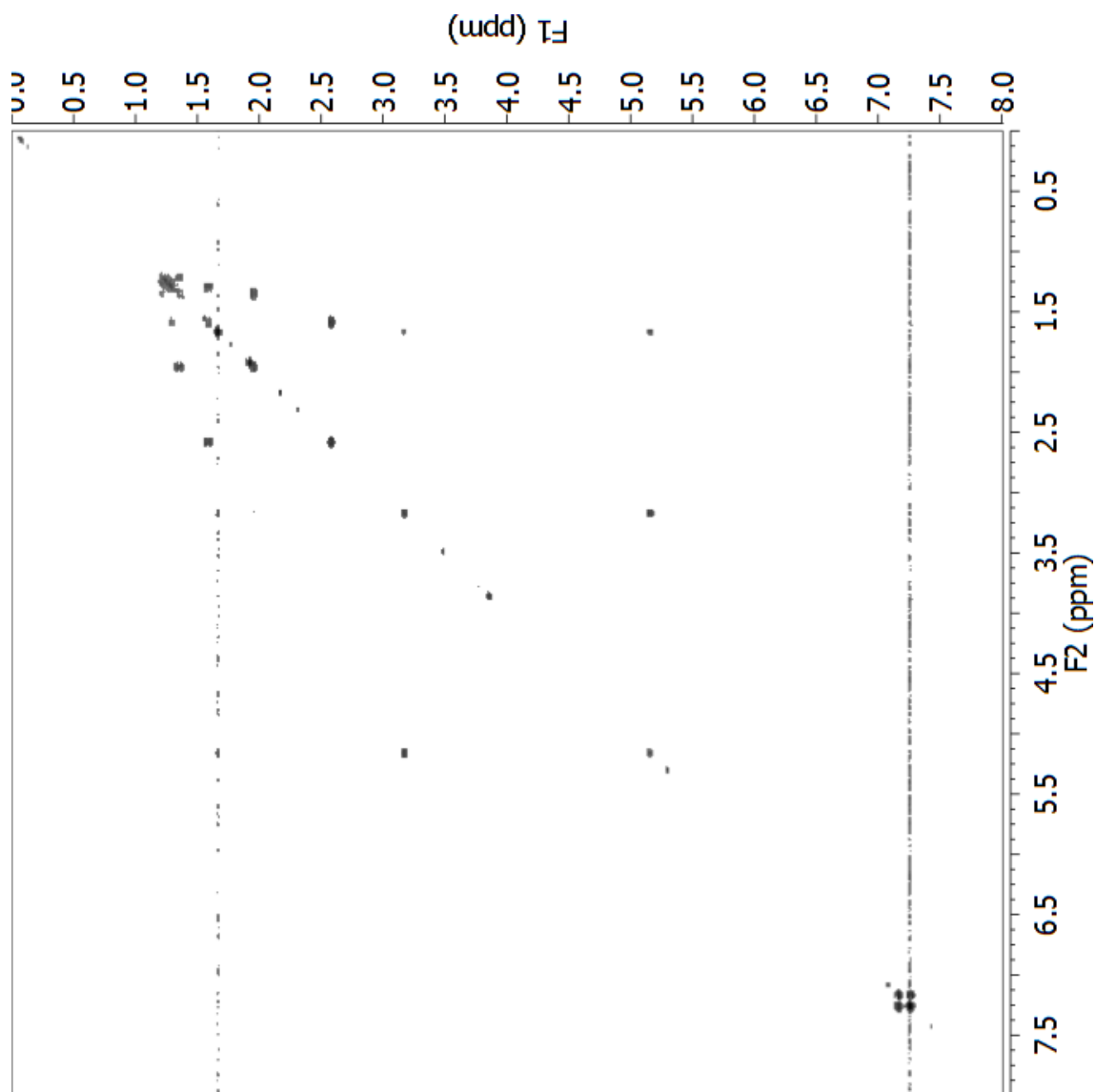


^{13}C NMR spectrum of lehuaide F (**70**) (150 MHz, CDCl_3).

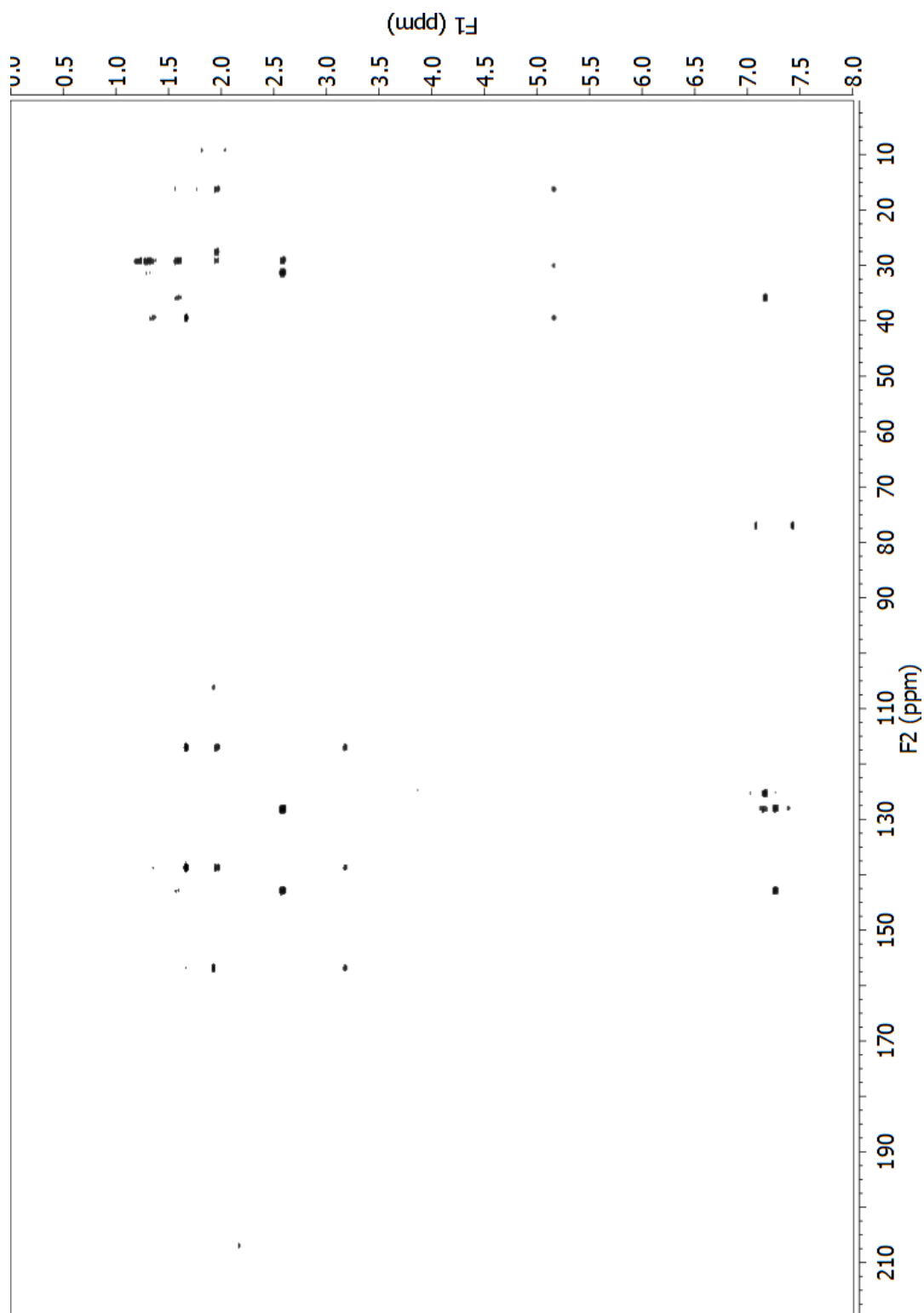
Lehualide G



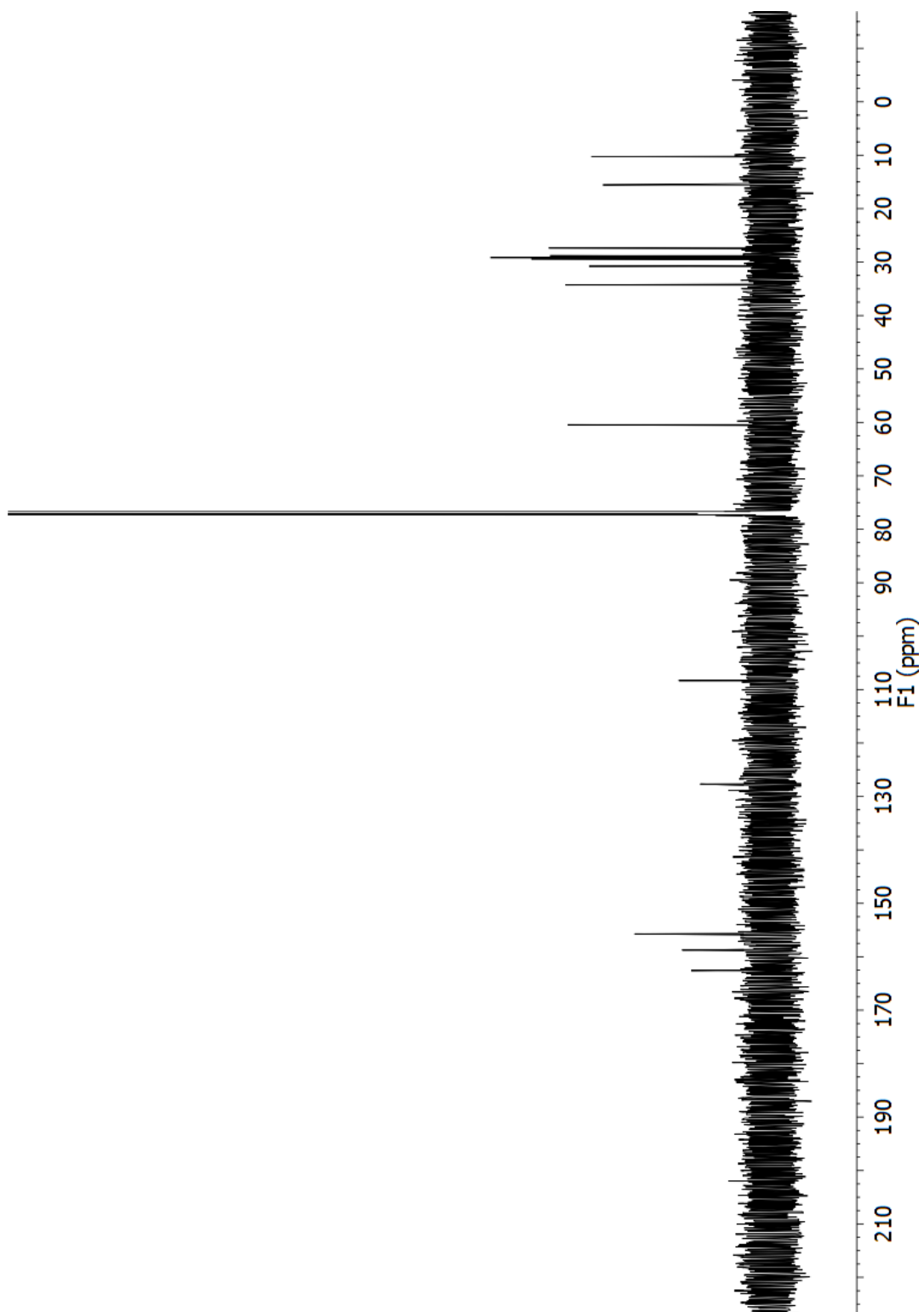
^1H NMR spectrum of lehualide G (**71**) (600 MHz, CDCl_3).



COSY spectrum of lehuaide G (**71**) (600 MHz, CDCl₃).

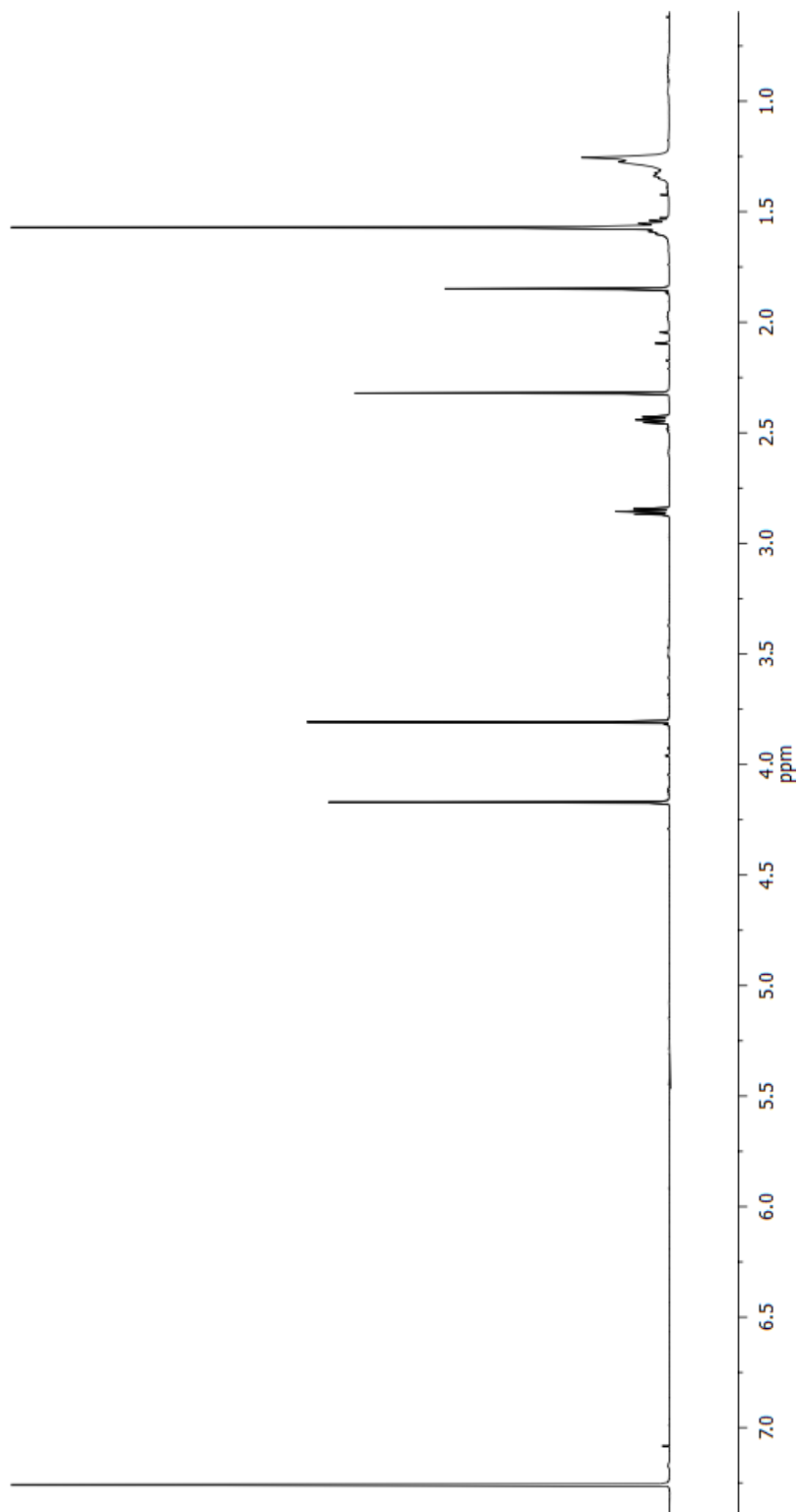


HMBC spectrum of lehuaide G (**71**) (600 MHz, CDCl_3).

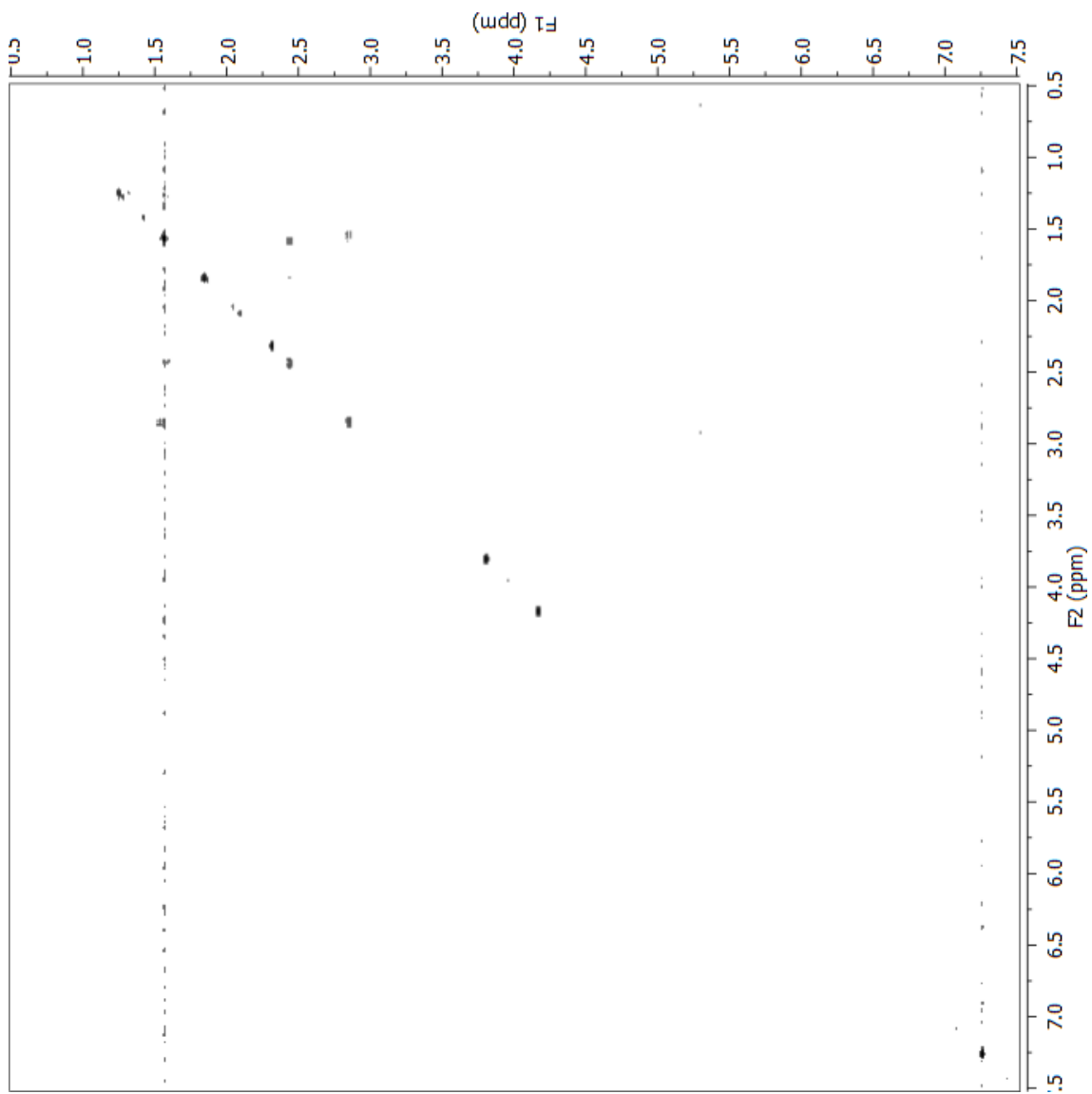


^{13}C NMR spectrum of lehuaide G (**71**) (150 MHz, CDCl_3).

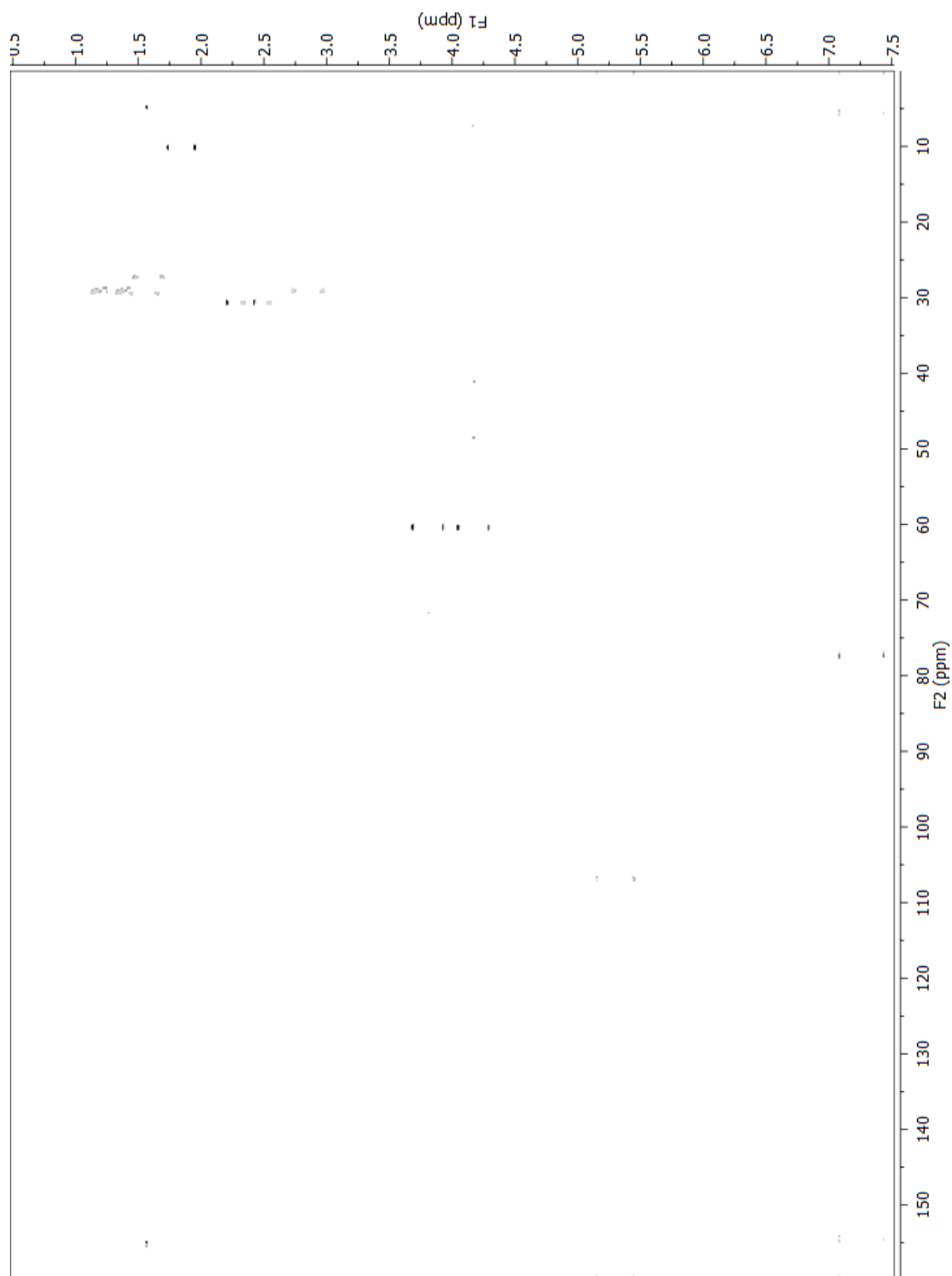
Lehualide H



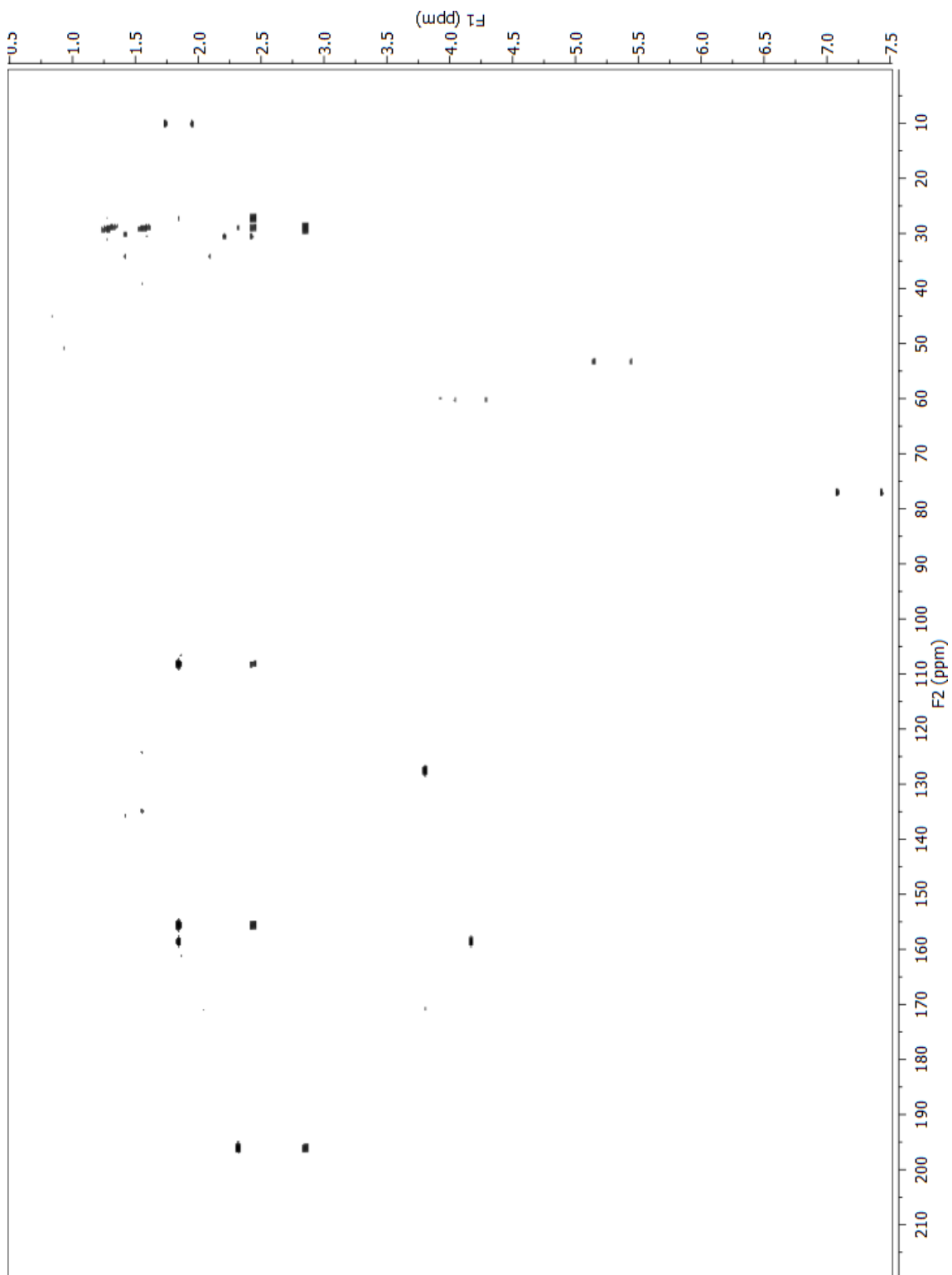
¹H NMR spectrum of lehualide H (**72**) (600 MHz, CDCl₃).



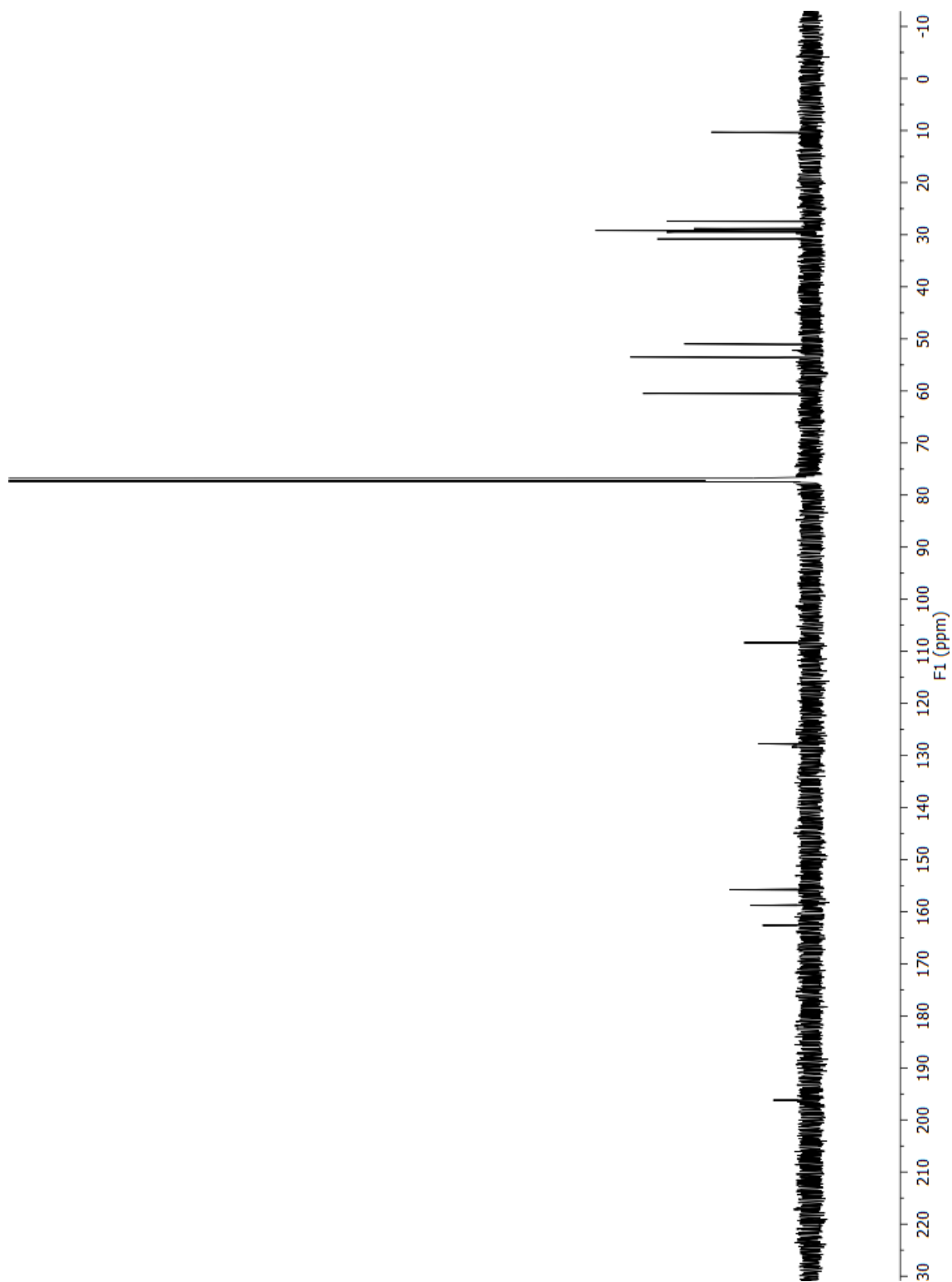
COSY spectrum of lehuaide H (**72**) (600 MHz, CDCl₃).



Fully-coupled HSQC spectrum of lehuaide H (**72**) (600 MHz, CDCl₃).

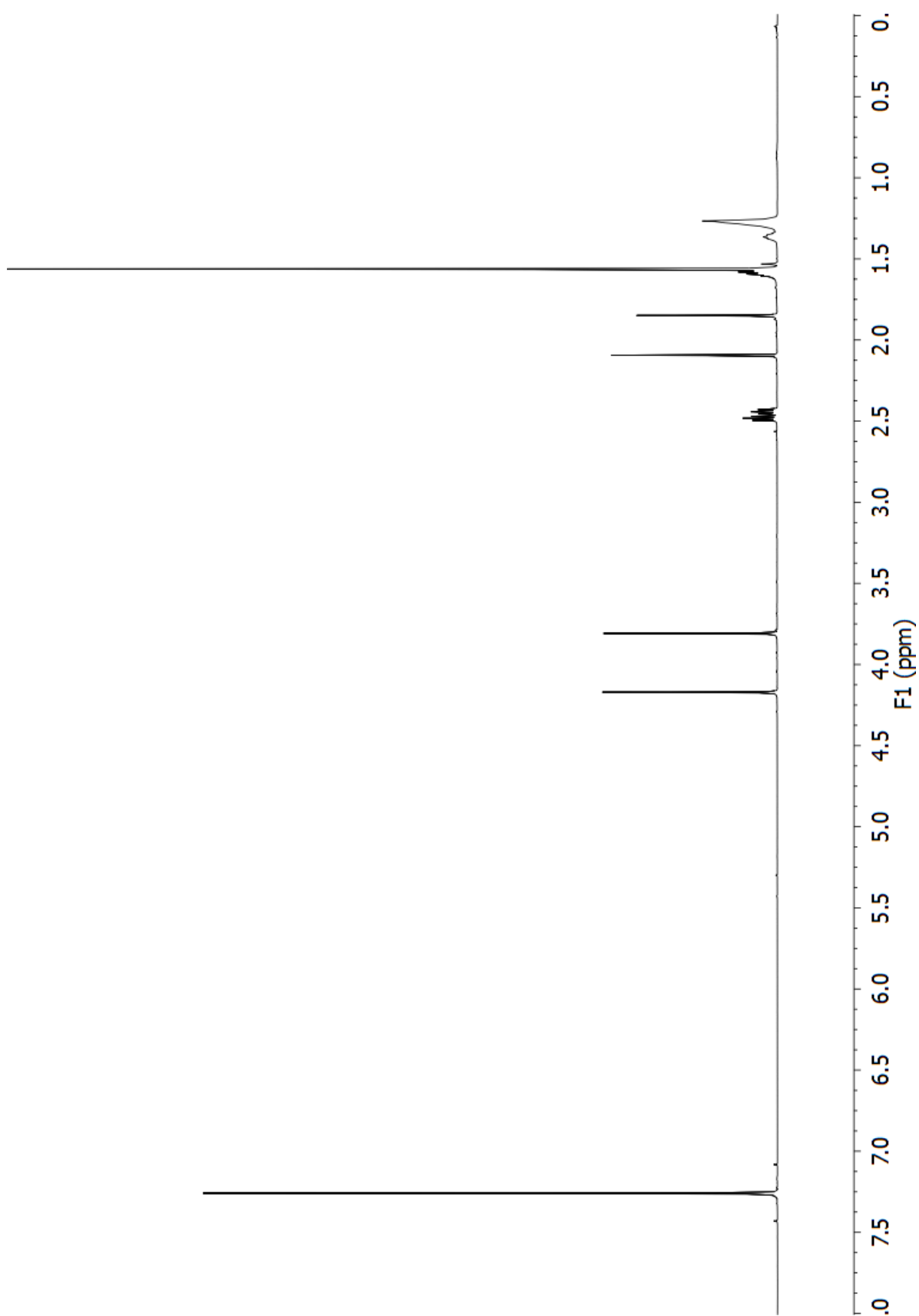


HMBC spectrum of lehuamide H (**72**) (600 MHz, CDCl₃).

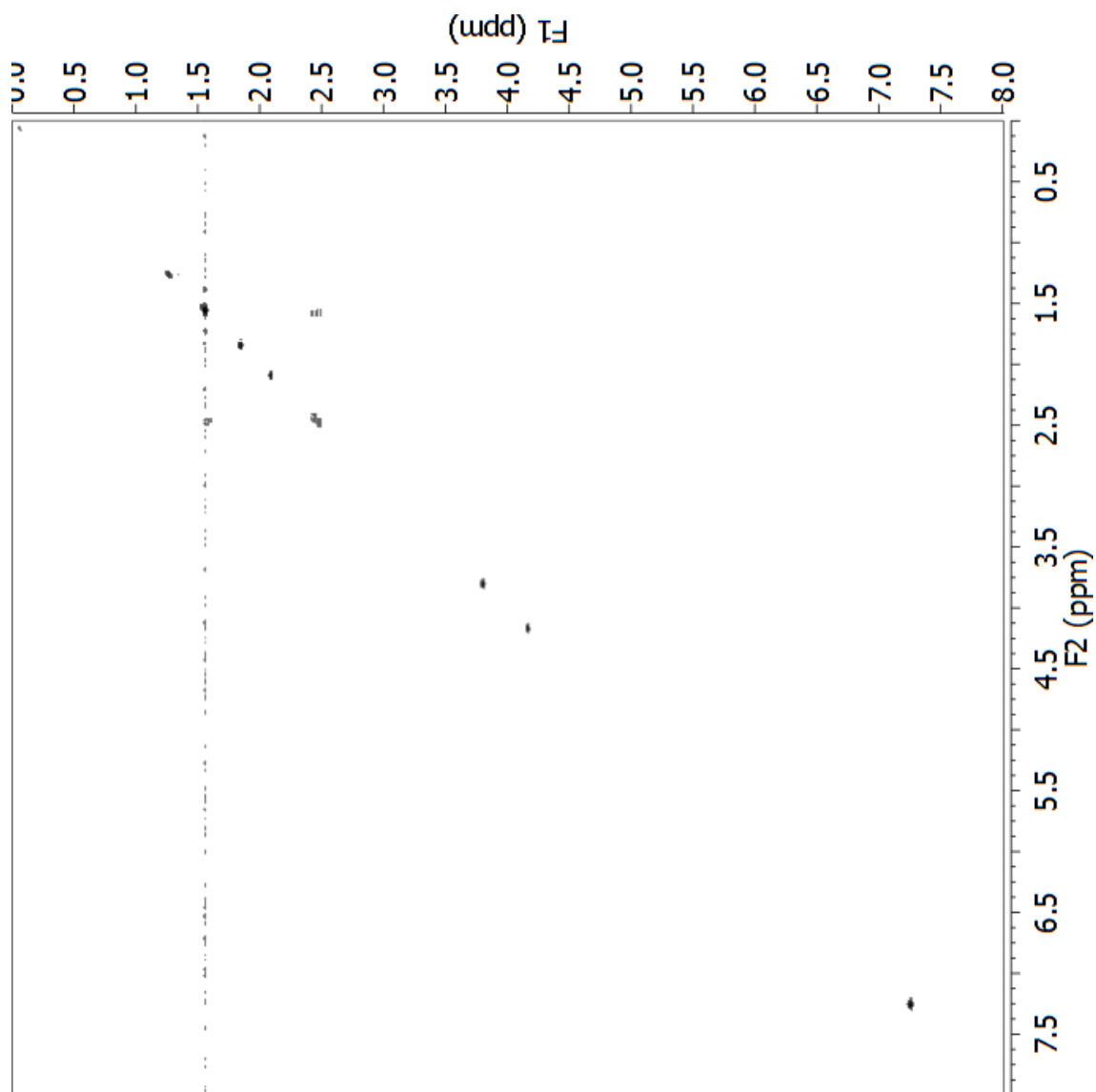


^{13}C NMR spectrum of lehuaide H (**72**) (150 MHz, CDCl_3).

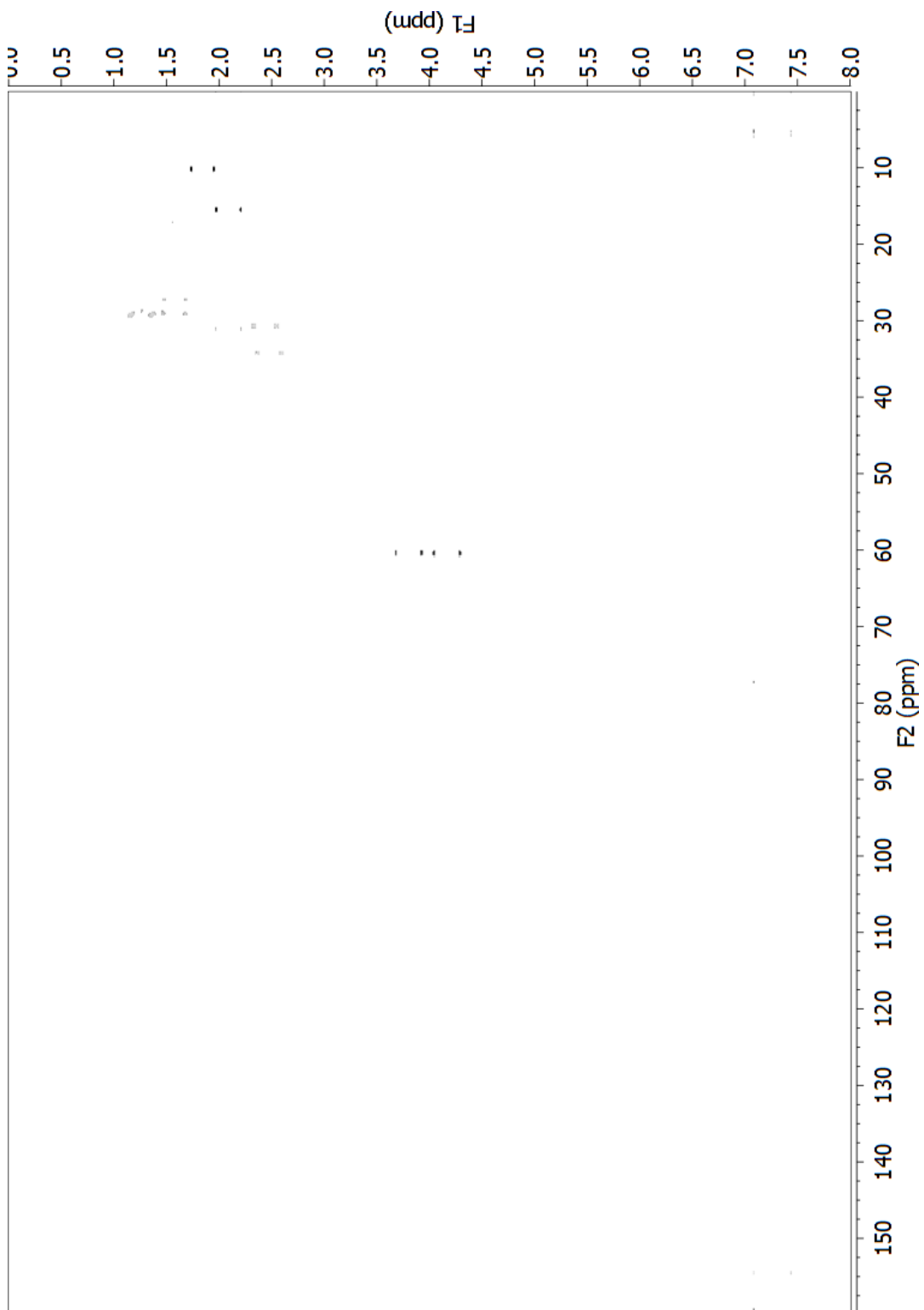
Lehualide I



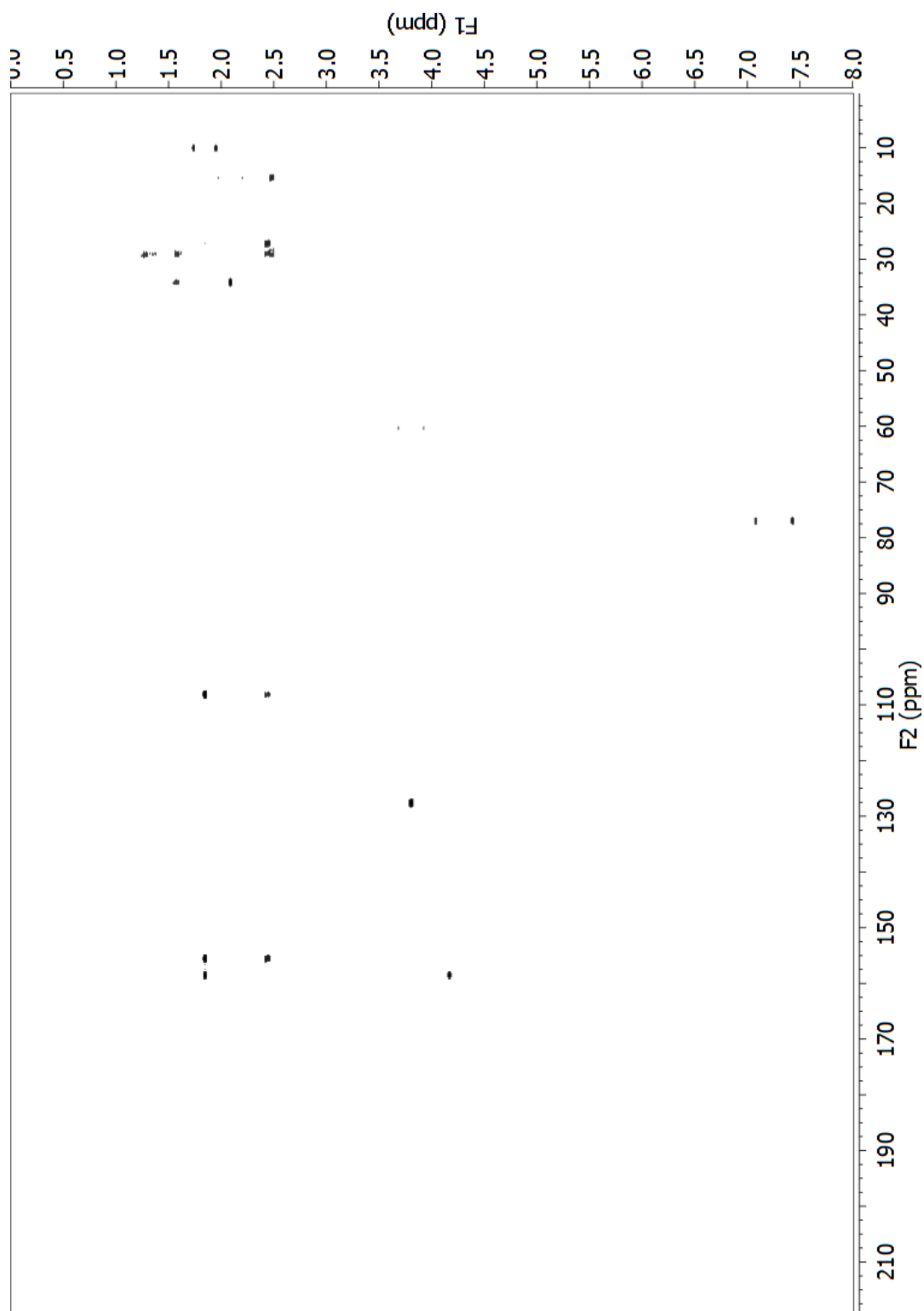
^1H NMR spectrum of lehualide I (**73**) (600 MHz, CDCl_3).



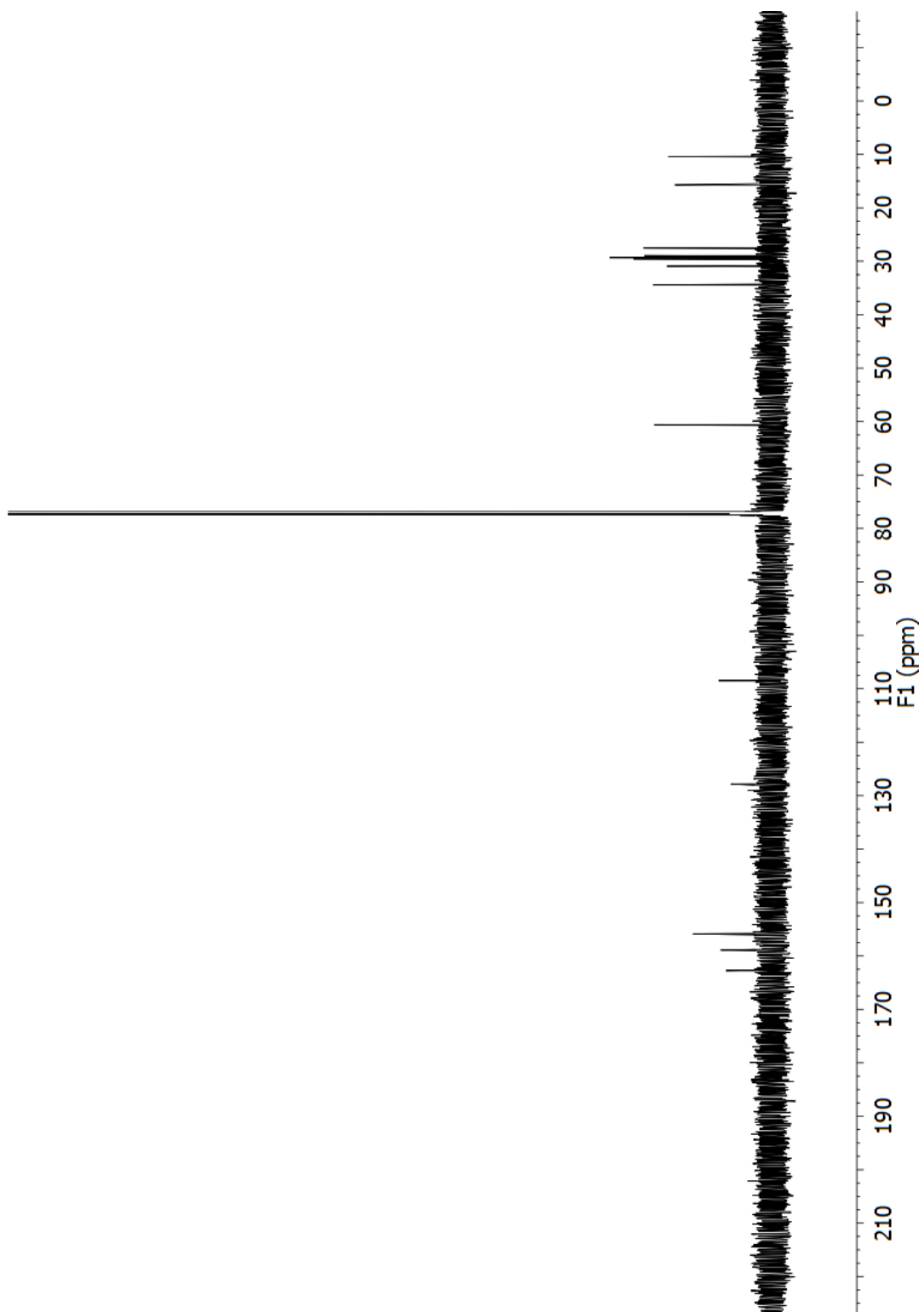
COSY spectrum of lehualide I (**73**) (600 MHz, CDCl₃).



Fully-coupled HSQC spectrum of lehuaide I (**73**) (600 MHz, CDCl₃).

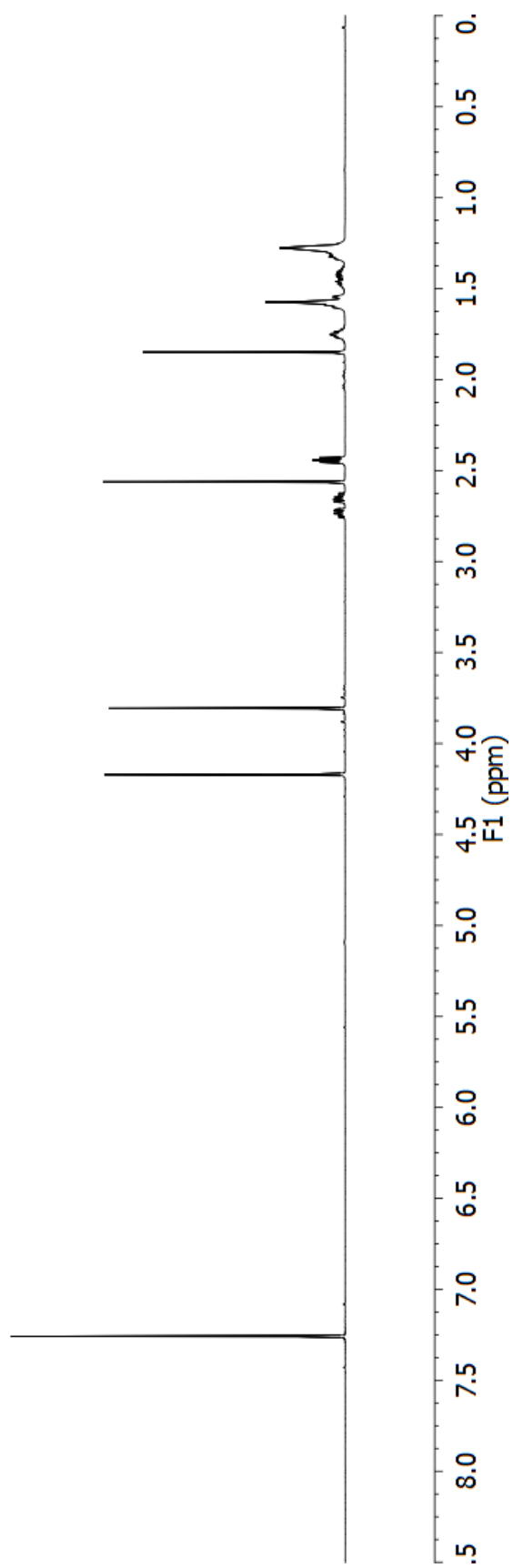


HMBC spectrum of lehuaide I (**73**) (600 MHz, CDCl₃).

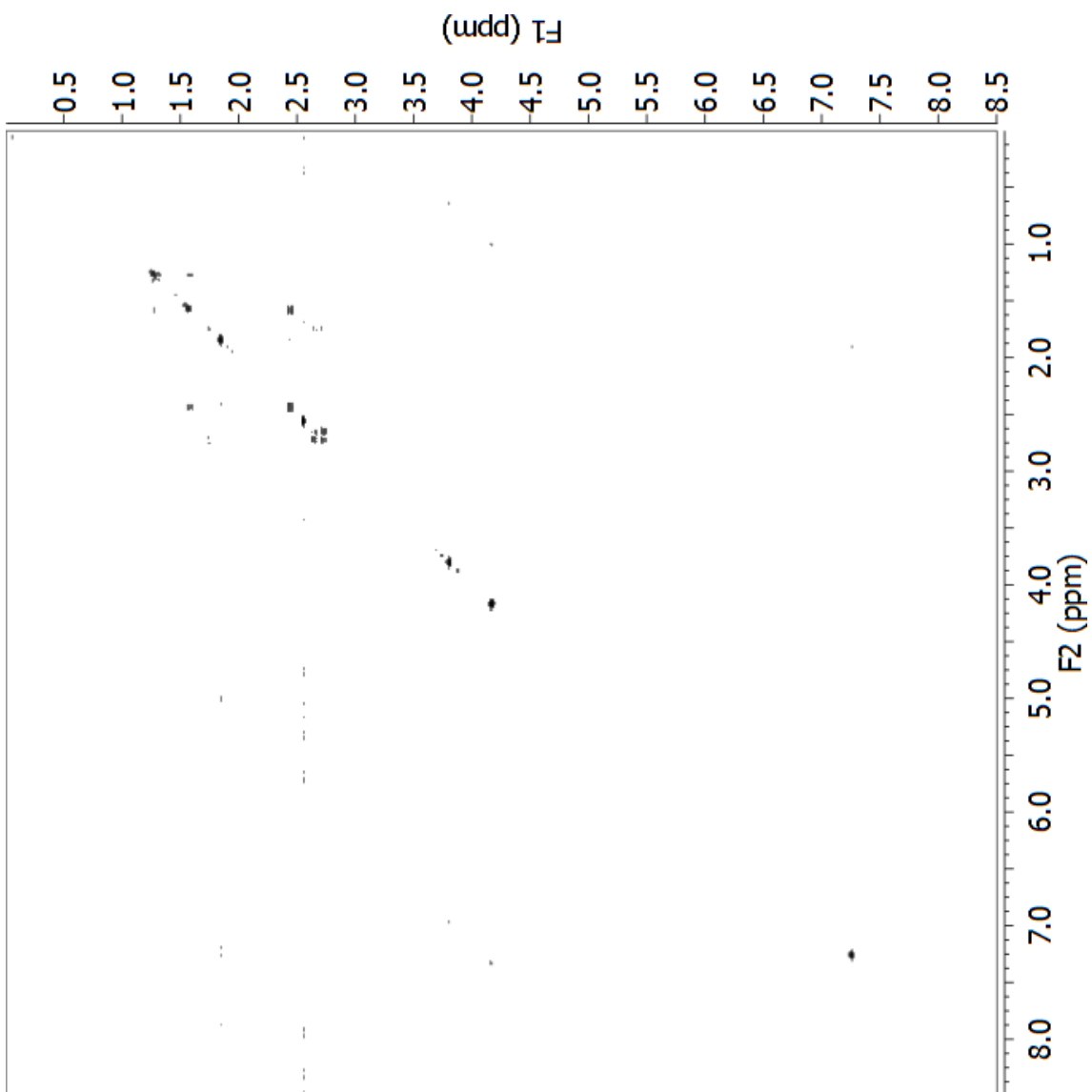


^{13}C NMR spectrum of lehuamide I (**73**) (150 MHz, CDCl_3).

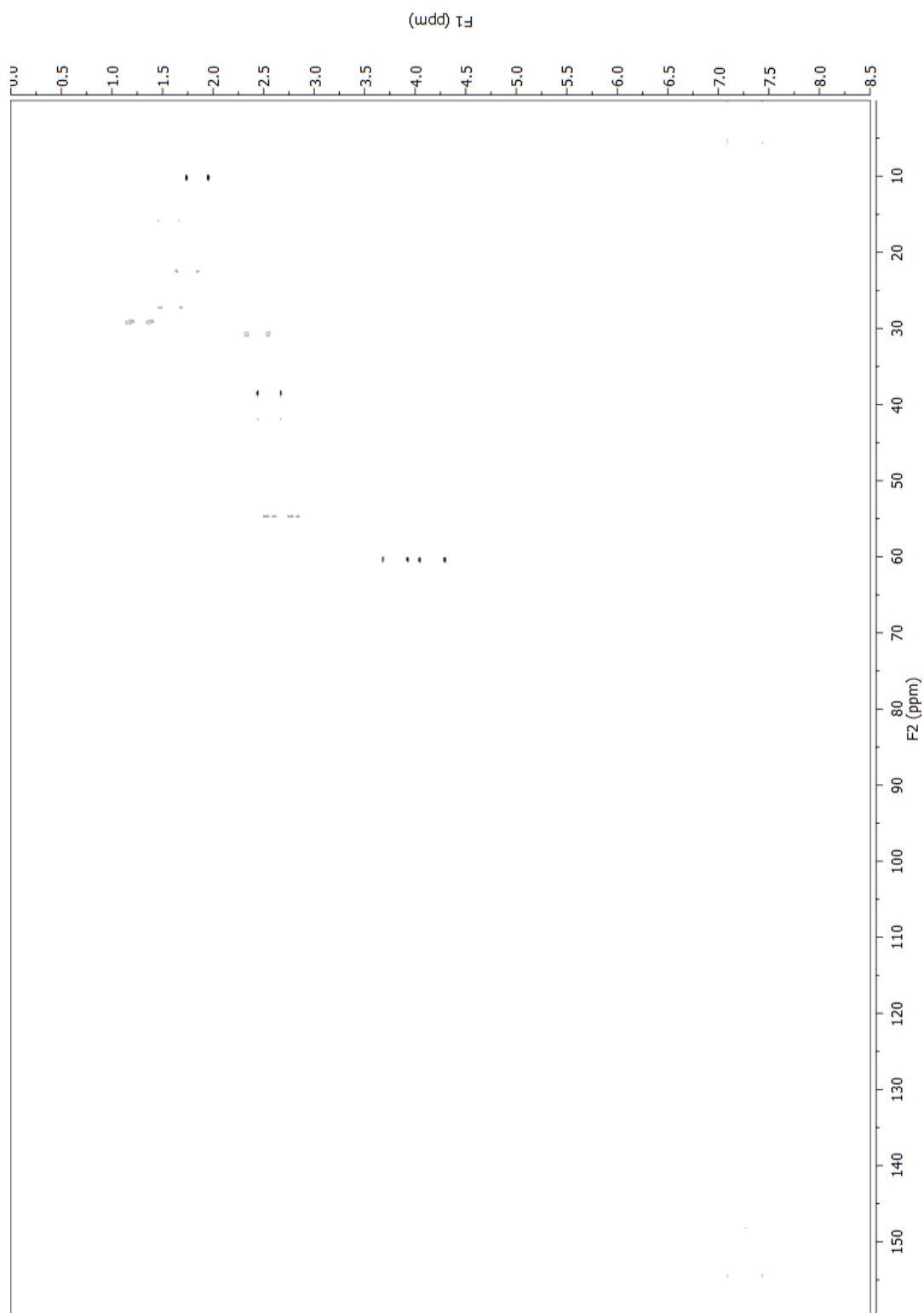
Lehualide J



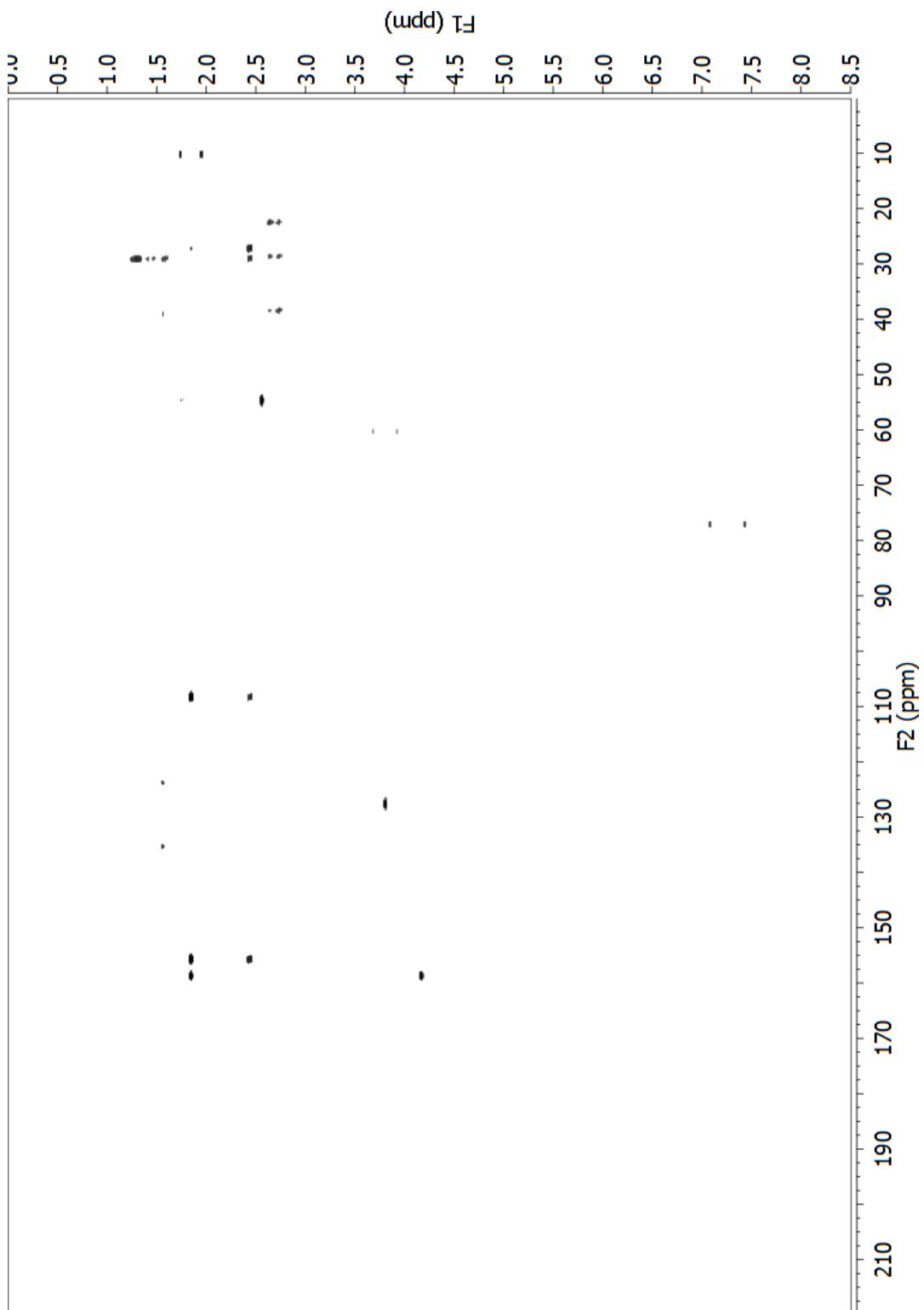
^1H NMR spectrum of lehualide J (**74**) (600 MHz, CDCl_3).



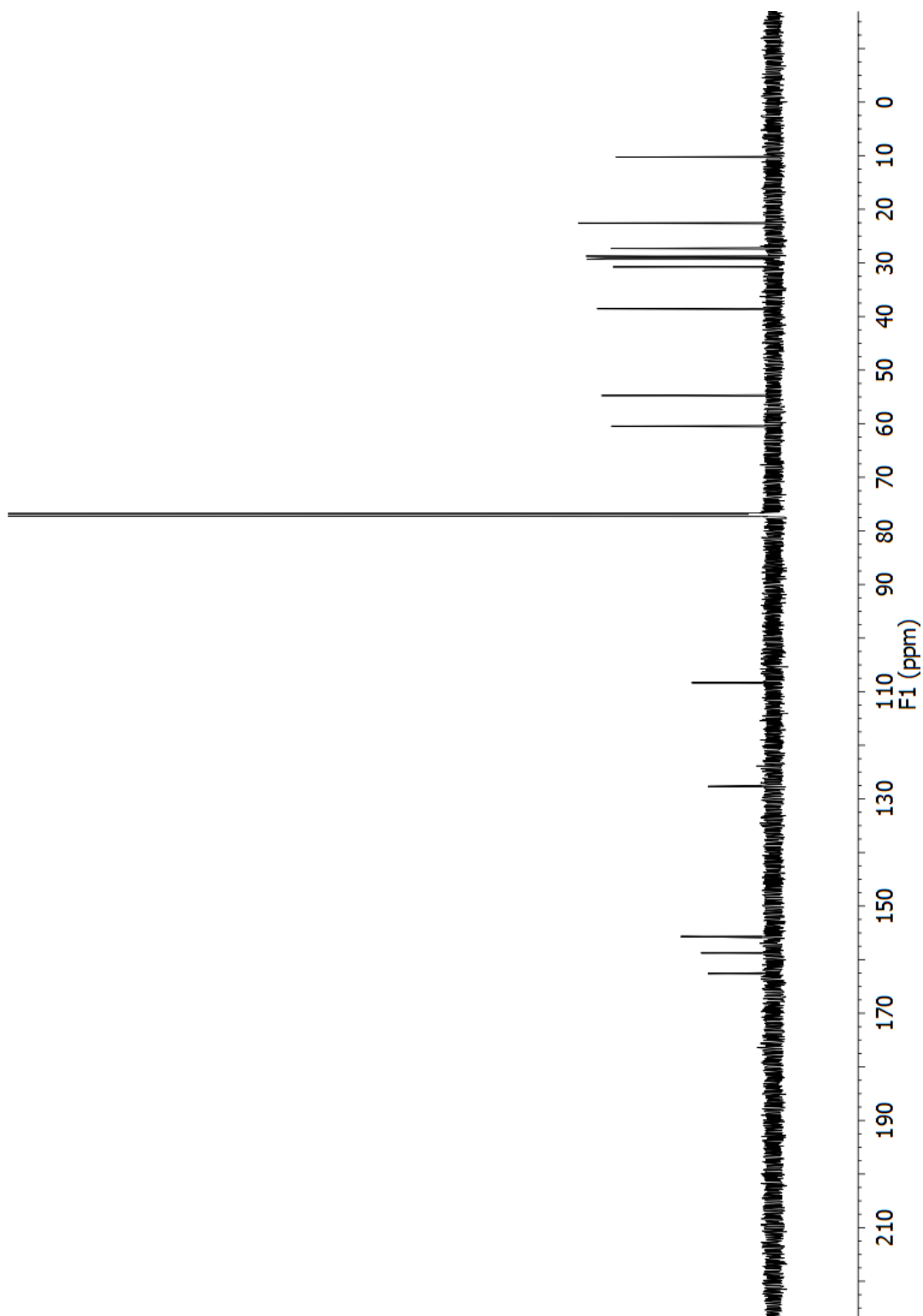
COSY spectrum of lehuaide J (**74**) (600 MHz, CDCl₃).



Fully-coupled HSQC spectrum of lehuaide J (**74**) (600 MHz, CDCl_3).

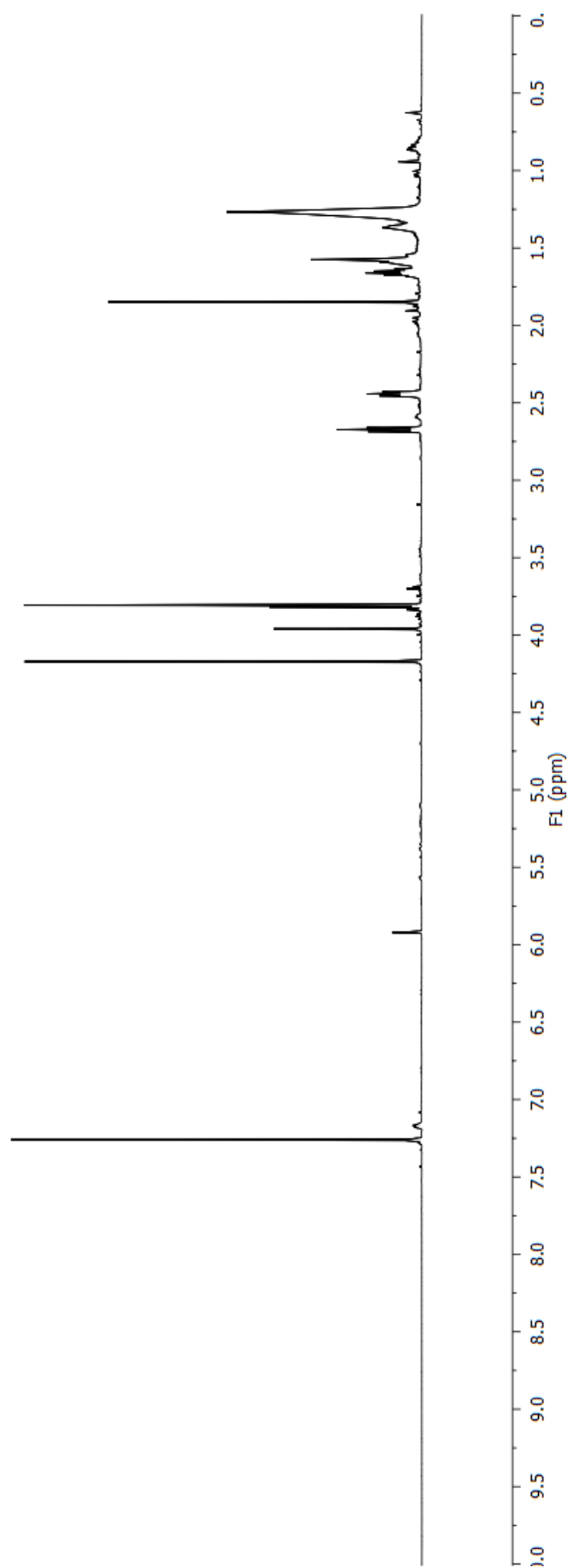


HMBC spectrum of lehuaide J (**74**) (600 MHz, CDCl₃).

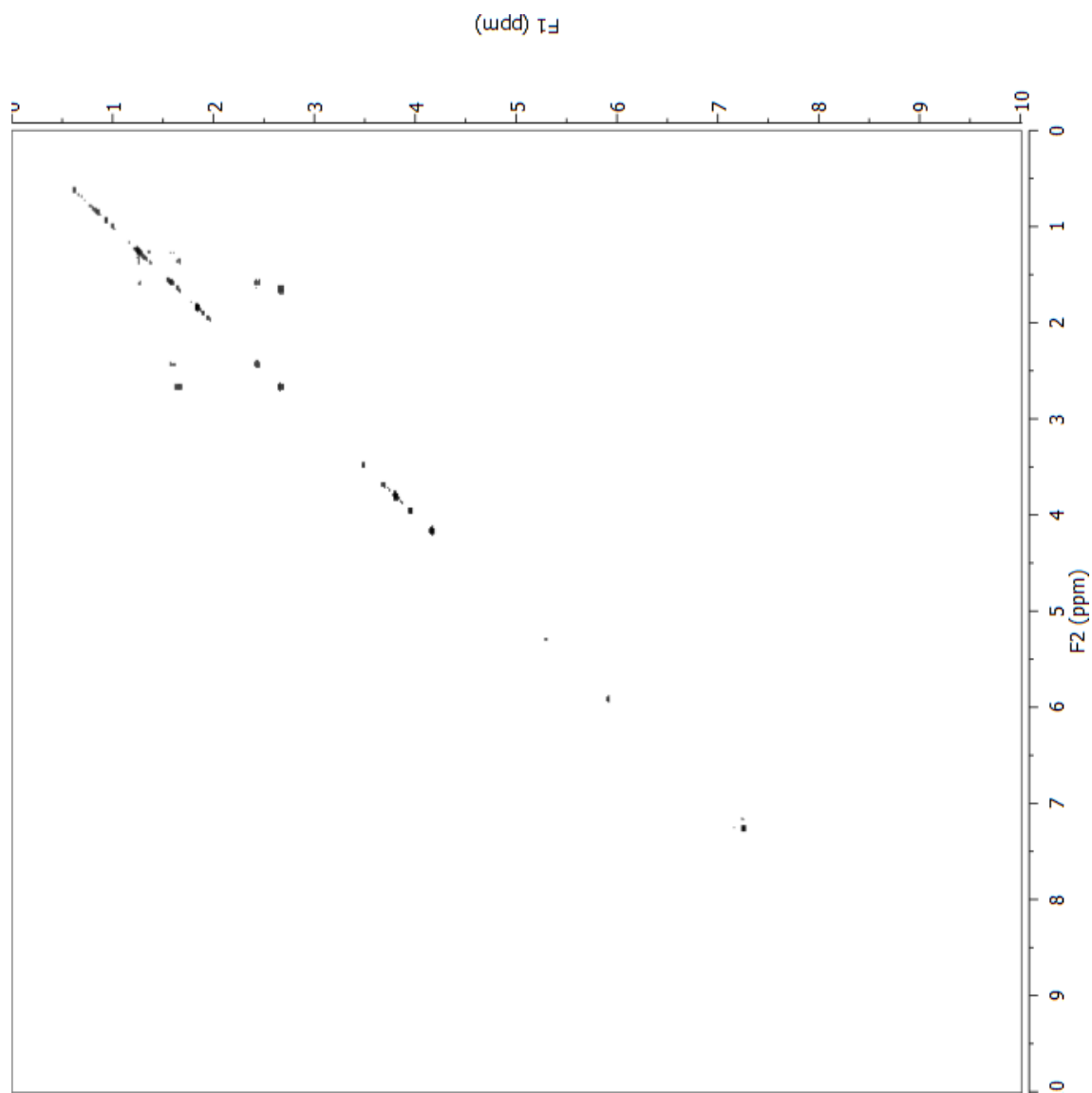


^{13}C NMR spectrum of lehuaide J (**74**) (150 MHz, CDCl_3).

Lehualide K



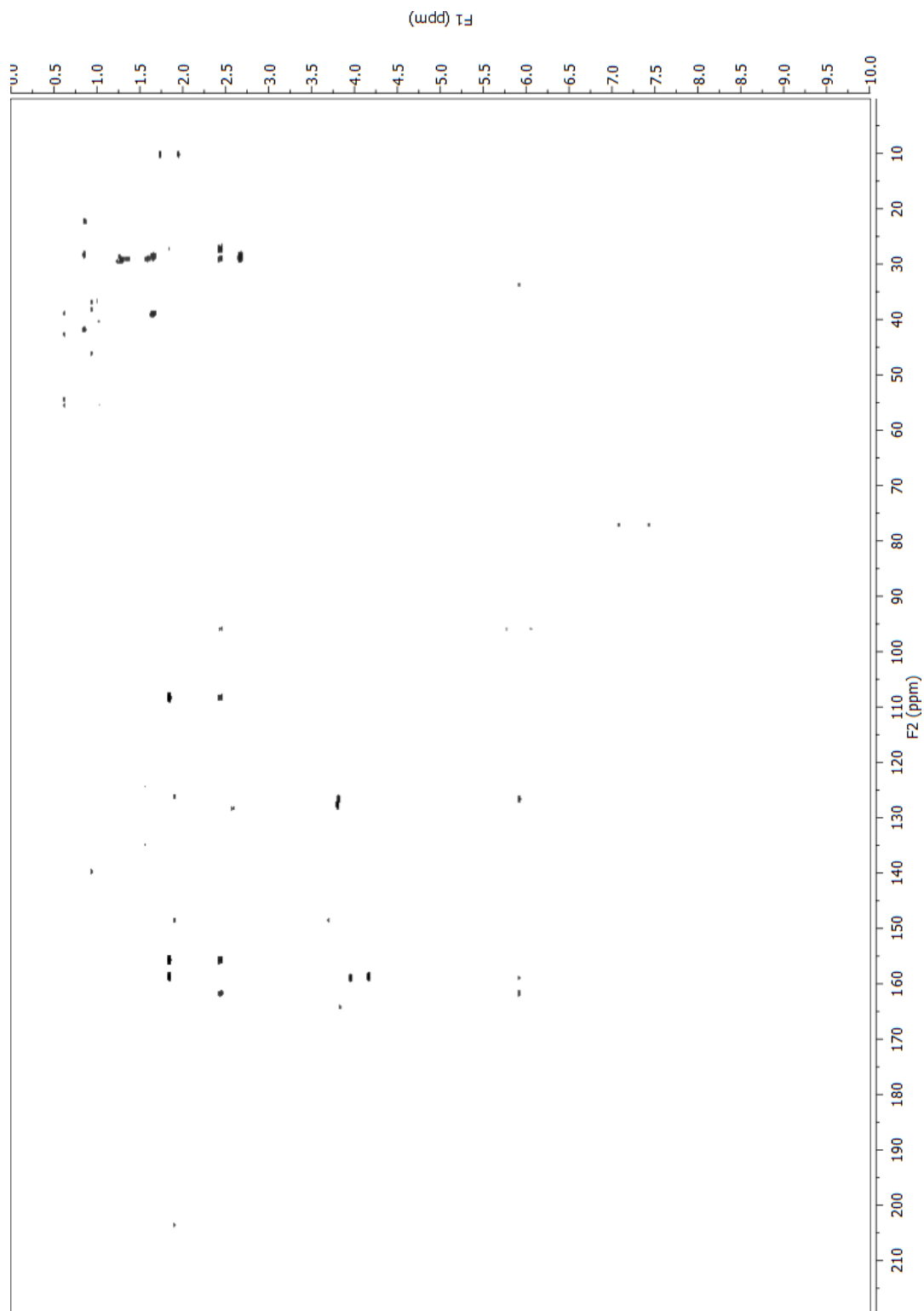
^1H NMR spectrum of lehualide K (**75**) (600 MHz, CDCl_3).



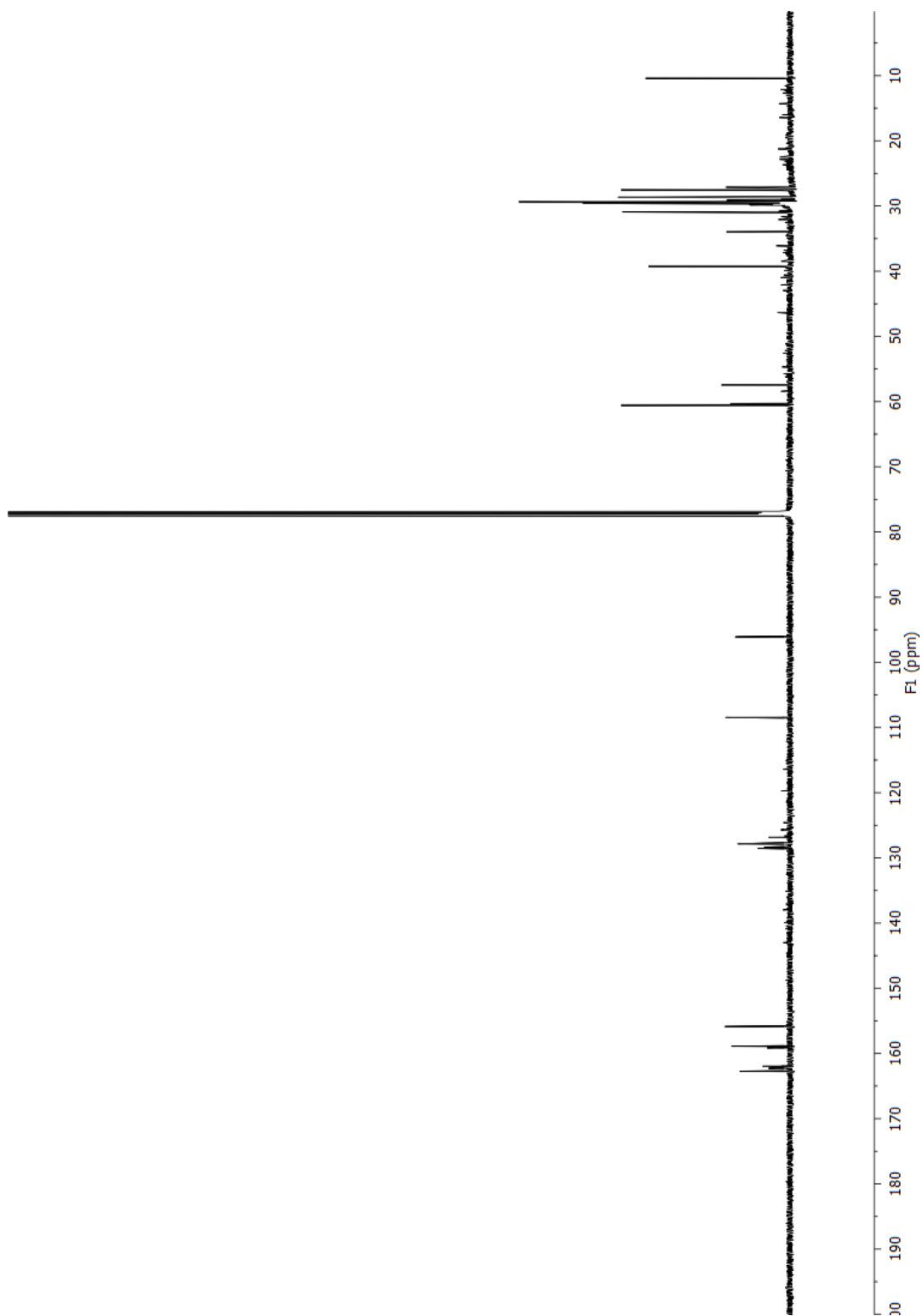
COSY spectrum of lehuaide K (**75**) (600 MHz, CDCl_3).



Fully-coupled HSQC spectrum of lehuaide K (**75**) (600 MHz, CDCl_3).



HMBC spectrum of lehuaide K (**75**) (600 MHz, CDCl_3).

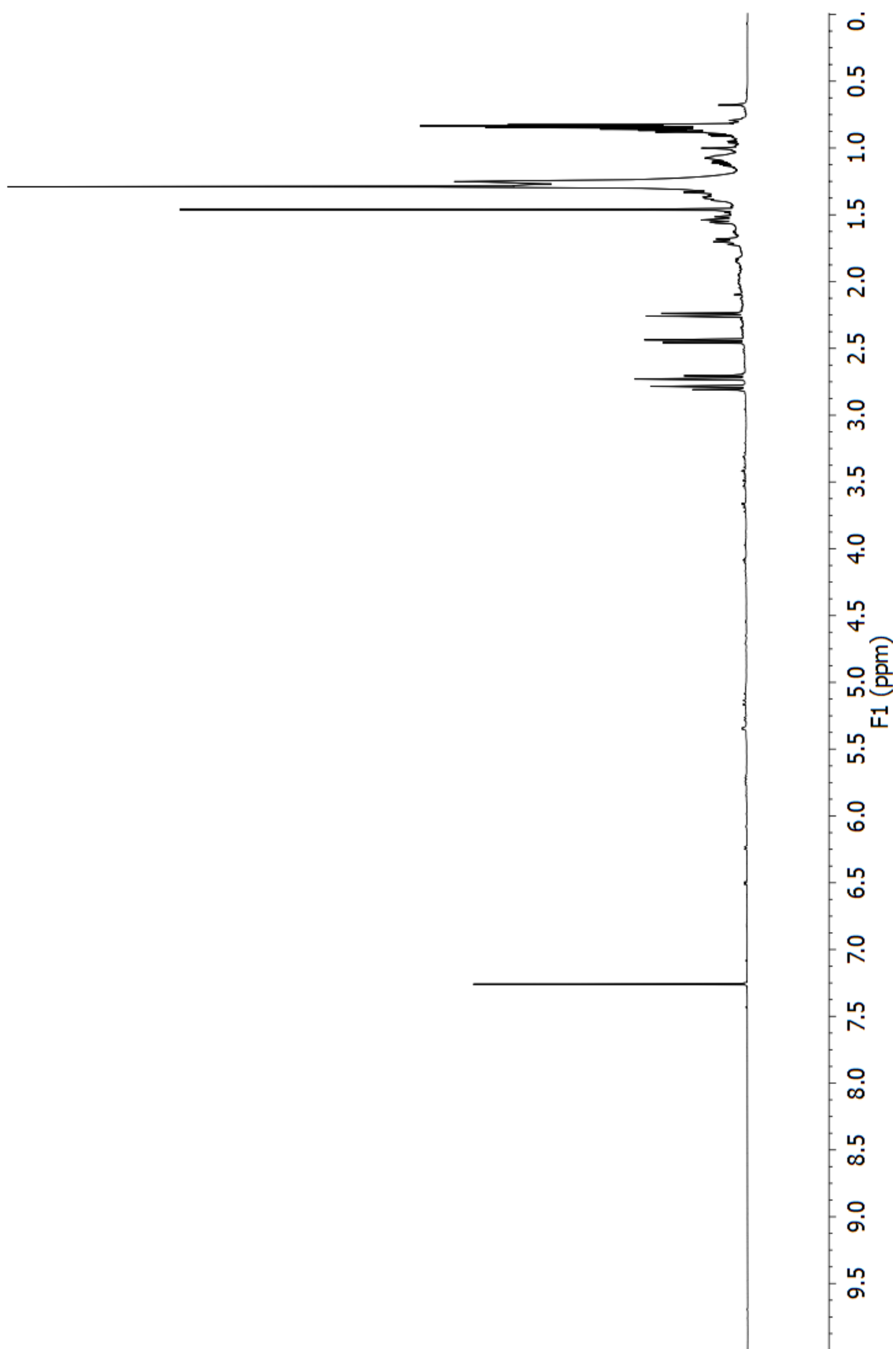


^{13}C NMR spectrum of lehuaide K (**75**) (150 MHz, CDCl_3).

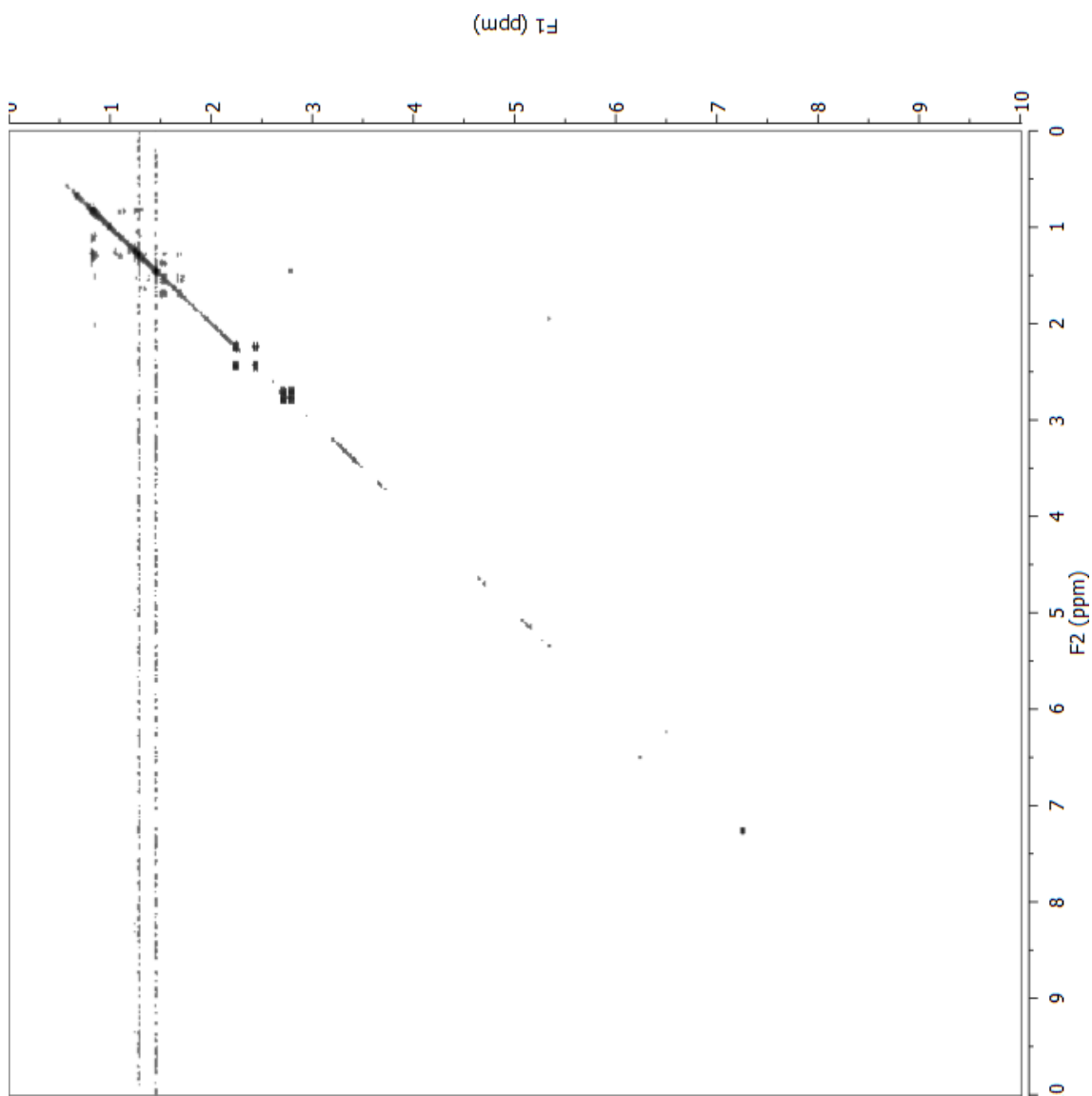
Appendix G

NMR Spectra of New Cyclic Peroxides

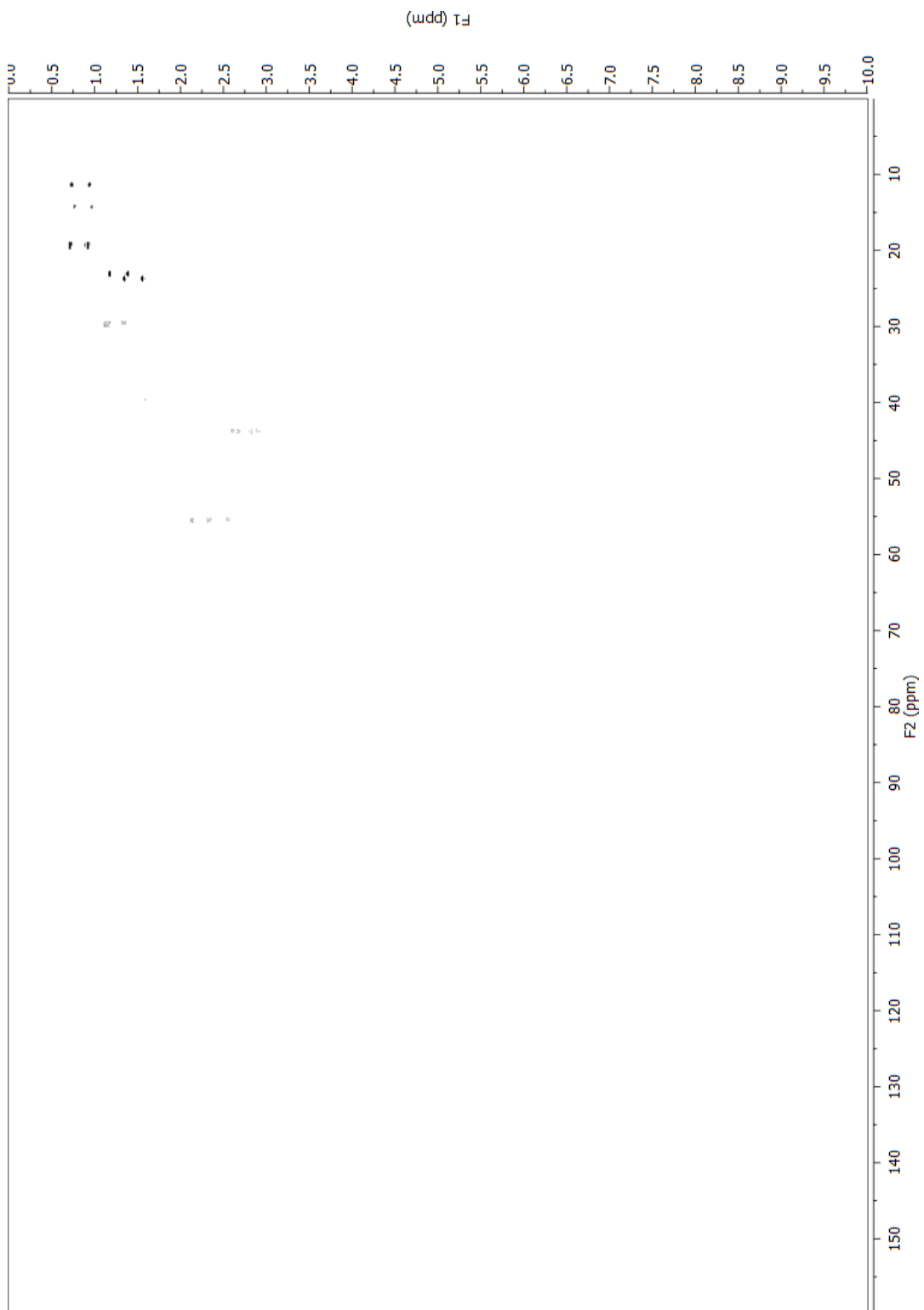
Epiplakinic Acid I



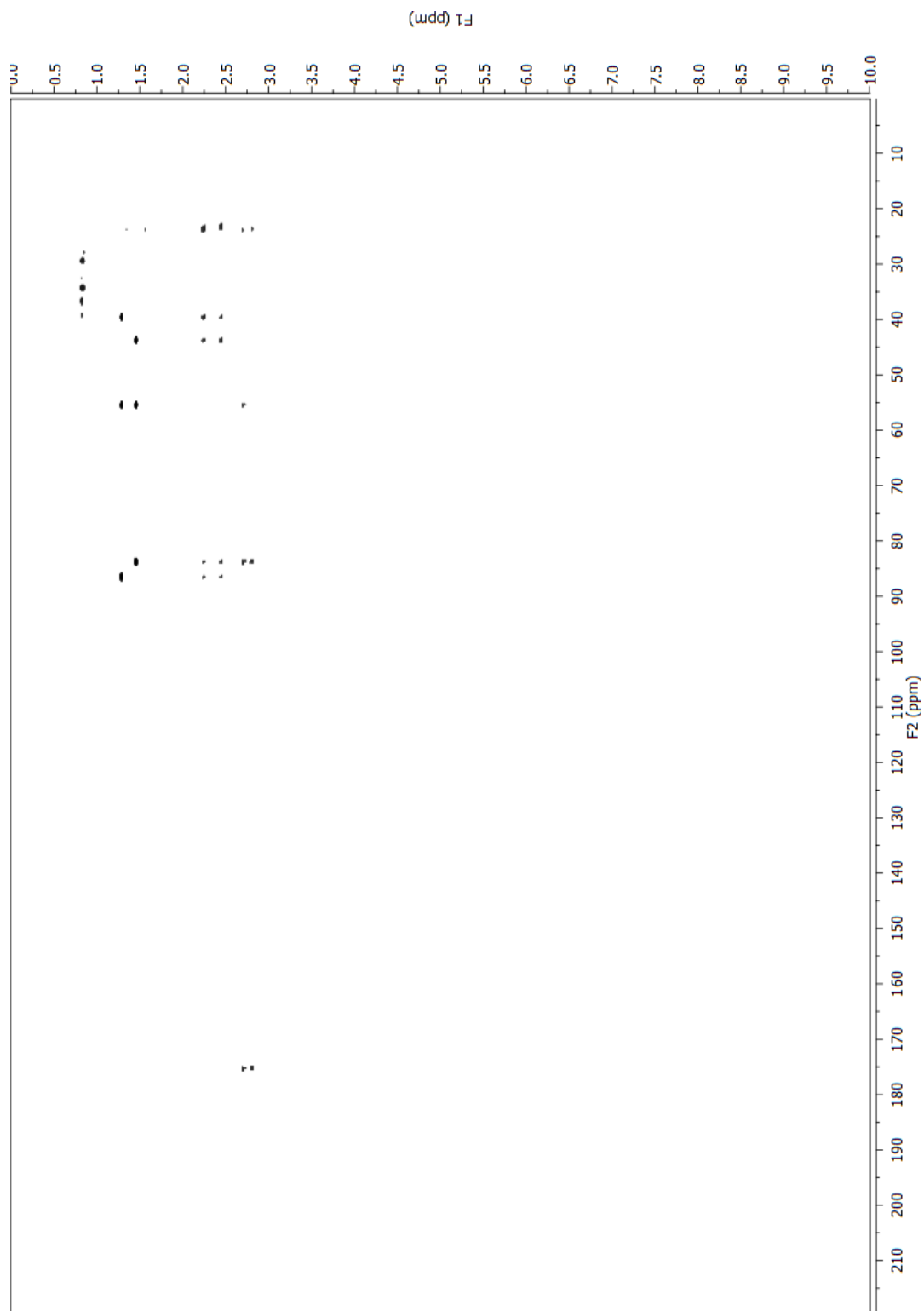
¹H NMR spectrum of epiplakinic acid I (**95**) (600 MHz, CDCl₃).



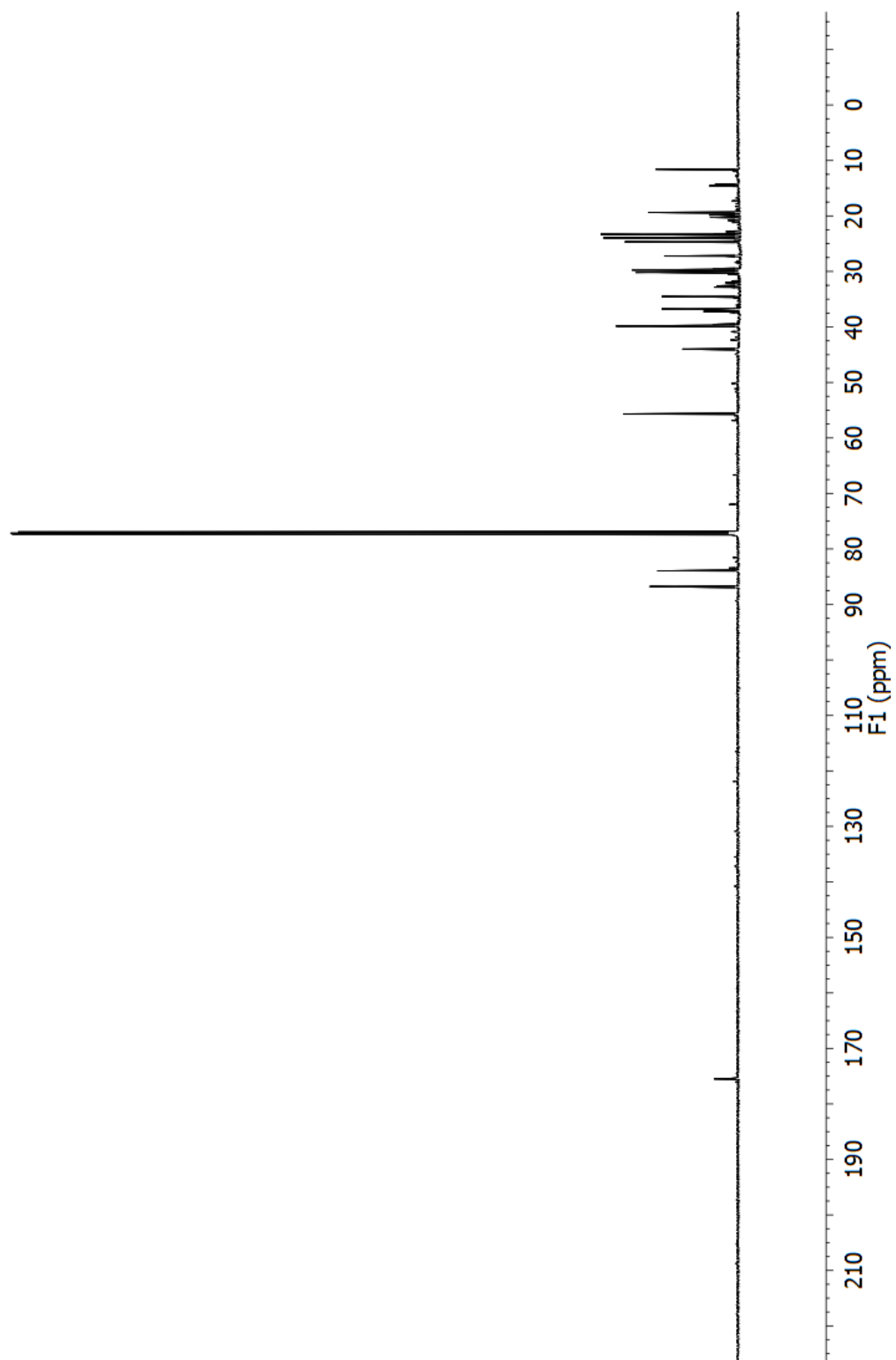
COSY spectrum of epiplakinic acid I (**95**) (600 MHz, CDCl₃).



Fully-coupled HSQC spectrum of epiplakinic acid I (**95**) (600 MHz, CDCl₃).

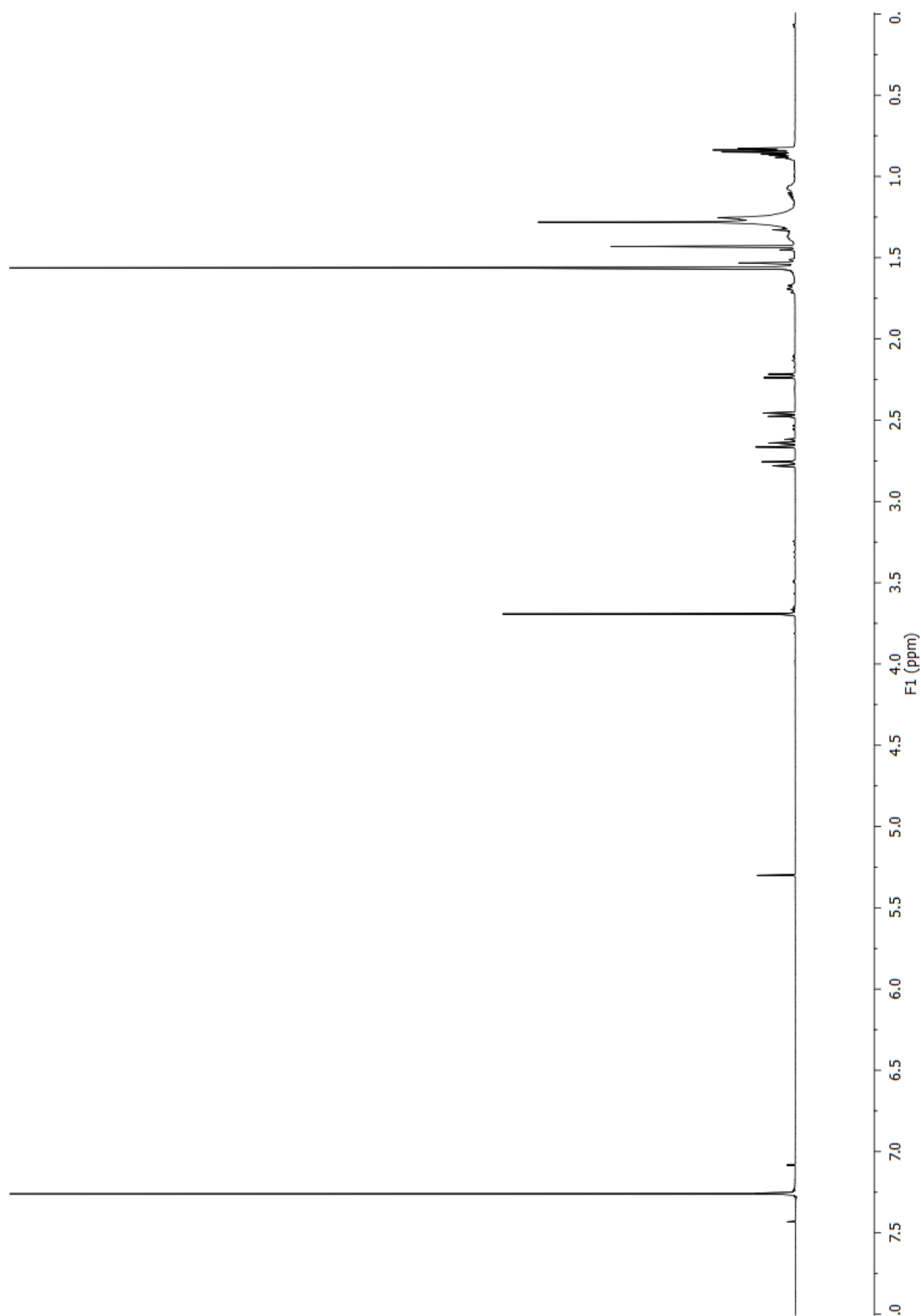


HMBC spectrum of epiplakinic acid I (**95**) (600 MHz, CDCl₃).

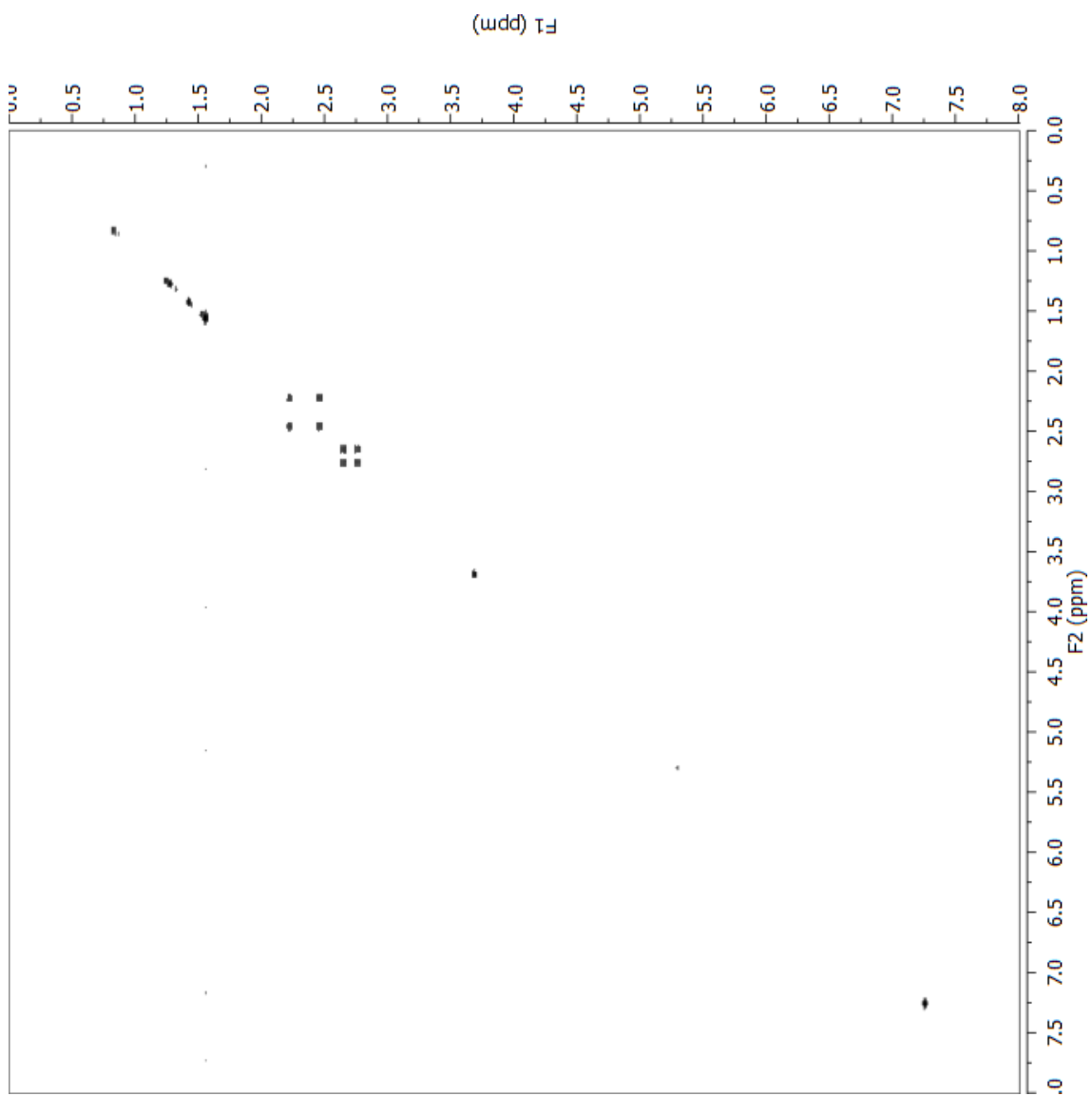


^{13}C NMR spectrum of epiplakinic acid I (**95**) (150 MHz, CDCl_3).

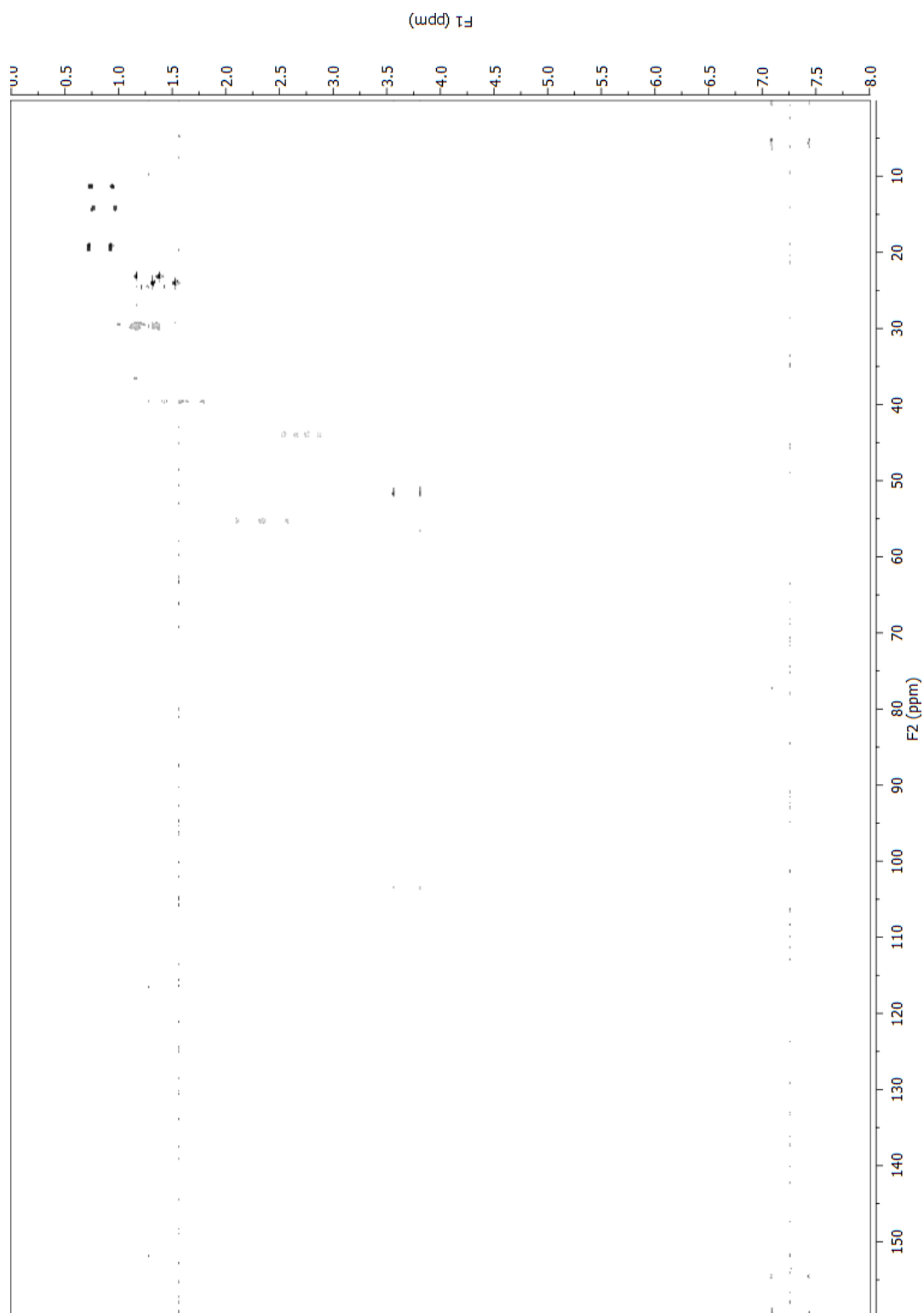
Epiplakinic Acid I Methyl Ester



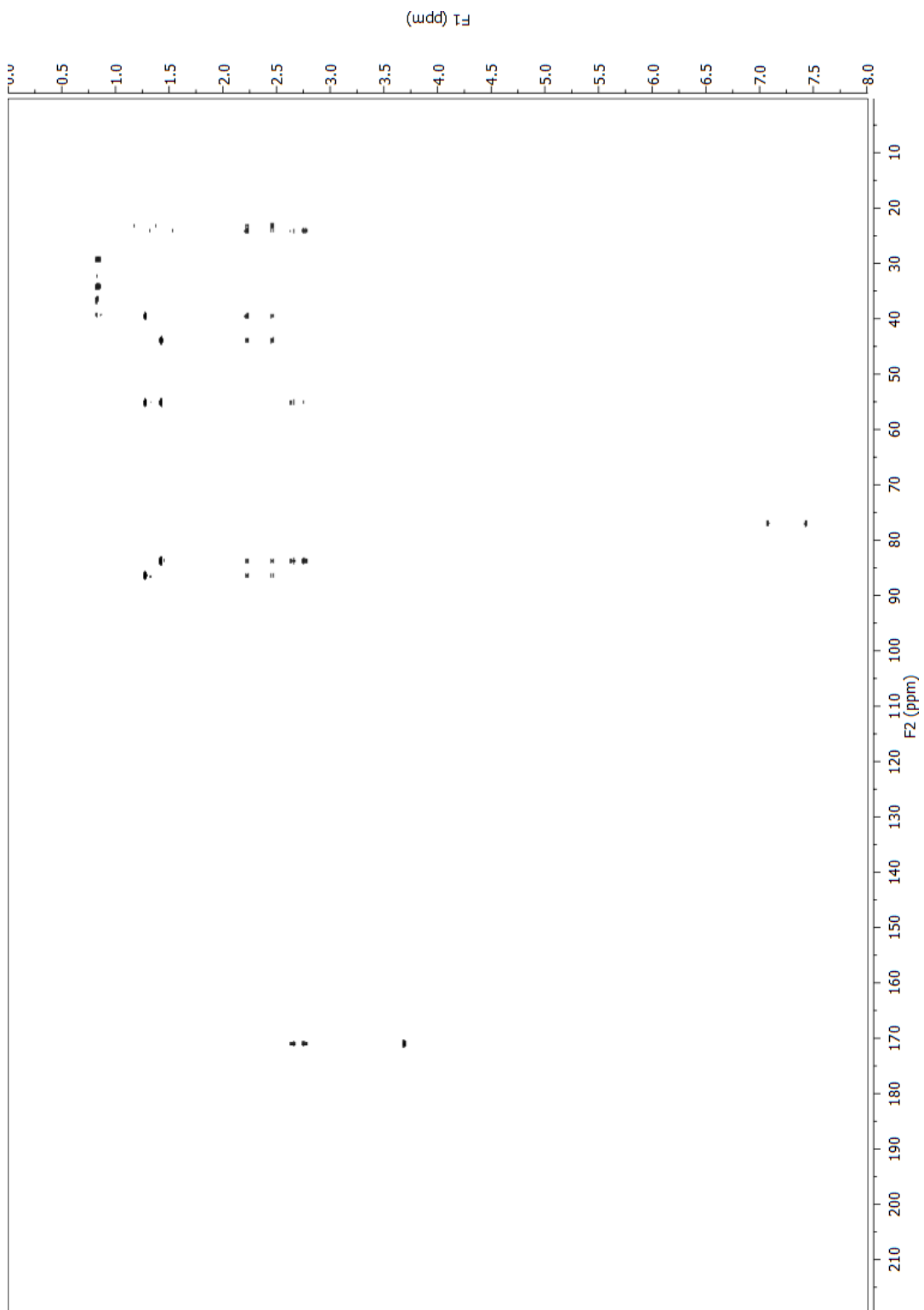
¹H NMR spectrum of epiplakinic acid I methyl ester (**96**) (600 MHz, CDCl₃).



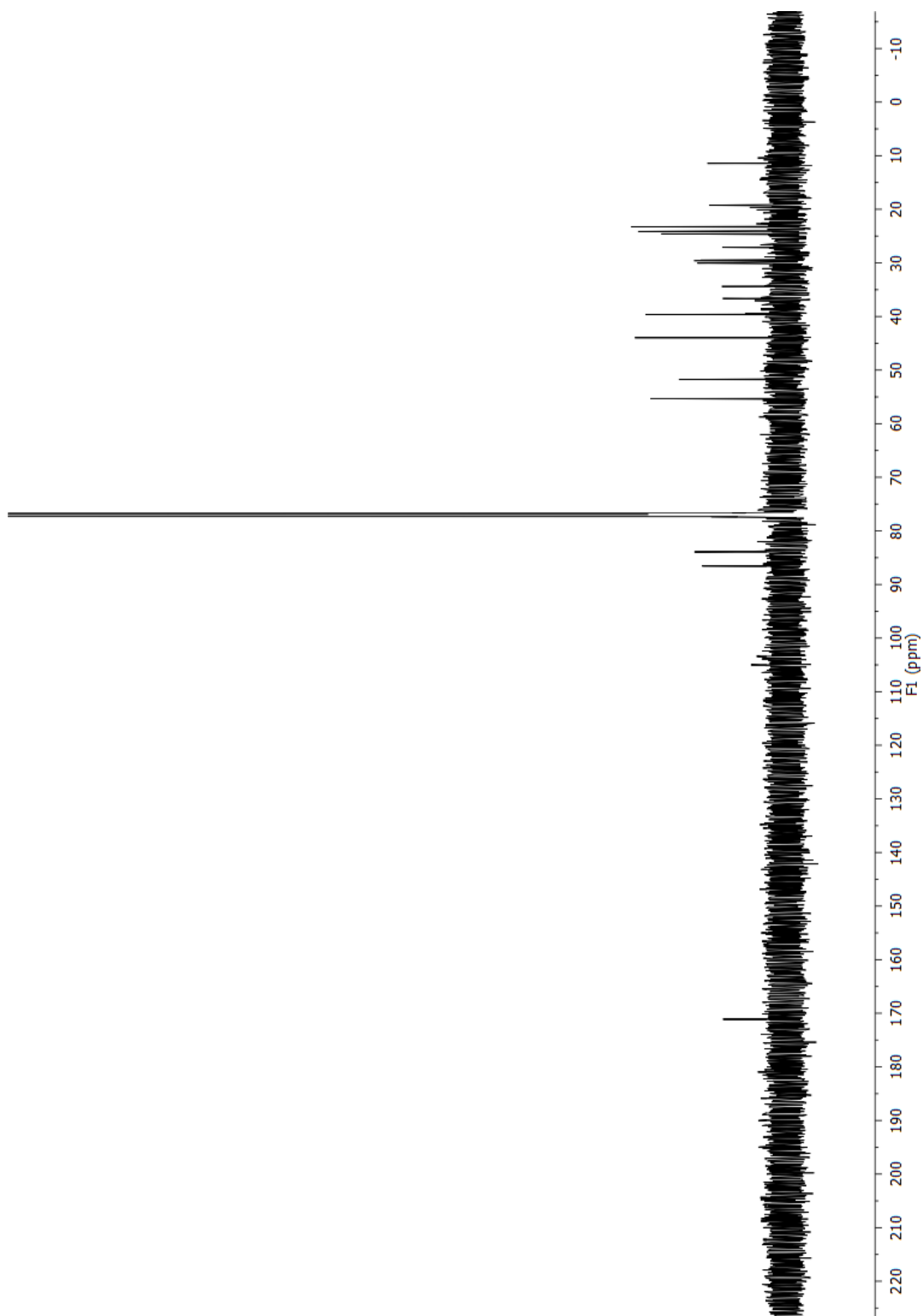
COSY spectrum of epiplakinic acid I methyl ester (**96**) (600 MHz, CDCl₃).



Fully-coupled HSQC spectrum of epiplakinic acid I methyl ester (**96**) (600 MHz, CDCl₃).

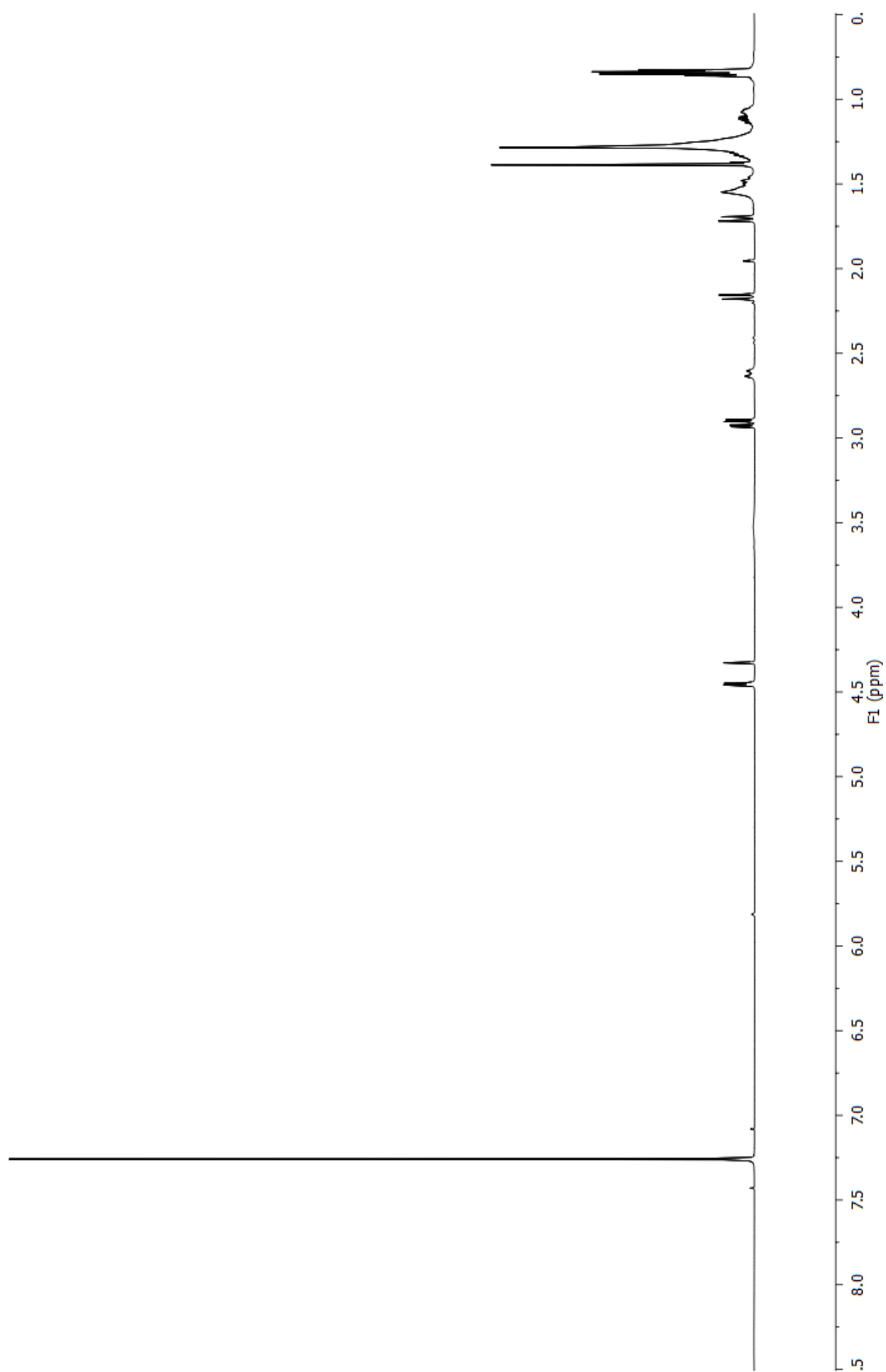


HMBC spectrum of epiplakinic acid I methyl ester (**96**) (600 MHz, CDCl₃).

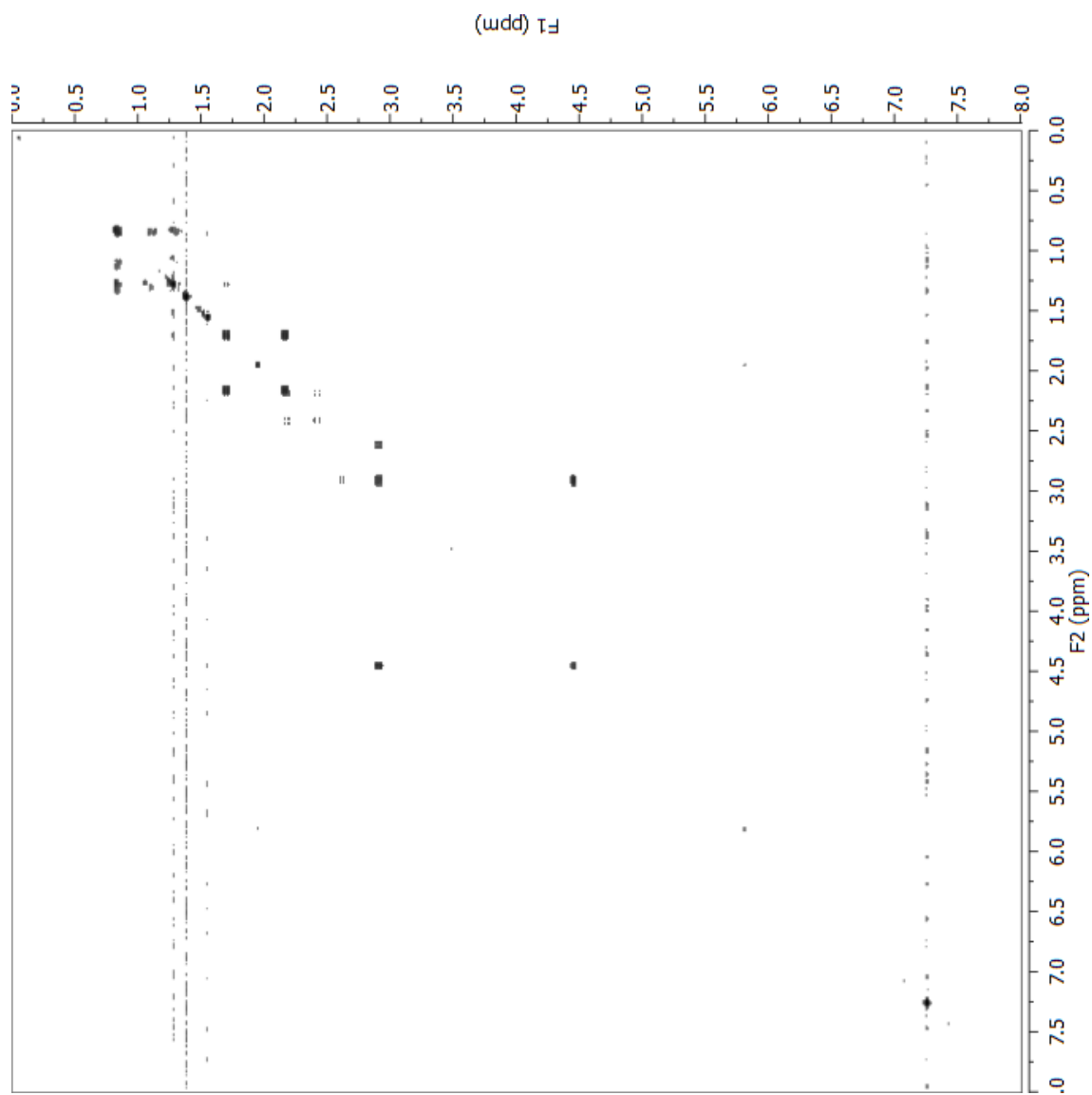


^{13}C NMR spectrum of epiplakinic acid I methyl ester (**96**) (150 MHz, CDCl_3).

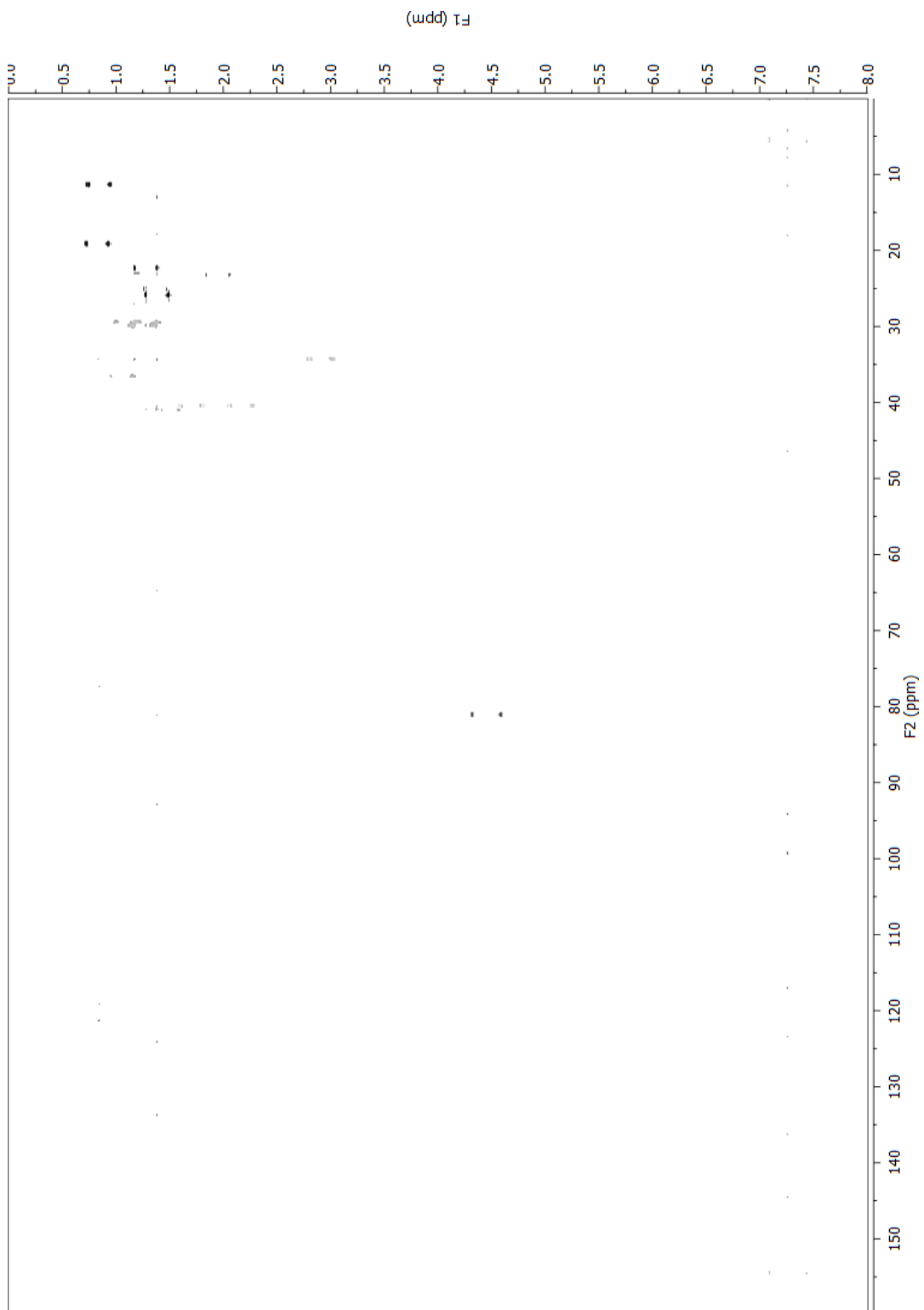
Plakortolide X



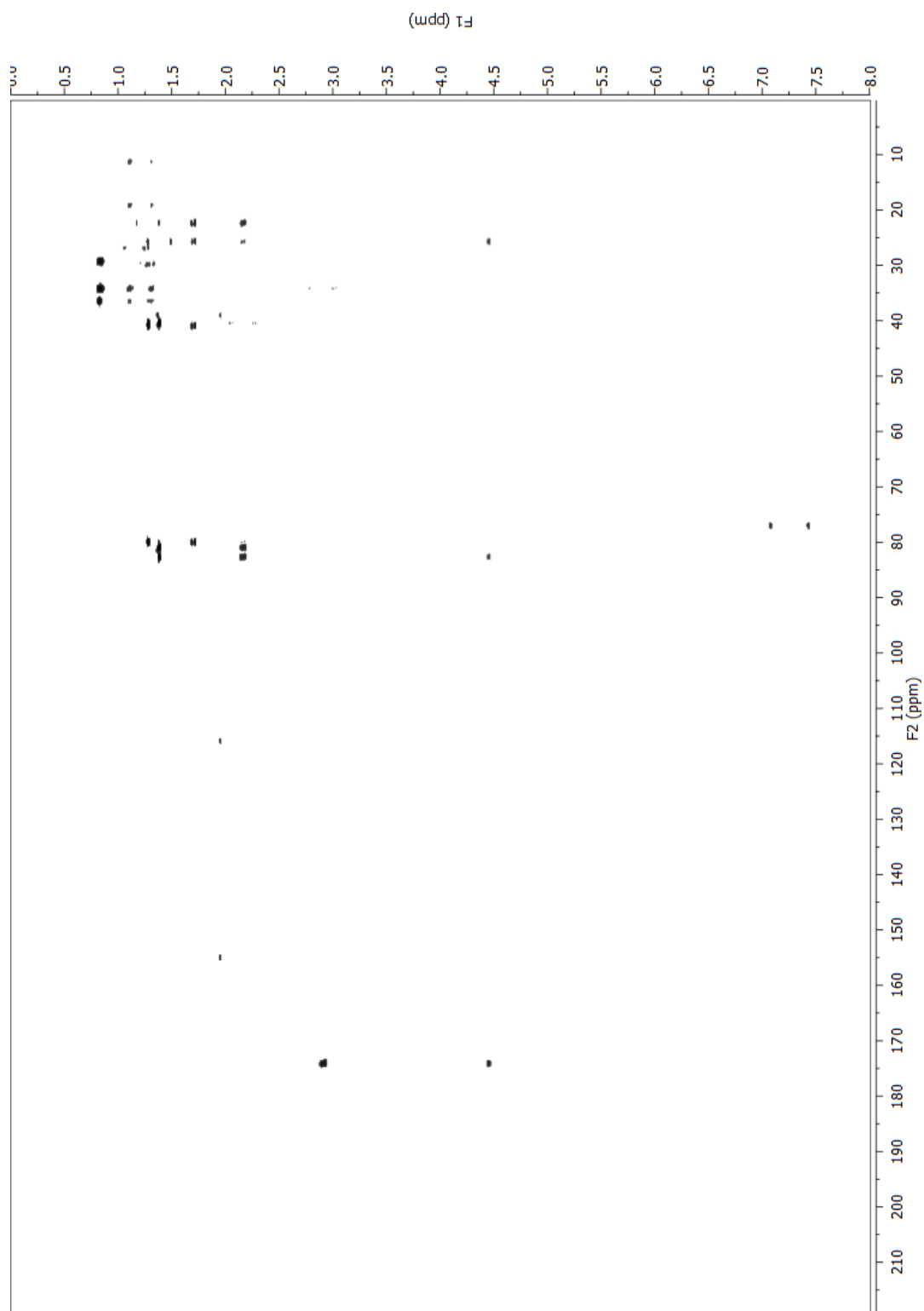
¹H NMR spectrum of plakortolide X (**97**) (600 MHz, CDCl₃).



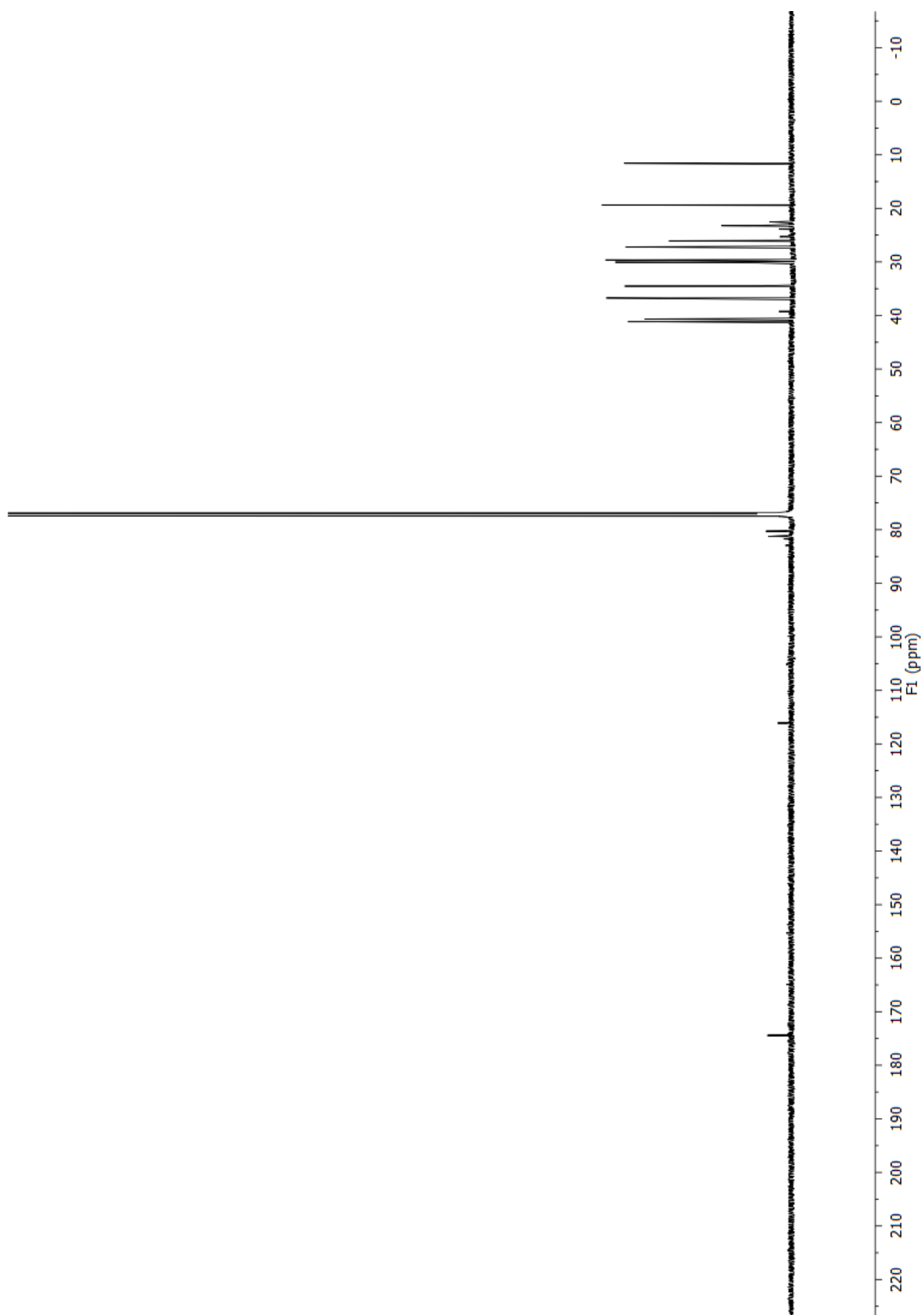
COSY spectrum of plakortolide X (**97**) (600 MHz, CDCl₃).



Fully-coupled HSQC spectrum of plakortolide X (**97**) (600 MHz, CDCl₃).

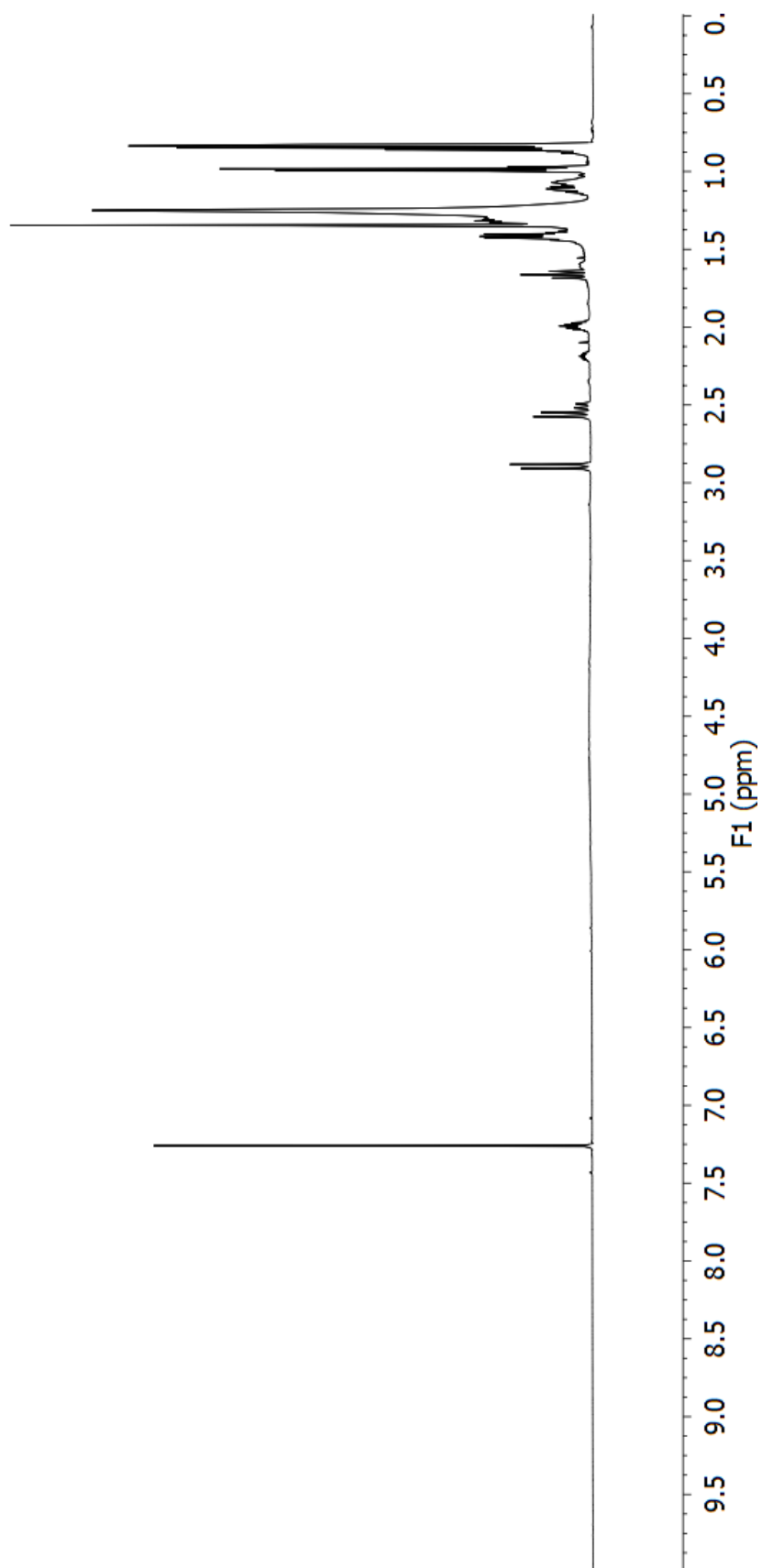


HMBC spectrum of plakortolide X (**97**) (600 MHz, CDCl₃).

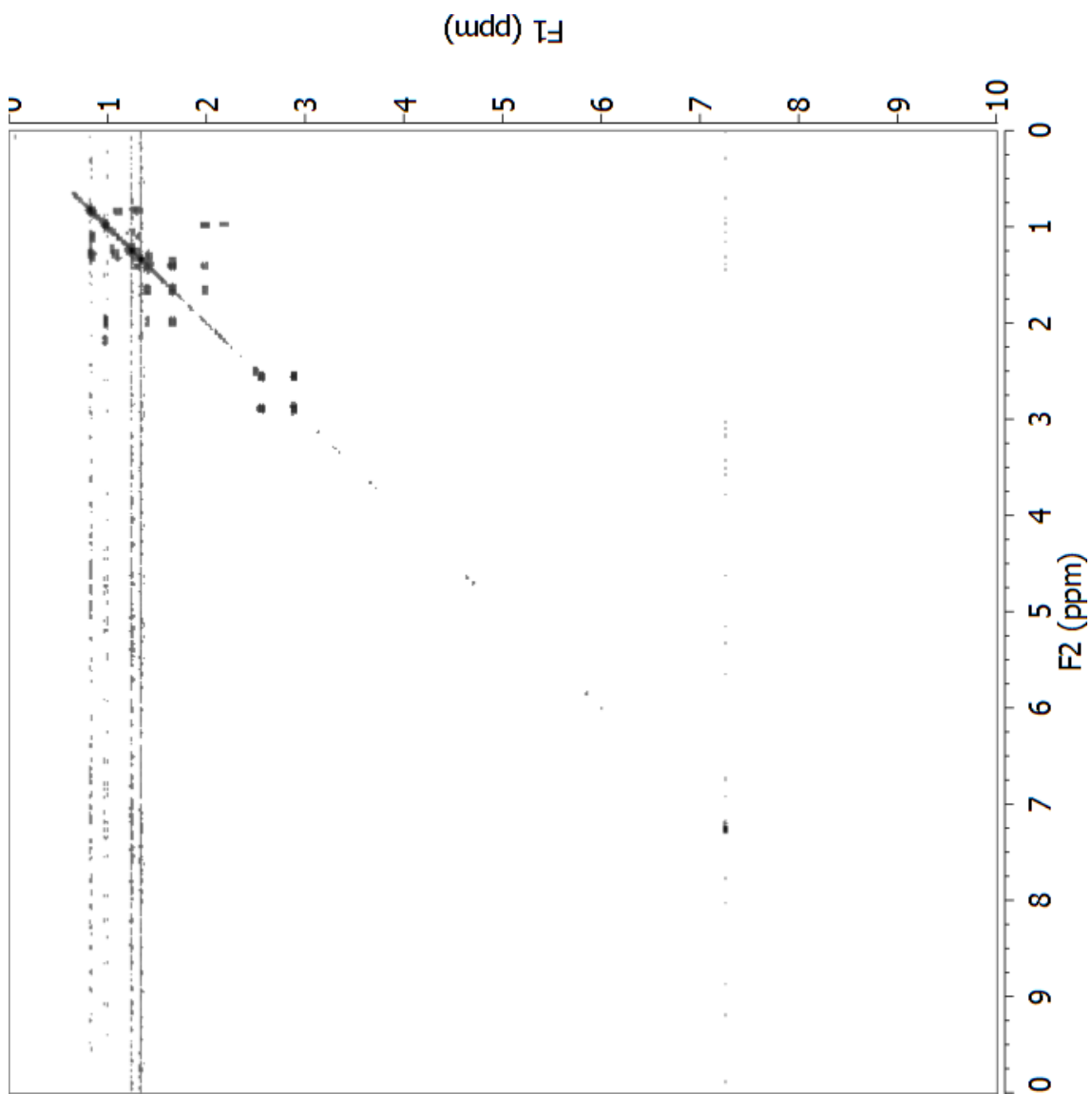


^{13}C NMR spectrum of plakortolide X (**97**) (150 MHz, CDCl_3).

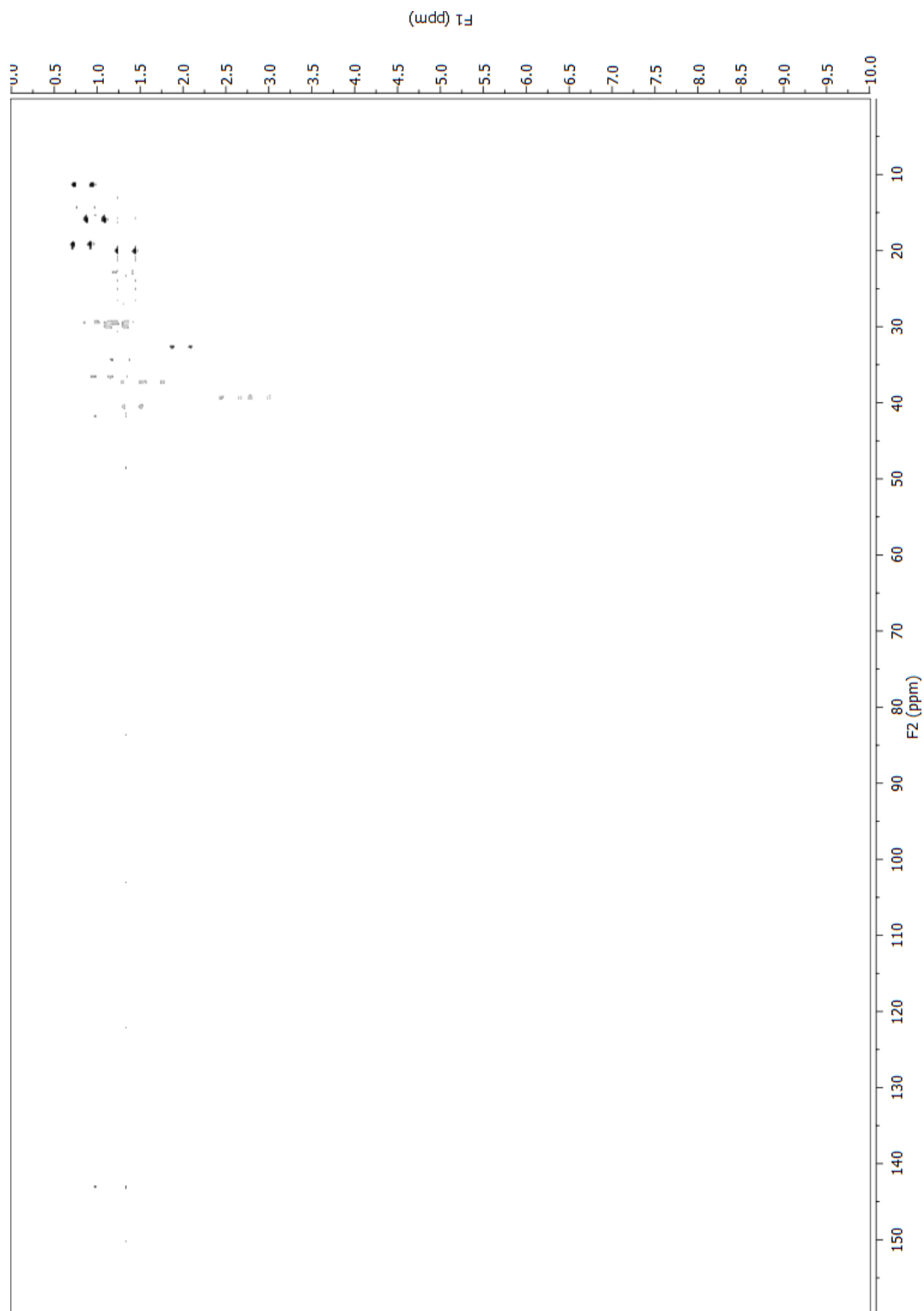
Cyclic peroxide **98**



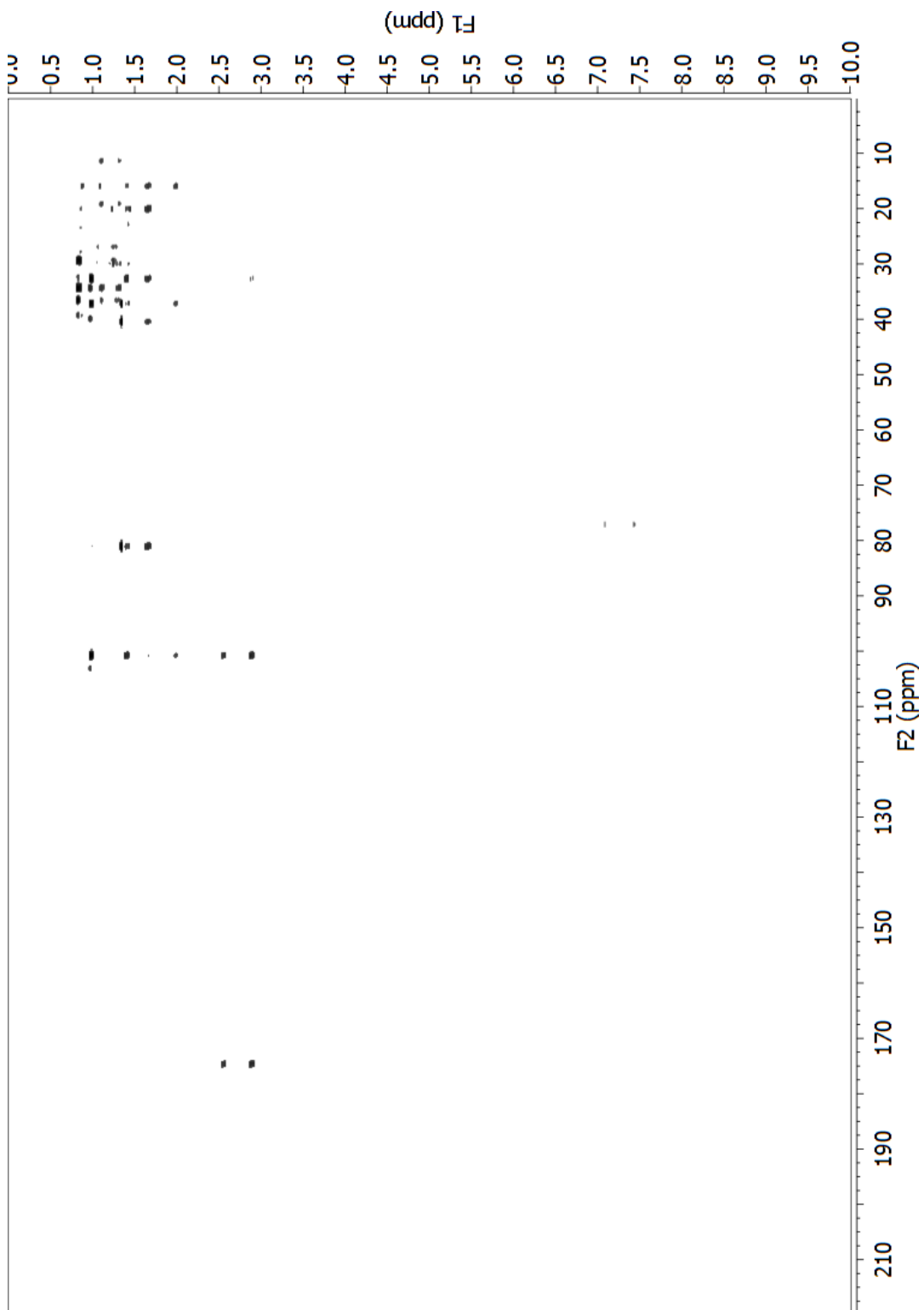
^1H NMR spectrum of cyclic peroxide **98** (600 MHz, CDCl_3).



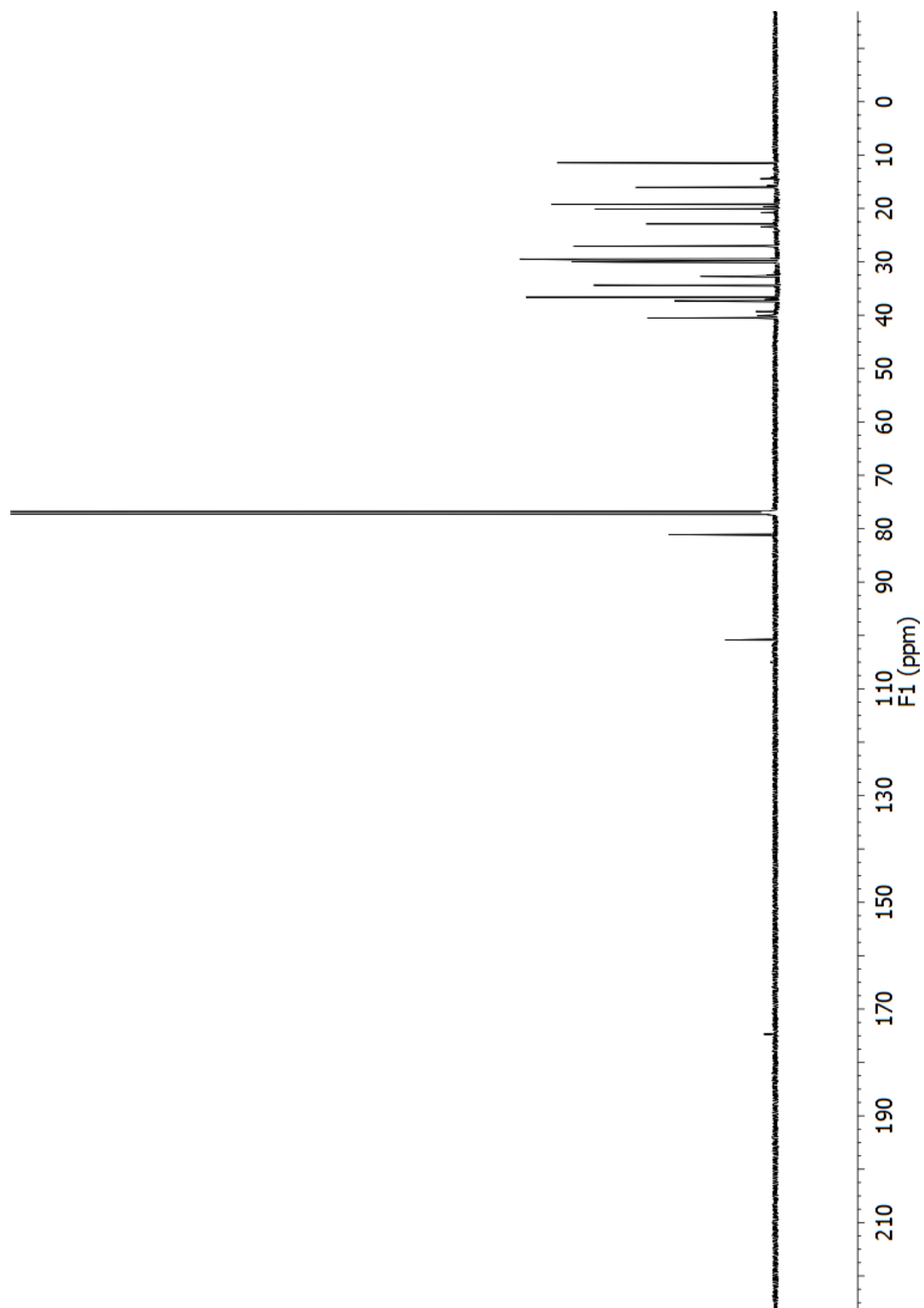
COSY spectrum of cyclic peroxide **98** (600 MHz, CDCl₃).



Fully-coupled HSQC spectrum of cyclic peroxide **98** (600 MHz, CDCl_3).



HMBC spectrum of cyclic peroxide **98** (600 MHz, CDCl_3).

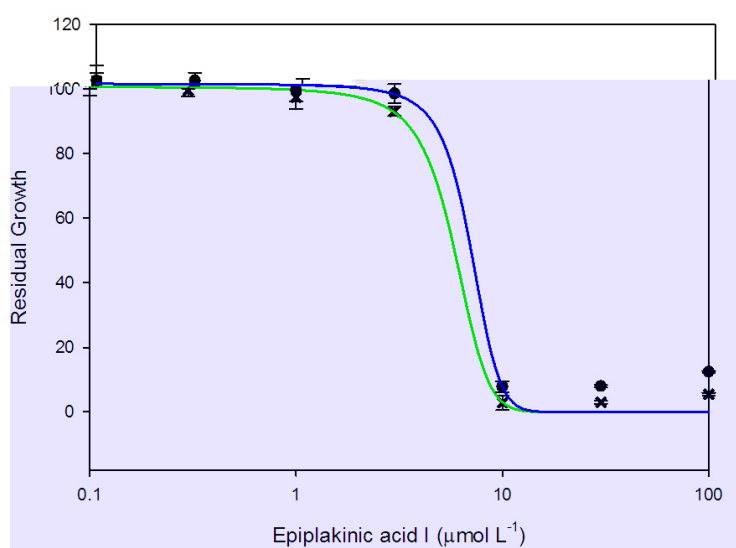


^{13}C NMR spectrum of cyclic peroxide **98** (150 MHz, CDCl_3).

Appendix H

Phenotypic Profile of 95

A



B

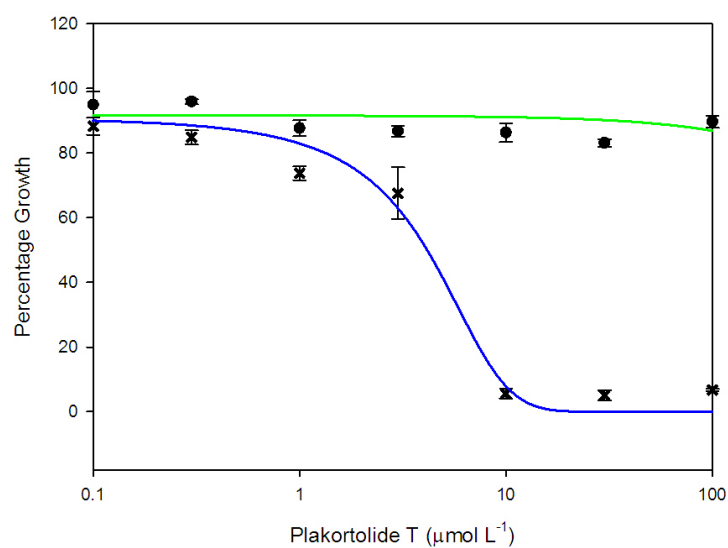
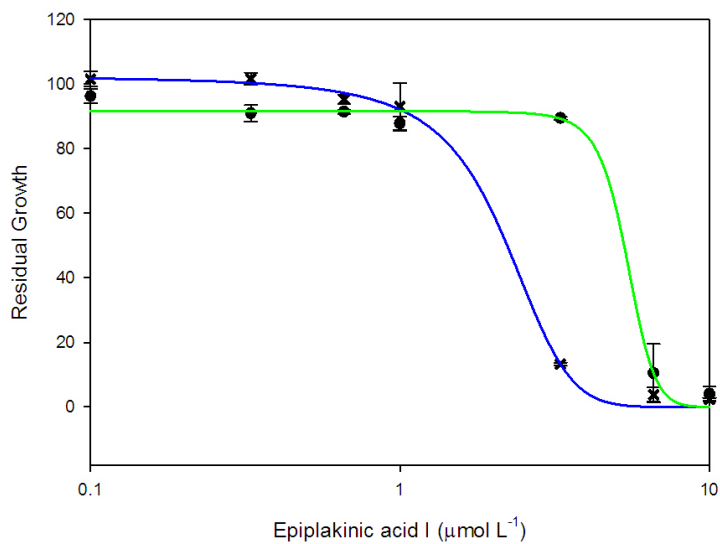


Figure H.1 Dose-response curves for epiplakinic acid I (**95**) and plakortolide X (**97**). **95** displays similar inhibition of both strains, while **97** only inhibits the Δpdr strain.

A: **95**, WT (—●—) and Δpdr (—×—) B: **97**, WT (—●—) and Δpdr (—×—)

A



B

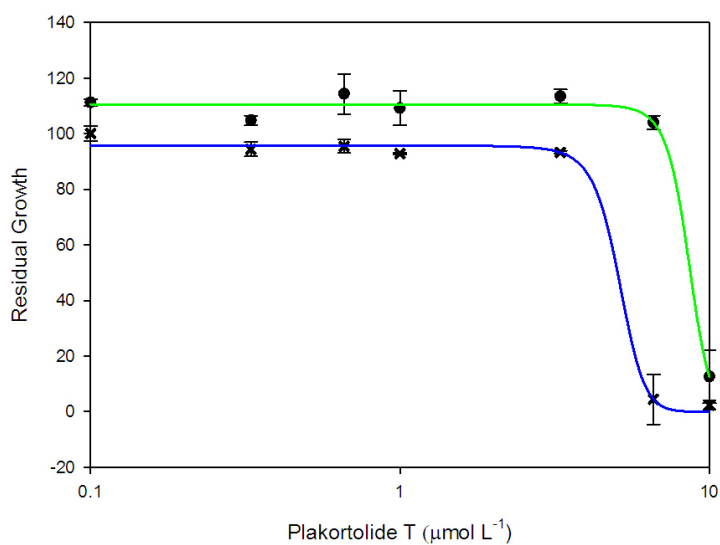


Figure H.2 Activity of epiplakinic acid I (**95**) and plakortolide X (**97**) is enhanced by high Ca^{2+} levels.

A: **95** (●) IC_{50} $4.98 \mu\text{mol L}^{-1}$ **95** and $50 \text{ mmol L}^{-1} \text{ CaCl}_2$ (×) IC_{50} $1.88 \mu\text{mol L}^{-1}$

B: **97** (●) IC_{50} $7.38 \mu\text{mol L}^{-1}$ **97** and $50 \text{ mmol L}^{-1} \text{ CaCl}_2$ (×) IC_{50} $4.68 \mu\text{mol L}^{-1}$

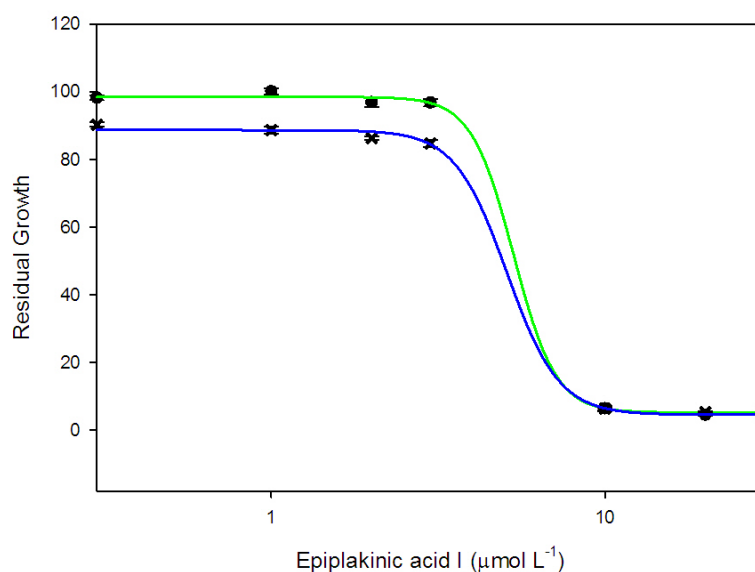


Figure H.3 Dose-response curves for epiplakinic acid I and plakortolide X in the presence of EGTA.

A: **95** (—x—) **95** and EGTA, 10 mmol L⁻¹ (—•—)

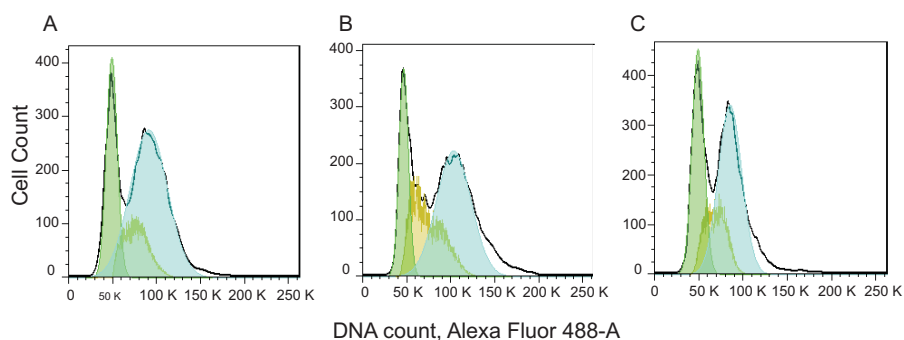


Figure H.4 Epiplakinic acid I (**95**) causes a 50% increase in S-phase population of cells treated at the IC₅₀, and increases the G₂ population when administered at the MIC.

A: DMSO, 1% B: **95**, IC₅₀ (3.45 μmol L⁻¹) C: **95**, MIC (10 μmol L⁻¹)

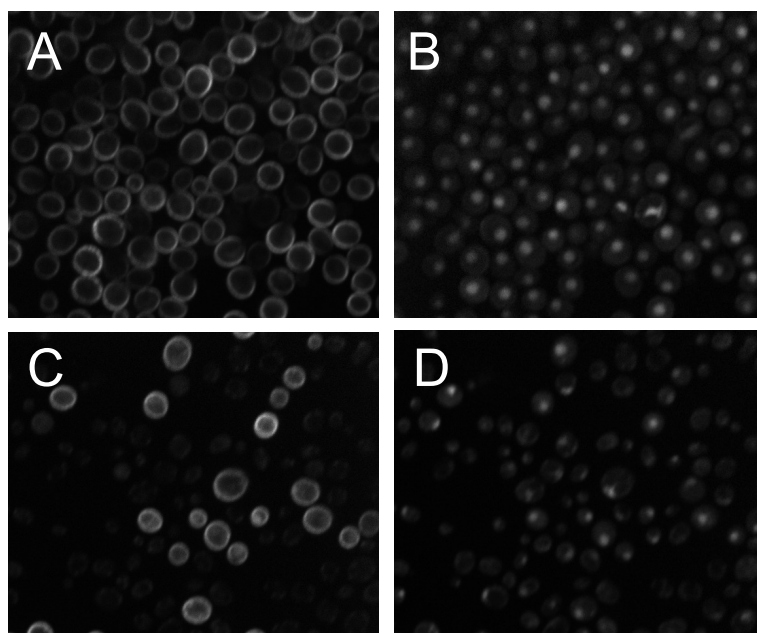


Figure H.5 Epiplakinic acid I (**95**) affects a decrease in cell size in *S. cerevisiae*. The red proteins mCherry and Red Star II localise to the cytoplasm and nucleus respectively, while the GFP-tagged Mrh1p resides in the plasma membrane.

A: DMSO (1%), 2 h, Mrh1-GFP B: DMSO (1%), 2 h, mCherry/Red Star II
 C: **95** ($10 \mu\text{mol L}^{-1}$), 2 h, Mrh1-GFP D: **95** ($10 \mu\text{mol L}^{-1}$), 2 h, mCherry/Red Star II

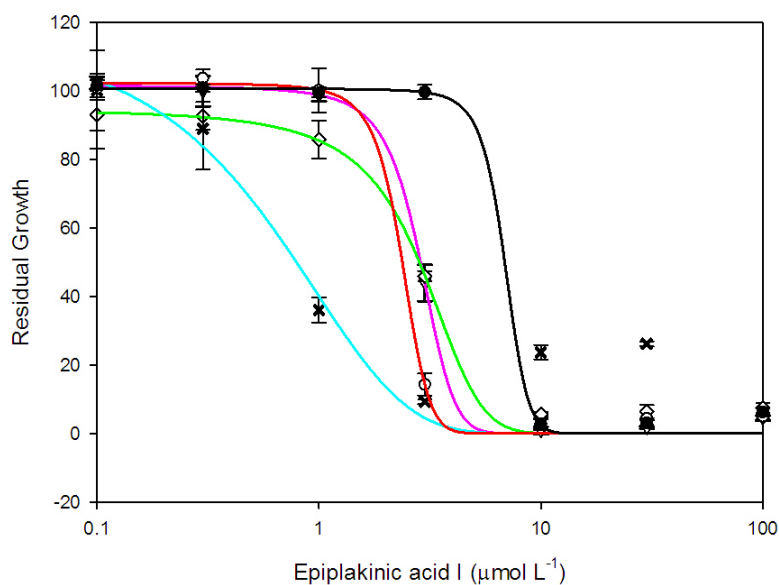
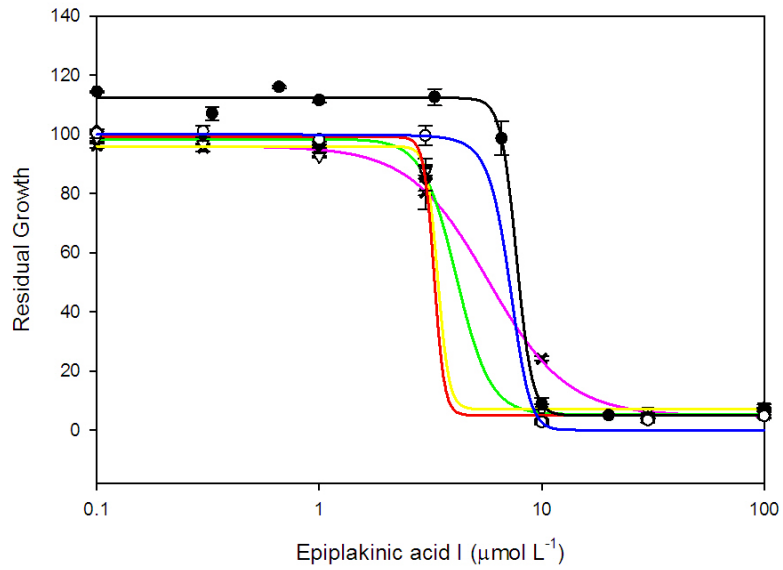


Figure H.6 Hypersensitivity of cytoskeletal mutants to epiplakinic acid I (**95**) relative to the BY4743 WT strain (—●—).

$\Delta RVS167$ (—▽—) IC_{50} $1.91 \mu\text{mol L}^{-1}$ $\Delta SLA1$ (—○—) IC_{50} $1.98 \mu\text{mol L}^{-1}$
 $\Delta SFP1$ (—×—) IC_{50} $2.80 \mu\text{mol L}^{-1}$ $\Delta RSA1$ (—◇—) IC_{50} $2.82 \mu\text{mol L}^{-1}$

A



B

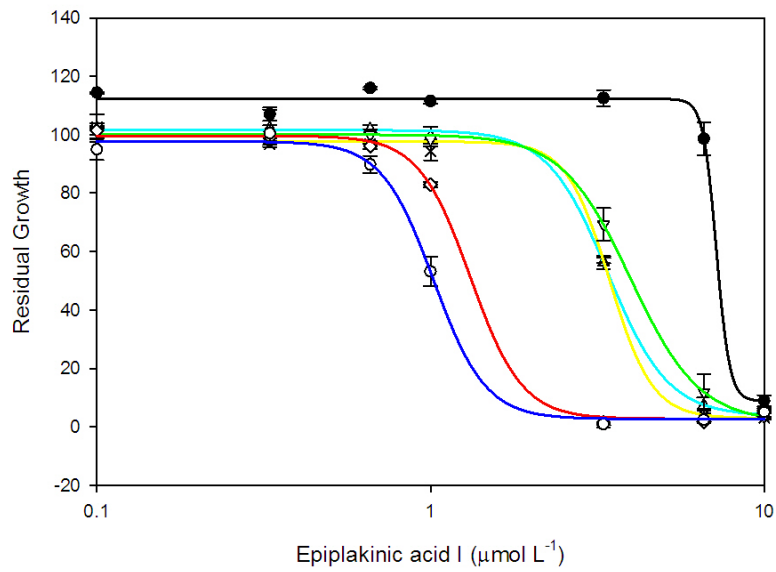


Figure H.7 Dose-response curves for epiplakinic acid I against Ca^{2+} -responsive deletions strains relative to the WT control.

A:	WT BY4743	(-●-)		$\Delta CNA1$	(-○-)	IC_{50} 3.77 $\mu\text{mol L}^{-1}$
	$\Delta CNA2$	(-△-)	IC_{50} 3.56 $\mu\text{mol L}^{-1}$	$\Delta CNB1$	(-▽-)	IC_{50} 3.53 $\mu\text{mol L}^{-1}$
	$\Delta CRZ1$	(-◇-)	IC_{50} 3.49 $\mu\text{mol L}^{-1}$	$\Delta HCM1$	(-×-)	IC_{50} 6.31 $\mu\text{mol L}^{-1}$
B:	WT BY4743	(-●-)		$\Delta CCH1$	(-△-)	IC_{50} 3.60 $\mu\text{mol L}^{-1}$
	$\Delta MID1$	(-◇-)	IC_{50} 3.28 $\mu\text{mol L}^{-1}$	$\Delta PMC1$	(-▽-)	IC_{50} 5.25 $\mu\text{mol L}^{-1}$
	$\Delta PMR1$	(-×-)	IC_{50} 3.36 $\mu\text{mol L}^{-1}$	$\Delta YGL167W$	(-○-)	IC_{50} 3.15 $\mu\text{mol L}^{-1}$

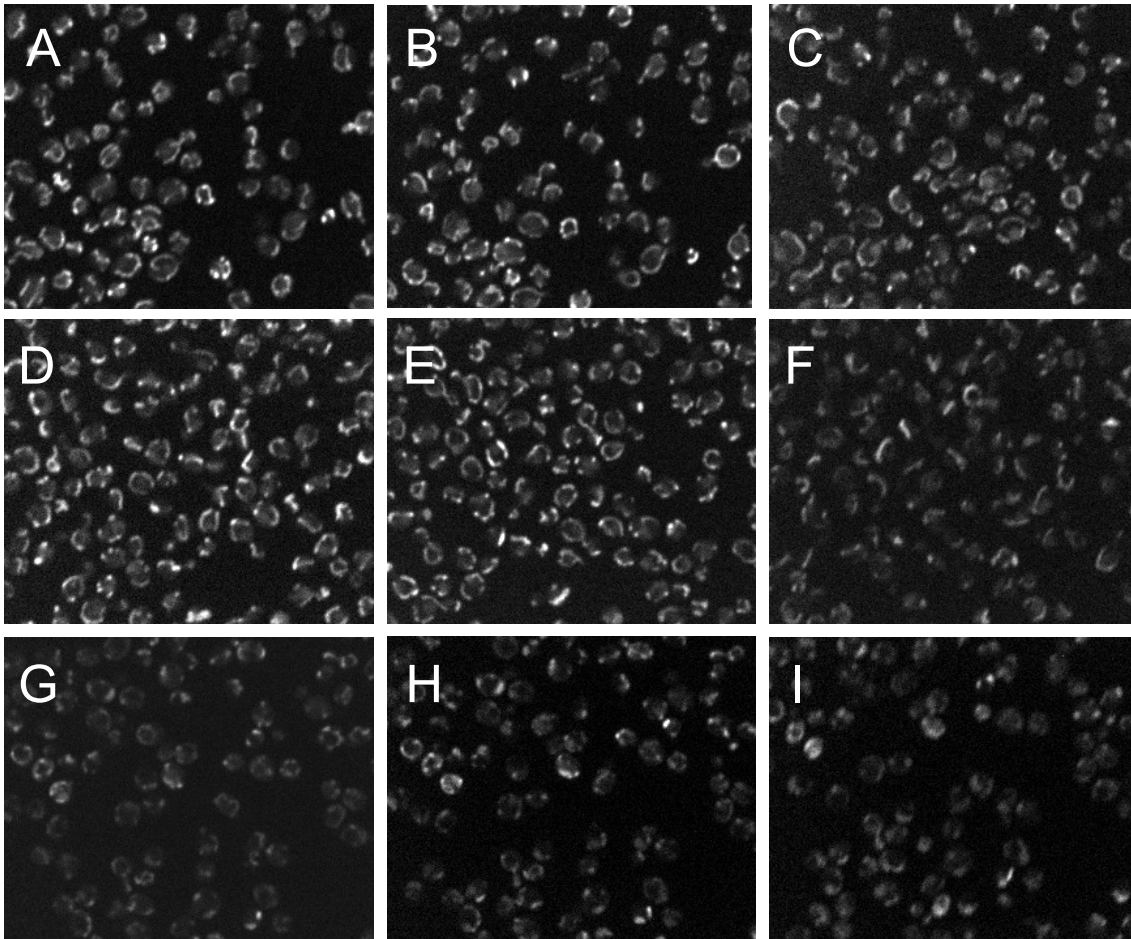


Figure H.8 Translocation studies in the Zrt1p-GFP, non-conclusive for endocytosis of the membrane pump in response to a rise in intracellular Zn^{2+} or exposure to **95**.

A: DMSO, 0 min B: DMSO, t = 10 min C: DMSO, t = 40 min
D: **95**, 0 min E: **95**, t = 10 min F: **95**, t = 40 min
G: ZnCl₂, 0 min H: ZnCl₂, t = 10 min I: ZnCl₂, t = 40 min

Appendix I

Chemical Genetic Profile of 95

Table I.1 Homozygous Profile of Epiplakinic Acid I (**95**).

Up Tag		Dn Tag	
Gene	z-score	Gene	z-score
SLA1	-5.809413688	SLA1	-4.410560386
VPS24	-4.972817922	RPS9B	-4.36002436
VPS28	-4.697856815	END3	-4.222755852
END3	-4.436000379	YER087W	-3.991511202
YIL157C	-4.334762811	STP22	-3.934688549
YOR019W	-4.161528418	GOS1	-3.911094923
CRZ1	-4.125482084	TPS2	-3.834067429
YOR161C	-4.048027013	VPS28	-3.741074729
YNL120C	-4.025318625	VPS36	-3.685492132
RVS161	-3.979063015	RGP1	-3.659586023
OCH1	-3.791609729	SNF7	-3.576692859
SNF7	-3.576648865	DBP7	-3.53354966
SLI15	-3.572018966	YBL054W	-3.48368878
BRO1	-3.457644953	SOD1	-3.444793226
APL2	-3.346409981	VAC7	-3.429958961
APT2	-3.269609242	GRR1	-3.37594831
VPS4	-3.205010706	YPL005W	-3.362444783
HCM1	-3.123723593	SPO74	-3.304200493
SFP1	-3.110038414	RCY1	-3.290998502
PFK2	-3.029516051	RVS167	-3.204320695
VPS24	-4.972817922	CSG2	-3.171599027
		DID2	-3.16113872
		CHS5	-3.147043804
		YLR338W	-3.093662482
		RSA1	-3.088253698
		IRS4	-3.057798815
		ARO7	-3.027509409

Bold font indicates genes with tag overlap.

Table I.2 Haploinsufficiency Profile of Epiplakinic Acid I (**95**).

Up Tag		Dn Tag	
Gene	z-score	Gene	z-score
YBL044W	-9.434195341	OST5	-11.41086097
EDE1	-8.904361216	KIN4	-10.08904761
YKL200C	-8.806319953	YLR123C	-9.940118526
UBP13	-8.521427816	VHS1	-8.40816393
ENT4	-8.259266665	INP52	-7.877981485
UBR2	-7.827602252	CAR2	-7.590762838
NDT80	-7.110771208	MRM2	-7.488420803
YMR316C-A	-6.806339037	RPS15	-7.405188592
YFR043C	-6.655317155	MRS1	-7.323103591
ELA1	-6.592775111	EUG1	-6.945223471
YOR298W	-6.477197383	YLR241W	-6.693412231
YJL163C	-6.472217167	SSP2	-6.651131162
THI12	-6.427515036	YDL206W	-6.526193924
YER139C	-6.341261909	COX17	-6.402868993
YNL187W	-6.334975414	YDR223W	-6.149852711
YLR202C	-6.334490923	YLR269C	-5.860689213
MAP2	-6.248179852	PHO36	-5.56226546
DDP1	-6.153337929	MAD3	-5.413899915
PCI8	-6.005399364	GAL3	-5.351678774
YBL083C	-5.881486314	PMT6	-5.279371881
AIM2	-5.838454891	HIS3	-5.175504603
YIL077C	-5.791565696	DAL7	-5.166777412
YDR084C	-5.644580502	FRM2	-5.115838933
LST4	-5.626825535	RPS14B	-5.023021712
AST1	-5.519434755	YER181C	-5.019790686
EUG1	-5.211588583	MRPL11	-5.003391004
ERV46	-5.210483898	YUH1	-4.97076341
PST1	-5.205556664	YGL232W	-4.866882063
YOR019W	-5.148338476	PTP1	-4.618553681
AZR1	-5.09881151	SLZ1	-4.617101441
PYK2	-5.056831381	RPS7A	-4.38453948
YIM1	-5.041111789	FOX2	-4.344719978
YPL245W	-4.960736203	RAX1	-4.334933264
SSA3	-4.867248834	RPL27A	-4.236754744
YFR055W	-4.766419283	MSN5	-4.222920612
YMR210W	-4.766383731	GGA1	-4.205278815
YKR017C	-4.659871866	PRP43	-4.189182085
ATH1	-4.642439614	GMH1	-3.90118805
PHO81	-4.441089116	RAD4	-3.86603065
MAF1	-4.410447644	GAC1	-3.745939683
YOR255W	-4.389717345	YSA1	-3.662090839
PCL1	-4.362060286	YGL082W	-3.599448702
STE13	-4.272390889	HHT1	-3.59855679
ASC1	-4.171738708	PXR1	-3.486747419
RPC10	-4.036284207	RPL39	-3.447685757
ASI1	-4.006071145	RPL33A	-3.422225152

Continued on following page ...

Bold font indicates genes with tag overlap.
Essential genes appear in blue.

Table I.3 Haploinsufficiency Profile of Epiplakinic Acid I Continued (**95**).

Up Tag		Dn Tag	
Gene	z-score	Gene	z-score
CIK1	-3.741965011	YIL086C	-3.212591118
RTS2	-3.886488775	TPS1	-3.410693771
YFR046C	-3.826413009	DIP5	-3.385823841
PDR8	-3.754045725	YGR107W	-3.132920087
YDR066C	-3.677657055	IMD3	-3.116253877
GNP1	-3.660006156	NAP1	-3.110696791
YJR015W	-3.656590627	YLL012W	-3.110245285
YOL048C	-3.646448665	MRPL16	-3.101164361
YIR003W	-3.6222659	ADO1	-3.086583503
YOS9	-3.599699728	MNE1	-3.015526831
RCL1	-3.536428723		
STP2	-3.501269521		
YLR400W	-3.420612012		
CRC1	-3.409312476		
SHU1	-3.28657986		
SIP1	-3.285653011		
FSH3	-3.2770514		
ABP140	-3.235341139		
YGL160W	-3.114316827		
YDR492W	-3.096230308		
YBR016W	-3.095670033		
YRA2	-3.020672642		
SUR2	-3.000979236		

Bold font indicates genes with tag overlap.
Essential genes appear in blue.

Table I.4 Functional Categories of Deletion Strains Resistant to Epiplakinic Acid I (**95**, $3 \mu\text{mol L}^{-1}$, z-score > 2).

GO Molecular Function	p-value	Gene deletion strain
Phosphatidylinositol transporter activity	0.000371781	SFH5 and CSR1
Phospholipase activity	0.000371781	PLB3, YOR022C, CSR1 and PLB3
FMN reductase activity	0.0062093	LOT6
NAD(P)H dehydrogenase (quinone) activity	0.0062093	LOT6
High affinity zinc ion uptake and transmembrane transporter activity	0.0062093	ZRT1
<i>bis</i> (5'-Adenosyl)-triphosphatase activity	0.0062093	HNT2
Phosphatidylserine catabolic process	0.0062093	PLB3
Regulation of fatty acid metabolic process	0.0062093	CSR1, PLB3 and YOR022C
Lipid transport	0.00733151	SFH5 and CSR1

Table I.5 Functional Categories of Heterozygous Deletion Strains Resistant to Epiplakinic Acid I (**95**, 2 $\mu\text{mol L}^{-1}$, z-score > 2).

GO Molecular Functions	p-value	Gene deletion strain
Structural constituent of ribosome	9.07E-05	RPS8A, RPS11A, RSM10, RPS13, RPS18A, RPL27B, RPS2, RPS21B, RSM22, RPS27A, RPL20A and RPS28A
SSU rRNA binding	0.00130933	RPS13 and RPS2
Inositol or phosphatidylinositol phosphatase activity	0.00587519	INM2 and INP52
S-adenosylmethionine-dependent methyltransferase activity	0.00309695	RSM22, NOP2 and YNL092W
Adenyl-nucleotide exchange factor activity	0.00320969	LHS1 and SIL1
Post-translational protein targeting to membrane, translocation	0.00748032	SBH1 and LHS1
SRP-dependent cotranslational protein targeting to membrane and translocation	0.00925952	SBH1 and SIL1
Structural constituent of nuclear pore	0.00444974	NUP192 and NSP1
Translation	6.78E-05	FMT1, RPS8A, SLM5, RPS11A, RSM10, RPS13, GCD6, RPS18A, RPL27B, RPS2, RPS0A, RPS20, RPL40A, RPS21B, RPL39, RSM22, RPS27A, MEF1, RPL37A, RPS30A, RPL13B, RPL20A, YNL040W, RPL16B, YNL122C, RPS28A, RPS6A, MSD1 and RPL43A
rRNA processing	0.00059314	RPS8A, RPS11A, RSM10, RPS13, GCD6, RPS18A, RPL27B, RPS2, RPS21B, RSM22, RPS27A, MEF1, RPL20A, YNL040W and RPS28A
rRNA export from nucleus	0.000640291	NUP84, RPS18A, RPS2, and RPS28A

Bibliography

1. Newman, D. J.; Cragg, G. M.; Snader, K. M. *Nat. Prod. Rep.* **2000**, *17*, 215–234.
2. *National Cancer Institute*, 2012. <http://www.cancer.gov/aboutnci/servingpeople/cancer-statistics/costofcancer>.
3. *New Zealand Cancer Society*, 2012. <http://www.cancernz.org.nz/divisions/auckland/about/cancer-statistics/>.
4. Newman, D. J.; Cragg, G. M. *J. Nat. Prod.* **2007**, *70*, 461–477.
5. Koehn, F. E.; Carter, G. T. *Nat. Rev. Drug Discov.* **2005**, *4*, 206–220.
6. Piggott, A.; Karuso, P. *Mar. Drugs* **2005**, *3*, 36–63.
7. Clardy, J.; Walsh, C. *Nature* **2004**, *432*, 829–837.
8. Oberlies, N. H.; Flora, S.; Weaver, A. L. *Chemistry International* **2003**, *25*, NA.
9. Thayer, A. *Chem. Eng. News* **2003**, *18*, 6.
10. Bentley, T. S.; Hanson, S. G. *2011 U.S. organ and tissue transplant cost estimates and discussion*, 2011.
11. Dickschat, J. S. *Beilstein J. Org. Chem.* **2011**, *7*, 1620–1621.
12. Stone, M. J.; Williams, D. H. *Mol. Microbiol.* **1992**, *6*, 29–34.
13. Berenbaum, M. R. *Proc. Natl. Acad. Sci. USA* **1995**, *92*, 2–8.
14. Haefner, B. *Drug Discov. Today* **2003**, *8*, 536–544.
15. Verdine, G. L. *Nature* **1996**, *384*, 11–13.
16. Hruby, V. J.; Shenderovich, M.; Lam, K. S.; Lebl, M. *Mol. Divers.* **1996**, *2*, 46–56.
17. Newman, D. J.; Cragg, G. M. *J. Nat. Prod.* **2012**, *75*, 311–335.
18. Lam, K. S. *Trends Microbiol.* **2007**, *15*, 279–289.
19. Paterson, I.; Anderson, E. A. *Science* **2005**, *310*, 451–453.
20. Feher, M.; Schmidt, J. M. *J. Chem. Inf. Comp. Sci.* **2002**, *43*, 218–227.
21. Lipinski, C. A.; Lombardo, F.; Dominy, B. W.; Feeney, P. J. *Adv. Drug Deliv. Rev.* **1997**, *23*, 3–25.
22. Stahura, F. L.; Xue, L.; Godden, J. W.; Bajorath, J. *J. Mol. Model.* **2000**, *6*, 550–562.
23. Stahura, F. L.; Godden, J. W.; Xue, L.; Bajorath, J. *J. Chem. Inf. Comp. Sci.* **2000**, *40*, 1245–1252.

24. Costantino, V.; Fattorusso, E.; Menna, M.; Tagliatalata-Scafati, O. *Curr. Med. Chem.* **2004**, *11*, 1671–1692.
25. Dandapani, S.; Marcaurelle, L. A. *Nature Chemical Biology* **2010**, *6*, 861–863.
26. Rosén, J.; Gottfries, J.; Muresan, S.; Backlund, A.; ; Oprea, T. I. *J. Med. Chem.* **2009**, *52*, 1953–1962.
27. *National Oceanic and Atmospheric Administration*, 2012. <http://www.noaa.gov/index.html>.
28. Blunt, J. W.; Munro, M. H. G. *MarinLit, Marine Literature Database*, 2011.
29. Luch, A. *Molecular, Clinical and Environmental Toxicology: Clinical Toxicology*; Springer, 2010; pp 68–69.
30. Anderson, W. H. *J. Ethnopharmacol.* **1988**, *23*, 121–126.
31. Hwang, D. F.; Noguchi, T. *Adv. Food Nutr. Res.* **2007**, *52*, 141–236.
32. Chau, R.; Kalaitzis, J. A.; Neilan, B. A. *Aquatic Toxicology* **2011**, *104*, 61–72.
33. *New World Encyclopaedia*, 2012. <http://www.newworldencyclopedia.org/>.
34. Pomati, F.; Burns, B. P.; Neilan, B. A. *App. Environmen. Microbiol.* **2004**, *70*, 4711–4719.
35. Molinski, T. F.; Dalisay, D. S.; Lievens, S. L.; Saludes, J. P. *Nat. Rev. Drug Discov.* **2009**, *8*, 69–85.
36. Miljanich, G. P. *Curr. Med. Chem.* **2004**, *11*, 3029–3040.
37. Müller, W. E. G.; Müller, I. M. *Integr. Comp. Biol.* **2003**, *43*, 281–292.
38. *Systema Porifera. A Guide to the Classification of Sponges*; Hooper, J. N. A., van Soest, R. W. M., Eds.; Kluwer Academic/Plenum Publishers: New York, 2002; Vol. 1.
39. Northcote, P. *Verbal communication*, 2011.
40. Newman, D. J.; Cragg, G. M.; Snader, K. M. *J. Nat. Prod.* **2003**, *66*, 1022–1037.
41. Bergmann, W.; Feeney, R. J. *J. Am. Chem. Soc.* **1950**, *72*, 2809–2810.
42. Bergmann, W.; Feeney, R. J. *J. Org. Chem.* **1951**, *16*, 981–987.
43. Bergmann, W.; Burke, D. C. *J. Org. Chem.* **1955**, *20*, 1501–1507.
44. Sipkema, D.; Franssen, M. C. R.; Osinga, R.; Tramper, J.; Wijffels, R. H. *Mar. Biotechnol.* **2005**, *7*, 142–162.
45. Wright, K. *Nature* **1986**, *323*, 283.
46. Ledford, H. *Nature* **2010**, *468*, 608–609.
47. Hirata, Y.; Uemura, D. *Pure Appl. Chem.* **1986**, *58*, 701–710.

48. Wojnar, J. M. *Isolation of New Secondary Metabolites from New Zealand Marine Invertebrates*, Ph.D. thesis, Victoria University of Wellington, 2008.
49. König, G. M.; Kehraus, S.; Seibert, S. F.; Abdel-Lateff, A.; Müller, D. *ChemBioChem* **2006**, *7*, 229–238.
50. Laroche, M.; Imperatore, C.; Grozdanov, L.; Costantino, V.; Mangoni, A.; Hentschel, U.; Fattorusso, E. *Marine Biology* **2007**, *151*, 1365–1373.
51. Faulkner, D. J.; Unson, M. D.; Bewley, C. A. *Pure Appl. Chem.* **1994**, *66*, 1983–1990.
52. Lee, O. O.; Wong, Y. H.; Qian, P.-Y. *Appl. Environ. Microbiol.* **2009**, *75*, 3513–3521.
53. Lee, O. O.; Yang, L. H.; Li, X.; Pawlik, J. R.; Qian, P.-Y. *Mar. Ecol. Prog. Ser.* **2007**, *339*, 25–40.
54. Lee, O. O.; Chui, P. Y.; Wong, Y. H.; Pawlik, J. R.; Qian, P.-Y. *Appl. Environ. Microbiol.* **2009**, *75*, 6147 – 5156.
55. *NationMaster*, 2012. NationMaster.com.
56. *The Official Site of Tonga Tourism*, 2011. <http://www.thekingdomoftonga.com/>.
57. Crews, P.; Kakou, Y.; Quinoa, E. *J. Am. Chem. Soc.* **1988**, *110*, 4365–4368.
58. Kakou, Y.; Crews, P.; Bakus, G. J. *J. Nat. Prod.* **1987**, *50*, 482–484.
59. Sashidhara, K. V.; White, K. N.; Crews, P. *J. Nat. Prod.* **2009**, *72*, 588–603.
60. Singh, A. J. *The Structure-Directed Isolation of New Secondary Metabolites from South Pacific Marine Sponges*, Ph.D. thesis, Victoria University of Wellington, 2012.
61. Tanaka, J.; Higa, T. *Tetrahedron Lett.* **1996**, *37*, 5535–5538.
62. Field, J. J.; Singh, A. J.; Kanakkanthara, A.; Halafhi, T.; Northcote, P. T.; Miller, J. H. *J. Med. Chem.* **2009**, *52*, 7328–7332.
63. Vuorela, P.; Leinonen, M.; Saikku, P.; Tammela, P.; Rauha, J. P.; Wennberg, T.; Vuorela, H. *Natural Products in the Process of Finding New Drug Candidates*; Bentham Science Publishers Ltd., 2004; Vol. 11, pp 1375–1389.
64. Rollinger, J. M.; Langer, T.; Stuppner, H. *Strategies for Efficient Lead Structure Discovery from Natural Products*; Bentham Science Publishers Ltd., 2006; Vol. 13, pp 1491–1507.
65. Hilton, B.; Martin, G. *J. Nat. Prod.* **2010**, *73*, 1465–1469.
66. Popplewell, W. L. *Isolation and Structural Elucidation of New Secondary Metabolites from New Zealand Red Algae*, Ph.D. thesis, Victoria University of Wellington, 2008.
67. Bertelli, D.; Lolli, M.; Papotti, G.; Bortolotti, L.; Serra, G.; Plessi, M. *J. Agric. Food. Chem.* **2010**, *58*, 8495–8501.

68. Kos̆ir, I. J.; Kidrič, J. *J. Agric. Food. Chem.* **2000**, *49*, 50–56.
69. Nilsson, M.; Duarte, I. F.; Almeida, C.; Delgadillo, I.; Goodfellow, B. J.; Gil, A. M.; Morris, G. A. *J. Agric. Food. Chem.* **2004**, *52*, 3736–3743.
70. Lambert, J. B.; Heckenbach, E. A.; Wu, Y.; Santiago-Blay, J. A. *J. Nat. Prod.* **2010**, *73*, 1643–1648.
71. Winssinger, N.; Barluenga, S. *Chem. Commun.* **2007**, 22–36.
72. Roe, S. M.; Prodromou, C.; O'Brien, R. *J. Med. Chem.* **1999**, *42*, 260–266.
73. Daux, W. L. W.; Charles, M. *Dev. Toxicol. Environ. Sci.* **1980**, *49*, 153–160.
74. Miksicek, R. J. *J. Steroid Biochem. Mol. Biol.* **1994**, *49*, 153–160.
75. Boone, C.; Bussey, H.; Andrews, B. J. *Nature Rev. Gen.* **2007**, *8*, 437–449.
76. Giaever, G.; Flaherty, P.; Kumm, J.; Proctor, M.; Nislow, C.; Jaramillo, D. F.; Chu, A. M.; Jordan, M. I.; Arkin, A. P.; Davis, R. W. *Nature* **2002**, *418*, 387–391.
77. Adomas, A.; Heller, G.; Olson, A.; Osborne, J.; Karlsson, M.; Nahalkova, J.; Zyl, L. V.; Sederoff, R.; Stenlid, J.; Finlay, R.; Asiegbu, F. *Tree Physiol.* **2008**, *28*, 888–897.
78. Taufu, T. *New Sesterterpenes from Marine Sponges from the Tropical Waters of the Kingdom of Tonga*, M.Sc. thesis, Victoria University of Wellington, 2010.
79. Woolner, V. H. *The Isolation and Structure Elucidation of Secondary Metabolites from Tongan Marine Organisms*, M.Sc. thesis, Victoria University of Wellington, 2012.
80. Gauvin, A.; Smadja, J.; Akinin, M.; Faure, R.; Gaydou, E.-M. *Can. J. Chem.* **2000**, *78*, 986–992.
81. Horton, P. A.; Longley, R. E.; Kelly-Borges, M.; McConnell, O. J.; Ballas, L. M. *J. Nat. Prod.* **1994**, *57*, 1374–1381.
82. Gunatilaka, A. A. L.; Gopichand, Y.; Schmitz, F. J.; Djerassi, C. *J. Org. Chem.* **1980**, *46*, 3860–3886.
83. Ioannou, E.; Abdel-Razik, A. F.; Zervou, M.; Christofidis, D.; Alexi, X.; Vagias, C.; Alexis, M. N.; Roussis, V. *Steroids* **2009**, *74*, 73–80.
84. Chan, A. *Unpublished PhD Research*, 2011, 2011.
85. Segraves, N. L.; Robinson, S. J.; Garcia, D.; Said, S. A.; Fu, X.; Schmitz, F. J.; Pietraszkiwicz, H.; Valeriote, F. A.; Crews, P. *J. Nat. Prod.* **2004**, *67*, 783–792.
86. Roll, D. M.; Scheuer, P. J.; Matsumoto, G. K.; Clardy, J. *J. Am. Chem. Soc.* **1983**, *105*, 6177–6178.
87. Harada, N.; Uda, H.; Kobayashi, M.; Shimizu, N.; Kitagawa, I. *J. Am. Chem. Soc.* **1989**, *111*, 5668–5674.

88. Vacher, H. L.; Quinn, T. M. *Geology and Hydrogeology of Carbonate Islands*; Elsevier, 1997; p 948.
89. Zhi-Daz, M.; Ning, X.; Pei, Z.; Shou-Zun, Z.; Chong-Sh, W.; Qi-Tai, Z. *Phytochemistry* **1991**, *30*, 4175–4177.
90. Lee, I.-S.; Ma, X.; Chai, H.-B.; Madulid, D. A.; Lamont, B. R.; O'Neill, M. J.; Besterman, J. M.; Farnsworth, N. R.; Soejarto, D. D.; Cordell, G. A.; Pezzuto, J. M.; Kinghorn, D. A. *Tetrahedron* **1995**, *51*, 21–28.
91. Chinou, I. *Curr. Med. Chem.* **2005**, *12*, 1295–1317.
92. Williams, J. *The cytotoxic and immunomodulatory properties of novel labdane diterpenes.*, 2010, January 2010.
93. Leahy, D. C. *Inhibition of Eukaryotes*, 2010-2011, 2010-2011.
94. London, C. A.; Abbas, A. K.; Kelso, A. *Veterinary Immunology and Immunopathology* **1998**, *63*, 37–44.
95. Mackay, I. R.; Leskovsek, N. V.; Rose, N. R. *J. Autoimmun.* **2008**, *30*, 5–11.
96. Javeed, A.; Ashraf, M.; Riaz, A.; Ghafoor, A.; Afzal, S.; Mukhtar, M. M. *Eur. J. Pharm. Sci.* **2009**, *38*, 283–290.
97. Kishore, R.; McMullen, M. R.; Cocuzzi, E.; Nagy, L. E. *Comp. Hepatol.* **2004**, *3*, S31.
98. Sosroseno, W.; Bird, P. S.; Seymour, G. J. *Anaerobe* **2009**, *15*, 95–98.
99. Girón, N.; Través, P. G.; Rodríguez, B.; López-Fontal, R.; Boscá, L.; Hortelano, S.; de las Heras, B. *Toxicol. Appl. Pharmacol.* **2008**, *228*, 179–189.
100. Zani, C. L.; Alves, T. M. A.; Queira, R.; Fontes, E. S.; Shin, Y. G.; Cordell, G. A. *Phytochemistry* **2000**, *53*, 877–880.
101. Cocker, J. D.; Halsall, T. G.; Bowers, A. *J. Chem. Soc.* **1956**, 4249–4262.
102. Tanaka, J.; Marriott, G.; Higa, T.; Higa, T. *J. Nat. Prod.* **2001**, *64*, 1468–1470.
103. Tasdemir, D.; Concepcion, G. P.; Mangalindan, G. C.; Harper, M. K.; Hajdu, E.; Ireland, C. M. *Tetrahedron* **2000**, *56*, 9025–9030.
104. Peters, R. J. *Nat. Prod. Rep.* **2010**, *27*, 1521–1530.
105. San-Martin, A.; Quezada, E.; Soto, P.; Palacios, Y.; Rovirosa, J. *Can. J. Chem.* **1996**, *74*, 2471–2475.
106. Diaz-Marrero, A.; Issi, N.; Canales, V.; Chamy, C.; San-Martın, A.; Darias, J.; Rovirosa, J. *Nat. Prod. Res.* **2008**, *22*, 1516–1520.
107. Diaz-Marrero, A. R.; Dorta, E.; Cueto, M.; Rovirosa, J.; San-Martin, A.; Loyola, A.; Darias, J. *Tetrahedron* **2003**, *59*, 4805–4809.
108. Gray, C. A.; Davies-Coleman, M. T.; McQuaid, C. *Nat. Prod. Lett.* **1998**, *12*, 47–53.

109. van Wyk, A. W. W.; Gray, C. A.; Whibley, C. E.; Osoniyi, O.; Hendricks, D. T.; Caira, M. R.; Davies-Coleman, M. T. *J. Nat. Prod.* **2008**, *71*, 420–425.
110. Knass, W.; Reuter, B.; Zapp, J. *J. Biochem.* **1997**, *326*, 449–454.
111. Walker, R. P.; Faulkner, D. J. *J. Org. Chem.* **1981**, *46*, 1098–1102.
112. Meccia, G.; Rosquete, C.; Rojas, L. B.; Feliciano, A. S. *Flavour Frag. J.* **2006**, *21*, 559–561.
113. Diaz, M. C.; van Soest, R. W. M. The Plakinidae: a Sytematic Review. *4th International Porifera Conference*, University of Amsterdam, 1994; pp 99–109.
114. Sandler, J. S.; Colin, P. L.; Hooper, J. N. A.; Faulkner, D. J. *J. Nat. Prod.* **2002**, *65*, 1258–1261.
115. Jiménez, C.; Quinoa, E.; Crews, P. *Tetrahedron Lett.* **1991**, *32*, 1843–1846.
116. Campagnuolo, C.; Fattorusso, E.; Tagliatela-Scafati, O. *Eur. J. Org. Chem.* **2003**, *2003*, 284–287.
117. Borrelli, F.; Campagnuolo, C.; Capasso, R.; Fattorusso, E.; Tagliatela-Scafati, O. *Eur. J. Org. Chem.* **2004**, *15*, 3227–3232.
118. Campagnuolo, C.; Fattorusso, C.; Fattorusso, E.; Ianaro, A.; Pisano, B.; Tagliatela-Scafati, O. *Org. Lett.* **2003**, *5*, 673–676.
119. Fattorusso, E.; Romano, A.; Scala, F.; Tagliatela-Scafati, O. *Molecules* **2008**, *13*, 1465–1471.
120. Murayama, T.; Ohizumi, Y.; Nakamura, H.; Sasaki, T.; Kobayashi, J. *Cell Mol. Life Sci.* **1989**, *45*, 898–899.
121. Smith, S.; Tsai, S.-C. *Nat. Prod. Rep.* **2007**, *24*, 1041–1072.
122. Higgs, M.; Faulkner, D. J. *J. Org. Chem.* **1978**, *43*, 3454–3457.
123. Davidson, B. S. *J. Org. Chem.* **1991**, *56*, 6722–6724.
124. Yong, K. W. L.; de Voss, J. J.; Hooper, J. N. A.; Garson, M. J. *J. Nat. Prod.* **2011**, *74*, 194–207.
125. Gochfeld, D. J.; Hamann, M. T. *J. Nat. Prod.* **2001**, *64*, 1477–1479.
126. Campagnuolo, C.; Fattorusso, E.; Romano, A.; Tagliatela-Scafati, O.; Basilico, N.; Parapini, S.; Taramelli, D. *Eur. J. Org. Chem.* **2005**, *2005*, 5077–5083.
127. del Sol Jiménez, M.; Garzón, S. P.; Rodríguez, A. D. *J. Nat. Prod.* **2003**, *66*, 655–661.
128. Williams, D. E.; Allen, T. M.; van Soest, R.; Behrisch, H. W.; Andersen, R. J. *J. Nat. Prod.* **2001**, *64*, 281–285.
129. Rudi, A.; Afanii, R.; Gravalos, L. G.; Akinin, M.; Gaydou, E.; Vacelet, J.; Kashman, Y. *J. Nat. Prod.* **2003**, *66*, 682–685.

130. Huang, X.-H.; van Soest, R.; Roberge, M.; Andersen, R. *J. Org. Lett.* **2003**, *6*, 75–78.
131. Berrue, F.; Thomas, O. P.; Laville, R.; Prado, S.; Golebiowski, J.; Fernandez, R.; Amade, P. *Tetrahedron* **2007**, *63*, 2328–2334.
132. Sata, N.; Abinsay, H.; Yoshida, W. Y.; Horgen, F. D.; Sitachitta, N.; Kelly, M.; Scheuer, P. J. *J. Nat. Prod.* **2005**, *68*, 1400–1403.
133. Jeso, V.; Micalizio, G. C. *J. Am. Chem. Soc.* **2010**, *132*, 11422–11424.
134. Barber, J. M.; Quek, N. C.; Leahy, D. C.; Miller, J. H.; Bellows, D. S.; Northcote, P. T. *J. Nat. Prod.* **2011**, *74*, 809–815.
135. Silverstein, R. M.; Webster, F. X. *Spectrometric Identification of Organic Compounds*, 6th ed.; John Wiley and Sons, 1997.
136. Nakagawa, A.; Ohno, H.; Miyano, K.; Omura, S. *J. Org. Chem.* **1980**, *45*, 3268–3274.
137. Lacey, M. J.; MacDonald, C. G.; Pross, A.; Shannon, J. S. *Aust. J. Chem.* **1970**, *23*, 1421–1429.
138. Schumacher, R. W.; Davidson, B. S. *Tetrahedron* **1995**, *51*, 10125–10130.
139. Baldwin, J. E.; Hackler, R. E.; Scott, R. M. *J. Chem. Soc.* **1969**, 1415–1416.
140. Kubec, R.; Kim, S.; McKeon, D. M.; Musah, R. A. *J. Nat. Prod.* **2002**, *65*, 960–964.
141. Ranu, B. C.; Dey, S. S.; Hajra, A. *Green Chemistry* **2003**, *5*, 44–46.
142. Kaczorowska, K.; Kolarska, Z.; Mitka, K.; Kowalski, P. *Tetrahedron* **2005**, *61*, 8315–8327.
143. Kowalski, P.; Mitka, K.; Ossowska, K.; Kolarska, Z. *Tetrahedron* **2005**, *61*, 1933–1953.
144. Shaabani, A.; Mirzaei, P.; Naderi, S.; Lee, D. G. *Tetrahedron* **2004**, *60*, 11415–11420.
145. Barbarella, G.; Dembech, P.; Garbesi, A.; Fava, A. *Org. Magn. Reson.* **1976**, *8*, 108–114.
146. Davies, J. A. *Adv. Inorg. Chem. Radiochem.* **1961**, *24*, 115–187.
147. Marks, H. S.; Hilson, J. A.; Leichtweis, H. C.; Stoewsand, G. S. *J. Agric. Food. Chem.* **1992**, *40*, 2098–101.
148. Abdel-Sattar, E.; El-Mekawy, S. *Nat. Prod. Res.* **2009**, *23*, 861–865.
149. Graham, S. K.; Lambert, L. K.; Pierens, G. K.; Hooper, J. N. A.; Garson, M. J. *Aust. J. Chem.* **2010**, *63*, 867–872.
150. Lake, R. J.; McCombs, J. D.; Blunt, J. W.; Munro, M. H. G.; Robinson, W. T. *Tetrahedron Lett.* **1988**, *29*, 4971–4972.

151. Lam, H. W.; Cooke, P. A.; Pattenden, G.; Bandaranayake, W. M.; Wickramasinghe, W. A. *J. Chem. Soc., Perkin Trans. 1* **1999**, 847–848.
152. Quinoa, E.; Crews, P. *Tetrahedron Lett.* **1987**, *28*, 3229–3232.
153. Schneemann, I.; Ohlendorf, B.; Zinecker, H.; Nagel, K.; Wiese, J.; Imhoff, J. F. *J. Nat. Prod.* **2010**, *73*, 1444–1447.
154. Zhang, Y.; Li, X.-M.; Feng, Y.; Wang, B.-G. *Nat. Prod. Res.* **2010**, *24*, 1036–1043.
155. Liu, D.; Li, X.-M.; Meng, L.; Li, C.-S.; Gao, S.-S.; Shang, Z.; Proksch, P.; Huang, C.-G.; Wang, B.-G. *J. Nat. Prod.* **2011**, *74*, 1787–1791.
156. Trisuwan, K.; Rukachaisirikul, V.; Sukpondma, Y.; Preedanon, S.; Phongpaichit, S.; Rungjindamai, N.; Sakayaroj, J. *J. Nat. Prod.* **2008**, *71*, 1323–1326.
157. Wang, C.-Y.; Wang, B.-G.; Brauers, G.; Guan, H.-S.; Proksch, P.; Ebel, R. *J. Nat. Prod.* **2002**, *65*, 772–775.
158. Cutignano, A.; Fontana, A.; Renzulli, L.; Cimino, G. *J. Nat. Prod.* **2003**, *66*, 1399–1401.
159. Ciavatta, M. L.; Manzo, E.; Nuzzo, G.; Villani, G.; Cimino, G.; Cervera, J. L.; Malaquias, M. A. E.; Gavagnin, M. *Tetrahedron Lett.* **2009**, *50*, 527–529.
160. Roviroso, J.; San-Martín, A. *Quím. Nova* **2006**, *29*, 52–53.
161. Hochlowski, J.; Coll, J.; Faulkner, D. J.; Clardy, J. *J. Am. Chem. Soc.* **1984**, *106*, 6748–50.
162. Kong, F.; Singh, M. P.; Carter, G. T. *J. Nat. Prod.* **2005**, *68*, 920–923.
163. Singh, M. P.; Kong, F.; Janso, J. E.; Arias, D. A.; Suarez, P. A.; Bernan, V. S.; Petersen, P. J.; Weiss, W. J.; Carter, G.; Greenstein, M. *J. Antibiot.* **2003**, *56*, 1033–1044.
164. Begley, T. P.; Xi, J.; Kinsland, C.; Taylor, S.; McLafferty, F. *Current Opin. Chem. Biol.* **1999**, *3*, 623–629.
165. White, P. J.; Millar, G.; Coggins, J. R. *Biochem. J.* **1988**, *251*, 313–322.
166. Yong, K. W. L.; Lambert, L. K.; Hayes, P. Y.; de Voss, J. J.; Garson, M. J. *J. Nat. Prod.* **2012**, *75*, 351–360.
167. Holland, H. L. *Nat. Prod. Rep.* **2001**, *18*, 171–181.
168. Motomasa Kondo Kobayashi, K.; Kitagawa, I. *Chem. Pharm. Bull.* **1993**, *41*, 1324–1326.
169. Xu, T.; Feng, Q.; Jacob, M. R.; Avula, B.; Mask, M. M.; Baerson, S. R.; Tripathi, S. K.; Mohammed, R.; Hamann, M. T.; Khan, I. A.; Walker, L. A.; Clark, A. M.; Agarwal, A. K. *Antimicrob. Agents Chemother.* **2011**, *55*, 1611–1621.
170. Qureshi, A.; Salvá, J.; Harper, M. K.; Faulkner, D. J. *J. Nat. Prod.* **1998**, *61*, 1539–1542.

171. Chen, Y.; Killday, K. B.; McCarthy, P. J.; Schimoler, R.; Chilson, K.; Selitrennikoff, C.; Pomponi, S. A.; Wright, A. E. *J. Nat. Prod.* **2001**, *64*, 262–264.
172. Jiménez-Romero, C.; Ortiz, I.; Vicente, J.; Vera, B.; Rodríguez, A. D.; Nam, S.; Jove, R. *J. Nat. Prod.* **2010**, *73*, 1694–1700.
173. Manzo, E.; Ciavatta, M. L.; Melck, D.; Schupp, P.; de Voogd, N.; Gavagnin, M. *J. Nat. Prod.* **2009**, *72*, 1547–1551.
174. Jungwirth, H.; Kuchler, K. *FEBS Letters* **2006**, *580*, 1131–1138.
175. Rogers, B.; Decottignies, A.; Kolaczowski, M.; Carvajal, E.; Balzi, E.; Goffeau, A. *J. Mol. Microbiol. Biotechnol.* **2001**, *3*, 207–214.
176. Sakemi, S.; Higa, T.; Anthoni, U.; Christophersen, C. *Tetrahedron* **1987**, *43*, 263–268.
177. Shen, Y.-C.; Prakash, C. V. S.; Kuo, Y.-H. *J. Nat. Prod.* **2001**, *64*, 324–327.
178. Wells, R. J. *Tetrahedron Lett.* **1976**, *17*, 2637–2638.
179. Toth, S. I.; Schmitz, F. J. *J. Nat. Prod.* **1994**, *57*, 123–127.
180. Patil, A. D.; Freyer, A. J.; Carte, B.; Johnson, R. K.; Lahouratate, P. *J. Nat. Prod.* **1996**, *59*, 219–223.
181. Tanaka, J.; Higa, T.; Suwanborirux, K.; Kokpol, U.; Bernardinelli, G.; Jefford, C. W. *J. Org. Chem.* **1993**, *58*, 2999–3002.
182. Butler, M. S.; Capon, R. J. *Aust. J. Chem.* **1993**, *46*, 1363–1374.
183. Fontana, A.; Cimino, G.; Gavagnin, M.; Lez, M. C. G.; Estornell, E. *J. Med. Chem.* **2001**, *44*, 2362–2365.
184. Reyes, F.; Rodríguez-Acebes, R.; Fernanández, R.; Bueno, S.; Francesch, A.; Cuevas, C. *J. Nat. Prod.* **2009**, *73*, 83–85.
185. Subrahmanyam, C.; Rao, C. V.; Anjaneyulu, V.; Satyanarayana, P.; Rao, P. V. S.; Ward, R. S.; Pelter, A. *Tetrahedron* **1992**, *48*, 3111–3120.
186. Alam, M.; Martin, G. E.; Zektzer, A. S.; Weinheimer, A. J.; Sanduja, R.; Ghuman, M. A. *J. Nat. Prod.* **1993**, *56*, 774–779.
187. Avery, M. A.; Fan, P.; Karle, J. M.; Bonk, J. D.; Miller, R.; Goins, D. K. *J. Med. Chem.* **1978**, *39*, 1885–1897.
188. Hommel, M. *J. Biol.* **2008**, *7*, 1–5.
189. Mayer, A. M. S.; Rodríguez, A. D.; Berlinck, R. G. S.; Hamann, M. T. *Biochim. Biophys. Acta* **2009**, *1790*, 283–308.
190. Kuria, K. A. M.; Chepkwony, H.; Govaerts, C.; Roets, E.; Busson, R.; de Witte, P.; Zupko, I.; Hoornaert, G.; Quirynen, L.; Maes, L.; Janssens, L.; Hoogmartens, J.; Laekeman, G. *J. Nat. Prod.* **2002**, *65*, 789–793.
191. Schneider, C.; Pratt, D. A.; Porter, N. A.; Brash, A. R. *Chem. Biol.* **2007**, *14*, 473–488.

192. Capon, R. J.; Macleod, J. K. *Tetrahedron* **1985**, *41*, 3391–3404.
193. Compagnone, R. S.; Piña, I. C.; Rangel, H. R.; Dagger, F.; Suárez, A. I.; Reddy, M. V. R.; Faulkner, D. J. *Tetrahedron* **1998**, *54*, 3057–3068.
194. Jung, M.; Ham, J.; Song, J. *Org. Lett.* **2002**, *4*, 2763–2765.
195. Ovenden, S. P. B.; Capon, R. J. *J. Nat. Prod.* **1999**, *62*, 214–218.
196. Capon, R. J.; MacLeod, J. K. *J. Nat. Prod.* **1987**, *50*, 225–229.
197. Patil, A. D.; Freyer, A. J.; Bean, M. F.; Carté, B. K.; Westley, J. W.; Johnson, R. K.; Lahouratate, P. *ChemInform.* **1996**, *27*, NA.
198. Carter, S.; Pitt, S. J.; Colyer, J.; Sitsapesan, R. *J. Mem. Biol.* **2011**, *240*, 21–33.
199. Paddon-Jones, G. C.; Hungerford, N. L.; Hayes, P.; Kitching, W. *Org. Lett.* **1999**, *1*, 1905–1907.
200. Mbaya, E.; Oules, B.; Caspersen, C.; Tacine, R.; Massinet, H.; Pennuto, M.; Chretien, D.; Munnich, A.; Rotig, A.; Rizzuto, R.; Rutter, G. A.; Paterlini-Brechot, P.; Chami, M. *Cell Death Differ.* **2010**, *17*, 1855–1866.
201. Rafiee, M. A.; Hadipour, N. L.; Naderi-manesh, H. *J. Chem. Inf. Model.* **2005**, *45*, 366–370.
202. D'Ambrosio, M.; Guerriero, A.; Deharo, E.; Debitus, C.; Munoz, V.; Pietra, F. *Helv. Chim. Acta* **1998**, *81*, 1285–1292.
203. Brenner, C. *Genome Biol.* **2004**, *5*, 1–4.
204. Wolfger, H.; Mamnun, Y. M.; Kuchler, K. *J. Biol. Chem.* **2004**, *279*, 11593–11599.
205. Hillenmeyer, M. E.; Fung, E.; Wildenhain, J.; Pierce, S. E.; Hoon, S.; Lee, W.; Proctor, M.; St. Onge, R. P.; Tyers, M.; Koller, D.; Altman, R. B.; Davis, R. W.; Nislow, C.; ; Giaever, G. *Science* **2008**, *320*, 362–365.
206. Goffeau, A. *Yeast* **1996**, *12*, 1603–1605.
207. Goffeau, A. et al. *Science* **1996**, *274*, 546, 563–7.
208. Yibmantasiri, P.; Leahy, D. C.; Busby, B. P.; Angermayr, S. A.; Sorgo, A. G.; Boeger, K.; Heathcott, R.; Barber, J. M.; Moraes, G.; Matthews, J. H.; Northcote, P. T.; Atkinson, P. H.; Bellows, D. S. *Mol. BioSyst.* **2012**, *8*, 902–912.
209. Lum, P. Y. et al. *Cell* **2004**, *116*, 121–137.
210. Parsons, A. B. et al. *Cell* **2006**, *126*, 611–625.
211. Baetz, K.; McHardy, L.; Gable, K.; Tarling, T.; Rebérioux, D.; Bryan, J.; Andersen, R. J.; Dunn, T.; Hieter, P.; Roberge, M. *Proc. Natl. Acad. Sci. USA* **2004**, *101*, 4525–4530.
212. Giaever, G.; Shoemaker, D. D.; Jones, T. W.; Liang, H.; Winzeler, E. A.; Astromoff, A.; Davis, R. W. *Nat. Genet.* **1999**, *21*, 278–283.

213. Deutschbauer, A. M.; Jaramillo, D. F.; Proctor, M.; Kumm, J.; Hillenmeyer, M. E.; Davis, R. W.; Nislow, C.; Giaever, G. *Genetics* **2005**, *169*, 1915–1925.
214. Giaever, G.; Flaherty, P.; Kumm, J.; Proctor, M.; Nislow, C.; Jaramillo, D. F.; Chu, A. M.; Jordan, M. I.; Arkin, A. P.; Davis, R. W. *Proc. Natl. Acad. Sci. USA* **2004**, *101*, 793–798.
215. Springer, M.; Weissman, J. S.; Kirschner, M. W. *Mol. Syst. Biol.* **2010**, *6*, 1–6.
216. Matthews, J. H. *The Molecular Pharmacology of Pateamine A*, Ph.D. thesis, Victoria University of Wellington, 2010.
217. Almeida, B.; Silva, A.; Mesquita, A.; Sampaio-Marques, B.; Rodrigues, F.; Ludovico, P. *BBA-Mol. Cell Res.* **2008**, *1783*, 1436–1448.
218. Edlind, T.; Smith, L.; Henry, K.; Katiyar, S.; Nickels, J. *Molecular Microbiology* **2002**, *46*, 1365–2958.
219. Zaragoza, D.; Ghavidel, A.; Heitman, J.; Schultz, M. C. *Mol. Cell Biol.* **1998**, *18*, 4463–4470.
220. Mayer, C.; Grummt, I. *Oncogene* **2006**, *25*, 6384–6391.
221. Herman, P. K. *Curr. Opin. Microbiol.* **2002**, 602–607.
222. Hartwell, L. H.; Culotti, J.; Pringle, J. R.; Reid, B. J. *Science* **1974**, *183*, 46–51.
223. Calzone, L. *Temporal organization of the budding yeast cell cycle: General principles and detailed simulations*, Ph.D. thesis, Virginia Polytechnic Institute and State University, 2003.
224. Coorey, N. *Innovative tools to discover potential drug-candidates*, M.Sc. thesis, Victoria University of Wellington, 2011, 2011.
225. Robinson, M. D.; Grigull, J.; Mohammad, N.; Hughes, T. R. *BMC Bioinformatics* **2002**, *3*, 1–5.
226. *Saccharomyces Genome Database*, 2012. <http://www.yeastgenome.org/>.
227. Hillenmeyer, M. E.; Ericson, E.; Davis, R. W.; Nislow, C.; Koller, D.; Giaever, G. *Genome Biol.* **2010**, *11*, 1–17.
228. Toret, C. P.; Drubin, D. G. *J. Cell Sci.* **2007**, *119*, 1501–1503.
229. Fingerman, I.; Nagaraj, V.; Norris, D.; Vershon, A. K. *Eukaryotic Cell* **2003**, *2*, 1061–1068.
230. Miyakawa, T.; Mizunuma, M. *Biosci. Biotechnol. Biochem.* **2007**, *71*, 633–645.
231. Gupta, S. S.; Ton, V.-K.; Beaudry, V.; Rulli, S.; Cunningham, K.; Rao, R. *J. Biol. Chem.* **2003**, *278*, 28831–28839.
232. Courchesne, W. E.; Ozturk, S. *Molecular Microbiology* **2003**, *47*, 223–234.
233. Peiter, E.; Fischer, M.; Sidaway, K.; Roberts, S. K.; Sanders, D. *FEBS Lett.* **2005**, *579*, 5697–5703.

234. Wang, H. G.; Pathan, N.; Ethell, I. M.; Krajewski, S.; Yamaguchi, Y.; Shibasaki, F.; McKeon, F.; Bobo, T.; Franke, T. F.; Reed, J. *Science* **1999**, *284*, 339–343.
235. Tsuzi, D.; Maeta, K.; Takatsume, Y.; Izawa, S.; Inoue, Y. *FEBS Lett.* **2004**, *569*, 301–306.
236. Gitan, R. S.; Luo, H.; Rodgers, J.; Broderius, M.; Eide, D. *J. Biol. Chem.* **1998**, *273*, 28617–28624.
237. Zhang, Y.-Q.; Rao, R. *J. Biol. Chem.* **2007**, *282*, 37844–37853.
238. Decuyper, J.-P.; Monaco, G.; Missiaen, L.; Smedt, H. D.; Parys, J. B.; Bultynck, G. *J. Aging Res.* **2011**, *2011*, 1–20.
239. Cyert, M. S. *Biochem. Biophys. Res. Commun.* **2003**, *311*, 1143–1150.
240. Shitamukai, A.; Hirata, D.; Sonobe, S.; Miyakawa, T. *J. Biol. Chem.* **2004**, *279*, 3651–3661.
241. Mulet, J. M.; Martin, D. E.; Loewith, R.; Hall, M. N. *J. Biol. Chem.* **2006**, *281*, 33000–33007.
242. Stathopoulos, A. M.; Cyert, M. S. *Genes Dev.* **1997**, *11*, 3432–3444.
243. Yoshimoto, H.; Saltsman, K.; Gasch, A. P.; Li, H. X.; Ogawa, N.; Botstein, D.; Brown, P. O.; Cyert, M. S. *J. Biol. Chem.* **2002**, *277*, 31079–31088.
244. Yarmola, E. G.; Somasundaram, T.; Boring, T. A.; Spector, I.; Bubba, M. R. *J. Biol. Chem.* **2000**, *275*, 28120–28127.
245. Martin, D. E.; Powers, T.; Hall, M. N. *Cell Metabolism* **2006**, *9*, 259–260.
246. Gulati, P.; Gaspers, L. D.; Dann, S. G.; Joaquin, M.; Nobukuni, T.; Natt, F.; Kozma, S. C.; Thomas, A. P.; Thomas, G. *Cell Metab.* **2008**, *7*, 456–465.
247. Kamble, C.; Jain, S.; Murphy, E.; Kim, K. *J. Biosci.* **2011**, *36*, 79–96.
248. Park, K. S.; Kim, T. K.; Kim, D. H. *Am. J. Physiol.* **1999**, *276*, 865–872.
249. Qiao, W.; Mooney, M.; Bird, A. J.; Winge, D. R.; Eide, D. *Biochemistry* **2006**, *106*, 8674–8679.
250. Gottlieb, H. E.; Kotlyar, V.; Nudelman, A. *J. Org. Chem.* **1997**, *62*, 7512–7515.
251. Amberg, D. C.; Burke, D. J.; Strathern, J. N. *Methods In Yeast Genetics*, English ed.; Cold Spring Harbor Laboratory Press, 2005.
252. Haase, S.; Reed, S. *Cell Cycle* **2002**, *1*, 132–136.
253. Peyser, B. D.; Irizarry, R.; Spencer, F. A. *Methods Mol. Biol.* **2008**, *416*, 369–381.
254. Jack, C. *Replicate removal script*; Victoria University of Wellington, 2012.
255. West, L. M. *The isolation of secondary metabolites from New Zealand marine sponges*, Ph.D. thesis, Victoria University of Wellington, 2001.